


Spectral Functions of the Holstein Polaron: Exact and Approximate Solutions

Petar Mitrić¹, Veljko Janković¹, Nenad Vukmirović¹, and Darko Tanasković¹
Institute of Physics Belgrade, University of Belgrade, Pregrevica 118, 11080 Belgrade, Serbia

 (Received 10 January 2022; revised 2 May 2022; accepted 5 August 2022; published 22 August 2022)

It is generally accepted that the dynamical mean field theory gives a good solution of the Holstein model, but only in dimensions greater than two. Here, we show that this theory, which becomes exact in the weak coupling and in the atomic limit, provides an excellent, numerically cheap, approximate solution for the spectral function of the Holstein model in the whole range of parameters, even in one dimension. To establish this, we make a detailed comparison with the spectral functions that we obtain using the newly developed momentum-space numerically exact hierarchical equations of motion method, which yields electronic correlation functions directly in real time. We crosscheck these conclusions with our path integral quantum Monte Carlo and exact diagonalization results, as well as with the available numerically exact results from the literature.

DOI: [10.1103/PhysRevLett.129.096401](https://doi.org/10.1103/PhysRevLett.129.096401)

The Holstein model is the simplest model that describes an electron that propagates through the crystal and interacts with localized optical phonons [1]. On the example of this model, numerous many-body methods were developed and tested [2]. The Holstein molecular crystal model is also very important in order to understand the role of polarons (quasiparticles formed by an electron dressed by lattice vibrations) in real materials [3]. This is still a very active field of research fueled by new directions in theoretical studies [4–12] and advances in experimental techniques [13].

The Holstein model can be solved analytically only in the limits of weak and strong electron-phonon coupling [14–16]. Reliable numerical results for the ground state energy and quasiparticle effective mass were obtained in the late 1990s using the density matrix renormalization group (DMRG) [17,18] and path integral quantum Monte Carlo (QMC) methods [19], and also within variational approaches [20–22]. At the time, numerically exact spectral functions for one-dimensional (1D) systems were obtained only within the DMRG method [17,18]. The main drawback of the QMC method is that it gives correlation functions in imaginary time and obtaining spectral functions and dynamical response functions is often impossible since the analytical continuation to the real frequency is a numerically ill-defined procedure. Interestingly, at finite temperature the spectral functions were obtained only very recently using finite- T Lanczos (FTLM) [23] and finite- T DMRG [24] methods. All these methods have their strengths and weaknesses depending on the parameter regime and temperature. As usually happens in a strongly interacting many-body problem, a complete physical picture emerges only by taking into account the solutions obtained with different methods.

The hierarchical equations of motion (HEOM) method is a numerically exact technique that has recently gained

popularity in the chemical physics community [25–28]. It has been used to explore the dynamics of an electron (or exciton) linearly coupled to a Gaussian bosonic bath. Within HEOM, we calculate the correlation functions directly on the real time (real frequency) axis [29]. Nevertheless, the applications of the HEOM method to the Holstein model [30–34] have been, so far, scarce because of the numerical instabilities stemming from the discreteness of the phonon bath on a finite lattice.

Along with numerically exact methods, a number of approximate techniques have been developed and applied to the Holstein model [35–38]. The dynamical mean field theory (DMFT) is a simple nonperturbative technique that has emerged as a method of choice for the studies of the Mott physics within the Hubbard model [39,40]. It can also be applied to the Holstein model giving numerically cheap results directly on the real frequency axis [41]. This method fully takes into account local quantum fluctuations and it becomes exact in the limit of infinite coordination number when the correlations become completely local. It was soon recognized [42,43] that the DMFT gives qualitatively correct spectral functions and conductivity for the Holstein model in three dimensions. In low-dimensional systems the solution is approximate as it neglects the nonlocal correlations and one might expect that the DMFT solution would not be accurate, particularly in one dimension. Surprisingly, to our knowledge, only the DMFT solution for the Bethe lattice was used in comparisons with the numerically exact results for the ground state properties in one dimension [20,44]. The quantitative agreement was rather poor, suggesting that the DMFT cannot provide a realistic description of the low-dimensional Holstein model due to the importance of nonlocal correlations [16,20,44].

In this Letter, we present a comprehensive solution of the 1D Holstein model: (i) We solve the DMFT equations in all

parameter regimes. At zero temperature we find a remarkable agreement of the DMFT ground state energy and effective mass with the available results from the literature in one, two, and three dimensions. (ii) For intermediate electron-phonon coupling, we obtain numerically exact spectral functions using the recently developed momentum-space HEOM approach [45]. For strong coupling we calculate the spectral functions using exact diagonalization (ED). We find a very good agreement with DMFT results and therefore demonstrate that the DMFT is rather accurate, in sharp contrast to current belief in the literature. (iii) We crosscheck the results with our QMC calculations in imaginary time. Overall, we demonstrate that the DMFT emerges as a unique method that gives close to exact spectral functions in the whole parameter space of the Holstein model, both at zero and at finite temperature.

Model and methods.—We study the 1D Holstein model given by the Hamiltonian

$$H = -t_0 \sum_i (c_i^\dagger c_{i+1} + \text{H.c.}) - g \sum_i n_i (a_i^\dagger + a_i) + \omega_0 \sum_i a_i^\dagger a_i. \quad (1)$$

Here, c_i^\dagger (a_i^\dagger) are the electron (phonon) creation operators, t_0 is the hopping parameter, and $n_i = c_i^\dagger c_i$. We consider dispersionless optical phonons of frequency ω_0 , and g denotes the electron-phonon coupling parameter. t_0 , \hbar , k_B , and lattice constant are set to 1. We consider the dynamics of a single electron in the band. It is common to define several dimensionless parameters: adiabatic parameter $\gamma = \omega_0/2t_0$, electron-phonon coupling $\lambda = g^2/2t_0\omega_0$, and $\alpha = g/\omega_0$. These parameters correspond to different physical regimes of the Holstein model shown schematically in Fig. 1(a).

In order to obtain reliable solutions in the whole parameter space, we use two approximate methods and three methods that are numerically exact. In the Holstein model, the DMFT reduces to solving the polaron impurity problem in the conduction electron band supplemented by the self-consistency condition [41]. The impurity problem can be solved in terms of the continued fraction expansion, giving the local Green's function on the real frequency axis (see Ref. [41] and Supplemental Material (SM) [46], Sec. I, for details). A crucial advantage of the DMFT for the Holstein model is that it becomes exact in both the weak coupling and in the atomic limit, and that it can be easily applied in the whole parameter space both at zero and at finite temperature. The DMFT equations can be solved on a personal computer in just a few seconds to a few minutes depending on the parameters. On general grounds, the DMFT is expected to work particularly well at high temperatures when the correlations become more local due to the thermal fluctuations [47,48]. We will compare the DMFT with the well-known self-consistent Migdal

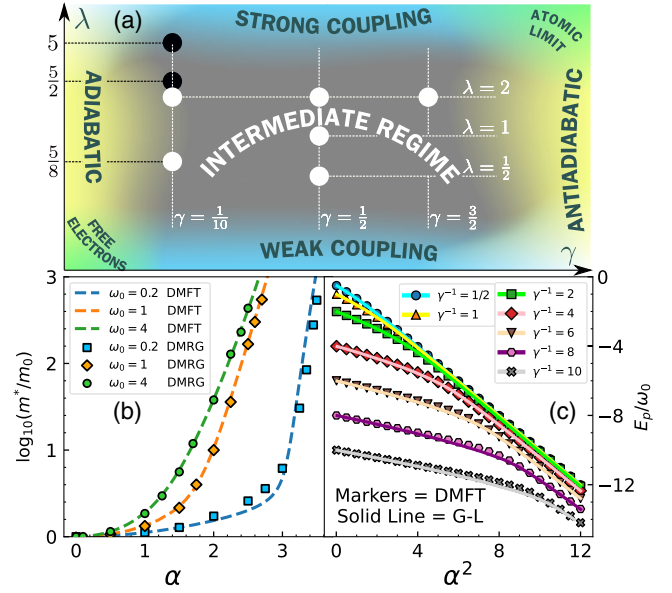


FIG. 1. (a) Schematic plot of different regimes in the (γ, λ) parameter space. The white (black) circles correspond to parameters for which both HEOM and QMC (just QMC) calculations were performed. The DMFT results are obtained in practically whole space of parameters. (b) Comparison of the DMFT and DMRG (taken from Refs. [17,20]) renormalized electron mass at $T = 0$. (c) Comparison of the ground state energy from the DMFT and the global-local variational approach (taken from Ref. [20]) at $T = 0$.

approximation (SCMA) [49], which becomes exact only in the weak coupling limit; see Sec. II of SM [46].

We have recently developed the momentum-space HEOM method [45] that overcomes the numerical instabilities originating from the discrete bosonic bath. Within this method we calculate the time-dependent greater Green's function $G^>(k, t)$, which presents the root of the hierarchy of the auxiliary Green's functions. The hierarchy is, in principle, infinite, and one actually solves the model by truncating the hierarchy at certain depth D . The HEOM are propagated independently for each allowed value of k up to long times ($\omega_0 t_{\max} \sim 500$). The propagation takes 5 to 10 hours on 16 cores per momentum k . The discrete Fourier transform is then used to obtain spectral functions without introducing any artificial broadening. Numerical error in the HEOM solution can originate from the finite-size effects since the method is applied on the lattice with N sites, and also from the finite depth D . We always use N and D , as given in SM [46], which correctly represent the thermodynamic limit. Generally, for larger g we need smaller N and larger D . This is why the ED method with a small number of sites could be a better option in the strong coupling regime. The ED method can be used more efficiently after the initial Hamiltonian is transformed by applying the Lang-Firsov transformation; see SM [46], Sec. III.

In the QMC method, we calculate the correlation function $C_k(\tau) = \langle c_k(\tau) c_k^\dagger \rangle_{T,0}$ in imaginary time. The thermal

expectation value is performed over the states with zero electrons and $c_k(\tau) = e^{\tau H} c_k e^{-\tau H}$. We use the path integral representation, the discretization of imaginary time, and analytical calculation of integrals over the phonon coordinates. We then evaluate a multidimensional sum over the electronic coordinates by a Monte Carlo method. This method is a natural extension of early works where such approach was applied just to thermodynamic quantities [50–52]. Details of the method are presented in Ref. [45].

Results at zero temperature.—In Fig. 1(b), we show the DMFT results for the electron effective mass at the bottom of the band, $m^*/m_0 = 1 - d\text{Re}\Sigma(\omega)/d\omega|_{E_p}$ (where $\Sigma(\omega)$ is the self-energy), over a broad range of parameters covering practically the whole parameter space in the (γ, λ) plane. We see that the mass renormalization is in striking agreement with the DMRG result [17,20] that presents the best available result from the literature. Small discrepancies are visible only for stronger interaction with small ω_0 . A similar level of agreement can be seen in the comparison of the ground state (polaron) energy E_p in Fig. 1(c). Here, the results obtained with variational global-local method [20,21] are taken as a reference. While the agreement in the weak coupling and in the atomic limit could be anticipated since the DMFT becomes exact in these limits, we find the quantitative agreement in the crossover regime between these two limits rather surprising, having in mind that the DMFT completely neglects nonlocal correlations. It is also interesting that this was not observed earlier. The only difference from the standard reference of Ciuchi *et al.* [41] is that we applied the DMFT to the 1D case, as opposed to the Bethe lattice. This is, however, a key difference. Otherwise the DMFT provides only a qualitative description of the Holstein model [3,16,20,44,53]. From the technical side, the only difference as compared to the case of the Bethe lattice is in the self-consistency equation. For obtaining a numerically stable and precise solution, it was crucial to use an analytical expression for the self-consistency relation (see Sec. IB in SM [46]). We have also calculated the effective mass for two- and three-dimensional lattices (see Sec. IC in SM [46]) and the agreement with the QMC calculation from Ref. [19] is excellent. This was now expected since the importance of nonlocal correlations decreases in higher dimensions. A comparison with the Bethe lattice effective mass is illustrated in SM [46], Sec. ID.

The next step is to check if the agreement with the numerically exact solution extends also to spectral functions. Typical results at $k = 0$ are illustrated in Fig. 2. We note that at $T = 0$ the DMFT quasiparticle peak is a delta function (broadened in Fig. 2), while satellite peaks are incoherent having intrinsic nonzero width. In HEOM, the peak broadening due to the finite lattice size N and finite propagation time t_{max} is generally much smaller than the Lorentzian broadening used in the insets of Figs. 2(a)–2(d). The weights of the DMFT and HEOM quasiparticle peaks

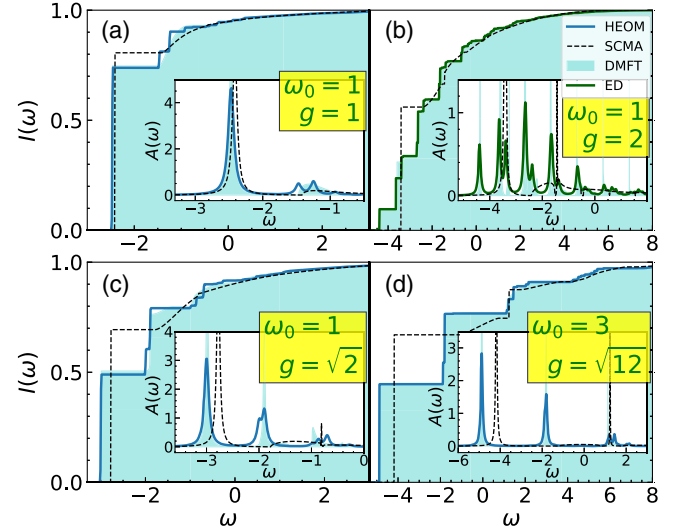


FIG. 2. (a)–(d) Integrated HEOM, DMFT, SCMA, and ED spectral weight, $I(\omega) = \int_{-\infty}^{\omega} d\nu A_k(\nu)$, for $k = 0$ and $T = 0$. The insets show comparisons of the spectral functions. $I(\omega)$ is obtained without broadening, whereas $A(\omega)$ is broadened by Lorentzians of half-width $\eta = 0.05$.

correspond to the m_0/m^* ratio. The satellite peaks are also very well captured by the DMFT solution in all parameter regimes. For $g = 1$ we can see two small peaks in the first satellite structure of the HEOM solution. We find very similar peaks also in the DMFT solution when applied on a lattice of the same size, which is here equal to 10 (see SM [46], Sec. IV). Hence, we conclude that these peaks are an artefact of the finite lattice size. In the strong coupling regime $\omega_0 = 1, g = 2$, the DMFT is compared with ED since the thermodynamic limit is practically reached for $N = 4$; see SM [46], Sec. IV. Here, we notice a pronounced excited quasiparticle peak [22,23] whose energy is below $E_p + \omega_0$. This peak, which consists of a polaron and a bound phonon, is also very well resolved within the DMFT solution. For parameters in Fig. 2(d) the lattice sites are nearly decoupled, approaching the atomic limit ($t_0 \ll g, \omega_0$), when the DMFT becomes exact (see Sec. V in SM [46]). For a comparison, we show also the SCMA spectral functions. As the interaction increases, the SCMA solution misses the position and the weight of the quasiparticle peak and the satellite peaks are not properly resolved. Further comparisons of zero temperature spectral functions are shown in Sec. VI of SM [46].

Results at finite temperature.—Reliable finite- T results for the spectral functions of the Holstein model have been obtained only very recently using the FTLM [23] and finite- T DMRG methods [24]. Here, we calculate the spectral functions using HEOM or ED and compare them extensively with the DMFT. The results are crosschecked using the QMC results in imaginary time.

Typical results for the spectral functions are shown in Fig. 3, while additional results for other momenta and other

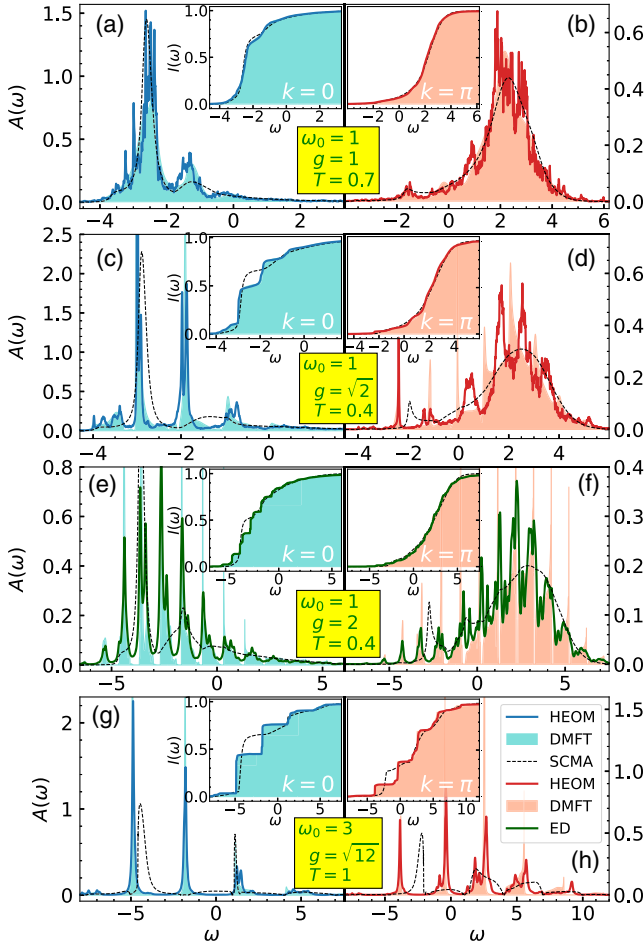


FIG. 3. (a)–(h) Spectral functions at $T > 0$ for $k = 0$ and $k = \pi$. In panels (e)–(f) only the ED results are broadened by Lorentzians of half-width $\eta = 0.05$, while all the curves are broadened in (g)–(h) with the same η . All insets are shown without broadening.

parameters are shown in Sec. VII of SM [46]. We see that for $T > 0$ the satellite peaks appear also below the quasiparticle peak. The agreement between the DMFT and the HEOM (ED) spectral functions is very good. The agreement remains excellent even for $g = 2$ where the electrons are strongly renormalized $m^*/m_0 \approx 10$, which is far away from both the atomic and weak coupling limits, where the DMFT is exact. A part of the difference between the DMFT and the HEOM (ED) results can be ascribed to the small finite-size effects in the HEOM and ED solutions, as detailed in SM [46], Sec. IV. In accordance with the presented results, it is not surprising that the self-energies are nearly k independent, as shown in SM [46], Sec. VIII. It is also instructive to examine the difference between the SCMA and DMFT (HEOM) solutions. For moderate interaction [Figs. 3(a) and 3(b)], the weight of the SCMA quasiparticle peak is nearly equal to the DMFT (HEOM) quasiparticle weight, and the overall agreement of spectral functions is rather good. This is not the case for stronger

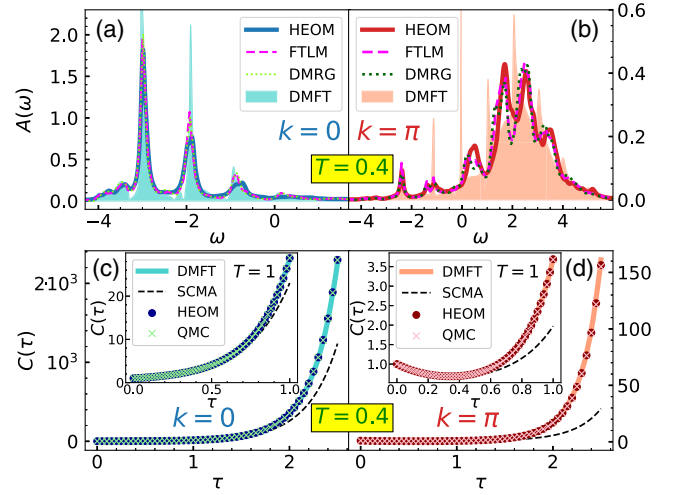


FIG. 4. (a), (b) Comparison of DMFT, HEOM, and finite- T DMRG and FTLM (taken from Ref. [24]) spectral functions at $T = 0.4$. All the lines are here broadened by Lorentzians of half-width $\eta = 0.05$. (c), (d) DMFT, QMC, HEOM, and SCMA imaginary time correlation functions at $T = 0.4$ ($T = 1$ in the insets). Here, $g = \sqrt{2}$, $\omega_0 = 1$.

electron-phonon coupling [Figs. 3(c)–3(h)] where the SCMA poorly approximates the true spectrum.

We observe that for $g = \sqrt{2}$ and $k = \pi$ the DMFT and HEOM satellite peaks are somewhat shifted with respect to one another; see Figs. 3(c) and 3(d). This is the most challenging regime for the DMFT, representing a crossover ($\lambda = 1$) between the small and large polaron. Nevertheless, the agreement remains very good near the quasiparticle peak for $k = 0$, which will be the most important for transport in weakly doped systems. In order to gain further confidence into the details of the HEOM spectral functions for $g = \sqrt{2}$, we compare them with the available results obtained within the finite- T DMRG and Lanczos methods. We find an excellent agreement, as shown in Figs. 4(a) and 4(b).

The DMFT and HEOM results are crosschecked with the path integral QMC calculations. The quantity that we obtain in QMC is the single electron correlation function in imaginary time, which can be expressed through the spectral function as $C_k(\tau) = \int_{-\infty}^{\infty} d\omega e^{-\omega\tau} A_k(\omega)$. Typical results are illustrated in Figs. 4(c) and 4(d), while extensive comparisons are presented in Sec. IX of SM [46]. At $T = 0.4$ we can see a small difference in $C_\pi(\tau)$ between the DMFT and QMC (HEOM) results. At $T = 1$, both for $k = 0$ and $k = \pi$, the difference in $C_k(\tau)$ is minuscule, well below the QMC error bar, which is smaller than the symbol size. This confirms that nonlocal correlations are weak. Similarly, as for the spectral functions, the SCMA correlation functions show clear deviation from other solutions. We, however, note that great care is needed when drawing conclusions from the imaginary axis data since a very small difference in the imaginary axis correlation functions can correspond to substantial differences in spectral functions.

Conclusions.—In summary, we have presented a comprehensive solution of the 1D Holstein polaron covering all parameter regimes. We showed that the DMFT is a remarkably good approximation in the whole parameter space. This approximation is simple, numerically efficient, and can also be easily applied in two and three dimensions. We successfully used momentum-space HEOM and ED methods for comparisons with the DMFT spectral functions both at zero and at finite temperature. The comparisons showed an excellent agreement between the spectral functions in most of the parameter space. For parameters that are most challenging for the DMFT, a very good agreement was found around $k = 0$ and a reasonably good agreement was obtained at larger values of k . All of the results are crosschecked with the imaginary axis QMC calculations and with the available results from the literature. Both the DMFT and HEOM methods are implemented directly in real frequency, without artificial broadening of the spectral functions. This will be crucial in order to calculate dynamical quantities and determine a potential role of the vertex corrections to conductivity by avoiding possible pitfalls of the analytical continuation, which we leave as a challenge for future work.

D. T. acknowledges useful discussions with V. Dobrosavljević. We thank J. Bonča for sharing with us the data from Ref. [23]. The authors acknowledge funding provided by the Institute of Physics Belgrade, through the grant by the Ministry of Education, Science, and Technological Development of the Republic of Serbia. Numerical simulations were performed on the PARADOX supercomputing facility at the Scientific Computing Laboratory, National Center of Excellence for the Study of Complex Systems, Institute of Physics Belgrade.

-
- [1] T. Holstein, *Ann. Phys. (N.Y.)* **8**, 325 (1959).
 [2] A. S. Alexandrov, *Polarons in Advanced Materials* (Springer, New York, 2007).
 [3] C. Franchini, M. Reticcioli, M. Setvin, and U. Diebold, *Nat. Rev. Mater.* **6**, 560 (2021).
 [4] L. Vidmar, J. Bonča, M. Mierzejewski, P. Prelovšek, and S. A. Trugman, *Phys. Rev. B* **83**, 134301 (2011).
 [5] B. Kloss, D. R. Reichman, and R. Tempelaar, *Phys. Rev. Lett.* **123**, 126601 (2019).
 [6] C. Brockett and E. Jeckelmann, *Phys. Rev. B* **95**, 064309 (2017).
 [7] N. Prodanović and N. Vukmirović, *Phys. Rev. B* **99**, 104304 (2019).
 [8] J. Stolpp, J. Herbrych, F. Dorfner, E. Dagotto, and F. Heidrich-Meisner, *Phys. Rev. B* **101**, 035134 (2020).
 [9] Y. Murakami, P. Werner, N. Tsuji, and H. Aoki, *Phys. Rev. B* **91**, 045128 (2015).
 [10] D. Jansen, J. Stolpp, L. Vidmar, and F. Heidrich-Meisner, *Phys. Rev. B* **99**, 155130 (2019).
 [11] J. H. Fetherolf, D. Golež, and T. C. Berkelbach, *Phys. Rev. X* **10**, 021062 (2020).
 [12] A. S. Mishchenko, N. Nagaosa, and N. Prokof'ev, *Phys. Rev. Lett.* **113**, 166402 (2014).
 [13] M. Kang, S. W. Jung, W. J. Shin, Y. Sohn, S. H. Ryu, T. K. Kim, M. Hoesch, and K. S. Kim, *Nat. Mater.* **17**, 676 (2018).
 [14] G. Mahan, *Many-Particle Physics* (Kluwer Academic, New York, 2000).
 [15] I. Lang and Y. A. Firsov, *Zh. Eksp. Teor. Fiz.* **43**, 1843 (1962) [*Sov. Phys. JETP* **16**, 1301 (1963)].
 [16] A. S. Alexandrov and J. T. Devreese, *Advances in Polaron Physics* (Springer, New York, 2010).
 [17] E. Jeckelmann and S. R. White, *Phys. Rev. B* **57**, 6376 (1998).
 [18] C. Zhang, E. Jeckelmann, and S. R. White, *Phys. Rev. B* **60**, 14092 (1999).
 [19] P. E. Kornilovitch, *Phys. Rev. Lett.* **81**, 5382 (1998).
 [20] A. H. Romero, D. W. Brown, and K. Lindenberg, *J. Chem. Phys.* **109**, 6540 (1998).
 [21] A. H. Romero, D. W. Brown, and K. Lindenberg, *Phys. Rev. B* **59**, 13728 (1999).
 [22] J. Bonča, S. A. Trugman, and I. Batistić, *Phys. Rev. B* **60**, 1633 (1999).
 [23] J. Bonča, S. A. Trugman, and M. Berciu, *Phys. Rev. B* **100**, 094307 (2019).
 [24] D. Jansen, J. Bonča, and F. Heidrich-Meisner, *Phys. Rev. B* **102**, 165155 (2020).
 [25] Y. Tanimura, *J. Chem. Phys.* **153**, 020901 (2020).
 [26] R.-X. Xu and Y. J. Yan, *Phys. Rev. E* **75**, 031107 (2007).
 [27] J. Jin, X. Zheng, and Y. J. Yan, *J. Chem. Phys.* **128**, 234703 (2008).
 [28] D. Hou, R. Wang, X. Zheng, N. H. Tong, J. H. Wei, and Y. J. Yan, *Phys. Rev. B* **90**, 045141 (2014).
 [29] Z. H. Li, N. H. Tong, X. Zheng, D. Hou, J. H. Wei, J. Hu, and Y. J. Yan, *Phys. Rev. Lett.* **109**, 266403 (2012).
 [30] L. Chen, Y. Zhao, and Y. Tanimura, *J. Phys. Chem. Lett.* **6**, 3110 (2015).
 [31] L. Song and Q. Shi, *J. Chem. Phys.* **142**, 174103 (2015).
 [32] L. Song and Q. Shi, *J. Chem. Phys.* **143**, 194106 (2015).
 [33] I. S. Dunn, R. Tempelaar, and D. R. Reichman, *J. Chem. Phys.* **150**, 184109 (2019).
 [34] Y. Yan, T. Xing, and Q. Shi, *J. Chem. Phys.* **153**, 204109 (2020).
 [35] M. Hohenadler, M. Aichhorn, and W. von der Linden, *Phys. Rev. B* **68**, 184304 (2003).
 [36] G. De Filippis, V. Cataudella, V. Marigliano Ramaglia, and C. A. Perroni, *Phys. Rev. B* **72**, 014307 (2005).
 [37] M. Berciu, *Phys. Rev. Lett.* **97**, 036402 (2006).
 [38] G. L. Goodvin, M. Berciu, and G. A. Sawatzky, *Phys. Rev. B* **74**, 245104 (2006).
 [39] A. Georges, G. Kotliar, W. Krauth, and M. J. Rozenberg, *Rev. Mod. Phys.* **68**, 13 (1996).
 [40] R. M. Martin, L. Reining, and D. M. Ceperley, *Interacting Electrons: Theory and Computational Approaches* (Cambridge University Press, Cambridge, England, 2016).
 [41] S. Ciuchi, F. de Pasquale, S. Fratini, and D. Feinberg, *Phys. Rev. B* **56**, 4494 (1997).
 [42] S. Fratini, F. de Pasquale, and S. Ciuchi, *Phys. Rev. B* **63**, 153101 (2001).
 [43] S. Fratini and S. Ciuchi, *Phys. Rev. Lett.* **91**, 256403 (2003).
 [44] L.-C. Ku, S. A. Trugman, and J. Bonča, *Phys. Rev. B* **65**, 174306 (2002).

- [45] V. Janković and N. Vukmirović, *Phys. Rev. B* **105**, 054311 (2022).
- [46] See Supplemental Material at <http://link.aps.org/supplemental/10.1103/PhysRevLett.129.096401> for detailed analysis and supporting data.
- [47] J. Vučičević, J. Kokalj, R. Žitko, N. Wentzell, D. Tanasković, and J. Mravlje, *Phys. Rev. Lett.* **123**, 036601 (2019).
- [48] A. Vranić, J. Vučičević, J. Kokalj, J. Skolimowski, R. Žitko, J. Mravlje, and D. Tanasković, *Phys. Rev. B* **102**, 115142 (2020).
- [49] A. Migdal, *Zh. Eksp. Teor. Fiz.* **34**, 1438 (1958) [*Sov. Phys. JETP* **7**, 996 (1958)].
- [50] H. De Raedt and A. Lagendijk, *Phys. Rev. Lett.* **49**, 1522 (1982).
- [51] H. De Raedt and A. Lagendijk, *Phys. Rev. B* **27**, 6097 (1983).
- [52] H. De Raedt and A. Lagendijk, *Phys. Rev. B* **30**, 1671 (1984).
- [53] O. S. Barišić, *Phys. Rev. B* **76**, 193106 (2007).

Supplemental Material: Spectral functions of the Holstein polaron: exact and approximate solutions

Petar Mitrić,¹ Veljko Janković,¹ Nenad Vukmirović,¹ and Darko Tanasković¹

¹*Institute of Physics Belgrade, University of Belgrade, Pregrevica 118, 11080 Belgrade, Serbia*

Here we present numerical results that complement the main text and we also show some technical details of the calculations. The Supplemental Material is organized as follows. The DMFT for the Holstein polaron is briefly reviewed in Sec. I. Numerical implementation of the DMFT self-consistency loop is presented in detail and it is used to calculate the mass renormalization in one, two and three dimensions and for the Bethe lattice as well. In Sec. II the self-consistent Migdal approximation is briefly reviewed and used as a benchmark for the DMFT in the weak-coupling limit. Sec. III presents the ED method. In Sec. IV we investigate how the results depend on the chain length N and on hierarchy depth D . Sec. V examines the DMFT solution close to the atomic limit. Additional DMFT, SCMA, ED and HEOM results for the spectral functions at $T = 0$ and $T > 0$ for various parameter values and for different momenta k are shown in Secs. VI and VII, respectively. The k -dependence of the self-energies is shown in Sec. VIII. A detailed comparison of the DMFT, HEOM and QMC correlation functions is presented in Sec. IX. Sec. X presents a numerical procedure that was used for the calculation of the integrated spectral weight. In Sec. XI we show that the different definitions of spectral functions used by various methods are all in agreement.

I. DMFT FOR THE HOLSTEIN POLARON

The DMFT solution for the Holstein polaron on the infinitely-connected Bethe lattice was presented by Ciuchi *et al.* in 1997 [S1]. Interestingly, to our knowledge, this method has not been so far implemented on a finite-dimensional lattice. Details of the implementation in 1d and in arbitrary number of dimensions are the main content of this Section.

A. Physical content of the DMFT approximation

The DMFT was developed in the early 1990's in the context of the Hubbard model [S2] and has since significantly contributed to our understanding of the systems with strong electronic correlations [S3]. The DMFT is a non-perturbative method that fully takes into account local quantum fluctuations. It becomes exact in the

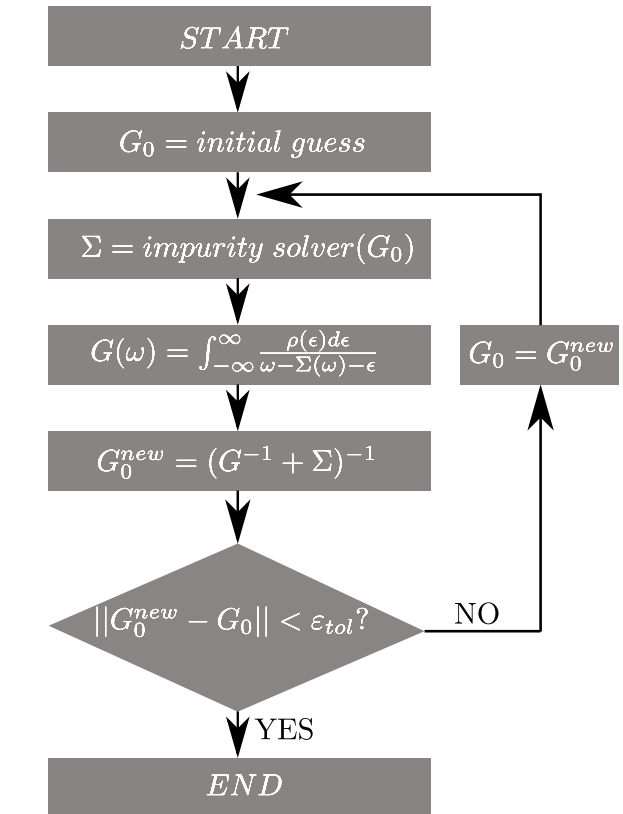


FIG. S1. DMFT self-consistency loop.

limit of infinite coordination number [S2], while it can be considered as an approximation in finite number of dimensions that keeps only local correlations by assuming that the self-energy $\Sigma(\omega)$ is \mathbf{k} -independent.

In practice, the DMFT reduces to solving the (Anderson) impurity problem in a frequency dependent Weiss field $G_0(\omega)$ that needs to be determined self-consistently. The bare propagator (Weiss field) $G_0(\omega)$ is responsible for the electron fluctuations between the impurity and the reservoir (conduction bath). On-site correlation is taken into account through the self-energy. The connection with the lattice problem is established by the requirement that the impurity self-energy $\Sigma_{\text{imp}}(\omega)$ is equal to the lattice self-energy $\Sigma_{ii}(\omega)$ (while the nonlocal components $\Sigma_{ij}(\omega)$ are equal to zero within DMFT) and that the impurity Green's function $G_{\text{imp}}(\omega)$ is equal to the local lattice Green's func-

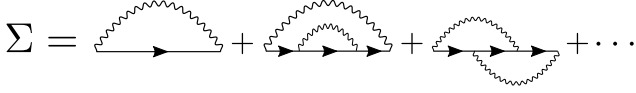


FIG. S2. First few DMFT Feynman diagrams of the self-energy in the expansion over G_0 .

tion $G_{ii}(\omega) = \frac{1}{N} \sum_{\mathbf{k}} G_{\mathbf{k}}(\omega)$. The DMFT equations are solved iteratively as shown schematically in Fig. S1. For a given bare propagator G_0 an *impurity solver* is used to obtain the self-energy, and then the self-consistency is imposed by the Dyson equation. The subscripts for the impurity and the local lattice Green's function are omitted since these two quantities coincide when the self-consistency is reached.

The DMFT solution for the Holstein polaron follows the general concepts introduced for the Hubbard model with an important simplification which comes from the fact that we consider the dynamics of just a single electron. We briefly review some key aspects and for details we refer the reader to Ref. [S1].

The self-energy for the polaron impurity, which is coupled to the reservoir by the bare propagator $G_0(\omega)$, can be simply expressed in a form of the continued-fraction expansion (CFE), which is in a sharp contrast with the Hubbard model where the numerical solution of the Anderson impurity model is the most difficult step. Here, the self-energy at $T = 0$ is simply given by

$$\Sigma(\omega) = \frac{g^2}{G_0^{-1}(\omega - \omega_0) - \frac{2g^2}{G_0^{-1}(\omega - 2\omega_0) - \frac{3g^2}{G_0^{-1}(\omega - 3\omega_0) - \dots}}} \quad (\text{S1})$$

(For a derivation and generalization to $T > 0$ see Ref. [S1].) This expansion has an infinite number of terms and in practice it needs to be truncated. In order to understand which condition needs to be fulfilled for a truncation, we will look at the diagrammatic expansion of the self-energy.

For a single electron (i.e. in the zero density limit) the Feynman diagrams of the self-energy consist of a single electron line accompanied by the lines that describe the emission and the absorption of phonons. There are no bubble diagrams and hence there is no renormalization of the phonon propagator. As an illustration, a diagrammatic expansion over $G_0(\omega)$ up to the order g^4 is shown in Fig. S2. These diagrams are included if we keep the terms up to the second stage in the CFE.

There are two important implications from this diagrammatic expansion. First, if we keep in the expansion terms up to the order g^{2N} then only the phonon states $|n\rangle$ with $n \leq N$ appear as intermediate states. Therefore, since the importance of the multiphonon effects

can be estimated by the parameter $\alpha^2 = g^2/\omega_0^2$ [S4], we need to keep $N \gg \alpha^2$ terms in the CFE. Second, we see that the vertex corrections (involving the phonons on the same site in the real-space representation [S5]) are included in the DMFT solution. This should be contrasted with the self-consistent Migdal approximation (SCMA) which completely neglects the vertex corrections in the self-energy. However, we note that one should be careful in making a direct comparison to the SCMA, since the DMFT diagrams are expanded using G_0 , unlike the SCMA.

B. Numerical implementation of the DMFT loop

We will now discuss step by step the self-consistency loop shown in Fig. S1. The DMFT loop starts by guessing the solution for the free propagator $G_0(\omega)$. Better guesses lead to fewer number of iterations, so depending on the parameter regime we take $G_0(\omega)$ to be either the Green's function in the Migdal approximation (S20) or the Green's function in the atomic limit (S25), since both of these expressions are analytically known. They correspond to the cases of very weak coupling and vanishing hopping, respectively. Next, the self-energy $\Sigma(\omega)$ is calculated using the impurity solver (S1) and its generalization to finite temperatures [S1]. In practice these are implemented using the recursion relations, which at finite temperature read as:

$$\Sigma(\omega) = G_0^{-1}(\omega) - G^{-1}(\omega), \quad (\text{S2a})$$

$$G(\omega) = \sum_{n=0}^{\infty} \frac{(1 - e^{-\omega_0/T})e^{-n\omega_0/T}}{G_0^{-1}(\omega) - A_n^{(0)}(\omega) - B_n^{(0)}(\omega)}, \quad (\text{S2b})$$

$$A_n^{(p)}(\omega) = \frac{(n-p)g^2}{G_0^{-1}(\omega + (p+1)\omega_0) - A_n^{(p+1)}(\omega)}, \quad (\text{S2c})$$

$$B_n^{(p)}(\omega) = \frac{(n+p+1)g^2}{G_0^{-1}(\omega - (p+1)\omega_0) - B_n^{(p+1)}(\omega)}, \quad (\text{S2d})$$

$$A_n^{(n)}(\omega) = 0, \quad B_n^{(\infty)}(\omega) = 0. \quad (\text{S2e})$$

Quantities $A_n^{(p)}$ and $B_n^{(p)}$ are determined recursively, starting from (S2e) and going back to (S2d) and (S2c). Then, $G(\omega)$ is calculated using (S2b), which enables us to use Dyson Eq. (S2a) to obtain $\Sigma(\omega)$. For $T = 0$ the equations simplify and the self-energy can be written as $\Sigma(\omega) = B_0^{(0)}(\omega)$, which coincides with Eq. (S1). The physical interpretation of the quantities in Eq. (S2) is the following: $G(\omega)$ is the interacting Green's function of the impurity. The quantity $A_n^{(0)}(\omega)$ is just a finite fraction that takes into account the emission of phonons. Similarly, $B_n^{(0)}(\omega)$ is an infinite continued fraction, which takes into account the absorption of phonons. The infinite fraction $B_n^{(0)}(\omega)$ can be calculated accurately even if we truncate it $B_n^{(N)}(\omega) = 0$,

taking N to be a number much larger than α^2 . The infinite series (S2b) can also be truncated by using the number of terms $n_{max} \gg T/\omega_0$ [S1].

Next step in the DMFT loop is calculating the local Green's function of the lattice using the self-energy $\Sigma(\omega)$ from the impurity solver. It is calculated as

$$G(\omega) = \int_{-\infty}^{\infty} \frac{\rho(\epsilon)d\epsilon}{\omega - \Sigma(\omega) - \epsilon}, \quad (\text{S3})$$

where $\rho(\epsilon)$ is the noninteracting density of states. This integral is convergent since we are integrating below the complex pole $\epsilon = \omega - \Sigma(\omega)$, as a consequence of the causality $\text{Im} \Sigma(\omega) < 0$. However, numerical instabilities can arise due to the fact that the complex pole can be arbitrarily close to the real axis. Hence, the numerical integration of Eq. (S3) requires additional care. In Sec. IB2 we present a numerical procedure which solves this problem. However, in the 1d case these numerical instabilities are completely avoided since Eq. (S3) admits an analytical solution, as shown in Sec. IB1.

Following the DMFT algorithm from Fig. S1, we now calculate the next iteration of the free propagator using the Dyson equation

$$G_0^{\text{new}}(\omega) = [G^{-1}(\omega) + \Sigma(\omega)]^{-1}. \quad (\text{S4})$$

We check if $|G_0^{\text{new}}(\omega) - G_0(\omega)| < \epsilon_{\text{tol}}$ (for each ω), where ϵ_{tol} is the tolerance parameter that we typically set to $\epsilon_{\text{tol}} \sim 10^{-4}$ or smaller. If this condition is satisfied, the DMFT loop terminates and Σ , G_0 and G are found. Otherwise, G_0^{new} is used in the impurity solver and the procedure is repeated until convergence is reached.

After the DMFT loop has been completed, we can use the calculated self-energy $\Sigma(\omega)$ to find the retarded Green's function of our original problem

$$G_{\mathbf{k}}(\omega) = \frac{1}{\omega - \Sigma(\omega) - \epsilon_{\mathbf{k}}}. \quad (\text{S5})$$

The spectral function is then simply given by

$$A_{\mathbf{k}}(\omega) = -\frac{1}{\pi} \text{Im} G_{\mathbf{k}}(\omega). \quad (\text{S6})$$

1. Self-consistency equation for the local Green's function in one dimension

Let us now show how the local Green's function (S3) can be analytically evaluated in a 1d system with nearest neighbor hopping t_0 . The noninteracting density of states reads as

$$\rho(\epsilon) = \frac{\theta(4t_0^2 - \epsilon^2)}{\pi\sqrt{4t_0^2 - \epsilon^2}}, \quad (\text{S7})$$

where θ is the Heaviside step function. Equation (S3) can be rewritten using the substitution $\epsilon = 2t_0 \sin x$

$$G(\omega) = \frac{1}{4t_0\pi} \int_{-\pi}^{\pi} \frac{dx}{B - \sin x}, \quad (\text{S8})$$

where we introduced

$$B = (\omega - \Sigma(\omega))/2t_0. \quad (\text{S9})$$

Additional substitution $z = e^{ix}$ leads us to

$$G(\omega) = -\frac{1}{2t_0\pi} \oint_C \frac{dz}{(z - z_+)(z - z_-)}, \quad (\text{S10})$$

where this represents the counterclockwise complex integral over the unit circle C and $z_{\pm} = iB \pm \sqrt{1 - B^2}$. In order to apply the method of residues, we first need to find out if z_{\pm} are inside the complex unit circle $|z| = 1$. Causality implies that $\text{Im} \Sigma(\omega) < 0$ which means that $\text{Im} B > 0$. In this case one can show that $|z_+| < 1$ and $|z_-| > 1$, which means that only the pole at z_+ gives a non-vanishing contribution to the Eq. (S10)

$$G(\omega) = \frac{-i}{2t_0\sqrt{1 - B^2}} = \frac{1}{2t_0B\sqrt{1 - \frac{1}{B^2}}}. \quad (\text{S11})$$

In Eq. (S11) we wrote the solution in two ways. They are completely equivalent in our case when $\text{Im} B > 0$, but can otherwise give different results. Since B can be arbitrarily close to the real axis, it is important to ensure additional numerical stability by requiring that the expression for $G(\omega)$ satisfies that the $\text{Im} B = 0$ solution coincides with the solution in the limit $\text{Im} B \rightarrow 0$. This is not satisfied by the expressions in Eq. (S11), but it can be achieved by combining their imaginary and real parts

$$G(\omega) = \text{Re} \frac{1}{2t_0aB\sqrt{1 - \frac{1}{B^2}}} + i \text{Im} \frac{-i}{2t_0a\sqrt{1 - B^2}}. \quad (\text{S12})$$

2. Self-consistency equation for the local Green's function in arbitrary number of dimensions

Here we present a numerical procedure for the calculation of the local Green's function (S3) for arbitrary density of states $\rho(\epsilon)$, that completely eliminates the potential numerical singularity at $\epsilon = \omega - \Sigma(\omega)$. This is particularly important since the techniques presented in Sec. IB1 fail when the dispersion relation even slightly changes. It is also relevant in the higher-dimensional systems where the density of states is not necessarily analytically known.

Let us suppose that the self-energy and the density of states are known only on a finite, equidistant grid $\omega_0, \omega_1, \dots, \omega_{N-1}$, where $\Delta\omega = \omega_{i+1} - \omega_i$. Further, suppose that the density of states is vanishing outside some closed interval $[D_1, D_2]$ and that the grid is wide enough so that there are at least a couple of points outside that closed interval: $\rho(\omega_0) = \dots = \rho(\omega_3) = 0$ and $\rho(\omega_{N-1}) = \dots = \rho(\omega_{N-4}) = 0$. These are quite general assumptions that are always satisfied in the systems we are examining. The local Green's function can now be rewritten as

$$G(\omega) = \sum_{i=0}^{N-2} \int_{\omega_i}^{\omega_{i+1}} d\epsilon \frac{\rho(\epsilon)}{\omega - \Sigma(\omega) - \epsilon}. \quad (\text{S13})$$

At each sub-interval $[\omega_i, \omega_{i+1}]$ the density of states is only known at the endpoints, so it is natural to approximate it using a linear function

$$\rho(\epsilon) = a_i + b_i(\epsilon - \omega_i), \quad (\text{S14})$$

where $a_i = \rho(\omega_i)$, $b_i = (\rho(\omega_{i+1}) - \rho(\omega_i))/\Delta\omega$. Introducing a shorthand notation $\xi = \omega - \Sigma(\omega)$, we evaluate Eq. (S13) analytically

$$\begin{aligned} G(\omega) &= \sum_{i=0}^{N-2} b_i(\omega_i - \omega_{i+1}) \\ &+ \sum_{i=0}^{N-2} a_i [\ln(\xi - \omega_i) - \ln(\xi - \omega_{i+1})] \\ &+ \sum_{i=0}^{N-2} b_i(\xi - \omega_i) [\ln(\xi - \omega_i) - \ln(\xi - \omega_{i+1})]. \end{aligned} \quad (\text{S15})$$

The first line is just a telescoping series that is vanishing

$$\sum_{i=0}^{N-2} b_i(\omega_i - \omega_{i+1}) = \rho(\omega_0) - \rho(\omega_{N-1}) = 0. \quad (\text{S16})$$

The last two lines in Eq. (S15) can be transformed by shifting the indices $i+1 \rightarrow i$, taking into account that a few boundary terms are vanishing and using the identity $a_i - a_{i-1} = (\omega_i - \omega_{i-1})b_{i-1}$

$$\begin{aligned} G(\omega) &= \sum_{i=0}^{N-2} \frac{\rho(\omega_{i+1}) - 2\rho(\omega_i) + \rho(\omega_{i-1}))}{\Delta\omega} \\ &\times (\omega - \omega_i - \Sigma(\omega)) \ln(\omega - \omega_i - \Sigma(\omega)). \end{aligned} \quad (\text{S17})$$

This expression now has no numerical instabilities. This is most easily seen from the fact that it has the form $x \ln x$ which is well defined even in the limit $x \rightarrow 0$, where it vanishes. Of course, the results were obtained by using the linear interpolation of the density of states.

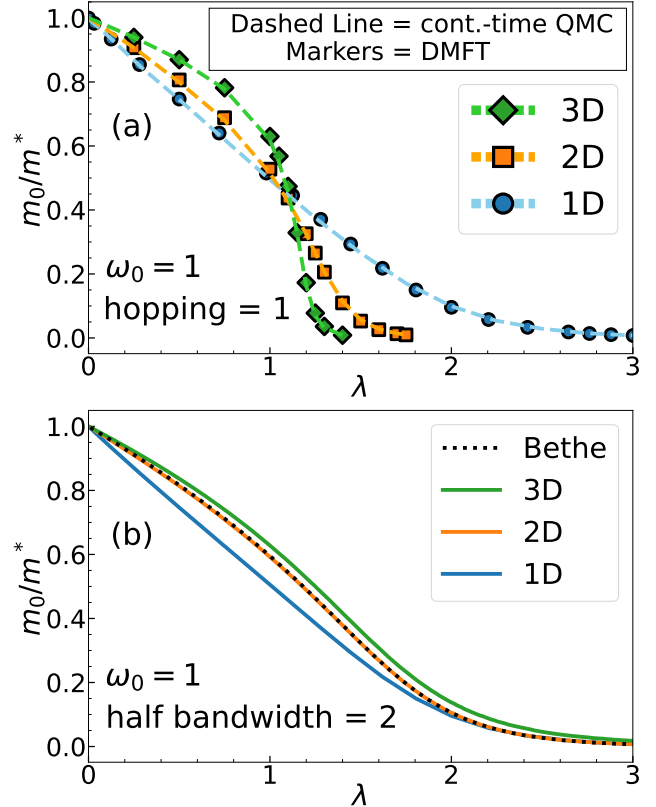


FIG. S3. (a) Continuous-time QMC (taken from Ref. S6) vs. DMFT mass renormalization in 1d, 2d and 3d, with $\omega_0 = 1$. (b) Comparison of the DMFT mass renormalization on different lattices.

This is completely justified if $\rho(\epsilon)$ is smooth or has finitely many cusps. However, the presence of van Hove singularities in $\rho(\epsilon)$ may require some special analytical treatment around them.

C. Effective mass in 1d, 2d and 3d

The DMFT mass renormalization is calculated in one, two and three dimensions. These are then compared to the continuous-time path-integral quantum Monte Carlo (QMC) results from Ref. S6. In that paper it was noted that the numerical accuracy of the QMC method is 0.1% – 0.3%. The results are presented in Fig. S3(a). We note that the definition of λ and γ is slightly different than the one we gave in the main text. Here

$$\lambda = \frac{g^2}{\omega_0 W/2}; \quad \gamma = \frac{\omega_0}{W/2}, \quad (\text{S18})$$

where $W/2$ is the half bandwidth. This coincides with our previous definition in 1d, but gives an extra normalization in higher dimensions.

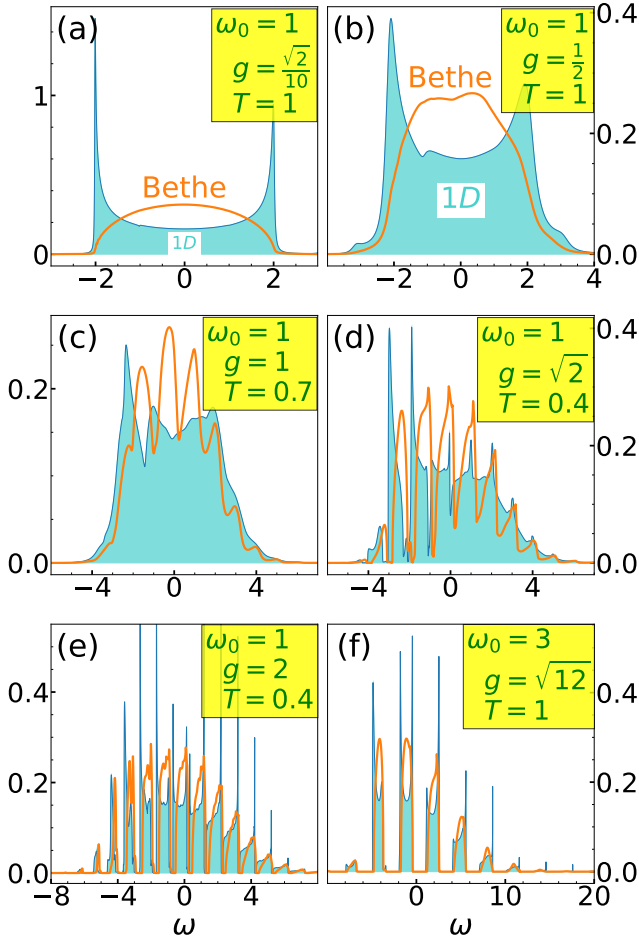


FIG. S4. 1d vs Bethe DMFT local spectral functions.

D. Comparisons with the Bethe lattice results

In the main text we emphasized that the misconception about the validity of the DMFT in 1d appeared since only the DMFT results on the Bethe lattice were used in comparisons with other methods [S7, S8]. In this section we illustrate why such comparison is inappropriate.

The main difference in practical implementation, compared to 1d, can be ascribed to the self-consistency condition for the Bethe lattice (corresponding to the semi-elliptic density of states) which can be formulated using a simple algebraic equation [S1]

$$G_0(\omega) = \left(\omega - \frac{(W/2)^2}{4} G(\omega) \right)^{-1}. \quad (\text{S19})$$

In Fig. S3(b) we compare the DMFT mass renormalization on different lattices using the same half-bandwidth. There is a clear discrepancy between the 1d and the Bethe lattice results, in accordance with the already mentioned earlier works.

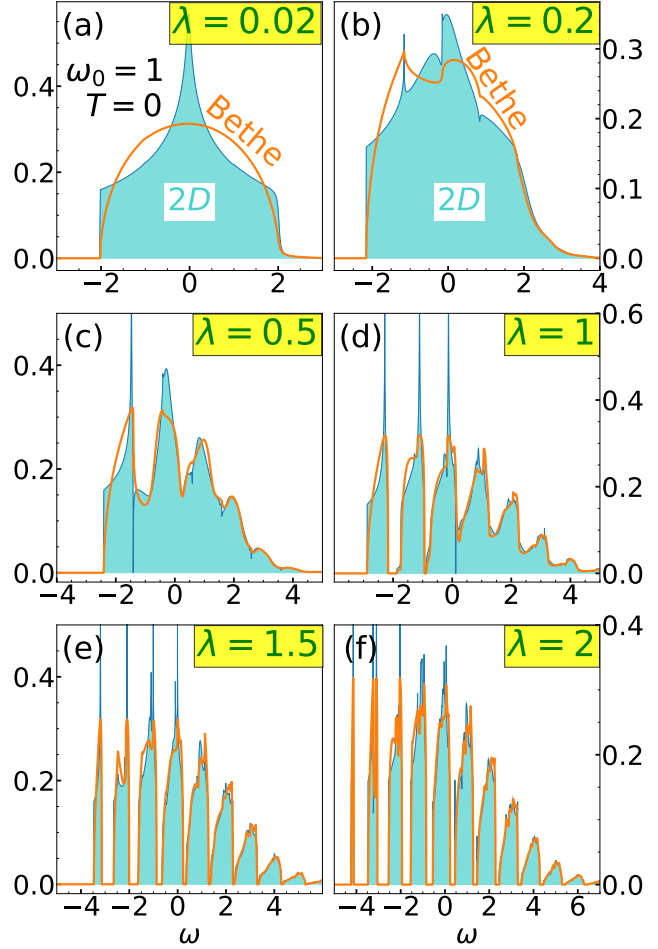


FIG. S5. 2d vs Bethe DMFT local spectral functions.

The Bethe lattice lacks a dispersion relation since it has no translational symmetry. Therefore in Fig. S4 we compare only the local spectral functions $A(\omega) = -\frac{1}{\pi} \text{Im} G(\omega) = -\frac{1}{\pi} \text{Im} \frac{1}{N} \sum_k G_k(\omega)$ of the Bethe and 1d lattice. For small couplings, the spectral functions resemble the noninteracting density of state and we find a large discrepancy, as shown in panels (a) and (b). In contrast, close to the atomic limit in Fig. S4(f) spectral functions become more alike. We note that the regimes at panels (c)-(f) are the same as in Fig. 3 from the main text.

It is rather surprising that there is a striking agreement between the effective mass for 2d and the Bethe lattice as shown in Fig. S3(b), even though the noninteracting density of states are different, Fig. S5(a). Interestingly, we can see from Fig. S5 that the local spectral functions become very similar already for moderate interactions.

II. WEAK-COUPLING LIMIT

In this section we introduce the self-consistent Migdal approximation (SCMA) and use it as a benchmark for the DMFT in the weak-coupling limit, where SCMA is exact. More importantly, we can examine a deviation of SCMA from DMFT for stronger couplings, which is shown in the main text and in the following sections of the SM.

A. Migdal approximation

The Migdal approximation [S9], as shown in Fig. S6, is defined by taking into account only the lowest order Feynman diagram in the perturbation expansion of the self-energy.

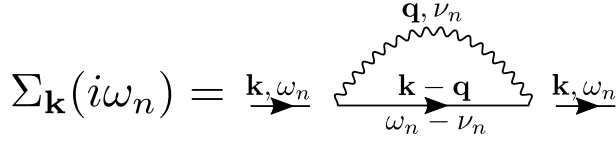


FIG. S6. Feynman diagrams of the self-energy in the Migdal approximation

Due to its simplicity it can be evaluated analytically

$$\Sigma_k(\omega) = g^2(b+1)S(\omega - \omega_0) + g^2bS(\omega + \omega_0), \quad (\text{S20})$$

where $b \equiv b(\omega_0) = (e^{\omega_0/T} - 1)^{-1}$ and

$$S(\omega) = (\omega^2 - 4t_0^2)^{-1/2} \quad \text{for } \omega > 0,$$

while the solution for $\omega < 0$ can be obtained by noting that $\text{Im}S(\omega)$ and $\text{Re}S(\omega)$ are symmetric and antisymmetric functions, respectively. However, this solution is accurate only for very small coupling g . For larger coupling a much better solution is obtained within the self-consistent Migdal approximation.

B. Self-consistent Migdal approximation

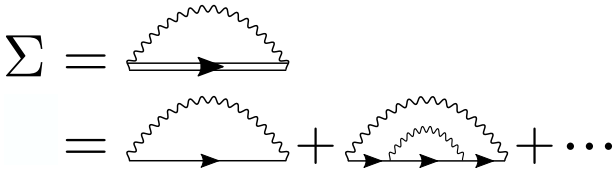


FIG. S7. Feynman diagrams in the SCMA approximation.

In the SCMA, free fermionic propagator from Fig. S6 is replaced with the interacting propagator, as shown in

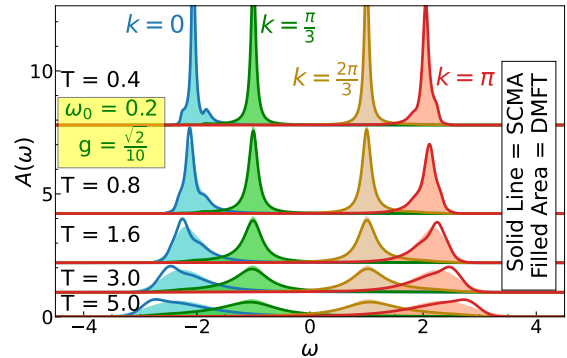
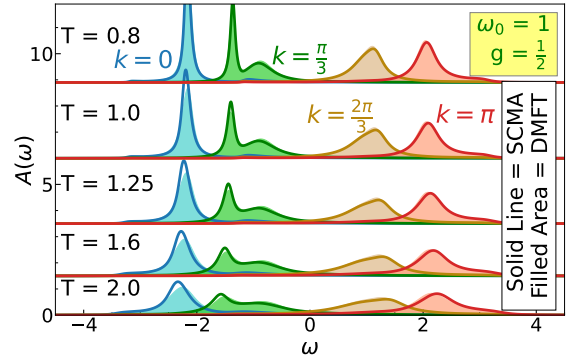
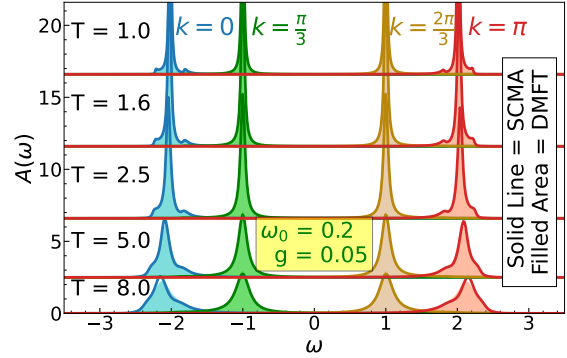
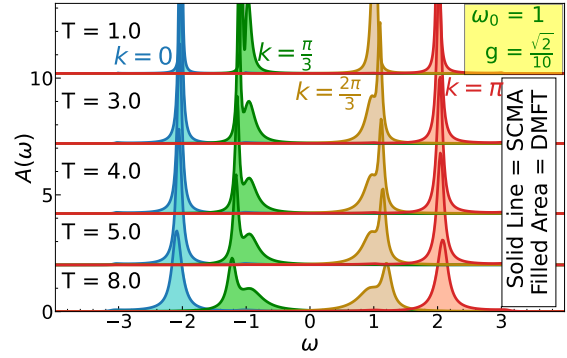


FIG. S8. DMFT vs. SCMA spectral functions in the weak-coupling regime.

Fig. S7. The corresponding equation for the self-energy can be written as

$$\Sigma_k(\omega) = g^2(b+1)G(\omega - \omega_0) + g^2bG(\omega + \omega_0), \quad (\text{S21})$$

where $G(\omega) = \frac{1}{N} \sum_k G_k(\omega)$ is the local Green's function. Equation (S21) needs to be solved self-consistently, since the Green's function can be expressed in terms of the self-energy (via the Dyson equation).

Using the expansion with respect to the free propagator, the formal solution for the self-energy can be written as an infinite series of non-crossing diagrams, as shown in Fig. S7. We see that the first term represents the Feynman diagram in the Migdal approximation. It is thus not at all surprising that the SCMA range of validity is much larger than the one-shot Migdal approximation.

We note that the SCMA self-energy is momentum-independent, which follows from Eq. (S21), making this method numerically cheap.

C. DMFT vs. SCMA in the weak coupling limit

A comparison of the DMFT and SCMA spectral functions in the weak coupling limit is shown in Fig. S8. Results almost fully coincide. As the electron-phonon coupling increases, the SCMA spectral functions starts to deviate from the exact solution, as we see from the main text and from the remaining part of the Supplemental Material.

III. STRONG COUPLING: EXACT DIAGONALIZATION

In the strong coupling regime we can approach the solution in the thermodynamic limit by using a small number of lattice sites. In SM Sec. IV we show that for $g = 2$, $\omega_0 = 1$ we are close to thermodynamic limit by considering a chain of just $N = 4$ sites. In this case we can reach a solution using the exact diagonalization (ED). In the following we describe our implementation of the ED method.

We calculate the spectral function by diagonalizing the Holstein Hamiltonian in the space spanned by the vectors $U c_i^\dagger |n_1 n_2 \dots n_N\rangle$, where n_i is the number of phonons at site $i \in \{1, \dots, N\}$, satisfying $\sum_i n_i < n_{\max}$, while U is the unitary operator of the Lang-Firsov transformation [S10] given as

$$U = e^{\frac{g}{\omega_0} \sum_i c_i^\dagger c_i (a_i - a_i^\dagger)}. \quad (\text{S22})$$

Both N and n_{\max} need to be increased until convergence is reached. The spectral function is then calculated as

$$A_{\mathbf{k}}(\omega) = \frac{1}{Z_p} \sum_p e^{-\beta E_p} \sum_e \delta(\omega + E_p - E_e) |\langle p | c_{\mathbf{k}} | e \rangle|^2, \quad (\text{S23})$$

where $|p\rangle$ denotes purely phononic states, the energy of which is E_p , $|e\rangle$ denotes the states with one electron and arbitrary number of phonons, the energy of which is E_e and $Z_p = \sum_p e^{-\beta E_p}$ is the phononic partition function.

We found that convergent results for the spectral function when $g = 2$, $\omega_0 = 1$, $N = 4$ could be obtained for $n_{\max} = 16$. The results are shown in Figs. S16-S21, as well as in Figs. 2(b) and 3(e)-(f) of the main text. The spectral functions at \mathbf{k} points different than $k = \frac{2\pi}{N}i$, $i \in \{0, \dots, N-1\}$ were obtained by employing so-called twisted boundary conditions, that is by changing the terms in the Hamiltonian $t_0 c_i^\dagger c_{i+1} \rightarrow t_0 e^{i\phi} c_i^\dagger c_{i+1}$ and $t_0 c_{i+1}^\dagger c_i \rightarrow t_0 e^{-i\phi} c_{i+1}^\dagger c_i$. The spectral function obtained from such a modified Hamiltonian corresponds then to the spectral function at $k + \phi$.

IV. FINITE-SIZE EFFECTS AND HEOM DEPTH

The numerically exact HEOM, QMC and ED methods are implemented on a 1d lattice of length N . Results which are representative of the thermodynamic limit can be obtained by taking large enough N . Furthermore, the hierarchy of HEOM needs to be truncated using sufficient depth D . In the ED method the number of phonons in the Hilbert space need to be specified. All of these parameters should be as large as possible, but the practical numerical implementation is restricted by the available computer memory. Finite- N and finite- D analysis was performed in all parameter regimes where we have HEOM results. In Figs. S9, S10, and S11 we briefly illustrate such analysis in the intermediate and strong coupling regime.

The optimal value of D strongly depends on the interaction strength and temperature. For large interaction we need large D since many phonon states are populated even at $T = 0$. Similarly, larger temperature also requires larger HEOM depth. As illustrated in Fig. S9(a)-(b), for $\omega_0 = 1$, $g = 1$ the convergence is nearly reached already for $D = 6$. For $g = \sqrt{2}$ (Fig. S10(a)-(b)), we need slightly larger D . However, in the strong-coupling regime for $g = 2$ we need much larger D , and from a comparison with the ED results for $N = 4$ in Fig. S11 we can conclude that the HEOM result has rather well converged only for $D = 17$. We can also observe that the results at $k = 0$ typically converge faster with respect to D than the results at $k = \pi$.

The value N for which the spectral functions correspond to those in the thermodynamic limit also depends on the

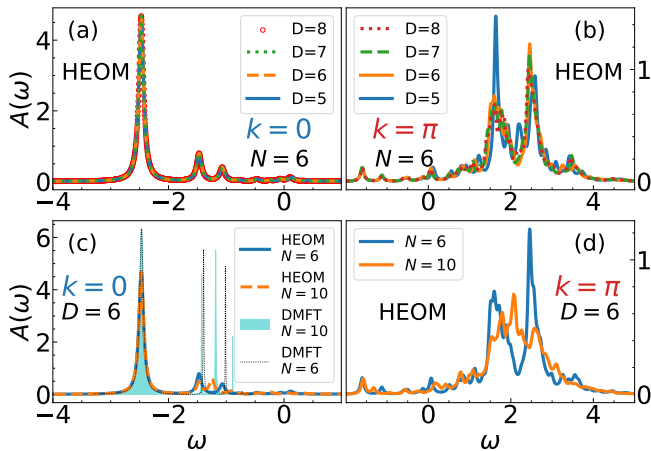


FIG. S9. Finite- N and finite- D effects in the HEOM method at intermediate coupling $\omega_0 = 1$, $g = 1$, $T = 0$, which is the same regime as in Fig. 2(a) of the main text. Here we use Lorentzian broadening with $\eta = 0.05$.

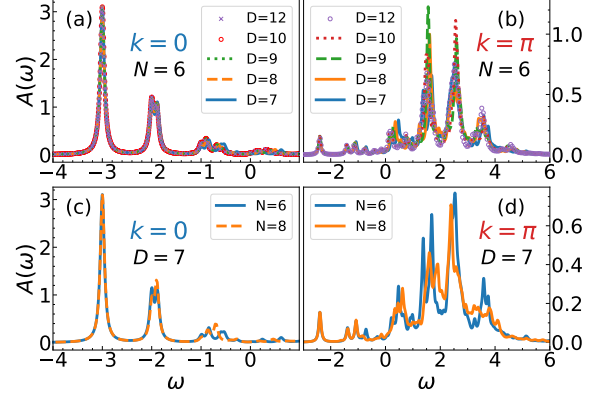


FIG. S10. Finite- N and finite- D effects in the HEOM at intermediate coupling $\omega_0 = 1$, $g = \sqrt{2}$, $T = 0$, which is the same regime as in Fig. 2(c) of the main text. Here we use Lorentzian broadening with $\eta = 0.05$.

parameter regime: for larger interaction g and for higher T the chain length N can be smaller, while for smaller g and lower T we need larger N . In panels (c) and (d) of Figs. S9 and S10 we see that for intermediate coupling there is some difference in spectral functions for $N = 6$ and $N = 10$ ($N = 8$). At $k = 0$ it is particularly visible in the first satellite structure for $g = 1$. Remarkably, the DMFT on a finite lattice $N = 6$ ($N = 10$) predicts very similar satellite structure as HEOM for the same N . This indicates that the correct satellite peak in Fig. 2(a) of the main text should be closer to DMFT, while HEOM results have some artefacts because of the finite lattice size. On the other hand, for $g = 2$ it is enough to set $N = 4$, as we now demonstrate.

It is very efficient to analyze the finite-size effects using the DMFT applied on a finite system with N sites. This is very simple to implement in the DMFT loop. The only difference is in the self-consistency equation: instead of the integral over the density of states, the local Green function is obtained as an average over the k vectors

$$G(\omega) = \frac{1}{N} \sum_{i=1}^N G_{k_i}(\omega). \quad (\text{S24})$$

We can see from Fig. S12 that there is very little difference between $N = 4$, $N = 6$ and thermodynamic limit for $g = 2$, $\omega_0 = 1$. We showed only the results for $T = 0.4$, but we checked that the conclusions remain true even for $T = 0$. Therefore, setting $N = 4$ in HEOM and ED calculations is enough. This left enough computer memory to use large $D = 17$ in HEOM calculations. Then all three methods give very similar spectral functions as seen in Fig. S11.

Fig. S13 shows the DMFT finite-size effects close to the atomic limit, both for the spectral function $A_k(\omega)$ and

for the self-energy $\Sigma(\omega)$. The spectral functions are not strongly N -dependent. On the other hand, the details of the self-energy are much more sensitive to finite-size effects. Finite N results show a kind of a stripe pattern, while $N = \infty$ results are smoother.

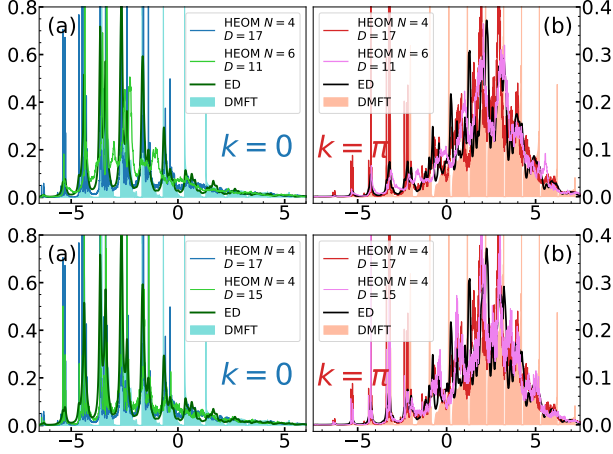


FIG. S11. Finite- N and finite- D effects in the strong coupling regime $\omega_0 = 1$, $g = 2$, $T = 0.4$, which is the same regime as in Figs. 3(e)-(f) of the main text. ED spectral functions ($N = 4$) are shown using Lorentzian broadening with $\eta = 0.05$, while other methods are shown without broadening. DMFT results are in thermodynamic limit.

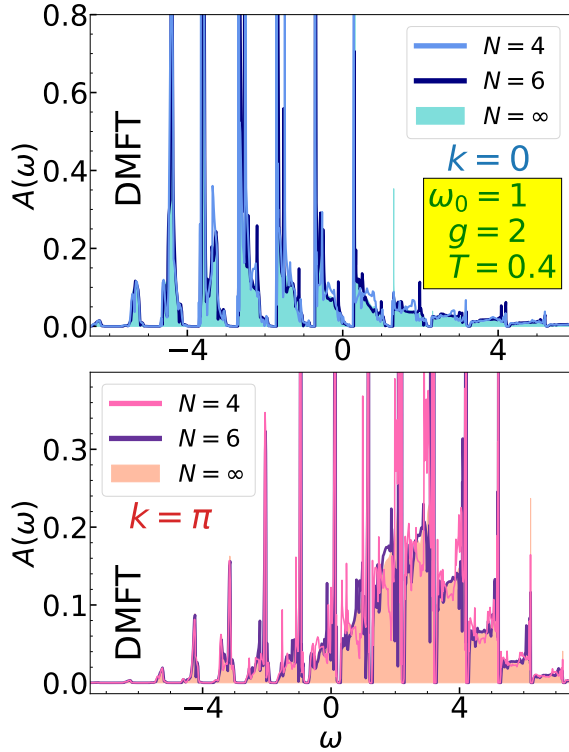


FIG. S12. DMFT spectral functions for different N .

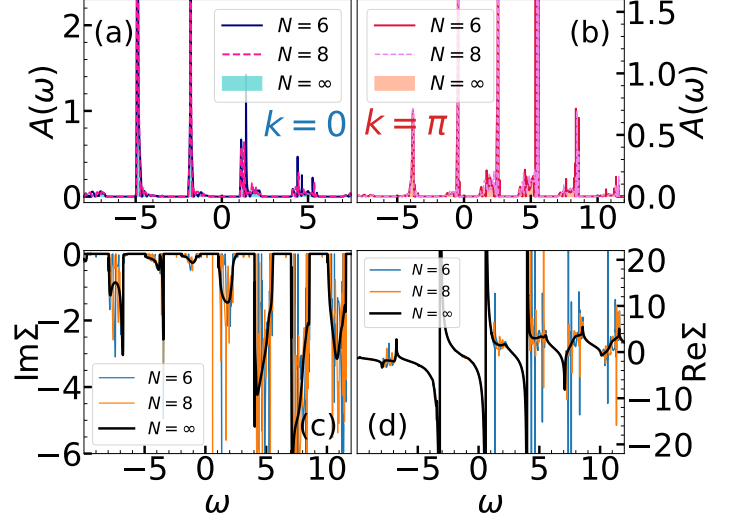


FIG. S13. DMFT finite-size effects close to the atomic limit $\omega_0 = 3$, $g = \sqrt{12}$, $T = 1$

V. ATOMIC LIMIT

Here we investigate the DMFT solution close to the atomic limit. For decoupled sites ($t_0 = 0$), using the Lang-Firsov transformation [S4, S10], the Green's function at $T = 0$ is given by

$$G(\omega) = \sum_{n=0}^{\infty} \frac{\alpha^{2n} e^{-\alpha^2}}{n!} \frac{1}{\omega - n\omega_0 - E_p + i0^+}, \quad (\text{S25a})$$

and at $T > 0$

$$G(\omega) = \sum_{n=-\infty}^{\infty} \frac{I_n \left(2\alpha^2 \sqrt{b(b+1)} \right)}{\omega - n\omega_0 - E_p + i0^+} e^{-(2b+1)\alpha^2 + n\omega_0/2T}. \quad (\text{S25b})$$

Here $E_p = -g^2/\omega_0$ is the ground-state energy, I_n are the modified Bessel functions of the first kind and $b \equiv b(\omega_0) = (e^{\omega_0/T} - 1)^{-1}$. We see that the atomic limit spectrum consists of a series of delta functions at a distance ω_0 from each other. At $T = 0$ the lowest energy peak is at $\omega = E_p$, which corresponds to the ground-state (polaron) energy. At finite temperatures more delta peaks emerge even below the polaron peak.

The integrated DMFT spectral weight at $T = 0$ is shown in Fig. S14 and compared to the exact atomic limit. It was calculated using the numerical procedure introduced in Sec. X. $I(\omega)$ features jumps at frequencies where $A(\omega)$ has peaks and the height of those jumps is equal to the weight of the peaks. Nonzero hopping in the DMFT solution introduces small momentum dependence of $I_k(\omega)$, which is why Fig. S14 shows the result averaged over all momenta. A more detailed comparison is presented in Table S1. It shows the numerical values of the DMFT $I(\omega)$ at the positions of delta peaks (for a given k and averaged over many k) in comparison with the analytical $t_0 = 0$ result from Eq. (S25a). These delta peaks, positioned at $n\omega_0 + E_p$, have the weights equal to $\alpha^{2n} e^{-\alpha^2}/n!$ for $n = 0, 1, \dots$

For $T > 0$, the peaks are located both below and above E_p . The DMFT spectra averaged over k are shown in Fig. S15. They have a characteristic fork-shaped form at low T , which is the consequence of the 1d density of states. The weight of the peaks are very close to the analytical result $I_n(2\alpha^2 \sqrt{b(b+1)}) e^{-(2b+1)\alpha^2 + n\omega_0/2T}$. These spectral weights, averaged over momenta k , are given in Table S2.

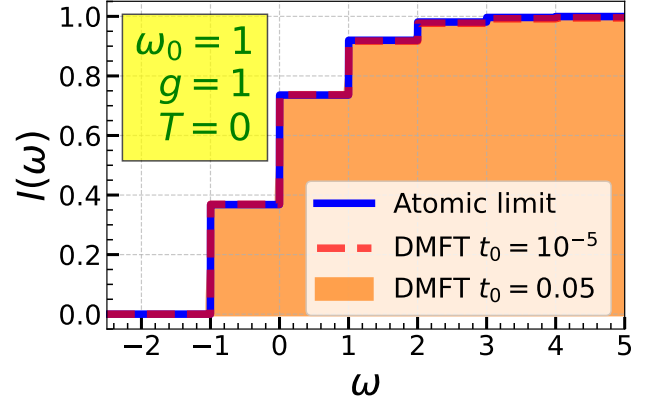


FIG. S14. DMFT integrated spectral weight for $t_0 = 0.05$ (shaded) and $t_0 = 10^{-5}$ (red dashed line) averaged over all momenta, $I(\omega) = \frac{1}{N} \sum_k \int_{-\infty}^{\omega} A_k(\nu) d\nu$, in comparison to the exact $t_0 = 0$ result (blue solid line).

TABLE S1. Integrated spectral weight $I(\omega)$ for $\omega_0 = 1$, $g = 1$ at $T = 0$. The exact atomic limit corresponds to $t_0 = 0.00$. For $t_0 = 10^{-5}$ the DMFT solution has no k -dependence within the specified accuracy. We denote the k -values to be 'av.' if the answer is averaged over all momenta.

k	ω	-2	-1	0	1	2	3
	t_0						
	0.00	0.00	0.37	0.74	0.92	0.98	1.0
all	10^{-5}	0.00	0.37	0.74	0.92	0.98	1.0
av.	0.05	0.00	0.37	0.73	0.92	0.98	1.0
0	0.05	0.00	0.40	0.76	0.94	0.99	1.0
$\pi/2$	0.05	0.00	0.37	0.74	0.92	0.98	1.0
π	0.05	0.00	0.33	0.71	0.91	0.98	0.99

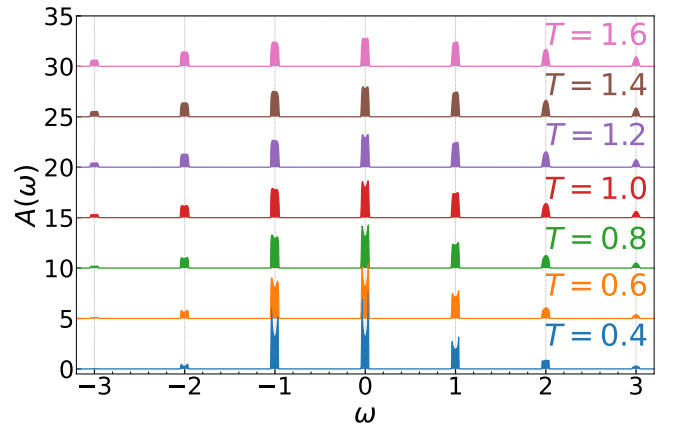


FIG. S15. DMFT spectral functions $A(\omega) = \frac{1}{N} \sum_k A_k(\omega)$ for $\omega_0 = 1$, $g = 1$, $t_0 = 0.05$, at several temperatures.

TABLE S2. Spectral weights of the peaks located at $\omega = n\omega_0 + E_p$ for $n = -2, -1, 0, 1, 2, 3$. The DMFT spectra, obtained for $t_0 = 0.05$, are averaged over k . The atomic limit values ($t_0 = 0.00$) are obtained from the analytical formula. Here $\omega_0 = 1, g = 1$.

T	ω t_0	-2	-1	0	1	2	3
0.4	0.00	0.03	0.34	0.35	0.19	0.07	0.02
0.4	0.05	0.03	0.34	0.34	0.18	0.07	0.02
0.6	0.00	0.06	0.30	0.33	0.19	0.08	0.02
0.6	0.05	0.06	0.30	0.33	0.19	0.08	0.02
0.8	0.00	0.09	0.27	0.30	0.19	0.09	0.03
0.8	0.05	0.09	0.27	0.30	0.19	0.09	0.03
1.0	0.00	0.10	0.25	0.28	0.19	0.09	0.04
1.0	0.05	0.10	0.25	0.28	0.19	0.10	0.04
1.2	0.00	0.11	0.23	0.26	0.19	0.10	0.04
1.2	0.05	0.11	0.23	0.26	0.19	0.10	0.04
1.4	0.00	0.12	0.21	0.24	0.19	0.11	0.05
1.4	0.05	0.12	0.21	0.24	0.19	0.11	0.05

VI. SPECTRAL FUNCTIONS AT $T = 0$: ADDITIONAL RESULTS

Spectral functions and integrated spectral weights at $T = 0$ for $k = 0$ are shown in Fig. 2 of the main text. In Figs. S16 - S18, we show the results for additional momenta. We note that the integrated spectral weight was calculated without broadening, using the numerical scheme described in Sec. X. The spectral functions are shown with a small Lorentzian broadening η ,

$$A_\eta(\omega) = \frac{1}{\pi} \int_{-\infty}^{\infty} d\nu \frac{\eta A(\nu)}{\eta^2 + (\omega - \nu)^2}, \quad (\text{S26})$$

We see that there is a very good agreement between DMFT and HEOM/ED results. In every regime where HEOM was implemented, we checked that the results were well converged with respect to the lattice size N and the maximum hierarchy depth D . These values are shown in Table S3.

We note that the HEOM/ED method imposes the periodic boundary conditions on a finite lattice. This means that the HEOM/ED spectral functions are available only for a discrete values of momenta, unlike the DMFT which is calculated in the thermodynamical limit. Results for additional k -values are obtained using twisted boundary conditions.

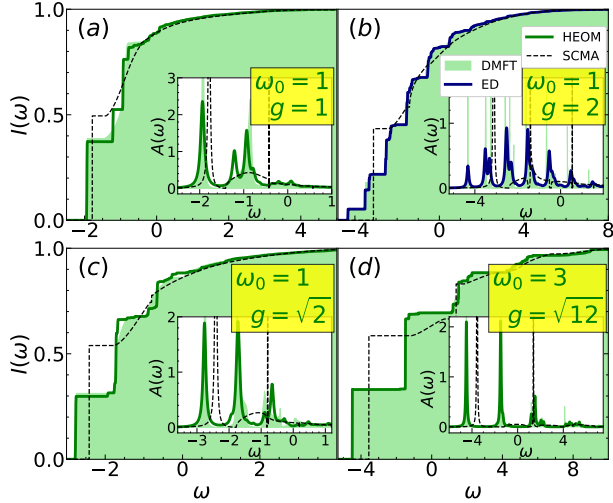


FIG. S16. Integrated spectral weight at $T = 0$ with no broadening. The insets show spectral functions with $\eta = 0.05$ Lorentzian broadening. Different panels have the following values of the momenta: (a) $k = \frac{8\pi}{25}$, (b) $k = \frac{\pi}{4}$, (c) $k = \frac{\pi}{4}$, (d) $k = \frac{\pi}{3}$.

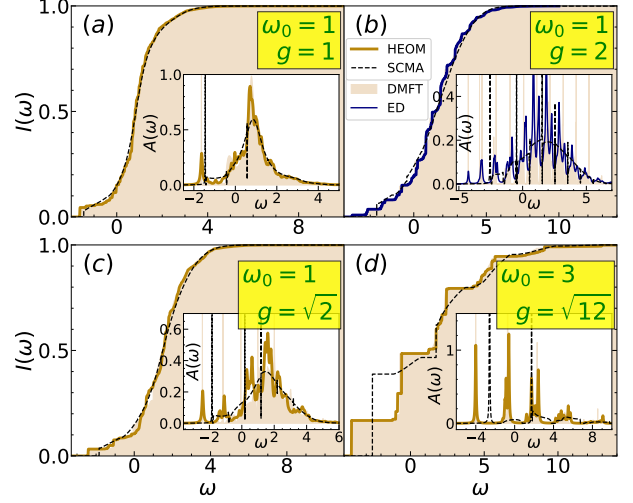


FIG. S17. Integrated spectral weight at $T = 0$ with no broadening. The insets show spectral functions with $\eta = 0.05$ Lorentzian broadening. Different panels have the following values of the momenta: (a) $k = \frac{16\pi}{25}$, (b) $k = \frac{3\pi}{4}$, (c) $k = \frac{3\pi}{4}$, (d) $k = \frac{2\pi}{3}$.

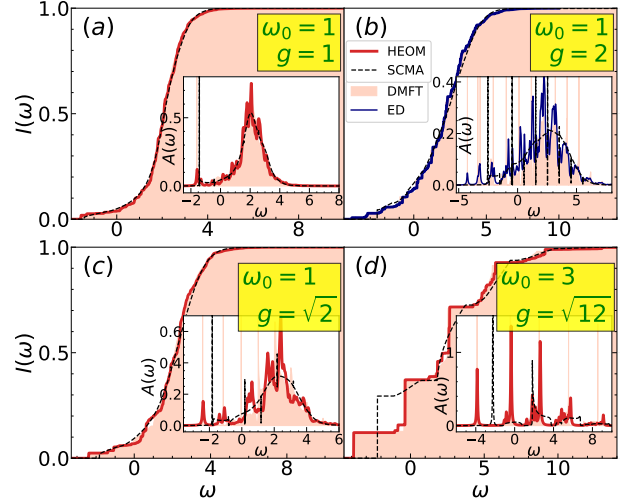


FIG. S18. Integrated spectral weight at $T = 0$ with no broadening. The insets show spectral functions with $\eta = 0.05$ Lorentzian broadening. Every panel is calculated for $k = \pi$.

TABLE S3. Lattice size N and the maximum hierarchy depth D used in the HEOM calculations which correspond to Figs. S16-S18 and Fig. 2 from the main text.

Parameters	N	D
$\omega_0 = 1 \quad g = 1$	10	6
$\omega_0 = 1 \quad g = \sqrt{2}$	8	7
$\omega_0 = 3 \quad g = \sqrt{12}$	6	9

VII. SPECTRAL FUNCTIONS AT $T > 0$: ADDITIONAL RESULTS

Spectral functions for $k = 0$ and $k = \pi$, shown in Fig. 3 of the main text, are supplemented with the results for different k in Fig. S19. Overall, the agreement of DMFT and HEOM/ED spectra is very good which confirms that the nonlocal correlations are not pronounced. Results for different temperatures are shown in Figs. S20 and S21. We checked that the HEOM results are well converged with respect to lattice size N and maximum hierarchy depth D . The values of N and D , used in the calculations, are shown in Table S4.

TABLE S4. Lattice size N and the maximum hierarchy depth D used in the HEOM calculations which correspond to Figs. S19 - S21 and Fig. 3 from the main text.

Parameters	N	D
$\omega_0 = 1$ $g = 1$ $T = 0.7$	10	6
$\omega_0 = 1$ $g = 1$ $T = 1$	10	6
$\omega_0 = 1$ $g = \sqrt{2}$ $T = 0.4$	8	8
$\omega_0 = 1$ $g = \sqrt{2}$ $T = 0.6$	8	7
$\omega_0 = 1$ $g = \sqrt{2}$ $T = 0.8$	8	7
$\omega_0 = 1$ $g = 2$ $T = 0.4$	4	17
$\omega_0 = 3$ $g = \sqrt{12}$ $T = 1$	6	9

It is common to present the spectral functions as color plots in the $k-\omega$ plane. In Fig. S22 we show the DMFT color plot for parameters as in Figs. S19 - S21. For comparison purposes, in Fig. S23 we also show the DMFT color plot for the same parameters as in the finite- T Lanczos results from Fig. 2 of Ref. [S11]. Small difference in DMFT vs. Lanczos method color plots is due to the more pronounced peaks in the DMFT spectra.

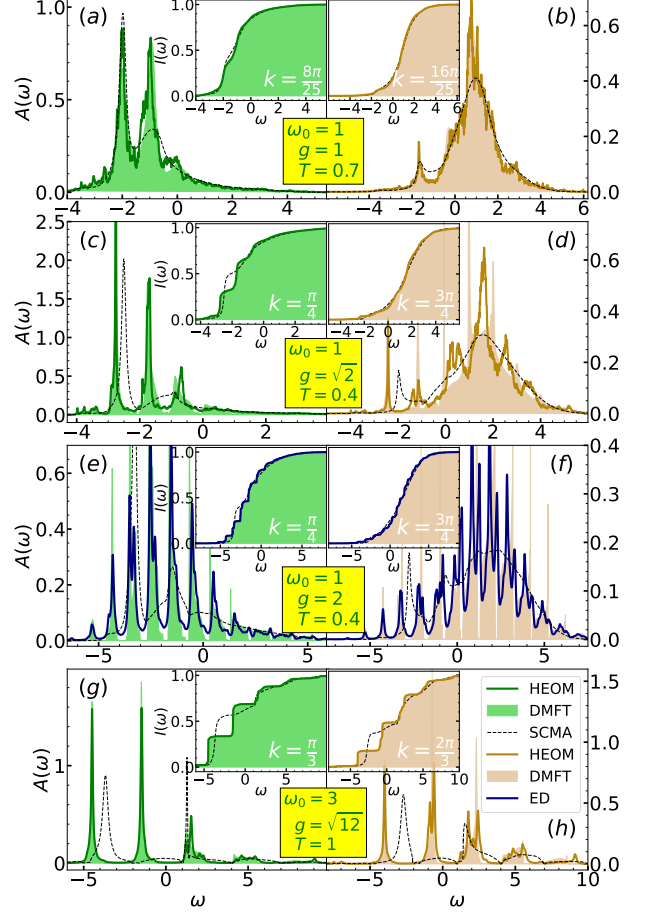


FIG. S19. HEOM, DMFT, SCMA and ED spectral functions for different parameters. On the left panels $\pi/4 \leq k \leq \pi/3$, whereas $\pi/2 \leq k \leq 3\pi/4$ on the right. The integrated spectral weight is presented in the insets without broadening. In panels (g) and (h) Lorentzian broadening with $\eta = 0.05$ is used for all spectral functions, while only ED is broadened in (e) and (f) using the same η .

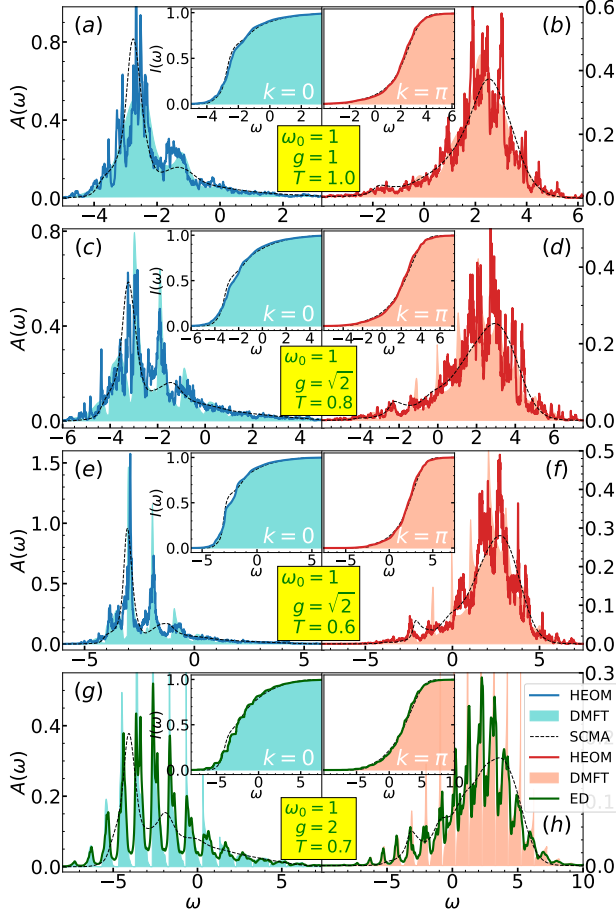


FIG. S20. HEOM, DMFT, SCMA and ED spectral functions for different parameters. On the left panels $k = 0$, whereas $k = \pi$ on the right. The integrated spectral weight is presented in the insets without broadening. The Lorentzian broadening with $\eta = 0.05$ is used only for ED spectral functions.

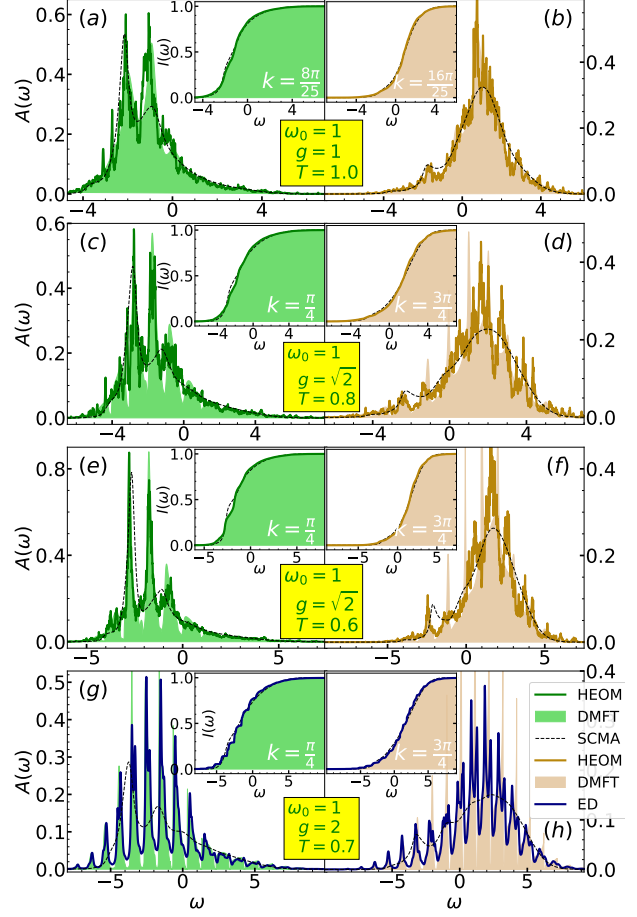


FIG. S21. HEOM, DMFT, SCMA and ED spectral functions for different parameters. On the left panels $\pi/4 \leq k \leq \pi/3$, whereas $\pi/2 \leq k \leq 3\pi/4$ on the right. The integrated spectral weight is presented in the insets without broadening. The Lorentzian broadening with $\eta = 0.05$ is used only for ED spectral functions.

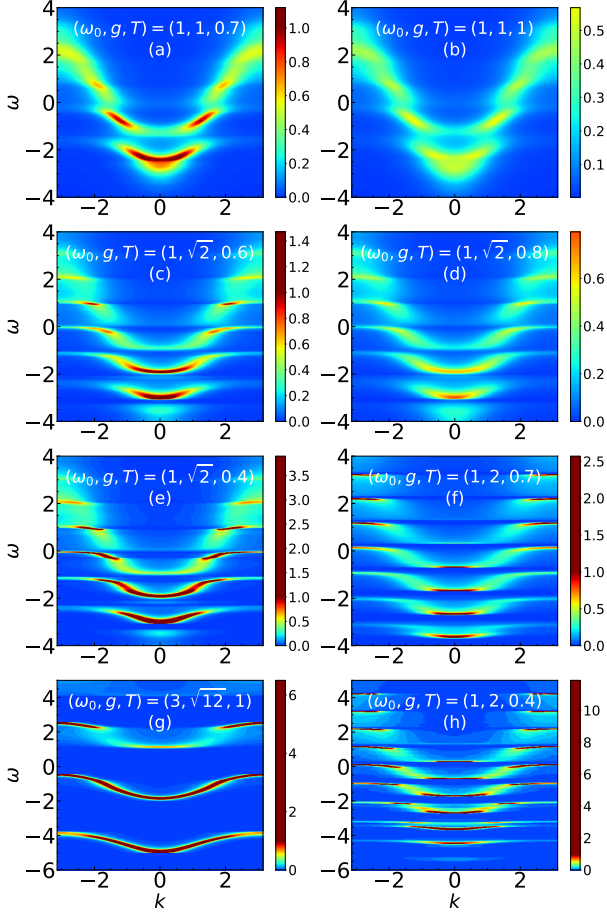


FIG. S22. The DMFT spectral functions $A_k(\omega)$ for parameters as in Figs. S19 - S21. The same color coding is used in all plots.

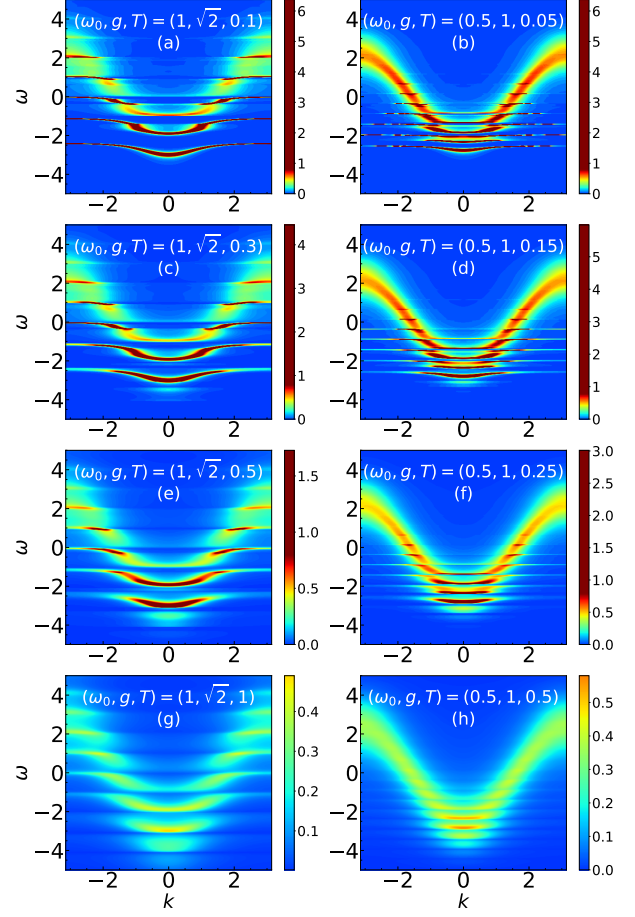


FIG. S23. The DMFT spectral functions $A_k(\omega)$ for parameters as in Fig. 2 of Ref. [S11]. The same color coding is used in all plots.

VIII. HEOM SELF-ENERGIES

The results for the spectral functions, as well as for the effective mass and ground state energy, have shown that the DMFT gives an excellent approximate solution of 1d Holstein model in the whole parameter space. This indicates that the self-energy is approximately local which we explicitly demonstrate in this Section. Since $\Sigma_k(\omega) = \Sigma_{-k}(\omega)$ we will show only the results for $k \geq 0$.

In Fig. S24 we present the HEOM and DMFT self-energies in the intermediate coupling regime. Panels (a) and (b) of Fig. S24 show that the self-energies are nearly local, whereas the DMFT solution interpolates in between. The self-energy is approximately local also for $g = \sqrt{2}$, Fig. S24(c)-(d). There is a visible discrepancy only at higher momenta, which reflects in a shift of the spectral functions with respect to the DMFT solution in Fig. 3d of the main text.

The results for the strong coupling are presented in Fig. S25. The DMFT solution for $\text{Im}\Sigma$ falls to zero between the peaks, as opposed to the HEOM solution where such behavior is observed only for the first few peaks. This is why, for the sake of clarity, the DMFT self-energy is omitted. This is consistent with Fig. S11 where the HEOM results feature the dips, while DMFT solution has gaps. Nevertheless, the presented HEOM results are enough to conclude that the self-energy is nearly local. This is particularly important conclusion since these parameters correspond to strongly renormalized effective mass, $m^*/m \approx 10$.

The regime close to the atomic limit is investigated in Fig. S26. Panels (c) and (d) show that the results are

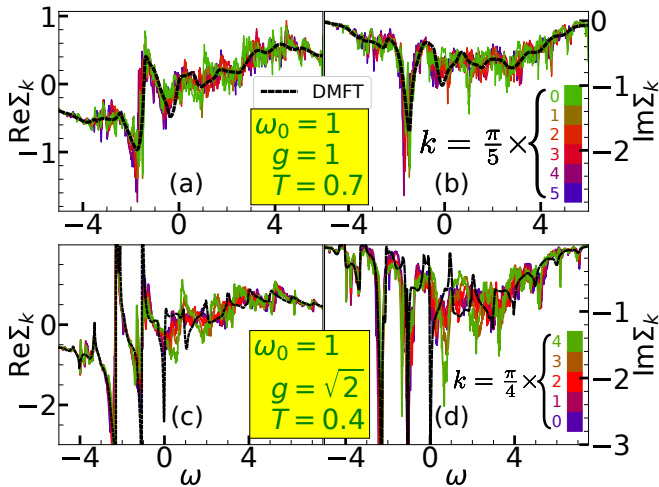


FIG. S24. HEOM and DMFT self-energies for intermediate coupling.

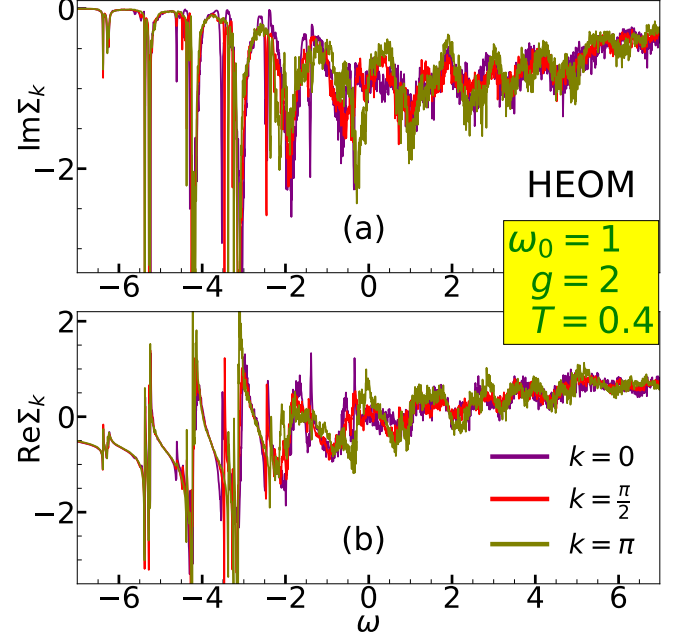


FIG. S25. HEOM self-energies for strong coupling. Here $N = 4$ and $D = 17$.

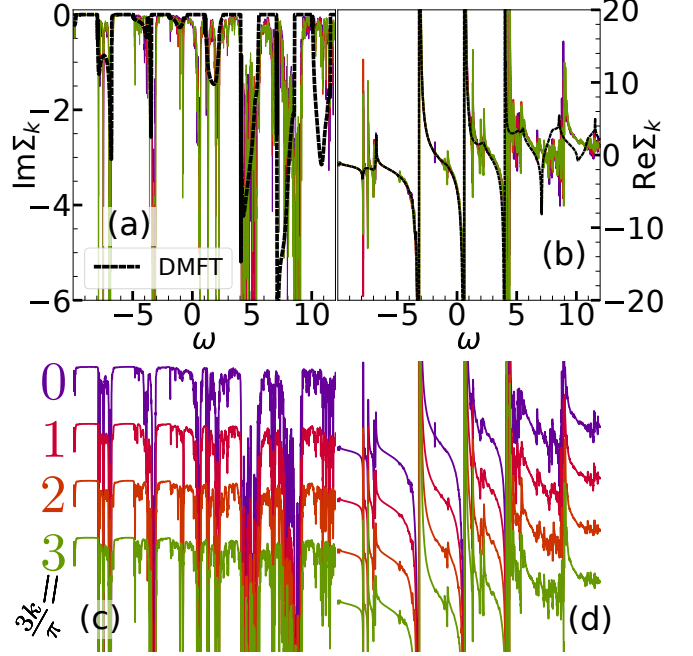


FIG. S26. Panels (a) and (b) show HEOM and DMFT self-energies close to the atomic limit $\omega_0 = 3$, $g = \sqrt{12}$, $T = 1$. Panels (c)-(d) show the same HEOM results as in (a)-(b) but shifted for different values of momenta k .

nearly local, but have a kind of stripe pattern, unlike the DMFT solution which is in thermodynamic limit. This is here just a consequence of the finite-size effects, as

shown in Fig. S13. As discussed in Sec. IV, even though the finite-size effects are visible as stripes in the self-energies, they will not significantly affect the spectral functions. This is why we see a very good agreement between the DMFT and $N = 6$ HEOM spectral functions in panels (g) and (h) of Fig. 3 in the main text.

IX. CORRELATION FUNCTIONS

Here we present a detailed comparison between QMC, HEOM and DMFT correlation functions. The QMC correlation function is defined by

$$C_k(\tau) = \langle c_k(\tau)c_k^\dagger \rangle_{T,0}, \quad (\text{S27})$$

where $c_k(\tau) = e^{\tau H} c_k e^{-\tau H}$ and $0 \leq \tau \leq 1/T$. In Sec. XID we proved the following relation

$$C_k(\tau) = \int_{-\infty}^{\infty} d\omega e^{-\omega\tau} A_k(\omega). \quad (\text{S28})$$

Eq. (S28) can now be used to check whether the spectral functions that we calculated using other methods are consistent with the QMC results. A calculation of the spectral functions from the QMC data would assume an analytical continuation which is an ill-defined procedure, particularly problematic when the spectrum has several pronounced peaks. Therefore, we have to settle for a comparison on the imaginary axis.

Fig. S27 shows the imaginary time QMC, DMFT and HEOM correlation functions and their deviation from the QMC result, for parameters as in Fig. 4 of the main text. We see that the deviation is very small, the relative discrepancy being just a fraction of a percent at $T = 1$. The discrepancy between the DMFT and QMC increases at lower temperatures when the nonlocal correlations are expected to be more important, but it remains quite small even at $T = 0.4$. As we can see, the DMFT gives better results at $k = 0$ than at $k = \pi$.

In Fig. S28 we present the correlation function comparison over a broad set of parameters. The DMFT, HEOM and QMC are in excellent agreement, with the relative discrepancy of the order of one percent for $\tau \sim 1/T$. The SCMA results are also included for comparison.

From Eq. (S28) we see that the correlation function unevenly treats different frequencies from the spectral function. Because of the exponential term, it takes into account low-frequency contributions with much larger weight. Thus, the correct DMFT and HEOM predictions about correlation function reveal that the low-frequency parts of the corresponding spectral functions behave appropriately and fall off fast enough. This is very important property for calculating quantities where the low-frequency part gives large contribution to the result, which would be the case for optical conductivity. Let us now estimate how much a Gaussian centered at frequency a ,

$$A_k^G(\omega) = \frac{W}{\sigma\sqrt{2\pi}} e^{-\frac{(\omega-a)^2}{2\sigma^2}}, \quad (\text{S29})$$

would contribute to the correlation function. Here W is the spectral weight and σ is the standard deviation

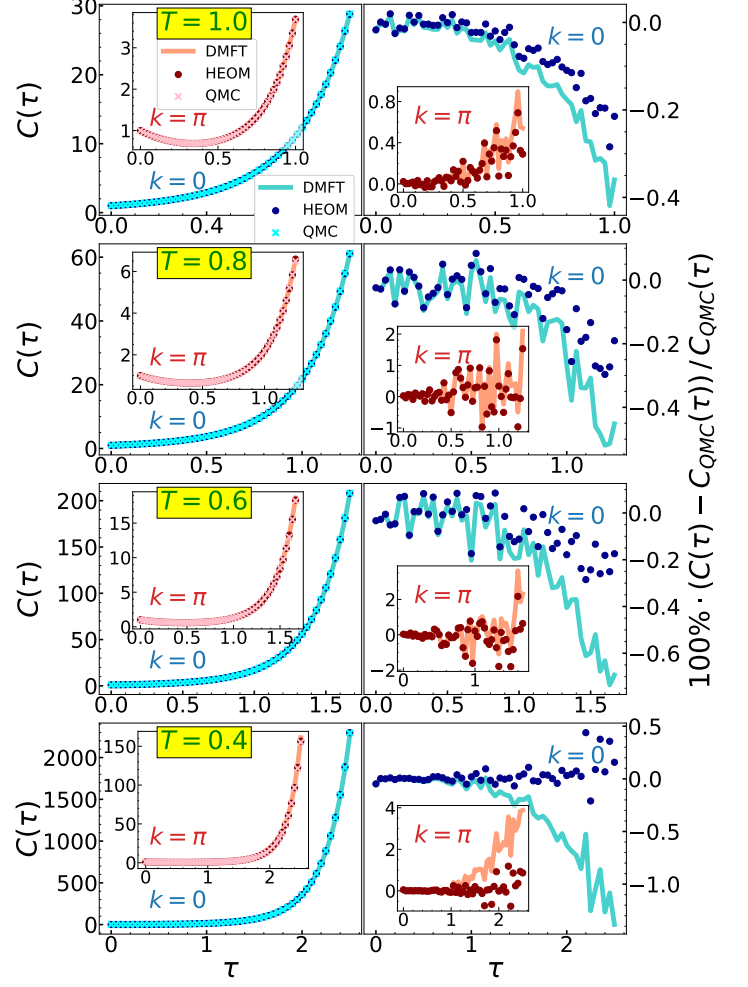


FIG. S27. DMFT, HEOM and QMC correlation functions for $\omega_0 = 1$, $g = \sqrt{2}$ at $k = 0$ and $k = \pi$ at several temperatures. The right panels show the relative discrepancy between DMFT and HEOM results with respect to QMC.

of the Gaussian. This could model a tiny peak present due to the noise, or a real physical contribution. The corresponding part of the correlation function C_k^G can be singled out since Eq. (S28) is linear in A_k . It can be evaluated analytically, giving

$$C_k^G(\tau) = W e^{\frac{\sigma^2 + 2}{2} - a\tau}. \quad (\text{S30})$$

We see that the spectral weight contributes linearly, while the position of the delta peak contributes exponentially (note that a can be negative). The width of the Gaussian σ , as well as the imaginary time τ , are quadratic inside the exponential. Hence, Eq. (S30) explicitly shows that precise calculation of the correlation function requires very accurate spectral functions at low frequencies. Even a small error or noise can produce a completely wrong result. Reliable comparison of $C_k(\tau)$

was made possible only due to the high precision of both DMFT and HEOM calculations.

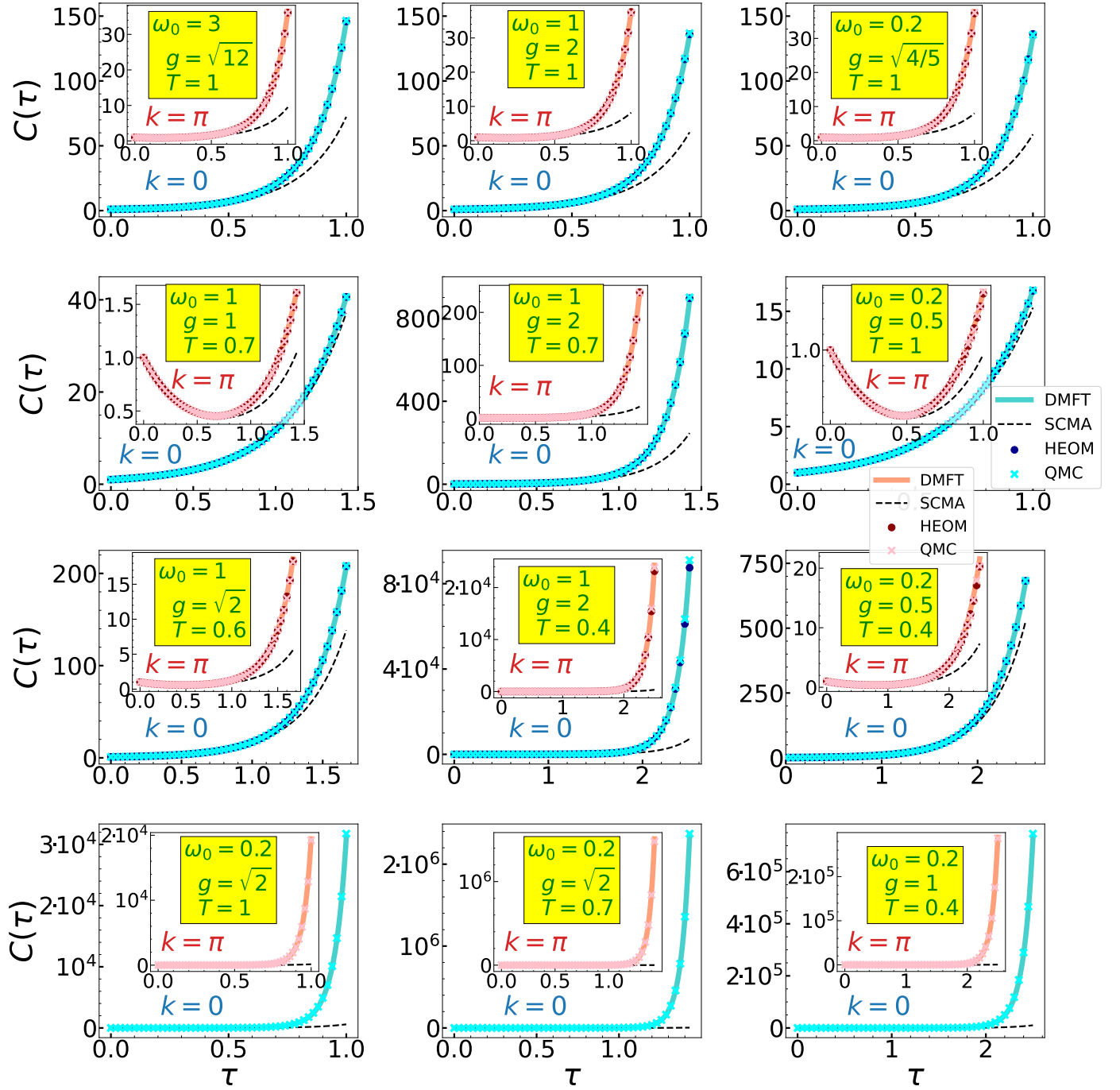


FIG. S28. Comparison of DMFT, HEOM, QMC and SCMA correlation functions over a wide range of parameters. The HEOM results are not available for the parameters in the last row.

X. TECHNICAL NOTE: NUMERICAL CALCULATION OF THE INTEGRATED SPECTRAL WEIGHT

We describe a numerical scheme for calculating the integrated spectral weight. Integrated spectral weight is defined as

$$I_k(\omega) = \int_{-\infty}^{\omega} A_k(\nu) d\nu, \quad (\text{S31})$$

where $A_k(\nu)$ is the spectral function. Straightforward numerical integration of Eq. (S31) can sometimes lead to the conclusion that the spectral sum rule $I_k(\infty) = 1$ is violated. This happens because the numerical representation of $A_k(\nu)$ on a finite grid does not detect the possible presence of delta function peaks without introducing artificial broadening. This is why our numerical scheme calculates $I_k(\omega)$ directly from the self-energy $\Sigma(\omega)$.

Let us suppose that the self-energy data $\{\Sigma_0, \Sigma_1, \dots, \Sigma_{N-1}\}$ are known on a grid $\{\omega_0, \omega_1, \dots, \omega_{N-1}\}$. The integrated spectral weight can then be rewritten as

$$\begin{aligned} I_k(\omega_l) &= -\frac{1}{\pi} \text{Im} \int_{-\infty}^{\omega_l} \frac{d\nu}{\nu - \Sigma(\nu) - \varepsilon_k} \\ &\approx -\frac{1}{\pi} \text{Im} \sum_{q=0}^{l-1} \int_{\omega_q}^{\omega_{q+1}} \frac{d\nu}{\nu - \Sigma(\nu) - \varepsilon_k}. \end{aligned} \quad (\text{S32})$$

The delta peaks in Eq. (S32) occur whenever our subintegral function is (infinitely) close to the singularity, i.e. when $\text{Im}\Sigma(\nu) \rightarrow 0^-$ and $\nu - \text{Re}\Sigma(\nu) - \varepsilon_k \approx 0$. These are most easily taken into account by using the linear interpolation of the denominator in Eq. (S32) and evaluating the integral analytically

$$\begin{aligned} I_k(\omega_l) &\approx -\frac{1}{\pi} \text{Im} \sum_{q=0}^{l-1} \int_{\omega_q}^{\omega_{q+1}} \frac{d\nu}{\nu - \varepsilon_k - [\Sigma_q + \Sigma'_q(\nu - \omega_q)]} \\ &= -\frac{1}{\pi} \text{Im} \sum_{q=0}^{l-1} \frac{1}{1 - \Sigma'_q} \ln \left[\frac{\omega_{q+1} - \varepsilon_k - \Sigma_{q+1}}{\omega_q - \varepsilon_k - \Sigma_q} \right], \end{aligned} \quad (\text{S33})$$

where $\Sigma'_q = (\Sigma_{q+1} - \Sigma_q)/(\omega_{q+1} - \omega_q)$. In the last line of Eq. (S33) we used that $\ln x - \ln y = \ln(x/y)$, which holds since $\text{Im}\Sigma_q < 0$ (for every q).

In the limit when $\Delta\omega_q = \omega_{q+1} - \omega_q$ is small, Eq. (S33) predicts that the contribution which corresponds to the interval (ω_q, ω_{q+1}) is equal to

$$\frac{1}{1 - \frac{\Sigma_{q+1} - \Sigma_q}{\omega_{q+1} - \omega_q}} \approx \frac{1}{1 - \partial_\omega \Sigma}, \quad (\text{S34})$$

if the interval contains a delta peak, whereas it is

$$-\frac{1}{\pi} \text{Im} \left[\frac{\Delta\omega_q}{\omega_q - \varepsilon_k - \Sigma_q} \right] \quad (\text{S35})$$

otherwise. The analytical result for the contribution of the delta peak coincides with Eq. (S34), while Eq. (S35) is exactly the term we would get using the standard Riemann sum. Having in mind that the Riemann sum approach is completely justified in the absence of delta peaks, we conclude that the integration scheme presented in Eq. (S33) is perfectly well-suited for the calculation of the integrated spectral weight.

XI. TECHNICAL NOTE: EQUIVALENCE OF SPECTRAL FUNCTIONS FROM DIFFERENT DEFINITIONS

Throughout this paper we compared spectral and correlation functions obtained with various methods. Each method uses different definition of the spectral function. The purpose of this Section is to show that all of them are equivalent in the case we are considering, which is a single electron in a system. We also present the relation which connects the spectral function with the imaginary-time correlation function obtained from QMC calculation.

A. Spectral function from greater Green's function

In the HEOM method, the most natural starting point is the greater Green's function [S12]

$$G_{\mathbf{k}}^>(t) = -i \left\langle c_{\mathbf{k}}(t) c_{\mathbf{k}}^{\dagger} \right\rangle_{T,0}. \quad (\text{S36})$$

Here $c_{\mathbf{k}}$ and $c_{\mathbf{k}}^{\dagger}$ are the electron annihilation and creation operators, while

$$c_{\mathbf{k}}(t) = e^{iHt} c_{\mathbf{k}}(0) e^{-iHt}.$$

The notation $\langle \dots \rangle_{T,0}$ denotes the thermal average over the space of states containing zero electrons

$$\langle x \rangle_{T,0} = \frac{\sum_p \langle p | e^{-H_{\text{ph}}/T} x | p \rangle}{\sum_p \langle p | e^{-H_{\text{ph}}/T} | p \rangle} = \frac{1}{Z_p} \sum_p \langle p | e^{-H_{\text{ph}}/T} x | p \rangle. \quad (\text{S37})$$

Here $|p\rangle$ denotes the states containing no electrons and arbitrary number of phonons, H_{ph} is purely phononic part of the Hamiltonian and Z_p is the phononic partition function. The spectral function is now defined as

$$A_{\mathbf{k}}(\omega) = -\frac{1}{2\pi} \text{Im} G_{\mathbf{k}}^>(\omega), \quad (\text{S38})$$

where

$$G_{\mathbf{k}}^>(\omega) = \int_{-\infty}^{\infty} dt e^{i\omega t} G_{\mathbf{k}}^>(t). \quad (\text{S39})$$

These expressions can be cast into explicit form using the Lehmann spectral representation (using the basis of energy eigenstates $H|n\rangle = E_n|n\rangle$)

$$G_{\mathbf{k}}^>(t) = \frac{-i}{Z_p} \sum_{p,e} e^{-E_p/T} e^{iE_p t} \langle p | c_{\mathbf{k}} | e \rangle e^{-iE_e t} \langle e | c_{\mathbf{k}}^{\dagger} | p \rangle, \quad (\text{S40})$$

where $|e\rangle$ denotes the states containing one electron and an arbitrary number of phonons. The spectral function

can now be obtained by taking the Fourier transform of previous expression and using Eq. (S38)

$$A_{\mathbf{k}}(\omega) = \frac{1}{Z_p} \sum_p e^{-E_p/T} \sum_e \delta(\omega + E_p - E_e) |\langle p | c_{\mathbf{k}} | e \rangle|^2. \quad (\text{S41})$$

B. Spectral function from retarded and time-ordered Green's function

In the DMFT/SCMA, we can start from the time-ordered Green's function [S1] with just a single electron inserted into the system

$$G_{\mathbf{k}}(t) = -i \langle T c_{\mathbf{k}}(t) c_{\mathbf{k}}^{\dagger} \rangle_{T,0}. \quad (\text{S42})$$

As in the case of the greater Green's function, here we average only over the phonon degrees of freedom. This means that (S42) gives nonvanishing contribution only for $t > 0$

$$G_{\mathbf{k}}(t) = -i\theta(t) \langle c_{\mathbf{k}}(t) c_{\mathbf{k}}^{\dagger} \rangle_{T,0}. \quad (\text{S43})$$

In our case of a single electron in the system, this coincides with the retarded Green's function. Ref [S1] explains in detail how is this connected to the polaron impurity problem. Now, the spectral function can be obtained as

$$A_{\mathbf{k}}(\omega) = -\frac{1}{\pi} \text{Im} G_{\mathbf{k}}(\omega), \quad (\text{S44})$$

where

$$G_{\mathbf{k}}(\omega) = \lim_{\varepsilon \rightarrow 0^+} \int_{-\infty}^{\infty} dt e^{i(\omega+i\varepsilon)t} G_{\mathbf{k}}(t). \quad (\text{S45})$$

Let us now check whether the definitions of spectral functions from Secs. XIA and XIB are in agreement with one another. This can be easily checked by utilizing the Lehmann spectral representation

$$G_{\mathbf{k}}(t) = \frac{-i\theta(t)}{Z_p} \sum_{p,e} e^{-E_p/T} e^{i(E_p-E_e)t} |\langle p | c_{\mathbf{k}} | e \rangle|^2. \quad (\text{S46})$$

The spectral function is now obtained by performing the Fourier transform, using Eq. (S44) and the Plemelj-Sokhotski theorem $\text{Im} \lim_{\varepsilon \rightarrow 0^+} \frac{1}{x+i\varepsilon} = -\pi\delta(x)$. We obtain the result which coincides with (S41). Furthermore, these results also coincide with Eq. (S23). This confirms that all of these approaches are consistent with one another.

C. Spectral function from grand canonical ensemble

It is also quite common to work within the grand canonical ensemble, not restricting ourselves explicitly to a single electron in a system. Here we use the usual definition of the retarded Green's function

$$G_{\mathbf{k}}(t) = -i\theta(t) \left\langle \left\{ c_{\mathbf{k}}(t), c_{\mathbf{k}}^\dagger \right\} \right\rangle_T, \quad (\text{S47})$$

where

$$c_{\mathbf{k}}(t) = e^{iKt} c_{\mathbf{k}} e^{-iKt}, \quad (\text{S48})$$

$K = H - \mu N$ and N being the electron number operator. The notation $\langle \dots \rangle_T$ denotes the average value in the grand canonical ensemble and $\{, \}$ is the anticommutator. The spectral function is obtained by substituting $G_{\mathbf{k}}(t)$ from (S47) into Eqs. (S45) and (S44). A more explicit form can be obtained using the Lehmann spectral representation (using the basis of energy eigenstates $K|n\rangle = K_n|n\rangle$)

$$A_{\mathbf{k}}(\omega) = \frac{1}{Z} \sum_{n_1 n_2} e^{-\beta K_{n_1}} \left[|\langle n_1 | c_{\mathbf{k}} | n_2 \rangle|^2 \delta(K_{n_1} - K_{n_2} + \omega) + |\langle n_1 | c_{\mathbf{k}}^\dagger | n_2 \rangle|^2 \delta(K_{n_2} - K_{n_1} + \omega) \right], \quad (\text{S49})$$

where $Z = \text{Tr}(e^{-\beta K})$ is the partition function. Let us now consider what happens in the case we are interested in, which is the zero density limit. This corresponds to $\mu \rightarrow -\infty$.

We note first that the dominant terms in the partition function Z in this limit are from the states with zero electrons

$$Z = \sum_n e^{-\beta K_n} = \sum_p e^{-\beta K_p} = Z_p. \quad (\text{S50})$$

The states containing a larger number of electrons introduce an additional term $e^{\beta\mu N}$ which is exponentially small when $\mu \rightarrow -\infty$. Consequently, we have shown that Z from Eq. (S49) is the same as Z_p from Eq. (S41) in the limit $\mu \rightarrow -\infty$.

Next, we consider the sum in Eq. (S49). Due to the $e^{-\beta K_{n_1}}$ factor, the dominant contribution to the sum over n_1 comes from the states $|n_1\rangle$ containing zero electrons. The states containing a larger number of electrons introduce an additional term $e^{\beta\mu N}$ which is exponentially small when $\mu \rightarrow -\infty$. Therefore, the sum over n_1 in Eq. (S49) can be replaced by a sum over p , where $|p\rangle$ denote the states containing no electrons. The second term containing $\langle n_1 | c_{\mathbf{k}}^\dagger | n_2 \rangle$ in Eq. (S49) is then

zero, while the first term containing $\langle n_1 | c_{\mathbf{k}} | n_2 \rangle$ is different from zero only when $|n_2\rangle$ is the state containing one electron. The sum in Eq. (S49) then reads as

$$A_{\mathbf{k}}(\omega) = \frac{1}{Z_p} \sum_{p,e} e^{-\beta K_p} |\langle p | c_{\mathbf{k}} | e \rangle|^2 \delta(K_p - K_e + \omega), \quad (\text{S51})$$

We further note that the last equation can be also expressed in the form

$$A_{\mathbf{k}}(\omega - \mu) = \frac{1}{Z_p} \sum_{p,e} e^{-\beta E_p} |\langle p | c_{\mathbf{k}} | e \rangle|^2 \delta(E_p - E_e + \omega). \quad (\text{S52})$$

The right hand side in previous equation coincides with Eq. (S41). This proves that the spectral function within the grand canonical formalism needs to be considered in the limit $\mu \rightarrow -\infty$ and also the result needs to be shifted $A_{\mathbf{k}}(\omega) \rightarrow A_{\mathbf{k}}(\omega - \mu)$ if we want our result to coincide with Eq. (S41).

All of these results give us to flexibility to work within different formalisms knowing that all of them give the same result. Hence, we proved that the definitions of spectral functions within HEOM, DMFT, SCMA and ED are all in agreement.

D. Relation between the spectral function and imaginary-time correlation function

In QMC we calculate the quantity

$$C_{\mathbf{k}}(\tau) = \langle c_{\mathbf{k}}(\tau) c_{\mathbf{k}}^\dagger \rangle_{T,0}, \quad (\text{S53})$$

where

$$c_{\mathbf{k}}(\tau) = e^{\tau H} c_{\mathbf{k}} e^{-\tau H}. \quad (\text{S54})$$

Again, using the Lehmann spectral representation in Eq. (S53) we get

$$C_{\mathbf{k}}(\tau) = \frac{1}{Z_p} \sum_{p,e} e^{-\beta E_p} |\langle p | c_{\mathbf{k}} | e \rangle|^2 e^{\tau(E_p - E_e)}. \quad (\text{S55})$$

By performing straightforward integration, one then finds from Eqs. (S41) and (S55)





$$C_{\mathbf{k}}(\tau) = \int_{-\infty}^{\infty} d\omega e^{-\omega\tau} A_{\mathbf{k}}(\omega). \quad (\text{S56})$$

This proves Eq. (S28), which connects the correlation functions from QMC with spectral functions, obtained from other methods.


[S1] S. Ciuchi, F. de Pasquale, S. Fratini, and D. Feinberg, *Phys. Rev. B* **56**, 4494 (1997).

- [S2] A. Georges, G. Kotliar, W. Krauth, and M. J. Rozenberg, *Rev. Mod. Phys.* **68**, 13 (1996).
- [S3] R. M. Martin, L. Reining, and D. M. Ceperley, *Interacting Electrons: Theory and Computational Approaches* (Cambridge University Press, 2016).
- [S4] G. Mahan, *Many-Particle Physics* (Kluwer Academic, New York, 2000).
- [S5] O. S. Barišić, *Phys. Rev. B* **76**, 193106 (2007).
- [S6] P. E. Kornilovitch, *Phys. Rev. Lett.* **81**, 5382 (1998).
- [S7] A. H. Romero, D. W. Brown, and K. Lindenberg, *J. Comp. Phys.* **109**, 6540 (1998).
- [S8] L.-C. Ku, S. A. Trugman, and J. Bonča, *Phys. Rev. B* **65**, 174306 (2002).
- [S9] A. Migdal, *Zh. Eksp. Teor. Fiz.* **34**, 1438 (1958), [*Sov. Phys. JETP* **7**, 996 (1958)].
- [S10] I. Lang and Y. A. Firsov, *Zh. Eksp. Teor. Fiz.* **43**, 1843 (1962), [*Sov. Phys. JETP* **16**, 1301 (1963)].
- [S11] J. Bonča, S. A. Trugman, and M. Berciu, *Phys. Rev. B* **100**, 094307 (2019).
- [S12] V. Janković and N. Vukmirović, *Phys. Rev. B* **105**, 054311 (2022).

Cumulant expansion in the Holstein model: Spectral functions and mobility

Petar Mitrić , Veljko Janković , Nenad Vukmirović , and Darko Tanasković 

Institute of Physics Belgrade, University of Belgrade, Pregrevica 118, 11080 Belgrade, Serbia

 (Received 29 December 2022; revised 6 March 2023; accepted 17 March 2023; published 30 March 2023)

We examine the range of validity of the second-order cumulant expansion (CE) for the calculation of spectral functions, quasiparticle properties, and mobility of the Holstein polaron. We devise an efficient numerical implementation that allows us to make comparisons in a broad interval of temperature, electron-phonon coupling, and phonon frequency. For a benchmark, we use the dynamical mean-field theory which gives, as we have recently shown, rather accurate spectral functions in the whole parameter space, even in low dimensions. We find that in one dimension, the CE resolves well both the quasiparticle and the first satellite peak in a regime of intermediate coupling. At high temperatures, the charge mobility assumes a power law $\mu \propto T^{-2}$ in the limit of weak coupling and $\mu \propto T^{-3/2}$ for stronger coupling. We find that, for stronger coupling, the CE gives slightly better results than the self-consistent Migdal approximation (SCMA), while the one-shot Migdal approximation is appropriate only for a very weak electron-phonon interaction. We also analyze the atomic limit and the spectral sum rules. We derive an analytical expression for the moments in CE and find that they are exact up to the fourth order, as opposed to the SCMA where they are exact to the third order. Finally, we analyze the results in higher dimensions.

DOI: [10.1103/PhysRevB.107.125165](https://doi.org/10.1103/PhysRevB.107.125165)

I. INTRODUCTION

The cumulant expansion (CE) method presents an alternative to the usual Dyson equation approach in the calculation of spectral functions of interacting quantum many-particle systems [1]. In this method, we express the Green's function in real time as an exponential function of an auxiliary quantity $C(t)$, called the cumulant, which can be calculated perturbatively [2]. In the late 1960s, it was established that the lowest order CE gives the exact solution of the problem of a core hole coupled to bosonic excitations (plasmons or phonons) [3,4]. While there were early papers that emphasized the potential role of CE as an approximate method to treat the electronic correlations in metals beyond the GW approximation [5–8] and the electron-phonon interaction in semiconductors and narrow band metals beyond the Migdal approximation (MA) [9–11], a surge of studies of CE has appeared only recently.

Renewed interest has emerged due to the possibility of combining CE with *ab initio* band-structure calculations. The CE for the electron-phonon interaction was used to obtain the spectral functions of several doped transition-metal oxides [12,13], showing a favorable comparison with angle-resolved photoemission spectroscopy [14]. A particularly appealing feature of the CE approach is that it describes the quasiparticle part of the spectrum as well as the satellite structure (sidebands). Combining the CE with the Kubo formula for charge transport gives an attractive route to calculate mobility in semiconductors beyond the Boltzmann approach, which is applicable only for weak electron-phonon coupling [15]. This was very recently demonstrated for SrTiO₃ [16] and naphthalene [17]. CE was also applied to elemental metals where a correction to the standard MA is discussed [18]. Similarly, the CE is successfully used to treat the electronic correlations beyond the GW approximation [19–25]. Further-

more, CE was used to study absorption spectra in molecular aggregates representative of photosynthetic pigment-protein complexes [26–28].

Despite the wide use of the lowest order CE, there seems to be a lack of studies establishing its range of validity, which represents the central motivation for this paper. To achieve this, we turn to simplified models of the electron-phonon interaction. CE for the Fröhlich model [29,30] gives the ground-state energy and the effective mass similar to the exact quantum Monte Carlo calculations for moderate interaction [31]. This is in contrast to the Dyson-Migdal approach, which severely underestimates mass renormalization. A comparison of the corresponding spectral functions is, however, missing, since reliable quantum Monte Carlo results are not available due to the well-known problems with analytical continuation. The Holstein polaron model gives a unique opportunity to explore the applicability of the CE since various numerically exact methods are developed and applied to this model covering different parameter regimes [32–49]. This was the approach of a very recent work by Reichman and collaborators [50,51]. Still, there are several questions that remained unresolved. Most importantly, a comparison of spectral functions was made just for a small set of parameters on a finite-size lattice, where the benchmark spectral functions were available from the finite-temperature Lanczos results, while the charge transport was not examined.

In our recent work [52], we established that the dynamical mean-field theory (DMFT) [53] gives close to exact spectral functions of the Holstein polaron for different phonon frequencies, electron-phonon couplings, and temperatures even in low dimensions, covering practically the whole parameter space. This method is computationally very fast and precise, which makes us ideally positioned to perform comprehensive comparisons with the CE method, which is the goal of

this paper. Within the CE, we calculate the spectral functions and charge mobility for a broad set of parameters and make detailed comparisons with DMFT and (self-consistent) MA. We find that the one-shot MA is appropriate only for very weak electron-phonon coupling. The validity of the CE and self-consistent Migdal approximation (SCMA) is much broader and for intermediate interaction CE even outperforms SCMA. We also derive analytical CE expressions for the ground-state energy, renormalized mass, and scattering rate as well as the spectral sum rules, and make comparisons between the methods. We establish a power-law behavior for the charge mobility at high temperatures. We also compare the performance of different methods as the bandwidth is reduced toward the atomic limit.

The remaining part of the paper is organized as follows. In Sec. II, we introduce the CE method and present details of its implementation on the Holstein model. DMFT and SCMA are here introduced as benchmark methods. Representative spectral functions are shown in Sec. III from weak toward the strong coupling. The high-temperature and atomic limits are analyzed in detail, as well as the spectral sum rules. In Sec. IV, we present the results for the effective mass and ground-state energy. The temperature dependence of the electron mobility is analyzed in Sec. V, and Sec. VI contains our conclusions. Some details concerning numerical implementations and additional figures for various parameters are shown in the Appendix and in the Supplemental Material (SM) [54].

II. MODEL AND METHODS

The Holstein model is the simplest model of the lattice electrons interacting with the phonons. It assumes a local electron-phonon interaction and dispersionless phonons. The Hamiltonian is given by

$$H = -t_0 \sum_{\langle ij \rangle} (c_i^\dagger c_j + \text{H.c.}) - g \sum_i n_i (a_i^\dagger + a_i) + \omega_0 \sum_i a_i^\dagger a_i. \quad (1)$$

Here, t_0 is the hopping parameter between the nearest neighbors and ω_0 is the phonon frequency. c_i and a_i are the electron and the phonon annihilation operators, $n_i = c_i^\dagger c_i$, and g denotes the electron-phonon coupling strength. We set \hbar, k_B , elementary charge e , and lattice constant to 1. We also often use a parameter $\alpha = g/\omega_0$. We study the model in the thermodynamic limit (number of sites $N \rightarrow \infty$). Furthermore, we consider a dynamics of a single electron in the conduction band and treat the electrons as spinless, since we are interested only in weakly doped semiconductors. This is equivalent to setting the chemical potential far below the conduction band, i.e., considering the limit $\tilde{\mu} \rightarrow -\infty$. This case is often referred to as the Holstein polaron problem. We mostly focus on the one-dimensional (1D) system, but we also consider the system in 2D and 3D.

A. Cumulant expansion

1. General theory

The central quantity of this paper is the electron spectral function $A_{\mathbf{k}}(\omega) = (-1/\pi)\text{Im}G_{\mathbf{k}}(\omega)$, where \mathbf{k} is the momen-

tum and $G_{\mathbf{k}}(\omega)$ is the retarded Green's function in frequency domain [1]. Its exact evaluation is often a formidable task, which is why approximate techniques are usually employed. One needs to be careful with such approaches not to violate some analytic properties, such as the pole structure of the Green's function, the positivity of the spectral function, or the spectral sum rules. At least some of these properties can be easily satisfied if the Green's function is not calculated directly but instead through some auxiliary quantity, such as the self-energy $\Sigma_{\mathbf{k}}(\omega)$. In the latter case, the connection with the Green's function is established via the Dyson equation

$$G_{\mathbf{k}}(\omega) = \frac{1}{G_{\mathbf{k},0}(\omega)^{-1} - \Sigma_{\mathbf{k}}(\omega)} = \frac{1}{\omega - \varepsilon_{\mathbf{k}} - \Sigma_{\mathbf{k}}(\omega)}, \quad (2)$$

where $G_{\mathbf{k},0}(\omega)$ is the noninteracting Green's function and $\varepsilon_{\mathbf{k}}$ is the noninteracting dispersion relation.

An alternative to the Dyson equation based approaches is the so-called cumulant expansion method [19], in which the exponential ansatz is chosen for the Green's function in the time domain:

$$G_{\mathbf{k}}(t) = G_{\mathbf{k},0}(t)e^{C_{\mathbf{k}}(t)} = -i\theta(t)e^{-i\varepsilon_{\mathbf{k}}t}e^{C_{\mathbf{k}}(t)}. \quad (3)$$

Here, $\theta(t)$ is the Heaviside step function and $C_{\mathbf{k}}(t)$ plays the role of an auxiliary quantity which is called the cumulant. Both Eqs. (2) and (3) would correspond to the same Green's function in frequency and time domain if the cumulant $C_{\mathbf{k}}(t)$ and the self-energy $\Sigma_{\mathbf{k}}(\omega)$ could be evaluated exactly [1]. In practice, however, one of these approaches is expected to perform better. The spectral function within the CE can be obtained as follows:

$$A_{\mathbf{k}}(\omega + \varepsilon_{\mathbf{k}}) = \frac{1}{\pi} \text{Re} \int_0^\infty dt e^{i\omega t} e^{C_{\mathbf{k}}(t)}. \quad (4)$$

Equation (4) circumvents the Fourier transform of the whole Green's function $A_{\mathbf{k}}(\omega) = -\frac{1}{\pi}\text{Im}G_{\mathbf{k}}(\omega)$, which is useful in practice, as the free electron part $e^{-i\varepsilon_{\mathbf{k}}t}$ typically oscillates much more quickly than $e^{C_{\mathbf{k}}(t)}$.

The expression for $C_{\mathbf{k}}(t)$ in the lowest order perturbation expansion can be obtained by taking the leading terms in the Taylor expansion of the Dyson equation $G_{\mathbf{k}}(\omega) = (G_{\mathbf{k},0}(\omega)^{-1} - \Sigma_{\mathbf{k}}(\omega))^{-1} \approx G_{\mathbf{k},0}(\omega) + G_{\mathbf{k},0}(\omega)\Sigma_{\mathbf{k}}(\omega)G_{\mathbf{k},0}(\omega)$, taking its inverse Fourier transform and equating it to Eq. (3), where the cumulant in the exponent is replaced with its linear approximation $e^{C_{\mathbf{k}}(t)} \approx 1 + C_{\mathbf{k}}(t)$:

$$C_{\mathbf{k}}(t) = ie^{i\varepsilon_{\mathbf{k}}t} \int_{-\infty}^\infty \frac{d\omega}{2\pi} \frac{e^{-i\omega t} \Sigma_{\mathbf{k}}(\omega)}{(\omega - \varepsilon_{\mathbf{k}} + i0^+)^2}. \quad (5)$$

Using the spectral representation of the self-energy

$$\Sigma_{\mathbf{k}}(\omega) = \int \frac{d\nu}{\pi} \frac{|\text{Im}\Sigma_{\mathbf{k}}(\nu)|}{\omega - \nu + i0^+}, \quad (6)$$

and the contour integration over ω , Eq. (5) simplifies to [19]

$$C_{\mathbf{k}}(t) = \frac{1}{\pi} \int_{-\infty}^\infty d\omega \frac{|\text{Im}\Sigma_{\mathbf{k}}(\omega + \varepsilon_{\mathbf{k}})|}{\omega^2} (e^{-i\omega t} + i\omega t - 1). \quad (7)$$

The corresponding spectral function satisfies the first two sum rules, irrespective of $\Sigma_{\mathbf{k}}(\omega)$. This is a consequence of the behavior of $C_{\mathbf{k}}(t)$ for small t ; see Sec. III C. In general, $C_{\mathbf{k}}(t=0) = 0$ is sufficient for the first spectral sum rule $\int A_{\mathbf{k}}(\omega)d\omega = 1$ to be satisfied. The second sum rule

$\int A_{\mathbf{k}}(\omega)\omega d\omega = \varepsilon_{\mathbf{k}}$ can also be satisfied if we additionally impose that the cumulant's first derivative at $t = 0$ is vanishing, $\frac{dC_{\mathbf{k}}}{dt}(0) = 0$. Both of these conditions are satisfied by the cumulant function in Eq. (7), as it is a quadratic function of time for small arguments $e^{-i\omega t} + i\omega t - 1 \approx -\omega^2 t^2/2$ for $t \rightarrow 0$.

The application of Eq. (7) is facilitated by the fact that it does not contain any iterative self-consistent calculations. However, one needs to overcome the numerical challenges caused by the removable singularity at $\omega = 0$ and by the rapidly oscillating trigonometric factor $e^{-i\omega t}$ for large t . The latter is important for the weak electron-phonon couplings, where it is necessary to propagate $C_{\mathbf{k}}(t)$ up to long times until the Green's function is sufficiently damped out. The same problem occurs in other regimes as well (e.g., close to the atomic limit), where the Green's function does not attenuate at all; see Sec. II A 4.

The numerical singularity at $\omega = 0$ can be completely avoided if we consider the cumulant's second derivative

$$\frac{d^2 C_{\mathbf{k}}(t)}{dt^2} = \int_{-\infty}^{\infty} \frac{d\omega}{\pi} \text{Im} \Sigma_{\mathbf{k}}(\omega + \varepsilon_{\mathbf{k}}) e^{-i\omega t} \equiv 2e^{i\varepsilon_{\mathbf{k}} t} \tilde{\sigma}_{\mathbf{k}}(t), \quad (8)$$

where we used $\text{Im} \Sigma_{\mathbf{k}}(\omega) < 0$ and introduced $\tilde{\sigma}_{\mathbf{k}}(t) \equiv \int_{-\infty}^{\infty} \text{Im} \Sigma_{\mathbf{k}}(\omega) e^{-i\omega t} \frac{d\omega}{2\pi}$. Then, $C_{\mathbf{k}}(t)$ is obtained as a double integral over time of Eq. (8),

$$C_{\mathbf{k}}(t) = 2 \int_0^t dt' \int_0^{t'} dt'' e^{i\varepsilon_{\mathbf{k}} t''} \tilde{\sigma}_{\mathbf{k}}(t''), \quad (9)$$

where the lower boundaries of both integrals have to be zero, as guaranteed by the initial conditions $C_{\mathbf{k}}(0) = \frac{dC_{\mathbf{k}}}{dt}(0) = 0$. Using the Cauchy formula for repeated integration, this can also be written as a single integral:

$$C_{\mathbf{k}}(t) = 2 \int_0^t (t-x) e^{i\varepsilon_{\mathbf{k}} x} \tilde{\sigma}_{\mathbf{k}}(x) dx. \quad (10)$$

This completely removed the problem of numerical singularities. Still, the problem of rapid oscillations of the subintegral function remains due to the presence of $e^{i\varepsilon_{\mathbf{k}} x}$ term. In Sec. II A 3, we provide an elegant solution for this issue, focusing on the case of the Holstein model.

2. Asymptotic expansion for cumulant when $t \rightarrow \infty$

The asymptotic expansion of $C_{\mathbf{k}}(t)$ for large times, as we now demonstrate, completely determines the quasiparticle properties within this method. This is one of the main motivations for studying the $t \rightarrow \infty$ limit. From Eq. (8), we see that

$$\begin{aligned} i \frac{dC_{\mathbf{k}}}{dt}(t \rightarrow \infty) &= i \int_0^{\infty} \frac{d^2 C_{\mathbf{k}}(t)}{dt^2} dt \\ &= -\frac{i}{\pi} \int_{-\infty}^{\infty} d\omega |\text{Im} \Sigma_{\mathbf{k}}(\omega + \varepsilon_{\mathbf{k}})| \int_0^{\infty} dt e^{-i\omega t} \\ &= \Sigma_{\mathbf{k}}(\varepsilon_{\mathbf{k}}), \end{aligned} \quad (11)$$

where we used the identity $\int_0^{\infty} dt e^{-i\omega t} = \pi \delta(\omega) - i\mathcal{P} \frac{1}{\omega}$ and the Kramers-Kronig relations for the self-energy. Hence, the cumulant function $C_{\mathbf{k}}(t)$, and also the whole exponent in Eq. (3) is a linear function of time $C_{\mathbf{k}}(t) - i\varepsilon_{\mathbf{k}} t \approx -i\tilde{E}_{\mathbf{k}} t +$

const for $t \rightarrow \infty$, where

$$\tilde{E}_{\mathbf{k}} = \varepsilon_{\mathbf{k}} + \Sigma_{\mathbf{k}}(\varepsilon_{\mathbf{k}}). \quad (12)$$

As a consequence, the Green's function in Fourier space has a simple pole situated at $\tilde{E}_{\mathbf{k}}$, as seen from the following expression:

$$G_{\mathbf{k}}(\omega) = -i \int_0^{\infty} e^{it(\omega - \varepsilon_{\mathbf{k}} - \frac{iC_{\mathbf{k}}(t)}{t})} dt. \quad (13)$$

Therefore, quasiparticle properties are encoded in $\tilde{E}_{\mathbf{k}}$: its real and imaginary parts correspond to the quasiparticle energy and scattering rate, respectively. We note that, in our present analysis, we implicitly assumed that $\frac{dC_{\mathbf{k}}}{dt}(t \rightarrow \infty)$ exists and is finite. Although this is generally true, there are a few exceptions. In the Holstein model, the first assumption is violated at the atomic limit [$t_0 = 0$; see Eq. (28)], while the second assumption is violated at the adiabatic limit ($\omega_0 = 0$) for $k = 0$ or $k = \pm\pi$; see Eqs. (18) or (19).

The knowledge that we gained about the analytic properties of the $C_{\mathbf{k}}(t)$ provides us with an intuitive understanding of how the shape of the cumulant determines the shape of the spectral function. The asymptotic limits $t \rightarrow \infty$ [where $C_{\mathbf{k}}(t)$ is linear] and $t \rightarrow 0$ [where $C_{\mathbf{k}}(t)$ is quadratic] by themselves, to a large extent, describe only the simple one-peak spectral functions, while the crossover between these limits is responsible for the emergence of satellite peaks. This can be explained as follows: If the cumulant was quadratic over the whole t domain $C_{\mathbf{k}}(t) = ct^2$, the spectral function would have a simple Gaussian shape. Similarly, the Lorentzian shape would be obtained from the linear cumulant $C_{\mathbf{k}}(t) = ct$. This suggests that the simple crossover between quadratic (at small t) and linear (at large t) behaviors would also give a simple one-peak shape of the spectral function. The information about phonon satellites is thus completely encoded in the $C_{\mathbf{k}}(t)$ for intermediate times t , which depends on the system and approximation in which the cumulant function is calculated.

3. Second-order cumulant expansion for the Holstein model

Let us now concentrate on a specific example, the Holstein model on a hypercubic lattice in n dimensions. The second-order cumulant is given by Eq. (7), where the self-energy is taken to be in the MA $\Sigma_{\mathbf{k}}(\omega) = \Sigma^{\text{MA}}(\omega)$, i.e., of the second (lowest) order with respect to the electron-phonon coupling g . This is in accordance with the derivation from Sec. II A 1, since we restricted ourselves to the lowest order terms in the Taylor expansion of the Dyson equation and of $e^{C_{\mathbf{k}}(t)}$. An alternative derivation of this expression is given in Sec. I of the SM [54]. MA is briefly discussed in Sec. II B 1. For our present purpose, we only need the expression for the imaginary part of the self-energy

$$\text{Im} \Sigma^{\text{MA}}(\omega) = -\pi g^2 [(n_{\text{ph}} + 1)\rho(\omega - \omega_0) + n_{\text{ph}}\rho(\omega + \omega_0)], \quad (14)$$

where $n_{\text{ph}} = 1/(e^{\omega_0/T} - 1)$ is the Bose factor, $\rho(\omega) = \frac{1}{N} \sum_{\mathbf{k}} \delta(\omega - \varepsilon_{\mathbf{k}})$ is the density of electron states for the system of size N , which we take in the thermodynamic limit $N \rightarrow \infty$, and $\varepsilon_{\mathbf{k}} = -2t_0 \sum_{j=1}^n \cos k_j$ is the noninteracting dispersion relation.

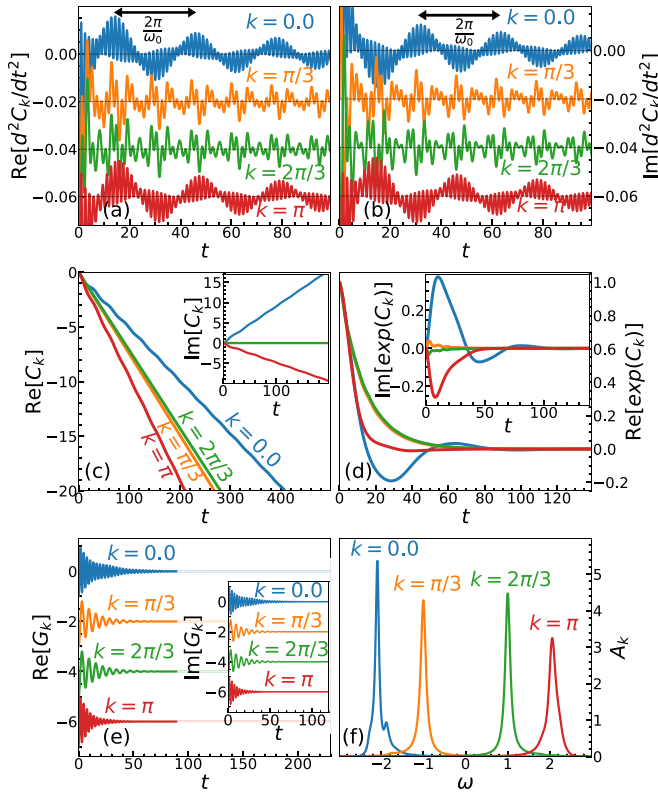


FIG. 1. (a)–(f) The cumulant, Green’s, and spectral function on the example of the one-dimensional Holstein model with the following values of the model parameters: $\omega_0 = 0.2$, $g = 0.2$, $T = 0.3$, and $t_0 = 1$.

The expression for the cumulant function, as seen from Eq. (10), is related to the inverse Fourier transform of $\text{Im}\Sigma^{\text{MA}}(\omega)$, which in turn is completely determined by the inverse Fourier transform of the density of states $\tilde{\rho}(t)$. The latter admits a closed-form solution

$$\begin{aligned} \tilde{\rho}(t) &= \int_{-\infty}^{\infty} \frac{d\omega e^{-i\omega t}}{(2\pi)^{n+1}} \int_{[0, 2\pi]^n} d^n \mathbf{k} \delta\left(\omega + 2t_0 \sum_{j=1}^n \cos k_j\right) \\ &= \frac{1}{2\pi} \left(\frac{1}{2\pi} \int_0^{2\pi} dk e^{2it_0t \cos k} \right)^n = \frac{J_0(2t_0t)^n}{2\pi}, \end{aligned} \quad (15)$$

where J_0 is the Bessel function of the first kind of order zero. Hence, Eqs. (10), (14), and (15) imply that the cumulant function can be written as

$$C_k(t) = -g^2 \int_0^t dx (t-x) iD(x) e^{ix\varepsilon_k} J_0(2t_0x)^n, \quad (16)$$

where $iD(t) = (n_{\text{ph}} + 1)e^{-i\omega_0 t} + n_{\text{ph}}e^{i\omega_0 t}$ is the phonon propagator in real time (for $t > 0$). In Fig. 1, we illustrate the cumulant function, as well as the corresponding Green’s function and spectral function. Figures 1(a) and 1(b) show the second derivative of the cumulant

$$\frac{d^2 C_k(t)}{dt^2} = -g^2 iD(t) e^{it\varepsilon_k} J_0(2t_0t)^n \quad (17)$$

to demonstrate the rapid oscillations that are also present in the cumulant itself. These are not easily observed by inspect-

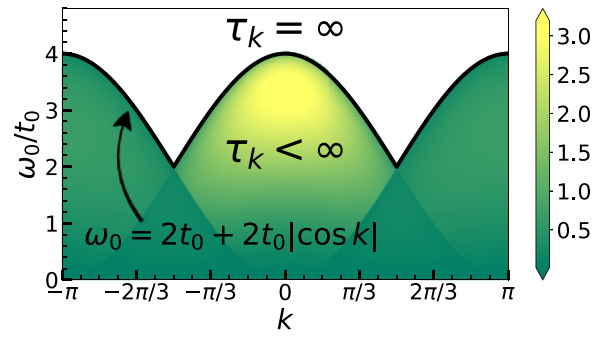


FIG. 2. Quasiparticle lifetime τ_k in the CE method for $T/t_0 = 2$ and $g/t_0 = 1$.

ing $C_k(t)$ directly, as the linear behavior dominates for large times. We observe that the $k = 0$ and $k = \pi$ results possess an oscillating envelope with period $2\pi/\omega_0$, while intermediate momenta have a much less regular structure. This can have direct consequences on the spectral functions, as the satellite peaks are expected to be at a distance ω_0 from each other. To be more explicit, oscillating envelopes suggest that there is a much higher chance for the occurrence of satellite peaks near the bottom ($k \approx 0$) and the top ($k \approx \pi$) of the band, than otherwise. However, that does not guarantee that the satellite peaks will in fact occur. Figure 1(c) shows that $\text{Re}C_k(t)$ is declining faster for $k > 0$ than for $k = 0$. As a consequence, $e^{C_k(t)}$ in Fig. 1(d) attenuates slower for $k = 0$, having enough time to complete a full period, while $k = \pi$ results are reminiscent of an overdamped oscillator. A similar, although much less evident, effect can be seen in the Green’s function itself; see Fig. 1(e). This is why the $k = \pi$ spectral function in Fig. 1(f) has a simple one-peak shape, while only the $k = 0$ result captures one small satellite peak.

From a numerical point of view, Eq. (16) is treated using Levin’s collocation method [55], which is reviewed in Appendix A. It provides a controlled, accurate, and numerically efficient way to integrate the product of trigonometric, Bessel, and some slowly varying function. This approach avoids using a dense t grid, which would otherwise be required, as the subintegral function in Eq. (16) has the same type of rapid oscillations present in $d^2 C_k(t)/dt^2$.

4. Lifetime

Another question of practical importance is how long we should propagate the cumulant function in real time until the corresponding Green’s function attenuates. A rough estimate of such quantity is given by the quasiparticle lifetime τ_k . The lifetime is given by $\tau_k = 1/(2|\text{Im}\tilde{E}_k|)$, where \tilde{E}_k is given by Eq. (12) and the self-energy is taken in the MA [see Eq. (14)]:

$$\begin{aligned} \tau_k^{-1} &= 2|\text{Im}\tilde{E}_k| = 2g^2 \frac{\theta(4t_0^2 - (\varepsilon_k - \omega_0)^2)}{\sqrt{4t_0^2 - (\varepsilon_k - \omega_0)^2}} (n_{\text{ph}} + 1) \\ &\quad + 2g^2 \frac{\theta(4t_0^2 - (\varepsilon_k + \omega_0)^2)}{\sqrt{4t_0^2 - (\varepsilon_k + \omega_0)^2}} n_{\text{ph}}. \end{aligned} \quad (18)$$

This is illustrated in Fig. 2. We observe that there is a considerable part of the parameter space where the lifetime is

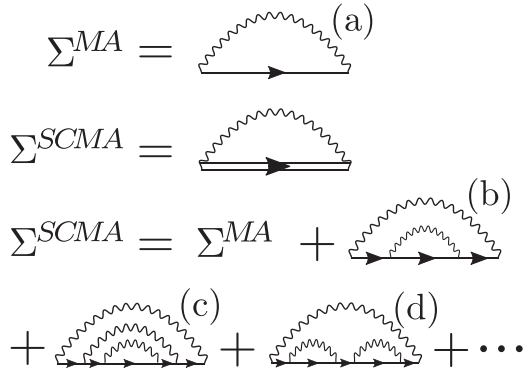


FIG. 3. Feynman diagrams in the Migdal approximation and the self-consistent Migdal approximation.

infinite, which means that the corresponding Green's function never attenuates. This occurs for $\omega_0 > 2t_0 + 2t_0|\cos k|$ in the case of finite temperatures, and for $\omega_0 > 4t_0 \sin^2 k/2$ in the $T = 0$ case. In these regimes, one could presume that this is reflected in the spectral functions through the appearance of Dirac delta peaks, which is not expected at finite temperatures. This illustrates one of the limitations of this method.

B. Benchmark methods

1. Migdal and self-consistent Migdal approximation

The Migdal approximation [56] is the simplest perturbation approach, whose self-energy is represented with a single, lowest order Feynman diagram, as shown in Fig. 3(a). The imaginary part of the self-energy is given by Eq. (14) in the case when there is just a single electron in the band, regardless of the dispersion relation or the number of dimensions of the system. The corresponding real part is obtained using the Kramers-Kronig relations, and in 1D reads as

$$\begin{aligned} \text{Re}\Sigma^{\text{MA}}(\omega) = & g^2(n_{\text{ph}} + 1) \frac{\theta((\omega - \omega_0)^2 - 4t_0^2)\text{sgn}(\omega - \omega_0)}{\sqrt{(\omega - \omega_0)^2 - 4t_0^2}} \\ & + g^2 n_{\text{ph}} \frac{\theta((\omega + \omega_0)^2 - 4t_0^2)\text{sgn}(\omega + \omega_0)}{\sqrt{(\omega + \omega_0)^2 - 4t_0^2}}. \end{aligned} \quad (19)$$

The range of validity of the MA can be extended if we substitute the noninteracting electron propagator in Fig. 3(a) with an interacting one. At the same time, the interacting propagator itself is expressed through the self-energy via the Dyson equation. These relations constitute the SCMA. Figure 3 illustrates that the SCMA self-energy consists of a series of noncrossing diagrams, whose lowest order coincides with the MA. Figure 3(b) shows the second-order contribution, while the third-order contributions are shown in Figs. 3(c) and 3(d).

Mathematically, the self-consistency relations are straightforwardly derived and, in our case, read as

$$\Sigma^{\text{SCMA}}(\omega) = g^2(n_{\text{ph}} + 1)G(\omega - \omega_0) + g^2 n_{\text{ph}}G(\omega + \omega_0), \quad (20a)$$

$$G(\omega) = \frac{1}{(2\pi)^n} \int_{-\pi}^{\pi} d^n \mathbf{k} \frac{1}{\omega - \varepsilon_{\mathbf{k}} - \Sigma^{\text{SCMA}}(\omega)}, \quad (20b)$$

where $G(\omega)$ is the local Green's function. We see that in the case of the Holstein model, the SCMA self-energy is \mathbf{k} independent.

2. Dynamical mean-field theory

Dynamical mean-field theory is a nonperturbative approximate method, that represents a natural generalization of the traditional mean-field theory [57]. It simplifies the original lattice problem by mapping it to a single site impurity problem, embedded into an external bath that is described with a frequency-dependent (i.e., dynamical) field $G_0(\omega)$, which needs to be determined self-consistently. This simplification is reflected on the self-energy, which is assumed to be \mathbf{k} -independent $\Sigma_{\mathbf{k}}(\omega) = \Sigma(\omega)$. The DMFT becomes exact in the limit of infinite dimensions or, equivalently, infinite coordination number.

In practice, $G_0(\omega)$ and $\Sigma(\omega)$ are determined self-consistently, by imposing that the local Green's function of the lattice problem

$$G(\omega) = \int_{-\infty}^{\infty} \frac{\rho(\epsilon)d\epsilon}{\omega - \Sigma(\omega) - \epsilon}, \quad (21)$$

and the self-energy $\Sigma(\omega)$ coincide with the corresponding quantities of the impurity problem. Here, $\rho(\epsilon)$ is the noninteracting density of states. The self-consistent loop is closed using the Dyson equation $G_0(\omega) = (G^{-1}(\omega) + \Sigma(\omega))^{-1}$. In the case of the Holstein model, the (polaron) impurity problem can be solved exactly, directly on the real-frequency axis, in terms of the continued fraction expansion [53]. Furthermore, in the one-dimensional case, Eq. (21) assumes a closed-form solution and reads as

$$G(\omega) = \text{Re} \frac{1}{2t_0 B(\omega) \sqrt{1 - \frac{1}{B(\omega)^2}}} + i \text{Im} \frac{-i}{2t_0 \sqrt{1 - B(\omega)^2}}, \quad (22)$$

where $B(\omega) = (\omega - \Sigma(\omega))/(2t_0)$; see Supplemental Material of Ref. [52]. We note that Eq. (22) can also be used for the SCMA in Eq. (20).

We have very recently shown [52], by using extensive comparisons with several numerically exact methods covering various parameter regimes, that the DMFT can provide a rather accurate solution for the Holstein polaron even in low dimension. Hence, the DMFT has emerged as a unique numerical method that gives close to exact spectral functions in practically the whole space of parameters, irrespective of the number of dimensions. This makes the DMFT an ideal benchmark method for comparisons with the CE results for the Holstein model.

III. SPECTRAL FUNCTIONS

In this section, we present the CE spectral functions of the 1D Holstein model. The DMFT is used as a benchmark, while MA and SCMA represent the main competitors and alternatives to the CE method. Section III A shows the results for $k = 0$, whereas heat plots and the $k = \pi$ results are shown in Sec. III B. High-temperature spectral functions and spectral sum rules are presented in Sec. III C. The behavior near the atomic limit is discussed in Sec. III D. We present only

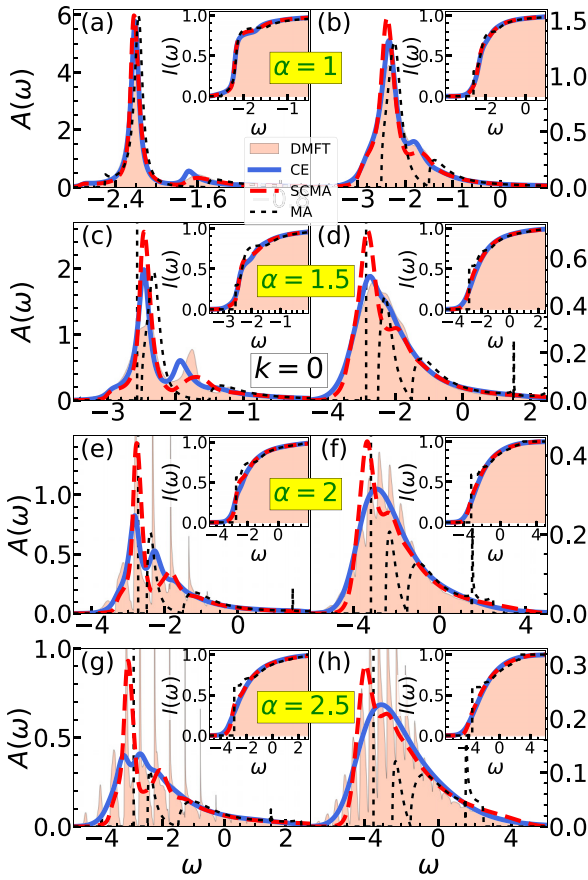


FIG. 4. (a)–(h) Spectral functions for $t_0 = 1$, $\omega_0 = 0.5$ and $k = 0$. In the left panels $T = 0.3$, while $T = 0.7$ in the right panels. Insets show the integrated spectral weights $I_k(\omega) = \int_{-\infty}^{\omega} A_k(v) dv$.

the results for $\omega_0 = 0.5$, while the results for other phonon frequencies and various momenta are shown in Sec. II of SM [54]. The 2D spectral functions are presented in Appendix B.

A. Low and intermediate temperatures for $k = 0$

In the weak-coupling limit $\alpha \rightarrow 0$, all these approximate methods (DMFT, CE, SCMA, MA) provide accurate results. In Fig. 4, we investigate how far from this strict limit each of our methods continues to give reasonably accurate spectral functions. In Fig. 4(a), we see that for $\alpha = 1$ all methods correctly capture the quasiparticle peak, which dominates in the structure of the spectrum. The MA satellite peak is slightly shifted towards higher frequencies, which becomes significantly more pronounced at higher temperatures; see Fig. 4(b). The limitations of the MA become more obvious for stronger couplings, where even the position and weight of the quasiparticle peak are inaccurate; see Figs. 4(c)–4(h).

While the quasiparticle properties of the CE and SCMA seem to be quite similar if α is not too large, some difference in satellite peaks is already visible in Figs. 4(b) and 4(c). Figure 4(c) shows that SCMA gives broader satellites than the DMFT benchmark, whereas CE slightly underestimates the position of the satellite. Neither CE nor SCMA can be characterized as distinctly better in this regime. On the other hand, Figs. 4(e) and 4(g) display a clear advantage of the CE.

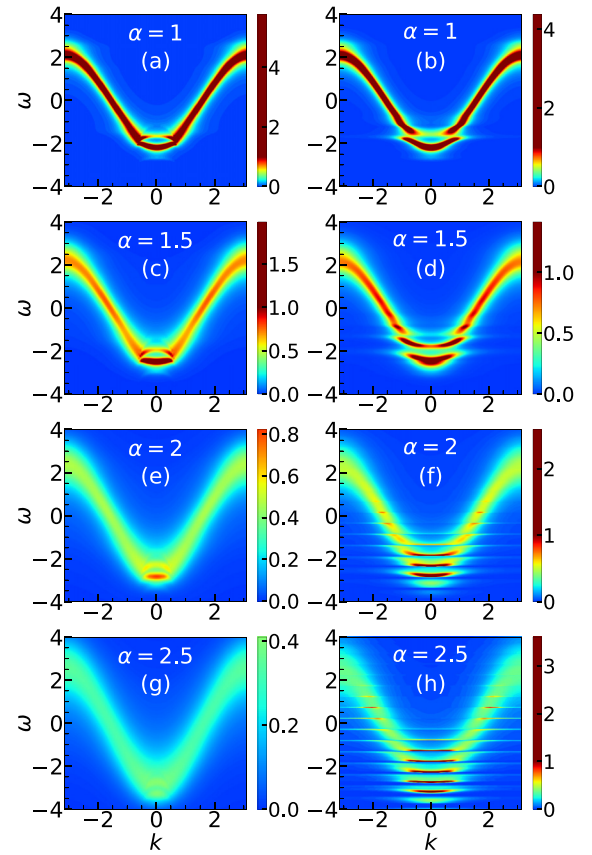


FIG. 5. (a)–(h) Heat maps of $A_k(\omega)$ for $t_0 = 1$, $\omega_0 = 0.5$, and $T = 0.3$. In the left panels, we present CE results, while the DMFT benchmark is presented in the right panel. All plots use the same color coding.

We see that it captures rather well the most distinctive features of the solutions, which are the first few satellites. This is not the case for SCMA.

Figures 4(f) and 4(h) demonstrate that the CE gives a rather quick crossover toward the high-temperature limit, as it predicts a simple broad one-peak structure for the spectral function already for $T = 0.7$. This large difference between the spectral functions for $T_1 = 0.3$ and $T_2 = 0.7$ can be understood by examining the ratio of their corresponding lifetimes $\tau(T_1)/\tau(T_2) = n_{\text{ph}}(T_2)/n_{\text{ph}}(T_1) \approx 8.5$. This implies that $\text{Re}C_k(t)$ for $T = 0.7$ has a much steeper slope as a function time, which suppresses the appearance of satellites, as explained in Sec. II A 3.

B. Low and intermediate temperatures for $k \neq 0$

To proceed with the analysis of the CE, we want to answer: (i) Whether the conclusions that we reached for $k = 0$ can be carried over to other momenta as well? (ii) Does CE continue to be better than SCMA at much higher temperatures? The first question is answered in Fig. 5, where we compare CE and DMFT heat plots. Figures 5(a) and 5(b) demonstrate that CE results are quite reminiscent of the DMFT results for $\alpha = 1$, even at nonzero momenta. The same conclusion holds for weaker couplings as well. On the other hand, there are differences between the results for somewhat stronger

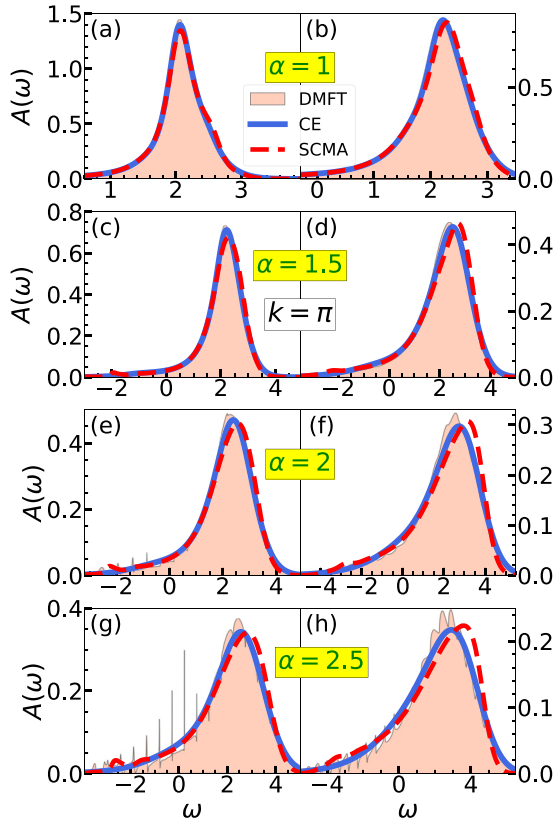


FIG. 6. (a)–(h) Spectral functions for $t_0 = 1$, $\omega_0 = 0.5$, and $k = \pi$. In the left panels $T = 0.3$, while $T = 0.7$ in the right panels.

coupling $\alpha = 1.5$, as shown in Figs. 5(c) and 5(d). While the polaron bands in both of these figures are convex, the CE predicts the first satellite to be concave, unlike the DMFT. In other words, CE predicts that the distance between the polaron peak and the satellites decreases as we increase the momentum. This is counterintuitive, as the satellites are perceived as the quasiparticle that absorbed or emitted a phonon, which should consequently be just at energy distance ω_0 apart. These limitations of the CE are much more pronounced for stronger electron-phonon couplings. While the DMFT solution in Figs. 5(f) and 5(h) exhibits a series of distinct bands, Figs. 5(e) and 5(g) demonstrate that the polaron and satellite bands of the CE merge into a single band at higher momenta. However, the most noticeable feature here is the fact that the CE is too smeared, as if the temperature is too high. This is a consequence of the fact that the lifetime in Eq. (18) scales as $\tau_{\mathbf{k}} \sim 1/g^2$. While the heat maps reveal noticeable discrepancies between the DMFT and CE for $k \neq 0$, it seems that these differences are much less pronounced around $k = \pi$. A more detailed comparison is presented in Fig. 6 that shows the results for the same regimes as in Fig. 4. The DMFT solution in Figs. 6(a)–6(d) shows that the main feature of the spectral function is a single broad peak for $\alpha \lesssim 1.5$, which is in agreement with the CE results. This is also the case for the SCMA, although we observe a slight tendency of the main peak to lean toward higher frequencies at higher temperatures. For larger interaction strengths, CE cannot fully reproduce the sharp peaks at lower frequencies of the low-temperature spectral function or the fine structure of the main peak at higher

temperatures; see Figs. 4(e)–4(h). Similarly, CE misses the quasiparticle peak as well, situated at low energy, although it is typically tiny and not (clearly) visible in Figs. 6(a)–6(h) (see Appendix C). A detailed comparison of the spectral functions for other momenta and phonon frequencies is presented in Sec. II of the SM [54].

Overall, we find that the CE gives the most accurate results for $k = 0$ and $k = \pi$ and that it is less accurate for other momenta. Although it cannot fully reproduce a tiny quasiparticle peak for $k = \pi$, it describes well a wide single-peak structure, which is the most prominent feature of the spectrum. A much larger discrepancy for $k = \pi$, between the CE and a reliable benchmark, was reported in Ref. [50] by examining the system on a finite lattice system with $N = 6$. In Appendix C, we examine the same parameter regime as in Ref. [50] and show that these discrepancies are significantly reduced in the thermodynamic limit.

C. Spectral functions at high temperatures and spectral sum rules

In Fig. 7, we show CE, SCMA, and DMFT spectral functions at high temperatures for the same electron-phonon couplings as in Figs. 4 and 6. We see that CE performs very well both for $k = 0$ and $k = \pi$. There are only small discrepancies at stronger interactions [see, e.g., Fig. 7(c)]. In contrast, the SCMA solution gets tilted relative to the DMFT and CE. In addition, it poorly reproduces the low-frequency part of the spectrum. It is not obvious whether the CE method is exact in the high-temperature limit $T \rightarrow \infty$. As we now demonstrate, this can be answered by examining the spectral sum rules:

$$\mathcal{M}_n(\mathbf{k}) = \int_{-\infty}^{\infty} A_{\mathbf{k}}(\omega) \omega^n d\omega. \quad (23)$$

These can be calculated both exactly,

$$\mathcal{M}_n^{\text{exact}}(\mathbf{k}) = \left\langle \underbrace{[\dots [c_{\mathbf{k}}, H], H] \dots, H]}_{n \text{ times}} c_{\mathbf{k}}^\dagger \right\rangle_T, \quad (24)$$

and within the CE approximation, where by combining Eqs. (4) and (23) we find

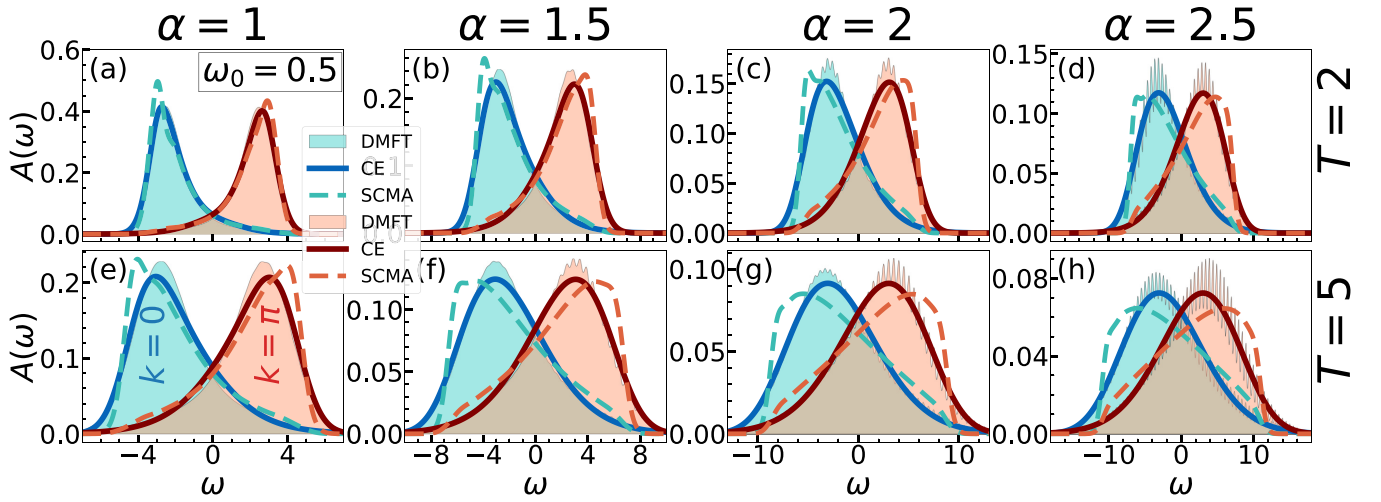
$$\begin{aligned} \mathcal{M}_n^{\text{CE}}(\mathbf{k}) &= \text{Re} \left[i^n \left(\frac{d}{dt} \right)^n e^{c_{\mathbf{k}}(t)} \right] \Big|_{t=0} \\ &\quad - \sum_{p=1}^n \binom{n}{p} (-\varepsilon_{\mathbf{k}})^p \mathcal{M}_{n-p}^{\text{CE}}(\mathbf{k}). \end{aligned} \quad (25)$$

The difference between these quantities $\mathcal{M}_n^{\text{CE}}(\mathbf{k}) - \mathcal{M}_n^{\text{exact}}(\mathbf{k})$ is zero for $n = 0$ and $n = 1$, as noted in Sec. II A 1. Higher order sum rules for the CE method are easily calculated, while the evaluation of the exact sum rules quickly becomes cumbersome for increasing n . The first five ($0 \leq n \leq 4$) sum rules were already calculated by Kornilovitch [58]

$$\mathcal{M}_2(\mathbf{k}) = \varepsilon_{\mathbf{k}}^2 + (2n_{\text{ph}} + 1)g^2, \quad (26a)$$

$$\mathcal{M}_3(\mathbf{k}) = \varepsilon_{\mathbf{k}}^3 + g^2\omega_0 + 2g^2(2n_{\text{ph}} + 1)\varepsilon_{\mathbf{k}}, \quad (26b)$$

$$\begin{aligned} \mathcal{M}_4(\mathbf{k}) &= \varepsilon_{\mathbf{k}}^4 + 2g^2\varepsilon_{\mathbf{k}}\omega_0 + g^2(2n_{\text{ph}} + 1) \\ &\quad \times (2t_0^2 + 3\varepsilon_{\mathbf{k}}^2 + \omega_0^2) + 3g^4(2n_{\text{ph}} + 1)^2. \end{aligned} \quad (26c)$$


 FIG. 7. (a)–(h) CE, DMFT, and SCMA spectral functions in 1D for $t_0 = 1$, $\omega_0 = 0.5$, and $k = 0, \pi$.

All of these are correctly predicted by the CE. However, the disagreement between $\mathcal{M}_n^{\text{exact}}$ and $\mathcal{M}_n^{\text{CE}}$ appears for $n = 5$, where we find

$$\begin{aligned} \mathcal{M}_5^{\text{exact}}(\mathbf{k}) &= \varepsilon_{\mathbf{k}}^5 + 3g^2\omega_0(2t_0^2 + \varepsilon_{\mathbf{k}}^2) + g^2\omega_0^3 \\ &\quad + 2g^2(2\varepsilon_{\mathbf{k}}^3 + 5g^2\omega_0 + \varepsilon_{\mathbf{k}}\omega_0^2 + 2t_0^2\varepsilon_{\mathbf{k}})(2n_{\text{ph}} + 1) \\ &\quad + 7g^4\varepsilon_{\mathbf{k}}(2n_{\text{ph}} + 1)^2, \end{aligned} \quad (27a)$$

$$\mathcal{M}_5^{\text{CE}}(\mathbf{k}) = \mathcal{M}_5^{\text{exact}}(\mathbf{k}) - 2g^4\varepsilon_{\mathbf{k}}(2n_{\text{ph}} + 1)^2. \quad (27b)$$

Hence, CE cannot be exact in the limit $T \rightarrow \infty$. However, we see that there are two limits where CE can potentially be exact: the weak-coupling limit $g \rightarrow 0$ and the atomic limit $\varepsilon_{\mathbf{k}} \rightarrow 0$. It turns out that CE is actually exact in both of these limits, as seen from Eqs. (3), (7), and (14) for the weak-coupling and Sec. III D for the atomic limit. We note that the SCMA gives correct sum rules only for $n \leq 3$ [42]. This is a consequence of the fact that SCMA ignores one of the fourth-order diagrams ($\sim g^4$) since it includes only the noncrossing diagrams. Also, we numerically checked that the DMFT results are in agreement with all of the sum rules that we listed above.

D. Atomic limit

In the atomic limit ($t_0 = 0$), the cumulant function can be evaluated exactly:

$$C(t) = \alpha^2(-2n_{\text{ph}} - 1 + it\omega_0 + iD(t)). \quad (28)$$

This follows from Eq. (16), using $J_0(0) = 1$. If we express the phonon propagator as $iD(t) = 2\sqrt{n_{\text{ph}}(n_{\text{ph}} + 1)} \cos[\omega_0(t + \frac{i}{2T})]$ and use the modified Jacobi-Anger identity

$$\begin{aligned} &e^{2\alpha^2\sqrt{n_{\text{ph}}(n_{\text{ph}}+1)}\cos[\omega_0(t+\frac{i}{2T})]} \\ &= \sum_{l=-\infty}^{\infty} I_l(2\alpha^2\sqrt{n_{\text{ph}}(n_{\text{ph}}+1)})e^{-il\omega_0 t} e^{\frac{l\omega_0}{2T}}, \end{aligned} \quad (29)$$

where I_l are the modified Bessel functions of the first kind, the spectral function [see Eqs. (3) and (4)] can be calculated

analytically and reads as

$$\begin{aligned} A(\omega) &= e^{-\alpha^2(2n_{\text{ph}}+1)} \\ &\quad \times \sum_{l=-\infty}^{\infty} I_l(2\alpha^2\sqrt{n_{\text{ph}}(n_{\text{ph}}+1)})e^{\frac{l\omega_0}{2T}} \delta(\omega + \alpha^2\omega_0 - l\omega_0). \end{aligned} \quad (30)$$

In the limit $T \rightarrow 0$, the previous expression reduces to

$$A(\omega) = e^{-\alpha^2} \sum_{l=0}^{\infty} \frac{\alpha^{2l}}{l!} \delta(\omega + \omega_0(\alpha^2 - l)). \quad (31)$$

This proves that CE gives correct results in the atomic limit, as Eqs. (30) and (31) coincide with the known exact results [1,44].

In contrast, the SCMA (let alone the MA) does not share this property, which is easy to show at zero temperature. In this case, Eq. (20a) and the Dyson equation imply that

$$G(\omega) = \frac{1}{\omega - g^2 G(\omega - \omega_0)}. \quad (32)$$

The previous equation can be solved by the iterative application of itself in terms of the continued fraction

$$G(\omega) = \frac{1}{\omega - \frac{g^2}{\omega - \omega_0 - \frac{g^2}{\omega - 2\omega_0 - \frac{g^2}{\omega - 3\omega_0 - \dots}}}}. \quad (33)$$

This does not coincide with Eq. (35) from Ref. [53], which represents the exact solution. Thus, SCMA cannot reproduce the correct result in the atomic limit.

While the CE is exact in the atomic limit ($t_0 = 0$), it is not immediately obvious how far from this limit it continues to give reliable results. This is why we now examine the regimes with small hopping parameter t_0 . Since the lifetime is infinitely large in some of these regimes (see Fig. 2), we introduce artificial attenuation η for the Green's function in real time by making a replacement $G(t) \rightarrow G(t)e^{-\eta t}$. The results are presented in Fig. 8. Here, the dotted line is the analytic solution in the atomic limit ($t_0 = 0$), determined by Eq. (30), where the Dirac delta functions have been replaced by Lorentzians of half-width η . It is used as a measure to see

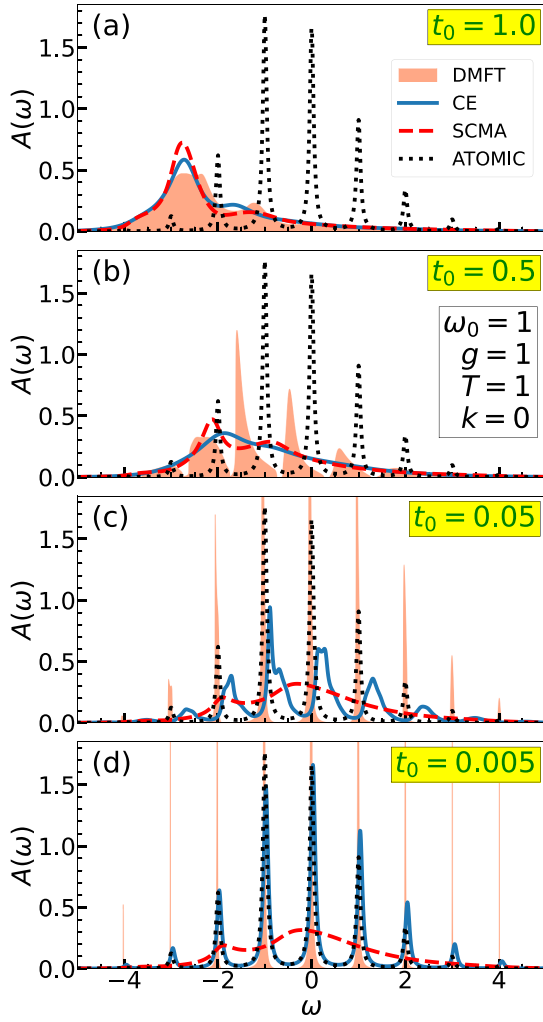


FIG. 8. (a)–(f) CE, DMFT, and SCMA spectral functions close to the atomic limit. Here, we use artificial Lorentzian broadening with half width set to $\eta = 0.05$.

how far the regime we are examining is from the exact atomic limit. In Fig. 8(a), we see that DMFT, SCMA, and CE spectral functions are in agreement. This regime is quite far from the atomic limit, as indicated by the dotted line. Figure 8(b) shows that the DMFT spectral function already consists of a series of peaks for $t_0 = 0.5$, while the CE and SCMA spectral functions are too flattened out. While the CE solution significantly improved in Fig. 8(c), it is still not giving satisfactory results, even though the DMFT suggests that we are already close to the atomic limit. Only for $t_0 \lesssim 0.005$ does the CE solution give accurate results; see Fig. 8(d). However, this is practically already at the atomic limit. It is interesting to note that while both the DMFT and the CE are exact in the weak-coupling and in the atomic limit, their behavior in other regimes can be quite different.

IV. QUASIPARTICLE PROPERTIES

We now investigate the quasiparticle properties obtained from the CE method and compare them extensively to the results obtained from the DMFT and SCMA. We note that

the lifetime within the CE was already studied in Sec. II A 4, so we supplement that study here with the results for the ground-state energy and the effective mass. Here we show the results in one, two, and three dimensions. Comparison with the MA ground-state energy, in the 1D case, is presented in Sec. III of the SM [54].

A. Ground-state energy

The polaron band dispersion $E_{p,\mathbf{k}}$ within the CE is given by the real part of Eq. (12), where the self-energy is taken in the MA:

$$E_{p,\mathbf{k}} = \varepsilon_{\mathbf{k}} + \text{Re}\Sigma^{\text{MA}}(\varepsilon_{\mathbf{k}}). \quad (34)$$

Since we deal with a single electron in the band, the ground-state energy E_p is given by $E_{p,\mathbf{k}=0}$ evaluated at zero temperature. In the 1D case, E_p is straightforwardly evaluated using Eq. (19) and reads as follows:

$$E_p^{1\text{D}} = -2t_0 - \frac{\alpha^2 \omega_0^2}{\sqrt{\omega_0^2 + 4\omega_0 t_0}}. \quad (35)$$

For the expression in higher dimensions, we need to go back to Eq. (14) that holds in any number of dimensions. At $T = 0$, it reads as

$$\text{Im}\Sigma^{\text{MA}}(\omega) = -\pi \alpha^2 \omega_0^2 \rho(\omega - \omega_0). \quad (36)$$

The real part of $\Sigma^{\text{MA}}(\omega)$ is obtained using the Kramers-Kronig relation

$$\text{Re}\Sigma^{\text{MA}}(\omega) = \pi \alpha^2 \omega_0^2 \mathcal{H}[\rho](\omega - \omega_0), \quad (37)$$

where $\mathcal{H}[\rho](\omega) = \mathcal{P} \int_{-\infty}^{\infty} \frac{d\nu}{\pi} \frac{\rho(\nu)}{\omega - \nu}$ is the Hilbert transform of the density of states $\rho(\omega)$ and \mathcal{P} is the Cauchy principle value. The evaluation of the Hilbert transform may be reduced to the evaluation of the Fourier transform \mathcal{F} , using the following identity:

$$\mathcal{F}^{-1}\mathcal{H}[\rho](t) = -i \text{sgn}(t) \mathcal{F}^{-1}[\rho](t). \quad (38)$$

The inverse Fourier transform of the density of states on the right-hand side was already calculated in Eq. (15) for the case of the hypercubic lattice with the nearest-neighbor hopping. Hence, $\mathcal{H}[\rho](\omega)$ is obtained by applying \mathcal{F} on both sides of Eq. (38),

$$\mathcal{H}[\rho](\omega) = \frac{1}{\pi} \int_0^{\infty} dx J_0(2t_0 x)^n \sin(x\omega), \quad (39)$$

where n is the number of dimensions. The polaron band dispersion then reads as

$$E_{p,\mathbf{k}} = \varepsilon_{\mathbf{k}} + \alpha^2 \omega_0^2 \int_0^{\infty} dx J_0(2t_0 x)^n \sin(x(\varepsilon_{\mathbf{k}} - \omega_0)). \quad (40)$$

E_p is thus a linear function with respect to α^2 , whose intercept is $\varepsilon_{\mathbf{k}}$, while its slope can be calculated accurately using the numerical scheme described in Appendix A. In the 2D case, it admits an analytical solution

$$E_p^{2\text{D}} = -4t_0 - \frac{2\alpha^2 \omega_0^2}{\pi(4t_0 + \omega_0)} K\left(\frac{4t_0}{4t_0 + \omega_0}\right), \quad (41)$$

where $K(k) = \int_0^{\pi/2} d\theta / \sqrt{1 - k^2 \sin^2 \theta}$ is the complete elliptic integral of the first kind. In the case $n = 3$, the integral

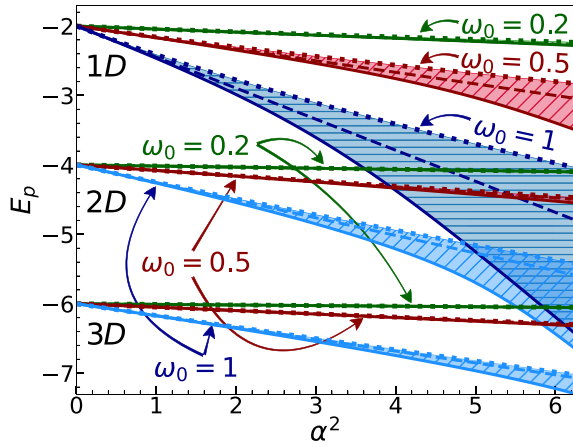


FIG. 9. Ground-state energy within the DMFT (solid line), CE (dashed line), and SCMA (dotted line). Here, $t_0 = 1$ and $T = 0$.

in Eq. (40) does not admit a closed-form solution and thus requires numerical calculation.

The polaron band dispersion $E_{p,\mathbf{k}}$ (and thus the ground state E_p) within the DMFT and SCMA is obtained numerically, as the smallest solution of the following equation:

$$E_{p,\mathbf{k}} = \varepsilon_{\mathbf{k}} + \text{Re}\Sigma(E_{p,\mathbf{k}}). \quad (42)$$

Results for the 1D, 2D, and 3D case are presented in Fig. 9. The DMFT benchmark, which is known to be very accurate [52], always gives the lowest ground-state energy predictions in comparison to the CE and SCMA. We see that CE always outperforms the SCMA, despite the fact that its predictions of the energy are always a linear function of α^2 . In the 1D case, we see that CE results for $\omega_0 = 0.5$ start to deviate more significantly from the DMFT just around $\alpha = 2.5$. Hence, the range of validity for the CE is similar as for the spectral functions in Fig. 4. The analogous conclusions can also be drawn from $\omega_0 = 1$ data as well. In contrast, all three methods seem to be in agreement for $\omega_0 = 0.2$ in the whole range of presented values of α . This is a consequence of the fact that the ground-state energy correction is small, as seen from Eqs. (35), (40), and (41) by fixing α and decreasing ω_0 . However, if we fix $g = \omega_0\alpha$ and then decrease ω_0 , the ground-state energy would change substantially [see, e.g., Eq. (35)], and the CE would certainly give poorer results.

Similar trends are observed in higher dimensions as well. Seemingly, the range of validity of the CE is increased in higher dimensions. However, one should keep in mind that the hopping parameter is always taken to be unity, which means that the bandwidth of the 2D and 3D systems are, respectively, two and three times larger than their 1D counterpart. Therefore, the correlation is weaker for a given coupling α .

B. Effective mass

Around the bottom ($|\mathbf{k}| \approx 0$) of the conduction band, the dispersion $E_{p,\mathbf{k}}$ assumes the following parabolic form:

$$E_{p,\mathbf{k}} \approx \text{const} + \frac{\mathbf{k}^2}{2m^*}, \quad (43)$$

where m^* is the effective mass, which we now calculate.

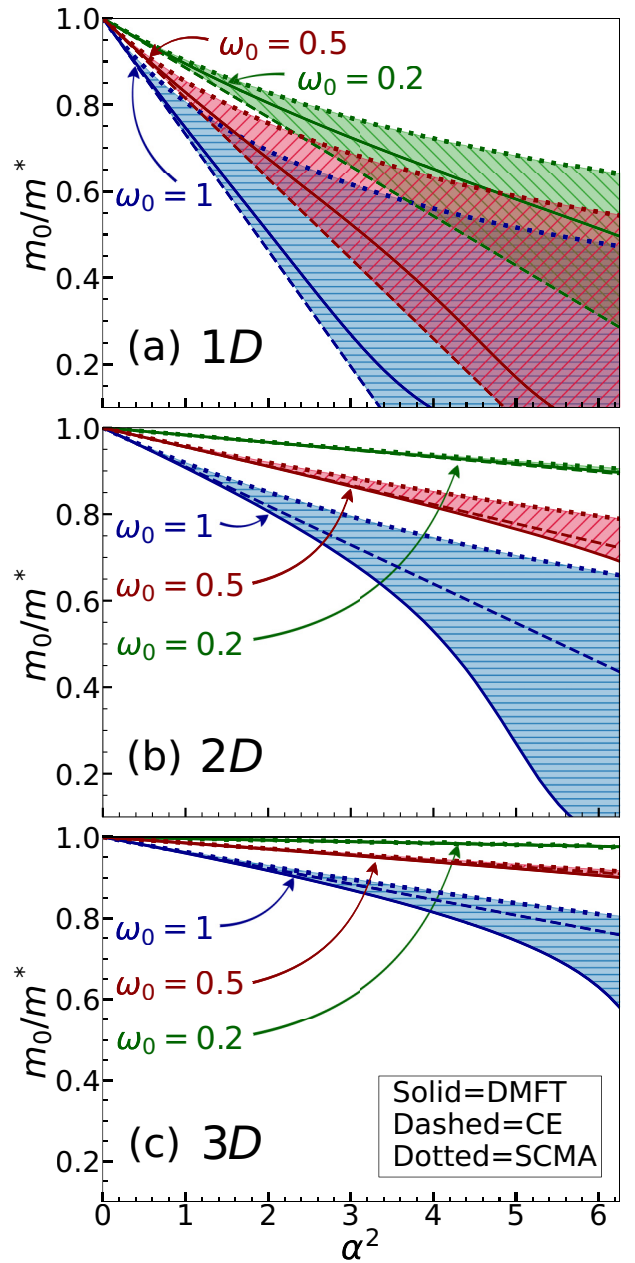


FIG. 10. Effective mass results within the DMFT, CE, and SCMA for $t_0 = 1$ and $T = 0$.

In the 1D case, one obtains the analytical result for the effective mass using Eqs. (19) and (34),

$$\left. \frac{m^*}{m_0} \right|_{1D, T=0} = \frac{1}{1 - \frac{(2t_0 + \omega_0)\alpha^2 \sqrt{\omega_0}}{(4t_0 + \omega_0)^{3/2}}}, \quad (44)$$

where $m_0 = 1/(2t_0)$ is the band mass which remains the same irrespective of the number of dimensions. Results for the higher number of dimensions are evaluated using Eq. (40). As for the ground-state energy, the 2D case admits an analytic solution

$$\left. \frac{m^*}{m_0} \right|_{2D, T=0} = \frac{1}{1 - \frac{2\alpha^2 \omega_0}{\pi(8t_0 + \omega_0)} E\left(\frac{4t_0}{4t_0 + \omega_0}\right)}, \quad (45)$$

where $E(k) = \int_0^{\pi/2} d\theta \sqrt{1 - k^2 \sin^2 \theta}$ is the complete elliptic integral of the second kind. Results in the n -dimensional case are given by

$$\left. \frac{m^*}{m_0} \right|_{T=0} = \frac{1}{1 + \pi \alpha^2 \omega_0^2 \left. \frac{d\mathcal{H}[\rho]}{d\omega} \right|_{\omega=-2n t_0 - \omega_0}}, \quad (46)$$

and require numerical calculation in the general case. From Eq. (46) we see that m_0/m^* is a linear function of α^2 . This linear behavior has to break down at one point, as m_0/m^* cannot be negative. This happens for strong interaction, where the CE is certainly not expected to be reliable. The mass renormalization within the DMFT and SCMA is calculated numerically as

$$\left. \frac{m^*}{m_0} \right|_{T=0} = 1 - \left. \frac{d\Sigma(\omega)}{d\omega} \right|_{\omega=E_p}, \quad (47)$$

where E_p is the ground-state energy. Results for the DMFT, CE, and SCMA effective mass in different parameter regimes and for different number of dimensions are presented in Fig. 10. In the 1D case, we see that the CE always underestimates, while the SCMA overestimates the results from the DMFT benchmark. Still, CE clearly outperforms the SCMA for $\omega_0 = 1$ and $\omega_0 = 0.5$, while the results in the vicinity of the adiabatic limit ($\omega_0 = 0.2$) seem to be equally well (poor) represented by both methods.

In the higher-dimensional case, we see that the CE is always a clearly better approximation than the SCMA, while both of them overestimate the DMFT predictions. As for the ground-state energy, we emphasize again that the hopping parameter was set to 1. As a consequence, the system has a larger bandwidth in the higher-dimensional case and, therefore, the correlations are weaker.

V. MOBILITY

The mobility is defined as the DC conductivity, normalized to the concentration of charge carriers n_e (and their unit charge which we set to $e = 1$), i.e., $\mu = \sigma^{\text{DC}}/n_e$. It can be calculated using the Kubo formalism, which relates μ to the current-current correlation function [1]. The latter can be written as a sum of the so-called bubble part, which is completely determined by the spectral functions $A_{\mathbf{k}}(\omega)$ and the vertex corrections. Within the DMFT, the vertex corrections vanish [57,59], while estimating their contribution in the general case is beyond the scope of this paper. In the following, we calculate the mobility solely from the bubble part.

In the case of a 1D system with a single spinless electron in the band, the mobility in the bubble approximation can be written as [1,60]

$$\mu = \frac{4\pi t_0^2}{T} \frac{\sum_{\mathbf{k}} \int_{-\infty}^{\infty} dv A_{\mathbf{k}}(v)^2 e^{-v/T} \sin^2 k}{\sum_{\mathbf{k}} \int_{-\infty}^{\infty} dv A_{\mathbf{k}}(v) e^{-v/T}}. \quad (48)$$

The processing time required for the calculation of μ within the CE method rises linearly with the number of k points we sum over. This is not the case for the DMFT and SCMA, as their self-energies are k independent and thus need to be calculated only once for a given parameter set. In every parameter regime the CE was applied to, we checked that 64 sampling points in the Brillouin zone are enough to be representative of

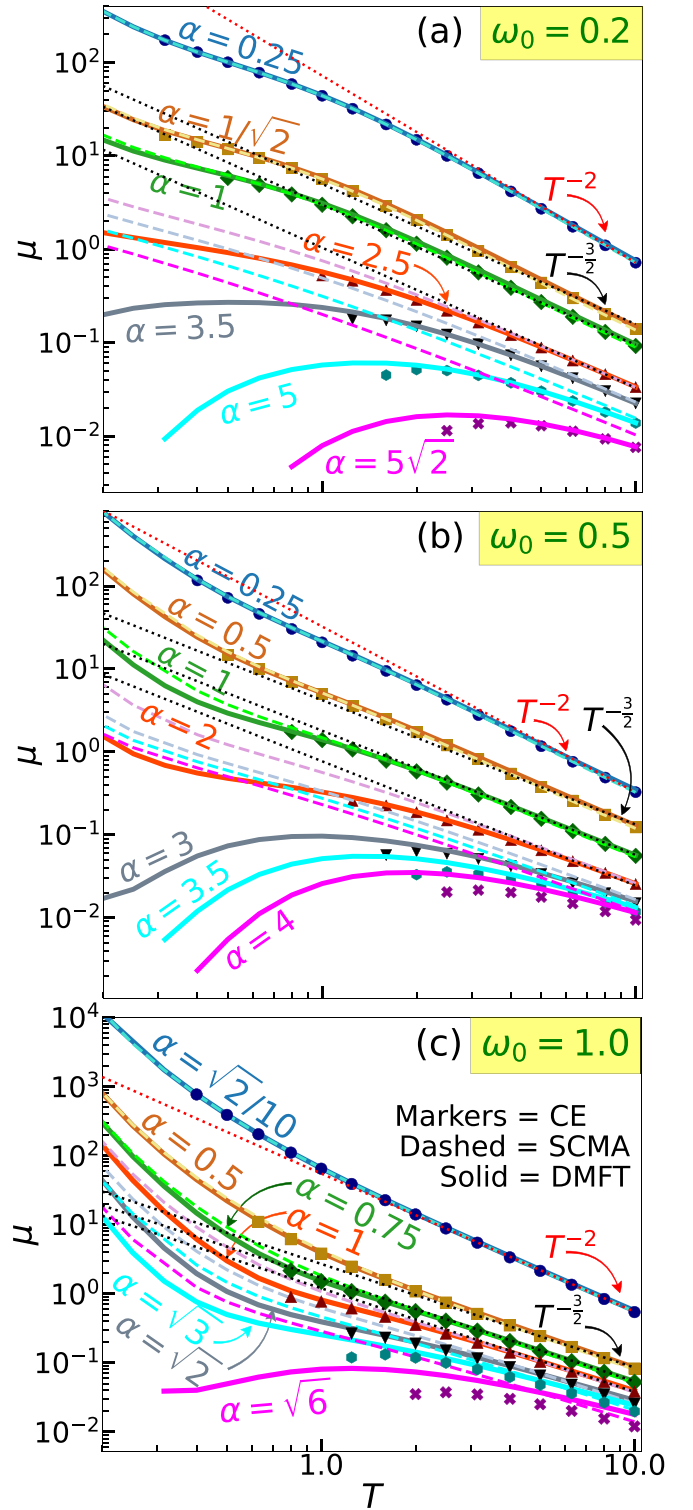


FIG. 11. Temperature dependence of the mobility for the CE, DMFT, and SCMA. The dotted red (black) lines are auxiliary lines with the power law behavior $\mu \propto T^{-2}$ ($\mu \propto T^{-3/2}$). Here $t_0 = 1$.

the thermodynamic limit. This was also crosschecked using the DMFT.

The exponential term $e^{-v/T}$ in Eq. (48) has some important implications. Despite the factor $\sin^2 k$, it implies that the largest contribution to the mobility most commonly comes

from the spectral functions around the bottom of the band ($k \approx 0$), as they are typically situated at lower frequencies with respect to their higher momentum counterparts. This is actually helpful, as we have seen that the CE is more reliable for $k \approx 0$ than for $0 < k < \pi$. However, $e^{-\nu/T}$ also introduces numerical instabilities, as even a small numerical noise of $A_k(\nu)$ at $\nu \ll -1$ will be inflated and give an enormous overall error in the mobility. This is why the integrals in Eq. (48) require introducing some kind of negative frequency cutoff $\int_{-\infty}^{\infty} \rightarrow \int_{-\Lambda}^{\infty}$. We always check that the mobility results converge with respect to Λ . This is easily done in both the DMFT and SCMA due to the high numerical accuracy of our numerical implementations. The convergence with respect to Λ is much harder to achieve within the CE, as the Green's functions are initially calculated in the time domain and require the use of numerical Fourier transform. We have implemented a well-known interpolation scheme [61] to increase the precision of the Fourier transform. Still, the numerical noise at low temperatures and strong interactions prevented us from precisely calculating the mobility in these regimes. We show only the data where an accurate calculation was possible.

In Fig. 11, we present numerical results for the temperature dependence of the electron mobility. For weak electron-phonon coupling, all methods are in agreement; see Fig. 11(a) for $\alpha \leq 1$ and Figs. 11(b) and 11(c) for $\alpha \leq 0.5$. Electron-phonon scattering is weak in these regimes, which is why the quasiparticle lifetime τ_k is long, and the linear time dependence dominates in the cumulant function. The spectral function and its square can thus be approximated as $A_k(\omega) \approx \delta(\omega - E_{p,k})$ and $A_k^2(\omega) \approx \frac{\tau_k}{\pi} \delta(\omega - E_{p,k})$, where δ is the Dirac delta function and $E_{p,k}$ is given by Eq. (34). The mobility from Eq. (48) thus simplifies to

$$\mu_{\text{weak}} \approx \frac{4t_0^2}{T} \frac{\sum_k \tau_k e^{-E_{p,k}/T} \sin^2 k}{\sum_k e^{-E_{p,k}/T}}. \quad (49)$$

At high temperatures, Eq. (49) further simplifies as $e^{-E_{p,k}/T} \approx 1$. In this case, the lifetime is inversely proportional to the temperature $\tau_k \propto 1/T$, as seen from Eq. (18), which implies the power-law behavior of the mobility $\mu_{\text{weak}} \propto 1/T^2$. This conclusion holds only for very weak electron-phonon couplings, where the assumption of weak scattering is still satisfied despite the high temperatures; see Figs. 11(a) and 11(b) for $\alpha = 0.25$ and Fig. 11(c) for $\alpha = \sqrt{2}/10$. This assumption is also violated at extremely high temperatures $T \rightarrow \infty$.

For stronger couplings, in the limit of high-temperatures $T \gg t_0, \omega_0$, the Green's function in the time domain is quickly damped, which is why $C_k(t)$ can be approximated with just the lowest order (quadratic) Taylor expansion around $t = 0$. Hence, Eqs. (3) and (17) imply that the Green's function can be written as

$$G_k(t) = -i\theta(t)e^{-i\varepsilon_k t} e^{-\frac{g^2}{2}(2n_{\text{ph}}+1)t^2}, \quad (50)$$

while the corresponding spectral function is given by the Gaussian:

$$A_k(\omega) = \frac{e^{-\frac{(\omega-\varepsilon_k)^2}{2g^2(2n_{\text{ph}}+1)}}}{\sqrt{2\pi g^2(2n_{\text{ph}}+1)}}. \quad (51)$$

Plugging this back into Eq. (48) and changing the sum over momenta to integral, we obtain

$$\mu_{\text{high-}T} = \frac{t_0}{g} \sqrt{\frac{\pi}{2n_{\text{ph}}+1}} \exp\left(-\frac{g^2(2n_{\text{ph}}+1)}{4T^2}\right) \frac{I_1\left(\frac{2t_0}{T}\right)}{I_0\left(\frac{2t_0}{T}\right)}, \quad (52)$$

where I_0 and I_1 are modified Bessel functions of the first kind, of zeroth and first orders, respectively. Equation (52) can be simplified by using the following approximations: $2n_{\text{ph}}+1 \approx 2T/\omega_0$ and $I_1(2t_0/T)/I_0(2t_0/T) \approx t_0/T$, that are valid for large T . Such a simplified formula coincides with the mobility obtained by combining the Einstein relation, between the mobility and diffusion coefficient, with the Marcus formula [45,62]. Furthermore, Eq. (52) implies the power-law behavior for the mobility $\mu_{\text{high-}T} \propto T^{-3/2}$, in the limit $T \gg t_0, \omega_0$. This is confirmed by our numerical results for a wide range of the electron-phonon coupling strengths, where all three methods are in agreement; see Fig. 11(a) for $1/\sqrt{2} \leq \alpha \leq 2.5$, Fig. 11(b) for $0.5 \leq \alpha \leq 2$, and Fig. 11(c) for $0.5 \leq \alpha \leq 1$.

While the SCMA gives satisfactory results for high temperatures and intermediate electron-phonon couplings, it deviates from the DMFT at lower temperatures [see, e.g., Fig. 11(a) for $\alpha = 2.5$ and Fig. 11(b) for $\alpha = 2$] and also for stronger coupling strengths [see, e.g., Fig. 11(a) for $\alpha > 2.5$ and Fig. 11(b) for $\alpha > 2$]. At these stronger couplings, the DMFT predicts the nonmonotonic mobility, where a region of decreasing mobility with decreasing temperature is ascribed to the hopping transport in phenomenological theories [38,62]. The strong coupling mobility is better described by the CE than SCMA, although low-temperature results are missing due to our inability to converge the results with respect to the cutoff Λ . In Appendix D, we also give mobility predictions of the MA.

VI. CONCLUSIONS AND OUTLOOK

In summary, we have presented a comprehensive analysis of the CE method in the context of the Holstein model. The second-order cumulant $C(t)$ is calculated in a broad temperature range for three vibrational frequencies $\omega_0/t_0 = 0.2, 0.5$, and 1, covering a regime from a weak to strong electron-phonon coupling. We mostly focused on the 1D system in the thermodynamic limit but some of the results are shown also in 2D and 3D. To avoid numerical instabilities and to reach high numerical precision, we derived a number of analytical expressions and we used the collocation method in calculations of the cumulant, as well as an interpolation scheme for the Fourier transform in corresponding calculations of the spectral functions. The quasiparticle properties, spectral functions, and charge mobility are shown in comparison to the DMFT and SCMA results. The DMFT, which gives close to the exact solution for the Holstein polaron throughout the parameter space [52], gave a valuable benchmark and facilitated a detailed analysis of the validity of the CE method.

At weak coupling (roughly corresponding to $m_0/m^* \gtrsim 0.9$) CE, DMFT, and SCMA give very similar spectral functions. Most of the spectral weight for $k = 0$ is in the quasiparticle peak, while even a small sideband (satellite) spectral weight is rather well reproduced in all three methods. As the interaction increases, a clear difference in the spectral functions

emerges. Nevertheless, the positions of the CE and DMFT quasiparticle and the first satellite peak at low temperatures are in rather good agreement. Furthermore, the overall spectral weight distribution is in a decent agreement even though the satellite peaks are more pronounced in DMFT for stronger electron-phonon coupling. Roughly speaking, there is a decent agreement in 1D up to the interactions corresponding to $m_0/m^* \sim 0.5$. Interestingly, the agreement between the CE and DMFT spectral functions persists also for $k = \pi$, although CE does not capture a tiny quasiparticle peak. In this case, the DMFT spectral weight almost merges to a single broad peak. We note that the difference for $k = \pi$ observed in Ref. [50] is solely due to considering a lattice of finite $N = 6$ size. The deviation of CE from the exact solution is most obvious for intermediate momenta where the CE solution merges to a single peak, while the satellite structure is seen in DMFT. At high temperatures, one might suspect that the CE would give the exact spectral functions. However, this is not the case, as we showed that the CE gives the exact spectral moments only up to the order $n = 4$. We note that in all these regimes, the CE gives slightly better results than the SCMA, while a single-shot MA is adequate only for very weak interactions.

The spectral functions were used to calculate the charge mobility from the Kubo formula without the vertex corrections. The agreement between DMFT and CE is quite good. This is the case even for stronger electron-phonon coupling where the CE even indicates nonmonotonic behavior of $\mu(T)$, with a region of increasing mobility with temperature which is usually assigned to hopping conduction in phenomenological theories. For strong electron-phonon coupling, the CE mobility results are shown only for $T \gtrsim t_0$ since a very small numerical noise at frequencies $\omega \ll E_p$ affects a precise calculation of mobility at lower temperatures. For high temperatures, the mobility assumes a universal form: For weak electron-phonon coupling $\mu \propto T^{-2}$, while for stronger coupling $\mu \propto T^{-3/2}$. These high-temperature limits can be obtained also analytically from the CE.

The CE method can be easily applied to different Hamiltonians, which makes it a particularly attractive method for the calculation of electronic properties beyond the weak-coupling limit in various systems. In particular, we argue that it will be most useful in calculations of charge mobility, as has already been done in *ab initio* calculations for SrTiO₃ [16] and naphthalene [17]. While our analysis may suggest that the DMFT appears computationally superior to CE, we note that the numerical efficiency that we achieved with DMFT is restricted to the Holstein model by virtue of the analytic solution for the impurity problem [53] and the local Green's function [52]. For predicting the properties of real materials, the numerical resources within the DMFT are vastly increased and also the issue of nonlocal correlations may emerge, while the CE remains simple and relatively inexpensive. Of course, for a definitive answer on the range of validity of CE in connection with *ab initio* calculations, one needs to perform a similar analysis for the Fröhlich model and for other models which can be used for realistic description of the electronic spectra and charge transport in real materials. A useful hint in this direction is provided by Ref. [51], which shows that the CE, around the bottom of the band, gives promising results for the spectral function even in the case when the phonons

have a dispersion [63]. Another very interesting question that we leave for further work is a possible contribution of vertex corrections to conductivity. Based on the weak coupling result [64], one might assume that their contribution is small for optical phonons, but this remains to be determined in the case of stronger coupling. Our high-temperature results for mobility may also be quite useful when analyzing a dominant type of electron-phonon coupling in real materials. Still, one needs to be cautious in such analyses since we see that at lower temperatures $\mu(T)$ does not assume a simple universal form.

ACKNOWLEDGMENTS

The authors acknowledge funding provided by the Institute of Physics Belgrade, through a grant by the Ministry of Science, Technological Development and Innovation of the Republic of Serbia. Numerical simulations were performed on the PARADOX supercomputing facility at the Scientific Computing Laboratory, National Center of Excellence for the Study of Complex Systems, Institute of Physics Belgrade.

APPENDIX A: NUMERICAL INTEGRATION SCHEME FOR THE HIGHLY OSCILLATING FUNCTIONS IN THE CE METHOD

We present a numerical integration scheme for the calculation of the cumulant function from Eq. (16). Since $C_k(t)$ will be expressed numerically on some t -grid [$t_0 = 0, t_1 \dots t_{G-1}$], it is much better to divide the integral \int_0^t from Eq. (16) into a sum of integrals of the form $\int_{t_{i-1}}^{t_i}$, where t_i are times from the previously defined t grid. In this manner, we do not integrate over the same interval multiple times. To shorten the notation, from now on, we denote $a \equiv t_{i-1}$ and $b \equiv t_i$. There are two different types of integrals in Eq. (16), and both of them have the following form:

$$I = \int_a^b dx g(x) e^{ir_1 x} J_0(r_2 x)^n, \quad (\text{A1})$$

where $g(x)$ is either a linear or a constant function, $r_1 = \varepsilon_{\mathbf{k}} \pm \omega_0$, and $r_2 = 2t_0$. Numerical integration of Eq. (A1) has already been studied by Levin for arbitrary r_1 and r_2 and slowly varying $g(x)$ [55]. In the rest of this Appendix, we review this method in the 1D ($n = 1$), 2D ($n = 2$), and 3D ($n = 3$) cases. The main idea is to rewrite the subintegral function as a scalar product of two columns $|\tilde{g}(x)\rangle$ and $|\tilde{J}(x)\rangle$, whose elements are functions:

$$I = \int_a^b dx \langle \tilde{g}(x) | \tilde{J}(x) \rangle. \quad (\text{A2})$$

Column $|\tilde{g}(x)\rangle$ consists exclusively of slowly varying functions, while $|\tilde{J}(x)\rangle$ contains highly oscillating functions, with the property that

$$\frac{d|\tilde{J}(x)\rangle}{dx} = \hat{A}(x)|\tilde{J}(x)\rangle, \quad (\text{A3})$$

where $\hat{A}(x)$ is a matrix of slowly varying functions. Then, the integral from Eq. (A2) can be written as

$$I = \int_a^b dx \frac{d}{dx} \langle \tilde{f}(x) | \tilde{J}(x) \rangle = \langle \tilde{f}(b) | \tilde{J}(b) \rangle - \langle \tilde{f}(a) | \tilde{J}(a) \rangle, \quad (\text{A4})$$

where $|\tilde{f}(x)\rangle$ satisfies

$$\left(\frac{d}{dx} + \hat{A}^\dagger(x) \right) |\tilde{f}(x)\rangle = |\tilde{g}(x)\rangle. \quad (\text{A5})$$

This is then, following Levin [55], solved by formally expanding $|\tilde{f}(x)\rangle = \sum_{k=1}^M u_k(x) [c_k \ d_k \ \dots]^T$ into a basis set of polynomials $u_k(x) = (x - \frac{a+b}{2})^{k-1}$ and determining the unknown polynomial coefficients $c_k, d_k \dots$ by imposing that Eq. (A5) is exactly satisfied at M uniformly distributed collocation points $x_j = a + \frac{(j-1)(b-a)}{M-1}$, $j = 1 \dots M$. The initial problem is thus reduced to a simple linear algebra problem.

1. 1D case

In the 1D case ($n = 1$), columns $|\tilde{g}(x)\rangle$ and $|\tilde{J}(x)\rangle$ assume the following form:

$$|\tilde{g}(x)\rangle = [g(x) \ 0]^T, \quad (\text{A6a})$$

$$|\tilde{J}(x)\rangle = e^{ir_1 x} [J_0(r_2 x) \ J_1(r_2 x)]^T, \quad (\text{A6b})$$

where $J_0(x)$ and $J_1(x)$ are the Bessel functions of the first kind, of zeroth and first order. The matrix $\hat{A}(x)$, such that Eq. (A3) holds, is given by

$$\hat{A}(x) = \begin{bmatrix} ir_1 & -r_2 \\ r_2 & ir_1 - \frac{1}{x} \end{bmatrix}. \quad (\text{A7})$$

The unknown coefficients c_k and d_k , which determine the column function

$$|\tilde{f}(x)\rangle = \sum_{k=1}^M u_k(x) [c_k \ d_k]^T, \quad (\text{A8})$$

are obtained from the following set of $2M$ linear equations:

$$\begin{bmatrix} \mathcal{C} & \mathcal{C}^d \\ \mathcal{D}^c & \mathcal{D} \end{bmatrix} \begin{bmatrix} c_1 \\ \vdots \\ c_M \\ d_1 \\ \vdots \\ d_M \end{bmatrix} = \begin{bmatrix} g(x_1) \\ \vdots \\ g(x_M) \\ 0 \\ \vdots \\ 0 \end{bmatrix}. \quad (\text{A9})$$

Here, $\mathcal{C}, \mathcal{C}^d, \mathcal{D}^c, \mathcal{D}$ are $M \times M$ matrices that read as

$$\mathcal{C}_{ij} = u'_j(x_i) - ir_1 u_j(x_i); \quad \mathcal{C}_{ij}^d = r_2 u_j(x_i), \quad (\text{A10a})$$

$$\mathcal{D}_{ij} = u'_j(x_i) - \left(ir_1 + \frac{1}{x_i} \right) u_j(x_i); \quad \mathcal{D}_{ij}^c = -r_2 u_j(x_i). \quad (\text{A10b})$$

2. 2D case

In the 2D case, the relevant quantities are given by

$$\begin{aligned} |\tilde{g}(x)\rangle &= [g(x) \ 0 \ 0]^T, \\ |\tilde{J}(x)\rangle &= e^{ir_1 x} [J_0(r_2 x)^2 \ J_0(r_2 x) J_1(r_2 x) \ J_1(r_2 x)^2]^T, \\ \hat{A}(x) &= \begin{bmatrix} ir_1 & -2r_2 & 0 \\ r_2 & ir_1 - \frac{1}{x} & -r_2 \\ 0 & 2r_2 & ir_1 - \frac{2}{x} \end{bmatrix}. \end{aligned} \quad (\text{A11})$$

The column $|\tilde{f}(x)\rangle = \sum_{k=1}^M u_k(x) [c_k \ d_k \ e_k]^T$ is determined by c_k, d_k , and e_k , which are obtained as a solution of the following system of $3M$ linear equations:

$$\begin{bmatrix} \mathcal{C} & \mathcal{C}^d & \mathcal{C}^e \\ \mathcal{D}^c & \mathcal{D} & \mathcal{D}^e \\ \mathcal{E}^c & \mathcal{E}^d & \mathcal{E} \end{bmatrix} \begin{bmatrix} c_1 \\ \vdots \\ c_M \\ d_1 \\ \vdots \\ e_1 \\ \vdots \end{bmatrix} = \begin{bmatrix} g(x_1) \\ \vdots \\ g(x_M) \\ 0 \\ \vdots \\ 0 \\ \vdots \end{bmatrix}. \quad (\text{A12})$$

Here, $\mathcal{C}, \mathcal{C}^d \dots \mathcal{E}$ are $M \times M$ matrices. Elements of \mathcal{C}_{ij} and \mathcal{C}_{ij}^d are the same as in Eq. (A10), while $\mathcal{C}_{ij}^e = \mathcal{E}_{ij}^c = 0$. All the other elements are given by

$$\begin{aligned} \mathcal{D}_{ij} &= u'_j(x_i) - \left(ir_1 + \frac{1}{x_i} \right) u_j(x_i), \\ \mathcal{E}_{ij} &= u'_j(x_i) - \left(ir_1 + \frac{2}{x_i} \right) u_j(x_i), \\ \mathcal{D}_{ij}^c &= -2r_2 u_j(x_i); \quad \mathcal{D}_{ij}^e = 2r_2 u_j(x_i); \quad \mathcal{E}_{ij}^d = -r_2 u_j(x_i). \end{aligned} \quad (\text{A13})$$

3. 3D case

The procedure that was presented so far is actually quite easily generalized to the 3D case as well. Here, the quantities of interest are easily derived and read as

$$\begin{aligned} |\tilde{g}(x)\rangle &= [g(x) \ 0 \ 0 \ 0]^T, \\ |\tilde{J}(x)\rangle &= e^{ir_1 x} [J_0(r_2 x)^3 \ J_0(r_2 x)^2 J_1(r_2 x) \\ &\quad J_0(r_2 x) J_1(r_2 x)^2 \ J_1(r_2 x)^3]^T, \\ \hat{A}(x) &= \begin{bmatrix} ir_1 & -3r_2 & 0 & 0 \\ r_2 & ir_1 - \frac{1}{x} & -2r_2 & 0 \\ 0 & 2r_2 & ir_1 - \frac{2}{x} & -r_2 \\ 0 & 0 & 3r_2 & ir_1 - \frac{3}{x} \end{bmatrix}, \\ \tilde{f}(x) &= \sum_{k=1}^M u_k(x) [c_k \ d_k \ e_k \ f_k]^T, \end{aligned} \quad (\text{A14})$$

where the coefficients c_k , d_k , e_k , and f_k satisfy

$$\begin{bmatrix} \mathcal{C} & \mathcal{C}^d & \mathcal{C}^e & \mathcal{C}^f \\ \mathcal{D}^c & \mathcal{D} & \mathcal{D}^e & \mathcal{D}^f \\ \mathcal{E}^c & \mathcal{E}^d & \mathcal{E} & \mathcal{E}^f \\ \mathcal{F}^c & \mathcal{F}^d & \mathcal{F}^e & \mathcal{F} \end{bmatrix} \begin{bmatrix} c_1 \\ \vdots \\ c_M \\ d_1 \\ \vdots \\ e_1 \\ \vdots \\ f_1 \\ \vdots \end{bmatrix} = \begin{bmatrix} g(x_1) \\ \vdots \\ g(x_M) \\ 0 \\ \vdots \\ 0 \\ \vdots \\ 0 \\ \vdots \end{bmatrix}. \quad (\text{A15})$$

Here \mathcal{C}_{ij} , \mathcal{C}_{ij}^d , \mathcal{C}_{ij}^e , \mathcal{D}_{ij} , \mathcal{D}_{ij}^e , \mathcal{E}_{ij}^c , and \mathcal{E}_{ij} are the same as in Eqs. (A10) and (A13), while $\mathcal{C}_{ij}^f = \mathcal{F}_{ij}^c = \mathcal{D}_{ij}^f = \mathcal{F}_{ij}^d = 0$. All other elements are given by

$$\begin{aligned} \mathcal{E}_{ij}^d &= -2r_2u_j(x_i); & \mathcal{E}_{ij}^f &= 3r_2u_j(x_i), \\ \mathcal{D}_{ij}^c &= -3r_2u_j(x_i); & \mathcal{F}_{ij}^e &= -r_2u_j(x_i), \\ \mathcal{F}_{ij} &= u'_j(x_i) - \left(ir_1 + \frac{3}{x_i}\right)u_j(x_i). \end{aligned} \quad (\text{A16})$$

Thus, our numerical scheme has been completely specified. We note that Eqs. (A10), (A13), and (A16) explicitly demonstrate that our numerical scheme is singular at $x = 0$. This does not pose any problems, as the subintegral function in our initial expression Eq. (A1) is not highly oscillatory around $x = 0$. Therefore, the trapezoid scheme can be applied there.

APPENDIX B: 2D SPECTRAL FUNCTIONS

We now examine the CE spectral functions in two dimensions and compare them to the results from DMFT and SCMA. We investigate the Hamiltonian from Eq. (1) on a square lattice and set \hbar , k_B and lattice constant to 1.

In the 2D case, the cumulant function is calculated from Eq. (16) by setting $n = 2$, and by exploiting the numerical integration scheme from Appendix A. The procedure for the implementation of the DMFT and SCMA is the same as explained in Sec. II B, with the only difference being that Eq. (22) no longer represents the solution for the local Green's function from Eqs. (20b) and (21). The local Green's function for the square lattice is obtained as follows. Let us introduce $B(\omega) \equiv (\omega - \Sigma(\omega))/(2t_0)$ and rewrite Eq. (21) as

$$G(\omega) = - \int_{-\infty}^{\infty} dx \tilde{\rho}(x) \int_{-\infty}^{\infty} d\varepsilon \frac{e^{ix\varepsilon}}{\varepsilon - 2t_0B(\omega)}. \quad (\text{B1})$$

The integral over ε can be solved using the residue theorem. It is thus important to note that the subintegral function has only a single pole at $\varepsilon_{\text{pole}} = 2t_0B(\omega)$ that is situated at the upper half-plane, i.e., $\text{Im}B(\omega) > 0$ (since $\text{Im}\Sigma(\omega) < 0$). Hence

$$G(\omega) = -2\pi i \int_{-\infty}^{\infty} dx \tilde{\rho}(x) e^{2ixt_0B(\omega)} \theta(x). \quad (\text{B2})$$

Here $\tilde{\rho}(x)$ is given by Eq. (15) for $n = 2$. Substituting this into Eq. (B2) and solving the integral gives

$$G(\omega) = \frac{K\left(\frac{2}{B(\omega)}\right)}{B(\omega)\pi t_0}, \quad (\text{B3})$$

where $K(k) \equiv \int_0^{\pi/2} d\theta / \sqrt{1 - k^2 \sin^2 \theta}$ is the complete elliptic integral of the first kind.

Results are presented in Fig. 12. We note that in Figs. 12(a)–12(d) [Figs. 12(i)–12(l)] the phonon frequency $\omega_0 = 0.2$ ($\omega_0 = 1$) is smaller (larger) than both of the temperatures $T_1 = 0.3$ and $T_2 = 0.7$ that we are considering. Therefore, we focus on Figs. 12(e)–12(h) where $T_1 < \omega_0 < T_2$, while other regimes can be analyzed analogously. We see that most of the spectral weight is concentrated in a smaller range of frequencies than in the 1D case; see Figs. 4 and 12(e)–12(h). This is a consequence of the fact that the hopping parameter is always set to unity, while the 2D bandwidth is twice as large in comparison with the bandwidth in the 1D system. Spectral functions from Figs. 12(e)–12(g) exhibit qualitatively similar behavior as results for the 1D system in Figs. 4(a)–4(d). Here, all methods are in agreement and predict that the quasiparticle peak dominates, while there is only a single tiny satellite structure that is more pronounced at higher temperatures. However, it seems that the satellites are more pronounced in the 1D spectral functions. A much more complicated multipeak structure is predicted by the DMFT in Fig. 10(h), where a large discrepancy can be observed in comparison to the CE and SCMA results. A better agreement is observed for higher temperatures.

It is interesting to note that while the DMFT frequently gave sharper peaks than other methods in 1D (see Fig. 4), here the roles are reversed. This is a consequence of the strong Van Hove singularity at the bottom of the band of a 1D system, which is highly relevant in our case when the concentration of electrons is very low, while the singularity in the 2D system is weaker and shifted to the center of the band.

APPENDIX C: A DETAILED STUDY OF THE SPECTRAL FUNCTION FOR $t_0 = \omega_0 = g = 1$ and $k = \pi$

In Sec. III, we concluded that the CE successfully captures the main features of the spectral functions both at the bottom of the band ($k \approx 0$) and at top of the band ($k \approx \pm\pi$) if the electron-phonon coupling is not too strong. Less promising results were reported in Ref. [50], where CE was examined on a finite lattice with $N = 6$ sites in the regime $t_0 = \omega_0 = g = 1$ and $k = \pi$, using the finite-temperature Lanczos method (FTLM) [44] as a benchmark. They found that the CE, in addition to the fact that it does not correctly reproduce a quasiparticle peak, predicts that the most prominent feature of the spectrum consists of only a single broad peak, whereas two distinct peaks are present in the FTLM solution. Here we show that this discrepancy between the CE and FTLM is significantly reduced in the thermodynamic limit.

Reference [50] emphasized that previous conclusions are valid only for low-temperature solutions, while CE becomes accurate for $T \geq \omega_0$. This was confirmed by the FTLM, whose spectral functions in this case look like a single broad

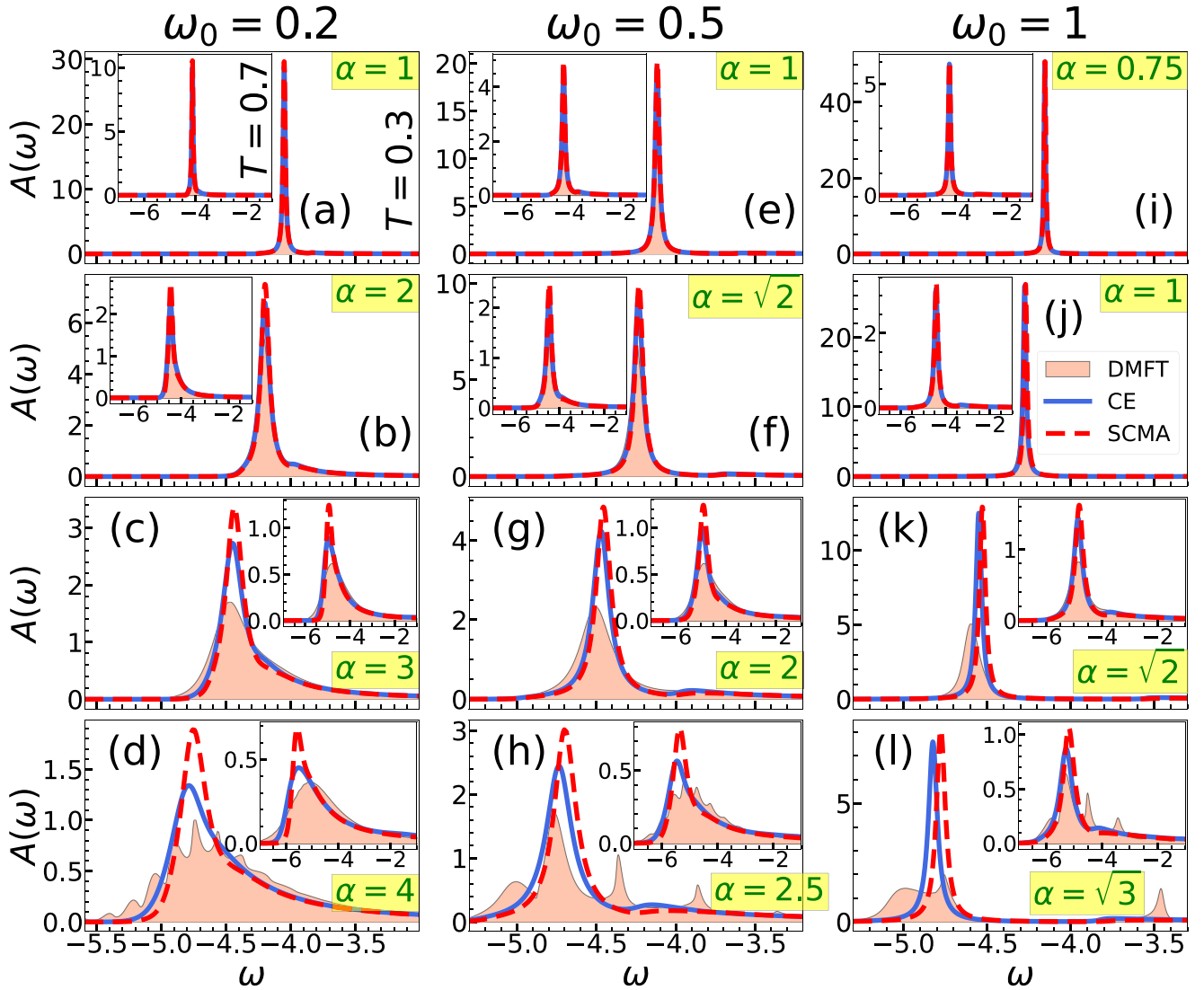


FIG. 12. (a)–(h) Comparison of the CE, DMFT, and SCMA spectral functions in 2D for $k = 0$ and $t_0 = 1$. The main panels show the results for $T_1 = 0.3$, while $T_2 = 0.7$ results are shown in the insets.

peak; see Fig. 1(c) from Ref. [50]. However, Fig. S9 in the Supplemental Material of Ref. [52] demonstrates that the spectral function in the thermodynamic limit for $t_0 = \omega_0 = g = 1$, $k = \pi$ consists of a broad single-peak structure even at $T = 0$. This conclusion was reached by carefully examining the finite-size effects using the numerically exact hierarchical equations of motion method (HEOM). It was established that the system with $N = 10$ lattice sites is representative of the thermodynamic limit, although much smaller systems are required for the $k = 0$ results. Furthermore, the same figure shows that two distinct peaks emerge for $N = 6$ and $k = \pi$, in accordance with the FTLM results. Hence, CE will provide much better results in the thermodynamic limit than previously expected. We note that for $t_0 = \omega_0 = g = 1$ and finite temperatures, one might expect that the required lattice size, representative of the thermodynamic limit, does not exceed $N = 10$, as the electron experiences much more scattering compared to the $T = 0$ case. This will be cross-checked independently (using the DMFT) in the rest of this Appendix for finite T , which satisfies the $T < \omega_0$ condi-

tion. In that case, we analyze the overall performance of the CE.

In Fig. 13(a), we show the FTLM data, (originally from Ref. [44]) used in Ref. [50], and compare them to the DMFT applied on a system of finite lattice size. We exploit the fact that the corresponding spectral functions (although certainly not as accurate in comparison with the exact solution) provide a rough estimate of how large N should be to faithfully represent the thermodynamic limit; see Sec. IV from the Supplemental Material of Ref. [52] for more details. In accordance with the FTLM results, we see that the DMFT spectral function for $N = 6$ also predicts distinct peaks around $\omega \approx 1.5$ and $\omega \approx 2.5$, although there is an additional peak around $\omega \approx 2$. Nevertheless, these results change drastically with increasing N and practically converge for $N = 10$. This is the same N as predicted by HEOM at $T = 0$. Therefore, the presented FTLM results are not representative of the thermodynamic limit. Additionally, Fig. 13(a) also shows that FTLM results for $T = 0.6$ and $T = 0.8$ are quite similar. Hence, our further analysis will be conducted for $T = 0.7$ case.

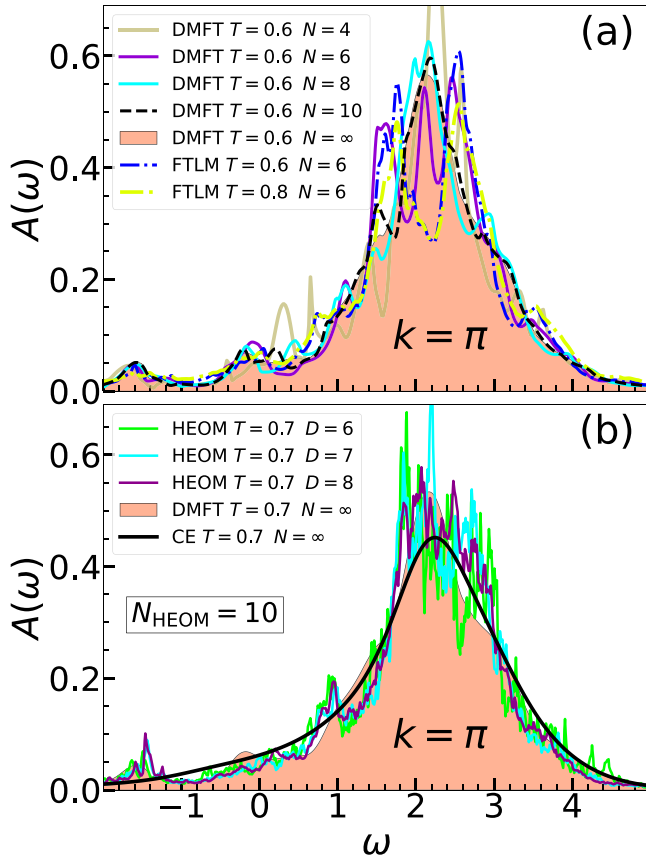


FIG. 13. CE, DMFT, FTLM, and HEOM spectral functions for $t_0 = \omega_0 = g = 1$. (a) Analysis of the finite-size effects. (b) Inspecting the convergence of HEOM data with respect to hierarchy depth D .

In Fig. 13(b), we present HEOM results for $N = 10$ and compare them to CE and DMFT. We note that HEOM has one additional parameter, the so-called hierarchy depth D . For details, we refer the reader to Ref. [47], but we only briefly mention that the numerically exact results are formally obtained in the limit $D \rightarrow \infty$. In practice, we always check whether the results converge with respect to D , which cannot be increased indefinitely, as finite computer memory presents a limiting factor. We see that the HEOM results have practically converged for $N = 10$ and $D = 8$. Here, the HEOM solution does not possess the two-peak structure predicted by the FTLM on a smaller lattice size ($N = 6$). It actually gives only a single, broad peak around $\omega \approx 2$, which is correctly reproduced by both the CE and the DMFT. Although the CE misses the quasiparticle peak around $\omega \approx -1.5$, we conclude that CE gives much more accurate results for the thermodynamic limit than for a finite system.

APPENDIX D: MOBILITY RESULTS FROM THE ONE-SHOT MIGDAL APPROXIMATION

In Sec. V, we presented and analyzed the mobility predictions from the CE, DMFT, and SCMA methods. Here, we supplement that study with the data from the one-shot MA (i.e., SCMA without self-consistency). The results are shown in Fig. 14. Since the mobility results have already been

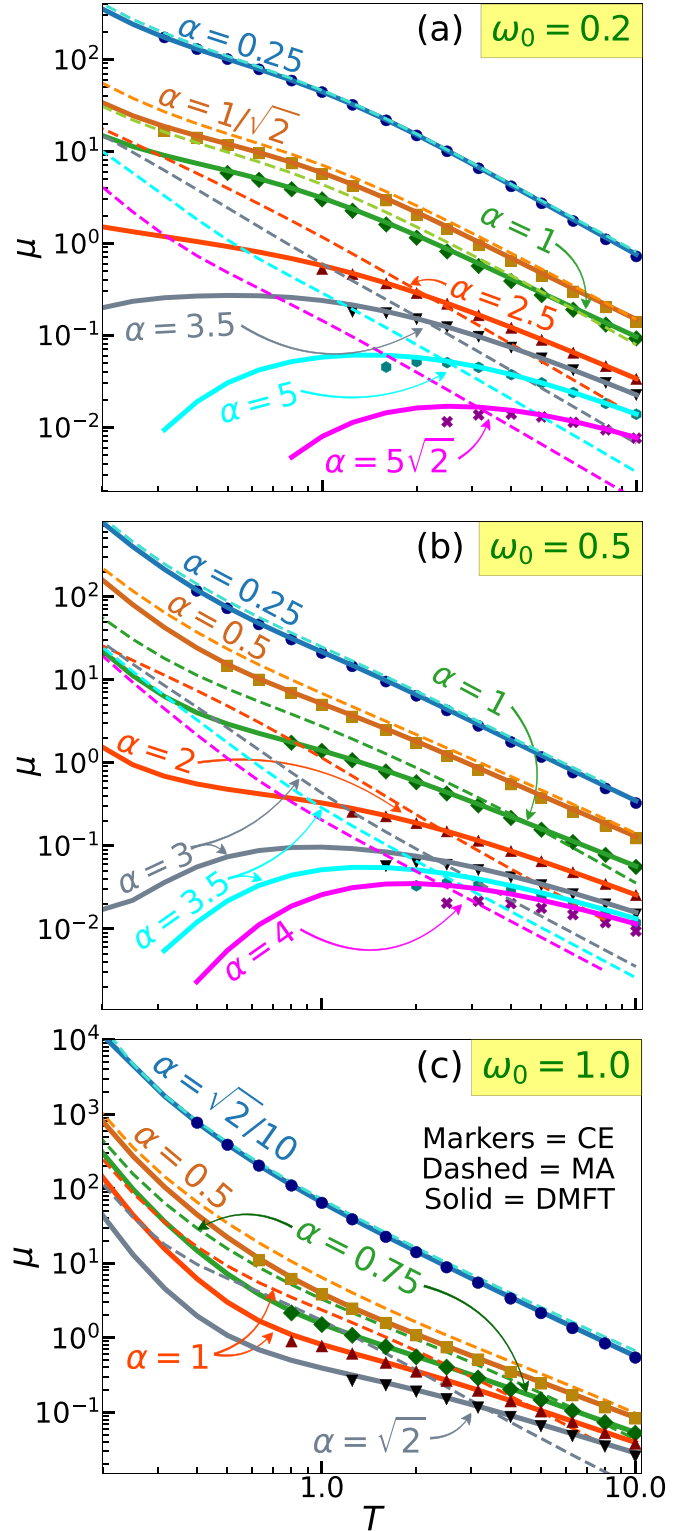


FIG. 14. Temperature dependence of the mobility within CE, DMFT, and MA. Here $t_0 = 1$.

thoroughly analyzed in Sec. V, we will here give only brief comments about the performance of the MA. Figure 14(a) shows that MA is practically useless for $\alpha \gtrsim 2.5$. Here, the results are not even qualitatively correct, regardless of the temperature. Even for $\alpha = 1$, the results are still not satisfactory:

the predictions for $T < 4$ ($T > 9$) overestimate (underestimate) the DMFT benchmark. MA proves to be reliable only for very weak interactions $\alpha \lesssim 1/\sqrt{2}$. Here, the results are better for higher temperatures. This is expected as the MA

takes into account only the lowest-order Feynman diagram, while the relevance of higher-order diagrams decreases as the temperature is increased. Similar analysis can be repeated for other phonon frequencies in Figs. 14(b) and 14(c).

-
- [1] G. Mahan, *Many-Particle Physics* (Kluwer Academic, New York, 2000).
- [2] R. Kubo, Generalized cumulant expansion method, *J. Phys. Soc. Jpn.* **17**, 1100 (1962).
- [3] B. I. Lundqvist, Characteristic structure in core electron spectra of metals due to the electron-plasmon coupling, *Phys. Kondens. Mater.* **9**, 236 (1969).
- [4] D. C. Langreth, Singularities in the x-ray spectra of metals, *Phys. Rev. B* **1**, 471 (1970).
- [5] L. Hedin, Effects of recoil on shake-up spectra in metals, *Phys. Scr.* **21**, 477 (1980).
- [6] L. Hedin, On correlation effects in electron spectroscopies and the *GW* approximation, *J. Phys.: Condens. Matter* **11**, R489 (1999).
- [7] F. Aryasetiawan, L. Hedin, and K. Karlsson, Multiple Plasmon Satellites in Na and Al Spectral Functions from *Ab Initio* Cumulant Expansion, *Phys. Rev. Lett.* **77**, 2268 (1996).
- [8] B. Holm and F. Aryasetiawan, Self-consistent cumulant expansion for the electron gas, *Phys. Rev. B* **56**, 12825 (1997).
- [9] G. D. Mahan, Phonon-broadened optical spectra: Urbach's rule, *Phys. Rev.* **145**, 602 (1966).
- [10] D. Dunn, Electron-Phonon Interactions in an insulator, *Can. J. Phys.* **53**, 321 (1975).
- [11] O. Gunnarsson, V. Meden, and K. Schönhammer, Corrections to Migdal's theorem for spectral functions: A cumulant treatment of the time-dependent Green's function, *Phys. Rev. B* **50**, 10462 (1994).
- [12] C. Verdi, F. Caruso, and F. Giustino, Origin of the crossover from polarons to Fermi liquids in transition metal oxides, *Nat. Commun.* **8**, 15769 (2017).
- [13] G. Antonius, Y.-H. Chan, and S. G. Louie, Polaron spectral properties in doped ZnO and SrTiO₃ from first principles, *Phys. Rev. Res.* **2**, 043296 (2020).
- [14] S. Moser, L. Moreschini, J. Jačimović, O. S. Barišić, H. Berger, A. Magrez, Y. J. Chang, K. S. Kim, A. Bostwick, E. Rotenberg, L. Forró, and M. Gironi, Tunable Polaronic Conduction in Anatase TiO₂, *Phys. Rev. Lett.* **110**, 196403 (2013).
- [15] F. Giustino, Electron-phonon interactions from first principles, *Rev. Mod. Phys.* **89**, 015003 (2017).
- [16] J.-J. Zhou and M. Bernardi, Predicting charge transport in the presence of polarons: The beyond-quasiparticle regime in SrTiO₃, *Phys. Rev. Res.* **1**, 033138 (2019).
- [17] B. K. Chang, J.-J. Zhou, N.-E. Lee, and M. Bernardi, Intermediate polaronic charge transport in organic crystals from a many-body first-principles approach, *npj Comput. Mater.* **8**, 63 (2022).
- [18] S. M. Story, J. J. Kas, F. D. Vila, M. J. Verstraete, and J. J. Rehr, Cumulant expansion for phonon contributions to the electron spectral function, *Phys. Rev. B* **90**, 195135 (2014).
- [19] J. J. Kas, J. J. Rehr, and L. Reining, Cumulant expansion of the retarded one-electron Green function, *Phys. Rev. B* **90**, 085112 (2014).
- [20] J. Lischner, D. Vigil-Fowler, and S. G. Louie, Satellite structures in the spectral functions of the two-dimensional electron gas in semiconductor quantum wells: A *GW* plus cumulant study, *Phys. Rev. B* **89**, 125430 (2014).
- [21] F. Caruso and F. Giustino, Spectral fingerprints of electron-plasmon coupling, *Phys. Rev. B* **92**, 045123 (2015).
- [22] J. S. Zhou, J. Kas, L. Sponza, I. Reshetnyak, M. Guzzo, C. Giorgetti, M. Gatti, F. Sottile, J. Rehr, and L. Reining, Dynamical effects in electron spectroscopy, *J. Chem. Phys.* **143**, 184109 (2015).
- [23] B. Gumhalter, V. Kovač, F. Caruso, H. Lambert, and F. Giustino, On the combined use of *GW* approximation and cumulant expansion in the calculations of quasiparticle spectra: The paradigm of Si valence bands, *Phys. Rev. B* **94**, 035103 (2016).
- [24] D. Vigil-Fowler, S. G. Louie, and J. Lischner, Dispersion and line shape of plasmon satellites in one, two, and three dimensions, *Phys. Rev. B* **93**, 235446 (2016).
- [25] J. S. Zhou, M. Gatti, J. J. Kas, J. J. Rehr, and L. Reining, Cumulant Green's function calculations of plasmon satellites in bulk sodium: Influence of screening and the crystal environment, *Phys. Rev. B* **97**, 035137 (2018).
- [26] J. Ma and J. Cao, Förster resonance energy transfer, absorption and emission spectra in multichromophoric systems. I. Full cumulant expansions and system-bath entanglement, *J. Chem. Phys.* **142**, 094106 (2015).
- [27] L. Cupellini, F. Lipparini, and J. Cao, Absorption and circular dichroism spectra of molecular aggregates with the full cumulant expansion, *J. Phys. Chem. B* **124**, 8610 (2020).
- [28] J. A. Nöthling, T. Mančal, and T. Krüger, Accuracy of approximate methods for the calculation of absorption-type linear spectra with a complex system-bath coupling, *J. Chem. Phys.* **157**, 095103 (2022).
- [29] J. P. Nery, P. B. Allen, G. Antonius, L. Reining, A. Miglio, and X. Gonze, Quasiparticles and phonon satellites in spectral functions of semiconductors and insulators: Cumulants applied to the full first-principles theory and the Fröhlich polaron, *Phys. Rev. B* **97**, 115145 (2018).
- [30] N. Kandolf, C. Verdi, and F. Giustino, Many-body Green's function approaches to the doped Fröhlich solid: Exact solutions and anomalous mass enhancement, *Phys. Rev. B* **105**, 085148 (2022).
- [31] A. S. Mishchenko, N. V. Prokof'ev, A. Sakamoto, and B. V. Svistunov, Diagrammatic quantum Monte Carlo study of the Fröhlich polaron, *Phys. Rev. B* **62**, 6317 (2000).
- [32] T. Holstein, Studies of polaron motion: Part I. The molecular-crystal model, *Ann. Phys.* **8**, 325 (1959).
- [33] I. Lang and Y. A. Firsov, Kinetic theory of semiconductors with low mobility, *Zh. Eksp. Teor. Fiz.* **43**, 1843 (1962) [*Sov. Phys. JETP* **16**, 1301 (1963)].
- [34] A. S. Alexandrov, *Polarons in Advanced Materials*, Springer Series in Materials Science, Vol. 103 (Springer, Dordrecht, 2007).

- [35] E. Jeckelmann and S. R. White, Density-matrix renormalization-group study of the polaron problem in the Holstein model, *Phys. Rev. B* **57**, 6376 (1998).
- [36] P. E. Kornilovitch, Continuous-Time Quantum Monte Carlo Algorithm for the Lattice Polaron, *Phys. Rev. Lett.* **81**, 5382 (1998).
- [37] A. H. Romero, D. W. Brown, and K. Lindenberg, Converging toward a practical solution of the Holstein molecular crystal model, *J. Chem. Phys.* **109**, 6540 (1998).
- [38] S. Fratini and S. Ciuchi, Dynamical Mean-Field Theory of Transport of Small Polarons, *Phys. Rev. Lett.* **91**, 256403 (2003).
- [39] S. Fratini and S. Ciuchi, Optical properties of small polarons from dynamical mean-field theory, *Phys. Rev. B* **74**, 075101 (2006).
- [40] C. Zhang, E. Jeckelmann, and S. R. White, Dynamical properties of the one-dimensional Holstein model, *Phys. Rev. B* **60**, 14092 (1999).
- [41] G. L. Goodvin, M. Berciu, and G. A. Sawatzky, Green's function of the Holstein polaron, *Phys. Rev. B* **74**, 245104 (2006).
- [42] M. Berciu, Green's Function of a Dressed Particle, *Phys. Rev. Lett.* **97**, 036402 (2006).
- [43] S. Ciuchi, E. Cappelluti, and S. Fratini, Optical properties of lattice/magnetic small polarons from DMFT, *J. Phys. Chem. Solids* **69**, 2164 (2008).
- [44] J. Bonča, S. A. Trugman, and M. Berciu, Spectral function of the Holstein polaron at finite temperature, *Phys. Rev. B* **100**, 094307 (2019).
- [45] N. Prodanović and N. Vukmirović, Charge carrier mobility in systems with local electron-phonon interaction, *Phys. Rev. B* **99**, 104304 (2019).
- [46] D. Jansen, J. Bonča, and F. Heidrich-Meisner, Finite-temperature density-matrix renormalization group method for electron-phonon systems: Thermodynamics and Holstein-polaron spectral functions, *Phys. Rev. B* **102**, 165155 (2020).
- [47] V. Janković and N. Vukmirović, Spectral and thermodynamic properties of the Holstein polaron: Hierarchical equations of motion approach, *Phys. Rev. B* **105**, 054311 (2022).
- [48] J. Bonča and S. A. Trugman, Electron removal spectral function of a polaron coupled to dispersive optical phonons, *Phys. Rev. B* **106**, 174303 (2022).
- [49] A. S. Mishchenko, N. Nagaosa, and N. Prokof'ev, Diagrammatic Monte Carlo Method for Many-Polaron Problems, *Phys. Rev. Lett.* **113**, 166402 (2014).
- [50] P. J. Robinson, I. S. Dunn, and D. R. Reichman, Cumulant methods for electron-phonon problems. I. Perturbative expansions, *Phys. Rev. B* **105**, 224304 (2022).
- [51] P. J. Robinson, I. S. Dunn, and D. R. Reichman, Cumulant methods for electron-phonon problems. II. The self-consistent cumulant expansion, *Phys. Rev. B* **105**, 224305 (2022).
- [52] P. Mitrić, V. Janković, N. Vukmirović, and D. Tanasković, Spectral Functions of the Holstein Polaron: Exact and Approximate Solutions, *Phys. Rev. Lett.* **129**, 096401 (2022).
- [53] S. Ciuchi, F. de Pasquale, S. Fratini, and D. Feinberg, Dynamical mean-field theory of the small polaron, *Phys. Rev. B* **56**, 4494 (1997).
- [54] See Supplemental Material at <http://link.aps.org/supplemental/10.1103/PhysRevB.107.125165> for additional figures and derivations.
- [55] D. Levin, Fast integration of rapidly oscillatory functions, *J. Comput. Appl. Math.* **67**, 95 (1996).
- [56] A. Migdal, Interaction between electrons and lattice vibrations in a normal metal, *Zh. Eksp. Teor. Fiz.* **34**, 1438 (1958) [*Sov. Phys. JETP* **7**, 996 (1958)].
- [57] A. Georges, G. Kotliar, W. Krauth, and M. J. Rozenberg, Dynamical mean-field theory of strongly correlated fermion systems and the limit of infinite dimensions, *Rev. Mod. Phys.* **68**, 13 (1996).
- [58] P. E. Kornilovitch, Photoemission spectroscopy and sum rules in dilute electron-phonon systems, *Europhys. Lett.* **59**, 735 (2002).
- [59] A. Khurana, Electrical Conductivity in the Infinite-Dimensional Hubbard Model, *Phys. Rev. Lett.* **64**, 1990 (1990).
- [60] S. Fratini, F. de Pasquale, and S. Ciuchi, Optical absorption from a nondegenerate polaron gas, *Phys. Rev. B* **63**, 153101 (2001).
- [61] W. H. Press, S. A. Teukolsky, W. T. Vetterling, and B. P. Flannery, *Numerical Recipes: The Art of Scientific Computing*, 3rd ed. (Cambridge University Press, Cambridge, 2007).
- [62] S. Fratini, D. Mayou, and S. Ciuchi, The transient localization scenario for charge transport in crystalline organic materials, *Adv. Funct. Mater.* **26**, 2292 (2016).
- [63] J. Bonča and S. A. Trugman, Dynamic properties of a polaron coupled to dispersive optical phonons, *Phys. Rev. B* **103**, 054304 (2021).
- [64] G. D. Mahan, Mobility of polarons, *Phys. Rev.* **142**, 366 (1966).

Supplemental Material: Cumulant expansion in the Holstein model: Spectral functions and mobility

Petar Mitrić, Veljko Janković, Nenad Vukmirović, and Darko Tanasković
Institute of Physics Belgrade, University of Belgrade, Pregrevica 118, 11080 Belgrade, Serbia

Here we supplement the main text by giving an alternative derivation of the cumulant function in Sec. I, additional spectral functions and heat maps in Sec. II, and a comparison of the 1D ground state energy using DMFT, CE, SCMA, and MA in Sec. III.

I. ALTERNATIVE DERIVATION OF THE CUMULANT FUNCTION IN THE CE METHOD

In Sec. XI of the Supplemental Material in Ref. [S1], we showed that the Green's function, if there is only a single electron in the band, can be written as

$$G_{\mathbf{k}}(t) = -i\theta(t)\langle c_{\mathbf{k}}(t)c_{\mathbf{k}}^{\dagger} \rangle_{T,0}, \quad (\text{S1})$$

where:

$$c_{\mathbf{k}}(t) = e^{iHt}c_{\mathbf{k}}e^{-iHt}, \quad (\text{S2a})$$

$$H = H_{\text{el}} + H_{\text{ph}} + H_{\text{el-ph}}, \quad (\text{S2b})$$

$$H_{\text{el}} = -t_0 \sum_{\langle ij \rangle} (c_i^{\dagger}c_j + \text{H.c.}) = \sum_{\mathbf{k}} \varepsilon_{\mathbf{k}} c_{\mathbf{k}}^{\dagger} c_{\mathbf{k}}, \quad (\text{S2c})$$

$$H_{\text{ph}} = \omega_0 \sum_i a_i^{\dagger} a_i = \omega_0 \sum_{\mathbf{k}} a_{\mathbf{k}}^{\dagger} a_{\mathbf{k}}, \quad (\text{S2d})$$

$$\begin{aligned} H_{\text{el-ph}} &= -g \sum_i c_i^{\dagger} c_i (a_i^{\dagger} + a_i) \\ &= -\frac{g}{\sqrt{N}} \sum_{\mathbf{k}, \mathbf{q}} c_{\mathbf{k}+\mathbf{q}}^{\dagger} c_{\mathbf{k}} (a_{\mathbf{q}} + a_{-\mathbf{q}}^{\dagger}). \end{aligned} \quad (\text{S2e})$$

Here, N is the number of sites (we take $N \rightarrow \infty$ in order to get the thermodynamic limit), while $\langle \dots \rangle_{T,0}$ denotes the thermal average over the states with no electrons

and arbitrary number of phonons

$$\langle x \rangle_{T,0} = \frac{\sum_{\{n_p\}} \langle 0, \tilde{n}_p | e^{-H_{\text{ph}}/T} x | 0, \tilde{n}_p \rangle}{\sum_{\{n_p\}} \langle 0, \tilde{n}_p | e^{-H_{\text{ph}}/T} | 0, \tilde{n}_p \rangle}. \quad (\text{S3})$$

For the rest of this section, an arbitrary state with n_p phonons and no electrons (since such state is not unique) will be denoted by $|0, \tilde{n}_p\rangle$, while $\sum_{\{n_p\}}$ represents the sum over all possible phonon configurations. We also introduce $|\mathbf{k}, \tilde{n}_p\rangle \equiv c_{\mathbf{k}}^{\dagger} |0, \tilde{n}_p\rangle$ and $Z_{\text{ph}} = \sum_{\{n_p\}} \langle 0, \tilde{n}_p | e^{-H_{\text{ph}}/T} | 0, \tilde{n}_p \rangle$.

Using the fact that $|0, \tilde{n}_p\rangle$ is an eigenstate of both the full and the phononic Hamiltonian $H|0, \tilde{n}_p\rangle = H_{\text{ph}}|0, \tilde{n}_p\rangle = n_p\omega_0|0, \tilde{n}_p\rangle$, we see how Eq. (S1) can be written in a more explicit form

$$G_{\mathbf{k}}(t) = \frac{-i\theta(t)}{Z_{\text{ph}}} \sum_{\{n_p\}} e^{i\omega_0 n_p t} e^{-n_p\omega_0/T} \langle 0, \tilde{n}_p | c_{\mathbf{k}} e^{-iHt} c_{\mathbf{k}}^{\dagger} | 0, \tilde{n}_p \rangle. \quad (\text{S4})$$

The term e^{-iHt} can be read off from

$$e^{iH_{\text{el}}t} e^{iH_{\text{ph}}t} e^{-iHt} = T_t \exp \left[-i \int_0^t dt_1 H_{\text{el-ph}}^{(I)}(t_1) \right], \quad (\text{S5})$$

which represents two different, but equivalent, forms for the evolution operator in the Dirac picture. Here, $H_{\text{el-ph}}^{(I)}$ is the electron-phonon interaction part of the Hamiltonian in the Dirac picture and T_t is the time-ordering operator. For the purely phononic part $e^{-iH_{\text{ph}}t}$ we use $\langle 0, \tilde{n}_p | e^{-iH_{\text{ph}}t} = e^{-i\omega_0 n_p t} \langle 0, \tilde{n}_p |$, while purely electronic part $e^{-iH_{\text{el}}t}$ is dealt with analogously $\langle 0, \tilde{n}_p | c_{\mathbf{k}} e^{-iH_{\text{el}}t} = e^{-i\varepsilon_{\mathbf{k}}t} \langle 0, \tilde{n}_p | c_{\mathbf{k}}$. Hence, Eq. (S4) becomes

$$G_{\mathbf{k}}(t) = -\frac{i\theta(t)}{Z_{\text{ph}}} e^{-i\varepsilon_{\mathbf{k}}t} \sum_{\{n_p\}} e^{-n_p\omega_0/T} \left\langle 0, \tilde{n}_p \left| c_{\mathbf{k}} T_t \exp \left[-i \int_0^t dt_1 H_{\text{el-ph}}^{(I)}(t_1) \right] c_{\mathbf{k}}^{\dagger} \right| 0, \tilde{n}_p \right\rangle \quad (\text{S6a})$$

$$\equiv -i\theta(t) e^{-i\varepsilon_{\mathbf{k}}t} \left\langle T_t e^{-i \int_0^t dt_1 H_{\text{el-ph}}^{(I)}(t_1)} \right\rangle_{T, \mathbf{k}}. \quad (\text{S6b})$$

The expressions of the form (S6b) have been extensively studied in the past. As shown in Eq. (6.10) of Kubo's cu-

mulant paper [S2], the expectation value with the time-ordering can be written as

$$\left\langle T_t e^{-i \int_0^t dt_1 H_{\text{el-ph}}^{(I)}(t_1)} \right\rangle_{T,\mathbf{k}} = \exp \left\langle T_t e^{-i \int_0^t dt_1 H_{\text{el-ph}}^{(I)}(t_1)} - 1 \right\rangle_{T,\mathbf{k},c} \equiv e^{C_{\mathbf{k}}(t)}, \quad (\text{S7})$$

where we defined the cumulant function $C_{\mathbf{k}}(t)$. The notation $\langle \dots \rangle_c$ denotes the so-called cumulant average. For our present purposes, we only need to know how the first two cumulant averages are defined:

$$\langle X_1 \rangle_c = \langle X_1 \rangle \quad (\text{S8a})$$

$$\langle X_1 X_2 \rangle_c = \langle X_1 X_2 \rangle - \langle X_1 \rangle \langle X_2 \rangle. \quad (\text{S8b})$$

In general, the cumulant average is defined using the ordinary average, by formally expanding the following expression in the Taylor series with respect to ξ_i and equating, order by order, the terms on the left- and the right-hand side

$$\left\langle \exp \sum_j \xi_j X_j \right\rangle = \exp \left\langle \left(\exp \sum_j \xi_j X_j \right) - 1 \right\rangle_c. \quad (\text{S9})$$

The -1 term on the right-hand side is motivated by the fact that the expectation value of the unity operator is equal to 1. While our paper focuses on the cumulant of the second order, there is actually an analytic formula that relates the cumulant average of any order with the

ordinary average [S3].

Let us now go back to Eq. (S6b) and use Eq. (S7) to obtain

$$G_{\mathbf{k}}(t) = -i\theta(t)e^{-i\varepsilon_{\mathbf{k}}t}e^{C_{\mathbf{k}}(t)}, \quad (\text{S10})$$

where

$$C_{\mathbf{k}}(t) = \sum_{j=1}^{\infty} \left\langle T_t \frac{(-i)^j}{j!} \int_0^t \prod_{m=1}^j dt_m H_{\text{el-ph}}^{(I)}(t_m) \right\rangle_{T,\mathbf{k},c}. \quad (\text{S11})$$

So far, everything was exact. The approximation, that we now introduce, consists of keeping only the first two terms in the previous equation ($j = 1$ and $j = 2$ terms) while neglecting everything else. This is known as the second-order cumulant expansion. In the $j = 1$ term, the cumulant average coincides with the ordinary average (see Eq. (S8a)), and hence vanishes due to Wick's theorem. As a consequence, the cumulant average can be simply replaced by the ordinary average in the case of $j = 2$ term as well; see Eq. (S8b). Therefore, the second-order cumulant function reads as

$$C_{\mathbf{k}}(t) = -\frac{1}{2} \int_0^t dt_1 \int_0^t dt_2 \left\langle T_t c_{\mathbf{k}} H_{\text{el-ph}}^{(I)}(t_1) H_{\text{el-ph}}^{(I)}(t_2) c_{\mathbf{k}}^\dagger \right\rangle_{T,0}. \quad (\text{S12})$$

For a straightforward application of Wick's theorem, it is customary to rewrite electron creation and annihilation operators in the Dirac picture. In order not to change the already existing time ordering in Eq. (S12), the annihilation operator is expressed in the final time

$c_{\mathbf{k}} = e^{i\varepsilon_{\mathbf{k}}t} c_{\mathbf{k}}^{(I)}(t)$, while the creation operator is expressed in the initial time $c_{\mathbf{k}}^\dagger = c_{\mathbf{k}}^{\dagger(I)}(0)$. If we also use the explicit form of $H_{\text{el-ph}}^{(I)}(t)$ from Eq. (S2e), the Eq. (S12) becomes

$$C_{\mathbf{k}}(t) = -\frac{g^2}{2N} e^{i\varepsilon_{\mathbf{k}}t} \int_0^t dt_1 \int_0^t dt_2 \left\langle T_t c_{\mathbf{k}}^{(I)}(t) \sum_{\mathbf{k}_1, \mathbf{q}_1} c_{\mathbf{k}_1 + \mathbf{q}_1}^{\dagger(I)}(t_1) c_{\mathbf{k}_1}^{(I)}(t_1) A_{\mathbf{q}_1}^{(I)}(t_1) \sum_{\mathbf{k}_2, \mathbf{q}_2} c_{\mathbf{k}_2 + \mathbf{q}_2}^{\dagger(I)} c_{\mathbf{k}_2}^{(I)}(t_2) A_{\mathbf{q}_2}^{(I)}(t_2) c_{\mathbf{k}}^{\dagger(I)}(0) \right\rangle_{T,0}, \quad (\text{S13})$$

where we introduced the shorthand notation for the phonon part $A_{\mathbf{q}} = a_{\mathbf{q}} + a_{-\mathbf{q}}^\dagger$. Eq. (S13) is now straightforwardly evaluated using Wick's theorem. Contraction between the phonon degrees of freedom gives [S4]

$$\left\langle T_t A_{\mathbf{q}_1}^{(I)}(t_1) A_{\mathbf{q}_2}^{(I)}(t_2) \right\rangle = \delta_{\mathbf{q}_1, -\mathbf{q}_2} iD(t_1 - t_2), \quad (\text{S14})$$

where $iD(t_1 - t_2) = (n_{ph} + 1)e^{-i\omega_0|t_1 - t_2|} + n_{ph}e^{i\omega_0|t_1 - t_2|}$ is the phonon propagator, while $n_{ph} = 1/(e^{\omega_0/T} - 1)$ is the Bose factor. Since we are working in the limit of vanishing electron density (single electron in a band), the contraction between the electron creation and annihilation operators does not have a hole part, and hence

reads as

$$\langle T_t c_{\mathbf{k}}^{(I)}(t_1) c_{\mathbf{q}}^{\dagger(I)}(t_2) \rangle = \delta_{\mathbf{k},\mathbf{q}} e^{-i\varepsilon_{\mathbf{k}}|t_1-t_2|} \theta(t_1-t_2). \quad (\text{S15})$$

Taking all of this into account, Eq. (S13) simplifies

$$C_{\mathbf{k}}(t) = -\frac{g^2}{2N} \sum_{\mathbf{q}} \int_0^t dt_1 \int_0^t dt_2 e^{i(\varepsilon_{\mathbf{k}}-\varepsilon_{\mathbf{q}})|t_2-t_1|} iD(t_2-t_1). \quad (\text{S16})$$

We can get rid of the absolute value by noticing that the contributions for $t_2 > t_1$ and for $t_2 < t_1$ are equal. It is thus sufficient to restrict ourselves to $t_2 > t_1$ and multiply everything by 2. Also, the expression can be further simplified if we use

$$e^{i(\varepsilon_{\mathbf{k}}-\varepsilon_{\mathbf{q}}\pm\omega_0)(t_2-t_1)} = \int_{-\infty}^{\infty} d\omega e^{-i\omega(t_2-t_1)} \delta(\omega+\varepsilon_{\mathbf{k}}-\varepsilon_{\mathbf{q}}\pm\omega_0).$$

Then, the whole \mathbf{q} dependence is inside the Dirac delta function, which in combination with the summation over \mathbf{q} gives

$$\sum_{\mathbf{q}} \delta(\omega + \varepsilon_{\mathbf{k}} - \varepsilon_{\mathbf{q}} \pm \omega_0) = N\rho(\omega + \varepsilon_{\mathbf{k}} \pm \omega_0), \quad (\text{S17})$$

where ρ is the density of states. It is now straightforward to show that Eq. (S16) reduces to

$$C_{\mathbf{k}}(t) = g^2 \int_{-\infty}^{\infty} d\omega \frac{e^{-i\omega t} + i\omega t - 1}{\omega^2} \times [(n_{ph} + 1)\rho(\omega + \varepsilon_{\mathbf{k}} - \omega_0) + n_{ph}\rho(\omega + \varepsilon_{\mathbf{k}} + \omega_0)]. \quad (\text{S18})$$

This expression can be rewritten in terms of the Migdal self-energy (see Eq. (14) from the main text) as follows

$$C_{\mathbf{k}}(t) = \frac{1}{\pi} \int_{-\infty}^{\infty} d\omega \frac{|\text{Im}\Sigma^{\text{MA}}(\omega + \varepsilon_{\mathbf{k}})|}{\omega^2} (e^{-i\omega t} + i\omega t - 1). \quad (\text{S19})$$

Hence, we gave an alternative derivation of the cumulant function $C_{\mathbf{k}}(t)$, where the self-energy in the Migdal approximation emerges more explicitly than in Eq. (7) of the main text.

We note that the cumulant expansion method that we have now presented is analogous to the linked cluster expansion for the thermodynamic potential F in statistical mechanics. This is a consequence of the same mathematical form of $C_{\mathbf{k}}(t) = \ln(G_{\mathbf{k}}(t)/G_{\mathbf{k},0}(t))$ and $F = \ln(Z/Z_0)$, where Z and Z_0 are the partition function of the full and noninteracting theories.

II. SPECTRAL FUNCTIONS

In Sec. III of the main text, we presented spectral functions $A(\omega)$ and heat maps for $\omega_0 = 0.5$. Here, we present a large number of results for $\omega_0 = 1$, $\omega_0 = 0.2$, as well as some additional results for $\omega_0 = 0.5$ that are organized as follows:

1. Results for $\omega_0 = 1$:

- Fig. S1: $A(\omega)$ in the weak coupling regime for a wide range of temperatures and momenta.
- Fig. S2: $A(\omega)$ in the weak, intermediate and strong electron-phonon coupling regimes for $k = 0$ and $k = \pi$:
 - Fig. S2i: $k = 0$ at $T = 0.4$ and $T = 1$.
 - Fig. S2ii: $k = \pi$ at $T = 0.4$ and $T = 1$.
 - Fig. S2iii: $k = 0, \pi$ at $T = 2$ and $T = 5$.
- Fig. S3: $A(\omega)$ in the weak, intermediate and strong electron-phonon coupling regimes for $k = \pi/3$ and $k = 2\pi/3$:
 - Fig. S3i: $T = 0.4$.
 - Fig. S3ii: $T = 1$.
 - Fig. S3iii: $T = 2$ and $T = 5$.
- Fig. S4: Heat maps
 - Fig. S4i: $T = 0.4$.
 - Fig. S4ii: $T = 1$.

2. Results for $\omega_0 = 0.5$:

- Fig. S3: $A(\omega)$ in the weak, intermediate, and strong electron-phonon coupling regimes for $k = \pi/3$ and $k = 2\pi/3$:
 - Fig. S5i: $T = 0.3$.
 - Fig. S5ii: $T = 0.7$.
 - Fig. S5iii: $T = 2$ and $T = 5$.

3. Results for $\omega_0 = 0.2$:

- Fig. S6: $A(\omega)$ in the weak, intermediate and strong coupling regimes for $k = 0$ and $k = \pi$:
 - Fig. S6i: $k = 0$ at $T = 0.3$ and $T = 0.7$.
 - Fig. S6ii: $k = \pi$ at $T = 0.3$ and $T = 0.7$.
 - Fig. S6iii: $k = 0, \pi$ at $T = 2$ and $T = 5$.
- Fig. S7: $A(\omega)$ in the weak, intermediate and strong coupling regimes for $k = \pi/3$ and $k = 2\pi/3$:
 - Fig. S7i: $T = 0.3$.
 - Fig. S7ii: $T = 0.7$.

– Fig. S7iii: $T = 2$ and $T = 5$.

• Fig. S8: Heat maps:

– Fig. S8i: $T = 0.3$.

– Fig. S8ii: $T = 0.7$.

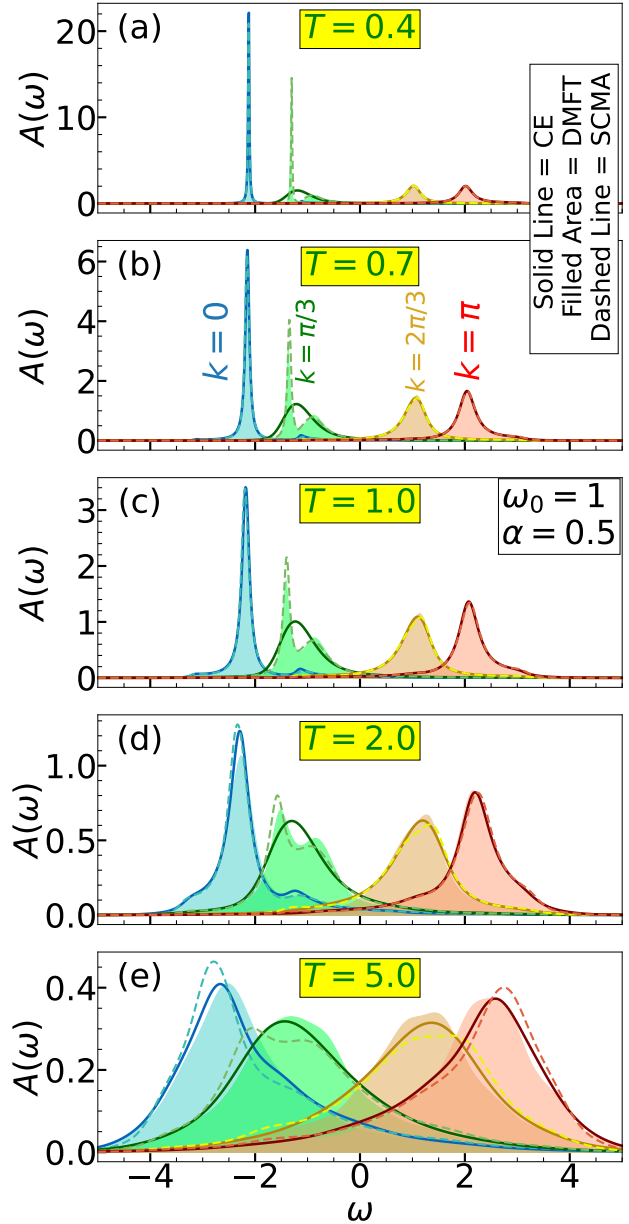
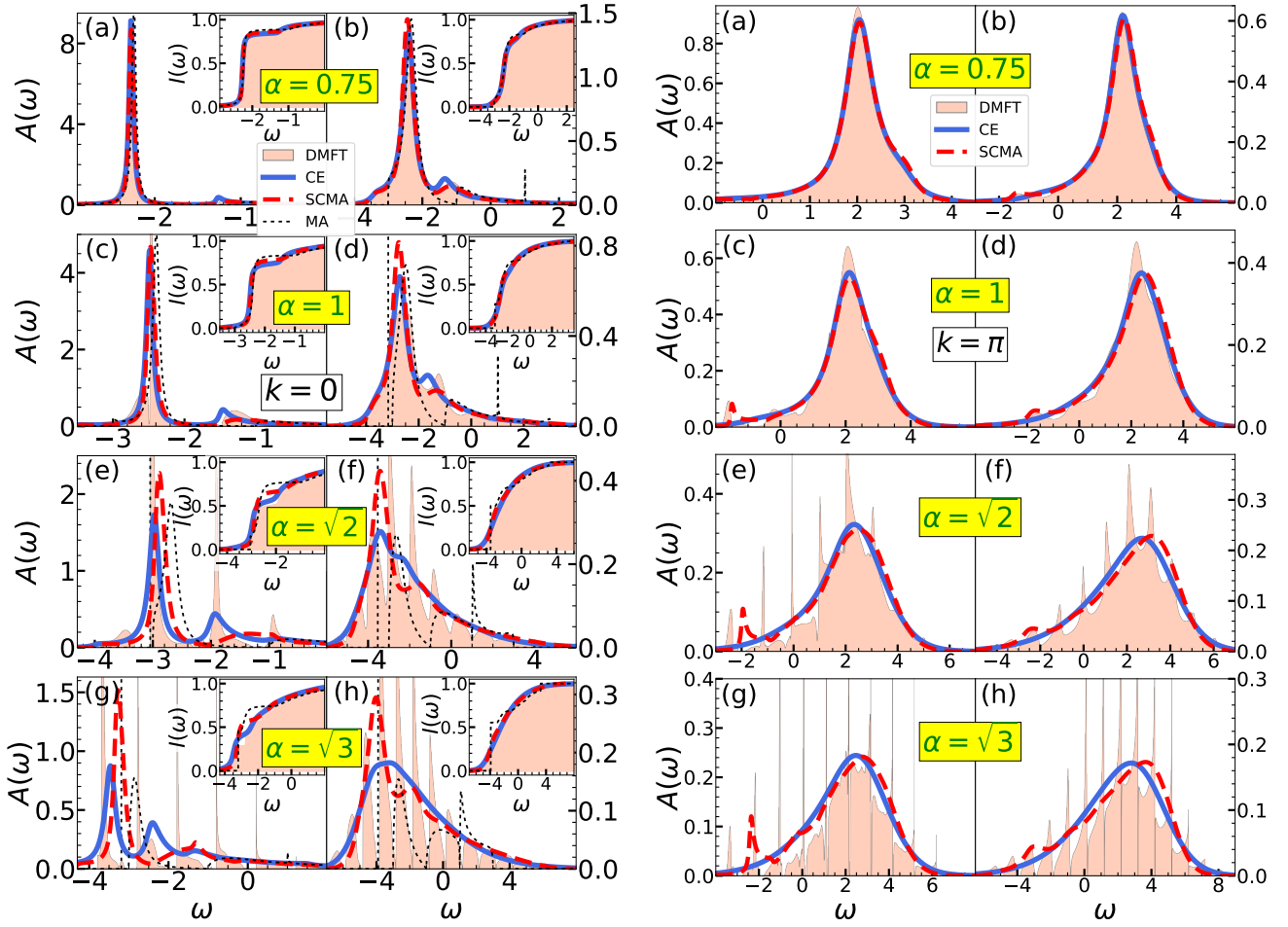
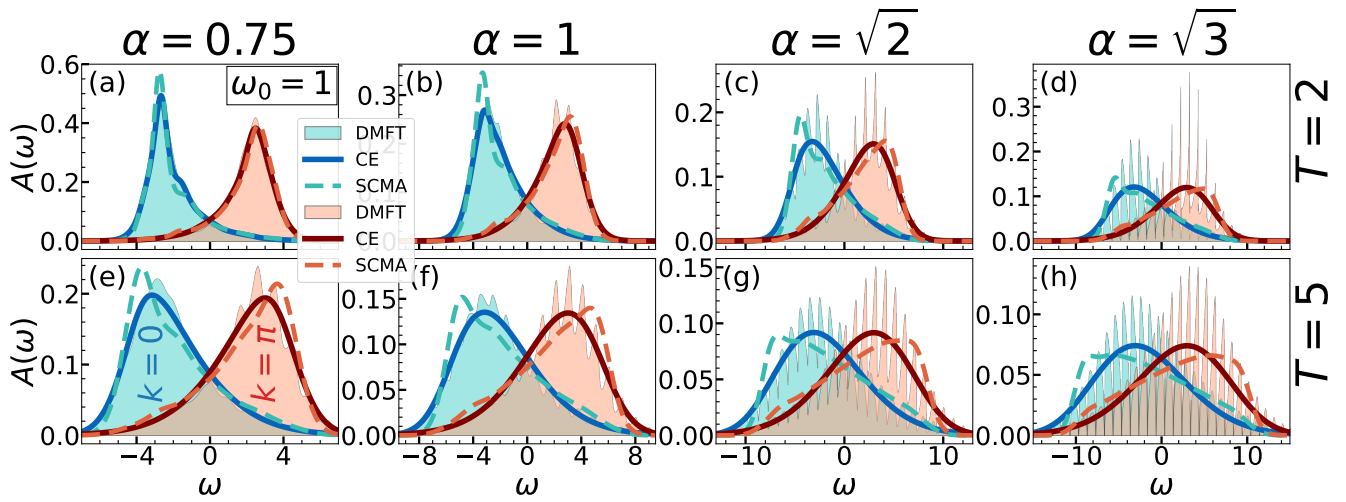


FIG. S1. (a)–(e) Comparison of CE, DMFT, and SCMA spectral functions in the weak coupling regime, for a wide range of temperatures. Here $t_0 = \omega_0 = 1$ and $\alpha = 0.5$.



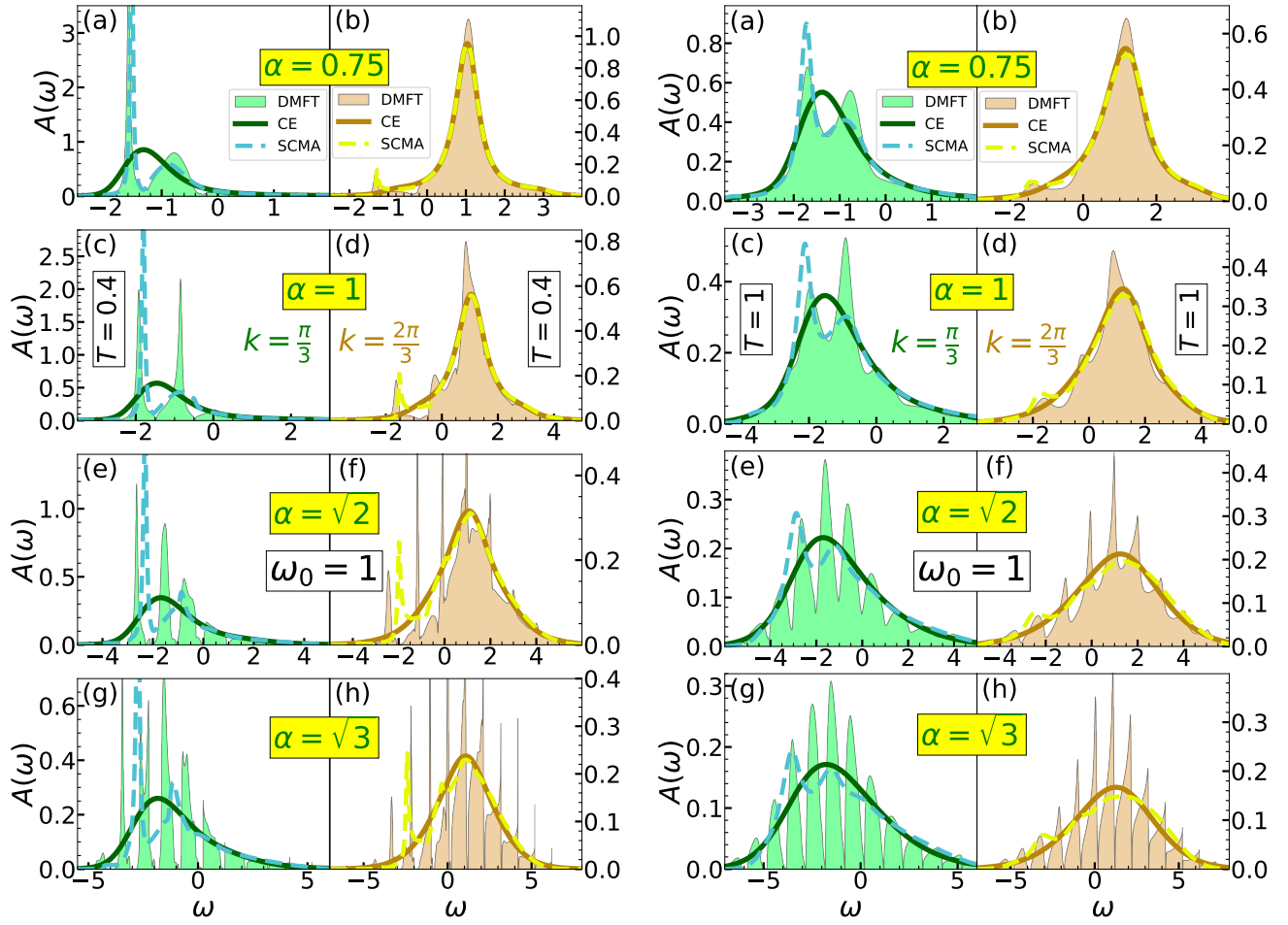
(i) (a)–(h) Spectral functions for $\omega_0 = 1$ and $k = 0$. In the left panels $T = 0.4$, while $T = 1$ in the right panels. Insets show the integrated spectral weights $I(\omega) = \int_{-\infty}^{\omega} A(\omega) d\omega$.

(ii) (a)–(h) Spectral functions for $\omega_0 = 1$ and $k = \pi$. In the left panels $T = 0.4$, while $T = 1$ in the right panels. Insets show the integrated spectral weights $I(\omega) = \int_{-\infty}^{\omega} A(\omega) d\omega$.



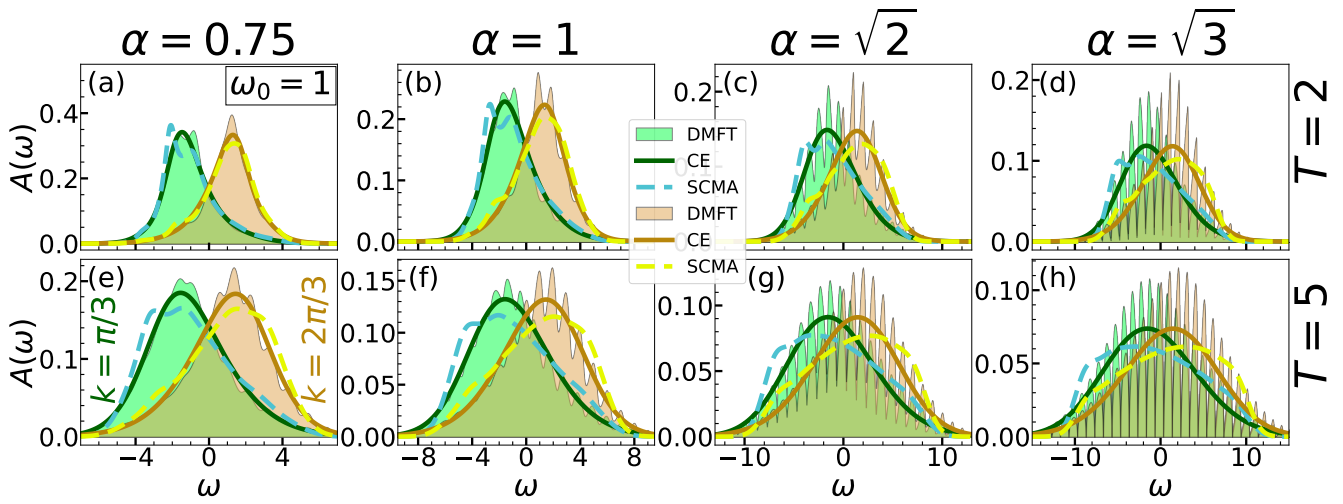
(iii) Spectral functions at higher temperatures for $\omega_0 = 1$ and $k = 0, \pi$.

FIG. S2. Comparison of the CE, DMFT, SCMA, and MA spectral functions in 1D for $t_0 = \omega_0 = 1$.



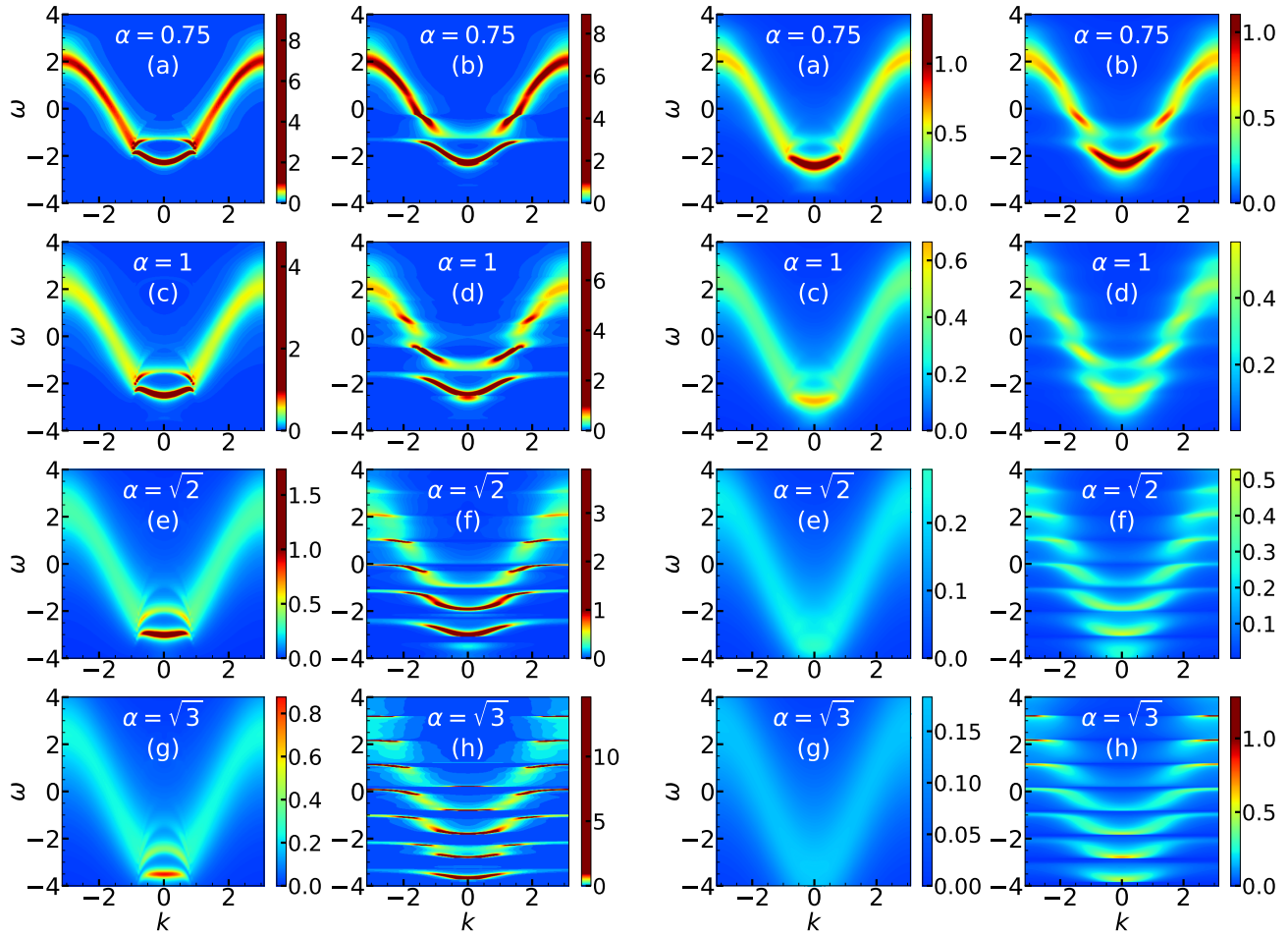
(i) (a)–(h) Spectral functions for $\omega_0 = 1$ and $T = 0.4$. In the left panels $k = \pi/3$, while $k = 2\pi/3$ in the right panels.

(ii) (a)–(h) Spectral functions for $\omega_0 = 1$ and $T = 1$. In the left panels $k = \pi/3$, while $k = 2\pi/3$ in the right panels.



(iii) Spectral functions at higher temperatures for $\omega_0 = 1$ and $k = \pi/3, 2\pi/3$.

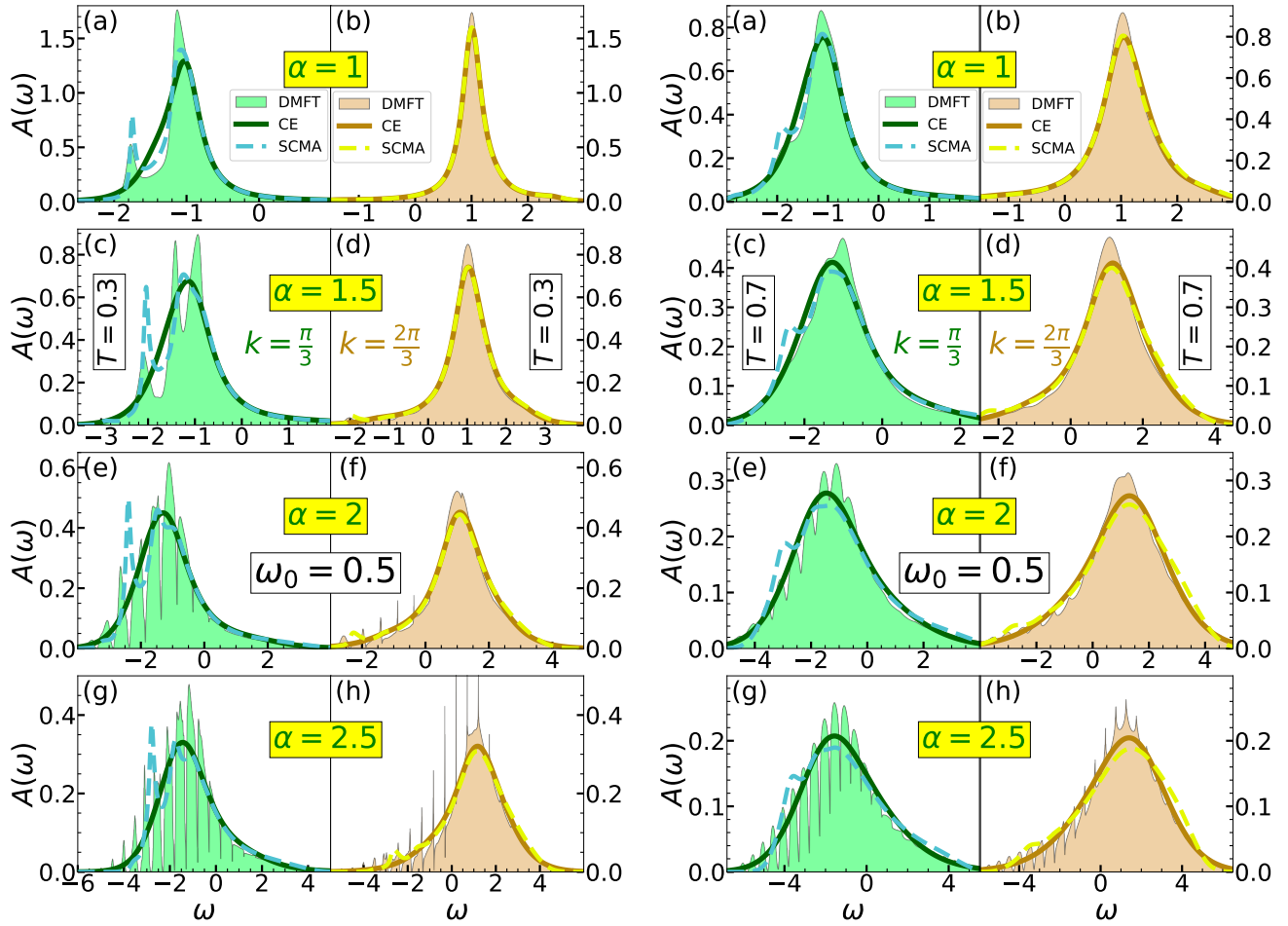
FIG. S3. Comparison of the CE, DMFT, and SCMA spectral functions in 1D for $t_0 = \omega_0 = 1$ and $k = \pi/3, 2\pi/3$.



(i) (a)–(h) Heat maps for $T = 0.4$. In the left panels, we present CE results, while the DMFT benchmark is presented in the right panels. All plots use the same color coding.

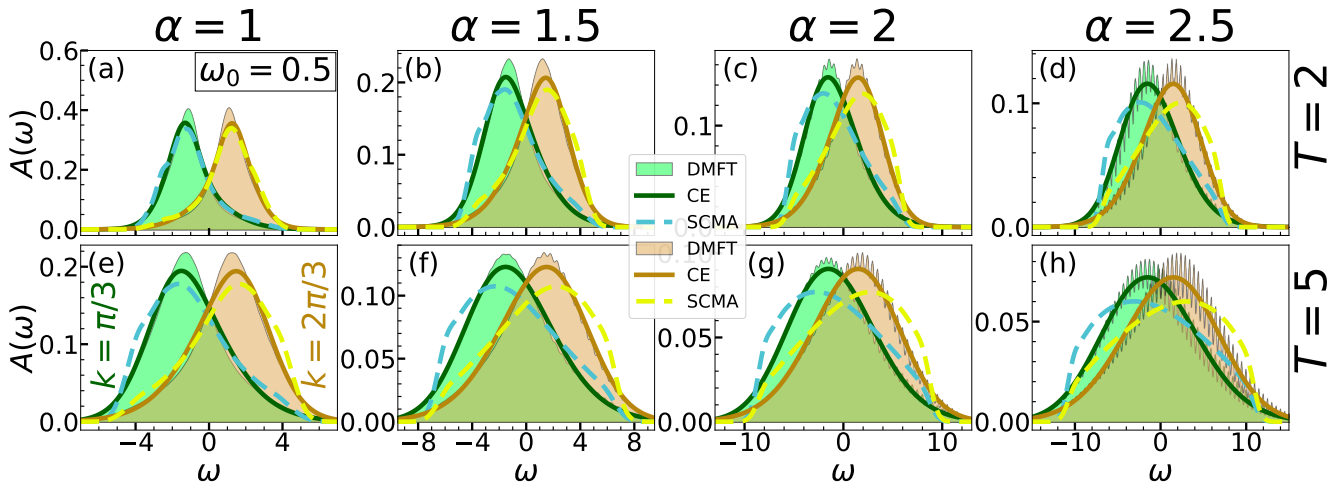
(ii) (a)–(h) Heat maps for $T = 1$. In the left panels, we present CE results, while the DMFT benchmark is presented in the right panels. All plots use the same color coding.

FIG. S4. Comparison of the CE and DMFT heat maps for $t_0 = \omega_0 = 1$.



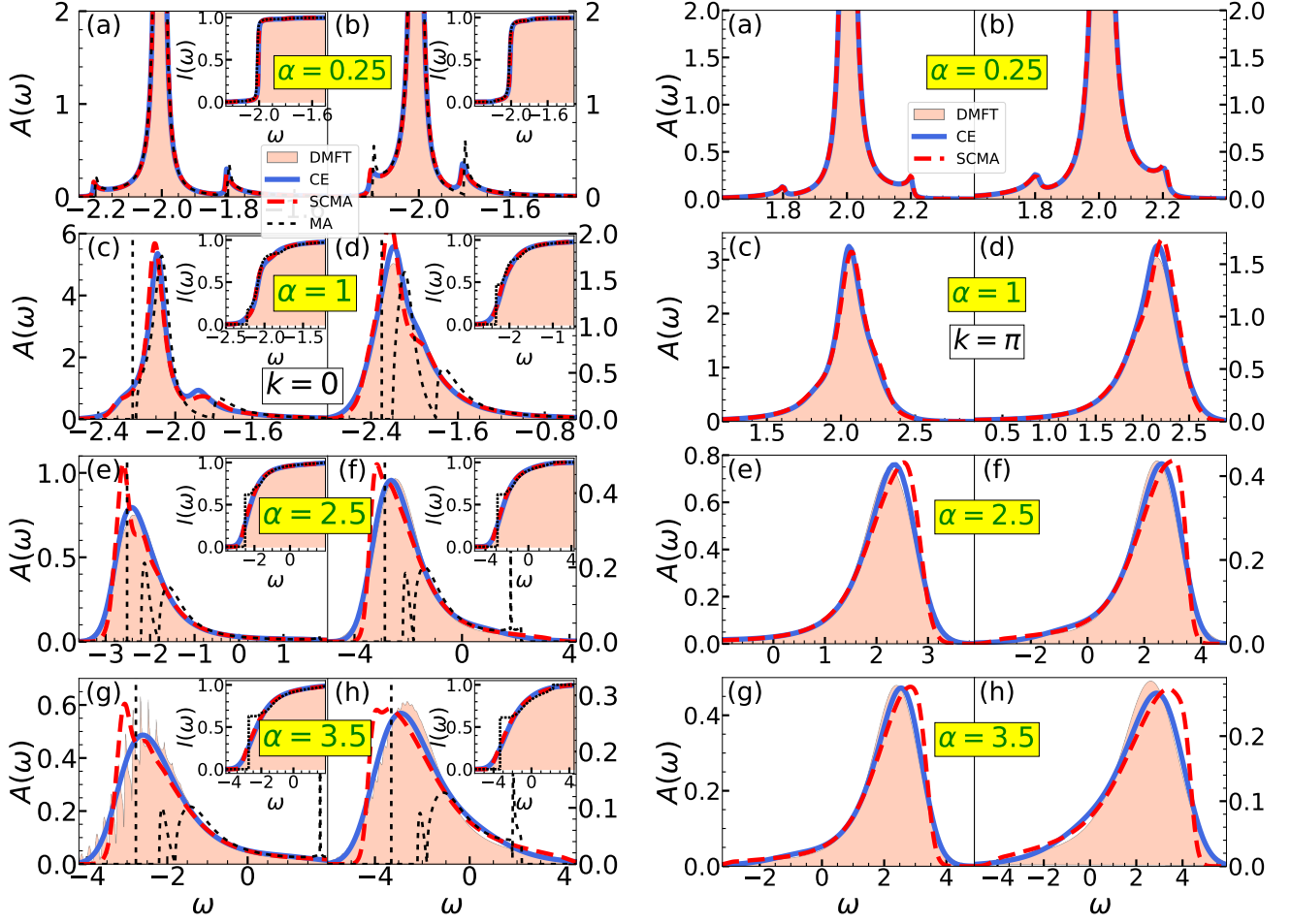
(i) (a)–(h) Spectral functions for $\omega_0 = 0.5$ and $T = 0.3$. In the left panels $k = \pi/3$, while $k = 2\pi/3$ in the right panels.

(ii) (a)–(h) Spectral functions for $\omega_0 = 0.5$ and $T = 0.7$. In the left panels $k = \pi/3$, while $k = 2\pi/3$ in the right panels.



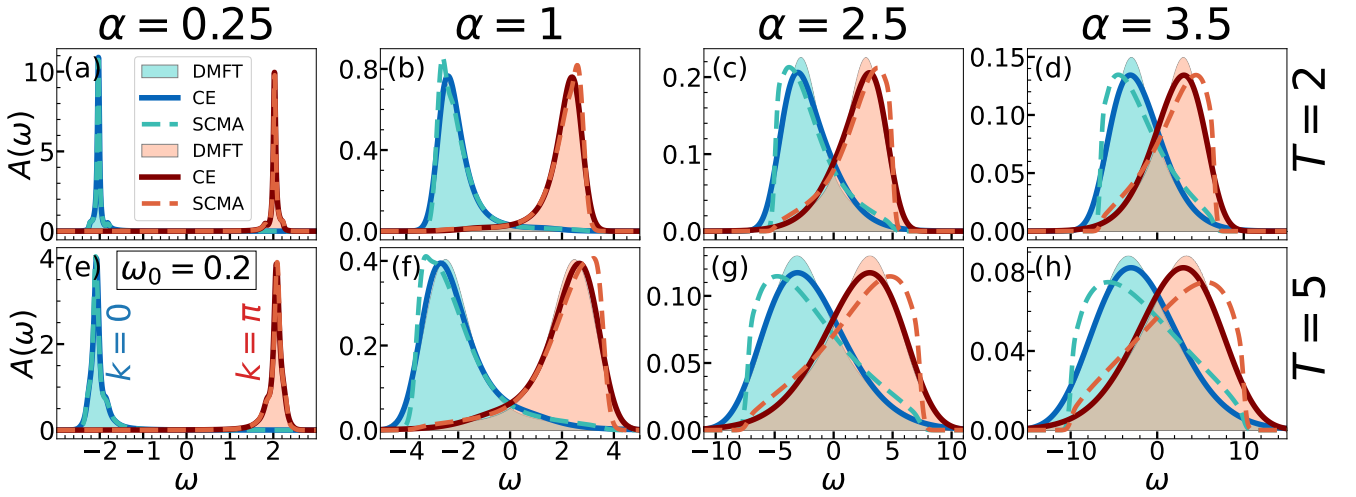
(iii) Spectral functions at higher temperatures for $\omega_0 = 0.5$ and $k = \pi/3, 2\pi/3$.

FIG. S5. Comparison of the CE, DMFT, and SCMA spectral functions in 1D for $t_0 = 1$, $\omega_0 = 0.5$ and $k = \pi/3, 2\pi/3$.



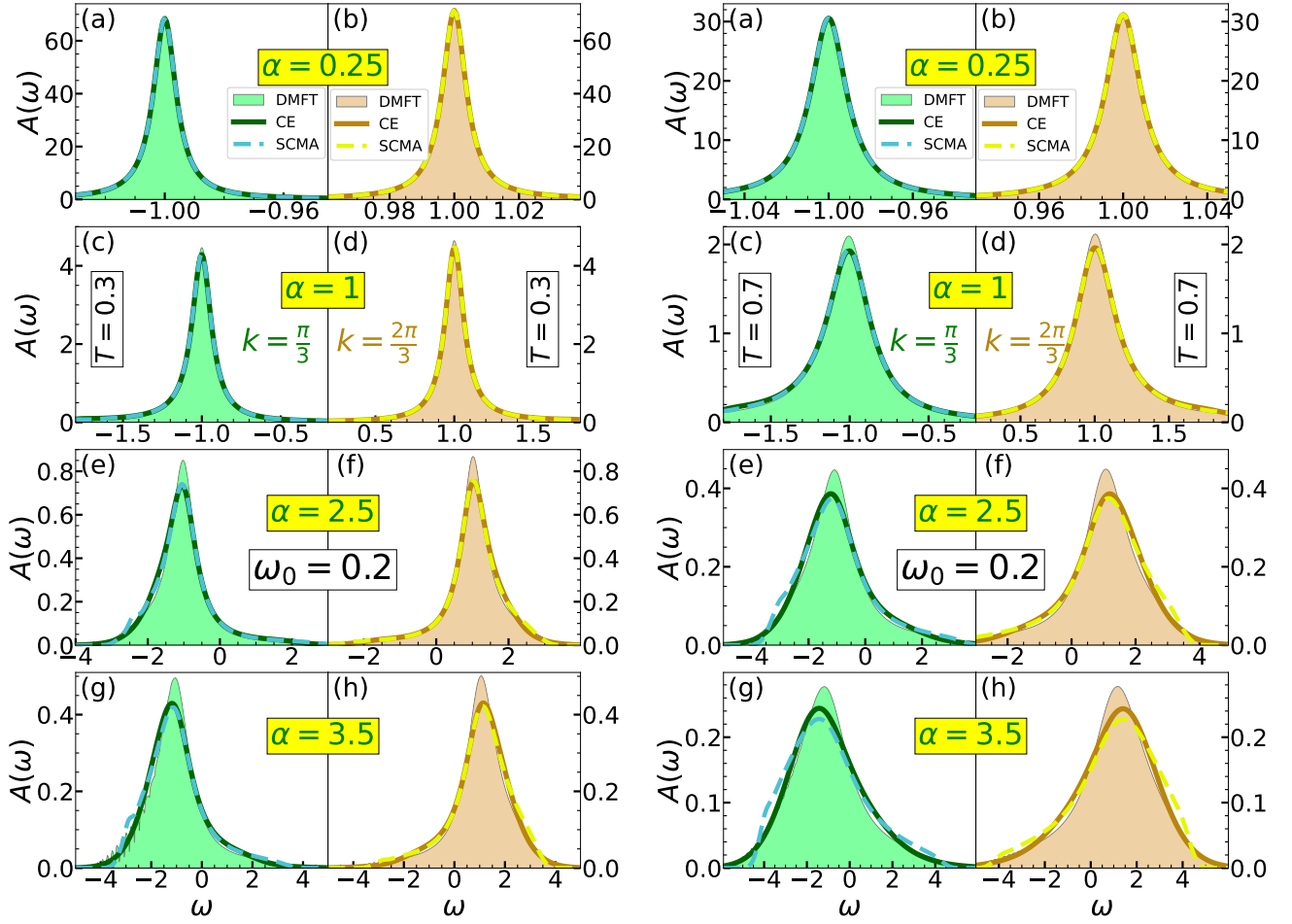
(i) (a)–(h) Spectral functions for $\omega_0 = 0.2$ and $k = 0$. In the left panels $T = 0.3$, while $T = 0.7$ in the right panels. Insets show the integrated spectral weight $I(\omega) = \int_{-\infty}^{\infty} A(\omega) d\omega$.

(ii) (a)–(h) Spectral functions for $\omega_0 = 0.2$ and $k = \pi$. In the left panels $T = 0.3$, while $T = 0.7$ in the right panels. Insets show the integrated spectral weight $I(\omega) = \int_{-\infty}^{\infty} A(\omega) d\omega$.



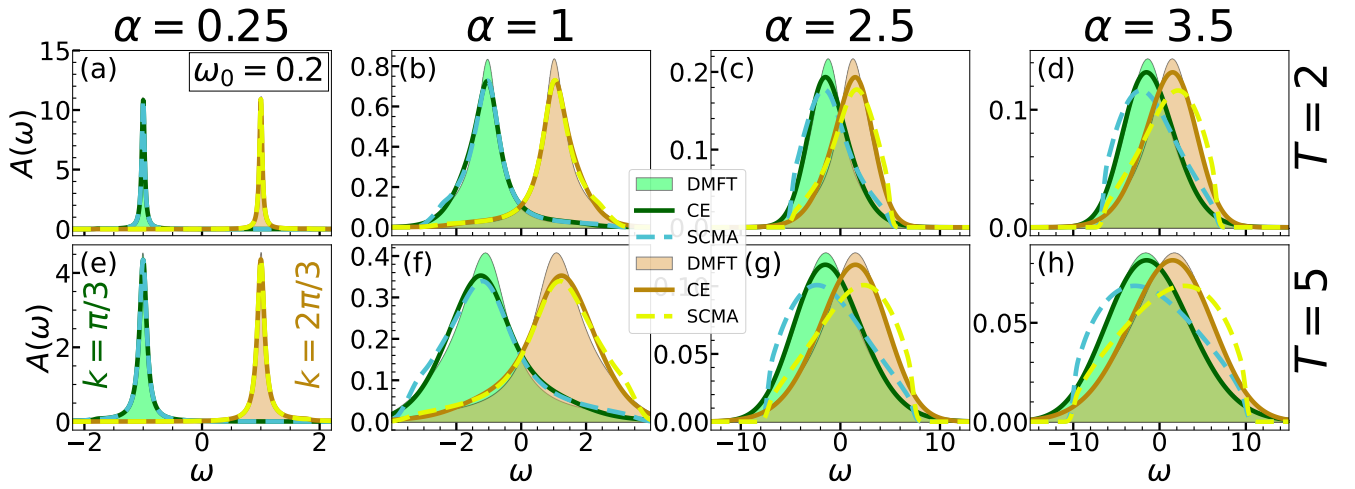
(iii) Spectral functions at higher temperatures for $\omega_0 = 0.2$ and $k = 0, \pi$.

FIG. S6. Comparison of the CE, DMFT, SCMA, and MA spectral functions in 1D for $t_0 = 1$, $\omega_0 = 0.2$, and $k = 0, \pi$.



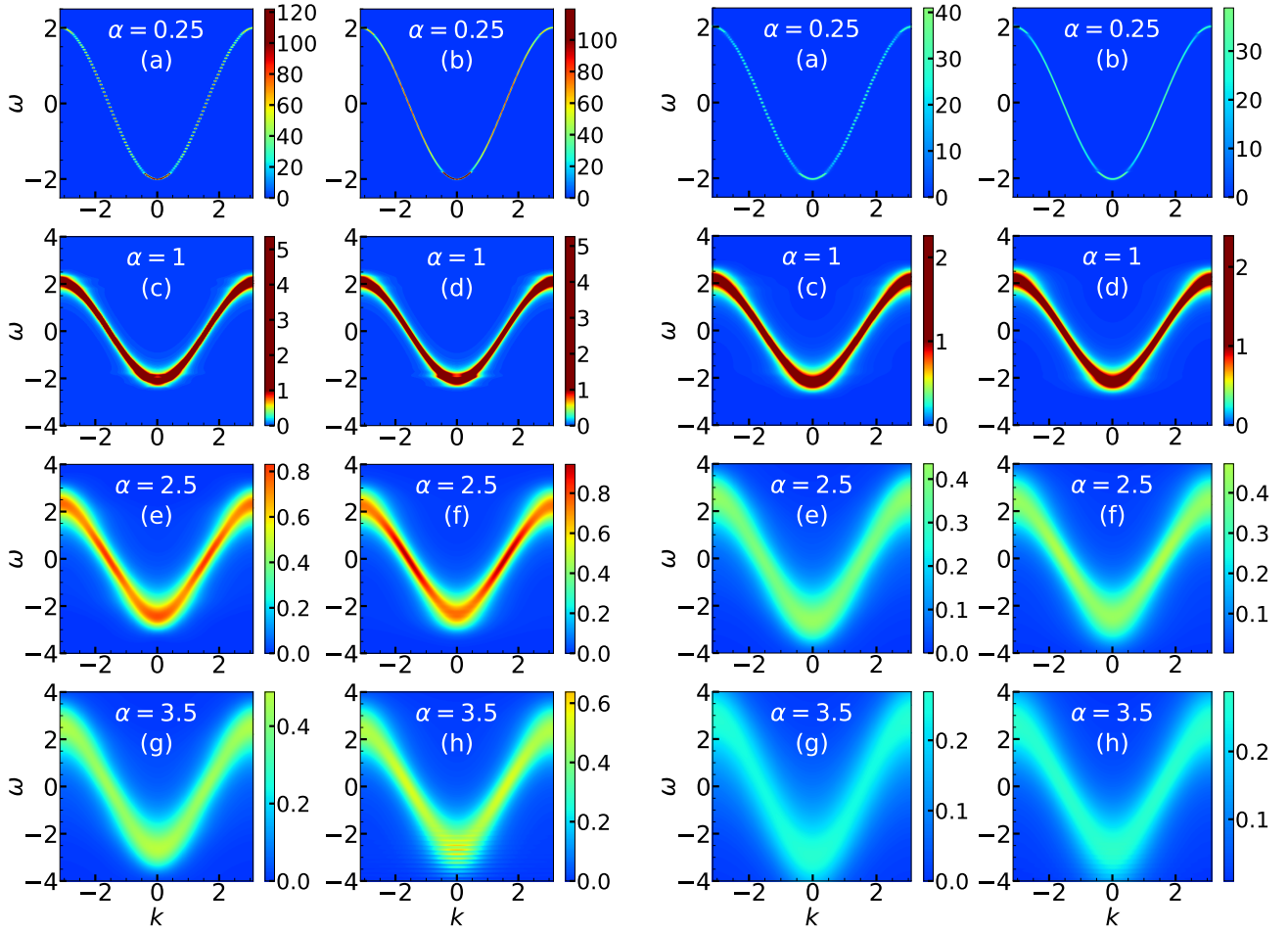
(i) (a)–(h) Spectral functions for $\omega_0 = 0.2$ and $T = 0.3$. In the left panels $k = \pi/3$, while $k = 2\pi/3$ in the right panels.

(ii) (a)–(h) Spectral functions for $\omega_0 = 0.2$ and $T = 0.7$. In the left panels $k = \pi/3$, while $k = 2\pi/3$ in the right panels.



(iii) Spectral functions at higher temperatures for $\omega_0 = 0.2$ and $k = \pi/3, 2\pi/3$.

FIG. S7. Comparison of the CE, DMFT, and SCMA spectral functions in 1D for $t_0 = 1$, $\omega_0 = 0.2$ and $k = \pi/3, 2\pi/3$.



(i) (a)–(h) Heat maps for $T = 0.3$. In the left panels, we present CE results, while the DMFT benchmark is presented in the right panels. Panels (c)–(h) use the same color coding, while panels (a) and (b) use different color coding.

(ii) (a)–(h) Heat maps for $T = 0.7$. In the left panels, we present CE results, while the DMFT benchmark is presented in the right panels. Panels (c)–(h) use the same color coding, while panels (a) and (b) use different color coding.

FIG. S8. Comparison of the CE and DMFT heat maps for $t_0 = 1$ and $\omega_0 = 0.2$.

III. QUASIPARTICLE PROPERTIES

In Sec. IV of the main text, we showed and analyzed the quasiparticle properties of CE, DMFT, and SCMA methods. Here we supplement that study by including the predictions of the Migdal approximation for the ground state energy in 1D. The results are shown in Fig. S9. We emphasize that the predictions of the DMFT benchmark are practically identical to the exact numerical results [S1]. These results readily demonstrate how much improvement to the simplest approximation (MA) is provided by including the self-consistency (SCMA) and by employing the cumulant expansion method (CE).

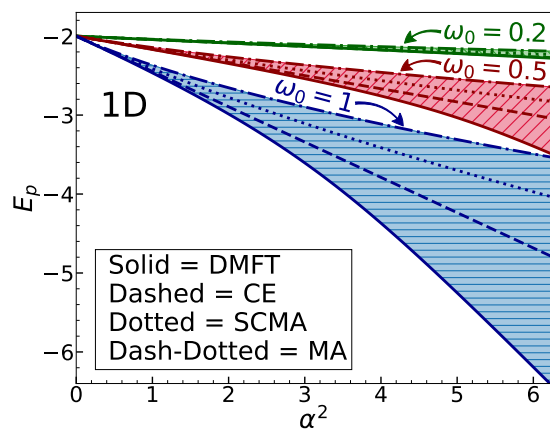















FIG. S9. Ground state energy within DMFT, CE, SCMA, and MA for the one-dimensional Holstein model with $t_0 = 1$.

- [S1] P. Mitrić, V. Janković, N. Vukmirović, and D. Tanasković, Spectral Functions of the Holstein Polaron: Exact and Approximate Solutions, *Phys. Rev. Lett.* **129**, 096401 (2022).
- [S2] R. Kubo, Generalized Cumulant Expansion Method, *Journal of the Physical Society of Japan* **17**, 1100

- (1962).
- [S3] E. Meeron, Series expansion of distribution functions in multicomponent fluid systems, *The Journal of Chemical Physics* **27**, 1238 (1957).
- [S4] G. Mahan, *Many-Particle Physics* (Kluwer Academic, New York, 2000).

Optical conductivity and vibrational spectra of the narrow-gap semiconductor FeGa₃C. Martin ¹, V. A. Martinez,² M. Opačić ³, S. Djurdjić-Mijin ³, P. Mitrić ³, A. Umičević ⁴, A. Poudel ¹, I. Sydoryk ¹,
Weijun Ren ^{5,6}, R. M. Martin ⁷, D. B. Tanner ², N. Lazarević ³, C. Petrovic ⁵ and D. Tanasković ³¹*School of Theoretical and Applied Sciences, Ramapo College of New Jersey, Mahwah, New Jersey 07430, USA*²*Department of Physics, University of Florida, Gainesville, Florida 32611, USA*³*Institute of Physics Belgrade, University of Belgrade, Pregrevica 118, 11080 Belgrade, Serbia*⁴*Vinča Institute of Nuclear Sciences, National Institute of the Republic of Serbia, University of Belgrade, P.O. Box 522, 11001 Belgrade, Serbia*⁵*Condensed Matter Physics and Materials Science Department, Brookhaven National Laboratory, Upton, New York 11973, USA*⁶*Shenyang National Laboratory for Materials Science, Institute of Metal Research, Chinese Academy of Sciences, Shenyang 110016, China*⁷*Department of Physics and Astronomy, Montclair State University, Montclair, New Jersey 07043, USA*

(Received 24 February 2023; accepted 10 April 2023; published 26 April 2023; corrected 5 May 2023)

Intermetallic narrow-gap semiconductors have been intensively explored due to their large thermoelectric power at low temperatures and a possible role of strong electronic correlations in their unusual thermodynamic and transport properties. Here we study the optical spectra and vibrational properties of FeGa₃ single crystal. The optical conductivity indicates that FeGa₃ has a direct band gap of ≈ 0.7 eV, consistent with density functional theory (DFT) calculations. Most importantly, we find a substantial spectral weight also below 0.4 eV, which is the energy of the indirect (charge) gap found in resistivity measurements and *ab initio* calculations. We find that the spectral weight below the gap decreases with increasing temperature, which indicates that it originates from the impurity states and not from the electronic correlations. Interestingly, we did not find any signatures of the impurity states in vibrational spectra. The infrared and Raman vibrational lines are narrow and weakly temperature dependent. The vibrational frequencies are in excellent agreement with our DFT calculations, implying a modest role of electronic correlations. Narrow Mössbauer spectral lines also indicate high crystallinity of the sample.

DOI: [10.1103/PhysRevB.107.165151](https://doi.org/10.1103/PhysRevB.107.165151)**I. INTRODUCTION**

Correlated narrow-gap semiconductors represent a class of materials known for their large thermopower at low temperatures and other anomalous transport and thermodynamic properties [1]. Three iron compounds among them, FeSi, FeSb₂, and FeGa₃, share some common features, but also show important differences. FeSi and FeSb₂ behave as insulators only at temperatures $T^* \lesssim 100$ K which corresponds to the energy much smaller than the band gap $E_g \approx 50$ meV [2–4]. A buildup of the in-gap spectral weight at temperatures $k_B T^* \ll E_g$, clearly seen in optical [5–8] and photoemission spectroscopy [9], is a signature of strong electronic correlations [10,11]. A crossover from a nonmagnetic insulator to a bad metal is accompanied by a large increase in the spin susceptibility which obtains Curie-Weiss form above room temperature [12,13]. This crossover leaves fingerprints also in the Raman vibrational spectra which become strongly temperature dependent. The width of vibrational peaks increases several times in the bad-metal region as compared to the low-temperature insulating state [14–16]. At temperatures near 10 K there is a large peak in the thermopower $|S|$ [17,18]. The exact role of the electronic correlations, in-gap states, anisotropy, and phonon drag in colossal thermopower found in FeSb₂ remains a subject of various studies and controversy [19–21].

FeGa₃ has a significantly larger band gap, $E_g \approx 0.4$ eV [22,23], than FeSi and FeSb₂ due to the stronger hybridization between 3*d* orbitals of Fe and 4*p* orbitals of Ga. The electronic structure calculations imply modest contribution of electronic correlations. Density functional theory (DFT) [24] and LDA+*U* [23] calculations give almost the same band structure, while dynamical mean field theory (DFT+DMFT) [25] gives only slightly reduced band gap. Nevertheless, the temperature dependence of dc resistivity is nontrivial: it strongly deviates from a simple activated transport at low temperatures, and features four distinct transport regimes which are associated with a presence of the in-gap states [22,23,25]. For $T \lesssim 5$ K ρ_{dc} has a power law temperature dependence consistent with the variable-range hopping transport driven by the localized in-gap states. In the interval $20 \lesssim T \lesssim 45$ K the charge transport is activated, but corresponds to a small gap of ≈ 40 meV between the in-gap states and the conduction band. Then, following a minimum in ρ_{dc} , there is a metalliclike transport up to ≈ 80 K which presumably corresponds to the regime where most of the in-gap electrons are already transferred to the conduction band. For $T > 300$ K the charge transport is activated, consistent with the wide gap $E_g \approx 0.4$ eV. The measurements show weak sample anisotropy and weak temperature dependence of magnetic susceptibility, whereas the DFT+DMFT calculations give small mass renormalization, as well as strong charge and spin

fluctuations [25]. A maximum in the Seebeck coefficient $|S|$ at $T \approx 15$ K is argued to be a consequence of the phonon-drag effect [23]. In this picture the in-gap states supply free charge carriers and the acoustic phonons cause an additional scattering of the electrons opposite to the direction of a temperature gradient, leading to the large thermoelectric power. Interestingly, to our knowledge, there has been so far only one infrared spectroscopy study of FeGa₃ in polycrystalline samples [26], restricted to room temperature and energies larger than 90 meV.

In this paper, we present infrared and Raman spectroscopy study of FeGa₃ single crystal in the temperature range between 4 and 300 K. The reflectance is measured in the energy interval between 30 and 24 000 cm⁻¹. The infrared and Raman active vibrational frequencies are in excellent agreement with our DFT calculations, indicating good crystallinity and a small influence of electronic correlations. Good crystallinity is corroborated also by measured Mössbauer spectra. The most prominent feature of the optical spectra is the existence of the in-gap states below the charge gap of approximately 0.4 eV. We observe a reduction of the in-gap spectral weight as the temperature increases to 300 K and conclude that this spectral weight originates from the impurities. Details of experimental and numerical methods are presented in Sec. II. The results are shown in Secs. III and IV contains our conclusions.

II. METHODS

Single crystals of FeGa₃ were grown as described previously [22]. For infrared measurements a small crystal was polished until a smooth surface of about 3 mm² area was obtained, then mounted on a helium-flow optical cryostat. The temperature dependence of reflectance was measured between 30 and 24 000 cm⁻¹, using a combination of two Fourier-transform infrared spectrometers: a Bruker 113v for far infrared (30–600 cm⁻¹) and a Bruker Vertex 70, with extended spectral range, from midinfrared to visible (100–24 000 cm⁻¹). Reflectance in visible and ultraviolet (12 000–50 000 cm⁻¹) was measured at room temperature only, using a Perkin-Elmer 650 UV/VIS grating spectrometer. As no temperature dependence was observed above about 12 000 cm⁻¹, all temperatures were merged with room temperature data in visible and ultraviolet parts of the spectrum. To capture correctly the width and line shape of lattice vibrations, the far-IR data were taken with a resolution of 0.5 cm⁻¹, while 2 cm⁻¹ or larger values were used at higher frequencies. Both gold and aluminum mirrors were used for reference, and in order to correct for surface roughness the sample was also gold coated, using a commercial Ted Pella Cressington 108 sputtering machine. Because of the polishing involved, the precise orientation of the electric field (polarization) with respect to the crystallographic axes of the samples is not clearly defined, hence we cannot discuss potential anisotropic optical properties.

Raman scattering measurements were performed using a TriVista557 Raman system, equipped with a nitrogen-cooled CCD detector, in backscattering micro-Raman configuration. Grating configuration was 1800/1800/2400 grooves/mm, in order to achieve the best possible resolution. The 514.5-nm

line of an Ar⁺/Kr⁺ gas laser was used as an excitation source and a microscope objective with factor 50 magnification was used for focusing the beam. All measurements were carried out with laser power less than 1.5 mW at the sample, in order to minimize local heating. Room temperature measurements were done in air, whereas for low temperature measurements the sample was placed in a KONTI CryoVac continuous flow cryostat, with a 0.5-mm-thick window. Spectra were corrected for the Bose factor.

The ⁵⁷Fe-Mössbauer spectrum of the FeGa₃ powdered sample was measured at room temperature in high ($\approx \pm 9$ mm/s) and low ($\approx \pm 2$ mm/s) Doppler velocity range. The spectra were collected in standard transmission geometry in constant acceleration mode using a ⁵⁷Co(Rh) source. The Doppler velocity scale was calibrated by using the Mössbauer spectrum of metallic α -Fe. The spectra were fitted by the RECOIL program [27]. The center shift value (CS) is quoted relative to the α -Fe (CS = 0).

First-principles DFT calculations of electronic structure and phonon frequencies were performed using the open-source QUANTUM-ESPRESSO package [28,29]. We employed the ultrasoft Vanderbilt-type pseudopotentials with Perdew-Burke-Ernzerhof exchange and correlation functional. For the Fe atom we considered 3s, 3p, 3d, and 4s as valence electrons (in total 16), while the Ga valence electrons were taken to be the electrons from 3d, 4s, and 4p orbitals (in total 13). Thus, a minimum of 110 bands was needed to perform the calculations since we have four formula units per unit cell, but we nevertheless considered 128 bands, which is a very convenient number for parallelization purposes. The plane wave kinetic energy cutoff was set to 70 Ry, which proved to be sufficient for all our calculations. The ionic relaxation, self-consistent, and normal mode calculations were performed using the Monkhorst-Pack scheme, with the k mesh of $8 \times 8 \times 8$, which corresponds to 75 k points in the irreducible part of the Brillouin zone. On the other hand, the density of states (DOS) calculation requires a much larger number of k points in order to be accurate, and hence we performed the non-self-consistent calculation with a k mesh of $12 \times 12 \times 12$ in order to calculate the DOS. We used density functional perturbation theory (DFPT) [30] in order to calculate the vibrational frequencies.

III. RESULTS

We first present the band structure calculations. These results are known from the literature, but we nevertheless show them for completeness and in order to put into context the analysis of the experimental data that follow. Then we present optical, Raman, and Mössbauer spectra.

A. DFT band structure

The semiconductor FeGa₃ belongs to the $P4_2/mnm$ space group and it has a tetragonal P -type lattice with lattice parameters $a=6.2628(3)$ Å and $c=6.5546(5)$ Å [31]. In the DFT calculations we used the lattice parameters from the experiment and relaxed only the fractional coordinates of the atoms. These coordinates, shown in Table I, are only slightly adjusted from their measured values.

TABLE I. Nonequivalent atomic positions from the DFT calculation.

Atom	$P\bar{4}n2$	x	y	z
Fe	4 <i>f</i>	0.34367	0.34367	0
Ga1	4 <i>c</i>	0	0.5	0
Ga2	8 <i>j</i>	0.15575	0.15575	0.26295

Figure 1 shows the dispersion relations and the density of states, calculated along the k path Z - R - A - Z - Γ - X - M - Γ in the Brillouin zone. Our results are very similar to previous work [23,32], showing that FeGa₃ is an indirect-gap semiconductor with the calculated band gap of 0.44 eV. The bands around the Fermi level are formed from the hybridized Fe 3*d* and Ga 4*p* orbitals.

B. Optical conductivity and infrared vibrational modes

The reflectance $R(\omega)$ measured at several temperatures between 25 and 300 K is shown in Fig. 2(a). Note that the spectra are shown on a logarithmic frequency scale so that we can distinguish both the low- and high-frequency features. The low-frequency reflectance is close to 1 which indicates a possible presence of the in-gap states that we will discuss in detail below. The far-infrared frequency region is shown on a linear scale in the inset. The peaks in $R(\omega)$ correspond to the infrared-active vibrational modes.

A better insight into the excitation spectrum can be obtained from the real part of the optical conductivity $\sigma_1(\omega)$. It corresponds to the imaginary part of the dielectric function, $\sigma_1(\omega) = \omega\epsilon_2(\omega)/4\pi$, describing the absorption of electromagnetic radiation [33,34]. Figure 2(b) shows $\sigma_1(\omega)$ obtained from the Kramers-Kronig transformation of $R(\omega)$. As this transformation involves integration of $R(\omega)$ from zero to infinity, we used extrapolation of our measurements. At high frequency ($\omega \rightarrow \infty$), the data were bridged with calculations of the dielectric function based on the x-ray photoabsorption, following the procedure described in Ref. [35]. For $\omega < 30 \text{ cm}^{-1}$ we set $R(\omega) = R(30 \text{ cm}^{-1})$, but we checked that $\sigma_1(\omega)$ is not sensitive to the precise form of $R(\omega)$ in the

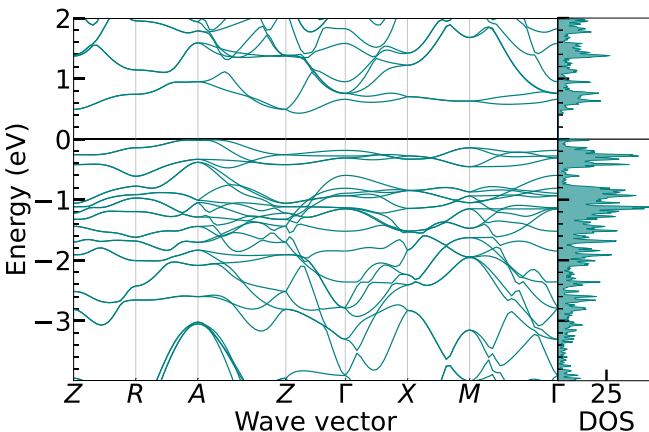


FIG. 1. DFT band structure of FeGa₃ and density of states in units states/(eV f.u.).

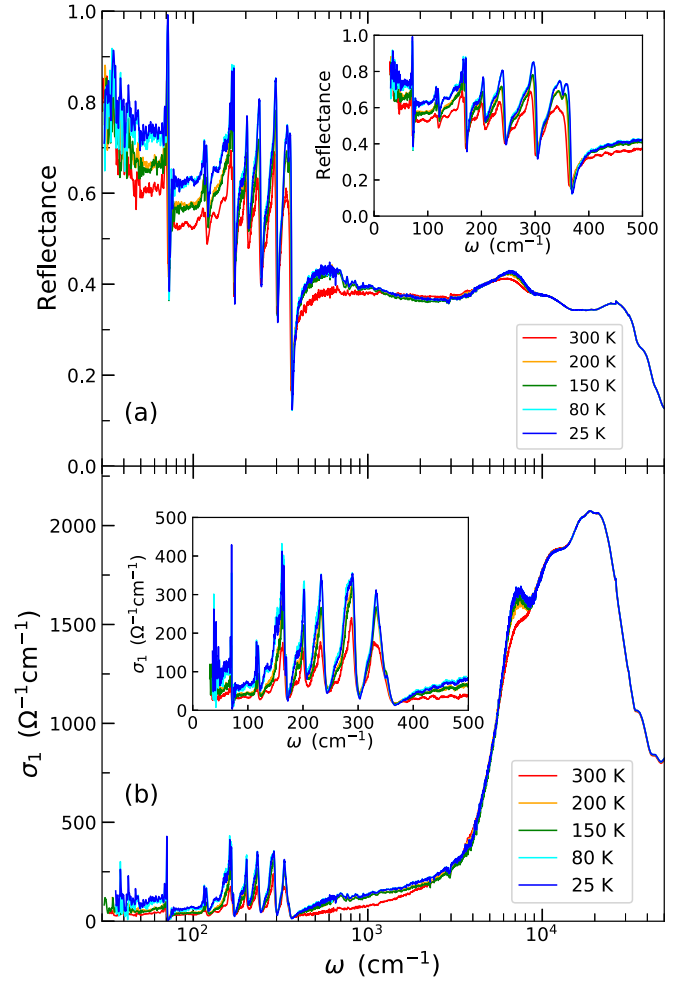


FIG. 2. Reflectance (a) and optical conductivity (b) as a function of frequency in the whole measured frequency range at several temperatures. The insets show the low-frequency data on a linear scale.

limit $\omega \rightarrow 0$. The same result is obtained using the Hagen-Rubens formula, $R(\omega) = 1 - A\sqrt{\omega}$, where A is a constant adjusted to fit the first several points from the measurements [33,34].

The optical conductivity at 25 and 300 K is shown in Fig. 3 on a linear energy (frequency) scale in units of eV. $\sigma_1(\omega)$ rapidly decreases for frequencies $\hbar\omega \lesssim 0.9 \text{ eV}$ (7000 cm^{-1}). This is consistent with the DFT band structure shown in Fig. 1. It gives the smallest direct gap of 0.67 eV near the Z point in the Brillouin zone, but in many regions of the Brillouin zone the gap is between 0.7 and 0.9 eV. At $\hbar\omega = E_g \approx 0.4 \text{ eV}$ the spectral weight is significantly reduced, yet it remains substantial also at $\hbar\omega < E_g$. We note that we did not attempt to calculate the optical spectra since a reliable calculation requires us to include the particle-hole interaction on a level of the Bethe-Salpeter equation, which is a very challenging task even for weakly interacting semiconductors [36,37]. A calculation of the optical spectra of FeGa₃ in the independent-particle approach poorly compares with our experiments [24]. On the other hand, our optical spectra for $\hbar\omega \gtrsim 0.5 \text{ eV}$ are

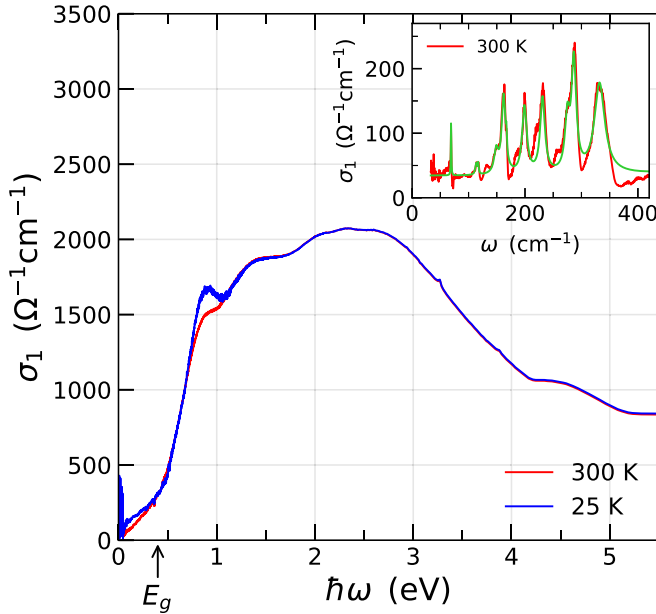


FIG. 3. Optical conductivity as a function of frequency at 25 and 300 K. The inset shows the infrared vibrational modes which are fitted by 11 Lorentzians. The green line corresponds to the cumulative fit.

in rather good agreement with the spectra on polycrystalline samples of Ref. [26].

Evidence that the spectral weight below E_g has origins in the impurity states can be obtained from analysis of the temperature dependence of $\sigma_1(\omega)$. At finite temperatures, in a standard band gap semiconductor a small spectral weight would appear just below E_g due to the phonon assisted excitations. The same amount of the spectral weight would recover just above the band edge, where the absorption becomes slightly lower due to the finite hole (electron) concentration in the valence (conduction) band at finite temperatures [33]. On the other hand, in FeSi and FeSb₂ a spectral gap is closed at higher temperatures due to the strong correlation effects. In this case, transfers of the spectral weight occur over the energy range much larger than the band gap. However, in our case the spectral weight at $T = 300$ K is reduced both below and above E_g [see Figs. 2(b) and 3]. The reduction of the spectral weight below E_g should correspond to the depopulation of the impurity band, which leads to the reduction in the light absorption for subgap energies [25]. Hence, we conclude that the spectral weight below E_g is due to impurity states. We note that a small surplus of Fe atoms in comparison to the stoichiometric ratio is found in wavelength dispersive x-ray spectroscopy [23]. Our conclusion is in line with the statement that the transfer of the electrons from the impurity states to the conduction band is a likely cause of the anomalous $d\rho/dT > 0$ resistivity temperature dependence around 100 K [20,25].

We now turn our attention to the far-infrared part of the spectrum from 50 to 350 cm^{-1} , which contains infrared vibrational modes. From the inset of Fig. 2(b) it appears that most of the phonon peaks are rather broad. However, that is not the case since several peaks, in fact, consist of two vi-

TABLE II. Irreducible representation of infrared-active modes and their frequencies. The measured frequencies are obtained at 300 K. Numerical values are obtained within DFPT calculation.

Irred. rep.	Expt. (cm^{-1})	Calc. (cm^{-1})
$E_u^{1,2}$	69.00	76.08
A_{2u}^1	113.50	107.61
$E_u^{3,4}$	117.50	116.18
$E_u^{5,6}$	149.85	161.78
A_{2u}^2	162.2	162.28
$E_u^{7,8}$	166.99	168.69
$E_u^{9,10}$	199.50	201.71
$E_u^{11,12}$	231.50	229.45
$E_u^{13,14}$	275.00	281.2
A_{2u}^3	287.30	296.61
$E_u^{15,16}$	332.50	329.0

brational modes with very close frequencies. The space group $P4_2/mmm$ has the corresponding point group $D_{4h}(4/mmm)$. Thus, all the normal modes are classified according to irreducible representations of $D_{4h}(4/mmm)$. The factor group analysis predicts 12 Raman and 11 infrared-active modes, along with ten silent and two acoustic modes:

$$\begin{aligned}
 \Gamma_{\text{Raman}} &= 3A_{1g} + 4E_g + 2B_{1g} + 3B_{2g}, \\
 \Gamma_{\text{IR}} &= 3A_{2u} + 8E_u, \\
 \Gamma_{\text{silent}} &= 2A_{2g} + 2A_{2u} + 4B_{1u} + 2B_{2u}, \\
 \Gamma_{\text{acoustic}} &= A_{2u} + E_u.
 \end{aligned} \tag{1}$$

The experimental data at 300 K are fitted with 11 Lorentz profile lines. Their cumulative contribution to the spectra is shown in green color in the inset of Fig. 3. A complete list of the corresponding phonon frequencies is shown in Table II. These frequencies were obtained at 300 K, but we see from the inset in Fig. 2(b) that the temperature dependence of the frequencies is weak. The changes are of the order of 1% in the temperature range between 25 and 300 K. The frequencies calculated within DFPT are in excellent agreement with measured frequencies. This implies that a crystallinity of the sample is very good, even though some surplus of Fe iron atoms is expected in comparison to the ideal composition [23]. In addition, excellent agreement between the calculated and measured frequencies indicates that the electronic correlations beyond the DFT are not strong, in line with the conclusions from DFT+ U [23] and DFT+DMFT [25] calculations.

C. Raman spectra

There are 12 Raman-active modes in FeGa₃ [see Eq. (1)]. Wyckoff positions of the atoms, their contributions to the Γ -point phonons, and the corresponding tensors for Raman active modes are given in Table III. Since observability of the Raman-active modes in backscattering configuration of the experiment strongly depends on the orientation of the sample, we first performed orientation dependent measurements. This was done by rotating the sample in the steps of 10°. The orientation of the sample which provided the best observability

TABLE III. Contributions of each atom to the Γ -point phonons for the $P4_2/mnm$ space group and the corresponding tensors for Raman active modes.

Space group $P4_2/mnm$		
Atoms	Irreducible representations	
Fe (4 <i>f</i>)	$A_{1g} + A_{2g} + A_{2u} + B_{1g} + B_{1u} + B_{2g} + E_g + 2E_u$	
Ga (4 <i>c</i>)	$A_{1u} + A_{2u} + B_{1u} + B_{2u} + 4E_u$	
Ga (8 <i>j</i>)	$2A_{1g} + A_{1u} + A_{2g} + A_{2u} + B_{1g} + 2B_{1u} + 2B_{2g} + B_{2u} + 3E_g + 3E_u$	
$A_{1g} = \begin{pmatrix} a & 0 & 0 \\ 0 & a & 0 \\ 0 & 0 & b \end{pmatrix}$	$B_{1g} = \begin{pmatrix} c & 0 & 0 \\ 0 & -c & 0 \\ 0 & 0 & 0 \end{pmatrix}$	$B_{2g} = \begin{pmatrix} 0 & d & 0 \\ d & 0 & 0 \\ 0 & 0 & 0 \end{pmatrix}$
${}^1E_g = \begin{pmatrix} c & 0 & 0 \\ 0 & 0 & e \\ 0 & e & 0 \end{pmatrix}$	${}^2E_g = \begin{pmatrix} 0 & 0 & -e \\ 0 & 0 & 0 \\ -e & 0 & 0 \end{pmatrix}$	

of Raman modes of various symmetries was used in further measurements.

Raman spectra of FeGa₃ single crystals, measured from the (011) plane of the sample, at temperature $T = 100$ K, for polarization plane angles within the range of 0° and 180° are presented in Fig. 4. We have identified 10 out of 12 Raman active modes. The assignment of modes was done in accordance with DFT calculations and polarization measurements. Peaks that exhibit the same polarization dependence were assigned with the same symmetry. Consequently, peaks at 146.58 and 331.80 cm^{-1} were assigned as A_{1g} and peaks at 127.99 and 269.98 cm^{-1} were assigned as B_{1g} . The phonon lines at 138.96, 179.01, and 264.40 cm^{-1} are assigned as E_g , whereas modes at 161.67, 238.27, and 321.43 cm^{-1} correspond to the B_{2g} symmetry modes. The full list of measured phonon

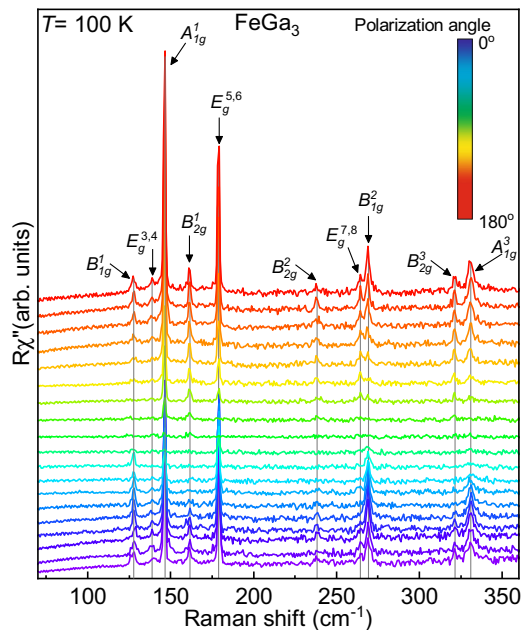


FIG. 4. Polarization-dependent Raman spectra of FeGa₃ single crystals. Measurements were performed with measuring step of 10° at temperature $T = 100$ K.

TABLE IV. Experimental Raman frequencies measured at 100 K and the corresponding values calculated within DFPT.

Irred. rep.	Expt. (cm^{-1})	Calc. (cm^{-1})
$E_g^{1,2}$		86.81
B_{1g}^1	127.99	125.52
$E_g^{3,4}$	138.96	139.06
A_{1g}^1	146.58	145.89
B_{1g}^1	161.67	161.51
$E_g^{5,6}$	179.01	165.09
A_{1g}^2		180.12
B_{2g}^2	238.27	239.62
$E_g^{7,8}$	264.40	258.94
B_{1g}^2	269.28	262.96
B_{2g}^3	321.43	318.53
A_{1g}^3	331.80	322.41

frequencies, along with their calculated values, is shown in Table IV.

There is a very good agreement between experimental and calculated phonon frequencies, with a discrepancy of less than 8%. A close match in experimental and theoretical results is not surprising knowing that the investigated material is semiconducting, with moderate electronic correlations. All of the observed phonon lines are sharp, with the full width at half maximum (FWHM) ≈ 2 cm^{-1} , and weakly temperature dependent. This indicates a good crystallinity of the sample and absence of a metal-insulator transition or magnetic ordering.

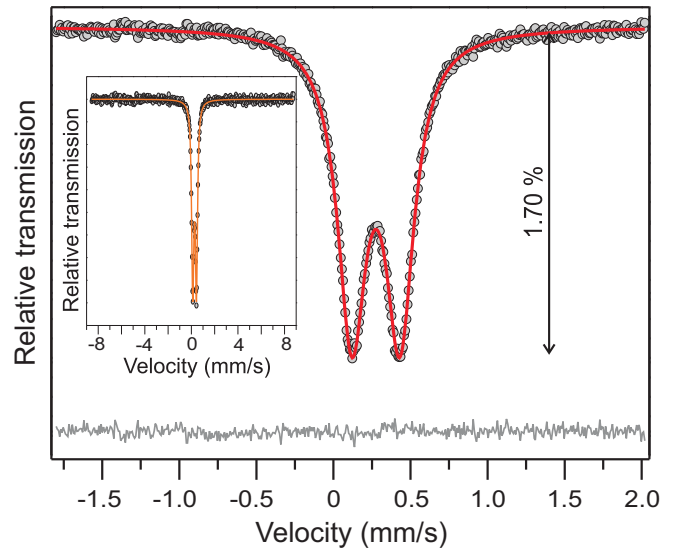


FIG. 5. Room temperature ${}^{57}\text{Fe}$ -Mössbauer spectra of the FeGa₃ sample recorded in the low-velocity range. Experimental data are presented by the solid circles and the fit is given by the red solid line. The difference (Calc. – Expt.) is shown by the dark gray line at the bottom of the figure. The vertical arrow denotes the relative position of the lowest experimental point with respect to the background (relative absorption of 1.70%). The absolute difference is less than 0.05%. The inset shows the room temperature spectrum of the FeGa₃ sample recorded within the high-velocity range. The orange line is just a guide for the eye.

D. Mössbauer spectra

The ^{57}Fe -Mössbauer spectroscopy was used to investigate quality and ordering of the prepared sample and to check for the presence of Fe-based impurity phases. The ^{57}Fe -Mössbauer spectra of the FeGa_3 are presented in Fig. 5. The spectrum recorded in the low-velocity range showed two absorption lines (doublet). In the spectrum recorded in the high-velocity range, beside the observed doublet, there is no indication of the magnetic hyperfine splitting. The thickness corrected FeGa_3 spectrum recorded in the low-velocity range was fitted with one Lorentzian-shaped doublet using the RECOIL program [27]. The obtained Mössbauer parameters for the measured doublet are center shift $\text{CS} = 0.28$ mm/s, quadrupole splitting $\Delta = 0.31$ mm/s, and FWHM of the Lorentzian lines is 0.22 mm/s. The obtained results closely match the hyperfine parameters for FeGa_3 from the literature [38–42]. A very small broadening of the resonance lines observed in the experiment is a strong indication that the sample is very well ordered and of high crystallinity.

IV. CONCLUSIONS

In summary, we have performed optical, Raman, and Mössbauer spectroscopy measurements of a narrow-gap semiconductor FeGa_3 , along with DFT band structure and vibrational frequencies calculation. We find that the optical conductivity decreases for frequencies below $\hbar\omega \approx 0.9$ eV consistent with the direct band gap observed in DFT calculations. Our most important finding is the appearance of the optical spectral weight below the charge (indirect) gap $E_g \approx 0.4$ eV. At room temperature the spectral weight below E_g diminishes as compared to the one at $T = 25$ K. Therefore,

we conclude that this spectral weight originates from the impurities and not from the correlation effects. Interestingly, we do not find signatures of the impurities in the vibrational spectra. Both the infrared and Raman lines are very narrow, as well as the Mössbauer spectral lines, which implies a good crystallinity of the sample. The calculated vibrational frequencies are in a very good agreement with the measurements, which indicates that the electronic correlations in FeGa_3 are not strong, in line with previous studies.

ACKNOWLEDGMENTS

A.U. acknowledges fruitful discussions with V. Ivanovski. C.M. acknowledges funding from the Research Honors Program at Ramapo College of New Jersey. M.O., S.Dj.-M., P.M., N.L., and D.T. acknowledge funding provided by the Institute of Physics Belgrade, through a grant by the Ministry of Science, Technological Development, and Innovation of the Republic of Serbia. A.U. acknowledges support provided by the Vinča Institute of Nuclear Sciences, through an agreement with the Ministry of Science, Technological Development, and Innovation of the Republic of Serbia. C.P. acknowledges support by the U.S. Department of Energy, Basic Energy Sciences, Division of Materials Science and Engineering, under Contract No. DE-SC0012704 (BNL), and W.R. was supported by the National Natural Science Foundation of China under Grants No. 51671192 and No. 51531008 (Shenyang). Numerical simulations were performed on the PARADOX supercomputing facility at the Scientific Computing Laboratory, National Center of Excellence for the Study of Complex Systems, Institute of Physics Belgrade.

-
- [1] J. M. Tomczak, Thermoelectricity in correlated narrow-gap semiconductors, *J. Phys.: Condens. Matter* **30**, 183001 (2018).
 - [2] Z. Schlesinger, Z. Fisk, H.-T. Zhang, M. B. Maple, J. DiTusa, and G. Aeppli, Unconventional Charge Gap Formation in FeSi, *Phys. Rev. Lett.* **71**, 1748 (1993).
 - [3] C.-H. Park, Z.-X. Shen, A. G. Loeser, D. S. Dessau, D. G. Mandrus, A. Migliori, J. Sarrao, and Z. Fisk, Direct observation of a narrow band near the gap edge of FeSi, *Phys. Rev. B* **52**, R16981 (1995).
 - [4] C. Petrovic, J. W. Kim, S. L. Bud'ko, A. I. Goldman, P. C. Canfield, W. Choe, and G. J. Miller, Anisotropy and large magnetoresistance in the narrow-gap semiconductor FeSb_2 , *Phys. Rev. B* **67**, 155205 (2003).
 - [5] A. Damascelli, K. Schulte, D. van der Marel, and A. A. Menovsky, Infrared spectroscopic study of phonons coupled to charge excitations in FeSi, *Phys. Rev. B* **55**, R4863 (1997).
 - [6] M. A. Chernikov, L. Degiorgi, E. Felder, S. Paschen, A. D. Bianchi, H. R. Ott, J. L. Sarrao, Z. Fisk, and D. Mandrus, Low-temperature transport, optical, magnetic and thermodynamic properties of $\text{Fe}_{1-x}\text{Co}_x\text{Si}$, *Phys. Rev. B* **56**, 1366 (1997).
 - [7] A. Perucchi, L. Degiorgi, R. Hu, C. Petrovic, and V. F. Mitrović, Optical investigation of the metal-insulator transition in FeSb_2 , *Eur. Phys. J. B* **54**, 175 (2006).
 - [8] A. Herzog, M. Marutzky, J. Sichelschmidt, F. Steglich, S. Kimura, S. Johnsen, and B. B. Iversen, Strong electron correlations in FeSb_2 : An optical investigation and comparison with RuSb_2 , *Phys. Rev. B* **82**, 245205 (2010).
 - [9] M. Arita, K. Shimada, Y. Takeda, M. Nakatake, H. Namatame, M. Taniguchi, H. Negishi, T. Oguchi, T. Saitoh, A. Fujimori, and T. Kanomata, Angle-resolved photoemission study of the strongly correlated semiconductor FeSi, *Phys. Rev. B* **77**, 205117 (2008).
 - [10] J. M. Tomczak, K. Haule, T. Miyake, A. Georges, and G. Kotliar, Thermopower of correlated semiconductors: Application to FeAs_2 and FeSb_2 , *Phys. Rev. B* **82**, 085104 (2010).
 - [11] J. M. Tomczak, K. Haule, and G. Kotliar, Signatures of electronic correlations in iron silicide, *Proc. Natl. Acad. Sci. USA* **109**, 3243 (2012).
 - [12] V. Jaccarino, G. K. Wertheim, J. H. Wernick, L. R. Walker, and S. Aarjns, Paramagnetic excited state of FeSi, *Phys. Rev.* **160**, 476 (1967).
 - [13] T. Koyama, Y. Fukui, Y. Muro, T. Nagao, H. Nakamura, and T. Kohara, Nuclear quadrupole resonance study of the electronic properties of the narrow-gap semiconductor FeSb_2 , *Phys. Rev. B* **76**, 073203 (2007).
 - [14] A.-M. Racu, D. Menzel, J. Schoenes, and K. Doll, Crystallographic disorder and electron-phonon coupling in $\text{Fe}_{1-x}\text{Co}_x\text{Si}$ single crystals: Raman spectroscopy study, *Phys. Rev. B* **76**, 115103 (2007).

- [15] N. Lazarević, Z. V. Popović, R. Hu, and C. Petrovic, Evidence for electron-phonon interaction in $\text{Fe}_{1-x}\text{M}_x\text{Sb}_2$ ($M = \text{Co}$ and Cr ; $0 \leq x \leq 0.5$) single crystals, *Phys. Rev. B* **81**, 144302 (2010).
- [16] N. Lazarević, M. M. Radonjić, D. Tanasković, R. Hu, C. Petrovic, and Z. V. Popović, Lattice dynamics of FeSb_2 , *J. Phys.: Condens. Matter* **24**, 255402 (2012).
- [17] B. C. Sales, E. C. Jones, B. C. Chakoumakos, J. A. Fernandez-Baca, H. E. Harmon, J. W. Sharp, and E. H. Volckmann, Magnetic, transport, and structural properties of $\text{Fe}_{1-x}\text{Ir}_x\text{Si}$, *Phys. Rev. B* **50**, 8207 (1994).
- [18] P. Sun, N. Oeschler, S. Johnsen, B. B. Iversen, and F. Steglich, Huge thermoelectric power factor: FeSb_2 versus FeAs_2 and RuSb_2 , *Appl. Phys. Express* **2**, 091102 (2009).
- [19] C. C. Homes, Q. Du, C. Petrovic, W. H. Brito, S. Choi, and G. Kotliar, Unusual electronic and vibrational properties in the colossal thermopower material FeSb_2 , *Sci. Rep.* **8**, 11692 (2018).
- [20] M. Battiato, J. M. Tomczak, Z. Zhong, and K. Held, Unified Picture for the Colossal Thermopower Compound FeSb_2 , *Phys. Rev. Lett.* **114**, 236603 (2015).
- [21] Q. Du, L. Wu, H. Cao, C.-J. Kang, C. Nelson, G. L. Pascut, T. Besara, T. Siegrist, K. Haule, G. Kotliar, I. Zaliznyak, Y. Zhu, and C. Petrovic, Vacancy defect control of colossal thermopower in FeSb_2 , *npj Quantum Mater.* **6**, 13 (2021).
- [22] Y. Hadano, S. Narazu, M. A. Avila, T. Onimaru, and T. Takabatake, Thermoelectric and magnetic properties of a narrow-gap semiconductor FeGa_3 , *J. Phys. Soc. Jpn.* **78**, 013702 (2009).
- [23] M. Wagner-Reetz, D. Kasinathan, W. Schnelle, R. Cardoso-Gil, H. Rosner, Y. Grin, and P. Gille, Phonon-drag effect in FeGa_3 , *Phys. Rev. B* **90**, 195206 (2014).
- [24] Z. P. Yin and W. E. Pickett, Evidence for a spin singlet state in the intermetallic semiconductor FeGa_3 , *Phys. Rev. B* **82**, 155202 (2010).
- [25] M. B. Gamža, J. M. Tomczak, C. Brown, A. Puri, G. Kotliar, and M. C. Aronson, Electronic correlations in FeGa_3 and the effect of hole doping on its magnetic properties, *Phys. Rev. B* **89**, 195102 (2014).
- [26] Y. V. Knyazev and Y. I. Kuz'min, The study of the structure of the electronic states of the FeGa_3 and RuGa_3 compounds by optical spectroscopy method, *Phys. Solid State* **59**, 2244 (2017).
- [27] K. Lagarec and D. G. Rancourt, *RECOIL, Mössbauer spectral analysis software for Windows* (University of Ottawa, Ottawa, Canada, 1998).
- [28] P. Giannozzi, S. Baroni, N. Bonini, M. Calandra, R. Car, C. Cavazzoni, D. Ceresoli, G. L. Chiarotti, M. Cococcioni, I. Dabo, A. D. Corso, S. de Gironcoli, S. Fabris, G. Fratesi, R. Gebauer, U. Gerstmann, C. Gougousis, A. Kokalj, M. Lazzeri, L. Martin-Samos *et al.*, Quantum espresso: a modular and open-source software project for quantum simulations of materials, *J. Phys.: Condens. Matter* **21**, 395502 (2009).
- [29] P. Giannozzi, O. Andreussi, T. Brumme, O. Bunau, M. B. Nardelli, M. Calandra, R. Car, C. Cavazzoni, D. Ceresoli, M. Cococcioni, N. Colonna, I. Carnimeo, A. D. Corso, S. de Gironcoli, P. Delugas, R. A. DiStasio, A. Ferretti, A. Floris, G. Fratesi, G. Fugallo *et al.*, Advanced capabilities for materials modelling with quantum espresso, *J. Phys.: Condens. Matter* **29**, 465901 (2017).
- [30] S. Baroni, S. de Gironcoli, A. Dal Corso, and P. Giannozzi, Phonons and related crystal properties from density-functional perturbation theory, *Rev. Mod. Phys.* **73**, 515 (2001).
- [31] U. Häussermann, M. Boström, P. Viklund, O. Rapp, and T. Björnängen, FeGa_3 and RuGa_3 : Semiconducting Intermetallic Compounds, *J. Solid State Chem.* **165**, 94 (2002).
- [32] Y. Imai and A. Watanabe, Electronic structures of semiconducting FeGa_3 , RuGa_3 , OsGa_3 , and RuIn_3 with the CoGa_3 - or the FeGa_3 -type structure, *Intermetallics* **14**, 722 (2006).
- [33] F. Wooten, *Optical Properties of Solids* (Academic Press, New York, 1972).
- [34] D. B. Tanner, *Optical Effects in Solids* (Cambridge University Press, New York, 2019).
- [35] D. B. Tanner, Use of x-ray scattering functions in Kramers-Kronig analysis of reflectance, *Phys. Rev. B* **91**, 035123 (2015).
- [36] S. Albrecht, L. Reining, R. Del Sole, and G. Onida, *Ab Initio* Calculation of Excitonic Effects in the Optical Spectra of Semiconductors, *Phys. Rev. Lett.* **80**, 4510 (1998).
- [37] M. Rohlfing and S. G. Louie, Electron-hole excitations and optical spectra from first principles, *Phys. Rev. B* **62**, 4927 (2000).
- [38] G. L. Whittle, P. E. Clark, and R. Cywinski, Vacancies and site occupation in Co-Ga-Fe alloys (Mössbauer study), *J. Phys. F* **10**, 2093 (1980).
- [39] I. Dézsi, I. Szűcs, C. Fetzter, and W. Keune, The local interactions of Co and Fe in β -phase $\text{Co}_x\text{Ga}_{(1-x)}$, *Acta Mater.* **46**, 3299 (1998).
- [40] N. Tsujii, H. Yamaoka, M. Matsunami, R. Eguchi, Y. Ishida, Y. Senba, H. Ohashi, S. Shin, T. Furubayashi, H. Abe, and H. Kitazawa, Observation of energy gap in FeGa_3 , *J. Phys. Soc. Jpn.* **77**, 024705 (2008).
- [41] G. R. Hearne, S. Bhattacharjee, B. P. Doyle, M. A. M. Ahmed, P. Musyimi, E. Carleschi, and B. Joseph, Pressure-induced disruption of the local environment of Fe-Fe dimers in FeGa_3 accompanied by metallization, *Phys. Rev. B* **98**, 020101(R) (2018).
- [42] D. Mondal, C. Kamal, S. Banik, A. Bhakar, A. Kak, G. Das, R. V. R., A. Chakrabarti, and T. Ganguli, Structural and electronic properties of $\text{Fe}(\text{Al}_x\text{Ga}_{1-x})_3$ system, *J. Appl. Phys.* **120**, 165102 (2016).

Correction: A typographical error in the fourth affiliation was introduced during the production cycle and has been fixed.

UNIVERSITY OF BELGRADE
FACULTY OF PHYSICS

Petar Mitrić

**SPECTRAL FUNCTIONS AND
MOBILITY OF THE HOLSTEIN
POLARON**

Doctoral Dissertation

Belgrade, 2023

УНИВЕРЗИТЕТ У БЕОГРАДУ
ФИЗИЧКИ ФАКУЛТЕТ

Петар Митрић

**СПЕКТРАЛНЕ ФУНКЦИЈЕ И
ПОКРЕТЉИВОСТ ХОЛШТАЈНОВОГ
ПОЛАРОНА**

докторска дисертација

Београд, 2023

Thesis Defense Committee

Thesis advisor:

Dr. Darko Tanasković
Research Professor
Institute of Physics Belgrade
University of Belgrade

Committee members:

Dr. Djordje Spasojević
Full Professor
Faculty of Physics
University of Belgrade

Dr. Božidar Nikolić
Associate Professor
Faculty of Physics
University of Belgrade

Dr. Antun Balaž
Research Professor
Institute of Physics Belgrade
University of Belgrade

Acknowledgments

This thesis was carried out at the Institute of Physics Belgrade, Scientific Computing Laboratory (SCL), under the guidance of Dr. Darko Tanasković. I would like to express my sincere gratitude to Darko for his boundless patience and immense enthusiasm for answering numerous questions that I placed upon him. He always had time for me, showing endless support and undivided attention. During our joint work, we often collaborated with Dr. Nenad Vukmirović and Dr. Veljko Janković from whom I also learned a lot. I thank them for always being willing to engage in discussions and provide valuable advice, even in times when I thought I didn't need one. I especially thank Dr. Antun Balaž, the head of SCL, not only for being a delightful boss, but also for being kind enough to invite me to join the SCL at a crossroads in my life. I'd also like to convey my appreciation to all my colleagues in the SCL group for a positive working atmosphere and their selfless willingness to help in a time of need.

Outside of the SCL, there are also individuals who have deeply affected my life, and in the process, imparted valuable lessons on me: Bogdan, Bane, Mihailo, Danilo and Siniša. Thank you all for being there for me when I needed you the most.

Finally, but most importantly, I thank my father, mother, sister, Keka, and the rest of my family. I don't need to explain why. They already know it all too well. I dedicate this thesis to them. After all, this thesis would not be possible without them. Even if it was, I wouldn't want to do it alone anyway.

Abstract

The electron-phonon interaction significantly affects the properties of semiconducting materials. Because of it, the phononic cloud can renormalize electrons, which leads to the emergence of polarons - a new quasiparticle that now, instead of the electron, plays the role of the current carrier in our system. The consequences of polaron formation are most easily studied using simplified models of electron-phonon systems. Among these models, the simplest one is the Holstein model, which successfully reproduces the most important polaronic effects. In practice, the Holstein model is used for testing and developing various theoretical methods that can subsequently be applied to more complex models or even real materials. The goal of this dissertation is to investigate the single-particle and transport properties of the Holstein model using different methods.

Until recently, it was widely accepted that the dynamical mean-field theory (DMFT) provides a good description of the single-particle properties of the Holstein model only in the cases of three-dimensional or even higher-dimensional systems. However, our results show that DMFT actually provides an excellent description of single-particle properties even in the one-dimensional case, regardless of the regime, which is determined by temperature, phonon frequency, and electron-phonon coupling strength. We have reached these conclusions by comparing the results obtained using this method, with the most reliable results currently available in the literature. Although DMFT is approximate, it is also a nonperturbative method that is exact in two different limits: in the weak coupling limit and in the atomic limit. Having in mind that DMFT neglects non-local correlations, which are most pronounced in the one-dimensional case, our conclusions about the high reliability of this method are expected to continue to hold in an arbitrary number of dimensions as well. This has been explicitly verified on the example of the effective mass in one-, two-, and three-dimensional cases. In addition, we have also presented a numerical procedure for the application of DMFT that requires very little computational resources. Therefore, this method allows us to easily generate a large amount of reliable results in different regimes, which can now be used to assess the quality of any other method. One such method that we intend to investigate more thoroughly is the cumulant expansion (CE) Method.

In contrast to DMFT, the CE is a perturbative method that does not rely on Dyson's equation for the calculation of the single-particle properties. Although CE does not provide reliable results in all regimes, the advantage of this method in comparison to the DMFT is that it can be easily applied to significantly more complex models, and even to real materials. Therefore, it is very important to determine in which parameter regimes can CE be expected to give an adequate description of the observed physical system. In this dissertation, this was investigated on the example of the Holstein model, by comparing the CE with the DMFT results, which we have already established as reliable. It turns out that, although CE is exact only in the weak coupling and atomic limits, reliable approximate predictions of this method are possible even for moderate interactions, where the corresponding spectral function accurately reproduces both the quasiparticle and the first satellite peak. This is signif-

icantly better than what would be obtained using the lowest-order perturbation theory. In addition, the high-temperature results of the CE look promising, although we proved, using the spectral sum rules, that this method cannot be exact in the limit $T \rightarrow \infty$.

For the study of transport properties, we focused on calculating mobility and a somewhat more general quantity, the optical conductivity. Within the framework of linear response theory, both of these quantities can be represented as the sum of the so-called bubble term, determined by the single-particle properties, and vertex corrections. The bubble term for mobility μ was calculated numerically, and detailed comparisons were made between the DMFT and CE predictions. We established that at high temperatures, the charge mobility assumes a power law $\mu \propto T^{-2}$ in the case of very weak coupling, and $\mu \propto T^{-3/2}$ for somewhat stronger coupling. We analytically proved that in the weak coupling and atomic limits of the Holstein model, the vertex corrections of mobility are vanishing. In all other regimes, the contribution of vertex corrections was examined numerically, by calculating the bubble term using the DMFT and by comparing it to the exact result from the literature.

Keywords: Holstein model, electron-phonon interaction, spectral functions, quasiparticle properties, dynamical mean field theory, cumulant expansion method, mobility, optical conductivity, vertex corrections, spectral sum rules

Research field: Physics

Research subfield: Condensed matter physics

UDC number: 538.9

Интеракција између електрона и фонона значајно утиче на особине полупроводничких материјала. Захваљујући њој, фононски облак може ренормализовати електрон и на тај начин довести до појаве поларона – нове квазичестице која сада, уместо електрона, постаје носилац струје у посматраном систему. Последице појаве поларона најлакше се проучавају помоћу поједностављених модела електрон-фононских система. Најједноставнији међу њима је Холштајнов модел, који успешно репродукује најважније поларонске ефекте. У пракси, Холштајнов модел се користи за тестирање и развој различитих теоријских метода који накнадно могу бити примењени на сложеније моделе или чак на реалне материјале. Циљ ове дисертације је проучавање једночестичних и транспортних особина Холштајновог модела коришћењем различитих метода.

До недавно, било је опште прихваћено да теорија динамичког средњег поља (ТДСП) даје добар опис једночестичних особина Холштајновог модела, али само у случају тродимензионих система или система са још већим бројем димензија. Међутим, наши резултати показују да ТДСП заправо даје сјајан опис једночестичних особина чак и у једнодимензионом случају, без обзира на режим који је одређен температуром, фреквенцијом фонона и јачином интеракције између електрона и фонона. До тог закључака дошли смо поређењем резултата овог метода са најпоузданијим резултатима тренутно доступних у литератури. Иако је ТДСП апроксимативан, он је такође и непертурбативан метод који је егзактан у два различита лимеса: у лимесу слабе електрон-фононске интеракције и у атомском лимесу. Имајући у виду да ТДСП занемарује нелокалне корелације које су најјаче у једнодимензионом случају, може се очекивати да наши закључци о великој поузданости овог метода остају на снази у произвољном броју димензија. То је било и експлицитно проверено на примеру ефективне масе квазичестице у случају једне, две и три димензије. Поред тога, изложили смо и нумеричку процедуру којом се ТДСП може применити коришћењем веома мало рачунарских ресурса. Стога, овај метод нам пружа могућност да веома једноставно генеришемо велику количину поузданих резултата у различитим режимима, који сада могу служити за оцену квалитета било ког другог метода. Један такав метод који желимо детаљније да испитамо зове се метод кумулантног развоја (МКР).

МКР је, за разлику од ТДСП, пертурбативан метод који се не ослања на коришћење Дајсонове једначине за израчунавање једночестичних особина система. Иако МКР не даје поуздане резултате у свим режимима, предност овог метода у односу на ТДСП је то што се он веома лако може применити и у знатно сложенијим моделима, па чак и у реалним материјалима. Зато је веома важно испитати у којим режимима се може очекивати да МКР даје адекватан опис посматраног физичког система. То је у овој дисертацији урађено на примеру Холштајновог модела, тако што смо резултате МКР-а поредили са

результатима ТДСП-а, за које смо већ утврдили да су поуздани. Испоставља се да, иако је МКР егзактан само у лимесу слабе електрон-фононске интеракције и атомском лимесу, поуздана апроксимативна предвиђања овог метода могућа су и за умерене интеракције, где одговарајућа спектрална функција добро репродукује и квазичестични и први сателитски пик. То је значајно боље него што бисмо добили теоријом пертурбације најнижег реда. Такође, резултати МКР-а при високим температурама изгледају обећавајући, али смо коришћењем спектралних сумационих правила аналитички показали да овај метод не може бити егзактан у лимесу $T \rightarrow \infty$.

За изучавање транспортних особина, усредсредили смо се на рачунање покретљивости и нешто општије величине, оптичке проводности. У оквиру теорије линеарног одзива, обе ове величине могу бити приказане као збир тзв. мехурастог члана, који је одређен једночестичним особинама, и тзв. вертексних корекција. Мехурасти члан за покретљивост μ је рачунат у оквиру ТДСП-а и МКР-а, и вршена су детаљна поређења. Утврдили смо да при високим температурама, температурна зависност мобилности задовољава $\mu \propto T^{-2}$ у случају веома слабе интеракције, и $\mu \propto T^{-3/2}$ у случају нешто јаче интеракције. Аналитички је показано да у лимесу слабе интеракције и у атомском лимесу нема вертексних корекција покретљивости у оквиру Холштајновог модела. У свим осталим режимима, вертексне корекције су испитиване нумерички, тако што је поређен мехурасти члан рачунат помоћу ТДСП-а и егзактан резултат који је преузет из литературе.

Кључне речи: Холштајнов модел, електрон-фононска интеракција, спектралне функције, квазичестичне особине, теорија динамичког средњег поља, метод кумулантног развоја, покретљивост, оптичка проводност, вертексне корекције, спектрална сумациона правила

Научна област: Физика

Област истраживања: Физика кондензоване материје

УДК број: 538.9

Contents

Thesis Defense Committee	v
Acknowledgments	vii
Abstract	ix
List of Figures	xxi
List of Tables	xxii
List of Abbreviations	xxv
List of Symbols	xxvii
I Introduction	1
1 Polaron Physics	3
1.1 Electron-Phonon Interaction in General	3
1.2 Polaron Concept	4
1.3 Holstein Model	4
1.3.1 Single Particle Properties	5
1.3.2 Transport Properties	6
1.4 Thesis Outline	7
2 Exploring the Holstein Model: Mathematical Foundations and Basic Results	8
2.1 Mathematical Foundations	8
2.1.1 One-Particle Green's Function: Definition	8
2.1.2 One-Particle Green's Function: Simplifications in the Limit of Vanishingly Small Electron Concentration $n_e \rightarrow 0$	9
2.2 Weak Coupling Regime: Migdal Approximation	11
2.3 Atomic Limit	13
2.4 Spectral Sum Rules	15

II	Single particle properties	17
1	Dynamical Mean-Field Theory	19
1.1	Introduction	19
1.2	Getting to Know DMFT: An Intuitive Approach	20
1.3	Renormalization of the Physical Quantities in the Limit of Infinite Number of Dimensions $d \rightarrow \infty$	24
1.3.1	Renormalization of the Hopping Parameter in the Limit $d \rightarrow \infty$	24
1.3.2	Renormalization of the Green's Function in the Limit $d \rightarrow \infty$	25
1.4	Self-energy in the Limit of an Infinite Number of Dimensions	26
1.5	Integrating out the Phononic Degrees of Freedom	29
1.6	Cavity Method	32
1.6.1	Overview	32
1.6.2	Cavity Construction	33
1.6.3	Expressing the Generating Functional in Terms of the Green's Functions	34
1.6.4	Expressing the Generating Functional in Terms of the Connected Green's Functions	35
1.6.5	Simplifications in the Limit $d \rightarrow \infty$	36
1.7	Holstein-Anderson Impurity Problem	38
1.8	Self-consistency Condition	41
1.8.1	Derivation of the Self-consistency Condition	41
1.8.2	Local Green's Function in the 1D Case	43
1.8.3	Local Green's Function in the Case of 2D Square Lattice	45
1.8.4	Numerical Scheme for Calculating the Local Green's Function in General case	46
1.9	Impurity Solver	48
1.9.1	Expressing Green's Function in Terms of a Resolvent of K	48
1.9.2	Expressing Green's Function in Terms of a Resolvent of K_0	49
1.9.3	Expressing a Resolvent of K_0 in Terms of a Free Green's Function G_0	50
1.9.4	Recurrence Relation for $G_{n,m}$	51
1.9.5	Final Solution of the Impurity Problem	52
1.9.6	Numerical Implementation of the Impurity Solver	52
2	Dynamical Mean-Field Theory: Numerical Results	54
2.1	Quasiparticle Properties	54
2.2	Spectral Functions for Weak Electron-phonon Coupling	57
2.2.1	Benchmark Method: Self-Consistent Migdal Approximation	57
2.2.2	DMFT vs. SCMA in the Weak Coupling Limit	59
2.3	Spectral Sum Rules	59
2.3.1	Introduction	59
2.3.2	Spectral Sum Rules: Exact Results	61
2.3.3	Spectral Sum Rules: SCMA Predictions	61
2.3.4	Spectral Sum Rules: DMFT Predictions	62
2.4	Atomic Limit	62
2.4.1	Atomic Limit at $T = 0$: DMFT Predictions	63
2.4.2	Atomic Limit at $T \neq 0$: DMFT Predictions	65
2.4.3	Atomic Limit at $T = 0$: SCMA Predictions	67
2.5	Spectral Function at Intermediate and Strong Electron-Phonon Coupling	67
2.5.1	Benchmark Method: Hierarchical Equations of Motion	67
2.5.2	Results at Finite Temperature	68
2.5.3	Heat Maps	73

2.5.4	Results at $T = 0$	74
2.5.5	HEOM Self-Energies	77
2.6	Imaginary Time Correlation Functions	79
3	Cumulant Expansion Method	83
3.1	Introduction	83
3.2	Cumulant Expansion: Theoretical Foundations	84
3.2.1	Theoretical Framework for the Calculation of the Second-Order Cumulant Function	84
3.2.2	Numerical Challenges when Applying the Second-order Cumulant Expansion	86
3.2.3	Asymptotic Expansion for Cumulant when $t \rightarrow \infty$	86
3.2.4	Alternative Derivation of the Cumulant Function	87
3.3	Second-Order Cumulant Expansion for the Holstein Model: Implementation and Basic Properties	91
3.3.1	Cumulant Function in the Holstein Model	91
3.3.2	Lifetime	92
3.4	Spectral Functions	93
3.4.1	Low and Intermediate Temperatures for $k = 0$	93
3.4.2	Low and Intermediate Temperatures for $k \neq 0$	95
3.4.3	Spectral Functions at High Temperatures and Spectral Sum Rules	96
3.4.4	Atomic Limit	98
3.5	Quasiparticle Properties	101
3.5.1	Ground State Energy	101
3.5.2	Effective Mass	103
3.6	2D Spectral Functions	105
3.7	Supplementary Results in a Wide Range of Parameter Regimes	106
III	Transport properties	115
1	Revisiting Linear Response Theory	117
1.1	Brief Overview and Introduction of the Most Important Quantities and Notation	117
1.2	Time Evolution of the Density Matrix	118
1.3	Linear Response Approach	119
1.4	Properties of Response and Relaxation Functions	121
1.4.1	Properties of $\phi_{BA}(t)$	121
1.4.2	Properties of $\Phi_{BA}(t)$	122
1.5	Generalized Susceptibility	123
2	Optical Conductivity from Linear Response Theory	125
2.1	Basic Definitions	125
2.2	Different Ways to Relate Optical Conductivity and Current-Current Correlation Functions	126
2.2.1	Expressions on a Real-Frequency Axis	126
2.2.2	Expressions on the Imaginary Axis	128
2.3	Optical Sum Rule	129
2.3.1	Optical Sum Rule in General	129
2.3.2	Optical Sum Rule for the Holstien Model	130
2.4	Diagrammatic Approach to Optical Conductivity	130
2.4.1	General Theory	130
2.4.2	Bubble Approximation	132

2.5	DMFT Optical Conductivity in the limit $d \rightarrow \infty$	134
3	Numerical Results for the Mobility: Comparison Between Different Methods	136
3.1	Technical Details	136
3.2	Results	137
4	Ward Identity and its Consequences	142
4.1	Introduction and Mathematical Formulation of the Ward identity	142
4.2	Proof of the Ward Identity	143
4.2.1	Definition of Correlation Function $\Lambda^\mu(r_1, r_2, r_3)$	143
4.2.2	Definition of $\tilde{\Gamma}^\mu$	144
4.2.3	Fourier Transform	145
4.2.4	Proof that $\tilde{\Gamma}^\mu(p, p + q) \equiv \Gamma^\mu(p, p + q)$	146
4.2.5	Differentiation under the Time-Ordering Operator	148
4.2.6	The Consequences of Charge Conservation on Λ^μ	149
4.2.7	Putting all the Pieces Together	151
4.3	Consequence of the Ward Identity	152
5	Vertex Corrections in the Holstein Model: Analytical Considerations	154
5.1	Introduction	154
5.2	The Limit of Weak Electron-Phonon Coupling	154
5.2.1	The Migdal Approximation and the Ward Identity	155
5.2.2	The Self-Consistent Migdal Approximation and the Ward Identity	156
5.2.3	Vertex Corrections of Mobility in the Weak Coupling Limit	157
5.3	Vertex Corrections in the Atomic Limit	158
6	Vertex Corrections in the Holstein Model: Numerical Considerations	159
6.1	Introduction and Benchmarks	159
6.2	Optical Conductivity in the Weak Coupling Regime	160
6.3	Optical Conductivity for Intermediate and Strong Electron-Phonon Coupling	162
6.4	Optical Conductivity Close to the Adiabatic Limit	166
6.4.1	Replacing Phonons with Static Disorder	166
6.4.2	Anderson Approach	168
6.4.3	Coherent Potential Approximation	169
6.4.4	Numerical Results	170
6.5	Optical Conductivity in the Regimes where the Phonon Frequency is Large	172
	Conclusions	175
V	Appendices	181
A	Numerical Fourier Transform of Green's functions	183
A.1	Transform $G(t) \rightarrow G(\omega)$	183
A.2	Transform $G(\omega) \rightarrow G(t)$	186
B	Numerical Integration Scheme for the Calculation of Highly-Oscillating Functions in the CE Method	189
B.1	Overview of the Main Ideas	189
B.2	1D Case	190

B.3	2D Case	191
B.4	3D Case	192
C	Current Operator in Quantum Mechanics	193
C.1	Introduction	193
C.2	Some General Remarks on the Definition of the Current Density Operator	194
C.3	Current Density Operator in the Case of a Continuum	195
C.4	Current Density Operator in the Case of a Lattice	196
C.4.1	Full Current Operator	196
C.4.2	Fourier Components of the Current Density Operator	197
C.5	Continuity Equation and its Consequences	201
C.6	General Form of the Current Operator	205
C.7	Some Properties of the (Paramagnetic) Current Operator	207
D	Using Continued Fraction Expansion for Representing Diagonal Elements of the Inverse of Tridiagonal Matrix	208
D.1	Statement of the Problem and Introduction of Notation	208
D.2	Some Useful Identities	209
D.3	Evaluation of $(M^{-1})_{nn}$ for Arbitrary n	211
E	Some General Operator Identities	212
F	Spectral Sum Rules: Numerical DMFT vs Analytical Results	214
	Bibliography	224
	Biography of the Author	231

List of Figures

I	Introduction	2
1.1	Schematic plot of different regimes of the 1D Holstein model in the (γ, λ) parameter space.	5
1.2	Schematic plot of the spectral function for $k = 0$ and $T = 0$	6
2.1	Feynman rules for the Holstein model.	9
II	Single particle properties	18
1.1	Mapping of the Holstein lattice problem to the Holstien-Anderson impurity problem	20
1.2	DMFT algorithm	23
1.3	Feynman diagrams for the self-energy.	27
1.4	Examples of diagrams that are not included in the skeleton expansion of the self-energy.	27
1.5	Visual proof that every two vertices have to be connected by at least three distinct paths.	28
1.6	Illustration of the cavity method.	32
1.7	Lowest order Feynman diagram for connected two-particle Green's function $G_{i_1 i_2 j_1 j_2}^{(0,c)}$.	37
1.8	Two different solutions for the local Green's function in 1D.	45
2.1	Comparison of the DMFT quasiparticle properties with reliable benchmarks.	55
2.2	(a) Continuous-time QMC vs. DMFT mass renormalization in 1d, 2d and 3d, with $\omega_0 = 1$. (b) Comparison of the DMFT mass renormalization on different lattices. . .	56
2.3	Comparison of DMFT local spectral functions on different lattices	57
2.4	Feynman diagrams for the self-consistent Migdal approximation.	58
2.5	The lowest Feynman diagram missing in the SCMA.	58
2.6	DMFT vs. SCMA spectral functions in the weak coupling regime.	60
2.7	DMFT integrated spectral weight for $t_0 = 0.05$ and $t_0 = 10^{-5}$ averaged over all momenta, $I(\omega) = \frac{1}{N} \sum_k \int_{-\infty}^{\omega} A_k(\nu) d\nu$, in comparison to the exact $t_0 = 0$ result. . . .	65
2.8	DMFT spectral functions $A(\omega) = \frac{1}{N} \sum_k A_k(\omega)$ for $\omega_0 = 1, g = 1, t_0 = 0.05$	66
2.9	DMFT, HEOM, SCMA, and ED finite temperature spectral functions and integrated spectral weights for $k = 0$ and $k = \pi$	70
2.10	DMFT, HEOM, SCMA, and ED finite temperature spectral functions and integrated spectral weights for $\pi/4 \leq k \leq \pi/3$ and $\pi/2 \leq k \leq 3\pi/4$	71

2.11	Additional DMFT, HEOM, SCMA, and ED results for spectral functions and integrated spectral weights.	72
2.12	DMFT results for systems with finite number of lattice sites.	72
2.13	DMFT heat maps for $A_{\mathbf{k}}(\omega)$	73
2.14	Integrated spectral weights and spectral functions, calculated using DMFT, HEOM, SCMA, and ED for $T = 0$ and $k = 0$	75
2.15	Integrated spectral weights and spectral functions, calculated using DMFT, HEOM, SCMA, and ED for $T = 0$ and $\pi/3 \leq k \leq \pi/4$	75
2.16	Integrated spectral weights and spectral functions, calculated using DMFT, HEOM, SCMA, and ED for $T = 0$ and $\pi/2 \leq k \leq 3\pi/4$	76
2.17	Integrated spectral weights and spectral functions, calculated using DMFT, HEOM, SCMA, and ED for $T = 0$ and $k = \pi$	76
2.18	Finite-size effects in the DMFT solution at intermediate coupling $\omega_0 = 1, g = 1, T = 0$	77
2.19	HEOM and DMFT self-energies for intermediate coupling.	78
2.20	(a)–(b) HEOM and DMFT self-energies close to the atomic limit $\omega_0 = 3, g = \sqrt{12}, T = 1$. (c)–(d) the same HEOM results in panels (a)–(b), but shifted for different values of momenta k	78
2.21	DMFT finite-size effects close to the atomic limit $\omega_0 = 3, g = \sqrt{12}, T = 1$	79
2.22	DMFT, HEOM, and QMC correlation functions for $\omega_0 = 1, g = \sqrt{2}$ at $k = 0$ and $k = \pi$, at several temperatures.	81
2.23	Comparison of DMFT, HEOM, QMC and SCMA correlation functions, over a wide range of parameters.	82
3.1	The cumulant, Green’s and spectral function on the example of the one-dimensional Holstein model with the following values of the model parameters: $\omega_0 = 0.2, g = 0.2, T = 0.3$ and $t_0 = 1$	92
3.2	Quasiparticle lifetime $\tau_{\mathbf{k}}$ in the CE method for $T/t_0 = 2$ and $g/t_0 = 1$	93
3.3	Spectral functions and integrated spectral weights for $t_0 = 1, \omega_0 = 0.5$ and $k = 0$	94
3.4	Heat maps of $A_{\mathbf{k}}(\omega)$ for $t_0 = 1, \omega_0 = 0.5$ and $T = 0.3$	96
3.5	Spectral functions for $t_0 = 1, \omega_0 = 0.5$ and $k = \pi$. In the left panels $T = 0.3$, while $T = 0.7$ in the right panels.	96
3.6	High-temperature CE, DMFT, and SCMA spectral functions in 1D for $t_0 = 1, \omega_0 = 0.5$, and $k = 0, \pi$	97
3.7	CE, DMFT, and SCMA spectral functions close to the atomic limit, for $k = 0$	100
3.8	Ground state energies, in the Holstein model, as a function of α^2 , for $t_0 = 1$ and $T = 0$	103
3.9	Effective mass results within the DMFT, CE, and SCMA for $t_0 = 1$ and $T = 0$	104
3.10	Comparison of the CE, DMFT, and SCMA spectral functions in a 2D Holstein model for $k = 0$ and $t_0 = 1$	105
3.11	Comparison of CE, DMFT, and SCMA spectral functions in the weak coupling regime, for a wide range of temperatures. Here $t_0 = \omega_0 = 1$ and $\alpha = 0.5$	107
3.12	Comparison of the CE, DMFT, SCMA, and MA spectral functions in 1D for $t_0 = \omega_0 = 1$	108
3.13	Comparison of the CE, DMFT, and SCMA spectral functions in 1D for $t_0 = \omega_0 = 1$ and $k = \pi/3, 2\pi/3$	109
3.14	Comparison of the CE and DMFT heat maps for $t_0 = \omega_0 = 1$	110
3.15	Comparison of the CE, DMFT, and SCMA spectral functions in 1D for $t_0 = 1, \omega_0 = 0.5$ and $k = \pi/3, 2\pi/3$	111
3.16	Comparison of the CE, DMFT, SCMA, and MA spectral functions in 1D for $t_0 = 1, \omega_0 = 0.2$, and $k = 0, \pi$	112

3.17 Comparison of the CE, DMFT, and SCMA spectral functions in 1D for $t_0 = 1$, $\omega_0 = 0.2$ and $k = \pi/3, 2\pi/3$ 113

3.18 Comparison of the CE and DMFT heat maps for $t_0 = 1$ and $\omega_0 = 0.2$ 114

III Transport properties 116

2.1 Feynman diagrams for the current-current correlation function. 131

2.2 Feynman diagrams for free vertices $\gamma^\alpha(\mathbf{p} + \mathbf{q}, \mathbf{p})$ and $\gamma^\alpha(\mathbf{p}, \mathbf{p} + \mathbf{q})$ 131

2.3 Alternative way to write Feynman diagrams for $\chi^{\mu\nu}$ 132

2.4 Another alternative way to write Feynman diagrams for $\chi^{\mu\nu}$ 134

2.5 An example of an irreducible two-particle vertex function $\tilde{\Lambda}$ 135

3.1 Temperature dependence of the mobility for the CE, DMFT, MA, and SCMA. 141

5.1 Renormalized vertex function Γ^μ needed for the Ward identity to be satisfied within the Migdal approximation. 155

5.2 Renormalized vertex function Γ^μ needed for the Ward identity to be satisfied within the self-consistent Migdal approximation. 157

6.1 Optical conductivities and current-current correlation functions in real and imaginary times in the weak coupling limit $\omega_0 = 1$, $\lambda = 0.01$ 161

6.2 Finite-size effects in the current-current correlation function for $\omega_0 = 1$, $\lambda = 0.01$, and $T = 1$ 162

6.3 Optical conductivities and current-current correlation functions in real and imaginary times in the intermediate coupling regime $\omega_0 = 1.0$, $\lambda = 0.5$ 163

6.4 Optical conductivities and real-time current-current correlation functions in the intermediate coupling regime $\omega_0 = 1.0$, $\lambda = 1.0$ 164

6.5 Optical conductivities and real-time current-current correlation functions in the strong coupling regime $\omega_0 = 1.0$, $\lambda = 2.0$ 165

6.6 Optical conductivities and real-time current-current correlation functions in the regime close to the adiabatic limit $\omega_0 = 1/3$, $\lambda = 1$ 171

6.7 Optical conductivities, normalized to the concentration of charge carriers, close to the antiadiabatic limit $\omega_0 = 3$ 172

Conclusions 176

V Appendices 182

List of Tables

2.1	Integrated spectral weight $I(\omega)$ for different momenta and hopping parameters at $T = 0$ and $\omega_0 = g = 1$	65
2.2	Spectral weights of individual peaks near the atomic limit, located at the frequency $\omega = n\omega_0 + E_p$, for $n = -2, -1, 0, 1, 2, 3$	66
2.3	Number of lattice sites N and the maximum hierarchy depth D used for the application of the HEOM method in different regimes at finite temperature	69
2.4	Number of lattice sites N and the maximum hierarchy depth D used for the application of the HEOM method in different regimes at $T = 0$	74
6.1	Number of lattice sites N and the maximum hierarchy depth D that correspond to HEOM/QMC results in Fig. 6.1.	161
6.2	Number of lattice sites N and the maximum hierarchy depth D that correspond to HEOM/QMC results in Figs. 6.3 and 6.4.	164
6.3	Number of lattice sites N and the maximum hierarchy depth D that correspond to HEOM results in Figs 6.6.	171
6.4	Number of lattice sites N and the maximum hierarchy depth D that correspond to the HEOM results in Fig. 6.7.	173
F.1	Spectral sum rules for $\omega_0 = 1.0, g = 1.0$ at different temperatures.	215
F.2	Sum rules for $\omega_0 = 1, g = \sqrt{2}$ at different temperatures.	216
F.3	Sum rules for $\omega_0 = 1, g = 0.5$ at different temperatures.	216
F.4	Sum rules for $\omega_0 = 1, g = 0.75$ at different temperatures.	217
F.5	Sum rules for $\omega_0 = 1, g = \sqrt{3}$ at different temperatures.	217
F.6	Sum rules for $\omega_0 = 0.2, g = 0.05$ at different temperatures.	218
F.7	Sum rules for $\omega_0 = 0.2, g = 0.2$ at different temperatures.	218
F.8	Sum rules for $\omega_0 = 0.2, g = 0.5$ at different temperatures.	219
F.9	Sum rules for $\omega_0 = 0.2, g = 0.75$ at different temperatures.	219
F.10	Sum rules for $\omega_0 = 0.2, g = 1.0$ at different temperatures.	220
F.11	Sum rules for $\omega_0 = 0.2, g = \sqrt{2}$ at different temperatures.	220
F.12	Sum rules for $\omega_0 = 0.5, g = 0.05$ at different temperatures.	221
F.13	Sum rules for $\omega_0 = 0.5, g = 0.2$ at different temperatures.	221
F.14	Sum rules for $\omega_0 = 0.5, g = 0.5$ at different temperatures.	222
F.15	Sum rules for $\omega_0 = 0.2, g = 0.75$ at different temperatures.	222
F.16	Sum rules for $\omega_0 = 0.5, g = 1.0$ at different temperatures.	223
F.17	Sum rules for $\omega_0 = 0.5, g = \sqrt{2}$ at different temperatures.	223

List of Abbreviations

CE	Cumulant Expansion
CPA	Coherent Potential Approximation
DMFT	Dynamical Mean Field Theory
DMRG	Density Matrix Renormalization Group
ED	Exact Diagonalization
FFT	Fast Fourier Transform
FTLM	Finite Temperature Lanczos Method
HEOM	Hierarchical Equations of Motion
MA	Migdal Approximation
QMC	Quantum Monte Carlo
QP	Quasiparticle
SCMA	Self-Consistent Migdal Approximation

List of Symbols

Symbol	Description
$c_{\mathbf{k}}^\dagger / c_{\mathbf{k}}$	electron creation/annihilation operator
$a_{\mathbf{k}}^\dagger / a_{\mathbf{k}}$	phonon creation/annihilation operator
t_0	hopping parameter
$\varepsilon_{\mathbf{k}}$	noninteracting electron dispersion relation
ω_0	Einstein frequency of phonon
g	electron-phonon coupling constant
T	temperature
β	inverse temperature $\beta = 1/T$
$G_{\mathbf{k}}(\omega)$	Green's function
$A_{\mathbf{k}}(\omega)$	spectral function
$\Sigma_{\mathbf{k}}(\omega)$	self-energy
$\rho(\omega)$	noninteracting density of electron states
$\tau_{\mathbf{k}}$	quasiparticle lifetime
m^*	renormalized mass
m_0	bare mass
μ	mobility
$\tilde{\mu}$	chemical potential
\mathcal{F}	Fourier transform operator
\mathcal{H}	Hilbert transform operator
d	number of dimensions of the system
n_e	concentration of electrons

Symbol	Description
N	number of lattice sites
V	volume of the system
\hat{T}_t	time ordering operator in real time
\hat{T}_τ	time ordering operator in imaginary time
\hat{N}	total number of electrons operator
$\tilde{\rho}$	density matrix
\mathcal{Z}	partition function
f	Fermi function
b	Bose function
n_{ph}	$n_{\text{ph}} = b(\omega_0)$
$W/2$	half bandwidth
χ_{BA}	generalized susceptibility
ϕ_{BA}	response function
Φ_{BA}	relaxation function
L_0, L_1	Liouville operators
$\mathcal{L}(t, t_0)$	evolution operator of the density matrix

Part I
Introduction

Polaron Physics

1.1 Electron-Phonon Interaction in General

Capturing the full many-body effects in systems with electron-phonon interaction remains one of the major ongoing challenges of the solid state physics [1–3]. Because of its ubiquity and importance for a wide range of phenomena, understanding the impact of electron-phonon interaction continues to attract considerable attention for both fundamental research and technical applications. The electron-phonon interaction is responsible for the temperature dependence of carrier mobility in semiconductors, Cooper pairing in superconductors, and a plethora of other phenomena as well [4–6]. It also enables the use of silicon in solar cells by allowing the absorption of visible light through phonon-assisted indirect gap transitions of electrons, which is crucial since the direct band gap of silicon is too large [7, 8]. These and many other examples justify a widespread interest in the study of the effects of electron-phonon interaction in a broad class of materials.

The electron-phonon system is described by the following Hamiltonian¹ [1, 2]

$$H = \sum_{n\mathbf{k}} \varepsilon_{n\mathbf{k}} c_{n\mathbf{k}}^\dagger c_{n\mathbf{k}} + \sum_{\mathbf{q}\nu} \omega_{\mathbf{q}\nu} a_{\mathbf{q}\nu}^\dagger a_{\mathbf{q}\nu} + \frac{1}{\sqrt{N}} \sum_{\substack{\mathbf{k}, \mathbf{q} \\ m\nu\nu}} g_{m\nu\nu}(\mathbf{k}, \mathbf{q}) c_{m\mathbf{k}+\mathbf{q}}^\dagger c_{n\mathbf{k}} \left(a_{\mathbf{q}\nu} + a_{-\mathbf{q}\nu}^\dagger \right), \quad (1.1)$$

where the phonon-phonon coupling and the higher order electron-phonon coupling² (with respect to atomic displacements) are neglected. The first term represents the free electron part of the Hamiltonian, with $\varepsilon_{n\mathbf{k}}$ and $c_{n\mathbf{k}}$ being the non-interacting dispersion relation and the electron annihilation operator, respectively. The second term is the free phonon part of the Hamiltonian. Here, $\omega_{\mathbf{q}\nu}$ is the phonon frequency, while $a_{\mathbf{q}\nu}$ is the phonon annihilation operator. The last term in Eq. (1.1) describes the electron-phonon interaction, where N is the total number of unit cells of our crystal lattice and $g_{m\nu\nu}(\mathbf{k}, \mathbf{q})$ is the electron-phonon coupling strength.

While the electron-phonon systems can be studied both by using the *ab initio* methods [2] and model Hamiltonians, this thesis will be focused on the latter. In this approach, the parameters from Eq. (1.1) $\varepsilon_{n\mathbf{k}}$, $\omega_{\mathbf{q}\nu}$, and $g_{m\nu\nu}(\mathbf{k}, \mathbf{q})$ are modeled such that the corresponding Hamiltonian in Eq. (1.1) captures the most significant properties of the system we are investigating. For example, in the case when an electron couples to long wavelength acoustical phonons, the electron-phonon coupling constant is of the following form $g_{m\nu\nu}(\mathbf{k}, \mathbf{q}) \propto \sqrt{|\mathbf{q}|}$. Although this type of interaction is present in every crystal, this is often neglected if there is a stronger electron-phonon coupling mechanism, such as the piezoelectric coupling $g_{m\nu\nu}(\mathbf{k}, \mathbf{q}) \propto \frac{1}{\sqrt{|\mathbf{q}|}}$ or the Fröhlich coupling $g_{m\nu\nu}(\mathbf{k}, \mathbf{q}) \propto \frac{1}{|\mathbf{q}|}$ [9, 10]. The latter is responsible for the emergence of new quasiparticles, called the *polarons*, which represent one of the central themes of this thesis.

¹We set $\hbar = 1$.

²These are important for describing the temperature-dependent band structures.

1.2 Polaron Concept

In ionic solids and polar semiconductors, the strongest electron-phonon coupling mechanism is the Fröhlich coupling. It arises due to the longitudinal optical oscillations of charged ionic cores which create an electric dipole moment that strongly couples to electrons. In the field-theoretical description, we say that the electron is renormalized due to its interaction with the cloud of phononic excitations, thus creating a new quasiparticle called the polaron. The introduction of the polaron concept led to a paradigm shift in which this new quasiparticle, characterized by its effective mass (which is different from the electron band mass) and lifetime, is now the current carrier in the system and hence significantly affects the transport properties of the material.

Historically, the origins of polaron physics can be traced back to Landau's 1933 seminal paper [11] in which he predicted the possibility of electron strongly distorting the crystal lattice, via the Coulomb interaction, and getting self-trapped in thus created potential well³. Although immobile, the electron, together with its surrounding potential well, can be recognized as an early manifestation of what would be later termed a polaron. This work was continued by Solomon Pekar who devised the first macroscopic semiclassical model of the polaron. Furthermore, he was the one who coined the term polaron and realized that this quasiparticle is actually mobile [12–15]. While the polaron's effective mass was also calculated within this semiclassical model [16], it was clear that further progress required a fully quantum mechanical and microscopic description of the polaron. In today's research, the most studied quantum models are the Fröhlich model [9, 17] and the Holstein model [18], but it should also be noted that there were also other early attempts of quantum approaches by Pekar [19], Bogoliubov [20] and Tyablikov [21].

1.3 Holstein Model

Although we motivated the polaron concept using the Fröhlich coupling (i.e., the Fröhlich model), the study of polarons in this thesis will actually be conducted in the *Holstein model*. This is the simplest electron-phonon model in which both the coupling and the phonon frequency from Eq. (1.1) are just constant numbers (i.e., momentum independent) [18]. This model was most commonly used to develop and test a variety of different many-body methods [22], which can then subsequently be used in more complex models. Nevertheless, the Holstein molecular crystal model is also very important in order to understand the role of polarons in real materials [23]. This is still a very active field of research fueled by new directions in theoretical studies [4, 24–31] and advances in experimental techniques [32].

The Holstein Hamiltonian is defined as follows

$$H = \underbrace{-t_0 \sum_{\langle ij \rangle} (c_i^\dagger c_j + H.c)}_{H_{\text{el}}} - \underbrace{g \sum_i n_i (a_i^\dagger + a_i)}_{H_{\text{el-ph}}} + \underbrace{\omega_0 \sum_i a_i^\dagger a_i}_{H_{\text{ph}}}. \quad (1.2)$$

Here, $c_i^\dagger (a_i^\dagger)$ are the electron (phonon) creation operators, t_0 is the hopping parameter, g is the electron-phonon coupling strength, ω_0 is the frequency of the dispersionless optical phonons, $n_i = c_i^\dagger c_i$, and the sum $\sum_{\langle ij \rangle}$ goes only over the nearest neighbors i and j . We note that the parameters t_0 , \hbar , k_B and lattice constant will be set to 1. Furthermore, we restrict ourselves to the case when the concentration of electrons in the system is vanishingly small⁴, and we treat the electrons as spinless. This is relevant for the study of weakly doped semiconductors.

Within this model, there are four important energy scales: the temperature T , the hopping parameter t_0 , the phonon frequency ω_0 , and the electron-phonon coupling constant g . The interplay of these

³It should be noted that Landau's original goal was to explain the F-centers.

⁴As we will see in the next chapter, this can also be interpreted as if there is only a single electron in the whole crystal.

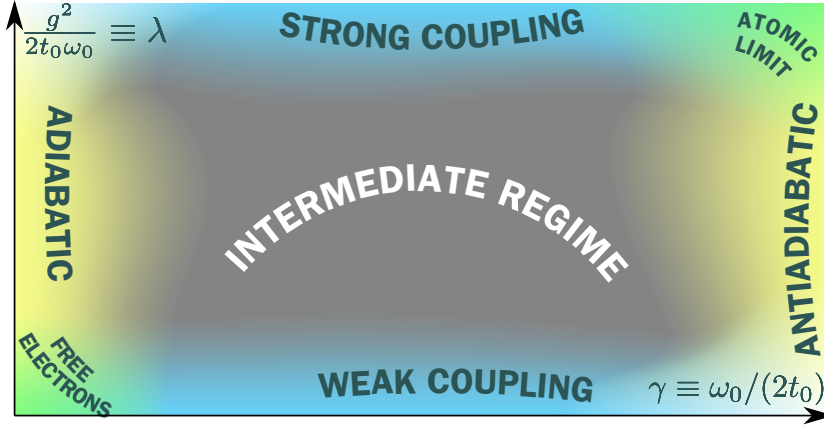


Figure 1.1: Schematic plot of different regimes of the 1D Holstein model in the (γ, λ) parameter space.

energy scales leads to a large number of parameter regimes. As shown in Fig. 1.1, to characterize these regimes it is common to introduce two dimensionless parameters⁵

$$\lambda = \frac{g^2}{\omega_0 W/2}; \quad \gamma = \frac{\omega_0}{W/2}, \quad (1.3)$$

where $W/2$ is the half bandwidth. Each of these parameter regimes is characterized by different single-particle and transport properties which, in this thesis, are investigated using the Green's function formalism [1, 33, 34].

1.3.1 Single Particle Properties

The central quantity for investigating the single-particle properties is the spectral function $A_k(\omega)$. If the interaction is not too strong and the temperature is not too high, the spectral function typically consists of a sharp quasiparticle peak (i.e., the *polaron peak*) and incoherent background; see Fig. 1.2. The incoherent part can be structureless or exhibit clearly separated features which are called satellite peaks [35]. The spectral function $A_k(\omega)$ can be interpreted as a probability density for an electron to have an energy ω . In addition, quasiparticle properties (ground state energy, effective mass, lifetime) are easily extracted from it (see Fig. 1.2). Furthermore, this quantity is also related to the spectrum of the angle-resolved photoelectron spectroscopy (ARPES) experiment [32, 35–37]. This is an experimental technique for probing a material's band structure, in which electrons, ionized by an incident photon beam, are analyzed in a detector. By measuring the number of detected electrons as a function of their kinetic energy and emission angle, it extracts the information about the momentum and binding energy of the electrons prior to ejection [35].

For the Holstein model, spectral functions can be evaluated analytically only in the weak coupling and the atomic limits [1, 38, 39]. Other regimes have, over the years, been investigated using a large number of numerical approaches. In particular, reliable numerical results for the ground state energy and quasiparticle effective mass were obtained in the late 1990's using the density matrix renormalization group (DMRG) [40, 41] and path integral quantum Monte Carlo (QMC) methods [42], and also within variational approaches [43–45]. At the time, numerically exact spectral functions for a one-dimensional (1D) system were restricted only to the $T = 0$ case, and were obtained only within the DMRG method [40, 41]. The main drawback of the QMC method is that it gives correlation functions in imaginary time and obtaining spectral functions and dynamical response functions is often

⁵In the 1D case $W/2 = 2t_0$, which is what we show in Fig. 1.1.

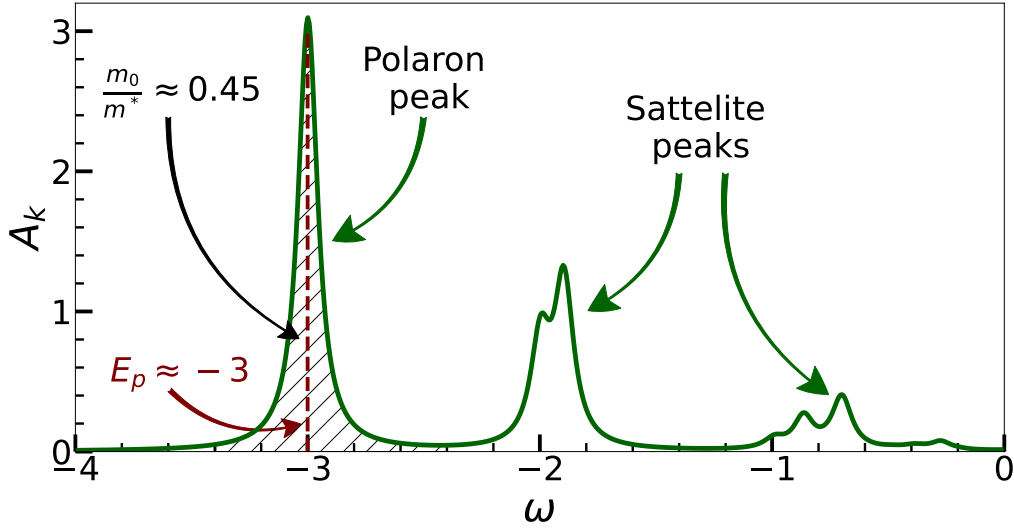


Figure 1.2: Schematic plot of the spectral function for $k = 0$ and $T = 0$, which illustrates some of the useful properties that can be easily extracted from the spectral function. For example, we see that the position of the polaron peak determines the ground state energy E_p , while its spectral weight determines the renormalization of the electron mass. We note that the polaron peak is actually a Dirac delta function in the Holstein model, but we used a Lorentzian broadening to make the figure more illustrative.

impossible since the analytical continuation to the real frequency is numerically ill-defined procedure. Interestingly, at finite temperatures the spectral functions were obtained only very recently using finite- T Lanczos (FTLM) [46] and finite- T DMRG [47] methods. All these methods have their strengths and weaknesses depending on the parameter regime and temperature. As usually happens in a strongly interacting many-body problem, a complete physical picture emerges only by taking into account the solutions obtained with different methods.

1.3.2 Transport Properties

Transport properties represent a step further from the investigation of just single-particle properties. One of the most important transport properties are the charge mobility⁶ and more generally, the optical conductivity. While both of these quantities are easily connected to experiments, their theoretical calculation is a notoriously difficult task. One of the ways to calculate these quantities in more general systems is by using the Boltzmann kinetic equation. A drawback of this approach is the fact that its domain of validity is not very large. For example, recently studied SrTiO_3 [48] and MoS_2 [32] have sufficiently strong electron-phonon interaction to fall outside the range where the Boltzmann approach is expected to give reliable results. These shortcomings of the Boltzmann approach were overcome by Kubo's linear response theory, which relates the optical conductivity to the current-current correlation function. However, it should be noted that although our task within this approach is thus reduced to the calculation of two-particle correlation functions, the linear response theory by itself does not provide a straightforward prescription to calculate them. In the Holstein model, various approaches have been used for the calculation of these quantities, such as the Hierarchical equations of motion [49], Quantum Monte Carlo [50], and many other methods as well [51–53]. However, obtaining reliable results in real materials still presents a challenge.

In Green's functions formalism, it is natural to express the current-current correlation function as

⁶The charge mobility is defined as a DC conductivity normalized to the concentration of charge carriers, and their unit charge.

a sum of two terms: the so-called *bubble term* and the so-called *vertex corrections*. The bubble term is solely determined by the single-particle Green's function and is thus, in conjunction with some other single-particle methods, often applied even in real materials. However, the contribution of vertex corrections is largely unknown and is often neglected without justification. This is why it is important to examine both the capabilities of different methods to calculate the bubble part, as well as determine the significance of vertex corrections. To answer these important questions, the Holstein model, due to its simplicity, presents an ideal starting point.

1.4 Thesis Outline

This thesis is divided into three parts. In the remaining portion of this part, we give an overview of some of the most basic known results concerning the single-particle properties of the Holstein model. We consider the two limiting cases (the weak coupling limit and the atomic limit) where the exact analytic solution is possible, and also show how the spectral sum rules are calculated in principle. In addition, we also briefly review the mathematical formalism that we use.

In Part II, the single-particle properties are studied in detail. Motivated by the highly local (i.e., almost k -independent) self-energy observed in Ref. [46], an idea arose to apply the DMFT in the Holstein model. A detailed review of this method is given in Chapter 1. In Chapter 2, we apply and thoroughly examine the DMFT in the Holstein model. We find that it provides an excellent, numerically cheap, approximate solution for the spectral functions and quasiparticle properties in the whole range of parameters, in an arbitrary number of dimensions. Surprisingly, a remarkable agreement with reliable benchmarks is observed even in 1D, where the nonlocal correlations are the strongest. In Chapter 3, another interesting many-body technique is examined - the cumulant expansion (CE) method. For this analysis, the DMFT was now used as a benchmark, which is justified because of our earlier findings. Due to the perturbative nature of the CE, it is not expected that it could outperform the DMFT. However, unlike the DMFT, the CE method is easily applied in any system, even in real materials, in a numerically inexpensive way. This is why it is extremely important to examine the range of validity of this increasingly popular method. As it turns out, the Holstein model is particularly useful for this purpose.

The transport properties are studied in Part III of this thesis. In Chapter 1, we briefly review Kubo's linear response theory [54]. This review is continued in Chapter 2 which focuses more specifically on the calculation of the optical conductivity. Here, we derive a variety of useful results such as the different relations between the current-current correlation function (both in real and in imaginary time) and the optical conductivity, the optical sum rule, the expression for the optical conductivity in the bubble approximation in terms of the spectral functions, the proof that there are no vertex corrections in the DMFT solution of optical conductivity, etc. The numerical results for the mobility in the bubble approximation are presented in Chapter 3. We compare the predictions of the CE, DMFT, as well as the (self-consistent) Migdal approximation. In addition, we analytically prove that the temperature dependence of mobility, at high temperatures, assumes a power law behavior. In Chapter 4 we prove the finite-temperature version of the Ward identity, and then using this result in Chapter 5 show that the bubble approximation within the MA and SCMA is actually in accordance with the conservation of charge. Furthermore, we demonstrate that the vertex corrections of mobility are vanishing in the cases of weak coupling and atomic limits. The vertex corrections in other regimes are studied numerically in Chapter 6.

Exploring the Holstein Model: Mathematical Foundations and Basic Results

In Sec. 1.3, we introduced the Holstein model: we defined the corresponding Hamiltonian, explained why this model continues to attract significant interest, and gave an overview of the most important results. In this chapter, we give formal mathematical definitions of the physical quantities that represent the backbone of this work¹, and also review some basic, already known [38, 55], analytic results which are essential for understanding the rest of this thesis.

2.1 Mathematical Foundations

The ground state energy, effective mass, spectral function, and correlation function in imaginary time are among the most important physical properties that characterize many physical systems. All of these quantities can be easily calculated if the one-particle Green's function $G_{\mathbf{k}}(t)$ is known. Even the optical conductivity, within the so-called bubble approximation, can be expressed using $G_{\mathbf{k}}(t)$. Therefore, it is of paramount importance to establish reliable methods of calculating this quantity within the Holstein model, for arbitrary values of parameters ω_0, g and T . A detailed discussion of these different methods will be postponed until Part II of this thesis. For now, we will give a definition of this quantity, show how it simplifies when the electron concentration is vanishingly small, which is the case of our interest, and briefly review how $G_{\mathbf{k}}(t)$ is connected to other physical quantities.

2.1.1 One-Particle Green's Function: Definition

The retarded one-particle Green's function² is defined as

$$G_{\mathbf{k}}(t) = -i\theta(t) \left\langle \left\{ c_{\mathbf{k}}(t), c_{\mathbf{k}}^{\dagger} \right\} \right\rangle_T, \quad (2.1)$$

where $\langle \dots \rangle_T$ denotes the average value in the grand canonical ensemble at temperature T , the curly brackets $\{, \}$ denote the anticommutator, while

$$c_{\mathbf{k}}(t) = e^{iKt} c_{\mathbf{k}} e^{-iKt}, \quad \text{and} \quad K = H - \tilde{\mu} \hat{N}. \quad (2.2)$$

Here, \hat{N} is the electron number operator. Although in some methods, such as the cumulant expansion, Green's function is calculated directly on the real-time axis, it is much more common to work with

¹Except for the transport properties - these are introduced in Part III of this thesis.

²For the remainder of this thesis, the abbreviated term "Green's function" refers to the one-particle Green's function, unless explicitly specified otherwise.

methods where the calculation is predominantly carried out in the frequency space

$$G_{\mathbf{k}}(\omega) = \lim_{\varepsilon \rightarrow 0^+} \int_{-\infty}^{\infty} dt e^{i(\omega+i\varepsilon)t} G_{\mathbf{k}}(t). \quad (2.3)$$

In fact, perturbation expansion is also usually performed in the Fourier space. The corresponding Feynman rules can be read off directly from the Hamiltonian in Eq. (1.2), and are summarized in Fig. 2.1.

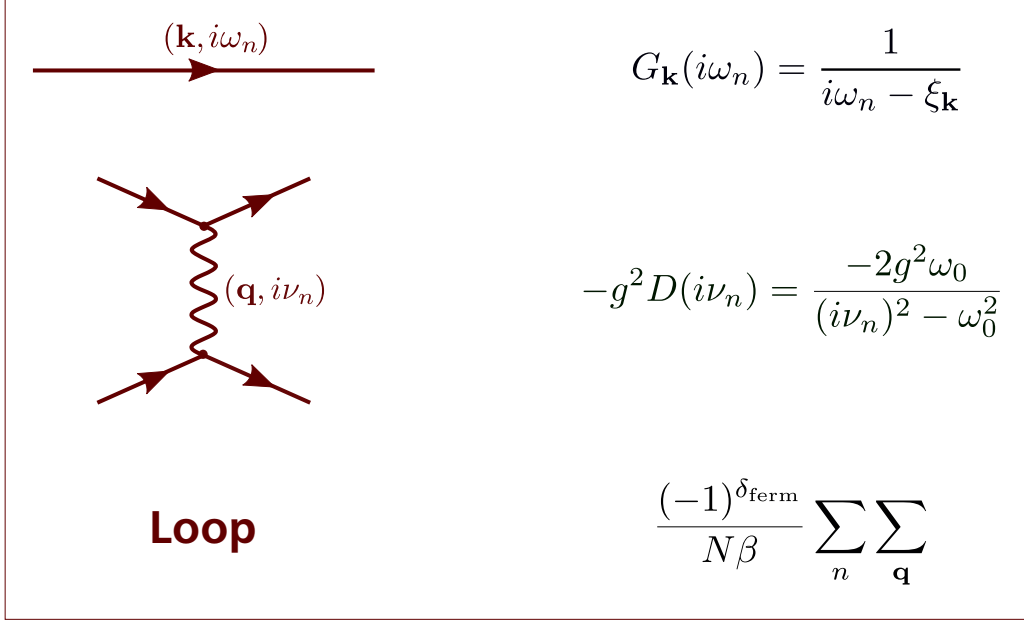


Figure 2.1: Feynman rules for the Holstein model. The quantity δ_{ferm} is equal to unity if the loop is fermionic, while being zero otherwise.

Furthermore, the Fourier space $G_{\mathbf{k}}(\omega)$ enables us to easily find the spectral function

$$A_{\mathbf{k}}(\omega) = -\frac{1}{\pi} \text{Im} G_{\mathbf{k}}(\omega), \quad (2.4)$$

which is closely connected to experiments through ARPES measurements. It is important to emphasize that throughout this whole thesis, we assume that the electron concentration is vanishingly small $n_e \rightarrow 0$. Some important simplifications arise in this limit, which we now investigate. In fact, we will see that this limit formally allows us to work in the canonical ensemble, with only a single electron in the entire system.

2.1.2 One-Particle Green's Function: Simplifications in the Limit of Vanishingly Small Electron Concentration $n_e \rightarrow 0$

In the grand canonical ensemble, the limit of vanishingly small concentration can be formally obtained by setting the chemical potential to be far below the conduction band $\tilde{\mu} \rightarrow -\infty$. This limit gives rise to some important simplifications. For example, it turns out that the phononic propagator remains unrenormalized [56]. This is easily understood because the creation and annihilation of electron-hole pairs are responsible for the renormalization of the phononic propagator, and there are no holes in the limit $n_e \rightarrow 0$. As a consequence, the most general self-energy Feynman diagram consists of a single fermion line, and an arbitrary number of attached phonon propagators. Another simplification arising in the limit $n_e \rightarrow 0$ is that we can formally redefine the Green's function, as if there is only a single electron in the whole system. We discuss this further in the following text.

Redefinition of the Green's Function

Starting from Eq. (2.1), let us expand that expression in the energy basis, i.e., let us use the Lehmann spectral representation

$$G_{\mathbf{k}}(t) = -i\theta(t)\langle c_{\mathbf{k}}(t)c_{\mathbf{k}}^{\dagger} \rangle_T - i\theta(t)\langle c_{\mathbf{k}}^{\dagger}c_{\mathbf{k}}(t) \rangle_T \quad (2.5a)$$

$$= \frac{-i\theta(t)}{\mathcal{Z}} \sum_n \langle n|e^{-\beta K} e^{iKt} c_{\mathbf{k}} e^{-iKt} c_{\mathbf{k}}^{\dagger}|n\rangle - \frac{i\theta(t)}{\mathcal{Z}} \sum_n \langle n|e^{-\beta K} c_{\mathbf{k}}^{\dagger} e^{iKt} c_{\mathbf{k}} e^{-iKt}|n\rangle. \quad (2.5b)$$

Here $\mathcal{Z} = \text{Tr} [e^{-\beta K}]$ is the partition function, and $|n\rangle$ is the energy basis $K|n\rangle = K_n|n\rangle$. This can be further simplified as follows

$$G_{\mathbf{k}}(t) = \frac{-i\theta(t)}{\mathcal{Z}} \sum_n e^{-\beta K_n} e^{iK_n t} \langle n|c_{\mathbf{k}} \mathbb{1} e^{-iKt} c_{\mathbf{k}}^{\dagger}|n\rangle - \frac{i\theta(t)}{\mathcal{Z}} \sum_n e^{-\beta K_n} e^{-iK_n t} \langle n|c_{\mathbf{k}}^{\dagger} \mathbb{1} e^{iKt} c_{\mathbf{k}}|n\rangle. \quad (2.6)$$

In the previous expression, we introduced the identity operator $\mathbb{1}$, which we now expand as $\mathbb{1} = \sum_m |m\rangle\langle m|$, and obtain

$$\begin{aligned} G_{\mathbf{k}}(t) &= \frac{-i\theta(t)}{\mathcal{Z}} \sum_{n,m} e^{-\beta K_n} e^{i(K_n - K_m)t} \langle n|c_{\mathbf{k}}|m\rangle \langle m|c_{\mathbf{k}}^{\dagger}|n\rangle \\ &\quad - \frac{i\theta(t)}{\mathcal{Z}} \sum_{n,m} e^{-\beta K_n} e^{-i(K_n - K_m)t} \langle n|c_{\mathbf{k}}^{\dagger}|m\rangle \langle m|c_{\mathbf{k}}|n\rangle. \end{aligned} \quad (2.7)$$

Since $e^{-\beta K_n} = e^{-\beta(E_n - \tilde{\mu}\hat{N})}$, only the terms where $|n\rangle$ has zero electrons and an arbitrary number of phonons can give a nonzero contribution to $G_{\mathbf{k}}(t)$. The second line of Eq. (2.7) thus has to be zero, since it contains $c_{\mathbf{k}}|n\rangle$. We are left with only the first line of Eq. (2.7), which corresponds to the first term on the right-hand side of Eq. (2.5a). Hence, we conclude that

$$G_{\mathbf{k}}(t) = \frac{-i\theta(t)}{\mathcal{Z}} \sum_{n,m} e^{-\beta K_n} e^{i(K_n - K_m)t} |\langle n|c_{\mathbf{k}}|m\rangle|^2 \quad (2.8a)$$

$$= \frac{-i\theta(t)}{\mathcal{Z}} \sum_n \langle n|e^{-\beta K} e^{iKt} c_{\mathbf{k}} e^{-iKt} c_{\mathbf{k}}^{\dagger}|n\rangle \quad (2.8b)$$

Furthermore, we note that the states $|n\rangle$ with zero electrons and an arbitrary number of phonons are also the only ones that give a contribution to the partition function

$$\mathcal{Z} = \sum_n \langle n|e^{-\beta K}|n\rangle = \sum_n e^{-\beta K_n} = \sum_n e^{-\beta E_n} e^{\beta \tilde{\mu} \hat{N}}. \quad (2.9)$$

This is seen as a consequence of the factor $e^{\beta \tilde{\mu} \hat{N}}$, which suppresses the contribution of states with a non-zero number of electrons in the $\tilde{\mu} \rightarrow \infty$ limit. In the following text, this partition function, with only the phononic contribution, will sometimes be denoted by \mathcal{Z}_p .

From Eq. (2.8a), we see that the Green's function in Fourier space can be calculated as

$$G_{\mathbf{k}}(\omega) = -\frac{i}{\mathcal{Z}} \sum_{n,m} |\langle m|c_{\mathbf{k}}^{\dagger}|n\rangle|^2 e^{-\beta K_n} \int_0^{\infty} dt e^{it(\omega + K_n - K_m)}. \quad (2.10)$$

The corresponding spectral function $A_{\mathbf{k}}(\omega) = -\frac{1}{\pi} \text{Im} G_{\mathbf{k}}(\omega)$ can be obtained using the following identity

$$\int_0^{\infty} dt e^{itx} = \pi \delta(x) + i\pi \mathcal{P} \frac{1}{x}, \quad (2.11)$$

giving

$$A_{\mathbf{k}}(\omega) = \frac{1}{\mathcal{Z}} \sum_{n,m} e^{-\beta K_n} |\langle m | c_{\mathbf{k}}^\dagger | n \rangle|^2 \delta(\omega + K_n - K_m). \quad (2.12)$$

We note that the states $|m\rangle$ have to contain exactly one electron, for the matrix element in Eq. (2.12) to be nonzero. Having in mind that the states $|n\rangle$ have zero electrons, it follows that $K_n - K_m = E_n - E_m + \tilde{\mu}$. Since $\tilde{\mu} \rightarrow -\infty$, we can ensure that the spectral weight of $A_{\mathbf{k}}(\omega)$ occurs at finite frequencies if we redefine the spectral function at the end of our calculation, using the following prescription $A_{\mathbf{k}}(\omega) \rightarrow A_{\mathbf{k}}(\omega + \tilde{\mu})$. An equivalent way to obtain the same result is to simply change $K \rightarrow H$. The redefined spectral function now reads as

$$A_{\mathbf{k}}(\omega) = \frac{1}{\mathcal{Z}} \sum_{n,m} e^{-\beta E_n} |\langle m | c_{\mathbf{k}}^\dagger | n \rangle|^2 \delta(\omega + E_n - E_m). \quad (2.13)$$

The corresponding Green's function on a real-time axis can be directly read off from Eq. (2.8b) by substituting $K \rightarrow H$. We note that, since the states $|n\rangle$ have zero electrons, we can also substitute $e^{-\beta H} \rightarrow e^{-\beta H_{\text{ph}}}$. Hence

$$G_{\mathbf{k}}(\omega) = \frac{-i\theta(t)}{\mathcal{Z}_p} \sum_n \langle n | e^{-\beta H_{\text{ph}}} e^{iHt} c_{\mathbf{k}} e^{-iHt} c_{\mathbf{k}}^\dagger | n \rangle = -i\theta(t) \langle c_{\mathbf{k}}(t) c_{\mathbf{k}}^\dagger \rangle_{T,0}, \quad (2.14)$$

where $c_{\mathbf{k}}(t)$ is now given by $c_{\mathbf{k}}(t) = e^{iHt} c_{\mathbf{k}} e^{-iHt}$, while $\langle \dots \rangle_{T,0}$ denotes the thermal average over the states with no electrons and an arbitrary number of phonons

$$\langle x \rangle_{T,0} = \frac{\sum_n \langle n | e^{-H_{\text{ph}}/T} x | n \rangle}{\sum_n \langle n | e^{-H_{\text{ph}}/T} | n \rangle}. \quad (2.15)$$

We see that with these new definitions of Green's (and spectral) function, it is as if there is only a single electron in the system. When using these definitions, we will say that we are working in a canonical ensemble. In the remainder of this thesis, depending on the problem, we will often switch back and forth between the canonical and grand canonical ensemble, but we will always take into account the prescription $A_{\mathbf{k}}(\omega) \rightarrow A_{\mathbf{k}}(\omega - \tilde{\mu})$ that is needed to relate these two.

2.2 Weak Coupling Regime: Migdal Approximation

As we already illustrated in Fig. 1.1, the Holstein model possesses quite a few parameter regimes. In general, finding a universal method that gives reliable results in all of these regimes is a challenging task. This is one of the goals of this thesis. However, the aim of this chapter is to get familiar with some already known results, originally derived by Migdal [55], which will help us to build an intuition and a foundation upon which other approaches will be based on.

Here, we explore the weak coupling limit of the Holstein model. In this case, a perturbative approach is possible. If g is very small, it is sufficient to take into account only the lowest-order Feynman diagram of the self-energy. This is known as the *Migdal approximation* (MA) [55]. In the grand canonical ensemble, the corresponding self-energy can be expressed as

$$\Sigma_{\mathbf{k}}(i\omega_n) = \begin{array}{c} \mathbf{q}, \nu_n \\ \text{wavy line} \\ \mathbf{k}, \omega_n \quad \xrightarrow{\quad} \quad \xrightarrow{\quad} \quad \mathbf{k}, \omega_n \\ \text{wavy line} \\ \mathbf{k} - \mathbf{q} \quad \omega_n - \nu_n \end{array} \quad (2.16)$$

$$= -\frac{g^2}{\beta N} \sum_{\mathbf{q}, \nu_n} \frac{1}{i\omega_n - i\nu_n - \xi_{\mathbf{k}-\mathbf{q}}} \frac{2\omega_0}{(i\nu_n)^2 - \omega_0^2}, \quad (2.17)$$

where $\xi_{\mathbf{k}} = \varepsilon_{\mathbf{k}} - \tilde{\mu}$. The sum over Matsubara frequencies can be performed using the well-known formula:

$$\frac{1}{\beta} \sum_{\nu_n} F(i\nu_n) = \sum_{\text{poles of } F} \text{Res}[-b(z)F(z)] \quad (2.18)$$

where $b(z) = \frac{1}{e^{\beta z} - 1}$ is the Bose function. In our case:

$$F(z) = \frac{1}{i\omega_n - z - \xi_{\mathbf{k}-\mathbf{q}}} \frac{2\omega_0}{z^2 - \omega_0^2} = \frac{-1}{z - i\omega_n + \xi_{\mathbf{k}-\mathbf{q}}} \left[\frac{1}{z - \omega_0} - \frac{1}{z + \omega_0} \right].$$

Thus, Eq. (2.17) simplifies to:

$$\begin{aligned} \Sigma_{\mathbf{k}}(i\omega_n) &= \frac{g^2}{N} \sum_{\mathbf{q}} \left[\frac{-b(\omega_0)}{\omega_0 - i\omega_n + \xi_{\mathbf{k}-\mathbf{q}}} + \frac{b(-\omega_0)}{-\omega_0 - i\omega_n + \xi_{\mathbf{k}-\mathbf{q}}} \right] \\ &\quad - \frac{g^2}{N} \sum_{\mathbf{q}} \left[\frac{b(i\omega_n - \xi_{\mathbf{k}-\mathbf{q}})}{i\omega_n - \xi_{\mathbf{k}-\mathbf{q}} - \omega_0} - \frac{b(i\omega_n - \xi_{\mathbf{k}-\mathbf{q}})}{i\omega_n - \xi_{\mathbf{k}-\mathbf{q}} + \omega_0} \right] \end{aligned}$$

The last expression can be further simplified if we use the following properties

$$b(-\omega_0) = -1 - b(\omega_0), \quad (2.19a)$$

$$b(i\omega_n - \xi_{\mathbf{k}-\mathbf{q}}) = -f(-\xi_{\mathbf{k}-\mathbf{q}}) = -1 + f(\xi_{\mathbf{k}-\mathbf{q}}), \quad (2.19b)$$

where we introduced the Fermi function $f(z) = \frac{1}{e^{\beta z} + 1}$, and take into account that we are working in the limit of vanishing electron concentration $\tilde{\mu} \rightarrow -\infty$, in which case $f(\xi_{\mathbf{k}-\mathbf{q}}) \approx 0$. Hence

$$\Sigma_{\mathbf{k}}(i\omega_n) = \frac{g^2}{N} \sum_{\mathbf{q}} \left[\frac{n_{\text{ph}} + 1}{i\omega_n - \xi_{\mathbf{k}-\mathbf{q}} - \omega_0} + \frac{n_{\text{ph}}}{i\omega_n - \xi_{\mathbf{k}-\mathbf{q}} + \omega_0} \right], \quad (2.20)$$

where we introduced $n_{\text{ph}} = b(\omega_0)$. We note that the right-hand side of the above expression is actually independent of \mathbf{k} . This is because the summation over \mathbf{q} permits us to use a substitution $\mathbf{q} \rightarrow \mathbf{k} - \mathbf{q}$. Furthermore, if we perform the Wick rotation $i\omega_n \rightarrow \omega + i0^+$, and use a prescription from Sec. 2.1.2 to formally switch to the canonical ensemble (i.e., the formalism when there is only a single electron in the system), the self-energy acquires the following form

$$\Sigma(\omega) = \frac{g^2}{N} \sum_{\mathbf{q}} \left[\frac{n_{\text{ph}} + 1}{\omega - \varepsilon_{\mathbf{q}} - \omega_0 + i0^+} + \frac{n_{\text{ph}}}{\omega - \varepsilon_{\mathbf{q}} + \omega_0 + i0^+} \right]. \quad (2.21)$$

By using the density of states $\rho(\varepsilon)$, we can get rid of the summation over the momenta, and rewrite the self-energy in the following form³

$$\Sigma(\omega) = g^2 \int d\varepsilon \left[\frac{n_{\text{ph}} + 1}{\omega - \varepsilon - \omega_0 + i0^+} + \frac{n_{\text{ph}}}{\omega - \varepsilon + \omega_0 + i0^+} \right] \rho(\varepsilon). \quad (2.22)$$

In Part. II of this thesis, we will see that the integrals of this type are quite relevant for a variety of methods. These will be studied in Secs. 1.8.2 and 1.8.3 of Part II. In particular, both of the terms in Eq. (2.22) are a special case of the much more general integral in Eq. (1.98) of Part II. Since Sec. 1.8.2 in Part II can be read independently of the other sections, we will not repeat the derivation of the solution and just use the end result. In the case of a 1D system with only the nearest neighbor hopping, we can use the solution in Eq. (1.108) of Part II, where we should substitute $B = \frac{\omega - \omega_0 + i0^+}{2t_0}$ and $B = \frac{\omega + \omega_0 + i0^+}{2t_0}$ for the first and the second term in Eq. (2.22), respectively.

³We set the volume of the unit cell to 1.

Remark 1. Expressions in Eq. (1.106) of Part II can also be used as a solution of the integral we are examining. However, then we always need to take into account the term $i0^+$. In contrast, Eq. (1.108) in Part II permits the $i0^+$ term to be dropped. This is why the latter form of the solution is much more convenient for numerical implementations.

We note that the solution we obtained for $\Sigma(\omega)$ can also be written in a more compact form

$$\Sigma(\omega) = g^2(n_{\text{ph}} + 1)S(\omega - \omega_0) + g^2n_{\text{ph}}S(\omega + \omega_0), \quad (2.23)$$

where $S(\omega)$ is determined by the following set of relations

$$S(\omega) = (\omega^2 - 4t_0^2)^{-1/2}, \quad \text{for } \omega > 0, \quad (2.24)$$

$$\text{Re}S(-\omega) = -\text{Re}S(\omega), \quad \text{for } \omega > 0, \quad (2.25)$$

$$\text{Im}S(-\omega) = \text{Im}S(\omega), \quad \text{for } \omega > 0. \quad (2.26)$$

Remark 2. The self-energy within the Migdal approximation can also be calculated in the 2D case. However, the analytic solution is not necessarily attainable on a general lattice. The difficulty lies in the calculation of the real part of $\Sigma(\omega)$. In contrast, $\text{Im}\Sigma(\omega)$ can always be expressed in terms of the noninteracting density of states. This is easily seen from Eq. (2.22), since the Plemelj-Sokhotski theorem

$$\frac{1}{x + i0^+} = \mathcal{P}\frac{1}{x} - i\pi\delta(x). \quad (2.27)$$

directly implies that

$$\text{Im}\Sigma(\omega) = -\pi g^2(n_{\text{ph}} + 1)\rho(\omega - \omega_0) - \pi g^2n_{\text{ph}}\rho(\omega + \omega_0). \quad (2.28)$$

2.3 Atomic Limit

The atomic limit corresponds to a regime where the atomic sites are completely decoupled, i.e., $t_0 = 0$. As a result, we can concentrate on just a single site, meaning that the relevant Hamiltonian reads as

$$H = -gc^\dagger c(a^\dagger + a) + \omega_0 a^\dagger a. \quad (2.29)$$

In this case, it is known that this Hamiltonian can be diagonalized by using a unitary, Lang-Fisrov transformation [1, 38]

$$U = e^{\frac{g}{\omega_0}c^\dagger c(a - a^\dagger)} \equiv e^S, \quad \text{where } S \equiv \frac{g}{\omega_0}c^\dagger c(a - a^\dagger). \quad (2.30)$$

To explicitly check this, let us first investigate how does this unitary transformation affect c and a . Using the Baker–Campbell–Hausdorff theorem, we see that

$$e^S c e^{-S} = c + [S, c] + \frac{1}{2!}[S, [S, c]] + \frac{1}{3!}[S, [S, [S, c]]] + \dots \quad (2.31)$$

Each of these terms is calculated straightforwardly

$$\begin{aligned} [S, c] &= \left[\frac{gc^\dagger c(a - a^\dagger)}{\omega_0}, c \right] = -\frac{g}{\omega_0}(a - a^\dagger)\{c^\dagger, c\}c = -\frac{g}{\omega_0}(a - a^\dagger)c \\ [S, [S, c]] &= \left[\frac{gc^\dagger c}{\omega_0}(a - a^\dagger), -\frac{g}{\omega_0}(a - a^\dagger)c \right] = \left(-\frac{g(a - a^\dagger)}{\omega_0} \right)^2 c \\ &\vdots \\ \underbrace{[S, [S, \dots [S, c]]]}_{n \text{ times}} &= \left(-\frac{g(a - a^\dagger)}{\omega_0} \right)^n c. \end{aligned} \quad (2.32)$$

Hence, we obtain

$$e^S c e^{-S} = \exp \left\{ -\frac{g}{\omega_0} (a - a^\dagger) \right\} c. \quad (2.33)$$

For a , the analysis is even simpler

$$\begin{aligned} e^S a e^{-S} &= a + [S, a] + \frac{1}{2!} [S, [S, a]] + \frac{1}{3!} [S, [S, [S, a]]] + \dots \\ [S, a] &= \frac{g c^\dagger c}{\omega_0} [a - a^\dagger, a] = \frac{g c^\dagger c}{\omega_0} \\ [S, [S, a]] &= 0, \end{aligned} \quad (2.34)$$

giving

$$e^S a e^{-S} = a + \frac{g c^\dagger c}{\omega_0}. \quad (2.35)$$

Therefore, the Hamiltonian is transformed as

$$\begin{aligned} e^S H e^{-S} &= -g e^S c^\dagger e^{-S} e^S c e^{-S} (e^S a^\dagger e^{-S} + e^S a e^{-S}) + \omega_0 e^S a^\dagger e^{-S} e^S a e^{-S} \\ &= -g c^\dagger e^{\frac{g}{\omega_0}(a-a^\dagger)} e^{-\frac{g}{\omega_0}(a-a^\dagger)} c \left(a^\dagger + \frac{g c^\dagger c}{\omega_0} + a + \frac{g c^\dagger c}{\omega_0} \right) \\ &\quad + \omega_0 \left(a^\dagger + \frac{g c^\dagger c}{\omega_0} \right) \left(a + \frac{g c^\dagger c}{\omega_0} \right) \\ &= \omega_0 a^\dagger a - \frac{g^2 c^\dagger c}{\omega_0}, \end{aligned} \quad (2.36)$$

where we used the fact that $(c^\dagger c)^2 = c^\dagger c$. As we see, the Hamiltonian has been diagonalized. Its ground-state energy can be directly read-off, and is given by

$$E_p = -\frac{g^2}{\omega_0}. \quad (2.37)$$

One can now proceed with the calculation of the Green's function. This is actually not completely trivial, even though the Hamiltonian has been diagonalized, due to the fact that $e^S c e^{-S}$ and $e^S a e^{-S}$ do not commute with each other. Nevertheless, this calculation is possible to perform completely analytically using the Feynman disentangling of operators [1], and the result reads as

$$G(\omega) = \sum_{n=0}^{\infty} \frac{\alpha^{2n} e^{-\alpha^2}}{n!} \frac{1}{\omega - n\omega_0 - E_p + i0^+}, \quad \text{for } T = 0, \quad (2.38a)$$

$$G(\omega) = \sum_{n=-\infty}^{\infty} \frac{I_n \left(2\alpha^2 \sqrt{n_{\text{ph}}(n_{\text{ph}} + 1)} \right)}{\omega - n\omega_0 - E_p + i0^+} e^{-(2n_{\text{ph}}+1)\alpha^2 + n\frac{\omega_0}{2T}}, \quad \text{for } T \neq 0. \quad (2.38b)$$

Here, $n_{\text{ph}} = (e^{\omega_0/T} - 1)^{-1}$, while I_n are the modified Bessel functions of the first kind. At $T = 0$, we see that the spectrum⁴ consists of the polaron (ground state) delta peak at $\omega = E_p$, which is the lowest energy peak, and a series of delta functions at a distance ω_0 from each other. Additionally, at finite temperatures, more delta peaks emerge even below the polaron peak.

⁴The spectrum $A(\omega) = -\frac{1}{\pi} \text{Im}G(\omega)$ is most easily obtained using Eq. (2.27).

2.4 Spectral Sum Rules

The n th spectral sum rule is defined as follows

$$\mathcal{M}_n(\mathbf{k}) = \int_{-\infty}^{\infty} d\omega A_{\mathbf{k}}(\omega) \omega^n. \quad (2.39)$$

In principle, knowing all the sum rules is equivalent to knowing the exact spectral function. Therefore, an important characteristic of a given method is its ability to correctly reproduce the spectral sum rules. However, as discussed by Ref. [53], it is much more important for a method to satisfy all the sum rules with decent accuracy, than to be able to reproduce only the first few of them exactly. Nevertheless, even the first few sum rules can give an important insight. In Part II of this thesis, we will use these to show that the so-called cumulant expansion method is not exact in the high-temperature limit.

Within the Holstein mode, it turns out that the arbitrary sum rule can be calculated analytically. One of the ways to do this is using the equation of motion technique, which we briefly review following along the line of Ref [57]. To apply this technique, we first notice that Eq. (2.39) can be rewritten as

$$\mathcal{M}_n(\mathbf{k}) = \left(i \frac{d}{dt} \right)^n \int_{-\infty}^{\infty} d\omega e^{-i\omega t} A_{\mathbf{k}}(\omega) \Big|_{t \rightarrow 0}. \quad (2.40)$$

Using Eq. (2.13), we obtain

$$\begin{aligned} \mathcal{M}_n(\mathbf{k}) &= \left(i \frac{d}{dt} \right)^n \frac{1}{\mathcal{Z}} \sum_{n,m} e^{-\beta E_n} \langle n | c_{\mathbf{k}} | m \rangle \langle m | c_{\mathbf{k}}^\dagger | n \rangle e^{-it(E_m - E_n)} \Big|_{t \rightarrow 0} \\ &= \left(i \frac{d}{dt} \right)^n \frac{1}{\mathcal{Z}} \sum_{n,m} e^{-\beta E_n} \langle n | e^{iHt} c_{\mathbf{k}} e^{-iHt} | m \rangle \langle m | c_{\mathbf{k}}^\dagger | n \rangle \Big|_{t \rightarrow 0} = \left(i \frac{d}{dt} \right)^n \langle c_{\mathbf{k}}(t) c_{\mathbf{k}}^\dagger \rangle \Big|_{t \rightarrow 0}. \end{aligned} \quad (2.41)$$

As a consequence of the Heisenberg equation of motion $\frac{dc_{\mathbf{k}}}{dt} = -i[c_{\mathbf{k}}, H]$, the above expression can be cast into a following form

$$\mathcal{M}_n(\mathbf{k}) = \left\langle \underbrace{[\dots [c_{\mathbf{k}}, H], H] \dots, H]}_{n \text{ times}} c_{\mathbf{k}}^\dagger \right\rangle_T. \quad (2.42)$$

Within the Holstein model, this can be evaluated for arbitrary n [57]. Although cumbersome, this calculation is completely straightforward. The end results for $0 \leq n \leq 8$ are listed in Sec. 2.3 of Part II.

Part II

Single particle properties

Dynamical Mean-Field Theory

1.1 Introduction

The DMFT is a simple non-perturbative technique that has emerged as a method of choice for the studies of the Mott physics within the Hubbard model [33, 58]. It was developed in the early 1990's [58] and has since significantly contributed to our understanding of the systems with strong electronic correlations [33]. This method fully takes into account local quantum fluctuations and it becomes exact in the limit of infinite coordination number (i.e., the limit of infinite dimensions $d \rightarrow \infty$), when the correlations become completely local, meaning that the self-energy $\Sigma(\omega)$ becomes \mathbf{k} -independent. It is approximate in the case of finite-dimensional systems, but its predictions are often reliable in 3D, where the coordination number is already quite large, such as $Z = 6$ in the case of a simple cubic lattice, or $Z = 12$ in the case of a face-centered cubic lattice.

It turns out that the DMFT can also be applied to the Holstein model *directly on the real frequency axis* [56], completely avoiding the use of numerically unstable analytical continuation. It was soon recognized [59, 60] that the DMFT gives qualitatively correct spectral functions and conductivity for the 3D Holstein model. Lowering the number of dimensions of the system increases the importance of non-local correlations. Thus, one might expect that the DMFT solution would not be as accurate in lower-dimensional systems, particularly in 1D. However, this was never explicitly checked, and only the DMFT solution for the Bethe lattice was used in comparisons with the numerically exact results for the ground state properties in one dimension [43, 61]. The quantitative agreement was rather poor suggesting that the DMFT cannot provide a realistic description of the low-dimensional Holstein model due to the importance of nonlocal correlations [39, 43, 61]. It turns out that this is actually a misconception. The FTLM results from Ref. [46] showed that the self-energy has only small \mathbf{k} dependence in the 1D Holstein model, for the regime when the electron-phonon coupling strength is comparable to the phonon frequency and the hopping parameter. Guided by this indication, we applied the DMFT in the case of a Holstein model for the finite-dimensional hypercubic lattice [62]. We solved the numerical instabilities that emerged, constructed a highly efficient numerical scheme, gave a comprehensive analysis of this method, and thus explicitly demonstrated that the DMFT can in fact give an accurate description of the single particle properties of the Holstein model in 1D. Having in mind that 1D is the least favorable case for the DMFT since the non-local correlations are the strongest, it is expected that reliable predictions of this method will persist in *any* number of dimensions as well.

In the subsequent sections of this chapter, we present a detailed review of the dynamical mean-field theory, following Refs. [58, 63] and references therein.

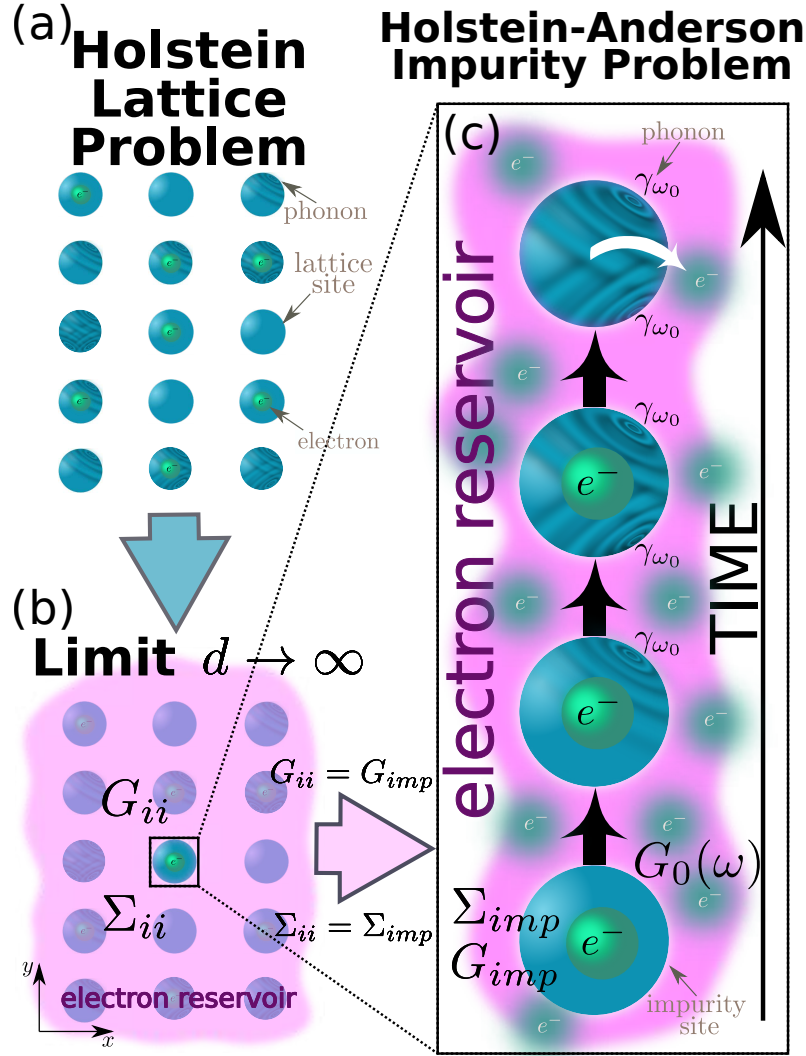


Figure 1.1: (a) Our original Holstein lattice problem. Blue and green balls represent lattice sites and electrons, respectively. Phonons are represented as little waves on blue balls. (b) In the $d \rightarrow \infty$ limit we can focus on just one single site, regarding everything else as an electron reservoir. In this limit the problem is fully characterized using only the local Green's function G_{ii} and local self-energy Σ_{ii} . (c) In the $d \rightarrow \infty$ limit the problem can be fully mapped to the impurity problem. The figure shows one possible scenario of the impurity's time evolution. Since the impurity problem is characterized by the impurity Green's function G_{imp} and impurity self-energy Σ_{imp} , the mapping is realized by equating $G_{ii} = G_{imp}$ and $\Sigma_{ii} = \Sigma_{imp}$.

1.2 Getting to Know DMFT: An Intuitive Approach

Before giving a formal derivation of the DMFT equations in the subsequent sections, let us first try to understand the foundational concepts using a less rigorous approach¹. Since DMFT is, as noted in Sec. 1.1, exact when $d \rightarrow \infty$, this limit will be used to motivate the main ideas behind this method. Let us start with the finite-dimensional Holstein lattice problem on a hypercubic lattice, shown in Fig. 1.1(a). Since all lattice sites are equivalent, let us focus on one arbitrary lattice site, which we call the *impurity*. One could now ask themselves, how does the impurity perceive its surroundings? In 1D, 2D, and 3D cases, it sees a discrete set of sites with a finite number ($2d$) of nearest neighbors. However, if we keep increasing the number of dimensions, the impurity's surroundings starts to acquire

¹This is also a convenient place to introduce the terminology that is standardly used.

a structureless form, which we call the (electron) *reservoir*. Thus, it is intuitively clear² that in the limit $d \rightarrow \infty$, our original Holstein lattice problem is equivalent (i.e., reduces to) an effective single-site problem, called the (Holstein-Anderson) *impurity* problem; see Fig. 1.1(b). This is simpler than the original problem, but much more sophisticated than the regular mean-field theory which reduces the original problem to a single-particle problem. In fact, the dynamics of the impurity problem is quite rich, and is illustrated in Fig. 1.1(c). We see that the electrons can hop back and forth between the impurity and the reservoir, and this dynamics can be described by introducing the so-called *Weiss* field $G_0(\omega)$, playing the role of the dynamical (i.e., frequency-dependent) mean-field. Furthermore, the impurity site can also accompany an arbitrary number of phonons, where the phonon frequency and electron-phonon coupling strength remain the same as in the lattice formulation of the problem, shown in panel 1.1(a).

The electron-phonon interaction on the impurity site is not taken into account by $G_0(\omega)$, which can thus be interpreted as a free propagator. The complete description of the impurity problem, therefore, requires the introduction of another quantity: the full (or interacting) Green's function $G_{\text{imp}}(\omega)$, which (in the time domain) represents the probability amplitude that the electron will stay at the impurity site. The interpretation of $G_0(\omega)$ and $G_{\text{imp}}(\omega)$ as the free and interacting Green's function suggests that we could also define the impurity self-energy using the Dyson equation

$$\Sigma_{\text{imp}}(\omega) = G_0^{-1}(\omega) - G_{\text{imp}}^{-1}(\omega). \quad (1.1)$$

Although this seems unnecessary at this point, this enables us to connect the lattice problem from panel 1.1(a) to the impurity problem from panels 1.1(b) and 1.1(c). To accomplish this, it is natural to require that $\Sigma_{\text{imp}}(\omega)$ and $G_{\text{imp}}(\omega)$ coincide with the corresponding quantities from the original lattice problem $\Sigma_{ii}(\omega)$ and $G_{ii}(\omega)$ respectively. This allows us to make the notation simpler in the following text by dropping the subscripts and simply writing

$$\Sigma_{\text{imp}}(\omega) = \Sigma_{ii}(\omega) = \Sigma(\omega); \quad G_{\text{imp}}(\omega) = G_{ii}(\omega) = G(\omega) \quad (1.2)$$

While all of this will be mathematically justified in the sections to come, it is important to note that none of this would be possible if the electron-phonon interaction was not local, meaning that all creation and annihilation operators of the interaction terms have to correspond to the same lattice site. Otherwise, there would be some more complicated interaction between the impurity site and the rest of the lattice, so we could not describe the full dynamics using only the two quantities which are connected via the Dyson equation: the self-energy Σ_{imp} (describing the interaction on the impurity site) and the Weiss field G_0 (describing the hopping, i.e., hybridization between the impurity and the rest of the system).

We have now successfully rewritten our original lattice problem as an impurity problem. However, two questions arise:

1. The Weiss field $G_0(\omega)$ is still unknown. How can we calculate this quantity?
2. Once $G_0(\omega)$ is known, how can we solve the impurity problem? Stated differently, how is the self-energy $\Sigma(\omega)$ calculated in the impurity problem if $G_0(\omega)$ is given?

²Although we give a rigorous proof of all of these statements in the following sections, this statement becomes much more apparent if we note that the self-energy becomes local $\Sigma_{ij}(\omega) = \Sigma_{ii}(\omega)\delta_{i,j}$ in the limit $d \rightarrow \infty$. This will be proved in Sec. 1.4 using the skeleton expansion of the self-energy and the fact that it features the Green's functions that scale as $G_{j_1 j_2} \propto 1/\sqrt{Z_{j_1 j_2}}$, where $Z_{j_1 j_2}$ represents the number of sites j_2 which are equivalent to site j_1 . This scaling can be seen as a consequence of the fact that $G_{j_1 j_2}$ is interpreted as the probability amplitude for a particle to hop from between sites j_1 and j_2 .

Starting with the second question, it turns out that the impurity problem can actually be solved completely analytically in terms of the continued fraction expansion. These can also be expressed as recursion relations which are much more convenient for numerical implementations. The derivation will be presented in Sec. 1.9, but for now we just list the results:

$$\Sigma(\omega) = G_0^{-1}(\omega) - G^{-1}(\omega), \quad (1.3a)$$

$$G(\omega) = \sum_{n=0}^{\infty} \frac{(1 - e^{-\omega_0/T})e^{-n\omega_0/T}}{G_0^{-1}(\omega) - A_n^{(0)}(\omega) - B_n^{(0)}(\omega)}, \quad (1.3b)$$

$$A_n^{(p)}(\omega) = \frac{(n-p)g^2}{G_0^{-1}(\omega + (p+1)\omega_0) - A_n^{(p+1)}(\omega)}, \quad (1.3c)$$

$$B_n^{(p)}(\omega) = \frac{(n+p+1)g^2}{G_0^{-1}(\omega - (p+1)\omega_0) - B_n^{(p+1)}(\omega)}, \quad (1.3d)$$

$$A_n^{(n)}(\omega) = 0, \quad B_n^{(\infty)}(\omega) = 0. \quad (1.3e)$$

Eq. (1.3) is known as the *impurity solver*: it takes $G_0(\omega)$ as an input, and provides $\Sigma(\omega)$ as an output. To use it, we first need to calculate the quantities $A_n^{(0)}$ and $B_n^{(0)}$, which are determined recursively, starting from (1.3e) and going back to (1.3d) and (1.3c). Then, $G(\omega)$ is calculated using (1.3b), which enables us to use Dyson Eq. (1.3a) to obtain $\Sigma(\omega)$. For $T = 0$ the equations simplify and the self-energy can be written as

$$\Sigma(\omega) = B_0^{(0)}(\omega). \quad (1.4)$$

Rewriting it as a continued fraction, $A_n^{(0)}(\omega)$ represents just a finite fraction that takes into account the emission of phonons, while $B_n^{(0)}(\omega)$ is an infinite continued fraction, which takes into account the absorption of phonons.

Let us now go back to the first question. The Weiss field $G_0(\omega)$, and thus the self-energy $\Sigma(\omega)$ can be determined using the self-consistency loop, as shown in Fig. 1.2. We start by using some initial guess for G_0 , and calculate $\Sigma(\omega)$ using the impurity solver. Then, we calculate the full Green's function $G(\omega)$ using

$$G(\omega) = G_{ii}(\omega) = \frac{1}{N} \sum_{\mathbf{k}} \frac{1}{\omega - \Sigma(\omega) - \varepsilon_{\mathbf{k}}} = \int_{-\infty}^{\infty} \frac{\rho(\varepsilon) d\varepsilon}{\omega - \Sigma(\omega) - \varepsilon}, \quad (1.5)$$

where N is the number of lattice sites, $\varepsilon_{\mathbf{k}}$ is the noninteracting dispersion relation, and $\rho(\varepsilon)$ is the noninteracting density of states. Then, the Weiss field in the next interaction $G_0^{\text{new}}(\omega)$ can be calculated via the Dyson equation. Now, we check whether

$$|G_0^{\text{new}}(\omega) - G_0(\omega)| < \varepsilon_{\text{tol}}, \quad (1.6)$$

where ε_{tol} is a fixed predetermined value of tolerance which is typically somewhere around $\varepsilon_{\text{tol}} \sim 10^{-4}$ or smaller. If Eq. (1.6) is satisfied, the DMFT loop terminates and Σ , G_0 and G are found. Otherwise, G_0^{new} is used in the impurity solver and the procedure is repeated until convergence is reached.

We note that the density of states $\rho(\varepsilon)$ in Eq. (1.5) is the only place where the lattice type comes into play. Hence, even though the DMFT equations were formally derived in the limit $d \rightarrow \infty$, the algorithm in Fig. 1.2 can also be used in finite-dimensional case, with appropriately chosen $\rho(\varepsilon)$. Of course, DMFT should then be regarded as an approximate method.

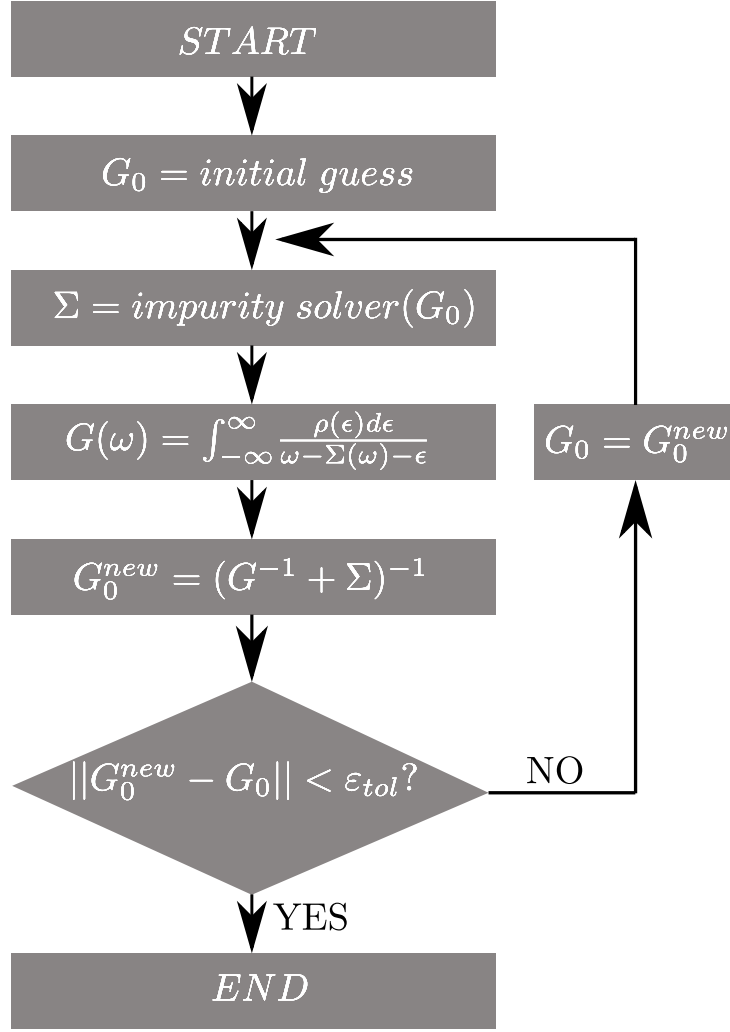


Figure 1.2: Visualization of the DMFT algorithm which connects $G_0(\omega)$, $\Sigma(\omega)$ and $G(\omega)$ self-consistently. The self-energy $\Sigma(\omega)$ takes into account all many-body effects on the impurity site, whereas $G_0(\omega)$ is the "free" impurity propagator which incorporates the effects of all other sites. $G(\omega)$ is the local Green's function.

It should also be mentioned that Eq. (1.5) admits an exact solution in 1D and 2D square lattices with nearest neighbour hopping (see Sec. 1.8):

$$G^{1D}(\omega) = \text{Re} \frac{1}{2t_0 a B(\omega) \sqrt{1 - \frac{1}{B(\omega)^2}}} + i \text{Im} \frac{-i}{2t_0 a \sqrt{1 - B(\omega)^2}}. \quad (1.7)$$

$$G^{2D}(\omega) = \frac{K\left(\frac{2}{B(\omega)}\right)}{B(\omega) \pi t_0}, \quad (1.8)$$

where $K(k) \equiv \int_0^{\pi/2} d\theta / \sqrt{1 - k^2 \sin^2 \theta}$ is the complete elliptic integral of the first kind, while

$$B(\omega) = (\omega - \Sigma(\omega)) / 2t_0. \quad (1.9)$$

In the rest of this chapter, we present a detailed derivation of the DMFT equations. We start by discussing the limit $d \rightarrow \infty$.

1.3 Renormalization of the Physical Quantities in the Limit of Infinite Number of Dimensions $d \rightarrow \infty$

Building upon the heuristic treatment from Secs. 1.1 and 1.2, we now present a more formal analysis of the limit $d \rightarrow \infty$ [58, 63, 64]. To begin with, it is important to note that this limit cannot be performed completely straightforwardly. Otherwise, as we will see, the kinetic energy might become infinitely larger than the potential energy, making this limit trivial. To avoid this, we will show that it is necessary to renormalize the hopping parameter as follows $t_0 \rightarrow t_0/\sqrt{2d}$. This will turn out to have direct consequences on the scaling of the Green's functions (with respect to d), and most importantly on the self-energy which ultimately proves to be momentum-independent in the $d \rightarrow \infty$ limit.

1.3.1 Renormalization of the Hopping Parameter in the Limit $d \rightarrow \infty$

Before starting our analysis it is important to point out that all energy quantities need to be normalized with respect to the number of lattice sites (or volume) and the concentration of charge carriers n_e in order to make them finite. This is not a property of the $d \rightarrow \infty$ limit, and needs to be done in the finite-dimensional case as well. The normalization with respect to the concentration of charge carriers is necessary since we are working in the limit when the chemical potential³ is $\tilde{\mu} \rightarrow -\infty$. In the following text, we will make our phrasing concise by simply using the term (kinetic or potential) energy, assuming that the given quantity is normalized appropriately.

Let us now determine the scaling of potential and kinetic energy with respect to d . Since the electron-phonon interaction is local in the Holstein model, we see that the potential energy scales as $\mathcal{O}(d^0)$. However, the electron kinetic part is different. The corresponding noninteracting kinetic energy can be written as

$$\frac{E_{\text{kin}}}{Nn_e} = \frac{\int_{-\infty}^{\infty} d\omega \omega e^{-\beta\omega} \rho(\omega)}{\int_{-\infty}^{\infty} d\omega e^{-\beta\omega} \rho(\omega)}, \quad (1.10)$$

where $\rho(\omega)$ is the density of states, which in the case of hypercubic lattice in d dimensions can be expressed as follows

$$\begin{aligned} \rho(\omega) &= \frac{1}{N} \sum_{\mathbf{k}} \delta(\omega - \varepsilon_{\mathbf{k}}) = \frac{1}{N} \sum_{\mathbf{k}} \delta\left(\omega + 2t_0 \sum_{j=1}^d \cos k_j\right) \\ &= \int_0^{2\pi} \cdots \int_0^{2\pi} \frac{d^d k}{(2\pi)^d} \delta\left(\omega + 2t_0 \sum_{j=1}^d \cos k_j\right), \end{aligned} \quad (1.11)$$

where we used that the noninteracting dispersion is $\varepsilon_{\mathbf{k}} = -2t_0 \sum_{j=1}^d \cos k_j$. Let us now interpret k_i as a random variable with a probability distribution $p(k_i) = \frac{1}{2\pi}$. Then, $\varepsilon_{\mathbf{k}}$ can be written as a sum

$$\varepsilon_{\mathbf{k}} = \sum_{j=1}^d Y_j, \quad (1.12)$$

where $Y_j = -2t_0 \cos k_j$ are also random variables, while Eq. (1.11) can be is the expectation value

$$\rho(\omega) = \left\langle \delta\left(\omega - \sum_{j=1}^d Y_j\right) \right\rangle, \quad (1.13)$$

³In the case when the chemical potential is finite, the normalization with respect to n_e is unnecessary.

which can be interpreted as the expectation value of the random variable $\varepsilon_{\mathbf{k}} = \sum_{j=1}^d Y_j$. Hence, according to the central limit theorem [65], in the limit $d \rightarrow \infty$, the density of states becomes a Gaussian

$$\rho(\omega) = \frac{1}{\sigma\sqrt{2\pi}} e^{-\frac{\omega^2}{2\sigma^2}}, \quad (1.14)$$

where the variance is determined by

$$\sigma^2 = d \langle Y^2 \rangle = 4dt_0^2 \int_0^{2\pi} \frac{dk}{2\pi} \cos^2 k = 2dt_0^2. \quad (1.15)$$

Plugging all of this back into Eq. (1.10), we see that the kinetic energy, in the limit of infinite number of dimensions, becomes

$$\frac{E_{\text{kin}}}{Nn_e} = \frac{-\beta\sigma^2 e^{\frac{\beta^2\sigma^2}{2}}}{e^{\frac{\beta^2\sigma^2}{2}}} = -\beta\sigma^2. \quad (1.16)$$

We conclude that, in order to make the kinetic energy scale the same way as the potential energy $\mathcal{O}(d^0)$, and in order keep the Gaussian variance finite, we need to renormalize the hopping parameter

$$t_0 \rightarrow \frac{t_0}{\sqrt{2d}}, \quad (1.17)$$

or equivalently to introduce a parameter t^* that is finite by definition and equal to $t^* = 2dt_0^2$.

1.3.2 Renormalization of the Green's Function in the Limit $d \rightarrow \infty$

Let us now inspect what are the consequences of the scaling $t_0 \propto 1/\sqrt{d}$ on the Green's functions $G_{ij}(\omega)$. Before we start, we note that in this section we will consider that the chemical potential is a large, but finite, negative number (instead of $\tilde{\mu} \rightarrow -\infty$). For all our purposes, this is physically equivalent, but makes the analysis somewhat easier since the energy now only needs to be normalized with respect to the number of lattice sites, and not with respect to the charge carrier concentration. We could have also done this in the previous section, in which case we would conclude that E_{kin}/N is finite if we renormalize the hopping parameter such that $t_0 \propto 1/\sqrt{d}$.

1.3.2.1 Renormalization of $G_{ij}(\omega)$ when i and j are Nearest Neighbours

The kinetic energy can be written as

$$E_{\text{kin}} = -t_0 \sum_i \sum_{j \in \delta_i} \langle c_i^\dagger c_j \rangle = it_0 \sum_i \sum_{j \in \delta_i} G_{ij}(t \rightarrow 0^-), \quad (1.18)$$

where δ_i denotes the sites that are nearest neighbours to site i . Since the system is translationally invariant, we conclude that $G_{ij} = G_{|i-j|}$, implying that the sum over i in Eq. (1.18) actually contains N identical terms. Thus, we conclude that

$$\frac{E_{\text{kin}}}{N} = it_0 \sum_{j \in \delta_i} G_{|i-j|}(t \rightarrow 0^-). \quad (1.19)$$

Since the left hand side scales as $\mathcal{O}(d^0)$, t_0 is scaled as $\mathcal{O}(d^{-\frac{1}{2}})$, and the sum $\sum_{j \in \delta_i}$ scales as $\mathcal{O}(d)$, we deduce that

$$G_{ij} \propto \frac{1}{\sqrt{d}}, \quad (1.20)$$

in the case when i and j are nearest neighbours.

1.3.2.2 Renormalization of $G_{ij}(\omega)$ in the Case of Arbitrary i and j

We first note that the scaling of Green's function with respect to d should not depend on the strength of electron-phonon coupling or the temperature. Hence, the scaling of G_{ij} can be determined by inspecting the free propagator at $T = 0$, which can be written as a resolvent [63]

$$G_{ij}(\omega) = \left\langle i \left| \frac{1}{\omega \mathbb{1} - \hat{t}} \right| j \right\rangle, \quad (1.21)$$

where $\mathbb{1}$ is the identity matrix, and \hat{t} is the hopping matrix⁴. The scaling of the Green's function G_{ij} with respect to d is thus solely a consequence of its functional dependence on t_0 . Therefore, one of the ways to proceed is to calculate the leading terms, with respect to t_0 , of the co-factors and determinant of the matrix $\omega \mathbb{1} - \hat{t}$. The ratio of these two quantities represents the leading term of Eq. (1.21). These are most easily calculated using

$$\begin{vmatrix} a_{11} & a_{12} & a_{13} & a_{14} & \dots \\ a_{21} & a_{22} & a_{23} & a_{24} & \dots \\ a_{31} & a_{32} & a_{33} & a_{34} & \dots \\ a_{41} & a_{42} & a_{43} & a_{44} & \dots \\ \vdots & \vdots & \vdots & \vdots & \ddots \end{vmatrix} = \sum_{\sigma} \text{sign}(\sigma) a_{1\sigma(1)} a_{2\sigma(2)} a_{3\sigma(3)} a_{4\sigma(4)} \dots, \quad (1.22)$$

where we sum over all possible permutations σ . Using this, we get

$$G_{ij} \propto d^{-\frac{1}{2} \|\mathbf{R}_i - \mathbf{R}_j\|}, \quad (1.23)$$

where $\|\mathbf{R} - \mathbf{R}'\|$ denotes the so-called Manhattan distance. It is defined by

$$\|\mathbf{R} - \mathbf{R}'\| = \sum_{r=1}^d |\mathbf{R}_r - \mathbf{R}'_r|. \quad (1.24)$$

This result could have been expected since it is in line with our physical intuition: since the hopping part of the Hamiltonian connects only the nearest neighbors, the particle needs $\|\mathbf{R}_i - \mathbf{R}_j\|$ hops in order to get from site i to site j . Due to the fact that the Green's function between nearest neighbors scales as $1/\sqrt{d}$ (see Eq. (1.20)), we could anticipate that $G_{ij} \propto (1/\sqrt{d})^{\|\mathbf{R}_i - \mathbf{R}_j\|}$. However, it is important to note that we cannot set $G_{ij} \rightarrow 0$, even in the strict limit $d \rightarrow \infty$. This is because, although G_{ij} gives infinitely small contribution, there are infinitely many paths that an electron can take. Thus, the overall contribution can be finite.

Our next task is to see what kind of implications does the scaling law of Green's function has on the self-energy.

1.4 Self-energy in the Limit of an Infinite Number of Dimensions

The self-energy can be written as a sum of one-particle irreducible Feynman diagrams, as shown in the first row of Fig. 1.3. Since the Green's functions are scaled as in Eq. (1.23), it is expected that this will have direct consequences on the self-energy: in fact, it turns out that the self-energy is local $\Sigma_{ij}(\omega) = \Sigma_{ii}(\omega) \cdot \delta_{i,j}$. In other words, the self-energy is momentum independent in the Fourier space $\Sigma_{\mathbf{k}}(\omega) = \Sigma(\omega)$. This was originally proved by Metzner and D. Vollhardt. Here, we review the proof of that statement.

In the first row of Fig. 1.3, the self-energy is written as a functional of the free propagator $\Sigma[G_0]$. It is also possible to express it as functional of the interacting propagator $\Sigma[G]$, by replacing the solid

⁴Hopping matrix looks the same as the Hamiltonian matrix if we set $g \rightarrow 0$ and $\omega_0 \rightarrow 0$.

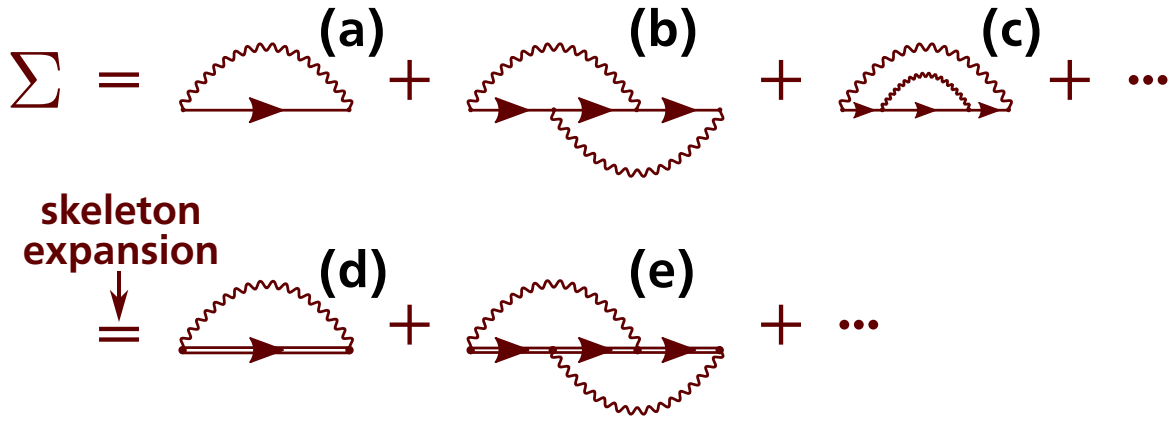


Figure 1.3: Feynman diagrams for the self-energy.

lines (noninteracting propagators) with double solid lines (interacting propagators), and omitting the diagrams that have the self-energy insertions (for example, see Fig. 1.4(a)) in order to avoid double counting of the diagrams. As a result, we get the so-called *skeleton expansion*, which is shown in the second row of Fig. 1.3. In Fig. 1.4 we show some diagrams that are omitted in the skeleton

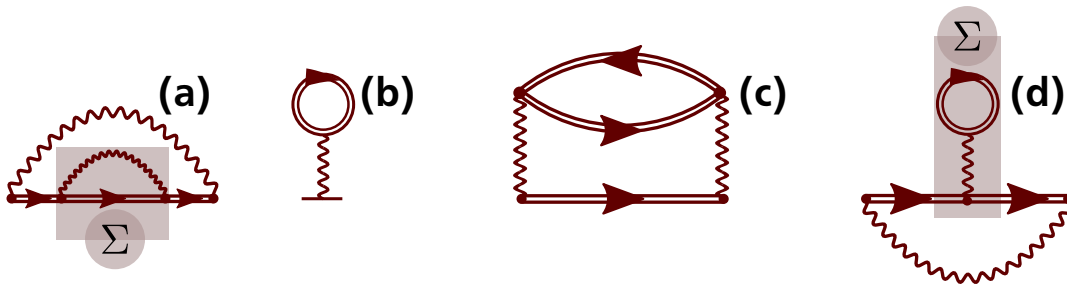


Figure 1.4: Examples of diagrams that are not included in the skeleton expansion of the self-energy. Panel (a) is not included as the fermion line has self-energy insertion. Panels (b) and (c) do not contribute in the limit of vanishing electron concentration, which is the case we are considering. Otherwise, these diagrams would be included. The diagram in panel (d) is not contributing in the limit of vanishing electron concentration, and in addition, it also has a self-energy insertion.

expansion, either due to the self-energy insertions or due to the fact that they do not contribute in the limit of vanishing electron concentration. We note that the derivation that we present (about the k -independence of the self-energy) will also work in the case when the electron concentration is finite, i.e., in the case when the diagrams in Figs. 1.4(b)–1.4(c) would be included.

To proceed, we first prove that every two vertices of the self-energy skeleton diagrams have to be connected by at least three distinct paths. We will prove this by contradiction. Suppose that there exist two vertices i and j (see panel 1.5(a)), in the skeleton expansion of the self-energy, that are connected by two or less distinct paths. We immediately see that a path between these necessarily has to exist, in order for the diagram to be connected; see Fig. 1.5(b). In fact, there also needs to be a second path between i and j . Otherwise, the diagram would not be one-particle irreducible. All three possibilities in which two paths can connect i and j are shown in Figs. 1.5(c₁)–1.5(c₃). Now, we need to establish what happens to the rest of the fermion lines that are not connected to anything. From the form of the bare electron-phonon vertex, we see that each fermion line is connected to either a vertex or to an ingoing/outgoing line. Thus, two fermion lines from Figs. 1.5(c₁)–1.5(c₃) have to be connected to an ingoing/outgoing line (there is only one ingoing and one outgoing line), while other two are somehow connected. As we supposed that there is no third path that connects i and j , Figs. 1.5(d₁)–1.5(d₄)

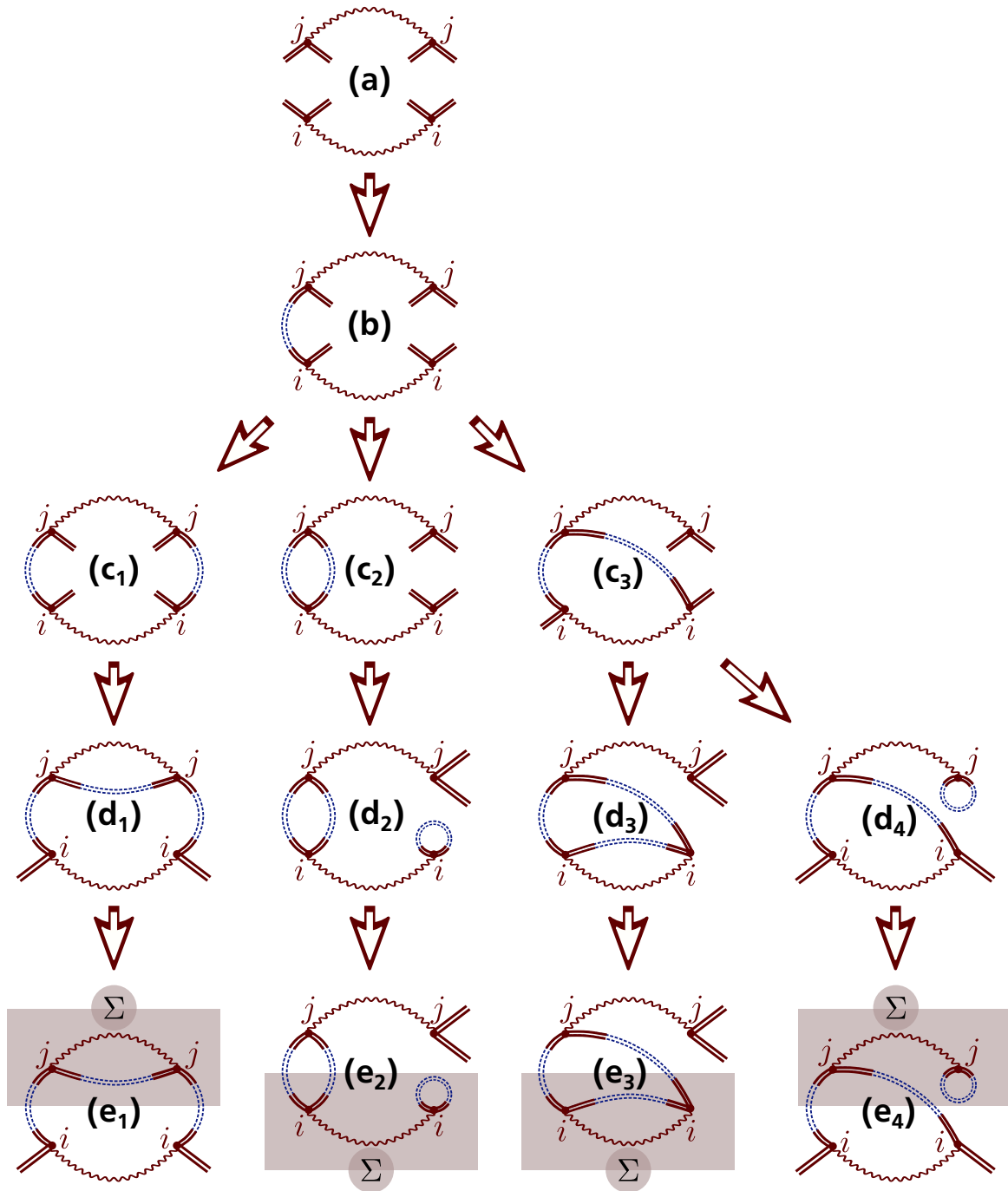


Figure 1.5: Visual proof that every two vertices (here denoted by i and j) have to be connected by at least three distinct paths (the blue dotted line denotes one distinct path, which does not have to go directly from i to j , and may traverse intermediate vertices in between.).

illustrate all forms that a diagram might assume. However, each of these diagrams has a self-energy insertion see Figs. 1.5(e₁)-1.5(e₄). Hence, these are not skeleton diagrams, which is a contradiction. We conclude that the assumption must have been false, which means that there are at least three distinct paths between each two vertices of the self-energy skeleton diagrams.

Let us now choose arbitrary vertex i , and keep it fixed. Then, for every other internal vertex j , we need to take into account at least three distinct paths between i and j , and the summation over j . The sites j , and thus the summation over j , can be divided into classes, such that each class consists of mutually equivalent sites. In each of these classes, $\|\mathbf{R}_i - \mathbf{R}_j\|$ is constant. Thus, the contribution of propagators, going from i to j is of the order of $\mathcal{O}(d^{-\frac{3}{2}}\|\mathbf{R}_i - \mathbf{R}_j\|)$, or less if we pass through some

additional sites between i and j (see Eq. (1.23)). Furthermore, the contribution of the sum over the class we are considering can be at most of the order of $\mathcal{O}(d^{\|\mathbf{R}_i - \mathbf{R}_j\|})$. The overall contribution for $i \neq j$ is thus of the order of $\mathcal{O}(d^{-\frac{1}{2}\|\mathbf{R}_i - \mathbf{R}_j\|})$, or less, while it is of the order of $\mathcal{O}(d^0)$ for $i = j$. From here, we can deduce that all propagators in the skeleton expansion of the self-energy are local propagators $G_{ii}(\omega)$. As a consequence, we do not have to worry about the conservation of momentum at the vertices. Furthermore, we can also see that the self-energy is diagonal in coordinate representation $\Sigma_{ij}(\omega) = \Sigma_{ii}(\omega)\delta_{i,j}$, i.e., momentum independent in Fourier space $\Sigma_{\mathbf{k}}(\omega) = \Sigma(\omega)$. This can be further confirmed from the definition of Fourier transform, using the translational invariance $\Sigma_{i,j}(\omega) = \Sigma_{i-j}(\omega)$

$$\Sigma_{\mathbf{k}}(\omega) = \sum_j e^{i\mathbf{k}\mathbf{R}_j} \Sigma_j(\omega). \quad (1.25)$$

As before, we can break the sum into the sum over different classes, and a sum within each class. Then, $\Sigma_j(\omega)$ scales as $\mathcal{O}(d^{-\frac{3}{2}\|\mathbf{R}_j\|})$, as there are at least three paths between site 0 and j . Furthermore, the sum over the elements of one class scales as $\mathcal{O}(d^{\|\mathbf{R}_j\|})$. Hence, only the term $j = 0$ gives a nonvanishing contribution in the limit $d \rightarrow \infty$, proving that the self-energy is indeed local.

Our next step is to prove that the Holstein lattice model can be mapped onto the impurity problem, in the limit $d \rightarrow \infty$. Before we do that, let us first reduce the number of degrees of freedom by integrating out the phonons. This way, the rest of the derivation will be completely analogous to the derivation in the Hubbard model.

1.5 Integrating out the Phononic Degrees of Freedom

The Hamiltonian in Eq. (1.2) defines the Holstein model. Equivalently, we can also switch to the functional formalism, where the partition function can be written as a path integral over the electronic and phononic degrees of freedom of e^{-S} , where S is the action of our theory. As we will see, the integral over the phononic degrees of freedom can be performed exactly as a consequence of the fact that the Hamiltonian (1.2) is linear with respect to a^\dagger and a . As a result, we get an effective action, where only the electronic degrees of freedom are left. Now the resulting electron-electron interaction is much more complicated: although still local, it is now time (i.e., frequency) dependent. These retardation effects are a compensation for the phonons⁵. Nevertheless, we will see that we can still perform an exact mapping to the impurity problem in the limit $d \rightarrow \infty$. This is a consequence of the fact that DMFT can capture temporal correlations exactly, while spatial correlations are neglected.

Let us now be more mathematically formal. Let ϕ be phononic field, and ψ Grassmann electron field. Then, the partition function can be written as follows [66, 67]

$$\mathcal{Z} = \int D[\bar{\psi}, \psi] \int D[\bar{\phi}, \phi] \exp \{ -S_{\text{el}}[\bar{\psi}, \psi] - S_{\text{ph}}[\bar{\phi}, \phi] - S_{\text{el-ph}}[\bar{\phi}, \phi, \bar{\psi}, \psi] \}, \quad (1.26)$$

where

$$S_{\text{el}}[\bar{\psi}, \psi] = \int_0^\beta d\tau \left[\sum_j \bar{\psi}_j(\tau) \left(\frac{\partial}{\partial \tau} - \tilde{\mu} \right) \psi_j(\tau) + H_{\text{el}}(\bar{\psi}, \psi) \right], \quad (1.27a)$$

$$S_{\text{ph}}[\bar{\phi}, \phi] = \int_0^\beta d\tau \left[\sum_j \bar{\phi}_j(\tau) \frac{\partial}{\partial \tau} \phi_j(\tau) + H_{\text{ph}}(\bar{\phi}, \phi) \right], \quad (1.27b)$$

$$S_{\text{el-ph}}[\bar{\phi}, \phi, \bar{\psi}, \psi] = \int_0^\beta d\tau H_{\text{el-ph}}[\bar{\phi}, \phi, \bar{\psi}, \psi]. \quad (1.27c)$$

⁵The analogous situation happens in a more familiar example of electrodynamics.

$H_{\text{el}}(\bar{\psi}, \psi)$, $H_{\text{ph}}(\bar{\phi}, \phi)$, and $H_{\text{el-ph}}[\bar{\phi}, \phi, \bar{\psi}, \psi]$ are given by⁶ Eq. (1.2), after we perform the substitution $c \rightarrow \psi(\tau)$, $c^\dagger \rightarrow \bar{\psi}(\tau)$, $a \rightarrow \phi(\tau)$, and $a^\dagger \rightarrow \bar{\phi}(\tau)$, which works both in the coordinate and Fourier space. Let us write these out explicitly:

$$H_{\text{el}} = -t_0 \sum_{\langle ij \rangle} (\bar{\psi}_i(\tau) \psi_j(\tau) + \bar{\psi}_j(\tau) \psi_i(\tau)) = \sum_{\mathbf{k}} \varepsilon_{\mathbf{k}} \bar{\psi}_{\mathbf{k}}(\tau) \psi_{\mathbf{k}}(\tau), \quad (1.28a)$$

$$H_{\text{ph}} = \omega_0 \sum_i \bar{\phi}_i(\tau) \phi_i(\tau) = \omega_0 \sum_{\mathbf{k}} \bar{\phi}_{\mathbf{k}}(\tau) \phi_{\mathbf{k}}(\tau), \quad (1.28b)$$

$$\begin{aligned} H_{\text{el-ph}} &= -g \sum_i \bar{\psi}_i(\tau) \psi_i(\tau) (\bar{\phi}_i(\tau) + \phi_i(\tau)) \\ &= -\frac{g}{\sqrt{N}} \sum_{\mathbf{k}, \mathbf{q}} \bar{\psi}_{\mathbf{k}+\mathbf{q}}(\tau) \psi_{\mathbf{k}}(\tau) (\bar{\phi}_{-\mathbf{q}}(\tau) + \phi_{\mathbf{q}}(\tau)) \\ &= -\frac{g}{\sqrt{N}} \sum_{\mathbf{q}} n_{-\mathbf{q}}(\tau) (\bar{\phi}_{-\mathbf{q}}(\tau) + \phi_{\mathbf{q}}(\tau)), \end{aligned} \quad (1.28c)$$

where $n_{\mathbf{q}} = \sum_{\mathbf{k}} \bar{\psi}_{\mathbf{k}} \psi_{\mathbf{k}+\mathbf{q}}$ is the Fourier transform of $n_i = \bar{\psi}_i \psi_i$. Let us now rewrite Eq. (1.26) as

$$\mathcal{Z} = \int D[\bar{\psi}, \psi] e^{-S_{\text{el}}[\bar{\psi}, \psi]} \underbrace{\int D[\bar{\phi}, \phi] \exp \{ -S_{\text{ph}}[\bar{\phi}, \phi] - S_{\text{el-ph}}[\bar{\phi}, \phi, \bar{\psi}, \psi] \}}_{\mathcal{Z}_1}. \quad (1.29)$$

If we integrate over $\bar{\phi}$ and ϕ , we can introduce S_1 such that $\mathcal{Z}_1 = \text{const} \cdot e^{-S_1[\bar{\psi}, \psi]}$, and the whole partition function can be written as

$$\mathcal{Z} = \text{const} \cdot \int D[\bar{\psi}, \psi] e^{-S_{\text{el}}[\bar{\psi}, \psi]} e^{-S_1[\bar{\psi}, \psi]} \equiv \text{const} \cdot \int D[\bar{\psi}, \psi] e^{-S_{\text{eff}}[\bar{\psi}, \psi]}. \quad (1.30)$$

Here, we introduced the so-called effective action $e^{-S_{\text{eff}}[\bar{\psi}, \psi]}$, where the phononic degrees of freedom have been integrated out. Calculating this quantity is the main task of this section.

To do so, we first perform the Fourier transform of the field operators from the imaginary time τ to the Matsubara frequency space, in order to get rid of the derivative with respect to τ in Eq. (1.27)

$$\phi_{\mathbf{q},n} = \frac{1}{\sqrt{\beta}} \int_0^\beta d\tau \phi_{\mathbf{q}}(\tau) e^{i\nu_n \tau}, \quad \phi_{\mathbf{q}}(\tau) = \frac{1}{\sqrt{\beta}} \sum_n \phi_{\mathbf{q},n} e^{-i\nu_n \tau}, \quad (1.31a)$$

$$\psi_{\mathbf{q},n} = \frac{1}{\sqrt{\beta}} \int_0^\beta d\tau \psi_{\mathbf{q}}(\tau) e^{i\omega_n \tau}, \quad \psi_{\mathbf{q}}(\tau) = \frac{1}{\sqrt{\beta}} \sum_n \psi_{\mathbf{q},n} e^{-i\omega_n \tau}, \quad (1.31b)$$

where $\nu_n = 2n\pi T$ and $\omega_n = (2n+1)\pi T$ are the bosonic and fermionic Matsubara frequencies respectively. Since $n_{-\mathbf{q}}$ consists of two fermionic operators, it is a bosonic operator. Hence:

$$n_{-\mathbf{q}}(\tau) = \frac{1}{\sqrt{\beta}} \sum_n n_{-\mathbf{q},n} e^{-i\nu_n \tau}, \quad (1.32a)$$

$$n_{-\mathbf{q},n} = \frac{1}{\sqrt{\beta}} \int_0^\beta d\tau n_{-\mathbf{q}}(\tau) e^{i\nu_n \tau} = \frac{1}{\sqrt{\beta}} \int_0^\beta d\tau \sum_{\mathbf{k}} \bar{\psi}_{\mathbf{k}+\mathbf{q}}(\tau) \psi_{\mathbf{k}}(\tau) e^{i\nu_n \tau}. \quad (1.32b)$$

⁶We note that Eq. (1.2) is written in the 1D case, while now we need to work in the d dimensional case. This is only reflected in H_{el} , which in this case reads as $H_{\text{el}} = -t_0 \sum_{\langle ij \rangle} (c_i^\dagger c_j + \text{H.c.}) = -\sum_{ij} t_{ij} c_i^\dagger c_j$, where $t_{ij} = t_0$ if i and j are nearest neighbours, while otherwise being $t_{ij} = 0$.

Now, plugging Eqs. (1.32), (1.31) into Eq. (1.28), and all of this into Eq. (1.27), we see that \mathcal{Z}_1 from Eq. (1.30) can be straightforwardly calculated as follows

$$\mathcal{Z}_1 = \int D[\bar{\phi}, \phi] \exp \left\{ - \sum_{\mathbf{q}, n} \bar{\phi}_{\mathbf{q}, n} (\omega_0 - i\nu_n) \phi_{\mathbf{q}, n} + \frac{g}{\sqrt{N}} \sum_{\mathbf{q}, n} n_{-\mathbf{q}, n} (\phi_{\mathbf{q}, -n} + \bar{\phi}_{-\mathbf{q}, n}) \right\}. \quad (1.33)$$

The factor g/\sqrt{N} multiplies two terms: let us make the substitution $n \rightarrow -n$ in the first of those terms and a substitution $\mathbf{q} \rightarrow -\mathbf{q}$ in the second of those terms

$$\mathcal{Z}_1 = \int D[\bar{\phi}, \phi] \exp \left\{ - \sum_{\mathbf{q}, n} \bar{\phi}_{\mathbf{q}, n} (\omega_0 - i\nu_n) \phi_{\mathbf{q}, n} + \frac{g}{\sqrt{N}} \sum_{\mathbf{q}, n} (n_{-\mathbf{q}, -n} \phi_{\mathbf{q}, n} + n_{\mathbf{q}, n} \bar{\phi}_{\mathbf{q}, n}) \right\}. \quad (1.34)$$

This is now a standard Gaussian integral that is calculated as follows

$$\int D[\bar{v}, v] e^{-\bar{v}Av + \bar{w}v + \bar{v}w'} = \frac{1}{\det A} e^{\bar{w}A^{-1}w'}. \quad (1.35)$$

Thus \mathcal{Z}_1 reduces to

$$\begin{aligned} \mathcal{Z}_1 &= \prod_{\mathbf{q}, n} \frac{1}{\omega_0 - i\nu_n} \exp \left\{ \frac{g^2}{N} \sum_{\mathbf{q}, n} \frac{n_{-\mathbf{q}, -n} n_{\mathbf{q}, n}}{\omega_0 - i\nu_n} \right\} \\ &= \prod_{\mathbf{q}, n} \frac{1}{\omega_0 - i\nu_n} \exp \left\{ \frac{g^2}{N} \sum_{\mathbf{q}, n} \frac{\omega_0}{\omega_0^2 + \nu_n^2} n_{-\mathbf{q}, -n} n_{\mathbf{q}, n} \right\}, \end{aligned} \quad (1.36)$$

where the last equality is obtained using the fact that $\sum_{\mathbf{q}, n} \frac{i\nu_n}{\omega_0^2 + \nu_n^2} n_{-\mathbf{q}, -n} n_{\mathbf{q}, n}$ is vanishing. This is seen as a consequence of the fact that the expression under the summation is an odd function of n . Hence, we finally obtain an expression for S_{eff} from Eq. (1.30)

$$\begin{aligned} S_{\text{eff}}[\bar{\psi}, \psi] &= S_{\text{el}}[\bar{\psi}, \psi] + S_1[\bar{\psi}, \psi] = S_{\text{el}}[\bar{\psi}, \psi] - \ln \mathcal{Z}_1 \\ &= S_{\text{el}}[\bar{\psi}, \psi] - \frac{g^2}{N} \sum_{\mathbf{q}, n} \frac{\omega_0}{\omega_0^2 + \nu_n^2} n_{-\mathbf{q}, -n} n_{\mathbf{q}, n} + \sum_{\mathbf{q}, n} \ln (\omega_0 - i\nu_n). \end{aligned} \quad (1.37)$$

The first and the last term represent the free electron and the free phonon action respectively, while the middle term represents the effective electron-electron interaction. Since we are interested in the electron Green's function, the free phonon action is unimportant, and will hence be dropped in the further analysis.

Let us now concentrate on the effective electron-electron interaction

$$S_{\text{eff}}^{\text{el-el}}[\bar{\psi}, \psi] = -\frac{g^2}{N} \sum_{\mathbf{q}, n} \frac{\omega_0}{\omega_0^2 + \nu_n^2} n_{-\mathbf{q}, -n} n_{\mathbf{q}, n}. \quad (1.38)$$

If we go back to the τ domain, we can explicitly see the retarded nature of effective electron-electron interaction

$$\begin{aligned} S_{\text{eff}}^{\text{el-el}}[\bar{\psi}, \psi] &= -\frac{g^2}{N} \sum_{\mathbf{q}} \frac{\omega_0}{\omega_0^2 + \nu_n^2} \frac{1}{\sqrt{\beta}} \int_0^\beta d\tau_1 \sum_{\mathbf{k}_1} \bar{\psi}_{\mathbf{k}_1 - \mathbf{q}}(\tau_1) \psi_{\mathbf{k}_1}(\tau_1) e^{i\nu_n \tau_1} \\ &\quad \times \frac{1}{\sqrt{\beta}} \int_0^\beta d\tau_2 \sum_{\mathbf{k}_2} \bar{\psi}_{\mathbf{k}_2 + \mathbf{q}}(\tau_2) \psi_{\mathbf{k}_2}(\tau_2) e^{-i\nu_n \tau_2}. \end{aligned} \quad (1.39)$$

If we now recall that the phonon propagator reads as

$$\begin{aligned} D_{\mathbf{q}}(\tau - \tau') &\equiv - \left\langle \hat{T}_{\tau} \left(a_{\mathbf{q}}(\tau) + a_{-\mathbf{q}}^{\dagger}(\tau) \right) \left(a_{\mathbf{q}}(\tau') + a_{-\mathbf{q}}^{\dagger}(\tau') \right) \right\rangle \\ &= \frac{1}{\beta} \sum_n \frac{2\omega_0}{(i\nu_n)^2 - \omega_0^2} e^{-i\nu_n(\tau - \tau')} \equiv D(\tau - \tau'), \end{aligned} \quad (1.40)$$

then Eq. (1.39) can be straightforwardly transformed to

$$S_{\text{eff}}^{\text{el-el}}[\bar{\psi}, \psi] = \frac{g^2}{2N} \int_0^{\beta} d\tau_2 \int_0^{\beta} d\tau_1 \sum_{\mathbf{q}, \mathbf{k}_1, \mathbf{k}_2} D(\tau_2 - \tau_1) \bar{\psi}_{\mathbf{k}_2 + \mathbf{q}}(\tau_2) \bar{\psi}_{\mathbf{k}_1 - \mathbf{q}}(\tau_1) \psi_{\mathbf{k}_1}(\tau_1) \psi_{\mathbf{k}_2}(\tau_2). \quad (1.41)$$

If we now also go back from the momentum to coordinate space, the whole S_{eff} can be written as⁷

$$\begin{aligned} S_{\text{eff}}[\bar{\psi}, \psi] &= \int_0^{\beta} d\tau \left\{ \sum_j \bar{\psi}_j(\tau) \left(\frac{\partial}{\partial \tau} - \tilde{\mu} \right) \psi_j(\tau) - t_0 \sum_{\langle ij \rangle} (\bar{\psi}_i(\tau) \psi_j(\tau) + \bar{\psi}_j(\tau) \psi_i(\tau)) \right. \\ &\quad \left. + \frac{g^2}{2} \int_0^{\beta} d\tau' D(\tau - \tau') \sum_j \bar{\psi}_j(\tau) \bar{\psi}_j(\tau') \psi_j(\tau') \psi_j(\tau) \right\} \end{aligned} \quad (1.42)$$

In order to see how this effective action is connected to the impurity problem, we use the so-called cavity method.

1.6 Cavity Method

1.6.1 Overview

In this section, we start analyzing how is our original lattice problem connected to the impurity problem, and how the exact mapping can be performed in the limit $d \rightarrow \infty$. To do this, we start from the effective action in Eq. (1.42) (see Fig. 1.6(a)) and separate the contribution from one arbitrary site (see Fig. 1.6(c)), its connection to the other sites (see Fig. 1.6(d)), and the rest of the lattice (see Fig. 1.6(b)). The site we selected plays the role of the impurity site, and everything else will be integrated over, in the functional formalism. Later, we will show that the resulting action coincides with the action of the impurity problem in the limit $d \rightarrow \infty$. This approach is known as the *cavity method*. Let us now present a more formal, mathematical derivation.

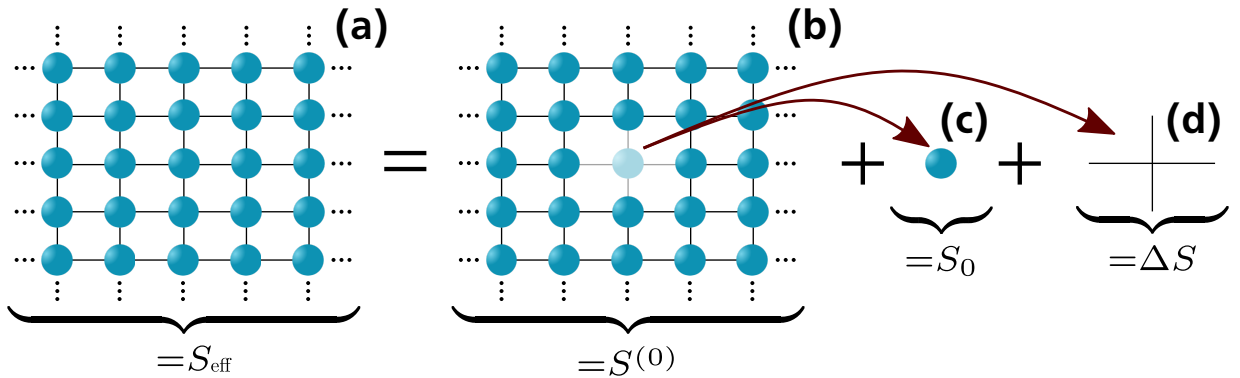


Figure 1.6: Illustration of the cavity method.

⁷As we discussed, the free phonon part will be dropped.

1.6.2 Cavity Construction

As we explained above, the effective action S_{eff} can be rewritten as follows

$$S_{\text{eff}} = S^{(0)} + S_0 + \Delta S, \quad (1.43)$$

where

$$S^{(0)} = \int_0^\beta d\tau \left\{ \sum_{i \neq 0} \bar{\psi}_i(\tau) \left(\frac{\partial}{\partial \tau} - \tilde{\mu} \right) \psi_i(\tau) - \sum_{i,j \neq 0} t_{ij} \bar{\psi}_i(\tau) \psi_j(\tau) \right. \\ \left. + \frac{g^2}{2} \int_0^\beta d\tau' D(\tau - \tau') \sum_{i \neq 0} \bar{\psi}_i(\tau) \bar{\psi}_i(\tau') \psi_i(\tau') \psi_i(\tau) \right\} \quad (1.44a)$$

$$S_0 = \int_0^\beta d\tau \left\{ \bar{\psi}_0(\tau) \left(\frac{\partial}{\partial \tau} - \tilde{\mu} \right) \psi_0(\tau) + \frac{g^2}{2} \int_0^\beta d\tau' D(\tau - \tau') \bar{\psi}_0(\tau) \bar{\psi}_0(\tau') \psi_0(\tau') \psi_0(\tau) \right\} \quad (1.44b)$$

$$\Delta S = - \int_0^\beta d\tau \underbrace{\sum_i [t_{i0} \bar{\psi}_i(\tau) \psi_0(\tau) + t_{0i} \bar{\psi}_0(\tau) \psi_i(\tau)]}_{\equiv -\Delta S(\tau)} = \int_0^\beta d\tau \Delta S(\tau). \quad (1.44c)$$

In order to make the notation somewhat simpler, we introduced $\Delta S(\tau)$ and also t_{ij} , that is nonzero only when i and j are nearest neighbors, in which case it is equal to t_0 . Now, we want to integrate over all ψ_i and $\bar{\psi}_i$ for $i \neq 0$ in Eq. (1.30). It is thus natural to rewrite the partition function as follows

$$\mathcal{Z} = \int D[\bar{\psi}_0, \psi_0] e^{-S_0} \int \prod_{i \neq 0} D[\bar{\psi}_i, \psi_i] e^{-S^{(0)} - \Delta S}. \quad (1.45)$$

While this cannot be calculated analytically in general, it is possible to express it in terms of the Green's functions. This can be done as follows

$$\int \prod_{i \neq 0} D[\bar{\psi}_i, \psi_i] e^{-S^{(0)} - \Delta S} = \int \prod_{i \neq 0} D[\bar{\psi}_i, \psi_i] e^{-S^{(0)}} \exp \left\{ - \int_0^\beta d\tau \Delta S(\tau) \right\} \\ = \int \prod_{i \neq 0} D[\bar{\psi}_i, \psi_i] e^{-S^{(0)}} \\ \times \exp \left\{ \int_0^\beta d\tau \sum_j [t_{j0} \bar{\psi}_j(\tau) \psi_0(\tau) + t_{0j} \bar{\psi}_0(\tau) \psi_j(\tau)] \right\}. \quad (1.46)$$

Using the fact that $t_{j0} = t_{0j}$, and introducing $\eta_j \equiv t_{j0} \psi_0$, the previous expression becomes

$$\int \prod_{i \neq 0} D[\bar{\psi}_i, \psi_i] e^{-S^{(0)} - \Delta S} = \int \prod_{i \neq 0} D[\bar{\psi}_i, \psi_i] e^{-S^{(0)}} \\ \times \exp \left\{ \int_0^\beta d\tau \sum_j [\bar{\eta}_j(\tau) \psi_j(\tau) + \bar{\psi}_j(\tau) \eta_j(\tau)] \right\}. \quad (1.47)$$

We derived that the right-hand side of Eq. (1.47) is actually a generating functional [67, 68] of a lattice with a cavity, where η_j and $\bar{\eta}_j$ represent the source terms. It is thus possible to immediately express $\int \prod_{i \neq 0} D[\bar{\psi}_i, \psi_i] e^{-S^{(0)} - \Delta S}$ in terms of the Green's functions. However, we will employ a more pedestrian approach.

1.6.3 Expressing the Generating Functional in Terms of the Green's Functions

In general, if S is the action of the theory⁸, then the Green's functions are defined as

$$\begin{aligned}
& (-1)^n G^{(n)}(\alpha_1 \tau_1 \dots \alpha_n \tau_n | \alpha_{2n} \tau_{2n} \dots \alpha_{n+1} \tau_{n+1}) \\
&= \frac{1}{\mathcal{Z}} \int \prod_i D[\bar{\psi}_{\alpha_i}, \psi_{\alpha_i}] e^{-S[\bar{\psi}_{\alpha_i}, \psi_{\alpha_i}]} \psi_{\alpha_1}(\tau_1) \dots \psi_{\alpha_n}(\tau_n) \bar{\psi}_{\alpha_{n+1}}(\tau_{n+1}) \dots \bar{\psi}_{\alpha_{2n}}(\tau_{2n}) \\
&= \frac{1}{\mathcal{Z}} \text{Tr} \left[e^{-\beta(H - \tilde{\mu}\hat{N})} \hat{T}_\tau c_{\alpha_1}(\tau_1) \dots c_{\alpha_n}(\tau_n) c_{\alpha_{n+1}}^\dagger(\tau_{n+1}) \dots c_{\alpha_{2n}}^\dagger(\tau_{2n}) \right] \\
&= \left\langle \hat{T}_\tau c_{\alpha_1}(\tau_1) \dots c_{\alpha_n}(\tau_n) c_{\alpha_{n+1}}^\dagger(\tau_{n+1}) \dots c_{\alpha_{2n}}^\dagger(\tau_{2n}) \right\rangle. \tag{1.48}
\end{aligned}$$

In the last two lines, we listed the corresponding expressions in the operator formalism. These can be used to easily switch between the functional and operator formalisms.

Going back to Eq. (1.47), we can expand the second line in the Taylor series

$$\begin{aligned}
& \int \prod_{i \neq 0} D[\bar{\psi}_i, \psi_i] e^{-S^{(0)} - \Delta S} \\
&= \int \prod_{i \neq 0} D[\bar{\psi}_i, \psi_i] e^{-S^{(0)}} \sum_{n=0}^{\infty} \frac{1}{n!} \left[\sum_j \int_0^\beta d\tau (\bar{\eta}_j(\tau) \psi_j(\tau) + \bar{\psi}_j(\tau) \eta_j(\tau)) \right]^n. \tag{1.49}
\end{aligned}$$

If we switched back to the operator formalism, there would be averaging over the field operators for $i \neq 0$, but not for $i = 0$, due to the factor $\int \prod_{i \neq 0} D[\bar{\psi}_i, \psi_i] e^{-S^{(0)}}$. Hence, terms with odd n in Eq. (1.49) are necessarily vanishing, as they have odd number of creation/annihilation operators that are averaged over. Thus

$$\begin{aligned}
& \int \prod_{i \neq 0} D[\bar{\psi}_i, \psi_i] e^{-S^{(0)} - \Delta S} \\
&= \int \prod_{i \neq 0} D[\bar{\psi}_i, \psi_i] e^{-S^{(0)}} \sum_{n=0}^{\infty} \sum_{j_1 \dots j_{2n}} \int_0^\beta d\tau_{j_1} \dots \int_0^\beta d\tau_{j_{2n}} \frac{1}{(2n)!} \\
&\times [\bar{\eta}_{j_1}(\tau_{j_1}) \psi_{j_1}(\tau_{j_1}) + \bar{\psi}_{j_1}(\tau_{j_1}) \eta_{j_1}(\tau_{j_1})] \dots [\bar{\eta}_{j_{2n}}(\tau_{j_{2n}}) \psi_{j_{2n}}(\tau_{j_{2n}}) + \bar{\psi}_{j_{2n}}(\tau_{j_{2n}}) \eta_{j_{2n}}(\tau_{j_{2n}})] \tag{1.50}
\end{aligned}$$

In the last line, when we multiply everything out, there are 2^{2n} terms (note that $(2n)! > 2^{2n}$ for $n > 1$). However, only terms with an equal number of creation and annihilation operators are nonzero, and there are only $\binom{2n}{n} = (2n)!/(n!)^2$ of these. Furthermore, all of these terms are equal. This can be seen as a consequence of: i) the fact that both $\bar{\eta}\psi$ and $\bar{\psi}\eta$ are bosonic (i.e., commuting); ii) the fact that we sum over $j_1 \dots j_{2n}$ and integrate over $\tau_{j_1} \dots \tau_{j_{2n}}$, thus we can always perform arbitrary permutation of indices. Hence, our expression simplifies as follows

$$\begin{aligned}
& \int \prod_{r \neq 0} D[\bar{\psi}_r, \psi_r] e^{-S^{(0)} - \Delta S} \\
&= \int \prod_{r \neq 0} D[\bar{\psi}_r, \psi_r] e^{-S^{(0)}} \sum_{n=0}^{\infty} \frac{1}{(2n)!} \sum_{i_1 \dots i_n} \sum_{j_1 \dots j_n} \int_0^\beta d\tau_{i_1} \dots \int_0^\beta d\tau_{i_n} \int_0^\beta d\tau_{j_1} \dots \int_0^\beta d\tau_{j_n} \\
&\times \binom{2n}{n} \bar{\eta}_{i_1}(\tau_{i_1}) \dots \bar{\eta}_{i_n}(\tau_{i_n}) \psi_{i_1}(\tau_{i_1}) \dots \psi_{i_n}(\tau_{i_n}) \bar{\psi}_{j_1}(\tau_{j_1}) \dots \bar{\psi}_{j_n}(\tau_{j_n}) \eta_{j_1}(\tau_{j_1}) \dots \eta_{j_n}(\tau_{j_n}). \tag{1.51}
\end{aligned}$$

⁸We are here just stating a general definition of Green's function. This is still not restricted to the case of the lattice with a cavity.

We will now move the source terms η to the left and rename the indices $j_1 \dots j_n \rightarrow j_n \dots j_1$, such that we obtain

$$\begin{aligned} & \int \prod_{r \neq 0} D[\bar{\psi}_r, \psi_r] e^{-S^{(0)} - \Delta S} \\ &= \int \prod_{r \neq 0} D[\bar{\psi}_r, \psi_r] e^{-S^{(0)}} \sum_{n=0}^{\infty} \frac{1}{(n!)^2} \sum_{i_1 \dots i_n} \sum_{j_1 \dots j_n} \int_0^\beta d\tau_{\bar{i}_1} \dots \int_0^\beta d\tau_{\bar{i}_n} \int_0^\beta d\tau_{j_1} \dots \int_0^\beta d\tau_{j_n} \\ & \times \bar{\eta}_{i_1}(\tau_{\bar{i}_1}) \dots \bar{\eta}_{i_n}(\tau_{\bar{i}_n}) \eta_{j_n}(\tau_{j_n}) \dots \eta_{j_1}(\tau_{j_1}) \psi_{i_1}(\tau_{\bar{i}_1}) \dots \psi_{i_n}(\tau_{\bar{i}_n}) \bar{\psi}_{j_n}(\tau_{j_n}) \dots \bar{\psi}_{j_1}(\tau_{j_1}). \end{aligned} \quad (1.52)$$

The $n = 0$ term is just the partition function for the lattice with a cavity

$$\mathcal{Z}^{(0)} = \int \prod_{i \neq 0} D[\bar{\psi}_i, \psi_i] e^{-S^{(0)}}. \quad (1.53)$$

If we separate this term, Eq. (1.52) becomes

$$\begin{aligned} & \int \prod_{r \neq 0} D[\bar{\psi}_r, \psi_r] e^{-S^{(0)} - \Delta S} \\ &= \mathcal{Z}^{(0)} + \mathcal{Z}^{(0)} \sum_{n=1}^{\infty} \frac{1}{(n!)^2} \sum_{i_1 \dots i_n} \sum_{j_1 \dots j_n} \int_0^\beta d\tau_{\bar{i}_1} \dots \int_0^\beta d\tau_{\bar{i}_n} \int_0^\beta d\tau_{j_1} \dots \int_0^\beta d\tau_{j_n} \\ & \times \bar{\eta}_{i_1}(\tau_{\bar{i}_1}) \dots \bar{\eta}_{i_n}(\tau_{\bar{i}_n}) \eta_{j_n}(\tau_{j_n}) \dots \eta_{j_1}(\tau_{j_1}) \\ & \times \frac{1}{\mathcal{Z}^{(0)}} \int \prod_{r \neq 0} D[\bar{\psi}_r, \psi_r] e^{-S^{(0)}} \psi_{i_1}(\tau_{\bar{i}_1}) \dots \psi_{i_n}(\tau_{\bar{i}_n}) \bar{\psi}_{j_n}(\tau_{j_n}) \dots \bar{\psi}_{j_1}(\tau_{j_1}). \end{aligned} \quad (1.54)$$

Using Eq. (1.48), we see that the last line of the previous expression represents the cavity Green's function. Hence

$$\begin{aligned} & \int \prod_{r \neq 0} D[\bar{\psi}_r, \psi_r] e^{-S^{(0)} - \Delta S} \\ &= \mathcal{Z}^{(0)} - \mathcal{Z}^{(0)} \sum_{n=1}^{\infty} \frac{(-1)^{n+1}}{(n!)^2} \sum_{i_1 \dots i_n} \sum_{j_1 \dots j_n} \int_0^\beta d\tau_{\bar{i}_1} \dots \int_0^\beta d\tau_{\bar{i}_n} \int_0^\beta d\tau_{j_1} \dots \int_0^\beta d\tau_{j_n} \\ & \times \bar{\eta}_{i_1}(\tau_{\bar{i}_1}) \dots \bar{\eta}_{i_n}(\tau_{\bar{i}_n}) \eta_{j_n}(\tau_{j_n}) \dots \eta_{j_1}(\tau_{j_1}) G_{i_1 \dots i_n, j_1 \dots j_n}^{(0)}(\tau_{\bar{i}_1} \dots \tau_{\bar{i}_n}, \tau_{j_1} \dots \tau_{j_n}), \end{aligned} \quad (1.55)$$

where $G^{(0)}$ represents the cavity Green's function.

1.6.4 Expressing the Generating Functional in Terms of the Connected Green's Functions

We managed to express the left-hand side of Eq. (1.55) in terms of the cavity Green's function. As we already noted, this was expected, as the left-hand side is actually a generating functional. Here, we will be more precise and define the generating functional $Z^{(0)}[\bar{\eta}, \eta]$ with a proper normalization⁹

$$Z^{(0)}[\bar{\eta}, \eta] = \frac{1}{\mathcal{Z}^{(0)}} \int \prod_{i \neq 0} D[\bar{\psi}_i, \psi_i] e^{-S^{(0)} - \Delta S}. \quad (1.56)$$

⁹The generating functional is normalized such that $Z^{(0)}[0, 0] = 1$

Let us remind ourselves that we started from Eq. (1.45), with the goal to calculate the effective action¹⁰ that is obtained when the integrals over all ψ_i , except for $i = 0$, have been carried out. It is thus much better to express $Z^{(0)}[\bar{\eta}, \eta]$ as an exponential of some function. In that sense, the result we obtained in Eq. (1.55) is not suitable in this particular form. Luckily, the solution to our problem is provided by the linked cluster theorem [68]: it tells us that the generating functional $Z^{(0)}[\bar{\eta}, \eta]$ can also be written as an exponential of the second term in Eq. (1.55), if we substitute $\mathcal{Z}^{(0)} \rightarrow 1$ and $G^{(0)} \rightarrow G^{(0,c)}$, where $G^{(0,c)}$ is the connected Green's function

$$\begin{aligned} & \int \prod_{r \neq 0} D[\bar{\psi}_r, \psi_r] e^{-S^{(0)} - \Delta S} = \mathcal{Z}^{(0)} Z^{(0)}[\bar{\eta}, \eta] \\ & = \mathcal{Z}^{(0)} \cdot \exp \left\{ - \sum_{n=1}^{\infty} \frac{(-1)^{n+1}}{(n!)^2} \sum_{i_1 \dots i_n} \sum_{j_1 \dots j_n} \int_0^\beta d\tau_{i_1} \dots \int_0^\beta d\tau_{i_n} \int_0^\beta d\tau_{j_1} \dots \int_0^\beta d\tau_{j_n} \right. \\ & \quad \left. \times \bar{\eta}_{i_1}(\tau_{i_1}) \dots \bar{\eta}_{i_n}(\tau_{i_n}) \eta_{j_n}(\tau_{j_n}) \dots \eta_{j_1}(\tau_{j_1}) G_{i_1 \dots i_n, j_1 \dots j_n}^{(0,c)}(\tau_{i_1} \dots \tau_{i_n}, \tau_{j_1} \dots \tau_{j_n}) \right\}. \end{aligned} \quad (1.57)$$

If we now go back to Eq. (1.45), we finally obtain

$$\begin{aligned} \tilde{S}_{\text{eff}} = S_0 + \sum_{n=1}^{\infty} \frac{(-1)^{n+1}}{(n!)^2} \sum_{i_1 \dots i_n} \sum_{j_1 \dots j_n} \int_0^\beta d\tau_{i_1} \dots \int_0^\beta d\tau_{i_n} \int_0^\beta d\tau_{j_1} \dots \int_0^\beta d\tau_{j_n} \\ \times \bar{\eta}_{i_1}(\tau_{i_1}) \dots \bar{\eta}_{i_n}(\tau_{i_n}) \eta_{j_n}(\tau_{j_n}) \dots \eta_{j_1}(\tau_{j_1}) G_{i_1 \dots i_n, j_1 \dots j_n}^{(0,c)}(\tau_{i_1} \dots \tau_{i_n}, \tau_{j_1} \dots \tau_{j_n}). \end{aligned} \quad (1.58)$$

1.6.5 Simplifications in the Limit $d \rightarrow \infty$

So far, all expressions that we derived are exact. Here, we can introduce the approximation such that only S_0 and the $n = 1$ term is kept in Eq. (1.58), while everything else is neglected. It turns out that in the limit $d \rightarrow \infty$ this is not an approximation, but actually an exact result. The main task of this section will be to prove this statement.

First of all, we note that $i_1 \dots i_n, j_1 \dots j_n$ are all nearest neighbors to site 0. This can be seen from the fact that $\eta_i = t_{i0}\psi_0$, and t_{i0} is nonzero only if i and 0 are nearest neighbors. Let us now use the scaling laws (with respect to d) of the hopping parameter and the Green's function, to see how the n -th term in Eq. (1.58) behaves in the limit $d \rightarrow \infty$.

The $n = 1$ term contains

$$\sum_{ij} \bar{\eta}_i \eta_j G_{ij}^{(0,c)}. \quad (1.59)$$

Each source term is of the form $\eta_i = t_{i0}\psi_0$, where $t_{i0} \propto 1/\sqrt{d}$, while $G_{ij}^{(0,c)} \propto d^{-\|\mathbf{R}_i - \mathbf{R}_j\|/2}$. As i and j are both nearest neighbours to site 0, and the lattice is hypercubic, we conclude: i) that we need at least two hops to go from i to j , which implies that $G_{ij}^{(0,c)} \propto 1/d$; ii) that $\sum_{ij} \propto d^2$. Combining all of this, we deduce that the $n = 1$ term scales as

$$\sum_{ij} \bar{\eta}_i \eta_j G_{ij}^{(0,c)} \propto d^2 \frac{1}{\sqrt{d}} \frac{1}{\sqrt{d}} \frac{1}{d} \propto \mathcal{O}(d^0), \quad (1.60)$$

which is finite in the limit $d \rightarrow \infty$.

A similar analysis can be conducted for the $n = 2$ term

$$\sum_{i_1, i_2, j_1, j_2} \bar{\eta}_{i_1} \bar{\eta}_{i_2} \eta_{j_2} \eta_{j_1} G_{i_1 i_2, j_1 j_2}^{(0,c)}. \quad (1.61)$$

¹⁰We note that we use the term effective action for both the action that is obtained by integrating out the phononic degrees of freedom and also for the action when we further integrate over ψ_i for $i \neq 0$. In mathematical expressions these will be denoted by S_{eff} and \tilde{S}_{eff} , respectively. In the text, the context will make it clear to which one we are referring.

The only nontrivial part is to determine how does $G_{i_1 i_2 j_1 j_2}^{(0,c)}$ scale with respect to d . We will illustrate this using the lowest-order Feynman diagram, shown in Fig. 1.7. From the diagram, we can read off

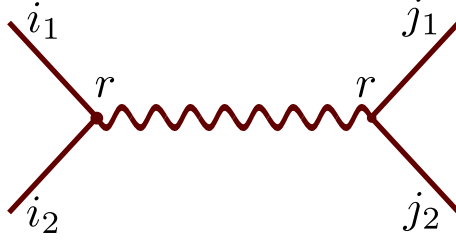


Figure 1.7: Lowest order Feynman diagram for connected two-particle Green's function $G_{i_1 i_2 j_1 j_2}^{(0,c)}$.

$$G_{i_1 i_2 j_1 j_2}^{(0,c)} \propto \sum_r G_{i_1 r}^{(0)} G_{i_2 r}^{(0)} G_{j_1 r}^{(0)} G_{j_2 r}^{(0)}. \quad (1.62)$$

We note that i_1, i_2, j_1, j_2 are all nearest neighbors to site 0, as seen from Eq. (1.61) and the fact that $\eta_i \propto t_{i0}$. If we take r from Eq. (1.62) to also be a nearest neighbor of site 0, such that it does not coincide with any of the indices i_1, i_2, j_1, j_2 , then we can conclude that: i) $\sum_r \propto d$; ii) we need exactly two hops to go from r to any one of i_1, i_2, j_1, j_2 , meaning that $G_{i_1 r}^{(0)} \propto 1/d$, $G_{i_2 r}^{(0)} \propto 1/d$, $G_{j_1 r}^{(0)} \propto 1/d$, $G_{j_2 r}^{(0)} \propto 1/d$. Thus, the two-particle Green's function from Eq. (1.62) scales as $G_{i_1 i_2 j_1 j_2}^{(0,c)} \propto 1/d^3$. Going back to Eq. (1.61), we see that in this case, the whole term $\sum_{i_1, i_2, j_1, j_2} \bar{\eta}_{i_1} \bar{\eta}_{i_2} \eta_{j_1} \eta_{j_2} G_{i_1 i_2 j_1 j_2}^{(0,c)}$ scales as $\propto d^4 (\frac{1}{\sqrt{d}})^4 \frac{1}{d^3} = \frac{1}{d}$, which vanishes in the limit $d \rightarrow \infty$. The same conclusion would be reached even if r was not the nearest neighbor of site 0. Let us now analyze what happens if r coincides with one of the indices i_1, i_2, j_1, j_2 . Without the loss of generality, let us assume that r coincides with i_1 . Then, Eq. (1.62) implies that

$$G_{i_1 i_2 j_1 j_2}^{(0,c)} \propto \frac{1}{\sqrt{d \|\mathbf{R}_{i_1} - \mathbf{R}_{i_2}\|}} \frac{1}{\sqrt{d \|\mathbf{R}_{i_1} - \mathbf{R}_{j_1}\|}} \frac{1}{\sqrt{d \|\mathbf{R}_{i_1} - \mathbf{R}_{j_2}\|}}. \quad (1.63)$$

If i_1, i_2, j_1, j_2 are all different, then $\|\mathbf{R}_{i_1} - \mathbf{R}_{i_2}\| = \|\mathbf{R}_{i_1} - \mathbf{R}_{j_1}\| = \|\mathbf{R}_{i_1} - \mathbf{R}_{j_2}\| = 2$, implying that $G_{i_1 i_2 j_1 j_2}^{(0,c)} \propto 1/d^3$. This is completely analogous to the case we previously analyzed, so we can immediately conclude that Eq. (1.61) scales as $1/d$, which vanishes in the limit of an infinite number of dimensions. If $i_1 = i_2 \neq j_1 \neq j_2$, then the Green's function falls off slower $G_{i_1 i_2 j_1 j_2}^{(0,c)} \propto 1/d^2$, but the sum in Eq. (1.61) now contributes only as d^3 . Hence, the scaling of Eq. (1.61) remains the same $\propto 1/d$. The same results are obtained even for $i_1 = i_2 = j_1 \neq j_2$, or $i_1 = i_2 = j_1 = j_2$. In these cases, the Green's function is falling off even slower (as the d is increased), but this is compensated by the fact that we are summing over fewer indices, so the contribution of the sum is smaller. We conclude that the $n = 2$ term completely vanishes in the limit $d \rightarrow \infty$.

Analogous reasoning can be used to show that all $n > 1$ terms in Eq. (1.58) vanish in the limit of an infinite number of dimensions, giving

$$\begin{aligned} \tilde{S}_{\text{eff}} &= S_0 + \sum_{ij} \int_0^\beta d\tau_i \int_0^\beta d\tau_j \bar{\eta}_i(\tau_i) \eta_j(\tau_j) G_{ij}^{(0,c)}(\tau_i, \tau_j) \\ &= \int_0^\beta d\tau \left\{ \bar{\psi}_0(\tau) \left(\frac{\partial}{\partial \tau} - \tilde{\mu} \right) \psi_0(\tau) + \frac{g^2}{2} \int_0^\beta d\tau' D(\tau - \tau') \bar{\psi}_0(\tau) \bar{\psi}_0(\tau') \psi_0(\tau') \psi_0(\tau) \right\} \\ &\quad + \sum_{ij} \int_0^\beta d\tau \int_0^\beta d\tau' t_{i0} \bar{\psi}_0(\tau) G_{ij}^{(0,c)}(\tau - \tau') \psi_0(\tau') t_{0j}. \end{aligned} \quad (1.64)$$

Let us now transform the first term, to be of the same form as the third term

$$\begin{aligned} \int_0^\beta d\tau \bar{\psi}_0(\tau) \left(\frac{\partial}{\partial \tau} - \tilde{\mu} \right) \psi_0(\tau) &= \int_0^\beta d\tau \bar{\psi}_0(\tau) \left(\frac{\partial}{\partial \tau} - \tilde{\mu} \right) \int_0^\beta d\tau' \delta(\tau - \tau') \psi_0(\tau') \\ &= \int_0^\beta d\tau \int_0^\beta d\tau' \bar{\psi}_0(\tau) \left[\left(\frac{\partial}{\partial \tau} - \tilde{\mu} \right) \delta(\tau - \tau') \right] \psi_0(\tau'). \end{aligned} \quad (1.65)$$

Hence, the effective action can be written as

$$\begin{aligned} \tilde{S}_{\text{eff}} &= \int_0^\beta d\tau \int_0^\beta d\tau' \bar{\psi}_0(\tau) \left[\left(\frac{\partial}{\partial \tau} - \tilde{\mu} \right) \delta(\tau - \tau') + \sum_{ij} t_{i0} t_{0j} G_{ij}^{(0)}(\tau - \tau') \right] \psi_0(\tau') \\ &\quad + \frac{g^2}{2} \int_0^\beta d\tau \int_0^\beta d\tau' D(\tau - \tau') \bar{\psi}_0(\tau) \bar{\psi}_0(\tau') \psi_0(\tau') \psi_0(\tau), \end{aligned} \quad (1.66)$$

where we substituted $G_{ij}^{(0,c)} \rightarrow G_{ij}^{(0)}$, since the one-particle Green's function is necessarily connected. In the following, we will see that this action has exactly the same form as the action for the Holstein-Anderson impurity problem. Thus, our next task is to precisely define what is the Holstein-Anderson impurity problem and to prove that its effective action coincides with Eq. (1.66). This will prove that the mapping of the lattice model to the impurity problem is exact in the limit $d \rightarrow \infty$.

1.7 Holstein-Anderson Impurity Problem

In this section, we will review the model in which a site, called the *impurity site*, is submerged into the so-called *electron bath*. The electrons in the bath are mutually noninteracting, but there exists a hybridization between them and the impurity site. Furthermore, the impurity site can contain an electron and phonons, while the interaction between them is of the Holstein type. Such a model is called the *Holstein-Anderson impurity problem* [56]. The main goal of this section is to convince ourselves that the action of the Holstein-Anderson impurity problem has exactly the same form as Eq. (1.66), meaning that there exists an exact mapping between the lattice problem in the limit $d \rightarrow \infty$, and the impurity problem. In the following sections, we will see that the impurity problem admits an exact analytic solution in terms of the continued fraction expansion [56]. This implies that the $d \rightarrow \infty$ lattice problem can also be solved exactly.

The Hamiltonian of the Holstein-Anderson impurity problem is given by

$$H = \underbrace{\sum_{\mathbf{k}} E_{\mathbf{k}} c_{\mathbf{k}}^\dagger c_{\mathbf{k}}}_{H_{\text{res}}} + \underbrace{\sum_{\mathbf{k}} \left(V_{\mathbf{k}} c_{\mathbf{k}}^\dagger d + \bar{V}_{\mathbf{k}} d^\dagger c_{\mathbf{k}} \right)}_{H_{\text{hybrid}}} + \underbrace{\omega_0 a^\dagger a}_{H_{\text{ph}}} - \underbrace{g d^\dagger d (a + a^\dagger)}_{H_{\text{int}}}. \quad (1.67)$$

Here, we explicitly see the contribution of the electrons in the bath H_{res} , hybridization between the impurity site and the bath H_{hybrid} , the free phonons H_{ph} , and the interaction between the phonons and the electrons on the impurity site H_{int} . Let us proceed in the functional formalism

$$\mathcal{Z} = \int D[\bar{\chi}, \chi] \int D[\bar{\psi}_{\mathbf{k}}, \psi_{\mathbf{k}}] \int D[\bar{\phi}, \phi] e^{-S[\bar{\psi}_{\mathbf{k}}, \psi_{\mathbf{k}}, \bar{\chi}, \chi, \bar{\phi}, \phi]}, \quad (1.68)$$

where S is the action, which can be written as

$$\begin{aligned} S[\bar{\psi}_{\mathbf{k}}, \psi_{\mathbf{k}}, \bar{\chi}, \chi, \bar{\phi}, \phi] &= S_{\text{imp}}[\bar{\chi}, \chi] + S_{\text{res}}[\bar{\psi}_{\mathbf{k}}, \psi_{\mathbf{k}}] + S_{\text{hybrid}}[\bar{\psi}_{\mathbf{k}}, \psi_{\mathbf{k}}, \bar{\chi}, \chi] \\ &\quad + S_{\text{ph}}[\bar{\phi}, \phi] + S_{\text{int}}[\bar{\chi}, \chi, \bar{\phi}, \phi], \end{aligned} \quad (1.69)$$

where

$$S_{\text{imp}}[\bar{\chi}, \chi] = \int_0^\beta d\tau \bar{\chi}(\tau) \frac{\partial}{\partial \tau} \chi(\tau), \quad (1.70a)$$

$$S_{\text{res}}[\bar{\psi}_{\mathbf{k}}, \psi_{\mathbf{k}}] = \int_0^\beta d\tau \sum_{\mathbf{k}} \bar{\psi}_{\mathbf{k}}(\tau) \left(\frac{\partial}{\partial \tau} + E_{\mathbf{k}} \right) \psi_{\mathbf{k}}(\tau), \quad (1.70b)$$

$$S_{\text{hybrid}}[\bar{\psi}_{\mathbf{k}}, \psi_{\mathbf{k}}, \bar{\chi}, \chi] = \int_0^\beta d\tau \sum_{\mathbf{k}} (V_{\mathbf{k}} \bar{\psi}_{\mathbf{k}}(\tau) \chi(\tau) + \bar{V}_{\mathbf{k}} \bar{\chi}(\tau) \psi_{\mathbf{k}}), \quad (1.70c)$$

$$S_{\text{ph}}[\bar{\phi}, \phi] = \int_0^\beta d\tau \bar{\phi}(\tau) \left(\frac{\partial}{\partial \tau} + \omega_0 \right) \phi(\tau), \quad (1.70d)$$

$$S_{\text{int}}[\bar{\chi}, \chi, \bar{\phi}, \phi] = -g \int_0^\beta d\tau \rho(\tau) (\phi(\tau) + \bar{\phi}(\tau)). \quad (1.70e)$$

Here, $\rho(\tau) = \bar{\chi}(\tau)\chi(\tau)$, while ψ, ϕ, χ represent the fields of the free electrons in the bath, phonons, and electrons on the impurity site, respectively.

Let us first integrate Eq. (1.68) over the phononic degrees of freedom ϕ . These are present only in terms S_{ph} and S_{int} . As in Sec. 1.5, we will rewrite these in the Matsubara frequency space (see Eqs. (1.31) and (1.32))

$$S_{\text{ph}}[\bar{\phi}, \phi] = \sum_n \bar{\phi}_n (\omega_0 - i\nu_n) \phi_n, \quad (1.71)$$

$$S_{\text{int}}[\bar{\chi}, \chi, \bar{\phi}, \phi] = -g \sum_n \rho_n (\phi_{-n} + \bar{\phi}_n). \quad (1.72)$$

Hence

$$\begin{aligned} \mathcal{Z} = & \int D[\bar{\chi}, \chi] \int D[\bar{\psi}_{\mathbf{k}}, \psi_{\mathbf{k}}] e^{-S_{\text{res}}[\bar{\psi}_{\mathbf{k}}, \psi_{\mathbf{k}}] - S_{\text{hybrid}}[\bar{\psi}_{\mathbf{k}}, \psi_{\mathbf{k}}, \bar{\chi}, \chi] - S_{\text{imp}}[\bar{\chi}, \chi]} \\ & \times \int D[\bar{\phi}, \phi] \exp \left\{ - \sum_n \bar{\phi}_n (\omega_0 - i\nu_n) \phi_n + g \sum_n \rho_{-n} \phi_n + g \sum_n \rho_n \bar{\phi}_n \right\}. \quad (1.73) \end{aligned}$$

The integral in the bottom line is completely analogous to the one in Eq. (1.34). Thus, we can simply read off the solution from Eq. (1.36)

$$\begin{aligned} \mathcal{Z} = & \int D[\bar{\chi}, \chi] \int D[\bar{\psi}_{\mathbf{k}}, \psi_{\mathbf{k}}] e^{-S_{\text{res}}[\bar{\psi}_{\mathbf{k}}, \psi_{\mathbf{k}}] - S_{\text{hybrid}}[\bar{\psi}_{\mathbf{k}}, \psi_{\mathbf{k}}, \bar{\chi}, \chi] - S_{\text{imp}}[\bar{\chi}, \chi]} \\ & \times \frac{1}{\prod_n (\omega_0 - i\nu_n)} \exp \left\{ g^2 \sum_n \frac{\omega_0}{\omega_0^2 + \nu_n^2} \rho_n \rho_{-n} \right\}. \quad (1.74) \end{aligned}$$

Next, we want to integrate over ψ . As before, we first express S_{res} and S_{hybrid} in Matsubara frequency space

$$S_{\text{res}}[\bar{\psi}_{\mathbf{k}}, \psi_{\mathbf{k}}] = \sum_{\mathbf{k}, n} \bar{\psi}_{\mathbf{k}, n} (E_{\mathbf{k}} - i\omega_n) \psi_{\mathbf{k}, n}, \quad (1.75)$$

$$S_{\text{hybrid}}[\bar{\psi}_{\mathbf{k}}, \psi_{\mathbf{k}}, \bar{\chi}, \chi] = \sum_{\mathbf{k}, n} (V_{\mathbf{k}} \bar{\psi}_{\mathbf{k}, n} \chi_n + \bar{V}_{\mathbf{k}} \bar{\chi}_n \psi_{\mathbf{k}, n}). \quad (1.76)$$

Plugging this back into Eq. (1.74)

$$\mathcal{Z} = \frac{1}{\prod_n (\omega_0 - i\nu_n)} \int D[\bar{\chi}, \chi] \exp \left\{ g^2 \sum_n \frac{\omega_0}{\omega_0^2 + \nu_n^2} \rho_n \rho_{-n} \right\} e^{-S_{\text{imp}}[\bar{\chi}, \chi]} \times \int D[\bar{\psi}_{\mathbf{k}}, \psi_{\mathbf{k}}] \exp \left\{ - \sum_{\mathbf{k}, n} \bar{\psi}_{\mathbf{k}, n} (E_{\mathbf{k}} - i\omega_n) \psi_{\mathbf{k}, n} - \sum_{\mathbf{k}, n} (V_{\mathbf{k}} \bar{\psi}_{\mathbf{k}, n} \chi_n + \bar{V}_{\mathbf{k}} \bar{\chi}_n \psi_{\mathbf{k}, n}) \right\}, \quad (1.77)$$

where the bottom line is again the Gaussian integral. However, this time we need to take into account that ψ is a Grassmann variable, so

$$\int D[\bar{\psi}, \psi] e^{-\bar{\psi} A \psi + \bar{\eta} \psi + \bar{\psi} \eta} = \det A \cdot e^{\bar{\eta} A^{-1} \eta}. \quad (1.78)$$

Hence, we obtain

$$\mathcal{Z} = \frac{\prod_{\mathbf{k}, m} (E_{\mathbf{k}} - i\omega_m)}{\prod_n (\omega_0 - i\nu_n)} \int D[\bar{\chi}, \chi] \exp \left\{ - S_{\text{imp}}[\bar{\chi}, \chi] + g^2 \sum_n \frac{\omega_0}{\omega_0^2 + \nu_n^2} \rho_n \rho_{-n} + \sum_{\mathbf{k}, n} |V_{\mathbf{k}}|^2 \bar{\chi}_n \frac{1}{E_{\mathbf{k}} - i\omega_n} \chi_n \right\}. \quad (1.79)$$

If we also express $S_{\text{imp}}[\bar{\chi}, \chi]$ in Matsubara frequency space

$$S_{\text{imp}}[\bar{\chi}, \chi] = \sum_n \bar{\chi}_n (-i\omega_n) \chi_n, \quad (1.80)$$

then we can simply read off the effective impurity action

$$S_{\text{eff}} = - \underbrace{\sum_n \bar{\chi}_n \left[i\omega_n - \sum_{\mathbf{k}} \frac{|V_{\mathbf{k}}|^2}{i\omega_n - E_{\mathbf{k}}} \right] \chi_n}_{\equiv - \sum_n \bar{\chi}_n G_0^{-1}(i\omega_n) \chi_n} - g^2 \sum_n \frac{\omega_0}{\omega_0^2 + \nu_n^2} \rho_n \rho_{-n}, \quad (1.81)$$

where we got rid of the terms in Eq. (1.79) that correspond to free phonons and free electrons from the reservoir, which is justified as we are interested only in the Green's function of the electrons on the impurity site. As indicated by the underbrace, the first term in Eq. (1.81) determines the free Green's function G_0 , which on the real-frequency axis reads as

$$G_0^{-1}(\omega) = \omega - \sum_{\mathbf{k}} \frac{|V_{\mathbf{k}}|^2}{\omega - E_{\mathbf{k}}}. \quad (1.82)$$

Let us now prove that Eq. (1.81) is of the same form as Eq. (1.66). To do so, we will rewrite Eq. (1.81) in terms of the fields χ in the τ domain. The first term in Eq. (1.81) can thus be expressed as follows

$$- \sum_n \bar{\chi}_n G_0^{-1}(i\omega_n) \chi_n = - \int_0^\beta d\tau \int_0^\beta d\tau' \bar{\chi}(\tau) G_0^{-1}(\tau - \tau') \chi(\tau'). \quad (1.83)$$

Remark 3. The last expression defines $G_0^{-1}(\tau - \tau')$ as an inverse Fourier transform of $G_0^{-1}(i\omega_n)$. Although it would be clearer if these quantities were denoted differently, this is standardly done in the literature.

The second term in Eq. (1.81) has the same form as the right-hand side of Eq. (1.38). Therefore, using the result in Eq. (1.41), we deduce that

$$-g^2 \sum_n \frac{\omega_0}{\omega_0^2 + \nu_n^2} \rho_n \rho_{-n} = \frac{g^2}{2} \int_0^\beta d\tau \int_0^\beta d\tau' \bar{\chi}(\tau) \bar{\chi}(\tau') \chi(\tau') \chi(\tau) D(\tau - \tau'), \quad (1.84)$$

where $D(\tau - \tau')$ is given by Eq. (1.40). Putting all of this together

$$S_{\text{eff}} = - \int_0^\beta d\tau \int_0^\beta d\tau' \bar{\chi}(\tau) G_0^{-1}(\tau - \tau') \chi(\tau') + \frac{g^2}{2} \int_0^\beta d\tau \int_0^\beta d\tau' \bar{\chi}(\tau) \bar{\chi}(\tau') \chi(\tau') \chi(\tau) D(\tau - \tau'). \quad (1.85)$$

Comparing Eqs. (1.81) and (1.66), we see that they have exactly the same form if we impose that

$$G_0^{-1}(\tau - \tau') = - \left(\frac{\partial}{\partial \tau} - \tilde{\mu} \right) \delta(\tau - \tau') - \sum_{ij} t_{i0} t_{0j} G_{ij}^{(0)}(\tau - \tau'). \quad (1.86)$$

1.8 Self-consistency Condition

1.8.1 Derivation of the Self-consistency Condition

While Eq. (1.86) connects the quantities G_0 and $G_{ij}^{(0)}$, neither of these quantities are initially known. As we will see, this requires the introduction of the self-consistently relation, which will be derived in this section.

We start from Eq. (1.86) in Fourier space¹¹:

$$G_0^{-1}(i\omega_n) = \tilde{\mu} + i\omega_n - \sum_{ij} t_{i0} t_{0j} G_{ij}^{(0)}(i\omega_n). \quad (1.87)$$

While on the left-hand side we have G_0^{-1} , which is a characteristic of the impurity problem, on the right-hand side there is $G_{ij}^{(0)}$, which represents the Green's function of the lattice with a cavity. We want to relate that quantity to the quantity we started from: the Green's function of a lattice without cavity [58]

$$G_{ij}^{(0)}(i\omega_n) = G_{ij}(i\omega_n) - \frac{G_{i0}(i\omega_n) G_{0j}(i\omega_n)}{G_{00}(i\omega_n)}. \quad (1.88)$$

This formula can be actually traced back to Hubbard [69]. Formally, it can be proved using the expansion around the atomic limit [58, 70], but it is also quite easy to understand it intuitively: the Green's function G_{ij} is interpreted as probability amplitude for the particle to propagate from j to i . This is also true for $G_{ij}^{(0)}$, but the electron in this case cannot propagate through site 0, because this site was removed. Hence, $G_{ij}^{(0)}$ can be obtained from G_{ij} by subtracting the paths that go through 0. Furthermore, in the limit we are considering $d \rightarrow \infty$, it turns out that we only need to take into account the paths that go once through 0, and these are given by $G_{i0}(i\omega_n) G_{0j}(i\omega_n)$. This last expression, however, has some double counting which is most easily explained using the example in the τ domain as follows: if the electron was to propagate from j at $\tau = 0$ to i at $\tau = \tilde{\tau}$, then one possible path is to first hop to site 0 at $\tau = \tilde{\tau}/3$, "wait" on the site 0 until $\tau = 2\tilde{\tau}/3$, and then hop to site i . As we explained, this contribution needs to be subtracted from $G_{ij}^{(0)}$. However, in the expression $G_{i0} G_{0j}$, the term G_{i0} takes into account paths in which the electron waits on the site 0 in the interval

¹¹See Remark 3.

$\tau \in (\tilde{\tau}/3, \tilde{\tau}/3 + \Delta t)$, while G_{0j} takes into account paths in which waiting on the site 0 happens in the interval $\tau \in (\tilde{\tau}/3 + \Delta t, 2\tilde{\tau}/3)$. But this is an overcounting, as all of these paths for different Δt , such that $0 \leq \Delta t \leq \tilde{\tau}/3$, physically represent the same path in which the electron waits at the site 0 in the interval $\tau \in (\tilde{\tau}/3, 2\tilde{\tau}/3)$. This overcounting can be easily taken into account in frequency space by using the normalization $G_{00}^{-1}(i\omega_n)$, as we did in Eq. (1.88).

Plugging Eq. (1.88) in Eq. (1.87), we get

$$\begin{aligned} G_0^{-1}(i\omega_n) &= \tilde{\mu} + i\omega_n - \sum_{ij} t_{i0}t_{0j}G_{ij}(i\omega_n) + G_{00}^{-1}(i\omega_n) \left(\sum_i t_{i0}G_{i0}(i\omega_n) \right) \left(\sum_j t_{0j}G_{0j}(i\omega_n) \right) \\ &= \tilde{\mu} + i\omega_n - \sum_{ij} t_{i0}t_{0j}G_{ij}(i\omega_n) + G_{00}^{-1}(i\omega_n) \left(\sum_j t_{j0}G_{j0}(i\omega_n) \right)^2. \end{aligned} \quad (1.89)$$

This can be further simplified if we use the Fourier representation of the Green's function as

$$\begin{aligned} \sum_j t_{j0}G_{j0}(i\omega_n) &= \sum_j t_{j0} \frac{1}{N} \sum_{\mathbf{k}} e^{-i\mathbf{k}\mathbf{R}_j} G_{\mathbf{k}}(i\omega_n) = \sum_{\mathbf{k}} G_{\mathbf{k}}(i\omega_n) \frac{1}{N} \underbrace{\sum_j t_{j0}e^{-i\mathbf{k}\mathbf{R}_j}}_{\varepsilon_{\mathbf{k}}} \\ &= \frac{1}{N} \sum_{\mathbf{k}} \varepsilon_{\mathbf{k}} G_{\mathbf{k}}(i\omega_n), \end{aligned} \quad (1.90)$$

and

$$\begin{aligned} \sum_{ij} t_{i0}t_{0j}G_{ij}(i\omega_n) &= \sum_{j_1j_2} t_{j_10}t_{0j_2} \frac{1}{N} \sum_{\mathbf{k}} e^{-i\mathbf{k}(\mathbf{R}_{j_1} - \mathbf{R}_{j_2})} G_{\mathbf{k}}(i\omega_n) \\ &= \frac{1}{N} \sum_{\mathbf{k}} G_{\mathbf{k}}(i\omega_n) \underbrace{\left(\sum_{j_1} t_{j_10}e^{-i\mathbf{k}\mathbf{R}_{j_1}} \right)^2}_{\varepsilon_{\mathbf{k}}^2} \\ &= \frac{1}{N} \sum_{\mathbf{k}} \varepsilon_{\mathbf{k}}^2 G_{\mathbf{k}}(i\omega_n), \end{aligned} \quad (1.91)$$

where $\varepsilon_{\mathbf{k}}$ is the noninteracting dispersion relation. Furthermore, since we proved that the self-energy is local, the Green's function is given by

$$G_{\mathbf{k}}(i\omega_n) = \frac{1}{i\omega_n - \varepsilon_{\mathbf{k}} - \Sigma(i\omega_n) + \tilde{\mu}} = \frac{1}{\xi - \varepsilon_{\mathbf{k}}}, \quad (1.92)$$

where we introduced the \mathbf{k} independent parameter $\xi \equiv i\omega_n + \tilde{\mu} - \Sigma(i\omega_n)$. Now, Eqs. (1.91) and (1.90) can be rewritten in terms of the local Green's function $G_{ii} = \sum_{\mathbf{k}} G_{\mathbf{k}}(i\omega_n)/N$ as

$$\begin{aligned} \frac{1}{N} \sum_{\mathbf{k}} \varepsilon_{\mathbf{k}} G_{\mathbf{k}}(i\omega_n) &= \frac{1}{N} \sum_{\mathbf{k}} \frac{\varepsilon_{\mathbf{k}} - \xi + \xi}{\xi - \varepsilon_{\mathbf{k}}} = \frac{1}{N} \sum_{\mathbf{k}} [-1 + \xi G_{\mathbf{k}}(i\omega_n)] \\ &= -1 + \xi \frac{1}{N} \sum_{\mathbf{k}} G_{\mathbf{k}}(i\omega_n) = -1 + \xi G_{ii}(i\omega_n) \end{aligned} \quad (1.93)$$

and

$$\begin{aligned} \frac{1}{N} \sum_{\mathbf{k}} \varepsilon_{\mathbf{k}}^2 G_{\mathbf{k}}(i\omega_n) &= \frac{1}{N} \sum_{\mathbf{k}} \varepsilon_{\mathbf{k}}^2 \frac{1}{\xi - \varepsilon_{\mathbf{k}}} = \frac{1}{N} \sum_{\mathbf{k}} \frac{\varepsilon_{\mathbf{k}}(\varepsilon_{\mathbf{k}} - \xi) + \varepsilon_{\mathbf{k}}\xi}{\xi - \varepsilon_{\mathbf{k}}} \\ &= \frac{\xi}{N} \sum_{\mathbf{k}} \frac{\varepsilon_{\mathbf{k}}}{\xi - \varepsilon_{\mathbf{k}}} = \frac{\xi}{N} \sum_{\mathbf{k}} \varepsilon_{\mathbf{k}} G_{\mathbf{k}}(i\omega_n) = -\xi + \xi^2 G_{ii}(i\omega_n), \end{aligned} \quad (1.94)$$

where we used the fact that the noninteracting dispersion relation is symmetric, i.e. $\sum_{\mathbf{k}} \varepsilon_{\mathbf{k}} = 0$. Let us now use all of these results in Eq. (1.89), to obtain

$$G_0^{-1}(i\omega_n) = \tilde{\mu} + i\omega_n - [-\xi + \xi^2 G_{ii}(\omega_n)] + G_{00}^{-1}(\omega_n) [-1 + \xi G_{ii}(i\omega_n)]^2. \quad (1.95)$$

As a consequence of the translational symmetry $G_{ii} = G_{00}$, so the previous expression simplifies and becomes

$$G_0^{-1}(i\omega_n) = \Sigma(i\omega_n) + G_{ii}^{-1}(i\omega_n). \quad (1.96)$$

This is the self-consistency relation we were looking for. It is actually just a Dyson equation. Since we are formulating our DMFT loop completely on the real-frequency axis, this result can be simply analytically continued by substituting $i\omega_n \rightarrow \omega$.

As we know, the local Green's function $G_{ii}(\omega)$ reads as

$$G_{ii}(\omega) = \frac{1}{N} \sum_{\mathbf{k}} G_{\mathbf{k}}(\omega) = \frac{1}{N} \sum_{\mathbf{k}} \frac{1}{\omega - \varepsilon_{\mathbf{k}} - \Sigma(\omega) + \tilde{\mu}}. \quad (1.97)$$

However, as we explained in Sec. 2.1.2 of Part I, in the limit (which we are considering) of vanishing electron density, we need to set the chemical potential far below the conduction band $\tilde{\mu} \rightarrow -\infty$, and at the end of the calculation redefine $\Sigma(\omega) \rightarrow \Sigma(\omega + \tilde{\mu})$, $G(\omega) \rightarrow G(\omega + \tilde{\mu})$. If we apply this prescription to Eq. (1.97), and use the substitution $\omega \rightarrow \omega - \tilde{\mu}$, we would obtain the result that looks the same as if the chemical potential $\tilde{\mu}$ was simply erased

$$G_{ii}(\omega) = \frac{1}{N} \sum_{\mathbf{k}} \frac{1}{\omega - \varepsilon_{\mathbf{k}} - \Sigma(\omega)} = \int d\varepsilon \frac{\rho(\varepsilon)}{\omega - \Sigma(\omega) - \varepsilon}. \quad (1.98)$$

In the last equality, we rewrote the result using the noninteracting density of states $\rho(\varepsilon)$. Although this result is exact in the limit $d \rightarrow \infty$, it actually enables us to easily apply DMFT as an approximate method in the finite-dimensional case as well. We just need to use the appropriate noninteracting density of states $\rho(\varepsilon)$.

Remark 4. *The DMFT formalism is applicable both to the case of a finite and infinite number of lattice sites N . The first equality in Eq. (1.98) is much better suited for the case of a finite N , whereas the second equality is better for the thermodynamic limit ($N \rightarrow \infty$).*

In the following, we will see that the integral in Eq. (1.98) can be solved exactly in the case of a 1D system and the 2D square lattice in thermodynamic limit.

1.8.2 Local Green's Function in the 1D Case

The straightforward numerical implementation of Eq. (1.98) may encounter issues, arising from the fact that we are working on a real frequency axis and the denominator can be very close to zero for certain ε . In Sec. 1.8.4 we will derive a numerical scheme that solves this problem. However, in 1D this problem can be solved even more directly, by explicitly solving the integral in Eq. (1.98).

To do so, we first need an expression for the 1D density of states $\rho(\varepsilon)$. It is given by

$$\rho(\varepsilon) = \frac{\theta(4t_0^2 - \varepsilon^2)}{\pi \sqrt{4t_0^2 - \varepsilon^2}}, \quad (1.99)$$

where θ is the Heaviside step function. Plugging this into Eq. (1.98) and using the substitution $\varepsilon = 2t_0 \sin x$, we obtain

$$G(\omega) = \frac{1}{4t_0\pi} \int_{-\pi}^{\pi} \frac{dx}{B(\omega) - \sin x}, \quad (1.100)$$

where we introduced an auxiliary quantity

$$B(\omega) = \frac{\omega - \Sigma(\omega)}{2t_0}. \quad (1.101)$$

Additional substitution $z = e^{ix}$ leads us to

$$G(\omega) = \frac{1}{4t_0\pi} \oint_{|z|=1} \frac{dz}{iz} \frac{1}{B(\omega) - \frac{1}{2i}(z - \frac{1}{z})} = \frac{1}{2t_0\pi} \oint_{|z|=1} \frac{dz}{-z^2 + 2izB(\omega) + 1}. \quad (1.102)$$

As we see, we obtained a counterclockwise complex integral over the unit circle $|z| = 1$. This integral can be solved using the method of residues. To do so, we express the polynomial in the denominator of Eq. (1.102) in its factorized form

$$-z^2 + 2izB(\omega) + 1 = -(z - z_+)(z - z_-), \quad (1.103)$$

where z_{\pm} are given by

$$z_{\pm} = iB(\omega) \pm \sqrt{1 - B(\omega)^2}. \quad (1.104)$$

Then, $G(\omega)$ becomes

$$G(\omega) = -\frac{1}{2t_0\pi} \oint_{|z|=1} \frac{dz}{(z - z_+)(z - z_-)}. \quad (1.105)$$

Lastly, to apply the method of residues, we need to determine which poles of the subintegral function are inside the contour we are integrating over, i.e., we need to find out whether z_{\pm} are inside the complex unit circle $|z| = 1$ or not. It turns out that $|z_+| < 1$, while $|z_-| > 1$, meaning that only the pole at z_+ gives a non-vanishing contribution to the Eq. (1.105). This can be proved as a consequence of the causality $\text{Im}\Sigma(\omega) < 0$, since it implies that $\text{Im}B(\omega) > 0$. Hence, the result is given by

$$G(\omega) = \frac{-i}{t_0} \frac{1}{z_+ - z_-} = \frac{-i}{\underbrace{2t_0\sqrt{1 - B(\omega)^2}}_{\equiv G^I(B)}} = \frac{1}{\underbrace{2t_0B(\omega)\sqrt{1 - \frac{1}{B(\omega)^2}}}_{G^{II}(B)}}}. \quad (1.106)$$

In Eq. (1.106), we wrote the solution in two ways: G^I and G^{II} . They are completely equivalent in our case when $\text{Im}B(\omega) > 0$, but can otherwise give different results. Since $B(\omega)$ can be arbitrarily close to the real axis, it is important to ensure additional numerical stability by requiring that the expression for $G(\omega)$ satisfies that the $\text{Im}B(\omega) = 0$ solution coincides with the solution in the limit $\text{Im}B(\omega) \rightarrow 0$. Neither expression in Eq. (1.106), fully satisfies this property. However, it turns out that

$$\text{Re} \lim_{\text{Im}B \rightarrow 0} G(B) = \text{Re}G^{II}(\text{Re}B) \neq \text{Re}G^I(\text{Re}B) \quad (1.107a)$$

$$\text{Im} \lim_{\text{Im}B \rightarrow 0} G(B) = \text{Im}G^I(\text{Re}B) \neq \text{Im}G^{II}(\text{Re}B) \quad (1.107b)$$

This is illustrated in Fig. 1.8. Hence, the desired property can be obtained by combining the imaginary and the real parts of different solutions G^I and G^{II} , as follows

$$G(\omega) = \text{Re} \frac{1}{2t_0B(\omega)\sqrt{1 - \frac{1}{B(\omega)^2}}} + i \text{Im} \frac{-i}{2t_0\sqrt{1 - B(\omega)^2}}. \quad (1.108)$$

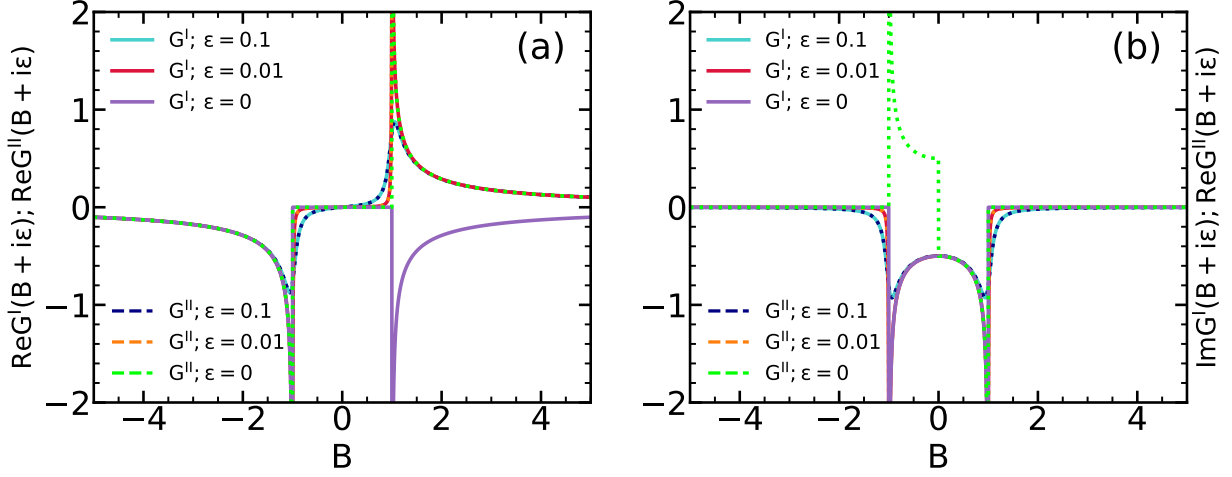


Figure 1.8: Two different solutions for the local Green's function in 1D. (a) Illustration that $\text{Re} \lim_{\varepsilon \rightarrow 0} G(B + i\varepsilon) = \text{Re}G^{II}(B) \neq \text{Re}G^I(B)$. (b) Illustration that $\text{Im} \lim_{\varepsilon \rightarrow 0} G(B + i\varepsilon) = \text{Im}G^I(B) \neq \text{Im}G^{II}(B)$. In both panels $B \in \mathbb{R}$.

1.8.3 Local Green's Function in the Case of 2D Square Lattice

Before presenting a numerical scheme for numerical implementation of Eq. (1.98), let us show that this integral can also be solved in the case of 2D square lattice as well.

First, let us rewrite Eq. (1.98) using the Fourier representation of the density of states ¹²

$$G(\omega) = \int_{-\infty}^{\infty} d\varepsilon \frac{1}{\omega - \Sigma(\omega) - \varepsilon} \cdot \int_{-\infty}^{\infty} dx e^{ix\varepsilon} \hat{\rho}(x). \quad (1.109)$$

If we now interchange the order of integrals, and use the auxiliary parameter $B(\omega)$ that we defined in Eq. (1.101), the previous expression becomes

$$G(\omega) = - \int_{-\infty}^{\infty} dx \hat{\rho}(x) \int_{-\infty}^{\infty} d\varepsilon \frac{e^{ix\varepsilon}}{\varepsilon - 2t_0 B(\omega)}. \quad (1.110)$$

The integral over ε can be solved using the residue theorem. It is thus important to notice that the subintegral function has only a single pole at $\varepsilon_{\text{pole}} = 2t_0 B(\omega)$, that is situated at the upper half-plane, i.e. $\text{Im}B(\omega) > 0$ (since $\text{Im}\Sigma(\omega) < 0$). Hence

$$G(\omega) = -2\pi i \int_{-\infty}^{\infty} dx \hat{\rho}(x) e^{2ixt_0 B(\omega)} \theta(x). \quad (1.111)$$

Up to now, everything was general. The only place where we actually specify the lattice we are working with is through a mathematical form of $\hat{\rho}(x)$, which we now calculate

$$\begin{aligned} \hat{\rho}(x) &= \frac{1}{2\pi} \int_{-\infty}^{\infty} d\varepsilon e^{-ix\varepsilon} \rho(\varepsilon) \\ &= \frac{1}{2\pi} \int_{-\infty}^{\infty} d\varepsilon e^{-ix\varepsilon} \cdot \frac{1}{N} \sum_{\mathbf{k}} \delta(\varepsilon - \varepsilon_{\mathbf{k}}) \\ &= \frac{1}{2\pi} \int_{-\infty}^{\infty} d\varepsilon e^{-ix\varepsilon} \cdot \frac{1}{(2\pi)^2} \int_0^{2\pi} dk_x \int_0^{2\pi} dk_y \delta(\varepsilon + 2t_0 \cos k_x + 2t_0 \cos k_y) \\ &= \frac{1}{(2\pi)^3} \int_0^{2\pi} dk_x \int_0^{2\pi} dk_y e^{-ix(-2t_0 \cos k_x - 2t_0 \cos k_y)} = \frac{1}{2\pi} \left[\frac{1}{2\pi} \int_0^{2\pi} dk e^{2it_0 x \cos k} \right]^2. \end{aligned} \quad (1.112)$$

¹²The Fourier transform of $\rho(\varepsilon)$ will be denoted by $\hat{\rho}(x)$

Hence, recognizing the integral representation of the Bessel function J_0 of the first kind of order zero, we get

$$\hat{\rho}(x) = \frac{J_0(2t_0x)^2}{2\pi}. \quad (1.113)$$

Plugging this back into Eq. (1.111), we finally obtain

$$G(\omega) = \frac{K\left(\frac{2}{B(\omega)}\right)}{B(\omega)\pi t_0}, \quad (1.114)$$

where $K(k) \equiv \int_0^{\pi/2} d\theta / \sqrt{1 - k^2 \sin^2 \theta}$ is the complete elliptic integral of the first kind.

1.8.4 Numerical Scheme for Calculating the Local Green's Function in General case

Here we finally present a numerical procedure for the calculation of the local Green's function (1.98) for arbitrary density of states $\rho(\epsilon)$, that completely eliminates the potential numerical singularity that can arise at $\epsilon = \omega - \Sigma(\omega)$.

Let us suppose that the self-energy and the density of states are known only on a finite, equidistant grid $\omega_0, \omega_1 \dots \omega_{N-1}$, where $\Delta\omega = \omega_{i+1} - \omega_i$. Further, suppose that the density of states is vanishing outside some closed interval $[D_1, D_2]$ and that the grid is wide enough so that there are at least a couple of points outside that closed interval: $\rho(\omega_0) = \dots = \rho(\omega_3) = 0$ and $\rho(\omega_{N-1}) = \dots = \rho(\omega_{N-4}) = 0$. These are quite general assumptions that are always satisfied in the systems we are examining. The local Green's function can now be rewritten as

$$G(\omega) = \sum_{i=0}^{N-2} \int_{\omega_i}^{\omega_{i+1}} d\epsilon \frac{\rho(\epsilon)}{\omega - \Sigma(\omega) - \epsilon}. \quad (1.115)$$

At each sub-interval $[\omega_i, \omega_{i+1}]$ the density of states is only known at the endpoints, so it is natural to approximate it using a linear function

$$\rho(\epsilon) = a_i + b_i(\epsilon - \omega_i), \quad (1.116)$$

where¹³ $a_i = \rho(\omega_i)$, $b_i = (\rho(\omega_{i+1}) - \rho(\omega_i))/\Delta\omega$. Plugging this into Eq. (1.115), and introducing a shorthand notation $\xi = \omega - \Sigma(\omega)$, we analytically evaluate that

$$\begin{aligned} G(\omega) &= \sum_{i=0}^{N-2} b_i(\omega_i - \omega_{i+1}) \\ &+ \sum_{i=0}^{N-2} a_i [\ln(\xi - \omega_i) - \ln(\xi - \omega_{i+1})] \\ &+ \sum_{i=0}^{N-2} b_i(\xi - \omega_i) [\ln(\xi - \omega_i) - \ln(\xi - \omega_{i+1})]. \end{aligned} \quad (1.117)$$

The first line is just a telescoping series that is vanishing

$$\sum_{i=0}^{N-2} b_i(\omega_i - \omega_{i+1}) = \rho(\omega_0) - \rho(\omega_{N-1}) = 0. \quad (1.118)$$

¹³Since we used a grid where the first and the last few points are outside of the interval where ρ is nonzero, then $a_0 = a_{N-2} = b_0 = \dots = b_3 = b_{N-3} = \dots = b_{N-1} = 0$.

The second line in Eq. (1.117) can be transformed by separating the two terms, shifting the indices $i + 1 \rightarrow i$ in the first term, and using the fact that $a_0 = a_{N-2} = 0$

$$\begin{aligned}
\sum_{i=0}^{N-2} a_i [\ln(\xi - \omega_i) - \ln(\xi - \omega_{i+1})] &= \sum_{i=1}^{N-2} a_i \ln(\xi - \omega_i) - \sum_{i=0}^{N-3} a_i \ln(\xi - \omega_{i+1}) \\
&= \sum_{i=0}^{N-3} a_{i+1} \ln(\xi - \omega_{i+1}) - \sum_{i=0}^{N-3} a_i \ln(\xi - \omega_{i+1}) \\
&= \sum_{i=0}^{N-3} [a_{i+1} - a_i] \ln(\xi - \omega_{i+1}) \\
&= \sum_{i=0}^{N-3} (\omega_{i+1} - \omega_i) b_i \ln(\xi - \omega_{i+1})
\end{aligned} \tag{1.119}$$

In the last line, we used the identity $a_i - a_{i-1} = (\omega_i - \omega_{i-1})b_{i-1}$. Plugging this back into Eq. (1.117) and using the fact that $b_{N-2} = 0$, we get:

$$\begin{aligned}
G(\omega) &= \sum_{i=0}^{N-3} (\omega_{i+1} - \omega_i) b_i \ln(\xi - \omega_{i+1}) \\
&\quad + \sum_{i=0}^{N-2} b_i (\xi - \omega_i) \ln(\xi - \omega_i) - \sum_{i=0}^{N-3} b_i (\xi - \omega_i) \ln(\xi - \omega_{i+1}) \\
&= \sum_{i=0}^{N-3} b_i (\omega_{i+1} - \xi) \ln(\xi - \omega_{i+1}) + \sum_{i=0}^{N-2} b_i (\xi - \omega_i) \ln(\xi - \omega_i)
\end{aligned} \tag{1.120}$$

By shifting the index in the first term, and using that $b_0 = 0$, we get:

$$G(\omega) = \sum_{i=1}^{N-2} (b_i - b_{i-1}) (\xi - \omega_i) \ln(\xi - \omega_i). \tag{1.121}$$

Since we are using the equidistant grid, it follows that

$$b_i - b_{i-1} = \frac{\rho(\omega_{i+1}) - 2\rho(\omega_i) + \rho(\omega_{i-1}))}{\Delta\omega}. \tag{1.122}$$

Finally, we obtain

$$G(\omega) = \sum_{i=1}^{N-2} \frac{\rho(\omega_{i+1}) - 2\rho(\omega_i) + \rho(\omega_{i-1}))}{\Delta\omega} (\omega - \omega_i - \Sigma(\omega)) \ln(\omega - \omega_i - \Sigma(\omega)) \tag{1.123}$$

This expression now has no numerical instabilities. This is most easily seen from the fact that it has the form $x \ln x$ which is well defined even in the limit $x \rightarrow 0$, where it vanishes. Of course, the results were obtained by using the linear interpolation of the density of states. This is completely justified if $\rho(\epsilon)$ is smooth or has finitely many cusps. However, the presence of van Hove singularities in $\rho(\epsilon)$ may require some special analytical treatment around them.

1.9 Impurity Solver

Holstein-Anderson impurity problem was introduced in Sec. 1.7. Its Hamiltonian is defined by Eq. (1.67). We showed that the corresponding effective action of this problem can be written as in Eq. (1.85), where the noninteracting Green's function G_0 was defined in Eq. (1.82). Now, our task is to find the impurity Green's function (i.e., the corresponding self-energy) for a given G_0 . We will use the same notation, as in Sec. 1.7, along with some new quantities that we now introduce

$$K = H - \tilde{\mu}\tilde{N} \quad (1.124a)$$

$$\tilde{N} = d^\dagger d \quad (1.124b)$$

$$H_0 = H - H_{\text{int}} \quad (1.124c)$$

$$K_0 = K - H_{\text{int}}. \quad (1.124d)$$

Remark 5. In Sec. 1.7, we integrated out the phononic degrees of freedom (that were present in H_{ph} and H_{int}) and obtained the retarded electron-electron interaction. Then, we integrated out the free electrons, and obtained the free Green's function G_0 . Hence, the free Green's function G_0 corresponds to the Hamiltonian $K - H_{\text{int}} - H_{\text{ph}} = K_0 - H_{\text{ph}}$ (from our notation, one might expect that the Green's function G_0 corresponds to the Hamiltonian K_0 , but this is not the case.).

1.9.1 Expressing Green's Function in Terms of a Resolvent of K

By definition, impurity Green's function is given by

$$G(t) = -i\theta(t)\langle\{d(t), d^\dagger\}\rangle_T, \quad (1.125)$$

where $d(t) = e^{iKt}de^{-iKt}$, $\{, \}$ is the anticommutator, and $\langle \dots \rangle_T$ denotes the average value in the grand canonical ensemble at temperature T . As explained in Sec. 2.1.2, in the limit of vanishing electron concentration $\tilde{\mu} \rightarrow -\infty$, the Green's function can also be written as

$$G(t) = -i\theta(t)\langle d(t), d^\dagger \rangle_T = \frac{-i\theta(t)}{\mathcal{Z}} \sum_n \langle n | e^{-\beta K} e^{iKt} d e^{-iKt} d^\dagger | n \rangle, \quad (1.126)$$

$$\mathcal{Z} = \sum_n \langle n | e^{-\beta K} | n \rangle = \sum_n e^{-\beta K_n}, \quad (1.127)$$

where $|n\rangle$, in both Eqs. (1.126) and (1.127), represents the eigenstates of K with zero electrons and an arbitrary number of phonons, while K_n are the corresponding eigenvalues $K|n\rangle = K_n|n\rangle$. Hence

$$G(t) = \frac{-i\theta(t)}{\mathcal{Z}} \sum_n e^{-\beta K_n} \langle n | d e^{-i(K-K_n)t} d^\dagger | n \rangle. \quad (1.128)$$

In the Fourier space, the corresponding relation reads as ¹⁴

$$G(\omega) = \frac{1}{\mathcal{Z}} \sum_n e^{-\beta K_n} \langle n | d \frac{1}{\omega - (K - K_n) + i0^+} d^\dagger | n \rangle. \quad (1.129)$$

In the case of the Holstein model $K_n = n\omega_0$, giving

$$\mathcal{Z} = \sum_n e^{-\beta\omega_0 n} = \frac{1}{1 - e^{-\beta\omega_0}}, \quad (1.130)$$

¹⁴The easiest way to see this, without calculation, is to notice that Eq. (1.128) has the same functional form as the Green function of the free particle $G(t) = -i\theta(t)e^{-i\varepsilon_k t}$. Since the corresponding quantity in the Fourier space is known to be $G(\omega) = \frac{1}{\omega - \varepsilon_k + i0^+}$, we can deduce Eq. (1.129).

and

$$G(\omega) = (1 - e^{-\beta\omega_0}) \sum_n e^{-\beta\omega_0 n} \langle n | d \frac{1}{\omega + n\omega_0 - K + i0^+} d^\dagger | n \rangle. \quad (1.131)$$

Since $|n\rangle$ is purely phononic state, it can be expressed as $|n\rangle = \frac{(a^\dagger)^n}{\sqrt{n!}} |0\rangle$. Furthermore, if we introduce auxiliary quantities $G_{n,m}(\omega)$, such that

$$G_{n,m}(\omega) = \left\langle 0 \left| \frac{a^n}{\sqrt{n!}} d \frac{1}{\omega - K + i0^+} d^\dagger \frac{(a^\dagger)^m}{\sqrt{m!}} \right| 0 \right\rangle, \quad (1.132)$$

then the impurity Green's function can be written as

$$G(\omega) = (1 - e^{-\beta\omega_0}) \sum_n e^{-\beta n\omega_0} G_{n,n}(\omega + n\omega_0). \quad (1.133)$$

In this expression, we represented the Green's function in terms of $G_{n,n}$, while these are connected to the resolvent. However, $G_{n,n}$ are still unknown. This will be solved by rewriting $G_{n,n}$ using a resolvent of the free Hamiltonian, and then expressing such quantity in terms of $G_0(\omega)$.

1.9.2 Expressing Green's Function in Terms of a Resolvent of K_0

Let us now try to express $\frac{1}{\omega - K + i0^+}$ from Eq. (1.132) in terms of $\frac{1}{\omega - K_0 + i0^+}$. To accomplish this, we start from this trivial identity, which is a consequence of Eq. (1.124d)

$$\omega + i0^+ - K_0 = \omega + i0^+ - K + H_{\text{int}}. \quad (1.134)$$

Then, we multiply both sides from the left by $\frac{1}{\omega + i0^+ - K_0}$ and from the right by $\frac{1}{\omega + i0^+ - K}$. We obtain

$$\frac{1}{\omega + i0^+ - K} = \frac{1}{\omega + i0^+ - K_0} - g \frac{1}{\omega + i0^+ - K_0} d^\dagger \mathbb{1} d (a + a^\dagger) \frac{1}{\omega + i0^+ - K}, \quad (1.135)$$

where we used the definition of H_{int} from Eq. (1.67), and conveniently placed the identity operator $\mathbb{1}$ that will be useful later. Now, the expression for $G_{n,m}$ can be obtained by multiplying both sides of Eq. (1.135) from the left by $\langle n | d$ and by $d^\dagger | m \rangle$ from the right, with $|n\rangle$ ($|m\rangle$) being a state with zero electrons and n (m) phonons

$$\underbrace{\langle n | d \frac{1}{\omega + i0^+ - K} d^\dagger | m \rangle}_{=G_{n,m}(\omega)} = \langle n | d \frac{1}{\omega + i0^+ - K_0} d^\dagger | m \rangle - g \langle n | d \frac{1}{\omega + i0^+ - K_0} d^\dagger \mathbb{1} d (a + a^\dagger) \frac{1}{\omega + i0^+ - K} d^\dagger | m \rangle. \quad (1.136)$$

By expanding the identity operator $\mathbb{1} = \sum_p |p\rangle \langle p|$, the bottom line becomes

$$\begin{aligned} & - g \langle n | d \frac{1}{\omega + i0^+ - K_0} d^\dagger d (a + a^\dagger) \frac{1}{\omega + i0^+ - K} d^\dagger | m \rangle \\ & = -g \sum_p \langle n | d \frac{1}{\omega + i0^+ - K_0} d^\dagger | p \rangle \langle p | d (a + a^\dagger) \frac{1}{\omega + i0^+ - K} d^\dagger | m \rangle. \end{aligned} \quad (1.137)$$

While $|n\rangle$ and $|m\rangle$ are purely phononic states, $|p\rangle$ is initially entirely general. However, upon closer examination of Eq. (1.137), we see that it too has to be purely phononic. This is most easily seen from the scalar product in the bottom line

$$\langle n | d \frac{1}{\omega + i0^+ - K_0} d^\dagger | p \rangle, \quad (1.138)$$

and the fact that K_0 conserves the number of electrons, while $|n\rangle$ is purely phononic. If we now use the fact that the field operators a and d commute, and utilize

$$a^\dagger|p\rangle = \sqrt{p+1}|p+1\rangle, \quad (1.139)$$

$$a|p\rangle = \sqrt{p}|p-1\rangle, \quad (1.140)$$

Eq. (1.137) becomes

$$\begin{aligned} & -g\langle n|d\frac{1}{\omega+i0^+-K_0}d^\dagger d(a+a^\dagger)\frac{1}{\omega+i0^+-K}d^\dagger|m\rangle \\ &= -g\sum_p\langle n|d\frac{1}{\omega+i0^+-K_0}d^\dagger|p\rangle\left(\sqrt{p+1}\langle p+1|d\frac{1}{\omega+i0^+-K}d^\dagger|m\rangle\right. \\ & \quad \left. +\sqrt{p}\langle p-1|d\frac{1}{\omega+i0^+-K}d^\dagger|m\rangle\right). \end{aligned} \quad (1.141)$$

The first term in the round brackets is $\sqrt{p+1}G_{p+1,m}(\omega)$, while the second term is $\sqrt{p}G_{p-1,m}(\omega)$. Hence

$$\begin{aligned} & -g\langle n|d\frac{1}{\omega+i0^+-K_0}d^\dagger d(a+a^\dagger)\frac{1}{\omega+i0^+-K}d^\dagger|m\rangle \\ &= -g\sum_p\langle n|d\frac{1}{\omega+i0^+-K_0}d^\dagger|p\rangle\left(\sqrt{p+1}G_{p+1,m}(\omega)+\sqrt{p}G_{p-1,m}(\omega)\right). \end{aligned} \quad (1.142)$$

Plugging this into Eq. (1.136), we find that

$$\begin{aligned} G_{n,m}(\omega) &= \langle n|d\frac{1}{\omega+i0^+-K_0}d^\dagger|m\rangle \\ & \quad -g\sum_p\langle n|d\frac{1}{\omega+i0^+-K_0}d^\dagger|p\rangle\left(\sqrt{p+1}G_{p+1,m}(\omega)+\sqrt{p}G_{p-1,m}(\omega)\right). \end{aligned} \quad (1.143)$$

In the following text, we will see how the resolvent $\langle n|d\frac{1}{\omega+i0^+-K_0}d^\dagger|m\rangle$ can be expressed in terms of G_0 . Hence, we will have a recurrence relation for $G_{n,m}$ that will turn out to be solvable.

1.9.3 Expressing a Resolvent of K_0 in Terms of a Free Green's Function G_0

Just as we explained in Remark 5, the free Green's function $G_0(\omega)$ corresponds to the Hamiltonian $K_0 - H_{\text{ph}}$. This Hamiltonian does not have any phonons. Hence, analogous to the derivation we presented in Sec. 1.9.1, we deduce that $G_0(\omega)$ must satisfy

$$G_0(\omega) = \langle 0|d\frac{1}{\omega+i0^+-(K_0-H_{\text{ph}})}d^\dagger|0\rangle, \quad (1.144)$$

as seen from Eq. (1.129) when the phononic degrees of freedom are removed. Our task is to explore the relationship between the resolvent $\langle n|d\frac{1}{\omega+i0^+-K_0}d^\dagger|m\rangle$ and Eq. (1.144):

$$\begin{aligned} \langle n|d\frac{1}{\omega+i0^+-K_0}d^\dagger|m\rangle &= \langle n|d\frac{1}{\omega+i0^+-(K_0-H_{\text{ph}})-H_{\text{ph}}}d^\dagger|m\rangle \\ &= \langle 0|d\frac{\delta_{n,m}}{(\omega-n\omega_0)+i0^+-(K_0-H_{\text{ph}})}d^\dagger|0\rangle \\ &= \delta_{n,m}G_0(\omega-n\omega_0), \end{aligned} \quad (1.145)$$

where in the second line we used that

- $|n\rangle$ and $|m\rangle$ are purely phononic and eigenstates of H_{ph} , i.e., $H_{\text{ph}}|n\rangle = n\omega_0|n\rangle$.
- $[K_0, H_{\text{ph}}] = 0$
- There are no phonons in the Hamiltonian $K_0 - H_{\text{ph}}$

1.9.4 Recurrence Relation for $G_{n,m}$

If we plug Eq. (1.145) into Eq. (1.143), we finally obtain a Recurrence relation for $G_{n,m}$

$$\begin{aligned}
G_{n,m}(\omega) &= \delta_{n,m}G_0(\omega - n\omega_0) - g \sum_p \delta_{n,p}G_0(\omega - n\omega_0) \left(\sqrt{p+1}G_{p+1,m}(\omega) + \sqrt{p}G_{p-1,m}(\omega) \right) \\
&= \delta_{n,m}G_0(\omega - n\omega_0) - gG_0(\omega - n\omega_0) \left(\sqrt{n+1}G_{n+1,m}(\omega) + \sqrt{n}G_{n-1,m}(\omega) \right) \\
&= \delta_{n,m}G_0(\omega - n\omega_0) - gG_0(\omega - n\omega_0) \sum_p \left(\sqrt{p}\delta_{n,p-1} + \sqrt{p+1}\delta_{n,p+1} \right) G_{p,m}(\omega). \quad (1.146)
\end{aligned}$$

If we use a shorthand notation

$$\begin{aligned}
G_{n,m} &\equiv G_{n,m}(\omega) \\
G_{0n} &\equiv G_0(\omega - n\omega_0) \quad (1.147a)
\end{aligned}$$

$$X_{n,p} \equiv \sqrt{p+1}\delta_{n,p+1} + \sqrt{p}\delta_{n,p-1}, \quad (1.147b)$$

then Eq. (1.146) can be written as

$$G_{n,m} = G_{0n}\delta_{n,m} - g \sum_p G_{0n}X_{n,p}G_{p,m}. \quad (1.148)$$

Furthermore, if we introduce the matrices \tilde{G} , \tilde{G}_0 , and \tilde{X} , such that their elements in the n -th row and m -th column of the matrix are given by $G_{n,m}$, $G_{0n}\delta_{n,m}$, and $X_{n,m}$, respectively, then the recurrence relation acquires the following form

$$\tilde{G} = \tilde{G}_0 - g\tilde{G}_0\tilde{X}\tilde{G}. \quad (1.149)$$

This looks like the Dyson equation. We solve it by rewriting it as

$$\left(1 + g\tilde{G}_0\tilde{X}\right)\tilde{G} = \tilde{G}_0, \quad (1.150)$$

and multiplying this whole expression by \tilde{G}_0^{-1} from the left and by \tilde{G}^{-1} from the right

$$\begin{aligned}
\tilde{G}^{-1} &= \tilde{G}_0^{-1} + g\tilde{X} \\
&= \begin{bmatrix} G_0^{-1}(\omega) & g\sqrt{1} & 0 & 0 & 0 & \dots \\ g\sqrt{1} & G_0^{-1}(\omega - \omega_0) & g\sqrt{2} & 0 & 0 & \dots \\ 0 & g\sqrt{2} & G_0^{-1}(\omega - 2\omega_0) & g\sqrt{3} & 0 \dots & \dots \\ 0 & 0 & g\sqrt{3} & G_0^{-1}(\omega - 3\omega_0) & g\sqrt{4} & \dots \\ 0 & 0 & 0 & g\sqrt{4} & G_0^{-1}(\omega - 4\omega_0) & \dots \\ \vdots & \vdots & \vdots & \vdots & \vdots & \ddots \end{bmatrix}. \quad (1.151)
\end{aligned}$$

Hence, $G_{n,m}$ is found by inverting this large matrix.

1.9.5 Final Solution of the Impurity Problem

Finite-Temperature Case

Let us now go back to Eq. (1.133). We see that we actually only need $G_{n,m}$ for $n = m$. To find these, we need to invert the matrix in Eq. (1.151) and take its n -th diagonal element. But this matrix is a symmetric tridiagonal matrix! A detailed solution of this problem, for a general symmetric tridiagonal matrix, was already presented in Appendix. D. Therefore, we apply Eq. (D.12), setting $b_n^2 = ng^2$ and $a_n = G_0^{-1}(\omega - n\omega_0)$, and finally obtain the solution of the impurity problem in terms of the continued fraction expansion.

$$G(\omega) = (1 - e^{-\beta\omega_0}) \sum_n e^{-\beta n\omega_0} G_{n,n}(\omega + n\omega_0), \quad (1.152a)$$

$$G_{n,n}(\omega + n\omega_0) = \frac{1}{G_0^{-1}(\omega) - A_n(\omega) - B_n(\omega)}, \quad (1.152b)$$

$$A_n(\omega) = \frac{ng^2}{G_0^{-1}(\omega + \omega_0) - \frac{(n-1)g^2}{G_0^{-1}(\omega+2\omega_0) - \frac{(n-2)g^2}{\ddots - \frac{g^2}{G_0^{-1}(\omega+(n-1)\omega_0) - \frac{g^2}{G_0^{-1}(\omega+n\omega_0)}}}}}, \quad (1.152c)$$

$$B_n(\omega) = \frac{(n+1)g^2}{G_0^{-1}(\omega - \omega_0) - \frac{(n+2)g^2}{G_0^{-1}(\omega-2\omega_0) - \frac{(n+3)g^2}{G_0^{-1}(\omega-3\omega_0) - \frac{(n+4)g^2}{\ddots}}}}}. \quad (1.152d)$$

At last, the self-energy is obtained via the Dyson equation

$$\Sigma(\omega) = G_0^{-1}(\omega) - G^{-1}(\omega). \quad (1.153)$$

Zero-Temperature Case

In the limit $T \rightarrow 0$ (i.e., $\beta \rightarrow \infty$), only the $n = 0$ term is contributing. Since $A_0(\omega) = 0$, we conclude that

$$G(\omega) = G_{0,0}(\omega) = \frac{1}{G_0^{-1}(\omega) - B_0(\omega)}. \quad (1.154)$$

Furthermore, using the Dyson equation, the self-energy reads as

$$\Sigma(\omega) \Big|_{T=0} = \frac{g^2}{G_0^{-1}(\omega - \omega_0) - \frac{2g^2}{G_0^{-1}(\omega-2\omega_0) - \frac{3g^2}{G_0^{-1}(\omega-3\omega_0) - \frac{4g^2}{\ddots}}}}}. \quad (1.155)$$

Remark 6. In the atomic limit ($t_0 = 0$), the Holstein lattice problem actually reduces to the Holstein-Anderson impurity problem, defined by Eq. (1.67), with $E_{\mathbf{k}} = V_{\mathbf{k}} = 0$. Hence, the expressions that we derived in this section actually represent the exact solution in the atomic limit, if we set $G_0^{-1}(\omega) = \omega$, as seen from Eq. (1.82).

1.9.6 Numerical Implementation of the Impurity Solver

The solution of the impurity problem (1.152) requires the calculation of continued fractions. Numerically, these quantities are calculated using iterative procedures that we formulate in the form of theorems:

Theorem 1. *Let*

- $A_n^{(n)}(\omega) \equiv 0$ and $A_n^{(k)}(\omega) \equiv 0$, for $k \geq n$.
- $A_n^{(p)}(\omega) = \frac{(n-p)g^2}{G_0^{-1}(\omega+(p+1)\omega_0) - A_n^{(p+1)}(\omega)}$, for $p < n$,

Then $A_n(\omega) = A_n^{(0)}(\omega)$.

Proof. Formally, this is proved using the method of induction. However, we will be less rigorous

$$\begin{aligned}
A_n^{(0)}(\omega) &= \frac{ng^2}{G_0^{-1}(\omega + \omega_0) - A_n^{(1)}(\omega)} = \frac{ng^2}{G_0^{-1}(\omega + \omega_0) - \frac{(n-1)g^2}{G_0^{-1}(\omega+2\omega_0) - A_n^{(2)}(\omega)}} = \dots \\
&= \frac{ng^2}{G_0^{-1}(\omega + \omega_0) - \frac{(n-1)g^2}{G_0^{-1}(\omega+2\omega_0) - \frac{(n-2)g^2}{G_0^{-1}(\omega+(n-1)\omega_0) - A_n^{(n-1)}(\omega)}}}} \\
&= \frac{ng^2}{G_0^{-1}(\omega + \omega_0) - \frac{(n-1)g^2}{G_0^{-1}(\omega+2\omega_0) - \frac{(n-2)g^2}{G_0^{-1}(\omega+(n-1)\omega_0) - \frac{g^2}{G_0^{-1}(\omega+n\omega_0)}}}}}. \tag{1.156}
\end{aligned}$$

This completes our proof. □

Theorem 2. *Let*

- $B_n^{(k=\infty)}(\omega) \equiv 0$,
- $B_n^{(k)}(\omega) = \frac{(n+k+1)g^2}{G_0^{-1}(\omega-(k+1)\omega_0) - B_n^{(k+1)}(\omega)}$

Then $B_n(\omega) = B_n^{(0)}(\omega)$.

Proof. This is also formally proved using the method of induction, but for the sake of brevity, we employ a less rigorous approach

$$\begin{aligned}
B_n^{(0)}(\omega) &= \frac{(n+1)g^2}{G_0^{-1}(\omega - \omega_0) - B_n^{(1)}(\omega)} = \frac{(n+1)g^2}{G_0^{-1}(\omega - \omega_0) - \frac{(n+2)g^2}{G_0^{-1}(\omega-2\omega_0) - B_n^{(2)}(\omega)}} = \dots \\
&= \frac{(n+1)g^2}{G_0^{-1}(\omega - \omega_0) - \frac{(n+2)g^2}{G_0^{-1}(\omega-2\omega_0) - \frac{(n+3)g^2}{G_0^{-1}(\omega-3\omega_0) - \frac{(n+4)g^2}{G_0^{-1}(\omega-4\omega_0) - \dots}}}}}. \tag{1.157}
\end{aligned}$$

□

This completes our derivation of DMFT equations.

Dynamical Mean-Field Theory: Numerical Results

The results that we present in this chapter are a product of our work that we published in Ref. [62].

2.1 Quasiparticle Properties

The quasiparticle properties (the ground state energy and the effective mass) are simple, yet important characteristics of a given physical system. There are various ways to obtain these quantities, but we will calculate them from the Green's functions formalism, as it will help us in assessing the quality of the DMFT method.

The DMFT method gives the \mathbf{k} -independent self-energy $\Sigma(\omega)$, from which the Green's function can be calculated as

$$G_{\mathbf{k}}(\omega) = \frac{1}{\omega - \varepsilon_{\mathbf{k}} - \Sigma(\omega)}. \quad (2.1)$$

The quasiparticle properties are encoded in the pole structure of this quantity, as guaranteed by the Lehmann spectral representation. Since there is only a single electron in the band, the Fermi wavevector is zero. Hence, to evaluate the ground-state energy E_p , we need to find the smallest ω , which we denote by E_p , such that the real part of the denominator of Eq. (2.1), at $T = 0$, is vanishing

$$E_p = \varepsilon_{\mathbf{k}=0} + \text{Re}\Sigma(\omega = E_p). \quad (2.2)$$

On the other hand, to find the renormalized mass m^* , we first introduce the renormalized energy $E(\mathbf{k})$ by generalizing Eq. (2.2) for arbitrary \mathbf{k} , and impose that it should be quadratic for small momenta

$$E(\mathbf{k}) = \varepsilon_{\mathbf{k}} + \text{Re}\Sigma(\omega = E(\mathbf{k})) \approx \text{const.} + \frac{\mathbf{k}^2}{2m^*}, \quad \text{around } |\mathbf{k}| \approx 0. \quad (2.3)$$

A practical way to calculate m^* is to notice that around the bottom of the band $\nabla_{\mathbf{k}}E(\mathbf{k}) \approx \mathbf{k}/m^*$. Hence, from Eq. (2.3) we deduce that around $|\mathbf{k}| \approx 0$ it holds that¹

$$\frac{\mathbf{k}}{m^*} = \nabla_{\mathbf{k}}E(\mathbf{k}) = \nabla_{\mathbf{k}}\varepsilon_{\mathbf{k}} + \nabla_{\mathbf{k}}\text{Re}\Sigma(\omega = E(\mathbf{k})) \approx \frac{\mathbf{k}}{m_0} + \left. \frac{\partial \text{Re}\Sigma(\omega)}{\partial \omega} \right|_{\omega=E_p} \nabla_{\mathbf{k}}E_{\mathbf{k}}, \quad (2.4)$$

where we introduced the band mass m_0 analogous to m^* in Eq. (2.3), when the renormalized energy is substituted with the nonrenormalized dispersion $E(\mathbf{k}) \rightarrow \varepsilon_{\mathbf{k}}$. Going back to Eq. (2.4), we see that m^* can be expressed in terms of the self-energy as follows

$$m^* = m_0 \left(1 - \left. \frac{\partial \text{Re}\Sigma(\omega)}{\partial \omega} \right|_{\omega=E_p} \right). \quad (2.5)$$

¹We use that $E(\mathbf{k} = 0) = E_p$.

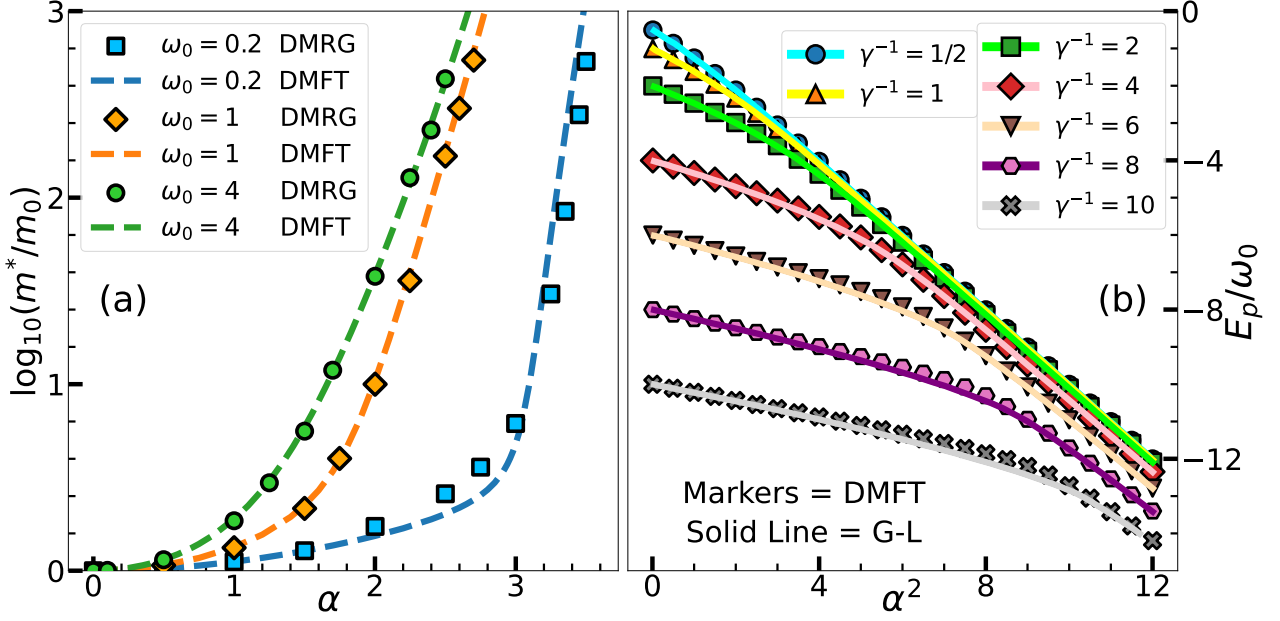


Figure 2.1: a) Comparison of the DMFT and DMRG (taken from Refs. [40, 43]) renormalized electron mass in the 1D system, at $T = 0$. (b) Comparison of the ground state energy from the DMFT and the global-local variational approach (taken from Ref. [43]) in the 1D system, at $T = 0$.

In the case of a tight-binding model on a hypercubic lattice in d dimensions, the band mass m_0 can be calculated using

$$\epsilon_{\mathbf{k}} = -2t_0 \sum_{i=1}^d \cos k_i \approx -2t_0 \sum_{i=1}^d \left(1 - \frac{k_i^2}{2}\right) = \text{const.} + t_0 \sum_{i=1}^d k_i^2 = \text{const.} + t_0 \mathbf{k}^2. \quad (2.6)$$

From here, it directly follows that $m_0 = 1/(2t_0)$, and this remains true irrespective of the number of dimensions.

Let us now examine some numerical results. We apply the DMFT algorithm from Fig. 1.2 to calculate the self-energy, and then use Eqs. (2.5) and (2.2) to calculate the quasiparticle properties. In Fig. 2.1(a) we show the DMFT results in 1D for the electron effective mass over a broad range of parameters, covering practically the whole parameter space in the (γ, λ) plane. We see that the mass renormalization is in striking agreement with the DMRG result [40, 43] which presents the best available result from the literature. Small discrepancies are visible only for stronger interaction with small ω_0 . A similar level of agreement can be seen in the comparison of the ground state (polaron) energy E_p in Fig. 2.1(b). Here, the results obtained with variational global-local method [43, 44] are taken as a reference. While the agreement in the weak coupling and in the atomic limit could be anticipated since the DMFT becomes exact in these limits, we find the quantitative agreement in the crossover regime between these two limits rather surprising, bearing in mind that the DMFT completely neglects nonlocal correlations.

We have also calculated the effective mass for two- and three-dimensional lattices (see Fig. 2.2(a)). We observe an excellent agreement with the continuous-time path-integral quantum Monte Carlo (QMC) calculation from Ref. [42], which has the reported numerical accuracy of 0.1% – 0.3%. This was now expected since the importance of nonlocal correlations decreases in higher dimensions.

It is interesting to note that none of this was not observed earlier. In the standard reference of Ciuchi *et al.* [56], the DMFT is applied only to the Bethe lattice, and this result was often used in comparison with other reliable results obtained on finite-dimensional lattices. Used in this way, it seems that the DMFT provides only a qualitative description of the Holstein model [23, 39, 43, 61, 71].

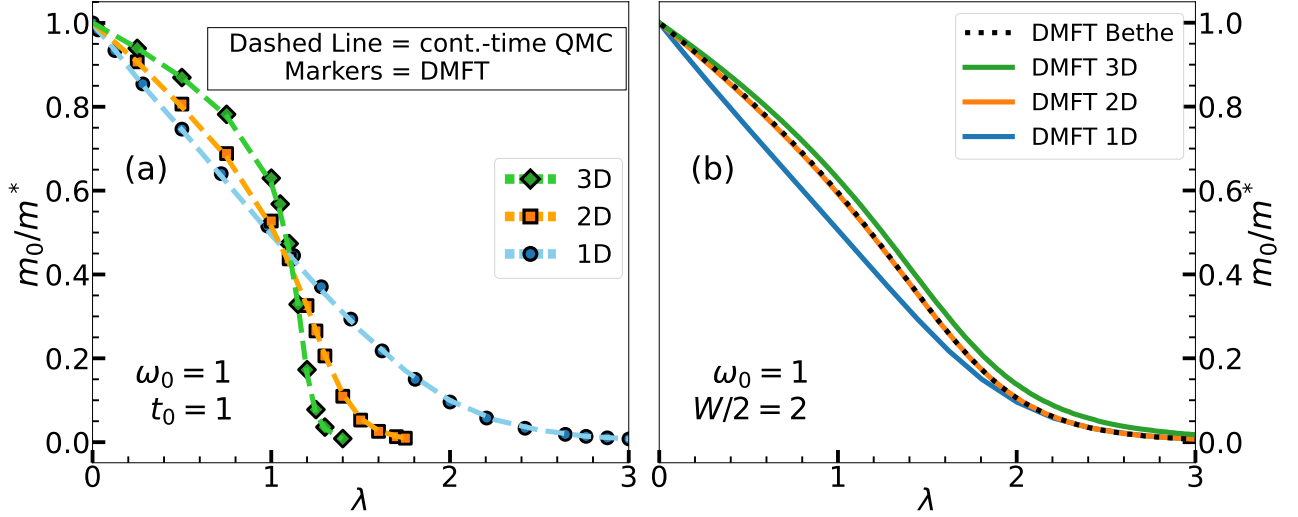


Figure 2.2: (a) Continuous-time QMC (taken from Ref. [42]) vs. DMFT mass renormalization in 1D, 2D and 3D, with $\omega_0 = 1$. (b) Comparison of the DMFT mass renormalization on different lattices. Here, the half-bandwidth $W/2$ is set to unity.

We illustrate this in Fig. 2.2(b), where we compare the renormalized mass results on a Bethe lattice, with the results obtained on 1D, 2D, and 3D lattices.

Remark 7. *The difference between the DMFT algorithm on different lattices lies in the self-consistency condition. In the 1D and 2D cases, these conditions are given by Eqs. (1.108) and (1.114), respectively. In the 3D case, we do not have a nice analytic solution, but Eq. (1.123) nevertheless gives a nice and stable result. A self-consistency condition for the Bethe lattice reads as*

$$G_0(\omega) = \left(\omega - \frac{(W/2)^2}{4} G(\omega) \right)^{-1}, \quad (2.7)$$

where $W/2$ is the half bandwidth.

It is rather surprising that there is a striking agreement between the effective mass for 2D and the Bethe lattice as shown in Fig. 2.2(b), even though the noninteracting densities of states are different. To make this analysis even more complete, we also provide comparisons between the 1D and 2D spectral functions with the spectral functions on a Bethe lattice; see Fig. 2.3. The Bethe lattice lacks a dispersion relation since it has no translational symmetry. Therefore in Fig. 2.3 we compare only the local spectral functions $A(\omega) = -\frac{1}{\pi} \text{Im} G(\omega) = -\frac{1}{\pi} \text{Im} \frac{1}{N} \sum_{\mathbf{k}} G_{\mathbf{k}}(\omega)$ of the Bethe, and finite-dimensional lattices. For small couplings, the spectral functions resemble the noninteracting density of state and we find a large discrepancy, as shown in panels (a) and (b). However, as the interaction increases the spectral functions become more alike. The agreement between 2D and Bethe results is very good, even for moderate interactions. Although these findings are completely unexpected, we will not delve further into their analysis, as our main focus is establishing the quality of DMFT method for the prediction of single-particle properties within the Holstein model.

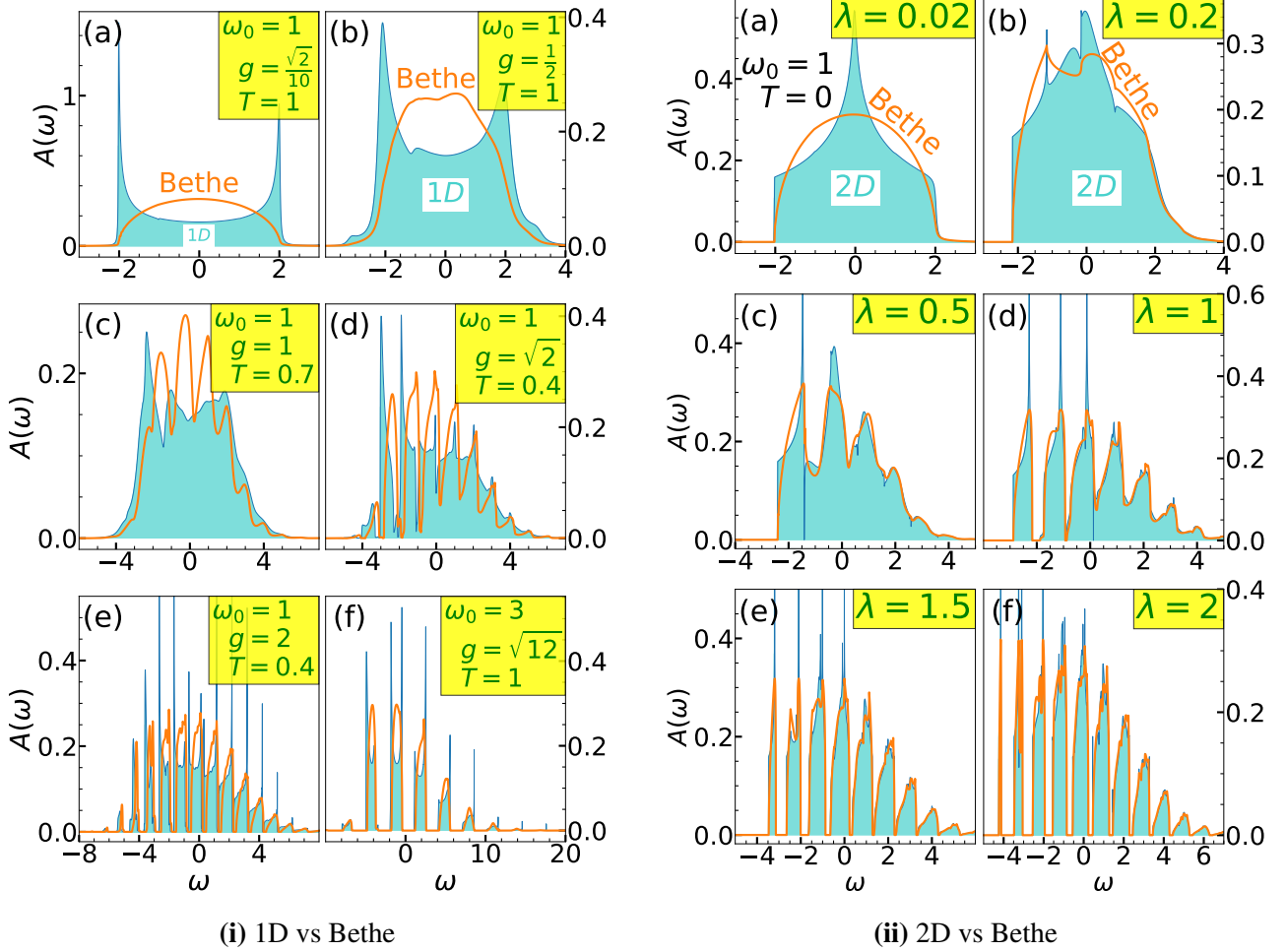


Figure 2.3: Comparison of DMFT local spectral functions on different lattices

2.2 Spectral Functions for Weak Electron-phonon Coupling

In the previous section, we demonstrated that the DMFT gives extremely accurate predictions of the quasiparticle properties. In doing so, we used a variety of different benchmarks from the literature. Since we now want to investigate the accuracy of DMFT spectral functions in the weak coupling limit, some benchmark methods are also needed here as well. One such promising candidate is the self-consistent Migdal approximation (SCMA).

2.2.1 Benchmark Method: Self-Consistent Migdal Approximation

In Sec. 2.2 of Part I, we introduced the one-shot Migdal approximation. It is a perturbative method that takes into account only the lowest-order Feynman diagram in the self-energy; see Eq. (2.17) of Part I. As such, it is accurate only for very small couplings g , and thus it is not a reliable benchmark for assessing the quality of the DMFT results in a somewhat broader range of parameter regimes. Luckily, a significant improvement can be easily constructed by generalizing the Migdal approximation, such that the noninteracting fermion propagator in Eq. (2.17) from Part I is substituted with the full (interacting) propagator; see the top row of Fig. 2.4. This equation needs to be supplemented by the Dyson equation, which relates the full Green's function back to the self-energy Σ^{SCMA} . Hence, these equations need to be solved self-consistently. This constitutes the SCMA method. We note that some further insight about this method can be gained if we expand the full Green's function in terms of the noninteracting Green's function: as shown in the bottom row of Fig. 2.4, in addition to the Migdal diagram in panel 2.4(b), SCMA consists of a series of non-crossing diagrams; see panels 2.4(c)–(e).

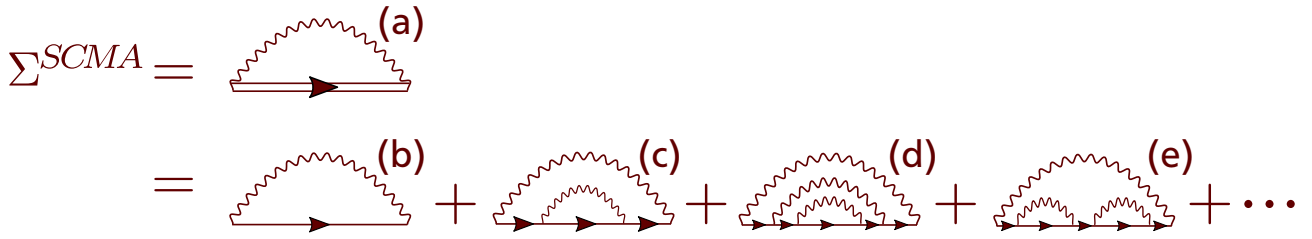


Figure 2.4: Feynman diagrams for the self-consistent Migdal approximation.

However, despite the fact that this series is infinite, it fails to reproduce even some low-order diagrams; see Fig. 2.5. This is one of the shortcomings of this method.

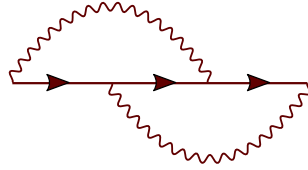


Figure 2.5: The lowest Feynman diagram missing in the SCMA.

Let us now derive the SCMA equations that are needed for the application of this method in practice. This derivation will be performed in the grand canonical ensemble. We will concentrate on the calculation of the self-energy since all single-particle properties are easily obtained from it. Using the Feynman rules (see Sec. 2.1.1 of Part I), we see that the self-energy from Fig 2.4(a) can be written as:

$$\Sigma_{\mathbf{k}}(i\omega_n) = -\frac{g^2}{\beta N} \sum_{\mathbf{q}, \nu_n} G_{\mathbf{k}-\mathbf{q}}(i\omega_n - i\nu_n) \frac{2\omega_0}{(i\nu_n)^2 - \omega_0^2}, \quad (2.8)$$

where $G_{\mathbf{k}}(i\omega_n - i\nu_n)$ is the full electron propagator. The frequency dependence of this quantity can be expressed explicitly using the spectral representation

$$G_{\mathbf{k}}(i\omega_n - i\nu_n) = \int d\xi \frac{A_{\mathbf{k}}(\xi)}{(i\omega_n - i\nu_n - \xi)}, \quad (2.9)$$

where $A_{\mathbf{k}}$ is the spectral function. Plugging this back into Eq. (2.8), we can perform the sum over Matsubara frequencies ν_n using a well-known trick

$$\frac{1}{\beta} \sum_{\nu_n} F(i\nu_n) = - \int_C \frac{dz}{2\pi i} F(z) b(z), \quad (2.10)$$

where $b(z) = 1/(e^{\beta z} - 1)$ is the Bose function and C is a counterclockwise contour around the poles and branch cuts of $F(z)$. Integral over z is easy to solve using the residue theorem, giving

$$\Sigma_{\mathbf{k}}(i\omega_n) = \frac{g^2}{N} \sum_{\mathbf{q}} \int d\xi A_{\mathbf{k}-\mathbf{q}}(\xi) \left[\frac{b(\omega_0) - b(i\omega_n - \xi)}{i\omega_n - \omega_0 - \xi} - \frac{b(-\omega_0) - b(i\omega_n - \xi)}{i\omega_n + \omega_0 - \xi} \right]. \quad (2.11)$$

This expression can be further simplified, using the properties of the Bose function $b(i\omega_n - \xi) = -f(-\xi)$ and $b(-\omega_0) = -1 - b(\omega_0)$, where we introduced the Fermi function as $f(z) = 1/(e^{\beta z} + 1)$. Furthermore, one should notice that the subintegral function in Eq. (2.11) is actually vanishingly small, unless ξ is extremely large. This is a consequence of the fact that the spectral function $A_{\mathbf{k}}(\xi)$ vanishes when we are very far away from $\xi = \xi(\mathbf{k}) = \varepsilon(\mathbf{k}) - \tilde{\mu}$, and in our case $\tilde{\mu} \rightarrow -\infty$. Hence, we can

restrict the integration in Eq. (2.11) to a domain of very large ξ . In that case we can approximate $f(\xi) \approx 0$ and $f(-\xi) \approx 1$. Combining all of these insights, we obtain

$$\Sigma_{\mathbf{k}}(i\omega_n) = \frac{g^2}{N} \sum_{\mathbf{q}} \int d\xi A_{\mathbf{k}-\mathbf{q}}(\xi) \left[\frac{n_{\text{ph}} + 1}{i\omega_n - \omega_0 - \xi} + \frac{n_{\text{ph}}}{i\omega_n + \omega_0 - \xi} \right], \quad (2.12)$$

where we introduced $n_{\text{ph}} = b(\omega_0)$. Once again, using the spectral representation from Eq. (2.9), the above expression can be written as

$$\Sigma_{\mathbf{k}}(i\omega_n) = \frac{g^2(1 + n_{\text{ph}})}{N} \sum_{\mathbf{q}} G_{\mathbf{k}-\mathbf{q}}(i\omega_n - \omega_0) + \frac{g^2 n_{\text{ph}}}{N} \sum_{\mathbf{q}} G_{\mathbf{k}-\mathbf{q}}(i\omega_n + \omega_0). \quad (2.13)$$

The right-hand side can be cast into an even simpler form if we use the fact that the local Green's function $G(\omega)$ can be written as $G(\omega) = \frac{1}{N} \sum_{\mathbf{q}} G_{\mathbf{k}-\mathbf{q}}(\omega)$. Furthermore, since this quantity is momentum-independent, we conclude that SCMA self-energy is also \mathbf{k} -independent. Therefore, after performing the Wick rotation $i\omega_n \rightarrow \omega + i0^+$ we finally obtain

$$\Sigma(\omega) = g^2(1 + n_{\text{ph}})G(\omega - \omega_0) + g^2 n_{\text{ph}} G(\omega + \omega_0). \quad (2.14)$$

The local Green's function on the right-hand is actually the same quantity that we already examined in Secs. 1.8.2, 1.8.3, and 1.8.4. Hence, depending on the lattice we are examining, Eqs. (1.108),(1.114), or (1.123), represent another relation between the Green's function and the self-energy. Each of these, in conjunction with Eq. (2.14), constitute a set of equations that are solved self-consistently. In practice, we start from the self-energy in the Migdal approximation and, depending on the lattice, use Eqs. (1.108),(1.114), or (1.123) to calculate the local Green's function. Then, Eq. (2.14) can be used to obtain the self-energy in the next interaction. This procedure is repeated over and over again, until the self-energy has converged.

2.2.2 DMFT vs. SCMA in the Weak Coupling Limit

A comparison of the DMFT and SCMA spectral functions, for weak electron-phonon coupling, is shown in Fig. 2.6. We note that no artificial broadening was used in any of the plots. As we see, the results almost fully coincide. This proves that DMFT is in fact reliable in the weak-coupling regime.

2.3 Spectral Sum Rules

2.3.1 Introduction

In the Sec. 2.4 of Part I, we defined the spectral sum rules in Eq. (2.39). Here, we will be examining the first few sum rules within the DMFT and SCMA. This analysis is relevant when the parameters g, T are not too large. This is because the spectral functions, in this case, have a simple one or two peak structure, as we already saw in Fig. 2.6. Hence, our goal is to support and somewhat extend the conclusions of the previous chapter.

In the previous sections, we always had a benchmark method that assessed the quality of our results. Since the spectral sum rules in the Holstein model can be calculated exactly [57], we will use these as our benchmark.

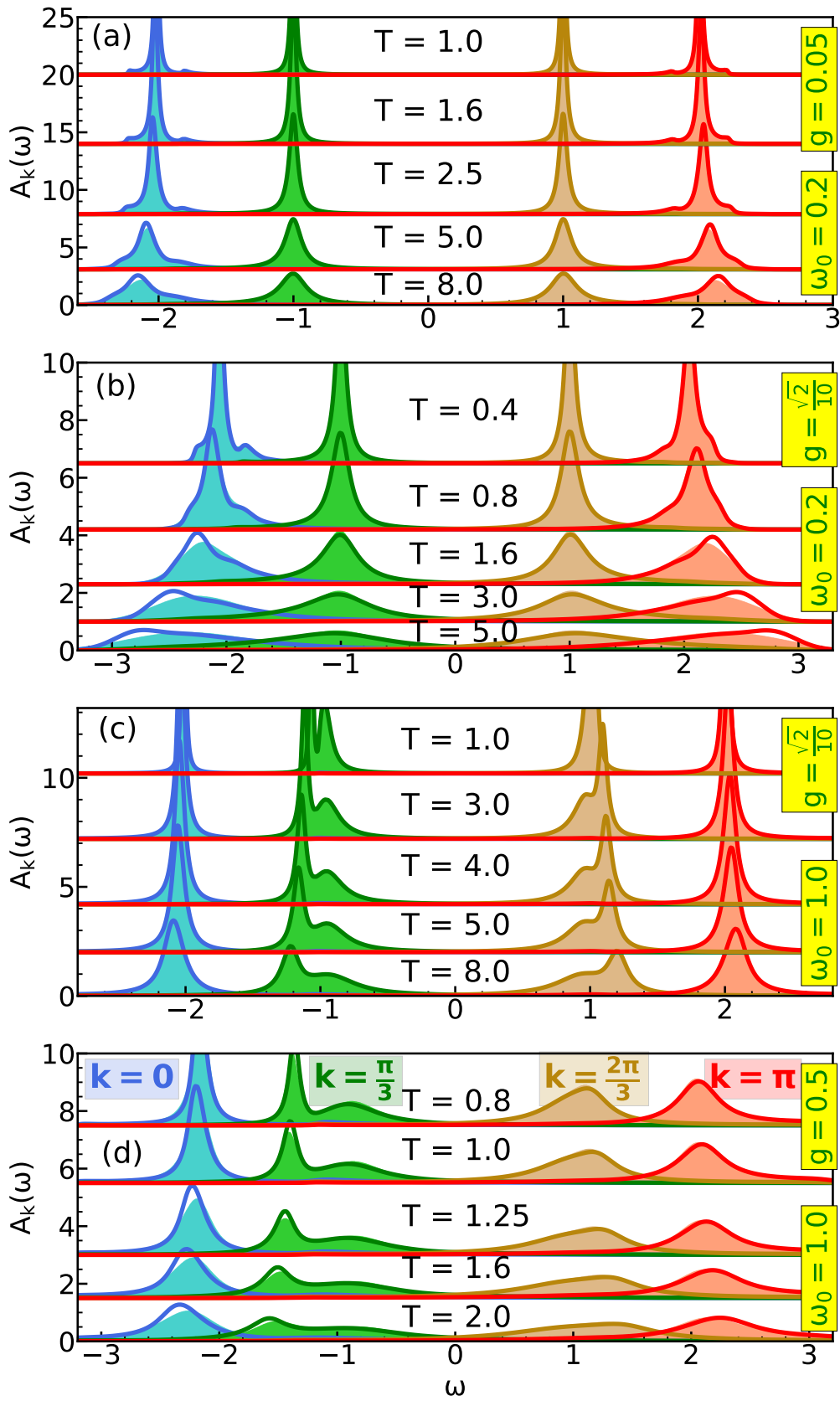


Figure 2.6: DMFT vs. SCMA spectral functions in the weak coupling regime.

2.3.2 Spectral Sum Rules: Exact Results

The spectral sum rules can be obtained using the expression we obtained in Eq. (2.42) of Part I. The results for $0 \leq n \leq 8$ read as

$$\mathcal{M}_0(\mathbf{k}) = 1, \quad (2.15a)$$

$$\mathcal{M}_1(\mathbf{k}) = \varepsilon_{\mathbf{k}}, \quad (2.15b)$$

$$\mathcal{M}_2(\mathbf{k}) = (2n_{\text{ph}} + 1)g^2 + \varepsilon_{\mathbf{k}}^2, \quad (2.15c)$$

$$\mathcal{M}_3(\mathbf{k}) = 2(2n_{\text{ph}} + 1)g^2\varepsilon_{\mathbf{k}} + g^2\omega_0 + \varepsilon_{\mathbf{k}}^3, \quad (2.15d)$$

$$\mathcal{M}_4(\mathbf{k}) = 3g^4(2n_{\text{ph}} + 1)^2 + g^2(2n_{\text{ph}} + 1)(3\varepsilon_{\mathbf{k}}^2 + 2t_0^2 + \omega_0^2) + 2g^2\omega_0\varepsilon_{\mathbf{k}} + \varepsilon_{\mathbf{k}}^4, \quad (2.15e)$$

$$\begin{aligned} \mathcal{M}_5(\mathbf{k}) &= 7g^4(2n_{\text{ph}} + 1)^2\varepsilon_{\mathbf{k}} + g^2(3\omega_0\varepsilon_{\mathbf{k}}^2 + 6t_0^2\omega_0 + \omega_0^3) \\ &\quad + (2n_{\text{ph}} + 1)(10g^4\omega_0 + g^2(4t_0^2\varepsilon_{\mathbf{k}} + 2\omega_0^2\varepsilon_{\mathbf{k}} + 4\varepsilon_{\mathbf{k}}^3)) + \varepsilon_{\mathbf{k}}^5, \end{aligned} \quad (2.15f)$$

$$\begin{aligned} \mathcal{M}_6(\mathbf{k}) &= \varepsilon_{\mathbf{k}}^6 + 15g^6(2n_{\text{ph}} + 1)^3 + g^4(2n_{\text{ph}} + 1)^2(12\varepsilon_{\mathbf{k}}^2 + 18t_0^2 + 15\omega_0^2) \\ &\quad + 10g^4\omega_0^2 + g^2(12t_0^2\omega_0\varepsilon_{\mathbf{k}} + 4\omega_0\varepsilon_{\mathbf{k}}^3 + 2\omega_0^3\varepsilon_{\mathbf{k}}) \\ &\quad + (2n_{\text{ph}} + 1)(22g^4\omega_0\varepsilon_{\mathbf{k}} + g^2(6t_0^2\varepsilon_{\mathbf{k}}^2 + 3\omega_0^2\varepsilon_{\mathbf{k}}^2 + 5\varepsilon_{\mathbf{k}}^4 + 12t_0^2\omega_0^2 + 6t_0^4 + \omega_0^4)), \end{aligned} \quad (2.15g)$$

$$\begin{aligned} \mathcal{M}_7(\mathbf{k}) &= 36g^6(2n_{\text{ph}} + 1)^3\varepsilon_{\mathbf{k}} + 21g^4\omega_0^2\varepsilon_{\mathbf{k}} \\ &\quad + g^2(18t_0^2\omega_0\varepsilon_{\mathbf{k}}^2 + 3\omega_0^3\varepsilon_{\mathbf{k}}^2 + 5\omega_0\varepsilon_{\mathbf{k}}^4 + 20t_0^2\omega_0^3 + 30t_0^4\omega_0 + \omega_0^5) \\ &\quad + (2n_{\text{ph}} + 1)^2(105g^6\omega_0 + g^4(41t_0^2\varepsilon_{\mathbf{k}} + 32\omega_0^2\varepsilon_{\mathbf{k}} + 18\varepsilon_{\mathbf{k}}^3)) \\ &\quad + (2n_{\text{ph}} + 1)g^4(36\omega_0\varepsilon_{\mathbf{k}}^2 + 108t_0^2\omega_0 + 56\omega_0^3) \\ &\quad + (2n_{\text{ph}} + 1)g^2(2\varepsilon_{\mathbf{k}}(12t_0^2\omega_0^2 + 6t_0^4 + \omega_0^4) + 8t_0^2\varepsilon_{\mathbf{k}}^3 + 4\omega_0^2\varepsilon_{\mathbf{k}}^3 + 6\varepsilon_{\mathbf{k}}^5) + \varepsilon_{\mathbf{k}}^7, \end{aligned} \quad (2.15h)$$

$$\begin{aligned} \mathcal{M}_8(\mathbf{k}) &= 105g^8(2n_{\text{ph}} + 1)^4 + g^6(2n_{\text{ph}} + 1)^3(64\varepsilon_{\mathbf{k}}^2 + 160t_0^2 + 210\omega_0^2) \\ &\quad + g^4(33\omega_0^2\varepsilon_{\mathbf{k}}^2 + 158t_0^2\omega_0^2 + 56\omega_0^4) \\ &\quad + g^2(24t_0^2\omega_0\varepsilon_{\mathbf{k}}^3 + 40t_0^2\omega_0^3\varepsilon_{\mathbf{k}} + 60t_0^4\omega_0\varepsilon_{\mathbf{k}} + 6\omega_0\varepsilon_{\mathbf{k}}^5 + 4\omega_0^3\varepsilon_{\mathbf{k}}^3 + 2\omega_0^5\varepsilon_{\mathbf{k}}) \\ &\quad + (2n_{\text{ph}} + 1)^2(236g^6\omega_0\varepsilon_{\mathbf{k}} + g^4(68t_0^2\varepsilon_{\mathbf{k}}^2 + 51\omega_0^2\varepsilon_{\mathbf{k}}^2 + 25\varepsilon_{\mathbf{k}}^4 + 258t_0^2\omega_0^2 + 94t_0^4 + 63\omega_0^4)) \\ &\quad + 280(2n_{\text{ph}} + 1)g^6\omega_0^2 + (2n_{\text{ph}} + 1)g^4(240t_0^2\omega_0\varepsilon_{\mathbf{k}} + 52\omega_0\varepsilon_{\mathbf{k}}^3 + 116\omega_0^3\varepsilon_{\mathbf{k}}) \\ &\quad + 3(2n_{\text{ph}} + 1)g^2\varepsilon_{\mathbf{k}}^2(12t_0^2\omega_0^2 + 6t_0^4 + \omega_0^4) \\ &\quad + (2n_{\text{ph}} + 1)g^2(10t_0^2\varepsilon_{\mathbf{k}}^4 + 5\omega_0^2\varepsilon_{\mathbf{k}}^4 + 7\varepsilon_{\mathbf{k}}^6 + 90t_0^4\omega_0^2 + 30t_0^2\omega_0^4 + 20t_0^6 + \omega_0^6) + \varepsilon_{\mathbf{k}}^8. \end{aligned} \quad (2.15i)$$

We note that the results for $0 \leq n \leq 4$ originally appeared in Ref. [57], $n = 5$ result was calculated in Ref. [62], while the results for $n = 6, 7, 8$ are presented here for the first time.

2.3.3 Spectral Sum Rules: SCMA Predictions

Berciu and collaborators [53, 72] introduced a nice method for determining how many sum rules a method we are examining satisfies, if we know its diagrammatic expansion (see Fig. 2.4) and the lowest order diagram that is missing from that expansion (see Fig. 2.5). We now briefly review that method, in the case of SCMA. Let

$$\widetilde{\mathcal{M}}_n(\mathbf{k}) \equiv \int d\omega \omega^n G_k(\omega). \quad (2.16)$$

Now, the spectral sum rules can be written as

$$\mathcal{M}_n(\mathbf{k}) = \int d\omega \omega^n A_k(\omega) = -\frac{1}{\pi} \text{Im} \widetilde{\mathcal{M}}_n(\mathbf{k}). \quad (2.17)$$

We note that the real part of the $\widetilde{\mathcal{M}}_n$ can even be infinite or undefined, since it is only the imaginary part that we are interested in. The Green's function from Eq. (2.16) can now be rewritten in terms of

the self-energy, using the Dyson equation ²

$$G_k(\omega) = \frac{1}{G_0^{-1}(\omega) - \Sigma_k(\omega)} = G_0(\omega) [1 + G_0(\omega)\Sigma_k(\omega) + (G_0(\omega)\Sigma_k(\omega))^2 + \dots], \quad (2.18)$$

while the self-energy itself can be expanded in the series with respect to the electron-phonon coupling strength g

$$\Sigma_k(\omega) = g^2\Sigma^{(2)}(\omega) + g^4\Sigma^{(4)}(\omega) + \dots \quad (2.19)$$

where $\Sigma^{(n)}(\omega)$ denotes the SCMA self-energy terms which have exactly n vertices. Plugging all of this back into (2.16), we get:

$$\begin{aligned} \widetilde{\mathcal{M}}_n = & \underbrace{\int d\omega \omega^n G_0(\omega)}_I + g^2 \underbrace{\int d\omega \omega^n G_0(\omega)^2 \Sigma^{(2)}(\omega)}_{II} \\ & + g^4 \underbrace{\int d\omega \omega^n G_0(\omega)^2 \Sigma^{(4)}(\omega)}_{III} + g^4 \underbrace{\int d\omega \omega^n G_0(\omega)^3 (\Sigma^{(2)}(\omega))^2}_{IV} + \dots \end{aligned} \quad (2.20)$$

Let us now see how much does each of these terms contribute to the spectral sum rules. Before we do that, we first need to notice that each of these terms has an integrand which is completely analytic in the upper-half complex ω plane. Hence, if the integrand is decaying faster than $\frac{1}{\omega}$, for $\omega \rightarrow \pm\infty$, we can close the complex contour from the upper half side³. Since there are no complex poles in the upper-half plane, the integral is vanishing. Hence, we conclude that if the integrand is decaying faster than $\frac{1}{\omega}$ for $\omega \rightarrow \pm\infty$, the corresponding term does not contribute to the spectral sum rule. Our task is thus reduced to finding the asymptotic expansion for each of the subintegral functions in Eq. (2.20).

In order to do this, we first note that $G_0(\omega) \propto \frac{1}{\omega}$, for $\omega \rightarrow \pm\infty$. Hence, the integrand in I behaves as $\propto \omega^{n-1}$, and this term contributes to spectral sum rules for arbitrary n . Before we analyze the second term, we first note that $g^2\Sigma^{(2)}(\omega)$ corresponds to the diagram shown in Fig. 2.4(b). This term has a single electron propagator, and hence contributes as $\Sigma^{(2)}(\omega) \propto \frac{1}{\omega}$, for $\omega \rightarrow \pm\infty$. The whole subintegral term II thus behaves as $\propto \omega^{n-3}$. We conclude that II contributes only for $n \geq 2$. Similarly, we see that $\Sigma^{(4)}(\omega) \propto \frac{1}{\omega^3}$, and hence both subintegral terms in III and IV behave as ω^{n-5} . These terms contribute for $n \geq 4$. However, SCMA does not faithfully reproduce all diagrams of fourth order. The one in Fig. 2.5 is missing. Hence, SCMA correctly predicts the spectral sum rules for $n = 0, 1, 2, 3$.

2.3.4 Spectral Sum Rules: DMFT Predictions

Within the DMFT, the spectral sum rules are calculated numerically. Results, over a large number of parameter regimes, are presented in Tables F.1–F.17, in Appendix F. We see a striking agreement with the exact results for all the sum rules that we calculated ($0 \leq n \leq 8$). This confirms our earlier findings that the DMFT is in fact reliable in the weak coupling limit.

2.4 Atomic Limit

The atomic limit is defined as a parameter regime where the hopping is vanishing $t_0 = 0$. In this case, the Holstein problem admits an exact analytic solution; see Sec. 2.3 in Part I. In fact, the DMFT should

²This is justified as we know that the spectral sum rules have the same, polynomial expression, irrespective of the coupling strength. Hence, if we derive the spectral sum rules for weak coupling, where this expansion is valid, we know that the sum rules continue to be valid even for other regimes.

³We could also close the contour from the lower-half side as well, but the upper half-side turns out to be much more convenient. This is allowed since the length of the contour grows linearly $2\pi R$ and there is no exponential term

also predict the exact solution. This can be seen as follows: in Chapter 1, we gave a detailed derivation of the DMFT equations and proved that they predict an exact result in the limit of infinite coordination number $Z \rightarrow \infty$. However, in the atomic limit, the sites are decoupled. This means that the result is independent of Z , enabling us to formally take the limit $Z \rightarrow \infty$. Since DMFT is exact in the $Z \rightarrow \infty$ limit, it follows that it also has to be exact in the atomic limit as well.

Here, we supplement this analysis by numerically investigating the DMFT solution close to the atomic limit. In addition, we will be discussing the predictions of the SCMA at the atomic limit.

2.4.1 Atomic Limit at $T = 0$: DMFT Predictions

In the $T = 0$ case, the exact Green's function in the atomic limit was already presented in Part I; see Eq. (2.38a). The corresponding spectral function is given by a series of delta peaks

$$A(\omega) = \sum_{n=0}^{\infty} \frac{\alpha^{2n} e^{-\alpha^2}}{n!} \delta(\omega - n\omega_0 - E_p), \quad (2.21)$$

where E_p is given by Eq. (2.37). We now want to compare this with the DMFT predictions close to the atomic limit ($t_0 = 0.05$ and $t = 10^{-5}$), in the regime $\omega_0 = g = 1$. Since Eq. (2.21) is given by a sum of Dirac delta functions, plotting this would require introducing some kind of artificial broadening. Instead, the comparison between DMFT and the exact result can be made using the momentum-averaged integrated spectral weights

$$I(\omega) = \frac{1}{N} \sum_k I_k(\omega), \quad (2.22a)$$

$$I_k(\omega) = \int_{-\infty}^{\omega} A_k(\nu) d\nu. \quad (2.22b)$$

The exact result for this quantity is a direct consequence of Eq. (2.21), and is given by

$$I^{\text{exact}}(\omega) = \sum_{n=0}^{\infty} \frac{\alpha^{2n} e^{-\alpha^2}}{n!} \theta(\omega - n\omega_0 - E_p), \quad (2.23)$$

where θ is the Heaviside step function. However, calculating $I(\omega)$ within DMFT is not completely straightforward. This is because DMFT, at $T = 0$ predicts that the polaron peak is a true Dirac delta function. In addition, there can be additional delta peaks in the DMFT solution. These delta peaks, without the use of artificial broadening, cannot be represented on a finite frequency grid, which is how $A_k(\nu)$ is stored on a computer. Hence, the information about the delta peaks will be missing if, *in our numerical implementation*, we simply calculate the spectral function as⁴ $A_k = -\frac{1}{\pi} \text{Im} G_k(\omega)$. Therefore, a straightforward numerical integration of Eq. (2.22b) would sometimes seemingly lead to the conclusion that the spectral sum rule $I_k(\infty) = 1$ is violated. This problem needs to be solved if we want to reliably calculate the expressions in Eq. (2.22).

Let us now present a numerical scheme that overcomes these issues. This is achieved by calculating $I_k(\omega)$ directly from the self-energy⁵ $\Sigma(\omega)$. Let us suppose that the self-energy data $\{\Sigma_0, \Sigma_1 \dots \Sigma_{N-1}\}$ are known on a dense grid $\{\omega_0, \omega_1 \dots \omega_{N-1}\}$, such that $\Delta\omega_q = \omega_{q+1} - \omega_q$ is small enough. The integrated spectral weight can then be rewritten as

$$I_k(\omega_l) = -\frac{1}{\pi} \text{Im} \int_{-\infty}^{\omega_l} \frac{d\nu}{\nu - \Sigma(\nu) - \varepsilon_k} \approx -\frac{1}{\pi} \text{Im} \sum_{q=0}^{l-1} \int_{\omega_q}^{\omega_{q+1}} \frac{d\nu}{\nu - \Sigma(\nu) - \varepsilon_k}. \quad (2.24)$$

⁴Of course, if we could perform the calculation analytically, delta peaks would be present.

⁵The self-energy keeps the information about the location of the delta peaks; see the text below Eq. (2.24).

At each interval $[\omega_q, \omega_{q+1}]$ the self-energy is known only at the endpoints. The linear interpolation of the subintegral function at each interval $[\omega_q, \omega_{q+1}]$ would correspond to trapezoid integration, which cannot take into account the already mentioned delta peaks. The delta peaks occur whenever our subintegral function is (infinitely) close to the singularity, i.e. when $\text{Im}\Sigma(\nu) \rightarrow 0^-$ and $\nu - \text{Re}\Sigma(\nu) - \varepsilon_k \approx 0$. Hence, these will be accounted for if we use the linear interpolation of the denominator itself instead of the whole subintegral function.

$$I_k(\omega_l) \approx -\frac{1}{\pi} \text{Im} \sum_{q=0}^{l-1} \int_{\omega_q}^{\omega_{q+1}} \frac{d\nu}{\nu - \varepsilon_k - [\Sigma_q + \Sigma'_q(\nu - \omega_q)]}, \quad (2.25)$$

where $\Sigma'_q = (\Sigma_{q+1} - \Sigma_q)/(\omega_{q+1} - \omega_q)$. This can now be evaluated analytically⁶

$$I_k(\omega_l) = -\frac{1}{\pi} \text{Im} \sum_{q=0}^{l-1} \frac{1}{1 - \Sigma'_q} \ln \left[\frac{\omega_{q+1} - \varepsilon_k - \Sigma_{q+1}}{\omega_q - \varepsilon_k - \Sigma_q} \right]. \quad (2.26)$$

Equation (2.26) is the solution to our problem, as it, by construction, correctly takes into account both the contribution of the Dirac delta peaks and the contribution of the rest of the spectral function.

Remark 8. *It is easy to see that the contribution of the term, which corresponds to the interval (ω_q, ω_{q+1}) , to Eq. (2.26) is equal to*

$$\frac{1}{1 - \frac{\Sigma_{q+1} - \Sigma_q}{\omega_{q+1} - \omega_q}} \approx \frac{1}{1 - \partial_\omega \Sigma}, \quad (2.27)$$

if the interval contains a delta peak, whereas it is

$$-\frac{1}{\pi} \text{Im} \left[\frac{1}{1 - \Sigma'_q} \ln \left(1 + \Delta\omega_q \frac{1 - \Sigma'_q}{\omega_q - \varepsilon - \Sigma_q} \right) \right] \approx -\Delta\omega_q \frac{1}{\pi} \text{Im} \left[\frac{1}{\omega_q - \varepsilon_k - \Sigma_q} \right] \quad (2.28)$$

otherwise. If we analytically took into account the contribution of the delta peak, it would coincide with Eq. (2.27), while Eq. (2.28) is exactly the term we would get using the standard Riemann sum in Eq. (2.22b). Having in mind that the Riemann sum approach is completely justified in the absence of delta peaks, we now explicitly see that the integration scheme presented in Eq. (2.26) is perfectly well-suited for the calculation of the integrated spectral weight.

Using the numerical scheme we just presented (see Eq. (2.26)), we can finally calculate the integrated spectral weight within the DMFT, and compare it to the exact analytical result from Eq. (2.23). The results are shown in Fig. 2.7, where we observe a remarkable agreement. We see that $I(\omega)$ features jumps at frequencies where $A(\omega)$ has peaks and the height of those jumps is equal to the weight of the peaks. Nonzero hopping in the DMFT solution introduces small momentum dependence of $I_k(\omega)$, which is why Fig. 2.7 shows the result averaged over all momenta. A more detailed comparison is presented in Table 2.1. It shows the numerical values of the DMFT $I(\omega)$ at the positions of delta peaks (for a given k and averaged over many k) in comparison with the analytical $t_0 = 0$ result from Eq. (2.23). These delta peaks, positioned at $n\omega_0 + E_p$, have the weights equal to $\alpha^{2n} e^{-\alpha^2}/n!$ for $n = 0, 1, \dots$. As expected, the DMFT is fully capable of reproducing the results at the atomic limit.

⁶For the calculation of this integral it is useful to exploit $\ln x - \ln y = \ln(x/y)$, which does not hold in general, but it can be used in our case since $\text{Im}\Sigma_q < 0$ (for every q).

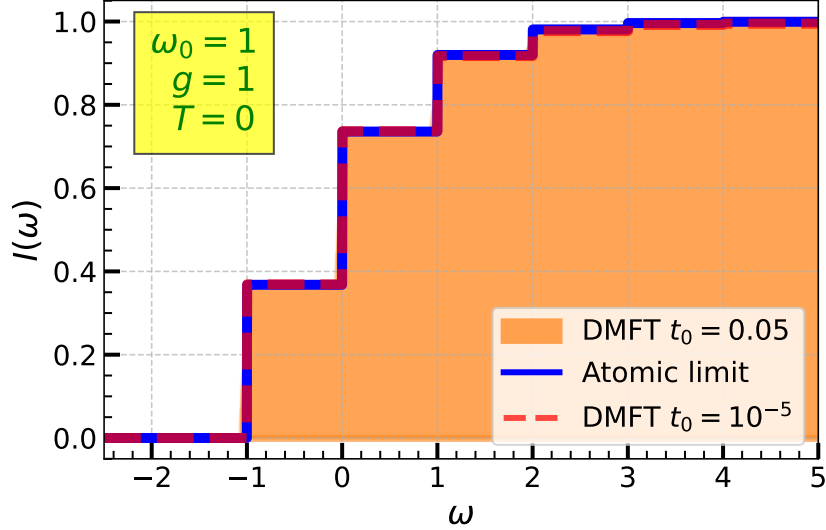


Figure 2.7: DMFT integrated spectral weight for $t_0 = 0.05$ (shaded) and $t_0 = 10^{-5}$ (red dashed line) averaged over all momenta, $I(\omega) = \frac{1}{N} \sum_k \int_{-\infty}^{\omega} A_k(\nu) d\nu$, in comparison to the exact $t_0 = 0$ result (blue solid line).

Table 2.1: Integrated spectral weight $I(\omega)$ for different momenta and hopping parameters at $T = 0$ and $\omega_0 = g = 1$. The exact atomic limit corresponds to $t_0 = 0.00$, and the corresponding results are depicted as shaded cells. For $t_0 = 10^{-5}$ the DMFT solution has no k -dependence within the specified accuracy, which is why the corresponding k -values are denoted as 'all'. We denote the k -values to be 'av.' if the answer is averaged over all momenta.

k	$t_0 \backslash \omega$	-2	-1	0	1	2	3
	0.00	0.00	0.37	0.74	0.92	0.98	1.0
all	10^{-5}	0.00	0.37	0.74	0.92	0.98	1.0
av.	0.05	0.00	0.37	0.73	0.92	0.98	1.0
0	0.05	0.00	0.40	0.76	0.94	0.99	1.0
$\pi/2$	0.05	0.00	0.37	0.74	0.92	0.98	1.0
π	0.05	0.00	0.33	0.71	0.91	0.98	0.99

2.4.2 Atomic Limit at $T \neq 0$: DMFT Predictions

Let us now consider the $T \neq 0$ case. At the atomic limit, Eq. (2.38b) from Part I implies that the spectral function is given by

$$A(\omega) = \sum_{n=-\infty}^{\infty} I_n \left(2\alpha^2 \sqrt{n_{\text{ph}}(n_{\text{ph}} + 1)} \right) e^{-(2n_{\text{ph}}+1)\alpha^2 + n\frac{\omega_0}{2T}} \delta(\omega - n\omega_0 - E_p), \quad (2.29)$$

while the corresponding integrated spectral weight reads as

$$I(\omega) = \sum_{n=-\infty}^{\infty} I_n \left(2\alpha^2 \sqrt{n_{\text{ph}}(n_{\text{ph}} + 1)} \right) e^{-(2n_{\text{ph}}+1)\alpha^2 + n\frac{\omega_0}{2T}} \theta(\omega - n\omega_0 - E_p). \quad (2.30)$$

The peaks are located at $n\omega_0 + E_p$, where n can now be both positive and negative integer.

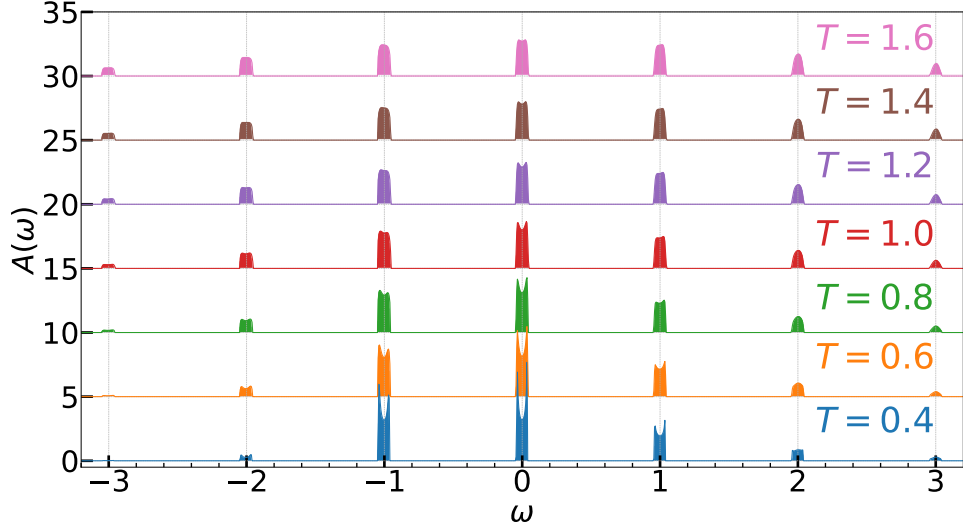


Figure 2.8: DMFT spectral functions $A(\omega) = \frac{1}{N} \sum_k A_k(\omega)$ for $\omega_0 = 1$, $g = 1$, $t_0 = 0.05$.

Table 2.2: Spectral weights of individual peaks located at $\omega = n\omega_0 + E_p$ for $n = -2, -1, 0, 1, 2, 3$. The DMFT spectra, obtained for $t_0 = 0.05$, are averaged over k . The atomic limit values ($t_0 = 0.00$) are obtained from the analytical formula and are depicted as shaded cells. Here $\omega_0 = 1$, $g = 1$.

T	ω t_0	-2	-1	0	1	2	3
0.4	0.00	0.03	0.34	0.35	0.19	0.07	0.02
0.4	0.05	0.03	0.34	0.34	0.18	0.07	0.02
0.6	0.00	0.06	0.30	0.33	0.19	0.08	0.02
0.6	0.05	0.06	0.30	0.33	0.19	0.08	0.02
0.8	0.00	0.09	0.27	0.30	0.19	0.09	0.03
0.8	0.05	0.09	0.27	0.30	0.19	0.09	0.03
1.0	0.00	0.10	0.25	0.28	0.19	0.09	0.04
1.0	0.05	0.10	0.25	0.28	0.19	0.10	0.04
1.2	0.00	0.11	0.23	0.26	0.19	0.10	0.04
1.2	0.05	0.11	0.23	0.26	0.19	0.10	0.04
1.4	0.00	0.12	0.21	0.24	0.19	0.11	0.05
1.4	0.05	0.12	0.21	0.24	0.19	0.11	0.05

Let us now compare these exact results for various temperatures with the DMFT predictions, in the parameter regime $\omega_0 = g = 1$. The DMFT spectra, averaged over k , are shown in Fig. 2.8. Even though no artificial broadening was used, these peaks have nonzero width, as a consequence of the nonzero hopping parameter ($t_0 = 0.05$). We note that the peaks themselves, at low temperature, do not have the Lorentzian shape. Instead, they are characteristically fork-shaped, which is the consequence of the 1D density of states (see Fig. 2.3i(a)). This property is only noticeable at small temperatures because the larger temperatures tend to smear it out. The weight of the peaks are very close to the analytical result $I_n(2\alpha^2 \sqrt{n_{\text{ph}}(n_{\text{ph}} + 1)})e^{-(2n_{\text{ph}} + 1)\alpha^2 + n \frac{\omega_0}{2T}}$, as seen from Table 2.2. This confirms the ability of the DMFT to correctly reproduce the results at the atomic limit.

2.4.3 Atomic Limit at $T = 0$: SCMA Predictions

Here, we present a formal proof that SCMA does not predict correct results at the atomic limit. We restrict our derivation to the $T = 0$ case. In the atomic limit ($t_0 = 0$) at $T = 0$, it holds that $n_{\text{ph}} \rightarrow 0$. Hence, the SCMA Eq. (2.14) reduces to

$$\Sigma(\omega) = g^2 G(\omega - \omega_0). \quad (2.31)$$

In addition, since the SCMA self-energy is k -independent, and the noninteracting dispersion vanishes in the atomic limit $\varepsilon_l = -2t_0 \cos k \rightarrow 0$, we see that in this limit the Green's function also loses its k dependence. Hence, the local Green's function from Eq. (2.31) can be written as

$$G(\omega) = \frac{1}{\omega - \Sigma(\omega)}. \quad (2.32)$$

Combining Eqs. (2.31) and (2.32), we obtain

$$\begin{aligned} \Sigma(\omega) = g^2 G(\omega - \omega_0) &= \frac{g^2}{\omega - \omega_0 - \Sigma(\omega - \omega_0)} = \frac{g^2}{\omega - \omega_0 - \frac{g^2}{\omega - 2\omega_0 - \Sigma(\omega - 2\omega_0)}} \\ &= \dots = \frac{g^2}{\omega - \omega_0 - \frac{g^2}{\omega - 2\omega_0 - \frac{g^2}{\omega - 3\omega_0 - \frac{g^2}{\dots}}}}. \end{aligned} \quad (2.33)$$

However, this does not coincide with the exact solution which is given by Eq. (1.155), where we should substitute $G(\omega) \rightarrow \omega^{-1}$, as explained in Remark 6. Therefore, SCMA cannot be exact in the atomic limit. Some numerical results of the SCMA in this limit will be given in the next section, and also in Sec. 3.4.4.

2.5 Spectral Function at Intermediate and Strong Electron-Phonon Coupling

2.5.1 Benchmark Method: Hierarchical Equations of Motion

The hierarchical equations of motion (HEOM) method is a numerically exact technique that has recently gained popularity in the chemical physics community [73–76]. It has been used to explore the dynamics of an electron (or exciton) which is linearly coupled to a Gaussian bosonic bath. One of the advantages of this method is that the correlation functions are calculated directly on the real-time (real-frequency) axis [77], avoiding the numerically ill-defined analytical continuation. However, the existence of numerical instabilities stemming from the discreteness of phonon bath on a finite lattice, explain why its application for the study of the Holstein model [78–82] were not more widespread in the past. Recently, these limitations were overcome using the momentum-space HEOM method, which was developed by Janković in Ref. [83]. He was the one who generated all the HEOM results, that we will be using as a benchmark, in this thesis.

Let us now give a brief overview of this method. Within HEOM, the central quantity that is calculated is the time-dependent greater Green's function, which is defined as $G^>(k, t) = -i\langle c_k(t)c_k^\dagger \rangle_{T,0}$. It turns out that we can represent it as a root $G^>(k, t) = G_0^{>,0}(k, t)$ of an infinite hierarchy of the so-called auxiliary Green's functions (AGFs) $G_n^{>,n}(k - k_n, t)$. Here, $n \geq 0$ is the number of the electron-phonon interaction events starting from the free-electron state of momentum k , while \mathbf{n} is a vector of nonnegative integers that fully describes each event (the phonon momentum and whether it is absorbed or emitted). The net momentum exchange between the electron and the phonons after n events is denoted

by k_n . The AGFs are mutually dependent: the equation of motion for the AGFs at depth n includes also the terms with AGFs at depths $n \pm 1$, with factors that are proportional to the electron-phonon coupling constant and to the phonon absorption/emission factors $\frac{1}{2}[\coth(\omega_0/(2T)) \pm 1]$. As a result, an infinite hierarchy of the equations for the AGFs is constructed. In practice, the hierarchy is truncated at a certain maximum depth D , so that all AGFs with $n > D$ are set to zero, after which the obtained set of differential equations is solved numerically.

Since the exact solution would theoretically correspond to $D \rightarrow \infty$, it is always necessary to check that the chosen D (which for numerical reasons has to be finite) was large enough so that the results have fully converged. In addition, HEOM method can only be applied to a system with a finite number of lattice sites N . Thus, if we want to describe the system in a thermodynamic limit (i.e., $N \rightarrow \infty$), we also need to keep increasing N until the convergence of the results, with respect to this parameter, is reached as well. However, we note that in practice N and D cannot be too large, due to computer memory issues. In addition, HEOM is computationally expensive. This is the price one has to pay for the results of such high quality that this method produces. The concrete values of N and D which one needs to take vary depending on the regime. For example, there is not much electron-phonon scattering in the weak coupling limit, which is why this regime requires large N and small D . In contrast, smaller N would be sufficient in the strong coupling limit, but the depth D should be much larger. In the case of intermediate electron-phonon coupling, which is the most relevant for us, Ref. [83] showed that even relatively small N (between 5 and 10) are representative of the thermodynamic limit.

2.5.2 Results at Finite Temperature

Typical results for the $k = 0$ and $k = \pi$ spectral functions are shown in Fig. 2.9, while additional results for other momenta and other parameters are shown in Figs. 2.10 and 2.11. We note that the convergence of the HEOM results with respect to N and D was always checked. Table 2.3 displays the values of these parameters, that are deemed sufficiently large for the results to be considered converged.

The agreement between DMFT and HEOM spectral functions is excellent for $\omega_0 = g = 1$; see panels Fig. 2.9(a)–2.9(b), where we note that the DMFT solution is a bit smoother than HEOM, due to the finite-size effects of the HEOM solution. Moreover, in this regime, even the SCMA method provides decent results: the weight of the SCMA quasiparticle (QP) peak is nearly equal to the DMFT/HEOM QP weight, and the overall agreement of spectral functions is rather good. This is not the case for stronger electron-phonon coupling (see panels 2.9(c)–2.9(h)) where the SCMA poorly approximates the true spectrum. In particular, we now see the numerical predictions of the SCMA near the atomic limit⁷ (see panels 2.9(g)–2.9(h)), complementing the results of Sec. 2.4.3. As expected, it gives completely incorrect predictions, in contrast to the DMFT which provides very reliable results.

However, the regime for $g = \sqrt{2}$ seems to pose some problems to the DMFT. We observe that for $g = \sqrt{2}$ and $k = \pi$ (see panel 2.9(d)) the DMFT and HEOM satellite peaks are somewhat shifted with respect to one another. This is the most challenging regime for the DMFT, representing a crossover ($\lambda = 1$) between the small and large polaron. Nevertheless, the agreement remains very good near the quasiparticle peak for $k = 0$ (see panel 2.9(c)), which will be the most important for transport in weakly doped systems.

Up to now, we have analyzed the DMFT solution for weak couplings (in Sec. 2.2), for intermediate couplings (in Figs. 2.9(a)–2.9(d)), and near the atomic limit (in Figs. 2.9(g)–2.9(h) and Sec. 2.4). To complete this analysis, let us now turn to the results at the strong coupling regime. The case when $g = 2$ should be a good representative of this regime. This can be concluded from Fig. 2.1, which shows that in this case, there is a strong renormalization of electron mass $m^*/m_0 \approx 10$. Unfortunately, the HEOM benchmark cannot easily converge in this regime with respect to maximum depth D , due to computer memory issues. In order to find an adequate benchmark, capable of providing reliable results for this regime, we first analyze the DMFT results, applied on a finite system with N sites (see

⁷Since we measure ω_0 and g in term of t_0 , the atomic limit corresponds to the regime of large ω_0 and g .

Chapter 1 and Remark 4 therein). The results are shown in Fig. 2.12. In the regime $g = 2, \omega_0 = 1$, we see that there is very little difference between the results for $N = 4, N = 6$, and the thermodynamic limit. Therefore, in this case, a lattice as small as $N = 4$ can be considered sufficiently large to be representative of the thermodynamic limit. This insight opens a pathway for the introduction of the exact diagonalization (ED) method as a benchmark in this regime. In the case of a lattice with $N > 4$, the application of the ED method would require too much computer memory. Luckily, as we have now demonstrated, $N = 4$ is sufficient in this case. We note that all the ED results were implemented by Nenad Vukmirović [62], and we just use them as a benchmark.

Remark 9. *Within the ED method, the spectral functions are calculated by diagonalizing the Holstein Hamiltonian in the space spanned by the vectors $U c_i^\dagger |n_1 n_2 \dots n_N\rangle$, where n_i is the number of phonons at site $i \in 1, \dots, N$, satisfying $\sum_i n_i < n_{\max}$, while U is the unitary operator of the Lang-Firsov transformation [38] given as*

$$U = e^{\frac{g}{\omega_0} \sum_i c_i^\dagger c_i (a_i - a_i^\dagger)}. \quad (2.34)$$

Both N and n_{\max} need to be increased until convergence is reached. The spectral function is then calculated as⁸

$$A_{\mathbf{k}}(\omega) = \frac{1}{\mathcal{Z}_p} \sum_{m_p} e^{-\beta E_{m_p}} \sum_{m_e} \delta(\omega + E_{m_p} - E_{m_e}) |\langle m_p | c_{\mathbf{k}} | m_e \rangle|^2, \quad (2.35)$$

where $|m_p\rangle$ denotes purely phononic states, the energy of which is E_{m_p} , $|m_e\rangle$ denotes the states with one electron and arbitrary number of phonons, the energy of which is E_{m_e} and $\mathcal{Z}_p = \sum_p e^{-\beta E_{m_p}}$ is the phononic partition function. It turns out that the convergent results, for the spectral function when $g = 2, \omega_0 = 1, N = 4$, are obtained for $n_{\max} = 16$.

The results are shown in Figs. 2.9(e)–2.9(f). We see a remarkable agreement between DMFT and ED, even though this regime is far away from both the atomic and weak coupling limits, where the DMFT is exact. The spectral functions in Figs. 2.10 and 2.11 can be analyzed analogously. Overall, we conclude that the agreement of DMFT and HEOM/ED spectra is very good, which implies that the nonlocal correlations are not pronounced.

Remark 10. *We note that the HEOM and ED methods impose periodic boundary conditions on a finite lattice. Hence, the momenta k can only take the values that are integer multiples of $2\pi/N$. Although additional values of k are obtained using the twisted boundary conditions, arbitrary values of k are not available. This is why different panels in Figs. 2.10 and 2.11ii do not always have the same values of momenta. Nevertheless, this is sufficient for our comparisons, since DMFT and SCMA are applied in the thermodynamic limit, meaning that we can easily calculate the results for arbitrary k .*

Table 2.3: Number of lattice sites N and the maximum hierarchy depth D used for the application of the HEOM method in different regimes at finite temperature

Parameters	N	D
$\omega_0 = 1 \quad g = 1 \quad T = 0.7$	10	6
$\omega_0 = 1 \quad g = 1 \quad T = 1$	10	6
$\omega_0 = 1 \quad g = \sqrt{2} \quad T = 0.4$	8	8
$\omega_0 = 1 \quad g = \sqrt{2} \quad T = 0.6$	8	7
$\omega_0 = 1 \quad g = \sqrt{2} \quad T = 0.8$	8	7
$\omega_0 = 3 \quad g = \sqrt{12} \quad T = 1$	6	9

⁸Plotting this result requires the introduction of some artificial broadening, due to the delta functions.

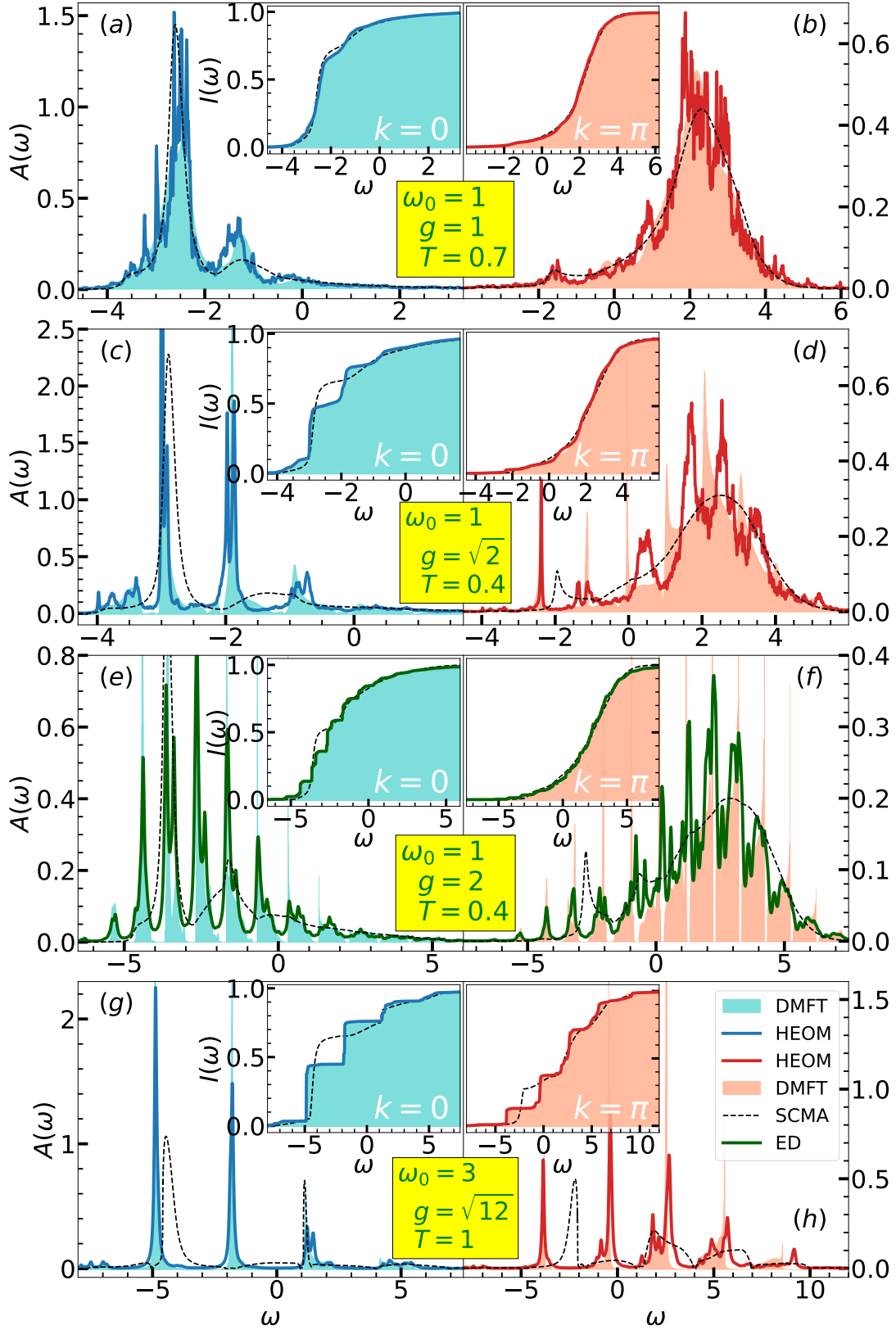


Figure 2.9: DMFT, HEOM, SCMA, and ED finite temperature spectral functions for different parameters. On the left panels $k = 0$, whereas $k = \pi$ on the right. The integrated spectral weight is presented in the insets without broadening. Lorentzian broadening (with a halfwidth $\eta = 0.05$) is only used for plotting the ED spectral functions in panels (e) and (f) and for plotting all spectral functions in panels (g) and (h).

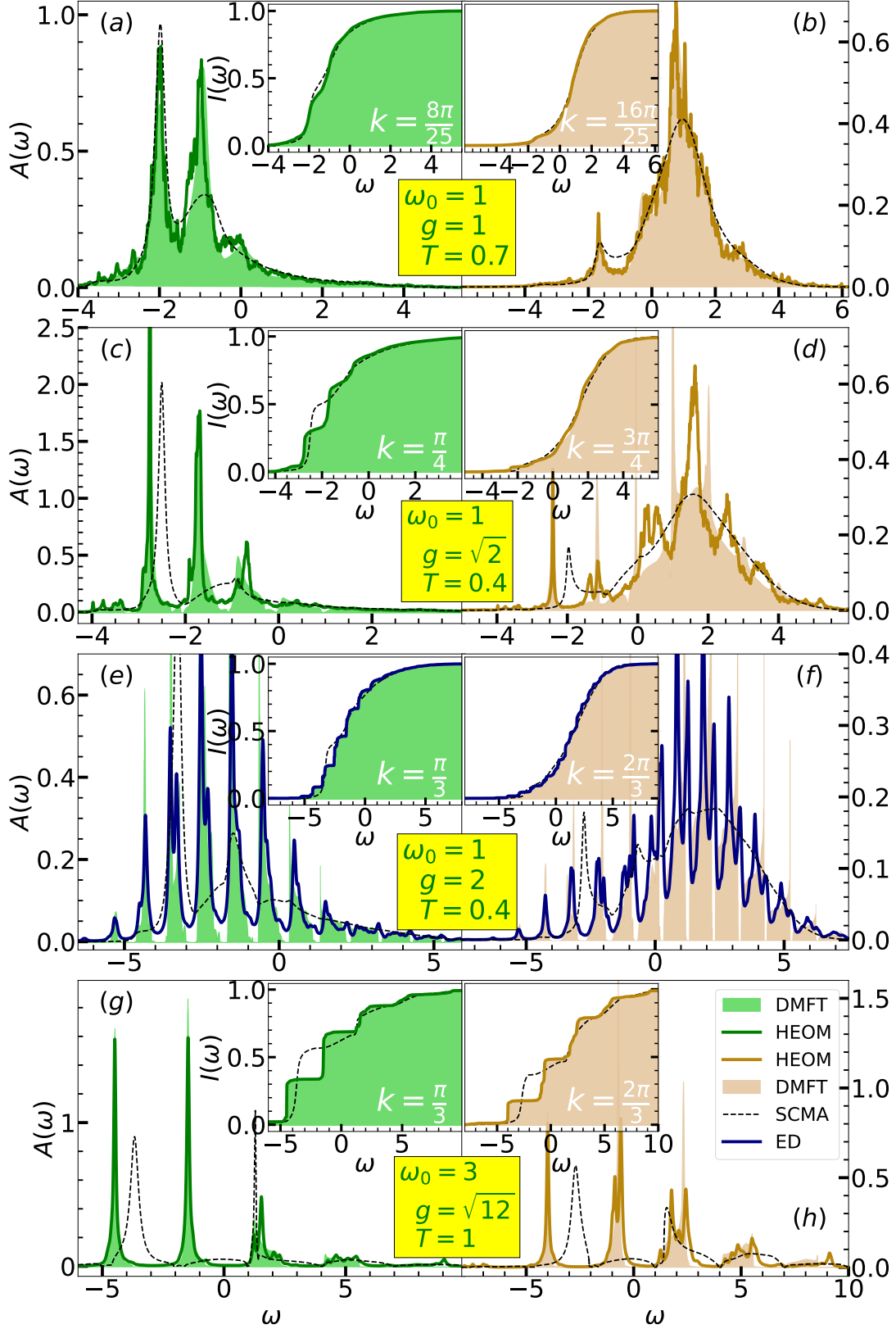
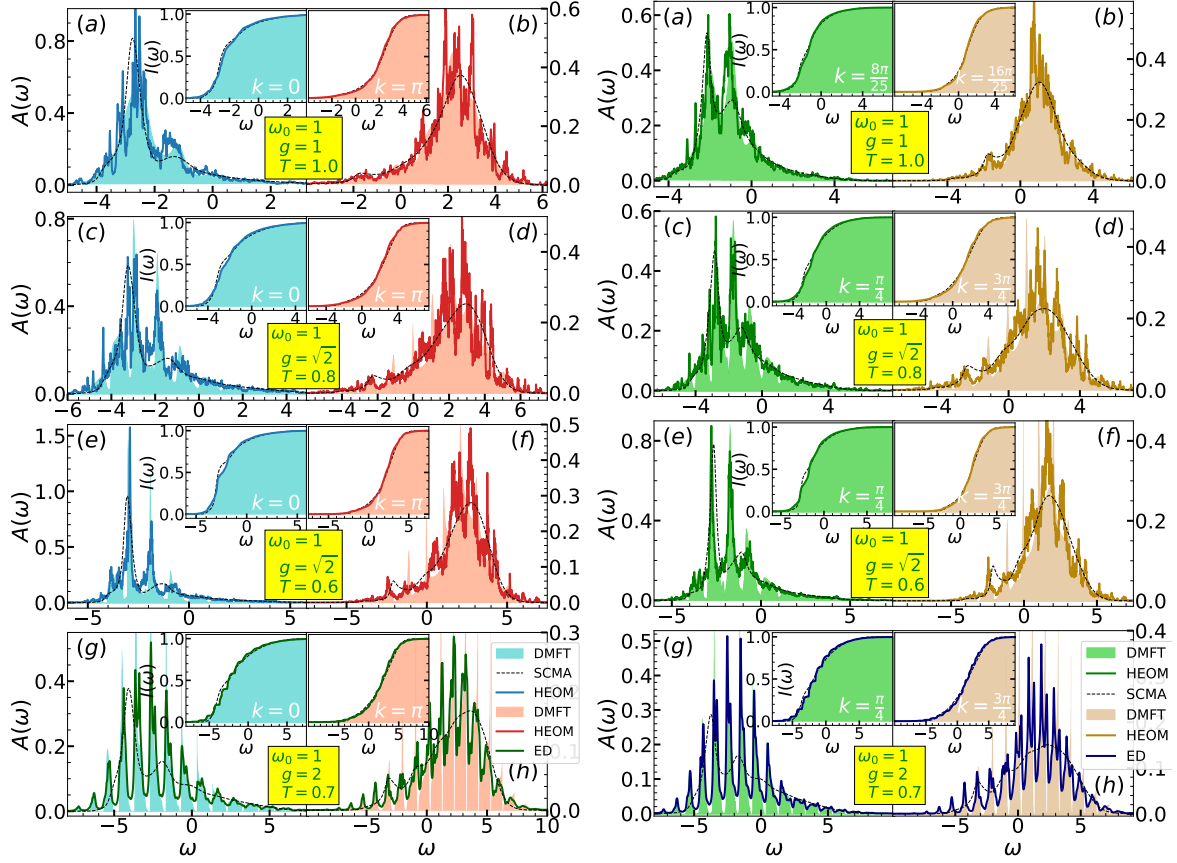


Figure 2.10: DMFT, HEOM, SCMA, and ED spectral functions for different parameters. On the left panels $\pi/4 \leq k \leq \pi/3$, whereas $\pi/2 \leq k \leq 3\pi/4$ on the right. The integrated spectral weight is presented in the insets without broadening. Lorentzian broadening (with a halfwidth $\eta = 0.05$) is only used for plotting the ED spectral functions in panels (e) and (f) and for plotting all spectral functions in panels (g) and (h).



(i) Results for $k = 0$ (left panels) and $k = \pi$ (right panels).

(ii) Results for $\pi/4 \leq k \leq \pi/3$ (left panels) and $\pi/2 \leq k \leq 3\pi/4$ (right panels).

Figure 2.11: DMFT, HEOM, SCMA, and ED spectral functions for different parameters. The integrated spectral weight is presented in the insets without broadening. Lorentzian broadening (with a halfwidth $\eta = 0.05$) is only used for plotting the ED spectral functions.

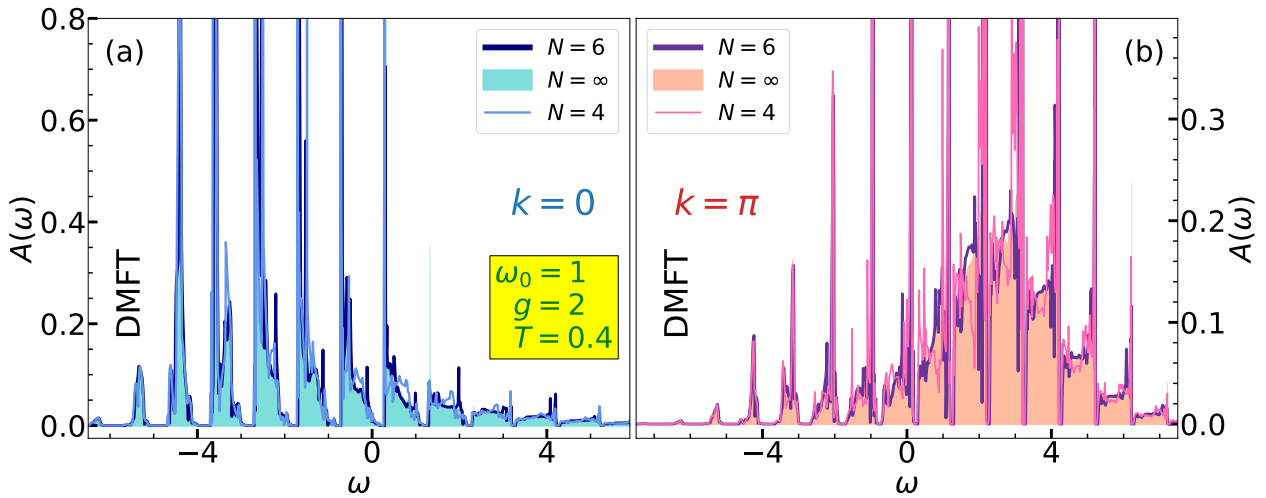
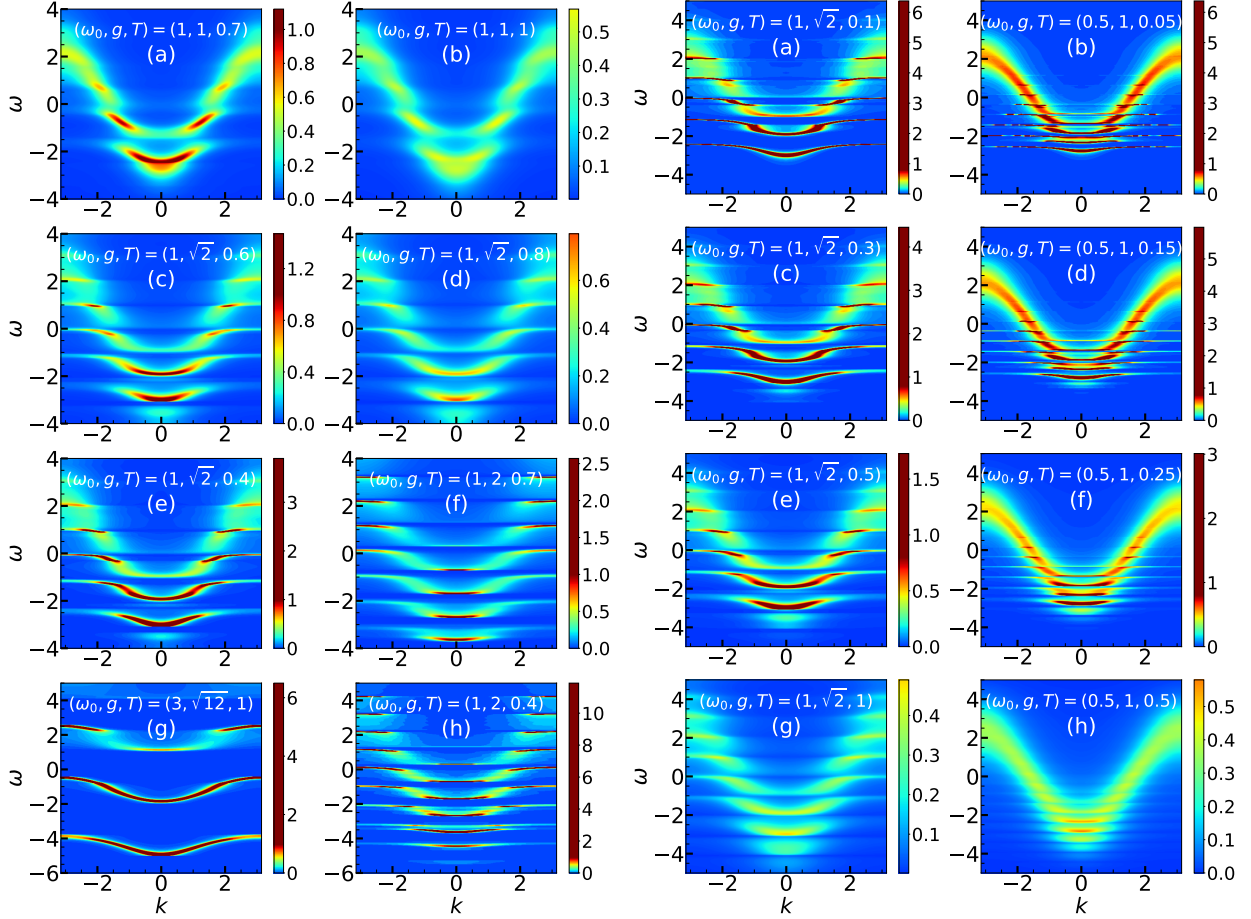


Figure 2.12: DMFT results for systems with finite number of lattice sites.

2.5.3 Heat Maps

In the previous section, we saw the DMFT spectral functions for different values of momenta. Another common way to present those results is by using the heat maps in the $k - \omega$ plane. In Fig. 2.13i we show the DMFT heat maps for the same parameters as in Figs. 2.9 - 2.11. For comparison purposes, in Fig. 2.13ii we also show the DMFT heat maps for the same parameters as in the finite- T Lanczos results from Fig. 2 of Ref. [46]. A small difference in DMFT vs. Lanczos method heat maps can be ascribed to the more pronounced peaks in the DMFT spectra.



(i) Parameter regimes are the same as in Figs. 2.9– 2.11. The same color coding is used in all plots.

(ii) Parameters regimes are the same as in Fig. 2 of Ref. [46]. The same color coding is used in all plots.

Figure 2.13: DMFT heat maps for $A_k(\omega)$.

2.5.4 Results at $T = 0$

The analysis from Sec. 2.5.2 can now also be repeated in the case of $T = 0$. The results, for the same values of ω_0 and g as in Figs 2.9– 2.11, are shown in Figs. 2.14– 2.17. As in Sec. 2.5.2, we note that the HEOM results represent a benchmark in all regimes except for $\omega_0 = 1$, $g = 2$, where this method requires too much computer memory to converge with respect to D . In this case, as a benchmark, we use the ED method. In the $g = 2$ regime, it turns out that $N = 4$ sites is large enough to represent the thermodynamic limit, as justified in Sec. 2.5.2. In all other regimes sufficiently large values of N and D , such that the results of the HEOM benchmark have fully converged, have always been used, and are presented in Table 2.4.

Typical results at $k = 0$ are illustrated in Fig. 2.14. The weights of the DMFT and HEOM quasiparticle peaks correspond to the m_0/m^* ratio. We note that at $T = 0$, the DMFT quasiparticle peak is a delta function, while satellite peaks are incoherent having intrinsic nonzero width. Hence, for illustration purposes, in the insets of Figs. 2.14– 2.17, the spectral functions are broadened, using a Lorentzian broadening with half-width $\eta = 0.05$. On the other hand, the main panels show the integrated spectral weights $I(\omega)$ without any broadening. These were calculated using the numerical scheme we presented in Sec. 2.4.1; see Eq. (2.26). A sharp jumps can be observed in $I(\omega)$ at frequencies where the Dirac delta peaks are situated in the spectral functions. In contrast to the DMFT results, all HEOM peaks have a finite width due to the finite lattice size N and finite propagation time t_{\max} . Nevertheless, to make a fair comparison with DMFT, we also use Lorentzian $\eta = 0.05$ broadening in HEOM spectral functions as well⁹. This Lorentzian broadening is generally much larger than the one arising from finite N and t_{\max} .

In panel 2.14(a), we see an excellent agreement between DMFT and HEOM quasiparticle peaks. However, there seems to be a small discrepancy in the satellite structure: while HEOM predicts two small peaks around $\omega \approx -1.25$ and $\omega \approx -1.47$, DMFT reproduces only a single broad structure. This discrepancy is a consequence of the small finite-size effects of the HEOM solution. We illustrate this in Fig. 2.18, where we apply the DMFT on a finite lattice with $N = 10$, which is the same size as the one used in HEOM; see Table 2.4. This is another demonstration that DMFT is in fact quite accurate.

A favorable comparison between DMFT and HEOM/ED is also visible in other regimes as well; see panels 2.14(b)– 2.14(c). In particular, in the strong coupling regime $\omega_0 = 1$, $g = 2$ (see panel 2.14(b)), the DMFT is even capable of capturing the so-called *excited QP peak*. This peak consists of a polaron and a bound phonon, and is situated at the energy below $E_p + \omega_0$, where E_p is the ground state energy [45, 46]. At a crossover regime between large and small polarons $\omega_0 = 1$, $g = \sqrt{2}$, the DMFT is giving excellent results for $k = 0$, but as in the finite temperature case, its predictions are shifted with respect to HEOM results for $k = \pi$; see Figs. 2.14(c) and 2.17(c). Lastly, for parameters in Fig. 2.14(d) the lattice sites are nearly decoupled, approaching the atomic limit ($t_0 \ll g, \omega_0$). Having in mind the finite temperature results from Sec. 2.5.2, and the fact that DMFT is exact in the atomic limit, its reliable predictions are now completely expected in this regime.

⁹Once again, we emphasize that the broadening is introduced only for plotting figures. All calculations are performed without any broadening.

Table 2.4: Number of lattice sites N and the maximum hierarchy depth D used for the application of the HEOM method in different regimes at $T = 0$

Parameters	N	D
$\omega_0 = 1 \quad g = 1$	10	6
$\omega_0 = 1 \quad g = \sqrt{2}$	8	7
$\omega_0 = 3 \quad g = \sqrt{12}$	6	9

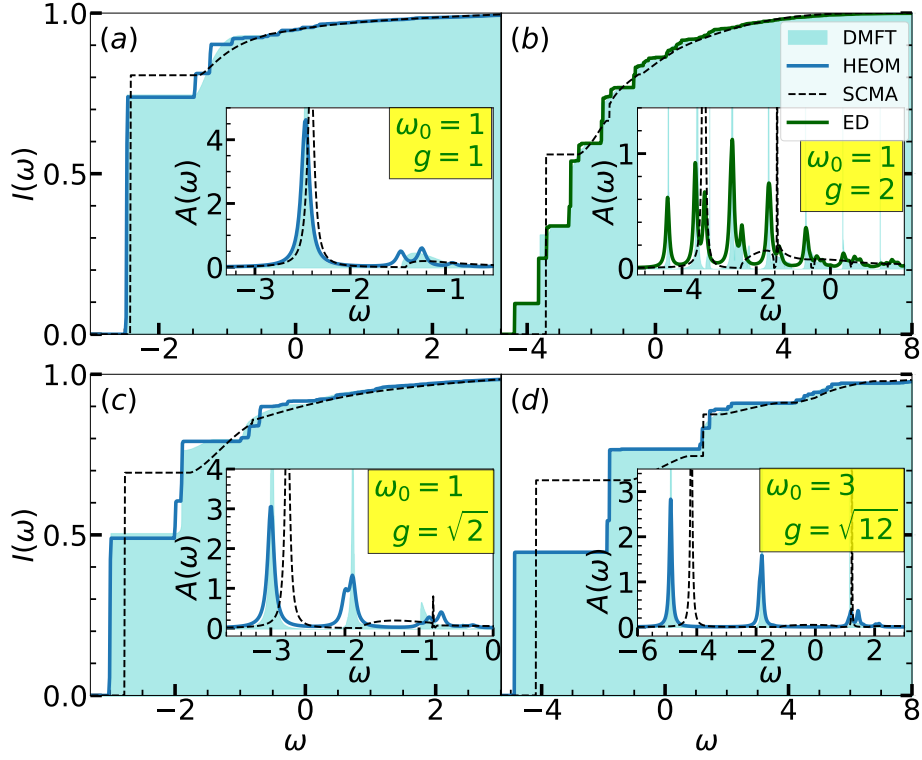


Figure 2.14: Integrated DMFT, HEOM, SCMA, and ED spectral weights, $I(\omega) = \int_{-\infty}^{\omega} d\nu A_k(\nu)$, for $k = 0$ and $T = 0$. The insets show comparisons of the spectral functions. $I(\omega)$ is obtained without broadening, whereas $A(\omega)$ is broadened by Lorentzians of halfwidth $\eta = 0.05$.

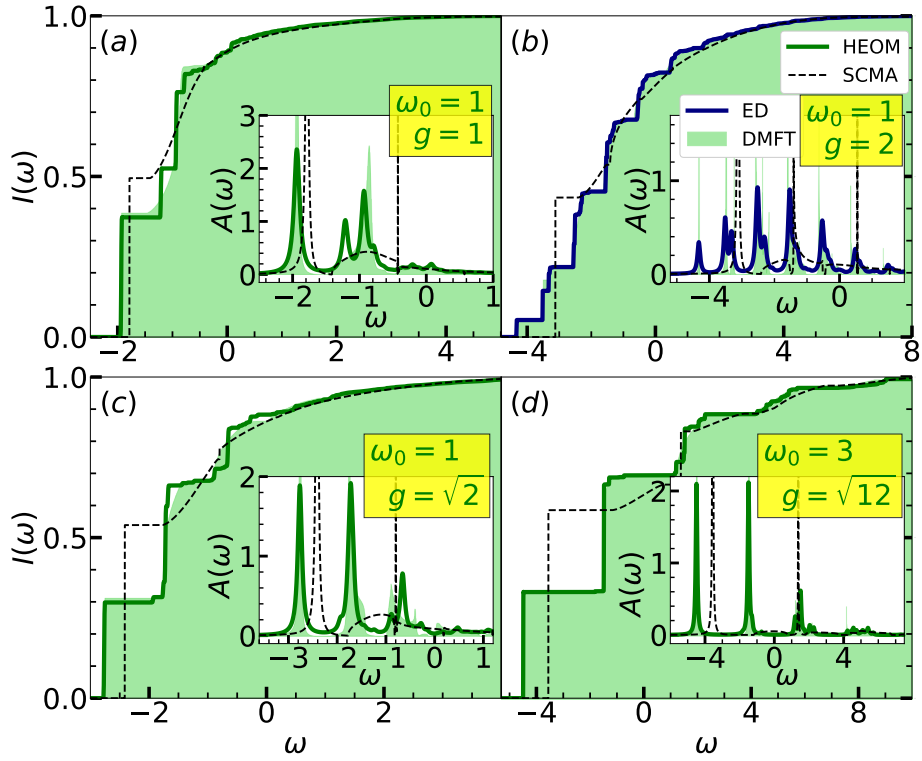


Figure 2.15: Integrated DMFT, HEOM, SCMA, and ED spectral weights, $I(\omega) = \int_{-\infty}^{\omega} d\nu A_k(\nu)$, at $T = 0$. The insets show comparisons of the spectral functions. $I(\omega)$ is obtained without broadening, whereas $A(\omega)$ is broadened by Lorentzians of halfwidth $\eta = 0.05$. Different panels have the following values of the momenta: (a) $k = \frac{8\pi}{25}$, (b) $k = \frac{\pi}{4}$, (c) $k = \frac{\pi}{4}$, (d) $k = \frac{\pi}{3}$.

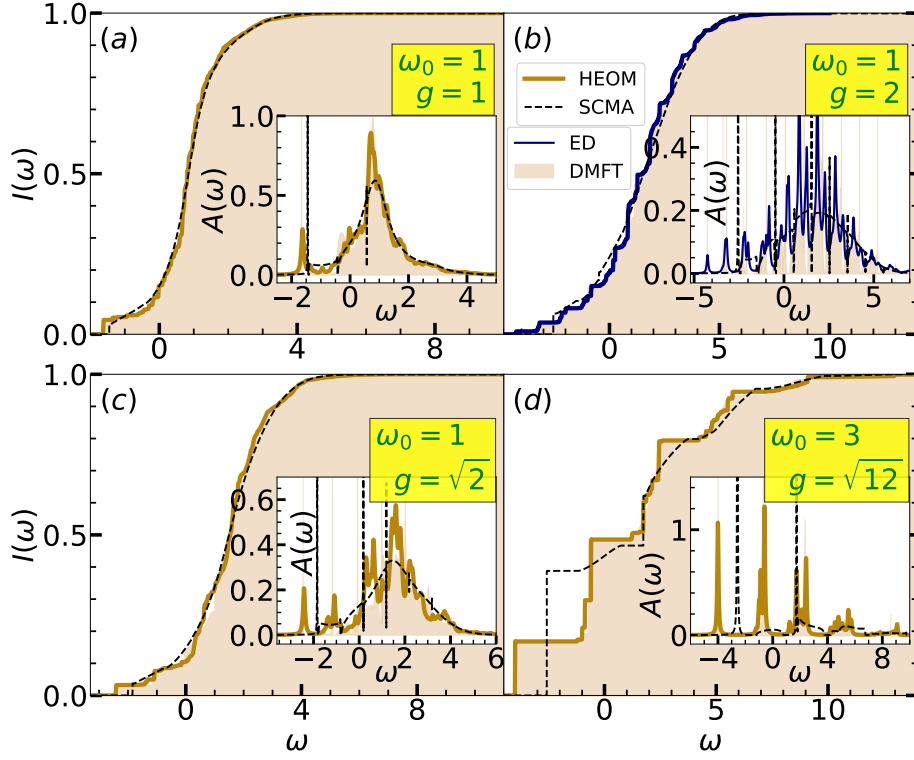


Figure 2.16: Integrated DMFT, HEOM, SCMA, and ED spectral weights, $I(\omega) = \int_{-\infty}^{\omega} d\nu A_k(\nu)$, at $T = 0$. The insets show comparisons of the spectral functions. $I(\omega)$ is obtained without broadening, whereas $A(\omega)$ is broadened by Lorentzians of halfwidth $\eta = 0.05$. Different panels have the following values of the momenta: (a) $k = \frac{16\pi}{25}$, (b) $k = \frac{3\pi}{4}$, (c) $k = \frac{3\pi}{4}$, (d) $k = \frac{2\pi}{3}$.

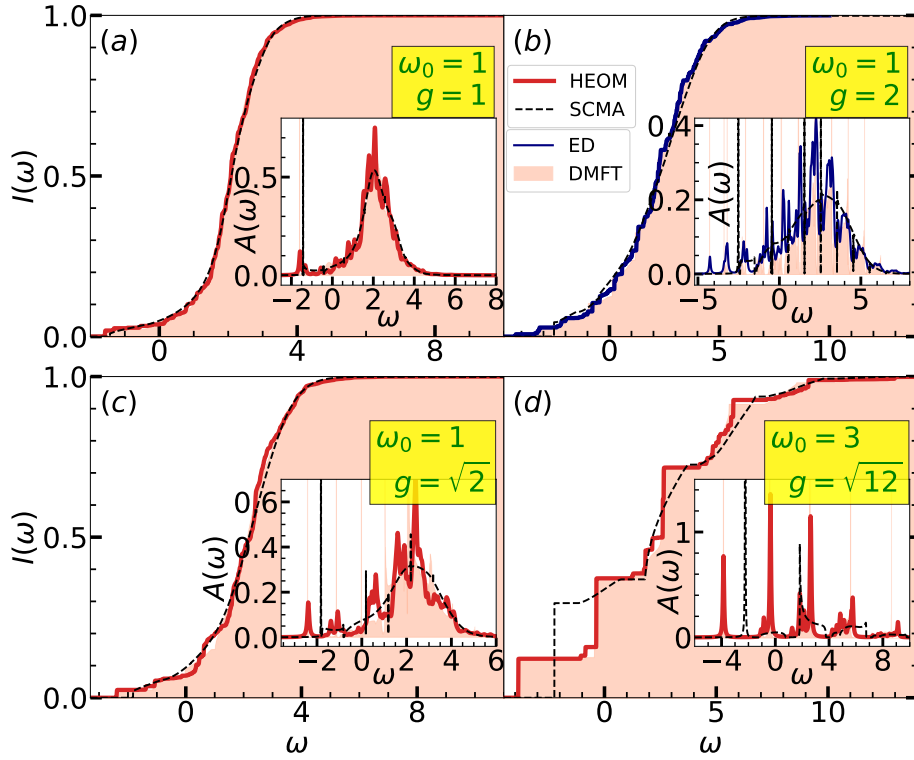


Figure 2.17: Integrated DMFT, HEOM, SCMA, and ED spectral weights, $I(\omega) = \int_{-\infty}^{\omega} d\nu A_k(\nu)$, for $T = 0$ and $k = \pi$. The insets show comparisons of the spectral functions. $I(\omega)$ is obtained without broadening, whereas $A(\omega)$ is broadened by Lorentzians of halfwidth $\eta = 0.05$.

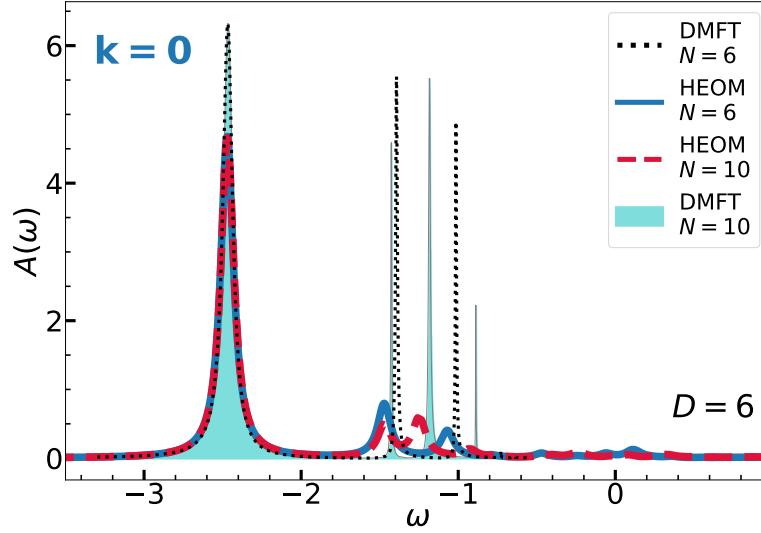


Figure 2.18: Finite-size effects in the DMFT solution at intermediate coupling $\omega_0 = 1$, $g = 1$, $T = 0$.

Other figures in this section support the conclusion that DMFT is an excellent approximate method in the whole parameter space. In contrast, we show that SCMA gives decent predictions only for $\omega_0 = 1$, $g = 1$. As the interaction increases, the SCMA solution misses the position and the weight of the quasiparticle peak, and the satellite peaks are not properly resolved.

Remark 11. *As in Sec. 2.5.2, we note that the HEOM/ED method imposes the periodic boundary conditions on a finite lattice. As a consequence, the HEOM/ED spectral functions are available only for momenta which are integer multiples of $2\pi/N$. Results for additional k -values are obtained using twisted boundary conditions. On the other hand, DMFT is calculated in the thermodynamical limit, and the corresponding spectral functions are thus easily obtained for arbitrary k .*

2.5.5 HEOM Self-Energies

The results for the spectral functions, as well as for the effective mass and ground state energy, have shown that the DMFT gives an excellent approximate solution of the 1D Holstein model in the whole parameter space. This indicates that the self-energy is approximately local. This will now be explicitly demonstrated using the HEOM results. Since $\Sigma_k(\omega) = \Sigma_{-k}(\omega)$ we will show only the results for $k \geq 0$.

In Fig. 2.19 we present the HEOM and DMFT self-energies in the intermediate coupling regime. Figs. 2.19(a) and 2.19(b) show that the self-energies are nearly local, whereas the DMFT solution interpolates in between. The self-energy is approximately local also for $g = \sqrt{2}$; see Figs. 2.19(c)–2.19(d). There is a visible discrepancy only at higher momenta, which reflects in a shift of the spectral functions with respect to the DMFT solution in Figs. 2.9(d) and 2.10(d).

The regime close to the atomic limit is investigated in Fig. 2.20. Panels (c) and (d) show that the results are nearly local, but have a kind of stripe pattern, unlike the DMFT solution. This is just a consequence of the finite-size effects. This can be seen by inspecting the DMFT solutions on lattices with different number of lattice sites N , as shown in Fig. 2.21, which demonstrates that while the spectral functions are not strongly N -dependent, the details of the self-energy are much more sensitive to finite-size effects. Here, we see a stripe pattern in the self-energies, but only in the case when the number of lattice sites N is finite. This is why we see a very good agreement between the DMFT and $N = 6$ HEOM spectral functions in Figs 2.9(g) and 2.9(h).

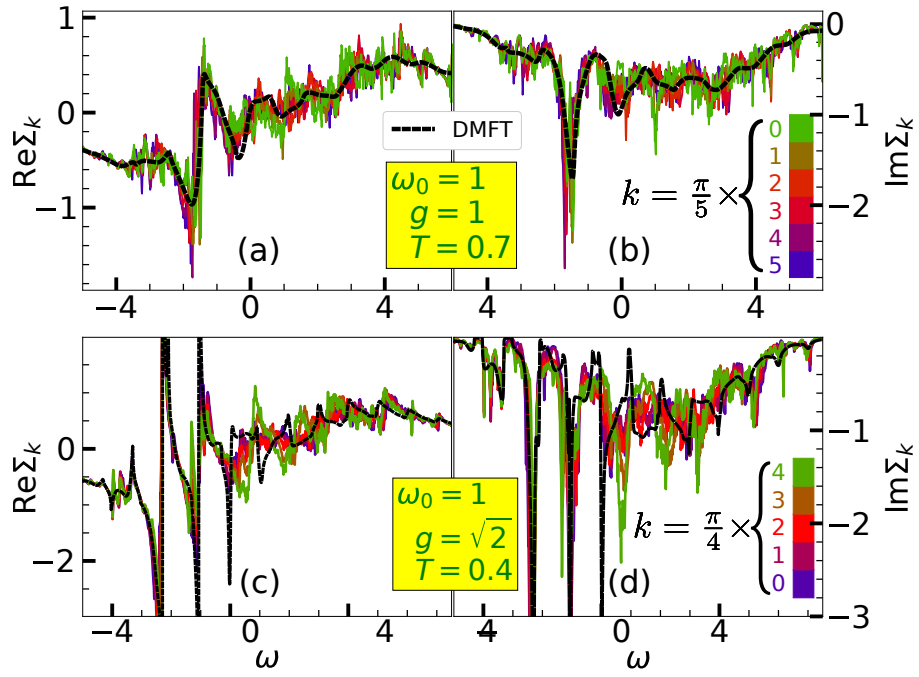


Figure 2.19: HEOM and DMFT self-energies for intermediate coupling.

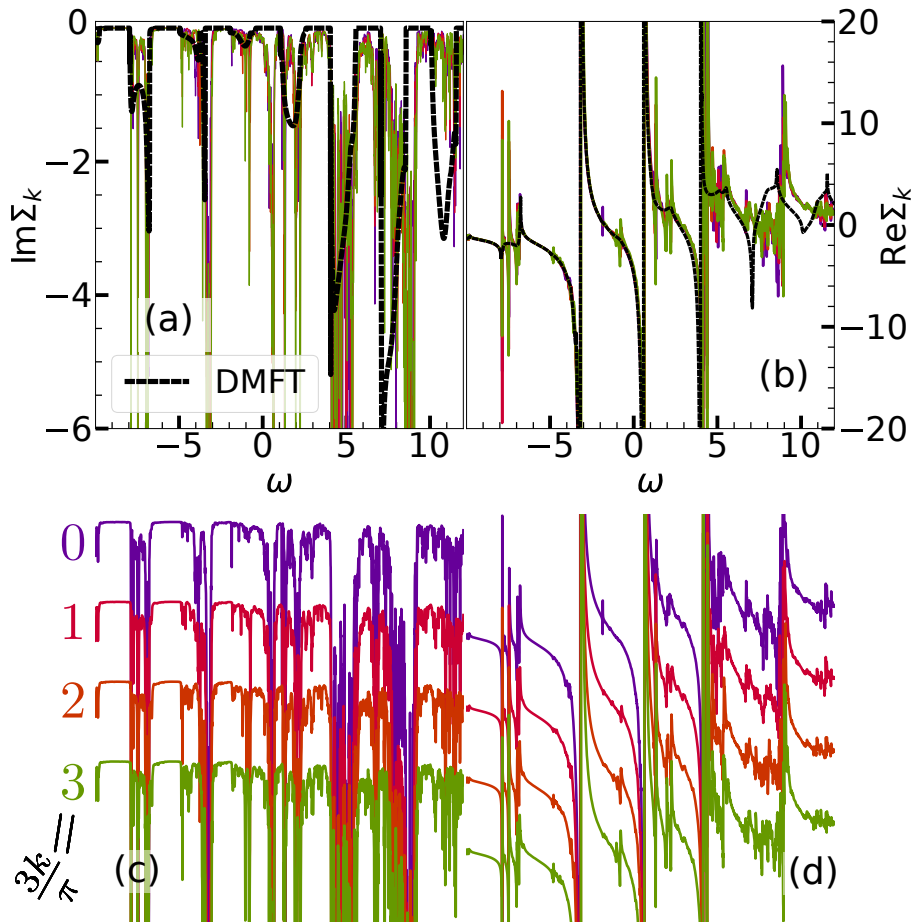


Figure 2.20: Panels (a) and (b) show HEOM and DMFT self-energies close to the atomic limit $\omega_0 = 3$, $g = \sqrt{12}$, $T = 1$. Panels (c)-(d) show the same HEOM results as in (a)-(b) but shifted for different values of momenta k .

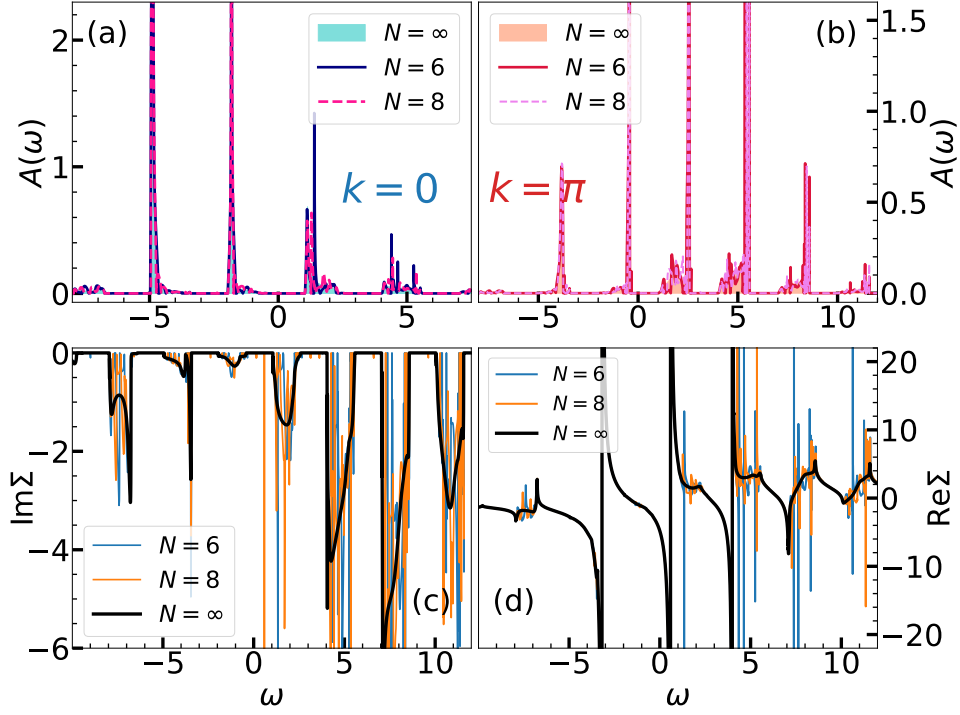


Figure 2.21: DMFT finite-size effects close to the atomic limit $\omega_0 = 3$, $g = \sqrt{12}$, $T = 1$.

2.6 Imaginary Time Correlation Functions

At the end of this chapter, let us perform yet another crosscheck of our conclusions, this time by calculating the correlation function on the imaginary time axis

$$C_{\mathbf{k}}(\tau) = \langle c_{\mathbf{k}}(\tau) c_{\mathbf{k}}^\dagger \rangle_{T,0}, \quad (2.36)$$

where $c_{\mathbf{k}}(\tau) = e^{\tau H} c_{\mathbf{k}} e^{-\tau H}$ and $0 \leq \tau \leq \beta = 1/T$. As a benchmark, we use a quantum Monte Carlo (QMC), which is capable of producing numerically exact results for $C_{\mathbf{k}}(\tau)$.

Remark 12. *To apply the QMC, the correlation function in Eq. (2.36) is expressed using the path integral representation of this quantity, and the imaginary time τ is discretized into small steps $\Delta\tau$. It turns out that the integral over phononic degrees of freedom is Gaussian, and can be evaluated analytically. Thus, the expression reduces to the multidimensional sum over the electronic coordinates. This is then calculated via the Monte Carlo method. We note that the QMC results that we use were obtained by Nenad Vukmirović. The details of the method are presented in Ref. [83]. This is a natural extension of early works where such an approach was applied just to thermodynamic quantities [84–86].*

Despite being numerically exact, QMC only provides the results on the imaginary time axis. This cannot be used to reliably obtain spectral functions, especially when the spectrum has several pronounced peaks, as the numerical continuation to the real-frequency axis is numerically ill-defined. However, the reverse procedure is achievable: $C_{\mathbf{k}}(\tau)$ can easily be calculated from $A_{\mathbf{k}}(\omega)$. Therefore, we have to settle for a comparison on the imaginary axis. The expression that relates these two quantities can be obtained by expressing $C_{\mathbf{k}}(\tau)$ in the energy basis, i.e., using the Lehmann spectral representation (this is done analogous to Sec. 2.1.2 in Part. I)

$$C_{\mathbf{k}}(\tau) = \frac{1}{Z} \sum_{m,n} e^{-\beta E_n} |\langle n | c_{\mathbf{k}} | m \rangle|^2 e^{\tau(E_n - E_m)}, \quad (2.37)$$

where $|n\rangle$, and $|m\rangle$ are states that have exactly zero and one electron, respectively, and an arbitrary number of phonons. Comparing this to Eq. (2.13) of Part I, we immediately conclude that

$$C_{\mathbf{k}}(\tau) = \int_{-\infty}^{\infty} d\omega e^{-\omega\tau} A_{\mathbf{k}}(\omega). \quad (2.38)$$

Equation (2.38) can now be used to check whether the spectral functions that we calculated using DMFT (and also HEOM and SCMA) are consistent with the QMC results.

Fig. 2.22 shows the imaginary time QMC, DMFT and HEOM correlation functions and their deviations from the QMC result, for the same ω_0 and g , as in Fig. 2.9(d). We see that deviations are very small, the relative discrepancy being just a fraction of a percent at $T = 1$. The discrepancy between the DMFT and QMC increases at lower temperatures when the nonlocal correlations are expected to be more important, but it remains quite small even at $T = 0.4$. We also see that the DMFT gives better results at $k = 0$ than at $k = \pi$. Furthermore, the SCMA correlation functions show a clear deviation from other solutions. This is in agreement with our findings in Sec. 2.5. However, as we see, great care is needed when drawing conclusions from the imaginary axis data since a very small difference in the imaginary axis correlation functions can correspond to substantial differences in spectral functions.

In Fig. 2.23 we present the correlation function comparison over a broad set of parameters. The DMFT, HEOM and QMC are in excellent agreement, with the relative discrepancy of the order of one percent for $\tau \sim 1/T$. The SCMA results are also included for comparison.

From Eq. (2.38) we see that the correlation function unevenly treats different frequencies from the spectral function. Because of the exponential term, it takes into account low-frequency contributions with much larger weight. Thus, the favorable comparison of DMFT and QMC reveals that the low-frequency parts of the corresponding spectral functions behave appropriately and fall off fast enough. This is a very important property for calculating quantities where the low-frequency part gives a large contribution to the result, which would be the case for optical conductivity.

Let us now estimate how much a Gaussian centered at frequency a ,

$$A_k^G(\omega) = \frac{W}{\sigma\sqrt{2\pi}} e^{-\frac{(\omega-a)^2}{2\sigma^2}}, \quad (2.39)$$

would contribute to the correlation function. Here W is the spectral weight and σ is the standard deviation of the Gaussian. This could model a tiny peak present due to the noise, or a real physical contribution. The corresponding part of the correlation function C_k^G can be singled out since Eq. (2.38) is linear in A_k . It can be evaluated analytically, giving

$$C_k^G(\tau) = W e^{\frac{\sigma^2\tau^2}{2} - a\tau}. \quad (2.40)$$

We see that the spectral weight contributes linearly, while the position of the delta peak contributes exponentially (note that a can be negative). The width of the Gaussian σ , as well as the imaginary time τ , are quadratic inside the exponential. Hence, Eq. (2.40) explicitly shows that precise calculation of the correlation function requires very accurate spectral functions at low frequencies. Even a small error or noise can produce a completely wrong result. Reliable comparison of $C_{\mathbf{k}}(\tau)$ was made possible only due to the high precision of both DMFT and HEOM calculations.

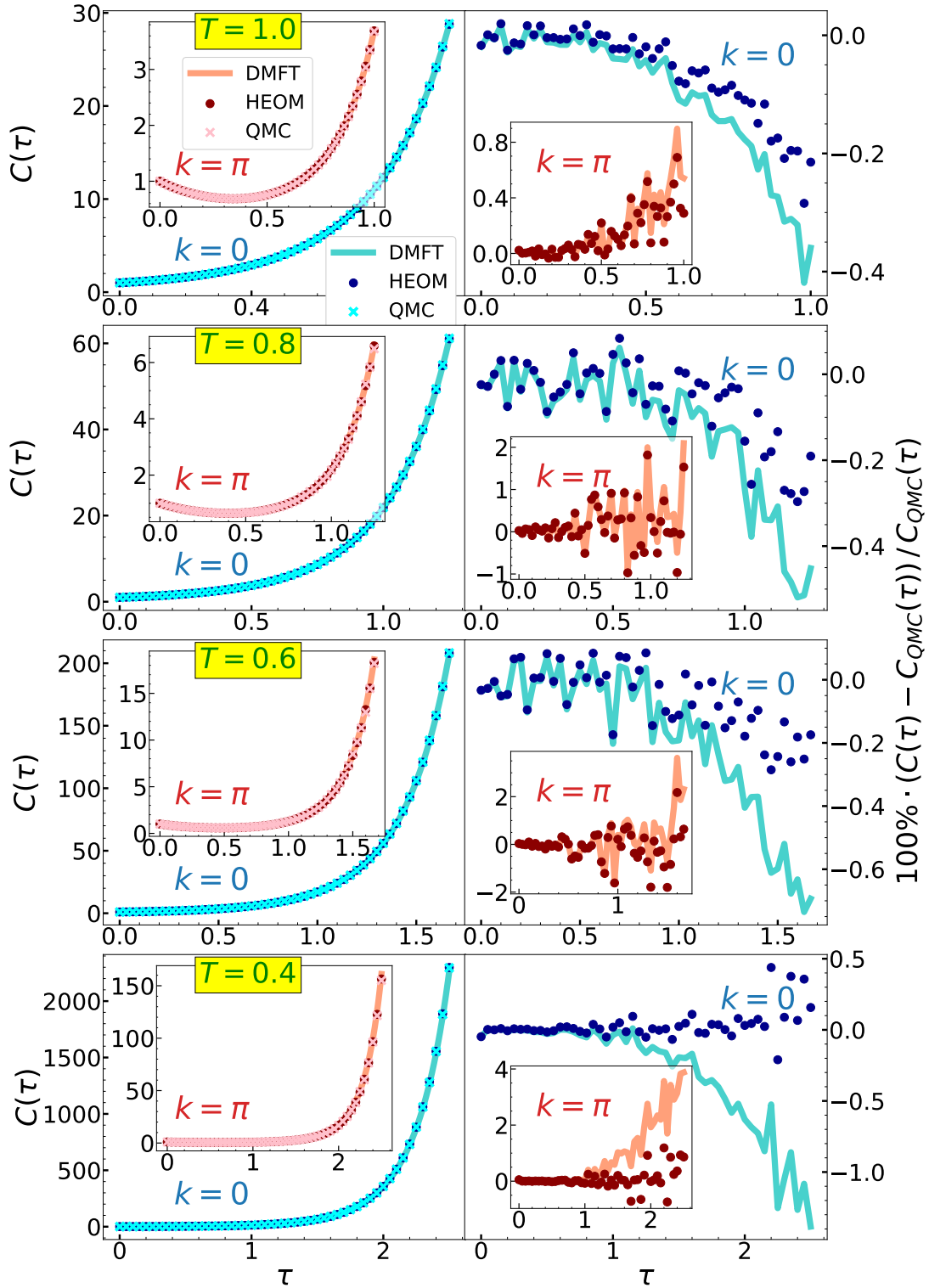


Figure 2.22: DMFT, HEOM, and QMC correlation functions for $\omega_0 = 1$, $g = \sqrt{2}$ at $k = 0$ and $k = \pi$, at several temperatures. The right panels show the relative discrepancy between DMFT and HEOM results with respect to QMC.

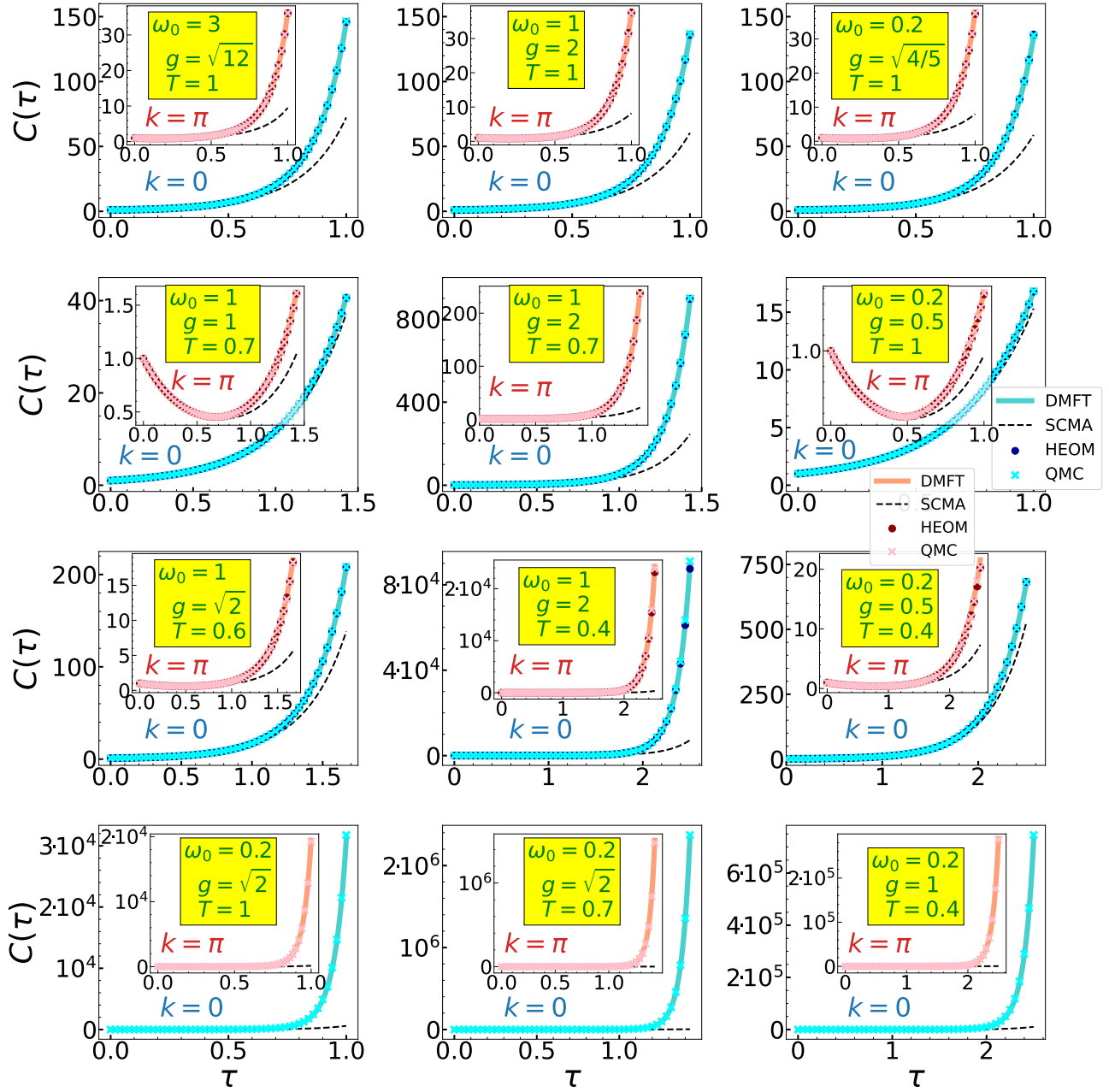


Figure 2.23: Comparison of DMFT, HEOM, QMC and SCMA correlation functions over a wide range of parameters. The HEOM results are not available for the parameters in the last row.

Cumulant Expansion Method

The results that we present in this chapter are a product of our work that we published in Ref. [87].

3.1 Introduction

The cumulant expansion (CE) method presents an alternative to the usual Dyson equation approach for the calculation of spectral functions of interacting quantum many-particle systems [1]. This approximation assumes that the Green's function can be written in an exponential form $G_{\mathbf{k}}(t) = G_{\mathbf{k},0}(t)e^{C_{\mathbf{k}}(t)}$. Here, $G_{\mathbf{k}}(t)$ and $G_{\mathbf{k},0}(t)$ represent the Green's functions of the full and noninteracting theory respectively, while $C_{\mathbf{k}}(t)$ is the auxiliary function, called the cumulant, that needs to be determined. This ansatz is based on the exact solution for the Green's function of the Lundqvist's X-ray model problem, which is of exponential form [88, 89]. This is another fermion-boson (core hole-plasmon) model, whose spectral functions exhibit multiple satellite peaks, analogous to the ones we observed in Chapter 2. Furthermore, it was shown that the cumulant approach gives a correct description of the valence electrons as well [90]. This suggests that the CE is well suited for the description of both the weak coupling and atomic limits, while its applicability in other regimes needs to be thoroughly investigated.

CE did not emerge recently. It was extensively used in the past for the studies of electron-phonon systems in metals, semiconductors, and insulators [91–93], as for plasmonic effects in metals and free electron gas [90, 94]. Recently, interest in this method has been renewed due to the possibility of combining CE with ab initio methods. Since then it has been applied to study spectra of a wide class of materials, including perovskite SrTiO₃ [95], transition-metal oxides ZnO and TiO₂ [95, 96], ionic insulators MgO and LiF [97] etc. Combining the CE with the Kubo formula for charge transport gives an attractive route to calculate mobility in semiconductors beyond the Boltzmann approach, which is applicable only for weak electron-phonon coupling [2]. This was very recently demonstrated for SrTiO₃ [98] and naphthalene [99]. CE was even applied to elemental metals Cu, Nb, Pb, Ta and V, showing that it gives substantial correction to the Migdal approximation in the case of stronger electron-phonon interaction [100]. Promising results in the case of plasmons have also been emerging, with significant attention being devoted to the combination of the well-known GW approximation with the CE [101–107]. Furthermore, CE was used to study absorption spectra in molecular aggregates representative of photosynthetic pigment-protein complexes [108–110]. Some theoretical progress in the development of the CE has also been made. As a solution to an uneven treatment of particles and holes, Kas et al. introduced the CE of the retarded Green's function, instead of the time-ordered one, which was commonly used at the time [111]. Generalizations of the CE are also being developed [112, 113].

Despite the attention that is paid to the theoretical aspect of this method, a thorough assessment of the range of validity and the limitations of CE is still lacking. One of the purposes of this work is to fill that gap in the literature. To achieve this, one can turn to simplified models of the electron-

phonon interaction where reliable benchmarks already exist. In the case of the Fröhlich model, CE gives the ground state energy and the effective mass [97, 114] similar to the exact QMC calculations for moderate interaction [115]. This is in contrast to the Dyson-Migdal approach which severely underestimates mass renormalization. However, a comparison of the corresponding spectral functions is missing, since reliable QMC results are not available due to the well-known problems with analytical continuation. In contrast, accurate results for the spectral functions are available in the Holstein model, as we have already seen in Chapter 2. Therefore, the Holstein polaron model gives a unique opportunity to explore the applicability of the CE in detail. Recently, a similar feat was conducted in Ref. [116]. Still, there are several questions that remain unresolved. Most importantly, a comparison of spectral functions was made just for a small set of parameters on a finite-size lattice, where the benchmark spectral functions were available from the finite-temperature Lanczos results [46], while the charge transport was not examined at all. On the other hand, our findings from Chapter 2, demonstrating that DMFT is an extremely cheap and accurate method, make us ideally positioned to perform a much more thorough analysis of the CE method, using the DMFT as a benchmark. In addition to calculating the 1D spectral functions in a wider range of parameter regimes compared to Ref. [116], we extend their results by providing a more comprehensive analysis which includes the spectral sum rules, quasiparticle properties, charge mobility, as well as the 2D spectral functions.

3.2 Cumulant Expansion: Theoretical Foundations

We have introduced the CE, as a method that assumes the Green's function to be of exponential form

$$G_{\mathbf{k}}(t) = G_{\mathbf{k},0}(t)e^{C_{\mathbf{k}}(t)} = -i\theta(t)e^{-i\varepsilon_{\mathbf{k}}t}e^{C_{\mathbf{k}}(t)}, \quad (3.1)$$

where $C_{\mathbf{k}}(t)$ is the so-called cumulant function. To apply this, we first need to find a way to calculate $C_{\mathbf{k}}(t)$. Usually, this is only done in the lowest-order perturbation theory. Such an approach bears the name the *second-order cumulant expansion*¹, and this will be one of the central themes of this thesis.

3.2.1 Theoretical Framework for the Calculation of the Second-Order Cumulant Function

Even though we introduced the cumulant expansion as an alternative to the Dyson approach, in the lowest-order perturbation theory the cumulant function is usually calculated from the self-energy in the Migdal approximation. This is justified because the CE actually improves the results given by the lowest-order self-energy, as will be demonstrated in the subsequent sections.

To derive the expression for the second-order cumulant function, we start from the leading terms in the Taylor expansion of the Dyson equation

$$G_{\mathbf{k}}(\omega) = (G_{\mathbf{k},0}(\omega)^{-1} - \Sigma_{\mathbf{k}}(\omega))^{-1} \approx G_{\mathbf{k},0}(\omega) + G_{\mathbf{k},0}(\omega)\Sigma_{\mathbf{k}}(\omega)G_{\mathbf{k},0}(\omega), \quad (3.2)$$

and take its inverse Fourier transform, equating it to the leading order terms in Eq. (3.1)

$$G_{\mathbf{k}}(t) = G_{\mathbf{k},0}(t)e^{C_{\mathbf{k}}(t)} \approx G_{\mathbf{k},0}(t) [1 + C_{\mathbf{k}}(t)]. \quad (3.3)$$

We obtain

$$\int \frac{d\omega}{2\pi} e^{-i\omega t} G_{\mathbf{k},0}(\omega) + \int \frac{d\omega}{2\pi} e^{-i\omega t} G_{\mathbf{k},0}(\omega)\Sigma_{\mathbf{k}}(\omega)G_{\mathbf{k},0}(\omega) = \cancel{G_{\mathbf{k},0}(t)} + G_{\mathbf{k},0}(t)C_{\mathbf{k}}(t), \quad (3.4)$$

¹The second-order cumulant expansion will often be abbreviated, and we will refer to it simply as the cumulant expansion.

where the first terms on both sides cancel each other out. This can be solved for $C_{\mathbf{k}}(t)$ by explicitly writing out the free Green's function as $G_{\mathbf{k},0}(t) = -i\theta(t)e^{-i\varepsilon_{\mathbf{k}}t}$, and restricting ourselves to positive times $t \geq 0$, which is justified since we are working with retarded quantities. We get

$$C_{\mathbf{k}}(t) = ie^{i\varepsilon_{\mathbf{k}}t} \int_{-\infty}^{\infty} \frac{d\omega}{2\pi} \frac{e^{-i\omega t} \Sigma_{\mathbf{k}}(\omega)}{(\omega - \varepsilon_{\mathbf{k}} + i0^+)^2}. \quad (3.5)$$

Using the spectral representation of the self-energy

$$\Sigma_{\mathbf{k}}(\omega) = \int_{-\infty}^{\infty} \frac{d\nu}{\pi} \frac{|\text{Im}\Sigma_{\mathbf{k}}(\nu)|}{\omega - \nu + i0^+}, \quad (3.6)$$

and the contour integration over ω , Eq. (3.5) simplifies to [111]

$$C_{\mathbf{k}}(t) = \frac{1}{\pi} \int_{-\infty}^{\infty} d\omega \frac{|\text{Im}\Sigma_{\mathbf{k}}(\omega + \varepsilon_{\mathbf{k}})|}{\omega^2} (e^{-i\omega t} + i\omega t - 1). \quad (3.7)$$

Since in our derivation, we restricted ourselves to the leading order terms in Eq. (3.1) and the Dyson equation, we conclude that the self-energy in Eq. (3.7) has to be in the lowest order (i.e., Migdal) approximation.

From our derivation, we now see all the positive aspects of the CE:

- It can be regarded as a post-processing method, which takes the Migdal self-energy as input and improves² those results by using Eqs. (3.7) and (3.1).
- In this derivation, we have not used any specifics of the model we are considering, implying that Eq. (3.7) is not restricted to the Holstein model, and can be easily combined even with *ab initio* methods.
- It is a one-shot method, meaning that it does not contain any iterative self-consistent calculations. This makes it numerically cheap.

Remark 13. One direct consequence of Eq. (3.7) is that

$$C_{\mathbf{k}}(t=0) = \left. \frac{dC_{\mathbf{k}}(t)}{dt} \right|_{t=0} = 0, \quad (3.8)$$

meaning that $C_{\mathbf{k}}(t)$ is a quadratic function of time around $t \approx 0$. This is important, since the cumulant function $C_{\mathbf{k}}(t)$ for small t is related to the Green's function in frequency space for large ω . In addition, $G_{\mathbf{k}}(\omega)$ for large frequencies is related to the spectral sum rules. The latter can be seen by starting from

$$\begin{aligned} G_{\mathbf{k}}(i\omega_n) &= \int_{-\infty}^{\infty} d\omega \frac{A_{\mathbf{k}}(\omega)}{i\omega_n - \omega} = \frac{1}{i\omega_n} \int_{-\infty}^{\infty} d\omega \frac{A_{\mathbf{k}}(\omega)}{1 - \frac{\omega}{i\omega_n}} \\ &\approx \frac{1}{i\omega_n} \int_{-\infty}^{\infty} d\omega A_{\mathbf{k}}(\omega) \left[1 + \frac{\omega}{i\omega_n} + \left(\frac{\omega}{i\omega_n} \right)^2 + \left(\frac{\omega}{i\omega_n} \right)^3 + \dots \right], \text{ for } i\omega_n \gg 1, \end{aligned} \quad (3.9)$$

and using the analytical continuation to the real-frequency axis $i\omega_n \rightarrow \omega + i0^+$, obtaining

$$G_{\mathbf{k}}(\omega) \approx \sum_{n=0}^{\infty} \frac{\mathcal{M}_n(\mathbf{k})}{\omega^{n+1}}, \text{ for } \omega \rightarrow \infty, \quad (3.10)$$

where $\mathcal{M}_n(\mathbf{k})$ is the n -th spectral sum rule, given by Eq. (2.39) from Part I.

Therefore, we conclude that the cumulant function for small times is related to the spectral sum rules. In general, $C_{\mathbf{k}}(t=0) = 0$ is sufficient for the first spectral sum rule $\int A_{\mathbf{k}}(\omega) d\omega = 1$ to be satisfied, while the second sum rule $\int A_{\mathbf{k}}(\omega) \omega d\omega = \varepsilon_{\mathbf{k}}$ is a consequence of both conditions in Eq. (3.8). In Sec. 3.4.3, we will see that within the Holstein model, additional spectral sum rules are satisfied as well.

²The fact that this method does actually improve the MA, will be demonstrated in the rest of this chapter.

3.2.2 Numerical Challenges when Applying the Second-order Cumulant Expansion

The cumulant function can be calculated directly from Eq. (3.7). However, there are some numerical challenges caused by the removable singularity at $\omega = 0$ and by the rapidly oscillating trigonometric factor $e^{-i\omega t}$ for large t . The latter is important for the weak electron-phonon couplings, where it is necessary to propagate $C_{\mathbf{k}}(t)$ up to long times until the Green's function is sufficiently damped out. The same problem occurs in other regimes as well (e.g., close to the atomic limit), where the Green's function does not attenuate at all; see Sec. 3.3.2.

The numerical singularity at $\omega = 0$ can be completely avoided if we consider the cumulant's second derivative

$$\frac{d^2 C_{\mathbf{k}}(t)}{dt^2} = \int_{-\infty}^{\infty} \frac{d\omega}{\pi} \text{Im}\Sigma_{\mathbf{k}}(\omega + \varepsilon_{\mathbf{k}}) e^{-i\omega t} \equiv 2e^{i\varepsilon_{\mathbf{k}}t} \tilde{\sigma}_{\mathbf{k}}(t), \quad (3.11)$$

where we used $\text{Im}\Sigma_{\mathbf{k}}(\omega) < 0$ and introduced

$$\tilde{\sigma}_{\mathbf{k}}(t) \equiv \int_{-\infty}^{\infty} \text{Im}\Sigma_{\mathbf{k}}(\omega) e^{-i\omega t} \frac{d\omega}{2\pi}. \quad (3.12)$$

Then, $C_{\mathbf{k}}(t)$ is obtained as a double integral over time of Eq. (3.11)

$$C_{\mathbf{k}}(t) = 2 \int_0^t dt' \int_0^{t'} dt'' e^{i\varepsilon_{\mathbf{k}}t''} \tilde{\sigma}_{\mathbf{k}}(t''), \quad (3.13)$$

where the lower boundaries of both integrals have to be zero, as guaranteed by the initial conditions that were given in Eq. (3.8). Using the Cauchy formula for repeated integration, this can also be written as a single integral

$$C_{\mathbf{k}}(t) = 2 \int_0^t (t-x) e^{i\varepsilon_{\mathbf{k}}x} \tilde{\sigma}_{\mathbf{k}}(x) dx. \quad (3.14)$$

This completely removed the problem of singularity at $\omega = 0$. Still, the problem of rapid oscillations of the subintegral function remains, due to the presence of $e^{i\varepsilon_{\mathbf{k}}x}$ term. In Sec. 3.3 we provide an elegant solution for this issue, focusing on the case of the Holstein model.

Once the cumulant function has been evaluated, Eq. (3.7) determines the Green's function, while the spectral function can be calculated as $A_{\mathbf{k}}(\omega) = (-1/\pi)\text{Im}G_{\mathbf{k}}(\omega)$. However, in practice, the free electron part $e^{-i\varepsilon_{\mathbf{k}}t}$ in Eq. (3.22) typically oscillates much more quickly than $e^{C_{\mathbf{k}}(t)}$. Hence, it is much more convenient to calculate

$$A_{\mathbf{k}}(\omega + \varepsilon_{\mathbf{k}}) = \frac{1}{\pi} \text{Re} \int_0^{\infty} dt e^{i\omega t} e^{C_{\mathbf{k}}(t)}, \quad (3.15)$$

and only subsequently shift the frequency axis $\omega \rightarrow \omega - \varepsilon_{\mathbf{k}}$ to obtain $A_{\mathbf{k}}(\omega)$.

3.2.3 Asymptotic Expansion for Cumulant when $t \rightarrow \infty$

In Remark 13, we investigated the cumulant function for small t and concluded that it behaves as a quadratic function of time, as $t \rightarrow 0$. In addition, we noted that such behavior has direct consequences on the spectral sum rules. Some further insight about the cumulant function can be gained by also inspecting its behavior for $t \rightarrow \infty$. For example, as we now demonstrate, the quasiparticle properties within CE are completely determined by the asymptotic expansion of $C_{\mathbf{k}}(t)$ for large times t . To see that, we start from Eq. (3.11) and obtain

$$i \frac{dC_{\mathbf{k}}}{dt}(t \rightarrow \infty) = i \int_0^{\infty} \frac{d^2 C_{\mathbf{k}}(t)}{dt^2} dt = -\frac{i}{\pi} \int_{-\infty}^{\infty} d\omega |\text{Im}\Sigma_{\mathbf{k}}(\omega + \varepsilon_{\mathbf{k}})| \int_0^{\infty} dt e^{-i\omega t} = \Sigma_{\mathbf{k}}(\varepsilon_{\mathbf{k}}), \quad (3.16)$$

where we used the identity $\int_0^\infty dt e^{-i\omega t} = \pi\delta(\omega) - i\mathcal{P}\frac{1}{\omega}$, and the Kramers-Kronig relations³ for the self-energy. From Eq. (3.16) and from the functional form of Eq. (3.7), we can conclude that the cumulant function $C_{\mathbf{k}}(t)$, and thus the whole exponent in Eq. (3.1) is a linear function of time

$$C_{\mathbf{k}}(t) - i\varepsilon_{\mathbf{k}}t \approx -i\tilde{E}_{\mathbf{k}}t + \text{const for } t \rightarrow \infty, \quad (3.19)$$

where

$$\tilde{E}_{\mathbf{k}} = \varepsilon_{\mathbf{k}} + \Sigma_{\mathbf{k}}(\varepsilon_{\mathbf{k}}). \quad (3.20)$$

As a consequence, the Green's function in Fourier space has a simple pole situated at $\tilde{E}_{\mathbf{k}}$, as seen from the following expression

$$\begin{aligned} G_{\mathbf{k}}(\omega) &= -i \int_0^\infty e^{it(\omega - \varepsilon_{\mathbf{k}} - \frac{iC_{\mathbf{k}}(t)}{t})} dt \\ &= -i \int_0^\Lambda e^{it(\omega - \varepsilon_{\mathbf{k}} - \frac{iC_{\mathbf{k}}(t)}{t})} dt - i \int_\Lambda^\infty \underbrace{e^{it(\omega - \varepsilon_{\mathbf{k}} - \frac{iC_{\mathbf{k}}(t)}{t})}}_{\approx e^{it(\omega - \tilde{E}_{\mathbf{k}})} \text{ for large enough } \Lambda} dt. \end{aligned} \quad (3.21)$$

Therefore, quasiparticle properties are encoded in $\tilde{E}_{\mathbf{k}}$: its real and imaginary parts correspond to the quasiparticle energy and scattering rate, respectively.

Remark 14. We note that, in our present analysis, we implicitly assumed that $\frac{dC_{\mathbf{k}}}{dt}(t \rightarrow \infty)$ exists and is finite. Although this is generally true, there are a few exceptions. In the Holstein model, the first assumption is violated at the atomic limit ($t_0 = 0$; see Eq. (3.53)), while the second assumption is violated at the adiabatic limit ($\omega_0 = 0$) for $k = 0$ or $k = \pm\pi$; see Eq. (3.45) or Eq. (2.23) from Part I.

The knowledge that we gained about the analytic properties of the $C_{\mathbf{k}}(t)$ provides us with an intuitive understanding of how the shape of the cumulant determines the shape of the spectral function. The asymptotic limits $t \rightarrow \infty$ (where $C_{\mathbf{k}}(t)$ is linear) and $t \rightarrow 0$ (where $C_{\mathbf{k}}(t)$ is quadratic) by themselves, to a large extent, describe only the simple one-peak spectral functions, while the crossover between these limits is responsible for the emergence of satellite peaks. This can be explained as follows: if the cumulant was quadratic over the whole t -domain $C_{\mathbf{k}}(t) = ct^2$, the spectral function would have a simple Gaussian shape. Similarly, the Lorentzian shape would be obtained from the linear cumulant $C_{\mathbf{k}}(t) = ct$. This suggests that the simple crossover between quadratic (at small t) and linear (at large t) behaviors would also give a simple one-peak shape of the spectral function. The information about phonon satellites is thus completely encoded in the $C_{\mathbf{k}}(t)$ for intermediate times t , which depends on the system and approximation in which the cumulant function is calculated.

3.2.4 Alternative Derivation of the Cumulant Function

So far, we derived the expression for the second-order cumulant expansion in terms of the self-energy. Let us now demonstrate how the cumulant function (not necessarily the second-order $C_{\mathbf{k}}(t)$) in the Holstein model can be calculated in general, not resorting to the use of the Dyson formalism.

³Kramers-Kronig relations for the self-energy read as

$$\text{Re}\Sigma_{\mathbf{k}}(\omega) = \text{Re}\Sigma_{\mathbf{k}}(\omega \rightarrow \infty) + \mathcal{P} \int \frac{d\omega'}{\pi} \frac{\text{Im}\Sigma_{\mathbf{k}}(\omega')}{\omega' - \omega}, \quad (3.17)$$

$$\text{Im}\Sigma_{\mathbf{k}}(\omega) = -\mathcal{P} \int \frac{d\omega'}{\pi} \frac{\text{Re}[\Sigma_{\mathbf{k}}(\omega')] - \Sigma_{\mathbf{k}}(\omega \rightarrow \infty)}{\omega' - \omega}, \quad (3.18)$$

but we restrict ourselves to the case when $\Sigma_{\mathbf{k}}(\omega \rightarrow \infty) = 0$, which is relevant in our case.

3.2.4.1 Setting up the Notation

In Eq. (2.14) of Part I, we showed that the Green's function can be written in the following form

$$G_{\mathbf{k}}(t) = -i\theta(t)\langle c_{\mathbf{k}}(t)c_{\mathbf{k}}^{\dagger} \rangle_{T,0}, \quad (3.22)$$

where $c_{\mathbf{k}}(t) = e^{iHt}c_{\mathbf{k}}e^{-iHt}$. For the sake of this section, it turns out that it is convenient to separate the Hamiltonian H as in Eq. (1.2) of Part I, into its electron part H_{el} , phonon part H_{ph} , and electron-phonon coupling part $H_{\text{el-ph}}$. These terms are given by⁴

$$H_{\text{el}} = -t_0 \sum_{\langle ij \rangle} \left(c_i^{\dagger} c_j + \text{H.c.} \right) = \sum_{\mathbf{k}} \varepsilon_{\mathbf{k}} c_{\mathbf{k}}^{\dagger} c_{\mathbf{k}}, \quad (3.23a)$$

$$H_{\text{ph}} = \omega_0 \sum_i a_i^{\dagger} a_i = \omega_0 \sum_{\mathbf{k}} a_{\mathbf{k}}^{\dagger} a_{\mathbf{k}}, \quad (3.23b)$$

$$H_{\text{el-ph}} = -g \sum_i c_i^{\dagger} c_i \left(a_i^{\dagger} + a_i \right) = -\frac{g}{\sqrt{N}} \sum_{\mathbf{k}, \mathbf{q}} c_{\mathbf{k}+\mathbf{q}}^{\dagger} c_{\mathbf{k}} \left(a_{\mathbf{q}} + a_{-\mathbf{q}}^{\dagger} \right). \quad (3.23c)$$

Remark 15. As explained in Sec. 2.1.2 of Part I, the symbol $\langle \dots \rangle_{T,0}$ in Eq. (3.22) denotes the thermal average over the states with no electrons and an arbitrary number of phonons. For the rest of this section, to avoid possible confusion, we introduce a more explicit notation $|0, \tilde{n}_p\rangle$, which denotes an arbitrary⁵ state with n_p phonons and no electrons. The sum over all possible phonon configurations will be denoted by $\sum_{\{n_p\}}$. Using these, the expectation value $\langle x \rangle_{T,0}$, for arbitrary x can be expressed as

$$\langle x \rangle_{T,0} = \frac{\sum_{\{n_p\}} \langle 0, \tilde{n}_p | e^{-H_{\text{ph}}/T} x | 0, \tilde{n}_p \rangle}{\sum_{\{n_p\}} \langle 0, \tilde{n}_p | e^{-H_{\text{ph}}/T} | 0, \tilde{n}_p \rangle}. \quad (3.24)$$

Furthermore, we also introduce $|\mathbf{k}, \tilde{n}_p\rangle \equiv c_{\mathbf{k}}^{\dagger} |0, \tilde{n}_p\rangle$ and $\mathcal{Z}_p = \sum_{\{n_p\}} \langle 0, \tilde{n}_p | e^{-H_{\text{ph}}/T} | 0, \tilde{n}_p \rangle$.

3.2.4.2 Theoretical Framework for the Calculation of the Cumulant Function of Arbitrary Order

Starting from Eq. (3.22), and using the fact that $|0, \tilde{n}_p\rangle$ is an eigenstate of both the full and the phononic Hamiltonian $H|0, \tilde{n}_p\rangle = H_{\text{ph}}|0, \tilde{n}_p\rangle = n_p\omega_0|0, \tilde{n}_p\rangle$ it follows that

$$G_{\mathbf{k}}(t) = \frac{-i\theta(t)}{\mathcal{Z}_p} \sum_{\{n_p\}} e^{i\omega_0 n_p t} e^{-n_p\omega_0/T} \langle 0, \tilde{n}_p | c_{\mathbf{k}} e^{-iHt} c_{\mathbf{k}}^{\dagger} | 0, \tilde{n}_p \rangle. \quad (3.25)$$

The term e^{-iHt} can be expressed using the identity that relates two different, but equivalent, forms for the evolution operator in the Dirac picture,

$$e^{iH_{\text{el}}t} e^{iH_{\text{ph}}t} e^{-iHt} = \hat{T}_t \exp \left[-i \int_0^t dt_1 H_{\text{el-ph}}^{(I)}(t_1) \right], \quad (3.26)$$

giving

$$e^{-iHt} = e^{-iH_{\text{ph}}t} e^{-iH_{\text{el}}t} \hat{T}_t \exp \left[-i \int_0^t dt_1 H_{\text{el-ph}}^{(I)}(t_1) \right]. \quad (3.27)$$

Here, $H_{\text{el-ph}}^{(I)}$ is the electron-phonon interaction part of the Hamiltonian in the Dirac picture and \hat{T}_t is the time-ordering operator. Using the fact that the purely phononic part $e^{-iH_{\text{ph}}t}$, and the purely electronic part $e^{-iH_{\text{el}}t}$ can be easily dealt with using

$$\langle 0, \tilde{n}_p | e^{-iH_{\text{ph}}t} = e^{-i\omega_0 n_p t} \langle 0, \tilde{n}_p |, \quad (3.28a)$$

⁴Here, N is the number of sites, that we take to be infinitely large $N \rightarrow \infty$, in order to get the thermodynamic limit.

⁵We say 'arbitrary' because such state is not unique.

$$\langle 0, \tilde{n}_p | c_{\mathbf{k}} e^{-iH_{\text{el}}t} = e^{-i\varepsilon_{\mathbf{k}}t} \langle 0, \tilde{n}_p | c_{\mathbf{k}}, \quad (3.28b)$$

we see that Eq. (3.25) becomes

$$G_{\mathbf{k}}(t) = -\frac{i\theta(t)}{\mathcal{Z}_p} e^{-i\varepsilon_{\mathbf{k}}t} \sum_{\{n_p\}} e^{-n_p\omega_0/T} \left\langle 0, \tilde{n}_p \left| c_{\mathbf{k}} \hat{T}_t \exp \left[-i \int_0^t dt_1 H_{\text{el-ph}}^{(I)}(t_1) \right] c_{\mathbf{k}}^\dagger \right| 0, \tilde{n}_p \right\rangle \quad (3.29a)$$

$$\equiv -i\theta(t) e^{-i\varepsilon_{\mathbf{k}}t} \left\langle \hat{T}_t e^{-i \int_0^t dt_1 H_{\text{el-ph}}^{(I)}(t_1)} \right\rangle_{T,\mathbf{k}}. \quad (3.29b)$$

The expressions of the form (3.29b) have been extensively studied in the past. As shown in Eq. (6.10) of Kubo's cumulant paper [117], the expectation value with the time-ordering can be written as

$$\left\langle \hat{T}_t e^{-i \int_0^t dt_1 H_{\text{el-ph}}^{(I)}(t_1)} \right\rangle_{T,\mathbf{k}} = \exp \left\langle \hat{T}_t e^{-i \int_0^t dt_1 H_{\text{el-ph}}^{(I)}(t_1)} - 1 \right\rangle_{T,\mathbf{k},c} \equiv e^{C_{\mathbf{k}}(t)}, \quad (3.30)$$

giving

$$C_{\mathbf{k}}(t) = \sum_{j=1}^{\infty} \left\langle \hat{T}_t \frac{(-i)^j}{j!} \int_0^t \prod_{m=1}^j dt_m H_{\text{el-ph}}^{(I)}(t_m) \right\rangle_{T,\mathbf{k},c}. \quad (3.31)$$

Therefore, where we finally found the expression for the cumulant function $C_{\mathbf{k}}(t)$ from Eq. (3.1). The notation $\langle \dots \rangle_c$ denotes the so-called cumulant average. In general, the cumulant average is defined using the ordinary average, by formally expanding the following expression in the Taylor series with respect to ξ_i and equating, order by order, the terms on the left- and the right-hand side

$$\left\langle \exp \sum_j \xi_j X_j \right\rangle = \exp \left\langle \left(\exp \sum_j \xi_j X_j \right) - 1 \right\rangle_c, \quad (3.32)$$

where the -1 term on the right-hand side is motivated by the fact that the expectation value of the unity operator is equal to 1. We note that there is actually an analytic formula that relates the cumulant average of any order with the ordinary average [118], but that will not be necessary for our present purposes.

3.2.4.3 Theoretical Framework for the Calculation of the Second-order Cumulant Function

In Sec. 3.2.4.2, everything was exact. Let us now demonstrate that the second-order cumulant from Eq. (3.7) corresponds to the approximation in which only the first two terms in Eq. (3.31) ($j = 1$ and $j = 2$ terms) are kept, while everything else is neglected. This is why this is known as the second-order cumulant expansion. To achieve this, we explicitly write out the first two cumulant averages in terms of the ordinary averages

$$\langle X_1 \rangle_c = \langle X_1 \rangle, \quad (3.33a)$$

$$\langle X_1 X_2 \rangle_c = \langle X_1 X_2 \rangle - \langle X_1 \rangle \langle X_2 \rangle. \quad (3.33b)$$

As we see from Eq. (3.33a), the cumulant average coincides with the ordinary average for $j = 1$, and hence vanishes when used in Eq. (3.31) due to Wick's theorem. As a consequence, the cumulant average can be simply replaced by the ordinary average in the case of $j = 2$ term as well; see Eq. (3.33b). Therefore, the second-order cumulant function reads as

$$C_{\mathbf{k}}(t) = -\frac{1}{2} \int_0^t dt_1 \int_0^t dt_2 \left\langle \hat{T}_t c_{\mathbf{k}} H_{\text{el-ph}}^{(I)}(t_1) H_{\text{el-ph}}^{(I)}(t_2) c_{\mathbf{k}}^\dagger \right\rangle_{T,0}. \quad (3.34)$$

For a straightforward application of Wick's theorem, it is customary to rewrite electron creation and annihilation operators in the Dirac picture. In order not to change the already existing time ordering in

Eq. (3.34), the annihilation operator is expressed in the final time $c_{\mathbf{k}} = e^{i\varepsilon_{\mathbf{k}}t}c_{\mathbf{k}}^{(I)}(t)$, while the creation operator is expressed in the initial time $c_{\mathbf{k}}^\dagger = c_{\mathbf{k}}^{\dagger(I)}(0)$. If we also use the explicit form of $H_{\text{el-ph}}^{(I)}(t)$ from Eq. (3.23c), the Eq. (3.34) becomes

$$C_{\mathbf{k}}(t) = -\frac{g^2}{2N}e^{i\varepsilon_{\mathbf{k}}t} \int_0^t dt_1 \int_0^t dt_2 \left\langle \hat{T}_t c_{\mathbf{k}}^{(I)}(t) \sum_{\mathbf{k}_1, \mathbf{q}_1} c_{\mathbf{k}_1+\mathbf{q}_1}^{\dagger(I)}(t_1) c_{\mathbf{k}_1}^{(I)}(t_1) A_{\mathbf{q}_1}^{(I)}(t_1) \sum_{\mathbf{k}_2, \mathbf{q}_2} c_{\mathbf{k}_2+\mathbf{q}_2}^{\dagger(I)} c_{\mathbf{k}_2}^{(I)}(t_2) A_{\mathbf{q}_2}^{(I)}(t_2) c_{\mathbf{k}}^{\dagger(I)}(0) \right\rangle_{T,0}, \quad (3.35)$$

where we introduced the shorthand notation for the phonon part $A_{\mathbf{q}} = a_{\mathbf{q}} + a_{-\mathbf{q}}^\dagger$. Equation (3.35) is now easily evaluated using Wick's theorem. Contraction between the phonon degrees of freedom gives [1]

$$\left\langle \hat{T}_t A_{\mathbf{q}_1}^{(I)}(t_1) A_{\mathbf{q}_2}^{(I)}(t_2) \right\rangle = \delta_{\mathbf{q}_1, -\mathbf{q}_2} iD(t_1 - t_2), \quad (3.36)$$

where $iD(t_1 - t_2) = (n_{ph} + 1)e^{-i\omega_0|t_1-t_2|} + n_{ph}e^{i\omega_0|t_1-t_2|}$ is the phonon propagator, while $n_{ph} = 1/(e^{\omega_0/T} - 1)$ is the Bose factor. Since we are working in the limit of vanishing electron density (single electron in a band), the contraction between the electron creation and annihilation operators does not have a hole part, and hence reads as

$$\left\langle \hat{T}_t c_{\mathbf{k}}^{(I)}(t_1) c_{\mathbf{q}}^{\dagger(I)}(t_2) \right\rangle = \delta_{\mathbf{k}, \mathbf{q}} e^{-i\varepsilon_{\mathbf{k}}|t_1-t_2|} \theta(t_1 - t_2). \quad (3.37)$$

Taking all of this into account, Eq. (3.35) simplifies

$$C_{\mathbf{k}}(t) = -\frac{g^2}{2N} \sum_{\mathbf{q}} \int_0^t dt_1 \int_0^t dt_2 e^{i(\varepsilon_{\mathbf{k}} - \varepsilon_{\mathbf{q}})|t_2-t_1|} iD(t_2 - t_1). \quad (3.38)$$

We can get rid of the absolute value by noticing that the contributions for $t_2 > t_1$ and for $t_2 < t_1$ are equal. It is thus sufficient to restrict ourselves to $t_2 > t_1$ and multiply everything by 2. Also, the expression can be further simplified if we use

$$e^{i(\varepsilon_{\mathbf{k}} - \varepsilon_{\mathbf{q}} \pm \omega_0)(t_2-t_1)} = \int_{-\infty}^{\infty} d\omega e^{-i\omega(t_2-t_1)} \delta(\omega + \varepsilon_{\mathbf{k}} - \varepsilon_{\mathbf{q}} \pm \omega_0).$$

Then, the whole \mathbf{q} dependence is inside the Dirac delta function, which in combination with the summation over \mathbf{q} gives

$$\sum_{\mathbf{q}} \delta(\omega + \varepsilon_{\mathbf{k}} - \varepsilon_{\mathbf{q}} \pm \omega_0) = N\rho(\omega + \varepsilon_{\mathbf{k}} \pm \omega_0), \quad (3.39)$$

where ρ is the density of states. It is now straightforward to show that Eq. (3.38) reduces to

$$C_{\mathbf{k}}(t) = g^2 \int_{-\infty}^{\infty} d\omega \frac{e^{-i\omega t} + i\omega t - 1}{\omega^2} [(n_{ph} + 1)\rho(\omega + \varepsilon_{\mathbf{k}} - \omega_0) + n_{ph}\rho(\omega + \varepsilon_{\mathbf{k}} + \omega_0)]. \quad (3.40)$$

This expression can be rewritten in terms of the Migdal self-energy (see Eq. (2.28) from Part I)

$$C_{\mathbf{k}}(t) = \frac{1}{\pi} \int_{-\infty}^{\infty} d\omega \frac{|\text{Im}\Sigma^{\text{MA}}(\omega + \varepsilon_{\mathbf{k}})|}{\omega^2} (e^{-i\omega t} + i\omega t - 1), \quad (3.41)$$

where we used the analytic property of self-energy $\text{Im}\Sigma < 0$.

Remark 16. We note that the cumulant expansion method that we have now presented is analogous to the linked cluster expansion for the thermodynamic potential in statistical mechanics. This is a consequence of the fact that both of these require evaluating quantities of the same mathematical form, $\ln(G_{\mathbf{k}}(t)/G_{\mathbf{k},0}(t))$ and $\ln(Z/Z_0)$, where Z and Z_0 are the partition function of the full and noninteracting theories.

3.3 Second-Order Cumulant Expansion for the Holstein Model: Implementation and Basic Properties

3.3.1 Cumulant Function in the Holstein Model

From now on, we exclusively concentrate on the Holstein model on a hypercubic lattice in d dimensions, in the thermodynamic limit $N \rightarrow \infty$. The expression for the cumulant function, as seen from Eqs. (3.14) and (3.12), is related to the inverse Fourier transform of $\text{Im}\Sigma^{\text{MA}}(\omega)$, which in turn is completely determined by the inverse Fourier transform of the density of states $\hat{\rho}(t)$; see Eq. (2.28) from Part I. The latter admits a closed-form solution⁶

$$\begin{aligned}\hat{\rho}(t) &= \int_{-\infty}^{\infty} \frac{d\omega e^{-i\omega t}}{(2\pi)^{d+1}} \int_{[0,2\pi]^d} d^d \mathbf{k} \delta\left(\omega + 2t_0 \sum_{j=1}^d \cos k_j\right) \\ &= \frac{1}{2\pi} \left(\frac{1}{2\pi} \int_0^{2\pi} dk e^{2it_0 t \cos k} \right)^d = \frac{J_0(2t_0 t)^d}{2\pi},\end{aligned}\quad (3.42)$$

where J_0 is the Bessel function of the first kind of order zero. Hence, Eqs. (3.14),(3.12), (2.28) from Part I, and (3.42) imply that the cumulant function can be written as

$$\boxed{C_{\mathbf{k}}(t) = -g^2 \int_0^t dx (t-x) iD(x) e^{ix\varepsilon_{\mathbf{k}}} J_0(2t_0 x)^d}, \quad (3.43)$$

where $iD(t) = (n_{\text{ph}} + 1)e^{-i\omega_0 t} + n_{\text{ph}}e^{i\omega_0 t}$ is the phonon propagator in real time (for $t > 0$).

In Fig. 3.1 we illustrate the cumulant function, as well as the corresponding Green's function and spectral function. Figs. 3.1(a) and 3.1(b) show the second derivative of the cumulant

$$\frac{d^2 C_{\mathbf{k}}(t)}{dt^2} = -g^2 iD(t) e^{it\varepsilon_{\mathbf{k}}} J_0(2t_0 t)^d, \quad \text{for } d = 1, \quad (3.44)$$

in order to demonstrate the rapid oscillations that are also present in the cumulant itself. These are not easily observed by inspecting $C_{\mathbf{k}}(t)$ directly, as the linear behavior dominates for large times. We observe that the $k = 0$ and $k = \pi$ results possess an oscillating envelope with period $2\pi/\omega_0$, while intermediate momenta have a much less regular structure. This can have direct consequences on the spectral functions, as the satellite peaks are expected to be at a distance ω_0 from each other. To be more explicit, oscillating envelopes suggest that there is a much higher chance for the occurrence of satellite peaks near the bottom ($k \approx 0$) and the top ($k \approx \pi$) of the band, than otherwise. However, that does not guarantee that the satellite peaks will in fact occur. Figure 3.1(c) shows that $\text{Re}C_{\mathbf{k}}(t)$ is declining faster for $k > 0$ than for $k = 0$. As a consequence, $e^{C_{\mathbf{k}}(t)}$ in Fig. 3.1(d) attenuates slower for $k = 0$, having enough time to complete a full period, while $k = \pi$ results are reminiscent of an overdamped oscillator. A similar, although much less evident, effect can be seen in the Green's function itself; see Fig. 3.1(e). This is why the $k = \pi$ spectral function in Fig. 3.1(f) has a simple one-peak shape, while only the $k = 0$ result captures one small satellite peak.

From a numerical point of view, Eq. (3.43) is treated using Levin's collocation method [119], which is reviewed in Appendix B. It provides a controlled, accurate, and numerically efficient way to integrate the product of trigonometric, Bessel, and some slowly-varying function. This approach avoids using a dense t -grid, which would otherwise be required, as the subintegral function in Eq. (3.43) has the same type of rapid oscillations present in $d^2 C_{\mathbf{k}}(t)/dt^2$.

⁶We note that this derivation is completely analogous to the one presented in Eq. (1.113), with the only difference being that the noninteracting dispersion relation now reads as $\varepsilon_{\mathbf{k}} = -2t_0 \sum_{j=1}^d \cos k_j$.

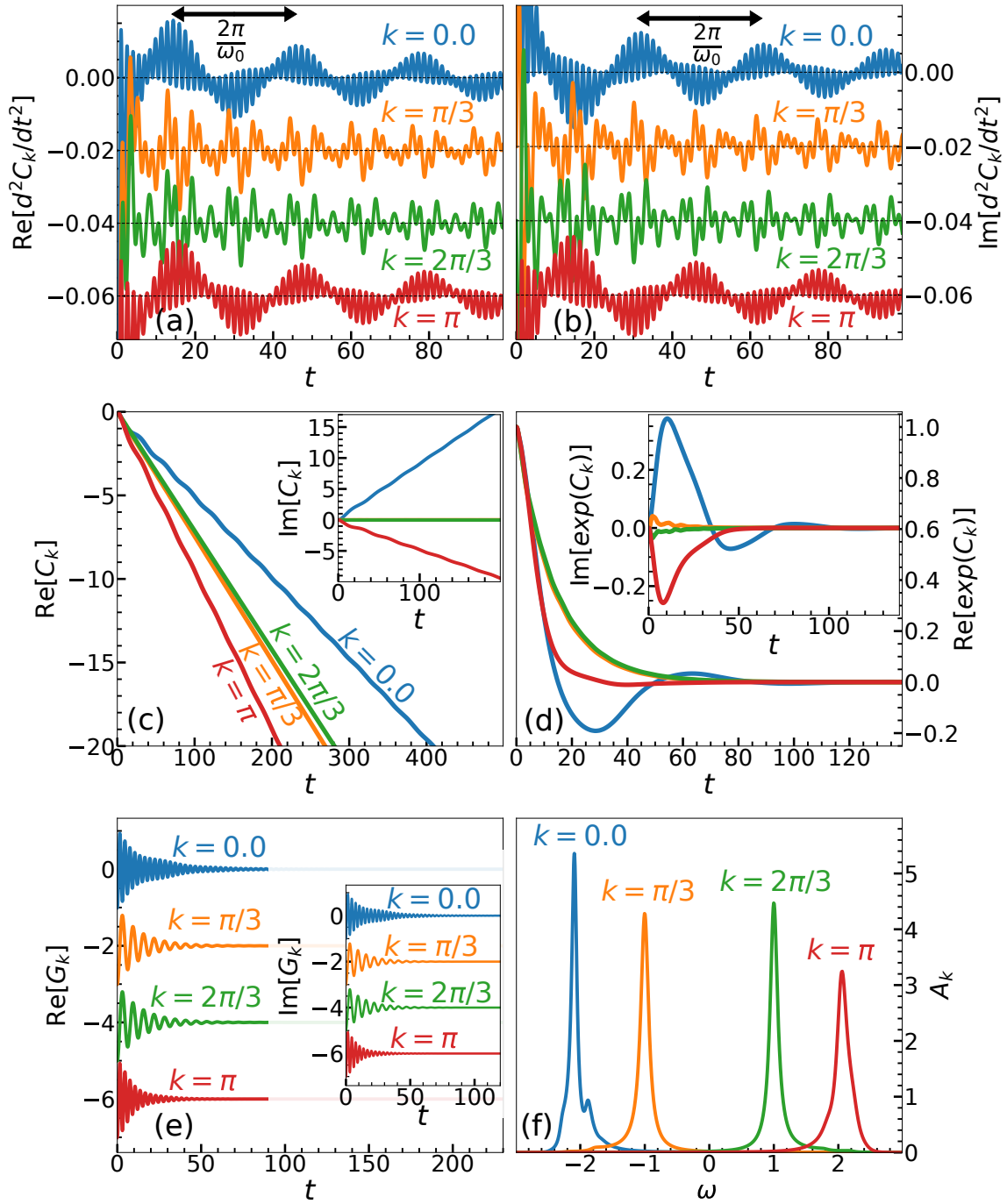


Figure 3.1: The cumulant, Green's and spectral function on the example of the one-dimensional Holstein model with the following values of the model parameters: $\omega_0 = 0.2$, $g = 0.2$, $T = 0.3$ and $t_0 = 1$.

3.3.2 Lifetime

Another question of practical importance is how long should we propagate the cumulant function in real-time until the corresponding Green's function attenuates. A rough estimate of such quantity is given by the quasiparticle lifetime τ_k . The lifetime is determined as $\tau_k = 1/(2|\text{Im}\hat{E}_k|)$, where \hat{E}_k is given by Eq. (3.20), while the self-energy is taken in the Migdal approximation (see Eq. (2.28) from Part I)

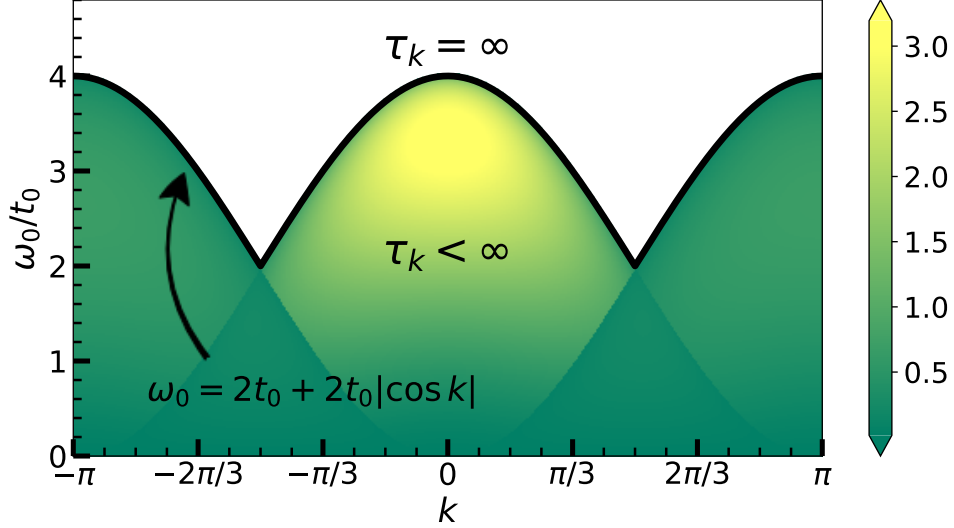


Figure 3.2: Quasiparticle lifetime τ_k in the CE method for $T/t_0 = 2$ and $g/t_0 = 1$.

$$\tau_k^{-1} = 2|\text{Im}\tilde{E}_k| = 2g^2 \frac{\theta(4t_0^2 - (\varepsilon_k - \omega_0)^2)}{\sqrt{4t_0^2 - (\varepsilon_k - \omega_0)^2}} (n_{\text{ph}} + 1) + 2g^2 \frac{\theta(4t_0^2 - (\varepsilon_k + \omega_0)^2)}{\sqrt{4t_0^2 - (\varepsilon_k + \omega_0)^2}} n_{\text{ph}}. \quad (3.45)$$

This is illustrated in Fig. 3.2. We observe that there is a considerable part of the parameter space where the lifetime is infinite, which means that the corresponding Green's function never attenuates. This occurs for $\omega_0 > 2t_0 + 2t_0|\cos k|$ in the case of finite temperatures, and for $\omega_0 > 4t_0 \sin^2 k/2$ in the $T = 0$ case. In these regimes, one could presume that this is reflected in the spectral functions through the appearance of Dirac delta peaks, which is not expected at finite temperatures. This illustrates one of the limitations of this method.

3.4 Spectral Functions

In this section, we present the CE spectral functions of the 1D Holstein model. The DMFT is used as a reliable benchmark, while MA and SCMA represent the main competitors and alternatives to the CE method. Sec. 3.4.1 shows the results for $k = 0$, whereas heat plots and the $k = \pi$ results are shown in Sec. 3.4.2. High-temperature spectral functions and spectral sum rules are presented in Sec. 3.4.3. The behavior near the atomic limit is discussed in Sec. 3.4.4. In these sections, we present only the results for $\omega_0 = 0.5$, while the results for other phonon frequencies and various momenta are shown in Sec. 3.7. Furthermore, we also calculate the 2D spectral functions, but these results will be postponed until Sec. 3.6.

3.4.1 Low and Intermediate Temperatures for $k = 0$

In the weak-coupling limit $\alpha \rightarrow 0$, all these approximate methods (DMFT, CE, SCMA, MA) provide accurate results. In Fig. 3.3 we investigate how far from this strict limit each of our methods continues to give reasonably accurate spectral functions. In Fig. 3.3(a), we see that for $\alpha = 1$ all methods correctly capture the QP peak, which dominates in the structure of the spectrum. The MA satellite peak is slightly shifted towards higher frequencies, which becomes significantly more pronounced at higher temperatures; see Fig. 3.3(b). The limitations of the MA become more obvious for stronger couplings, where even the position and the weight of the QP peak are inaccurate; see Figs. 3.3(c)–3.3(h).

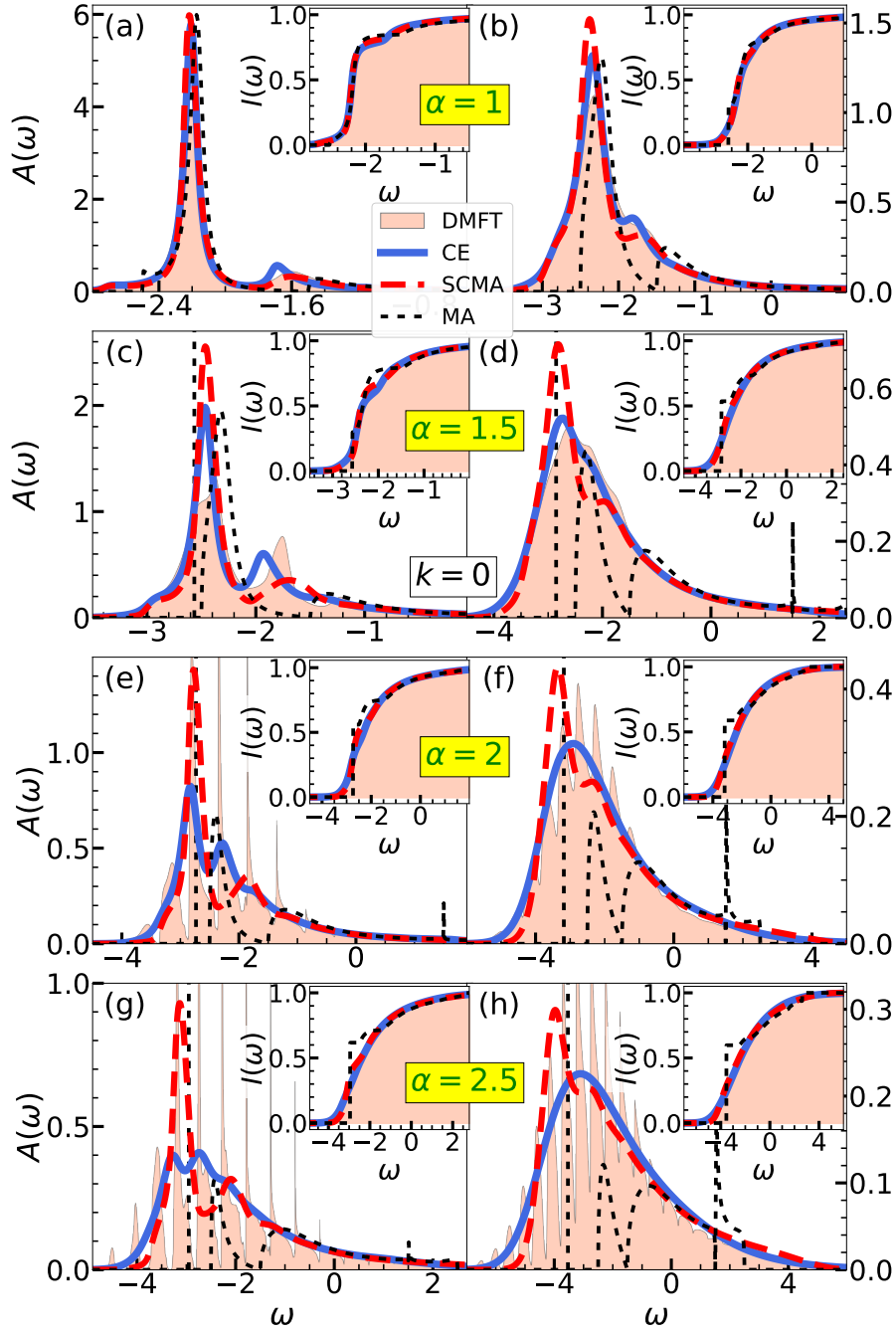


Figure 3.3: Spectral functions for $t_0 = 1$, $\omega_0 = 0.5$ and $k = 0$. In the left panels $T = 0.3$, while $T = 0.7$ in the right panels. Insets show the integrated spectral weights $I_k(\omega) = \int_{-\infty}^{\omega} A_k(\nu) d\nu$.

While the QP properties of the CE and SCMA seem to be quite similar if α is not too large, some difference in satellite peaks is already visible in Figs. 3.3(b) and 3.3(c). Figure 3.3(c) shows that SCMA gives broader satellites than the DMFT benchmark, whereas CE slightly underestimates the position of the satellite. Neither CE nor SCMA can be characterized as distinctly better in this regime. On the other hand, Figs. 3.3(e) and 3.3(g) display a clear advantage of the CE. We see that it captures rather well the most distinctive features of the solutions, which are the first few satellites. This is not the case for SCMA.

Figures 3.3(f) and 3.3(h) demonstrate that the CE gives a rather quick crossover toward the high-temperature limit, as it predicts a simple broad one-peak structure for the spectral function already for $T = 0.7$. This large difference between the spectral functions for $T_1 = 0.3$ and $T_2 = 0.7$ can be

understood by examining the ratio of their corresponding lifetimes $\tau(T_1)/\tau(T_2) = n_{\text{ph}}(T_2)/n_{\text{ph}}(T_1) \approx 8.5$. This implies that $\text{Re}C_k(t)$ for $T = 0.7$ has a much steeper slope as a function time, which suppresses the appearance of satellites, as explained in Sec. 3.3.

Remark 17. *Once again, we emphasize that the role of the DMFT is to help us decide whether CE or MA/SCMA gives more accurate results. It is not expected that a simple method like CE could outperform the nonperturbative DMFT, which is why some even more sophisticated method (like HEOM) was not included in the comparison. Furthermore, since the CE is built upon MA (see Eq. (3.7)), the very use of the CE needed to be justified by showing that it gives more reliable predictions than MA. This is seen from our $k = 0$ results, which demonstrate a much greater superiority of the CE (compared to MA) than one could have initially anticipated⁷. We checked that the same conclusions hold true even for other parameter regimes. Since MA gives vastly different results than all other methods (including benchmark) for stronger α , in the subsequent figures showcasing spectral functions, MA will be mostly omitted⁸, due to clarity, and our discussion will be mainly focused on comparing the quality of CE and SCMA methods. However, it should be noted that such a comparison is not completely fair, due to the fact that SCMA uses a self-consistent loop, while CE is a one-shot method.*

3.4.2 Low and Intermediate Temperatures for $k \neq 0$

To proceed with the analysis of the CE we want to answer:

- Whether the conclusions that we reached for $k = 0$ can be carried over to other momenta as well?
- Does CE continue to be better than SCMA at much higher temperatures?

The first question is answered in Fig. 3.4, where we compare CE and DMFT heat plots. Figures 3.4(a) and 3.4(b) demonstrate that CE results are quite reminiscent of the DMFT results for $\alpha = 1$, even at non-zero momenta. The same conclusion holds for weaker couplings as well. On the other hand, there are differences between the results for somewhat stronger coupling $\alpha = 1.5$, as shown in Figs. 3.4(c) and 3.4(d). While the polaron bands in both of these figures are convex, the CE predicts the first satellite to be concave, unlike the DMFT. In other words, CE predicts that the distance between the polaron peak and the satellites decreases, as we increase the momentum. This is counterintuitive, as the satellites are perceived as the QP that absorbed or emitted a phonon, which should consequently be just at energy distance ω_0 apart. These limitations of the CE are much more pronounced for stronger electron-phonon couplings. While the DMFT solution in Figs. 3.4(f) and 3.4(h) exhibits a series of distinct bands, Figs. 3.4(e) and 3.4(g) demonstrate that the polaron and the satellite bands of the CE merge into a single band at higher momenta. However, the most noticeable feature here is the fact that the CE is too smeared, as if the temperature is too high. This is a consequence of the fact that the lifetime in Eq. (3.45) scales as $\tau_k \sim 1/g^2$.

While the heat maps reveal noticeable discrepancies between the DMFT and CE for $k \neq 0$, it seems that these differences are much less pronounced around $k = \pi$. A more detailed comparison is presented in Fig. 3.5 that shows the results for the same regimes as in Fig. 3.3. The DMFT solution in Figs. 3.5(a)–3.5(d) shows that the main feature of the spectral function is a single broad peak for $\alpha \lesssim 1.5$, which is in agreement with the CE results. This is also the case for the SCMA, although we observe a slight tendency of the main peak to lean toward higher frequencies at higher temperatures. For larger interaction strengths, CE cannot fully reproduce the sharp peaks at lower frequencies of

⁷It should be noted that $k = 0$ results are the most important for the mobility and optical conductivity predictions in systems with low concentration of charge carriers, which we are interested in. The comparison of mobility predictions of different methods is shown in Sec. 3 of Part III.

⁸Some additional MA spectral functions will be showed in Sec. 3.7, while MA quasiparticle properties are briefly discussed in Sec. 3.5,

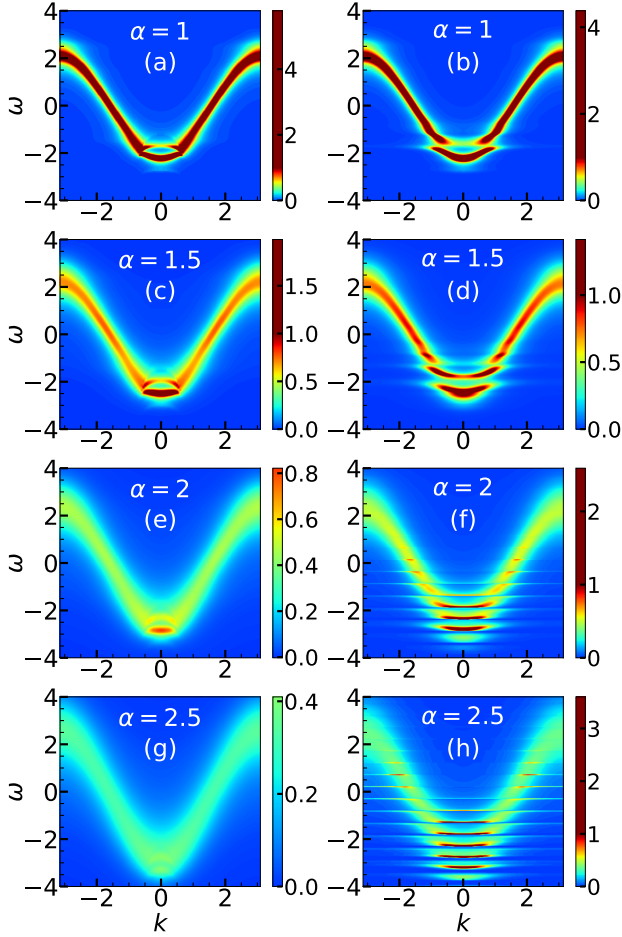


Figure 3.4: Heat maps of $A_k(\omega)$ for $t_0 = 1$, $\omega_0 = 0.5$ and $T = 0.3$. In the left panels, we present CE results, while the DMFT benchmark is presented in the right panels. All plots use the same color coding.

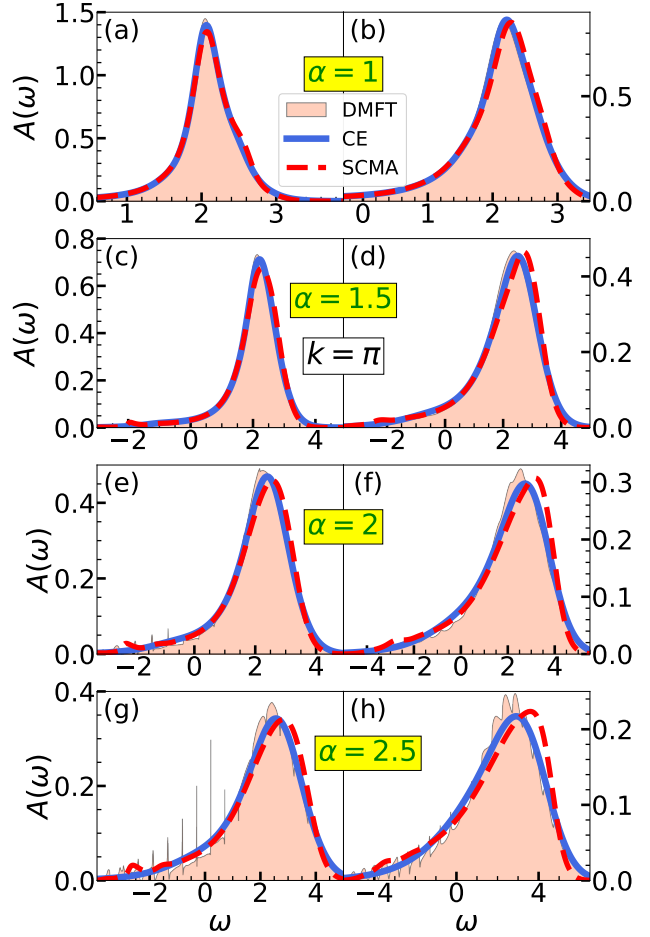


Figure 3.5: Spectral functions for $t_0 = 1$, $\omega_0 = 0.5$ and $k = \pi$. In the left panels $T = 0.3$, while $T = 0.7$ in the right panels.

the low-temperature spectral function or the fine structure of the main peak at higher temperatures; see Figs. 3.3(e)–3.3(h). Similarly, CE misses the quasiparticle peak as well, situated at low energy, although it is typically tiny and not (clearly) visible in Figs. 3.5(a)–3.5(h); see Appendix C in Ref. [87].

Overall, we find that the CE gives the most accurate results for $k = 0$ and $k = \pi$ and that it is less accurate for other momenta. Although it cannot fully reproduce a tiny quasiparticle peak for $k = \pi$, it describes well a wide single-peak structure, which is the most prominent feature of the spectrum. A much larger discrepancy for $k = \pi$, between the CE and a reliable benchmark, was reported in Ref. [116], by examining the system on a finite lattice system with $N = 6$. However, in Appendix C of Ref. [87] we examined the same parameter regime as in Ref. [116] and showed that these discrepancies are significantly reduced in the thermodynamic limit.

3.4.3 Spectral Functions at High Temperatures and Spectral Sum Rules

In Fig. 3.6 we show CE, SCMA, and DMFT spectral functions at high temperatures, for the same electron-phonon couplings as in Figs. 3.3 and 3.5. We see that CE performs very well, both for $k = 0$ and $k = \pi$. There are only small discrepancies at stronger interactions (see, e.g., Fig. 3.6(c)). In contrast, the SCMA solution gets tilted relative to the DMFT and CE. In addition, it poorly reproduces the low-frequency part of the spectrum. Although these promising CE results might lead one up to suspect that CE is exact in the high temperature limit $T \rightarrow \infty$, it is not immediately obvious whether

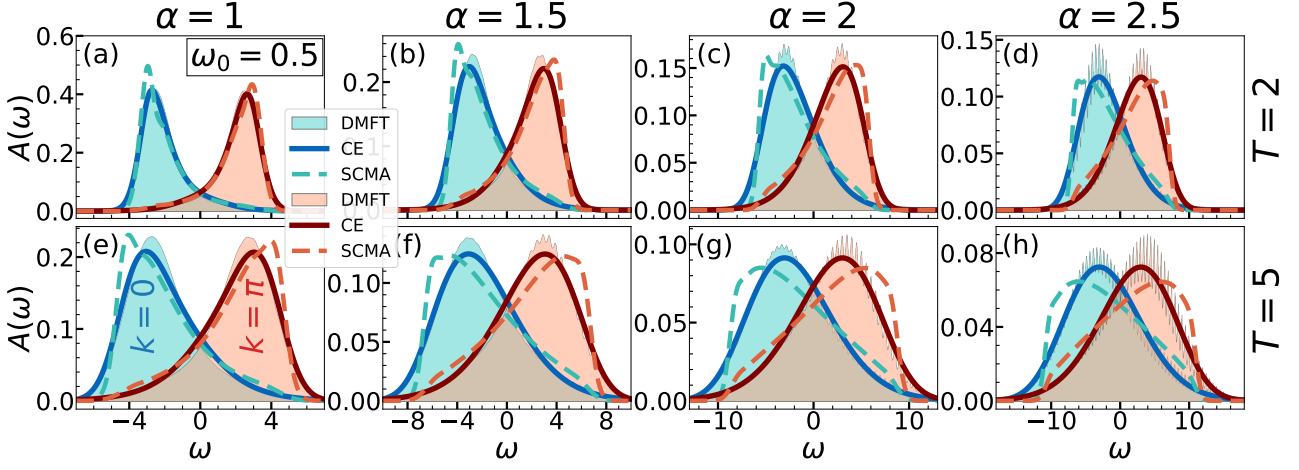


Figure 3.6: High-temperature CE, DMFT, and SCMA spectral functions in 1D for $t_0 = 1$, $\omega_0 = 0.5$, and $k = 0, \pi$.

this is true. As we now demonstrate, this can be answered by examining the spectral sum rules.

In Sec. 2.4 of Part I we showed how the exact n -th spectral sum rule $\mathcal{M}_n(\mathbf{k})$ is calculated in theory, while the specific expressions for $0 \leq n \leq 8$ were listed in Sec. 2.3.2. Let us now calculate the spectral sum rules within the CE method. To do so, we first define an auxiliary quantity

$$\mathcal{N}_n^{\text{CE}}(\mathbf{k}) = \int_{-\infty}^{\infty} A_{\mathbf{k}}^{\text{CE}}(\omega + \varepsilon_{\mathbf{k}}) \omega^n d\omega. \quad (3.46)$$

Using Eq. (3.15), we expand this quantity as follows

$$\begin{aligned} \mathcal{N}_n^{\text{CE}}(\mathbf{k}) &= \int_{-\infty}^{\infty} \frac{d\omega}{\pi} \omega^n \text{Re} \int_0^{\infty} dt e^{i\omega t} e^{C_{\mathbf{k}}(t)} = \frac{1}{\pi} \text{Re} \int_0^{\infty} dt e^{C_{\mathbf{k}}(t)} \int_{-\infty}^{\infty} d\omega \omega^n e^{i\omega t} \\ &= \frac{1}{\pi} \text{Re} \int_0^{\infty} dt e^{C_{\mathbf{k}}(t)} \frac{1}{i^n} \left(\frac{d}{dt} \right)^n \int_{-\infty}^{\infty} d\omega e^{i\omega t} = \frac{1}{\pi} \text{Re} \int_0^{\infty} dt e^{C_{\mathbf{k}}(t)} 2\pi (-i)^n \delta^{(n)}(t) \\ &= \text{Re} \left[i^n \left(\frac{d}{dt} \right)^n e^{C_{\mathbf{k}}(t)} \right] \Big|_{t=0}. \end{aligned} \quad (3.47)$$

If we now go back to Eq. (3.46) and use a substitution $\omega \rightarrow \omega - \varepsilon_{\mathbf{k}}$ we get

$$\begin{aligned} \mathcal{N}_n^{\text{CE}}(\mathbf{k}) &= \int_{-\infty}^{\infty} (\omega - \varepsilon_{\mathbf{k}})^n A_{\mathbf{k}}^{\text{CE}}(\omega) d\omega = \int_{-\infty}^{\infty} d\omega A_{\mathbf{k}}^{\text{CE}}(\omega) \sum_{m=0}^n \binom{n}{m} \omega^{n-m} (-\varepsilon_{\mathbf{k}})^m \\ &= \mathcal{M}_n^{\text{CE}}(\mathbf{k}) + \sum_{m=1}^n \binom{n}{m} (-\varepsilon_{\mathbf{k}})^m \mathcal{M}_{n-m}^{\text{CE}}(\mathbf{k}), \end{aligned} \quad (3.48)$$

where $\mathcal{M}_n^{\text{CE}}(\mathbf{k})$ is the n -th spectral sum rule, as predicted by the CE method. Moving the term with the sum to the left-hand side, and using Eq. (3.47), we obtain

$$\mathcal{M}_n^{\text{CE}}(\mathbf{k}) = \text{Re} \left[i^n \left(\frac{d}{dt} \right)^n e^{C_{\mathbf{k}}(t)} \right] \Big|_{t=0} - \sum_{m=1}^n \binom{n}{m} (-\varepsilon_{\mathbf{k}})^m \mathcal{M}_{n-m}^{\text{CE}}(\mathbf{k}). \quad (3.49)$$

This can be easily evaluated for arbitrary n using recursion and Eqs. (3.8) and (3.44). In fact, the following relation (which follows from Eq. (3.44)) makes this even easier

$$\left. \frac{d^{2+n}C_{\mathbf{k}}(t)}{dt^{2+n}} \right|_{t=0} = -g^2(n_{\text{ph}} + 1) [i(\varepsilon_{\mathbf{k}} - \omega_0)]^n {}_2F_1\left(\frac{1-n}{2}, -\frac{n}{2}; 1; \frac{4t_0^2}{(\varepsilon_{\mathbf{k}} - \omega_0)^2}\right) - g^2n_{\text{ph}} [i(\varepsilon_{\mathbf{k}} + \omega_0)]^n {}_2F_1\left(\frac{1-n}{2}, -\frac{n}{2}; 1; \frac{4t_0^2}{(\varepsilon_{\mathbf{k}} + \omega_0)^2}\right), \quad (3.50)$$

where ${}_2F_1$ is the hypergeometric function. However, since we are interested in only the first few sum rules, the general expression in Eq. (3.50) is not necessary.

The first five ($0 \leq n \leq 4$) sum rules read as:

$$\mathcal{M}_0^{\text{CE}}(\mathbf{k}) = 1, \quad (3.51a)$$

$$\mathcal{M}_1^{\text{CE}}(\mathbf{k}) = \varepsilon_{\mathbf{k}}, \quad (3.51b)$$

$$\mathcal{M}_2^{\text{CE}}(\mathbf{k}) = \varepsilon_{\mathbf{k}}^2 + (2n_{\text{ph}} + 1)g^2, \quad (3.51c)$$

$$\mathcal{M}_3^{\text{CE}}(\mathbf{k}) = \varepsilon_{\mathbf{k}}^3 + g^2\omega_0 + 2g^2(2n_{\text{ph}} + 1)\varepsilon_{\mathbf{k}}, \quad (3.51d)$$

$$\mathcal{M}_4^{\text{CE}}(\mathbf{k}) = \varepsilon_{\mathbf{k}}^4 + 2g^2\varepsilon_{\mathbf{k}}\omega_0 + g^2(2n_{\text{ph}} + 1)(2t_0^2 + 3\varepsilon_{\mathbf{k}}^2 + \omega_0^2) + 3g^4(2n_{\text{ph}} + 1)^2. \quad (3.51e)$$

All of these coincide with the exact sum rules from Eq. (2.15). However, for $n = 5$, we find that

$$\mathcal{M}_5^{\text{CE}}(\mathbf{k}) = \mathcal{M}_5(\mathbf{k}) - 2g^4\varepsilon_{\mathbf{k}}(2n_{\text{ph}} + 1)^2, \quad (3.52)$$

where $\mathcal{M}_5(\mathbf{k})$ is the exact result which is given by Eq. (2.15f). Since $g^4\varepsilon_{\mathbf{k}}(2n_{\text{ph}} + 1)^2$ is the leading order term (with respect to T) in the high-temperature limit, we conclude that CE cannot be exact when $T \rightarrow \infty$.

Remark 18. *To make this analysis more complete, we note that the SCMA gives correct sum rules only for $n \leq 3$; see Sec. 2.3.3 or Ref. [72]. On the other hand, in Appendix F we numerically checked that the DMFT results are in agreement with all the sum rules that we calculated analytically in Sec. 2.3.2 ($0 \leq n \leq 8$).*

3.4.4 Atomic Limit

The CE and the exact spectral sum rule in Eq. (3.52) coincide when $g \rightarrow 0$ or $t_0 \rightarrow 0$ (which means that $\varepsilon_{\mathbf{k}} \rightarrow 0$). These correspond to the weak coupling and the atomic limits, respectively. It turns out that the CE is actually exact in both of these limits. In this section, we prove this for the atomic limit, while for the weak coupling limit this follows by construction from Eqs. (3.1), (3.7) and (2.28) of Part I.

In the atomic limit ($t_0 = 0$) Eq. (3.43) greatly simplifies, since $J_0(2t_0t) = J_0(0) = 1$, so the cumulant function can be evaluated exactly⁹

$$C(t) = \alpha^2(-2n_{\text{ph}} - 1 + it\omega_0 + iD(t)). \quad (3.53)$$

If we express the phonon propagator $iD(t)$, given below Eq. (3.43), as

$$iD(t) = 2\sqrt{n_{\text{ph}}(n_{\text{ph}} + 1)} \cos \left[\omega_0 \left(t + \frac{i}{2T} \right) \right], \quad (3.54)$$

then the Green's function in the time domain reads as

$$G_{\mathbf{k}}(t) = -i\theta(t)e^{-\alpha^2(2n_{\text{ph}}+1)t} e^{i\alpha^2\omega_0 t} e^{2\alpha^2\sqrt{n_{\text{ph}}(n_{\text{ph}}+1)} \cos[\omega_0(t + \frac{i}{2T})]}. \quad (3.55)$$

To obtain the corresponding spectral function, we first need to do a Fourier transform which would be straightforward if the last exponential in the above equation was expressed in a plane wave representation. This can be achieved using the so-called modified Jacobi-Anger identity, which we formulate as a lemma:

⁹In the atomic limit there is no \mathbf{k} dependence, so we denote the cumulant function as $C(t)$ instead of $C_{\mathbf{k}}(t)$.

Lemma 1. For arbitrary $z, \theta \in \mathbb{C}$, it holds that

$$e^{z \cos \theta} = \sum_{l=-\infty}^{\infty} I_l(z) e^{-il\theta}, \quad (3.56)$$

where I_l are the modified Bessel function of the first kind.

Proof. Let us use the Euler representation of $\cos \theta$, and the Taylor expansion of the exponential function

$$\begin{aligned} e^{z \cos \theta} &= \exp \left[z \frac{e^{i\theta} + e^{-i\theta}}{2} \right] = e^{\frac{1}{2} z e^{i\theta}} e^{\frac{1}{2} z e^{-i\theta}} = \sum_{m=0}^{\infty} \frac{1}{m!} \left(\frac{z}{2} \right)^m e^{im\theta} \sum_{n=0}^{\infty} \frac{1}{n!} \left(\frac{z}{2} \right)^n e^{-in\theta} \\ &= \sum_{m=0}^{\infty} \sum_{n=0}^{\infty} \frac{1}{m!n!} \left(\frac{z}{2} \right)^{m+n} e^{i(m-n)\theta}. \end{aligned} \quad (3.57)$$

Using the substitution¹⁰ $l = m - n$, we obtain

$$e^{z \cos \theta} = \sum_{l=-\infty}^{\infty} \underbrace{\sum_{n=0}^{\infty} \frac{1}{(n+l)!n!} \left(\frac{z}{2} \right)^{2n+l}}_{=I_l(z)} e^{il\theta} = \sum_{l=-\infty}^{\infty} I_l(z) e^{il\theta}, \quad (3.58)$$

where we recognized a series representation for the modified Bessel function of the first kind [120]. Since the previous expression remains valid for arbitrary z and θ , we can use a substitution $\theta \rightarrow -\theta$ to finally prove our lemma

$$e^{z \cos \theta} = \sum_{l=-\infty}^{\infty} I_l(z) e^{-il\theta}. \quad (3.59)$$

□

Now, the plane wave representation of the last exponential in Eq. (3.55) is directly obtained using Eq. (3.59) with $z = 2\alpha^2 \sqrt{n_{\text{ph}}(n_{\text{ph}} + 1)} \cos \left[\omega_0 \left(t + \frac{i}{2T} \right) \right]$ and $\theta = \omega_0 \left(t + \frac{i}{2T} \right)$, giving

$$e^{2\alpha^2 \sqrt{n_{\text{ph}}(n_{\text{ph}} + 1)} \cos \left[\omega_0 \left(t + \frac{i}{2T} \right) \right]} = \sum_{l=-\infty}^{\infty} I_l \left(2\alpha^2 \sqrt{n_{\text{ph}}(n_{\text{ph}} + 1)} \right) e^{-il\omega_0 t} e^{\frac{l\omega_0}{2T}}, \quad (3.60)$$

The spectral function is now directly obtained and reads as

$$A(\omega) = e^{-\alpha^2(2n_{\text{ph}}+1)} \sum_{l=-\infty}^{\infty} I_l \left(2\alpha^2 \sqrt{n_{\text{ph}}(n_{\text{ph}} + 1)} \right) e^{\frac{l\omega_0}{2T}} \delta(\omega + \alpha^2\omega_0 - l\omega_0). \quad (3.61)$$

In the limit $T \rightarrow 0$, the terms for $l < 0$ are vanishing, while the rest of the expression can be simplified using

$$e^{\frac{l\omega_0}{2T}} = \left(\frac{n_{\text{ph}} + 1}{n_{\text{ph}}} \right)^{\frac{l}{2}}, \quad \text{and } I_l(x) \approx \frac{x^l}{2^l l!} \text{ as } x \rightarrow 0, \quad (3.62)$$

as follows

$$I_l \left(2\alpha^2 \sqrt{n_{\text{ph}}(n_{\text{ph}} + 1)} \right) e^{\frac{l\omega_0}{2T}} \approx \frac{\left(2\alpha^2 \sqrt{n_{\text{ph}}(n_{\text{ph}} + 1)} \right)^l}{2^l l!} \left(\frac{n_{\text{ph}} + 1}{n_{\text{ph}}} \right)^{\frac{l}{2}} \rightarrow \frac{\alpha^{2l}}{l!} \text{ as } T \rightarrow 0. \quad (3.63)$$

¹⁰ l goes from $-\infty$ to ∞

As a result, Eq. (3.61) simplifies in the $T \rightarrow 0$ limit, and we obtain

$$A(\omega) = e^{-\alpha^2} \sum_{l=0}^{\infty} \frac{\alpha^{2l}}{l!} \delta(\omega + \omega_0(\alpha^2 - l)). \quad (3.64)$$

We see that Eqs.(3.61) and (3.64) coincide with the exact results; see Eqs.(2.29) and (2.21). Therefore, this completes the proof that CE is exact in the atomic limit. \square

Remark 19. As we already proved in Sec. 2.4.3, the SCMA does not provide good results in the atomic limit. This is another advantage of the CE method compared to the SCMA.

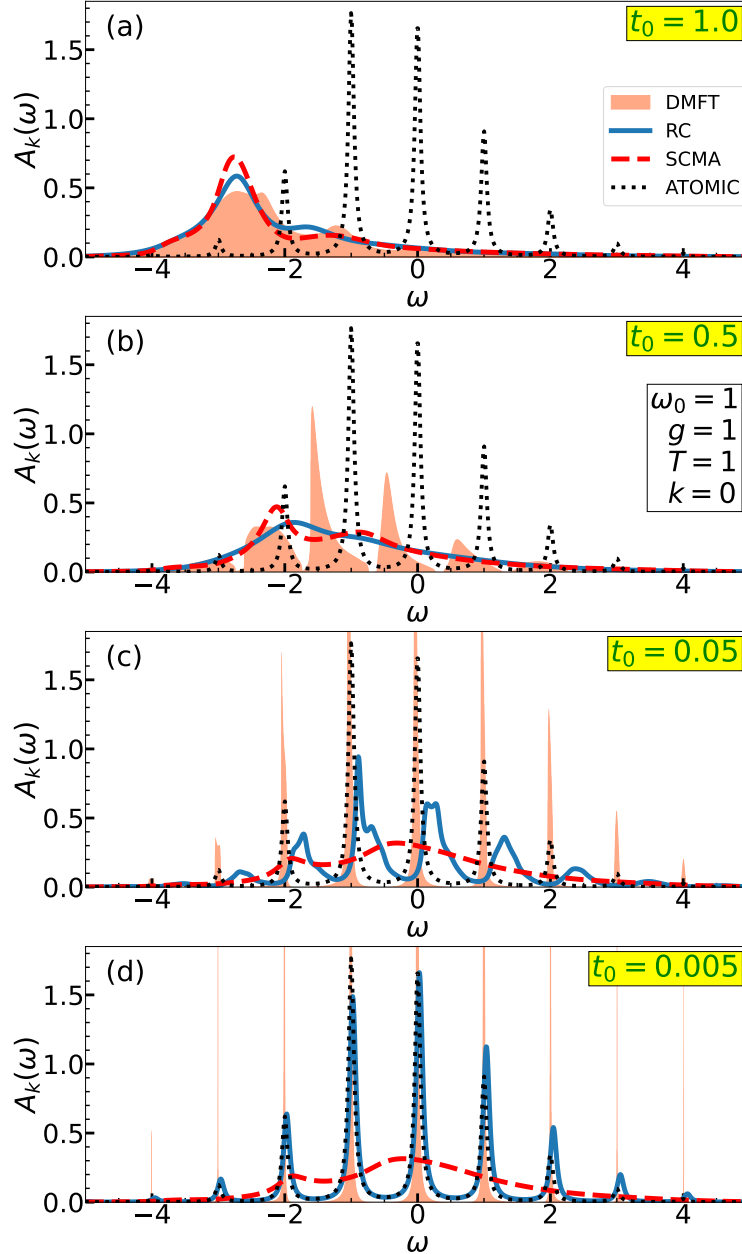


Figure 3.7: CE, DMFT, and SCMA spectral functions close to the atomic limit, for $k = 0$. Here, we use artificial Lorentzian broadening with half-width set to $\eta = 0.05$.

While the CE is exact in the atomic limit ($t_0 = 0$), it is not immediately obvious how far from this limit it continues to give reliable results. This is why we now examine the regimes with small

hopping parameter t_0 . Since the lifetime is infinitely large in some of these regimes (see Fig. 3.2), we introduce artificial attenuation η for the Green's function in real-time by making a replacement $G(t) \rightarrow G(t)e^{-\eta t}$. The results are presented in Fig. 3.7. As always, the DMFT represents a reliable benchmark, while the dotted line is the analytic solution at the atomic limit ($t_0 = 0$), determined by Eq. (3.61), where the Dirac delta functions have been replaced by Lorentzians of half-width η . It is used as a measure to see how far the regime we are examining, is from the exact atomic limit. In Fig. 3.7(a), we see that DMFT, SCMA, and CE spectral functions are in agreement. This regime is quite far from the atomic limit, as indicated by the dotted line. Figure 3.7(b) shows that the DMFT spectral function already consists of a series of peaks for $t_0 = 0.5$, while the CE and SCMA spectral functions are too flattened out. While the CE solution significantly improved in Fig. 3.7(c), it is still not giving satisfactory results, even though the DMFT suggests that we are already close to the atomic limit. Only for $t_0 \lesssim 0.005$ does the CE solution give accurate results; see Fig. 3.7(d). However, this is practically already at the atomic limit. It is interesting to note that while both the DMFT and the CE are exact in the weak-coupling and in the atomic limit, their behavior in other regimes can be quite different.

3.5 Quasiparticle Properties

We now investigate the quasiparticle properties obtained from the CE method and compare them extensively to the results obtained from the DMFT and SCMA. We note that the lifetime within the CE was already studied in Sec. 3.3.2, so we supplement that study here with the results for the ground state energy and the effective mass. Here we show the results in one, two, and three dimensions.

3.5.1 Ground State Energy

3.5.1.1 Analytical Results

The polaron band dispersion $E_{p,\mathbf{k}}$ within the CE is given by the real part of Eq. (3.20), where the self-energy is taken in the Migdal approximation

$$E_{p,\mathbf{k}} = \varepsilon_{\mathbf{k}} + \text{Re}\Sigma^{\text{MA}}(\varepsilon_{\mathbf{k}}). \quad (3.65)$$

Since we deal with a single electron in the band, the ground state energy E_p is given by $E_{p,\mathbf{k}=0}$ evaluated at zero temperature. In the one-dimensional case, E_p is straightforwardly evaluated using Eq. (2.23) from Part I, and reads as follows

$$E_p^{\text{1D}} = -2t_0 - \frac{\alpha^2 \omega_0^2}{\sqrt{\omega_0^2 + 4\omega_0 t_0}}. \quad (3.66)$$

For the expression in higher dimensions, we use Eq. (2.28) from Part I at $T = 0$, which holds in any number of dimensions

$$\text{Im}\Sigma^{\text{MA}}(\omega) = -\pi\alpha^2\omega_0^2\rho(\omega - \omega_0). \quad (3.67)$$

The real part of $\Sigma^{\text{MA}}(\omega)$, which we are interested in, is obtained using the Kramers-Kronig relation

$$\text{Re}\Sigma^{\text{MA}}(\omega) = \pi\alpha^2\omega_0^2\mathcal{H}[\rho](\omega - \omega_0), \quad (3.68)$$

where $\mathcal{H}[\rho](\omega) = \mathcal{P} \int_{-\infty}^{\infty} \frac{d\nu}{\pi} \frac{\rho(\nu)}{\omega - \nu}$ is the Hilbert transform of the density of states $\rho(\omega)$ and \mathcal{P} is the Cauchy principle value. The evaluation of the Hilbert transform may be reduced to the evaluation of the Fourier transform \mathcal{F} , using the following identity that we formulate in the form of a lemma

Lemma 2.

$$\mathcal{F}^{-1}\mathcal{H}[\rho](t) = -i \text{sgn}(t) \mathcal{F}^{-1}[\rho](t). \quad (3.69)$$

Proof. Let us first rewrite the Hilbert transform as the following convolution

$$\mathcal{H}[\rho](\omega) = \mathcal{P} \int \frac{d\nu}{\pi} \frac{\rho(\nu)}{\omega - \nu} = \frac{1}{\pi} \rho(\omega) * \mathcal{P} \left(\frac{1}{\omega} \right), \quad (3.70)$$

and apply \mathcal{F}^{-1} on both sides. Using the convolution theorem¹¹, we get

$$\mathcal{F}^{-1}\mathcal{H}[\rho](t) = \frac{1}{\pi} 2\pi \mathcal{F}^{-1}[\rho](t) \cdot \underbrace{\mathcal{F}^{-1} \left[\mathcal{P} \left(\frac{1}{\omega} \right) \right]}_{= \frac{1}{2i} \text{sgn}(t)}(t), \quad (3.71)$$

which proves Eq. (3.69). □

The right-hand side of Eq. (3.69) is analytically known, since the inverse Fourier transform of the density of states was already calculated in Eq. (3.42) for the case of the hypercubic lattice with the nearest neighbor hopping. Hence, $\mathcal{H}[\rho](\omega)$ can be obtained by applying \mathcal{F} on both sides of Eq. (3.69). If we further take into account that $J_0(2t_0t)$ from Eq. (3.42) is an even function of time, we get

$$\mathcal{H}[\rho](\omega) = \frac{1}{\pi} \int_0^\infty dx J_0(2t_0x)^d \sin(x\omega), \quad (3.72)$$

where d is the number of dimensions. The polaron band dispersion is then directly obtained from Eqs. (3.65), (3.68), and (3.72), and it reads as

$$E_{p,\mathbf{k}} = \varepsilon_{\mathbf{k}} + \alpha^2 \omega_0^2 \int_0^\infty dx J_0(2t_0x)^d \sin(x(\varepsilon_{\mathbf{k}} - \omega_0)). \quad (3.73)$$

As we already noted, the ground state energy E_p is then simply obtained by setting $\mathbf{k} = 0$ in the above expression. We see that E_p is thus a linear function with respect to α^2 , whose intercept is $\varepsilon_{\mathbf{k}=0}$, while its slope can be calculated accurately using the numerical scheme described in Appendix B.

In the two-dimensional case, it admits an analytical solution

$$E_p^{2D} = -4t_0 - \frac{2\alpha^2 \omega_0^2}{\pi(4t_0 + \omega_0)} K \left(\frac{4t_0}{4t_0 + \omega_0} \right), \quad (3.74)$$

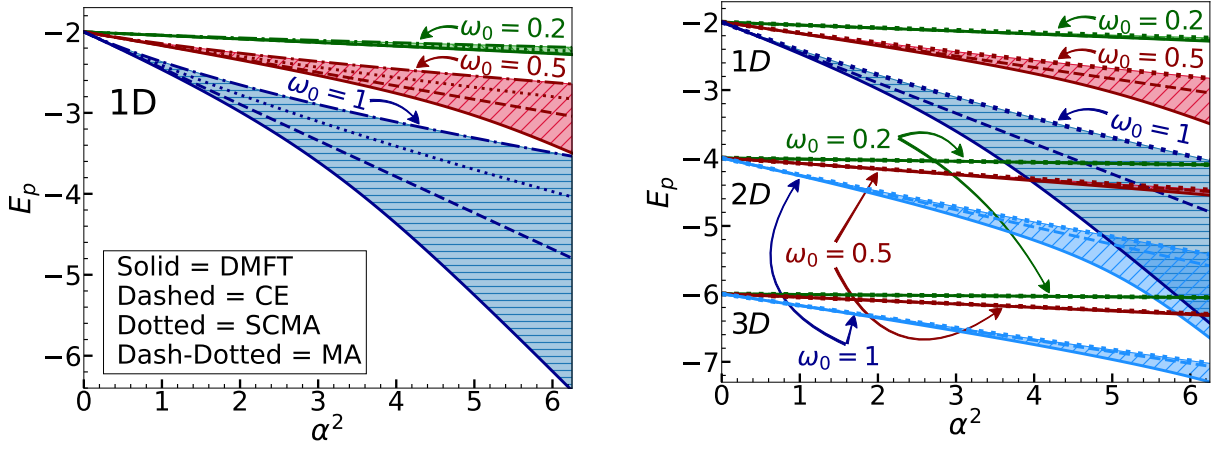
where $K(k) = \int_0^{\pi/2} d\theta / \sqrt{1 - k^2 \sin^2 \theta}$ is the complete elliptic integral of the first kind. In the case $d = 3$, the integral in Eq. (3.73) does not admit a closed-form solution and thus requires numerical calculation.

Remark 20. *The polaron band dispersion $E_{p,\mathbf{k}}$ (and thus the ground state E_p) within the DMFT and SCMA is obtained numerically, as we already explained in Sec. 2.1.*

3.5.1.2 Numerical Results

Numerical results are presented in Fig. 3.8. We emphasize once again that the results from Sec. 2.1 demonstrate that DMFT predictions are practically identical to the numerically exact results. Figure 3.8i shows that the DMFT always gives the lowest ground-state energy predictions, with CE being the closest approximation to DMFT. Following CE is the SCMA, while MA consistently exhibits the largest deviation from DMFT. These results readily demonstrate how much improvement to the one-shot MA is provided by including the self-consistency, and by employing the CE method.

¹¹Whether factor 2π appears in the convolution theorem or not depends on the convention for the Fourier transform that we use,



(i) Comparison of the DMFT, CE, SCMA, and MA for 1D.

(ii) Comparison of the DMFT (solid line), CE (dashed line), and SCMA (dotted line) in 1D, 2D, and 3D.

Figure 3.8: Ground state energies, in the Holstein model, as a function of α^2 , for $t_0 = 1$ and $T = 0$.

Furthermore, in the 1D case, we see that CE results for $\omega_0 = 0.5$ start to deviate more significantly from the DMFT just around $\alpha = 2.5$. Hence, the range of validity for the CE is similar as for the spectral functions in Fig. 3.3. While a distinction between the predictions of different methods is clearly seen for $\omega_0 = 1$, all three methods seem to be in agreement for $\omega_0 = 0.2$, in the whole range of presented values of α . This is a consequence of the fact that the ground state energy correction is small, as seen from Eqs. (3.66), (3.73) and (3.74) by fixing α and decreasing ω_0 . However, if we fix $g = \omega_0\alpha$ and then decrease ω_0 , the ground state energy would change substantially (see, e.g., Eq. (3.66)), and the CE would certainly give poorer results.

Similar trends are observed in higher dimensions as well; see Fig. 3.8ii. We see that CE always outperforms the SCMA, despite the fact that its predictions of the energy are always a linear function of α^2 . We note that it seems that the range of validity of all methods is increased in higher dimensions. However, one should keep in mind that the hopping parameter is always taken to be unity, which means that the bandwidth of the 2D and 3D systems are respectively 2 and 3 times larger than their one-dimensional counterpart. Therefore, the correlation is weaker for a given coupling α .

3.5.2 Effective Mass

3.5.2.1 Analytical Results

Around $|\mathbf{k}| \approx 0$, the dispersion $E_{p,\mathbf{k}}$ assumes the following parabolic form

$$E_{p,\mathbf{k}} \approx \text{const} + \frac{\mathbf{k}^2}{2m^*}, \quad (3.75)$$

where m^* is the effective mass, which we now calculate.

In the 1D case, one obtains the analytical result for the effective mass using Eqs. (3.65) and (2.23) from Part I, giving

$$\left. \frac{m^*}{m_0} \right|_{1D, T=0} = \frac{1}{1 - \frac{(2t_0 + \omega_0)\alpha^2\sqrt{\omega_0}}{(4t_0 + \omega_0)^{3/2}}}, \quad (3.76)$$

where $m_0 = 1/(2t_0)$ is the band mass; see Eq. (2.6) and the text below. Results for the higher number of dimensions are evaluated using Eq. (3.73). As for the ground state energy, the two-dimensional case admits an analytic solution

$$\left. \frac{m^*}{m_0} \right|_{2D, T=0} = \frac{1}{1 - \frac{2\alpha^2\omega_0}{\pi(8t_0 + \omega_0)} E\left(\frac{4t_0}{4t_0 + \omega_0}\right)}, \quad (3.77)$$

where $E(k) = \int_0^{\pi/2} d\theta \sqrt{1 - k^2 \sin^2 \theta}$ is the complete elliptic integral of the second kind. Results in the d -dimensional case are given by

$$\left. \frac{m^*}{m_0} \right|_{T=0} = \frac{1}{1 + \pi \alpha^2 \omega_0^2 \left. \frac{d\mathcal{H}[\rho]}{d\omega} \right|_{\omega=-2dt_0-\omega_0}}. \quad (3.78)$$

In general case, this requires the numerical calculation of the derivative of $\mathcal{H}[\rho](\omega)$, which for a given ω_0 and d is just a single number. From Eq. (3.78) we see that m_0/m^* is a linear function of α^2 . This linear behavior has to break down at one point, as m_0/m^* cannot be negative. This happens for strong interaction, where the CE is certainly not expected to be reliable.

Remark 21. *The mass renormalization within the DMFT and SCMA is calculated numerically, using Eq. (2.5), as we explained in Sec. 2.1.*

3.5.2.2 Numerical Results

Results for the DMFT, CE, and SCMA effective mass, in different parameter regimes and for different number of dimensions, are presented in Fig. 3.9.

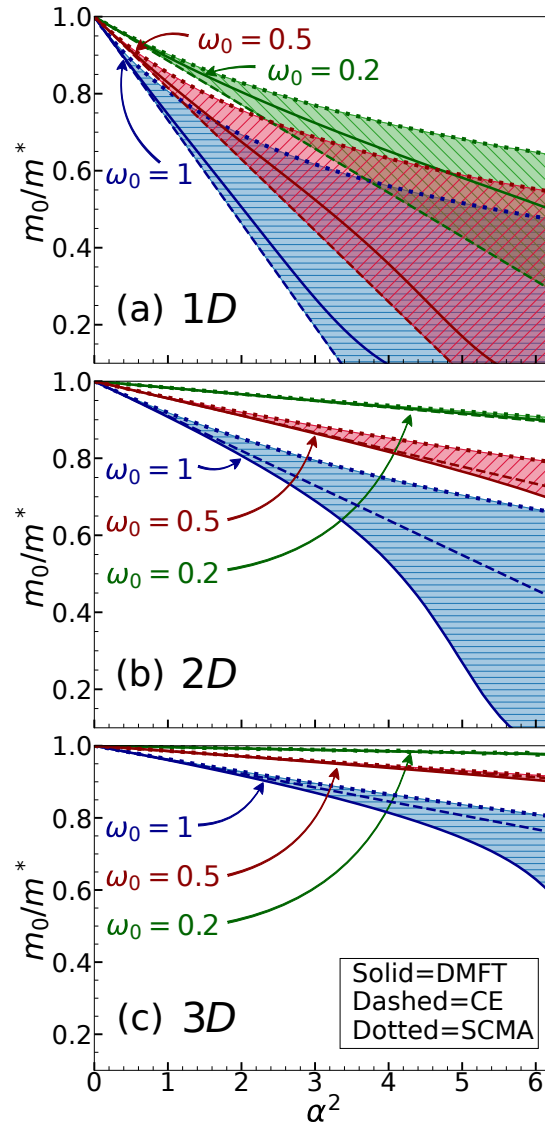


Figure 3.9: Effective mass results within the DMFT, CE, and SCMA for $t_0 = 1$ and $T = 0$.

In the one-dimensional case, we see that the CE always underestimates, while the SCMA overestimates the results from the DMFT benchmark. Still, CE clearly outperforms the SCMA for $\omega_0 = 1$ and $\omega_0 = 0.5$, while the results in the vicinity of the adiabatic limit ($\omega_0 = 0.2$) seem to be equally well (poor) represented by both of these methods.

In the higher-dimensional case, we see that the CE is always a clearly better approximation than the SCMA, while both of them overestimate the DMFT predictions. As for the ground state energy, we emphasize again that the hopping parameter was set to 1. As a consequence, the system has a larger bandwidth in the higher-dimensional case and, therefore, the correlations are weaker.

3.6 2D Spectral Functions

We now examine the CE spectral functions in a two-dimensional Holstein model, on a square lattice, and compare them to the results from DMFT and SCMA. Results are presented in Fig. 3.10. We note that in Figs. 3.10(a)–3.10(d), the phonon frequency $\omega_0 = 0.2$ is smaller, in the units of t_0 , than both of the temperatures ($T_1 = 0.3$ and $T_2 = 0.7$) that we are considering. Similarly, the phonon frequency in Figs. 3.10(i)–(l) is $\omega_0 = 1$, and is hence larger than both $T_1 = 0.3$ and $T_2 = 0.7$. Therefore, we focus

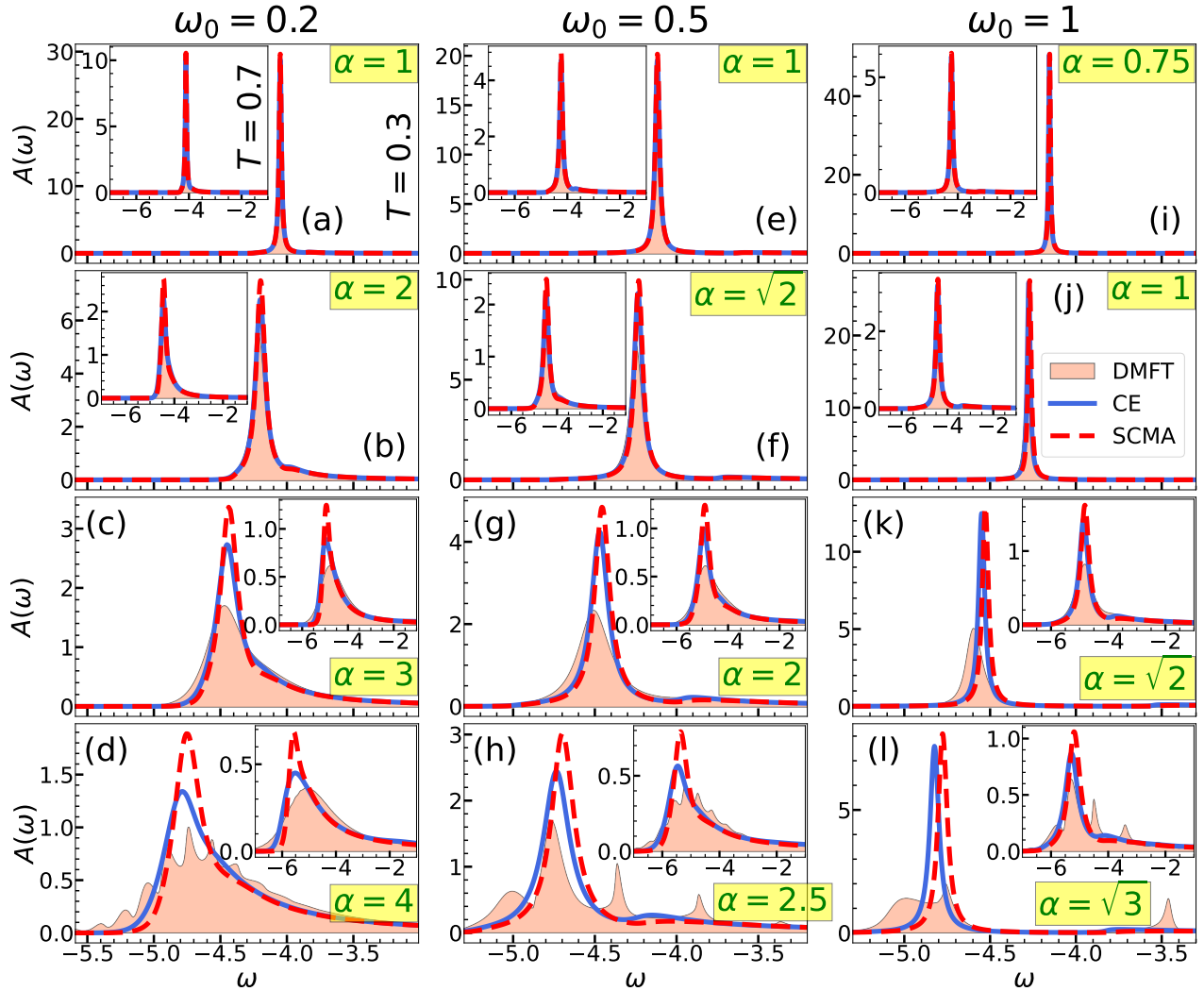


Figure 3.10: Comparison of the CE, DMFT, and SCMA spectral functions in a 2D Holstein model for $k = 0$ and $t_0 = 1$. The main panels show the results for $T_1 = 0.3$, while the results for $T_2 = 0.7$ are shown in insets.

on Figs. 3.10(e)–3.10(h) where $T_1 < \omega_0 < T_2$, while other regimes can be analyzed analogously. We see that most of the spectral weight is concentrated in a smaller range of frequencies than in the 1D case; see Figs. 3.3 and 3.10(e)–3.10(h). This is a consequence of the fact that the hopping parameter is always set to unity, while the 2D bandwidth is twice as large in comparison to the bandwidth in the 1D system. Regardless, spectral functions from Figs. 3.10(e)–3.10(g) exhibit qualitatively similar behavior as results for the one-dimensional system in Figs. 3.3(a)–3.3(d). Here, all methods are in agreement and predict that the quasiparticle peak dominates, while there is only a single tiny satellite structure that is more pronounced at higher temperatures. However, it seems that the satellites are more pronounced in the 1D spectral functions. A much more complicated multi-peak structure is predicted by the DMFT in Fig. 3.9(h), where a large discrepancy can be observed in comparison to the CE and SCMA results. A better agreement is observed for higher temperatures.

It is interesting to note that while the DMFT frequently gave sharper peaks than other methods in 1D (see Fig. 3.3), here the roles are reversed. This is a consequence of the strong Van Hove singularity at the bottom of the band of a 1D system, which is highly relevant in our case when the concentration of electrons is very low. On the other hand, the singularity in the 2D system is weaker and shifted to the center of the band.

3.7 Supplementary Results in a Wide Range of Parameter Regimes

In previous sections, we presented spectral functions $A_{\mathbf{k}}(\omega)$ and heat maps for $\omega_0 = 0.5$, and provided a comprehensive analysis of these results. Without further discussion, here we show a large number of results for $\omega_0 = 1$, $\omega_0 = 0.2$, as well as some additional results for $\omega_0 = 0.5$, that support our conclusions.

1. Results for $\omega_0 = 1$:

- Fig. 3.11: $A(\omega)$ in the weak coupling regime for a wide range of temperatures and momenta.
- Fig. 3.12: $A(\omega)$ in the weak, intermediate and strong electron-phonon coupling regimes for $k = 0$ and $k = \pi$:
 - Fig. 3.12i: $k = 0$ at $T = 0.4$ and $T = 1$.
 - Fig. 3.12ii: $k = \pi$ at $T = 0.4$ and $T = 1$.
 - Fig. 3.12iii: $k = 0, \pi$ at $T = 2$ and $T = 5$.
- Fig. 3.13: $A(\omega)$ in the weak, intermediate and strong electron-phonon coupling regimes for $k = \pi/3$ and $k = 2\pi/3$:
 - Fig. 3.13i: $T = 0.4$.
 - Fig. 3.13ii: $T = 1$.
 - Fig. 3.13iii: $T = 2$ and $T = 5$.
- Fig. 3.14: Heat maps
 - Fig. 3.14i: $T = 0.4$.
 - Fig. 3.14ii: $T = 1$.

2. Results for $\omega_0 = 0.5$:

- Fig. 3.13: $A(\omega)$ in the weak, intermediate, and strong electron-phonon coupling regimes for $k = \pi/3$ and $k = 2\pi/3$:
 - Fig. 3.15i: $T = 0.3$.
 - Fig. 3.15ii: $T = 0.7$.

- Fig. 3.15iii: $T = 2$ and $T = 5$.
3. Results for $\omega_0 = 0.2$:
- Fig. 3.16: $A(\omega)$ in the weak, intermediate and strong coupling regimes for $k = 0$ and $k = \pi$:
 - Fig. 3.16i: $k = 0$ at $T = 0.3$ and $T = 0.7$.
 - Fig. 3.16ii: $k = \pi$ at $T = 0.3$ and $T = 0.7$.
 - Fig. 3.16iii: $k = 0, \pi$ at $T = 2$ and $T = 5$.
 - Fig. 3.17: $A(\omega)$ in the weak, intermediate and strong coupling regimes for $k = \pi/3$ and $k = 2\pi/3$:
 - Fig. 3.17i: $T = 0.3$.
 - Fig. 3.17ii: $T = 0.7$.
 - Fig. 3.17iii: $T = 2$ and $T = 5$.
 - Fig. 3.18: Heat maps:
 - Fig. 3.18i: $T = 0.3$.
 - Fig. 3.18ii: $T = 0.7$.

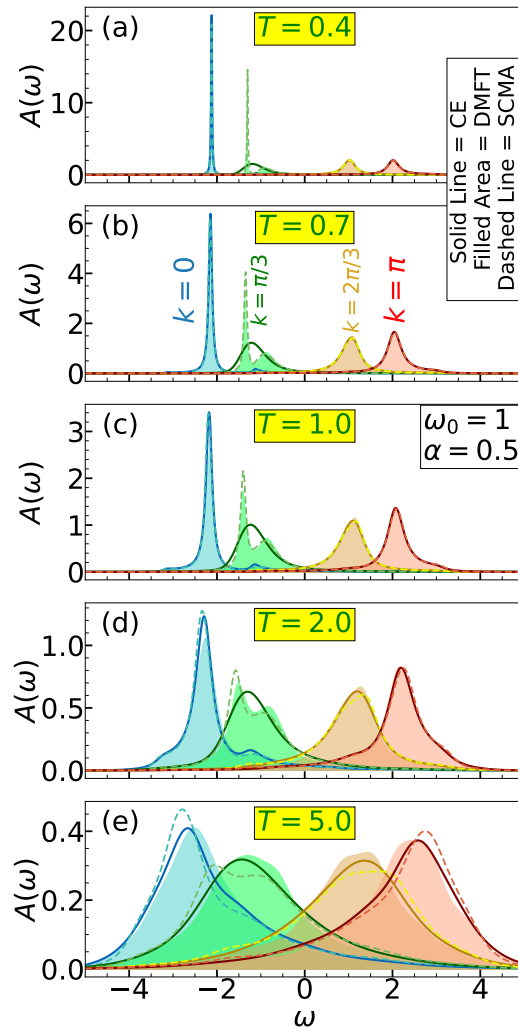
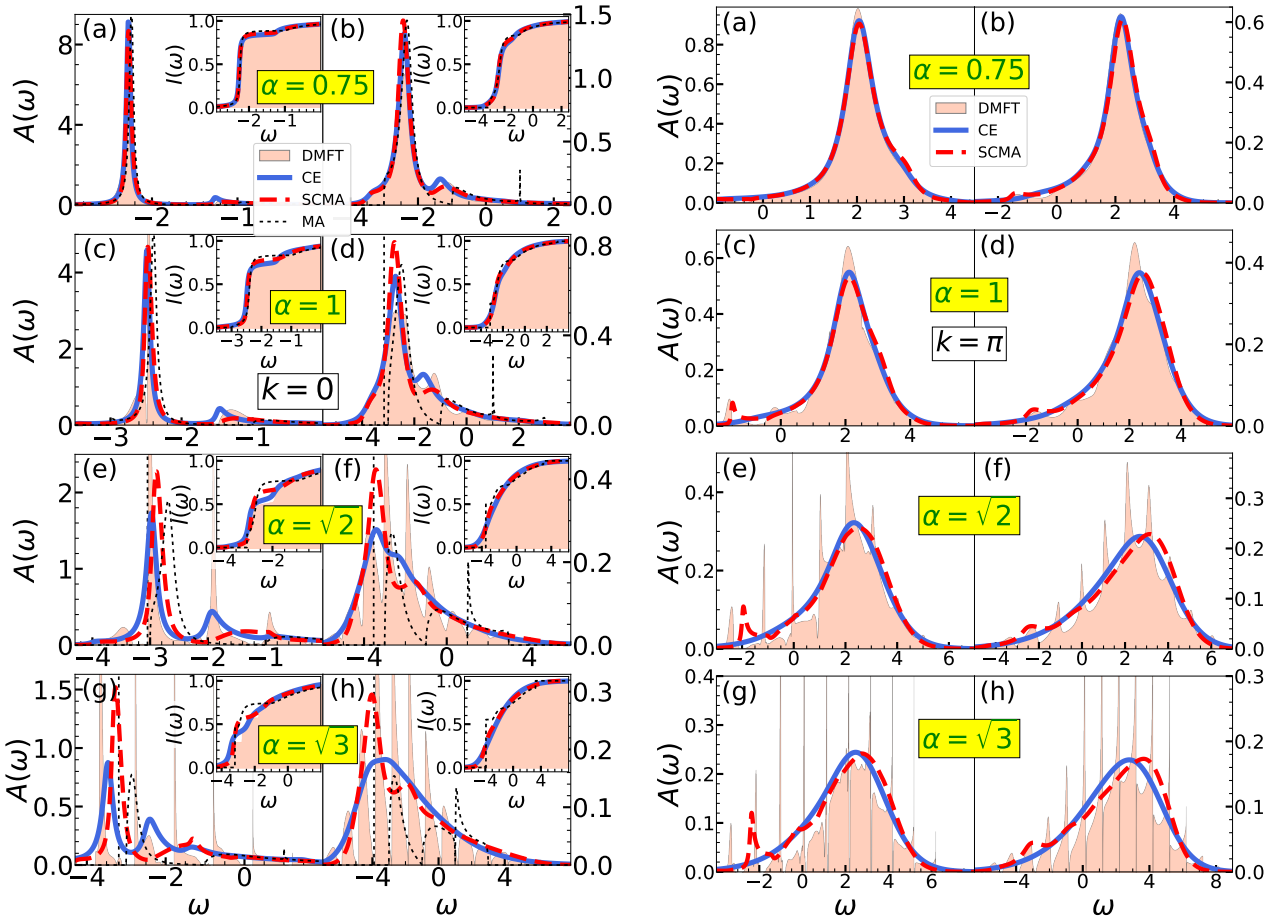
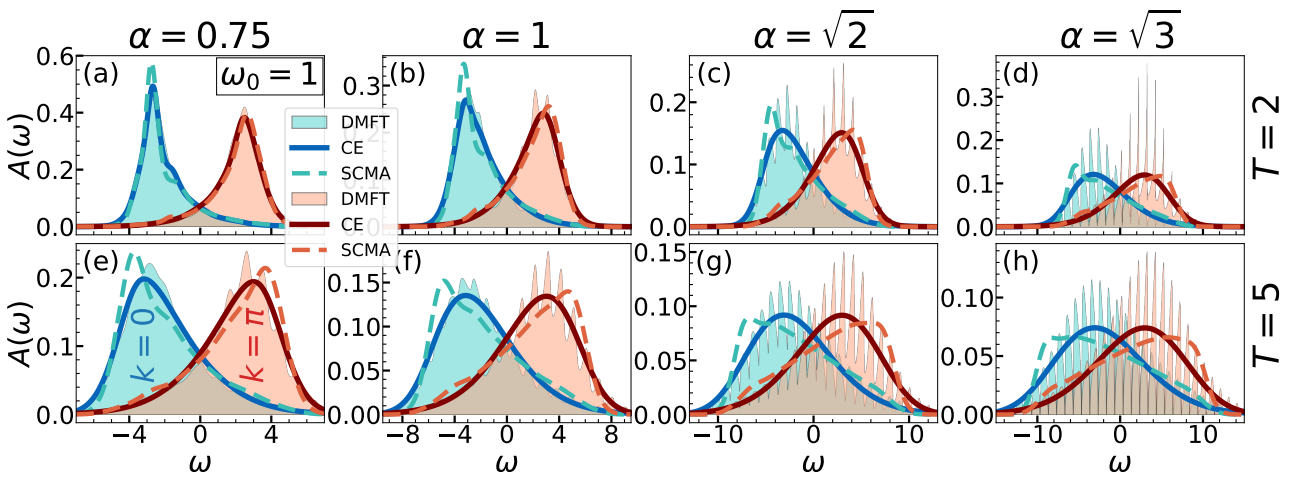


Figure 3.11: Comparison of CE, DMFT, and SCMA spectral functions in the weak coupling regime, for a wide range of temperatures. Here $t_0 = \omega_0 = 1$ and $\alpha = 0.5$.



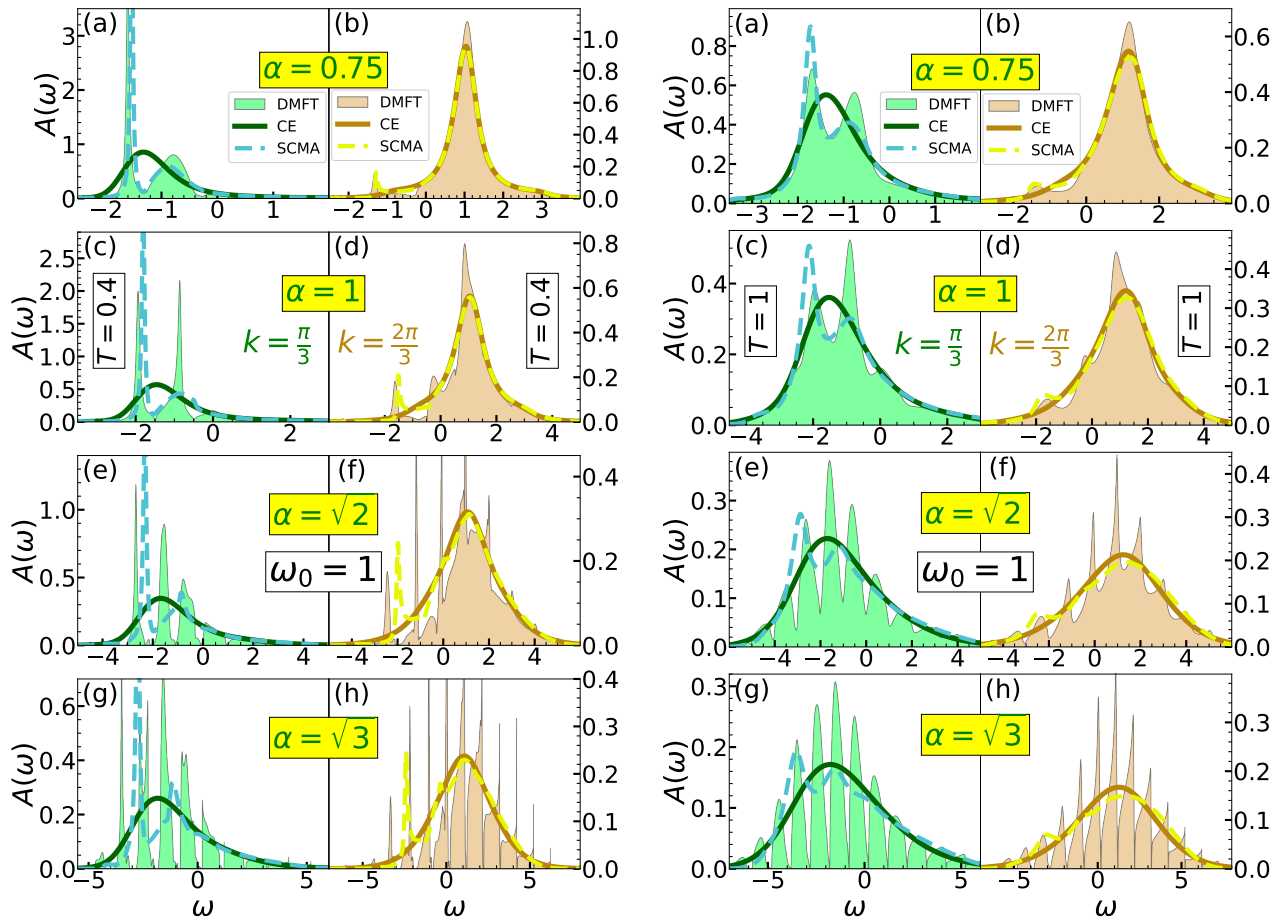
(i) Spectral functions for $\omega_0 = 1$ and $k = 0$. In the left panels $T = 0.4$, while $T = 1$ in the right panels. Insets show the integrated spectral weights $I(\omega) = \int_{-\infty}^{\infty} A(\omega) d\omega$.

(ii) Spectral functions for $\omega_0 = 1$ and $k = \pi$. In the left panels $T = 0.4$, while $T = 1$ in the right panels. Insets show the integrated spectral weights $I(\omega) = \int_{-\infty}^{\infty} A(\omega) d\omega$.



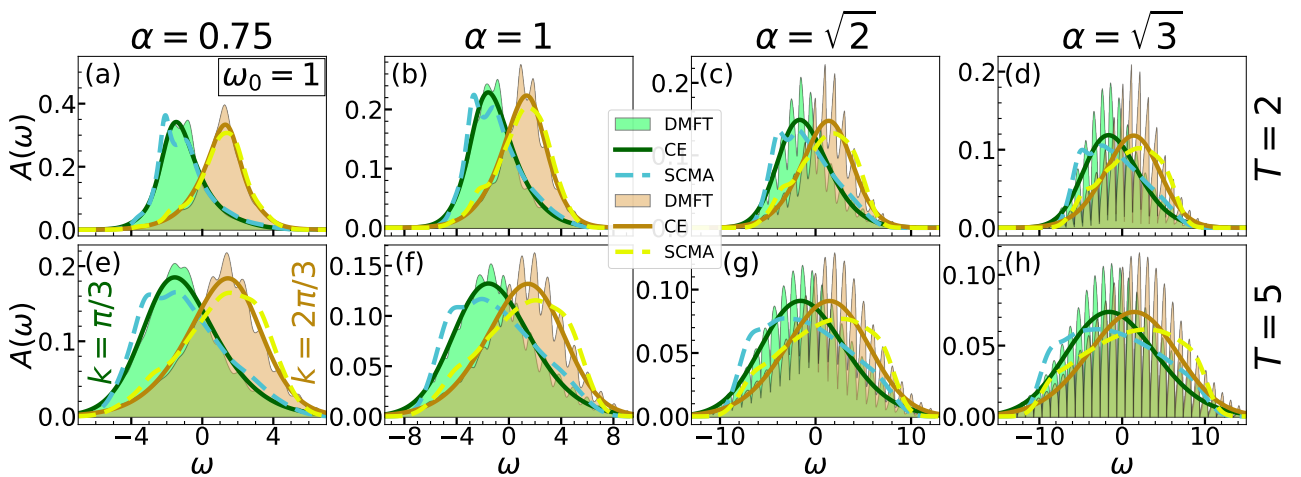
(iii) Spectral functions at higher temperatures for $\omega_0 = 1$ and $k = 0, \pi$.

Figure 3.12: Comparison of the CE, DMFT, SCMA, and MA spectral functions in 1D for $t_0 = \omega_0 = 1$.



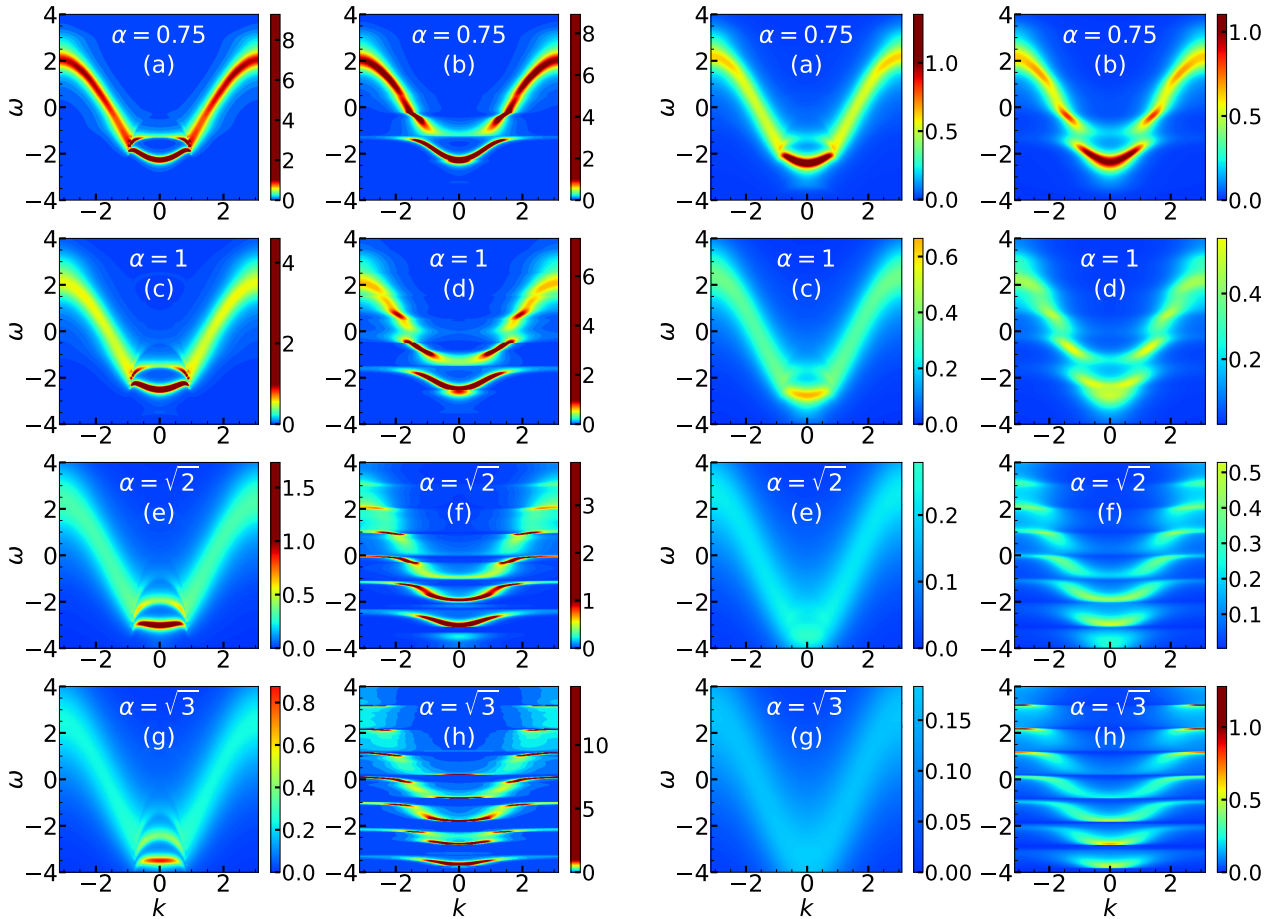
(i) Spectral functions for $\omega_0 = 1$ and $T = 0.4$. In the left panels $k = \pi/3$, while $k = 2\pi/3$ in the right panels.

(ii) Spectral functions for $\omega_0 = 1$ and $T = 1$. In the left panels $k = \pi/3$, while $k = 2\pi/3$ in the right panels.



(iii) Spectral functions at higher temperatures for $\omega_0 = 1$ and $k = \pi/3, 2\pi/3$.

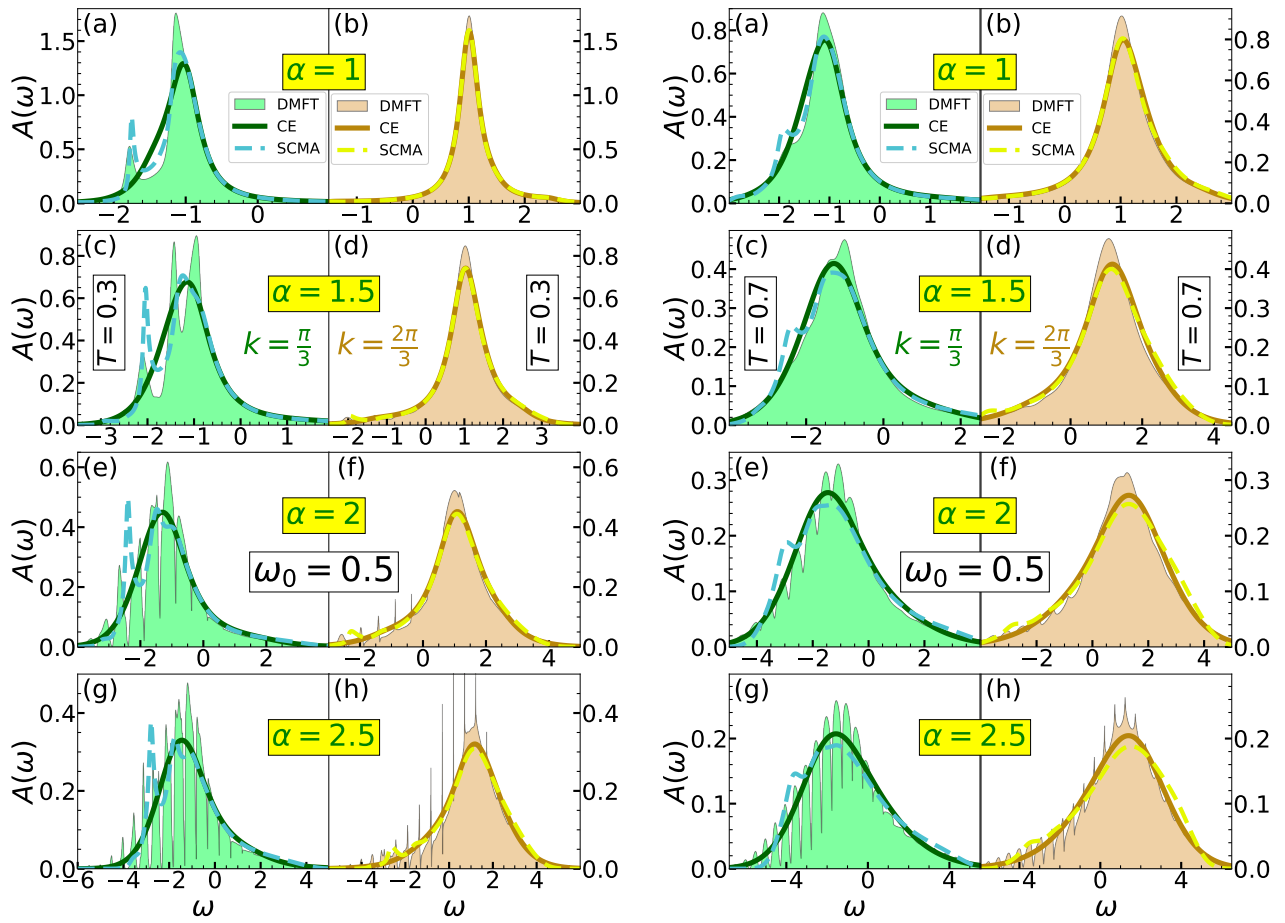
Figure 3.13: Comparison of the CE, DMFT, and SCMA spectral functions in 1D for $t_0 = \omega_0 = 1$ and $k = \pi/3, 2\pi/3$.



(i) Heat maps for $T = 0.4$. In the left panels, we present CE results, while the DMFT benchmark is presented in the right panels. All plots use the same color coding.

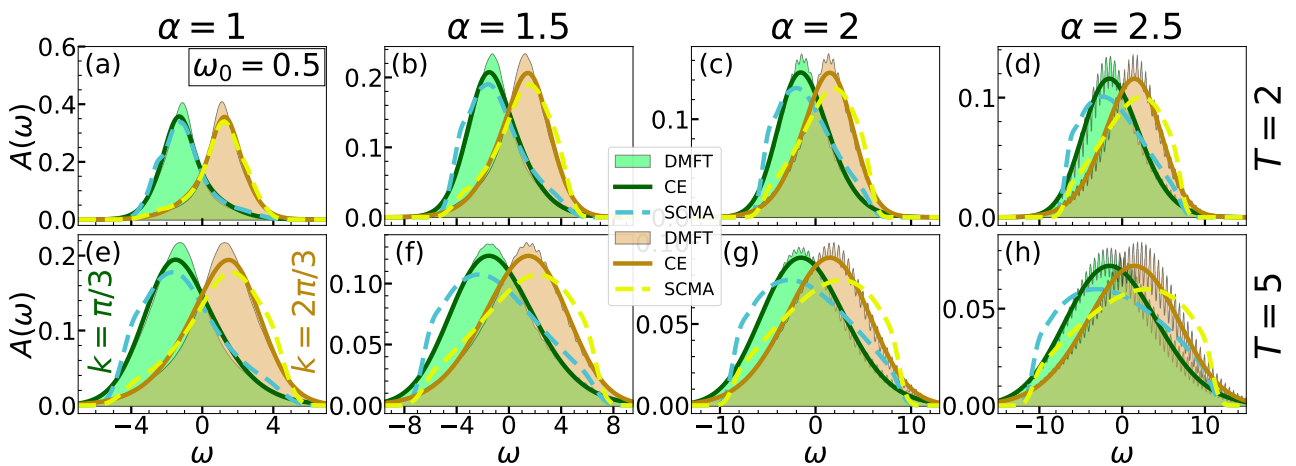
(ii) Heat maps for $T = 1$. In the left panels, we present CE results, while the DMFT benchmark is presented in the right panels. All plots use the same color coding.

Figure 3.14: Comparison of the CE and DMFT heat maps for $t_0 = \omega_0 = 1$.



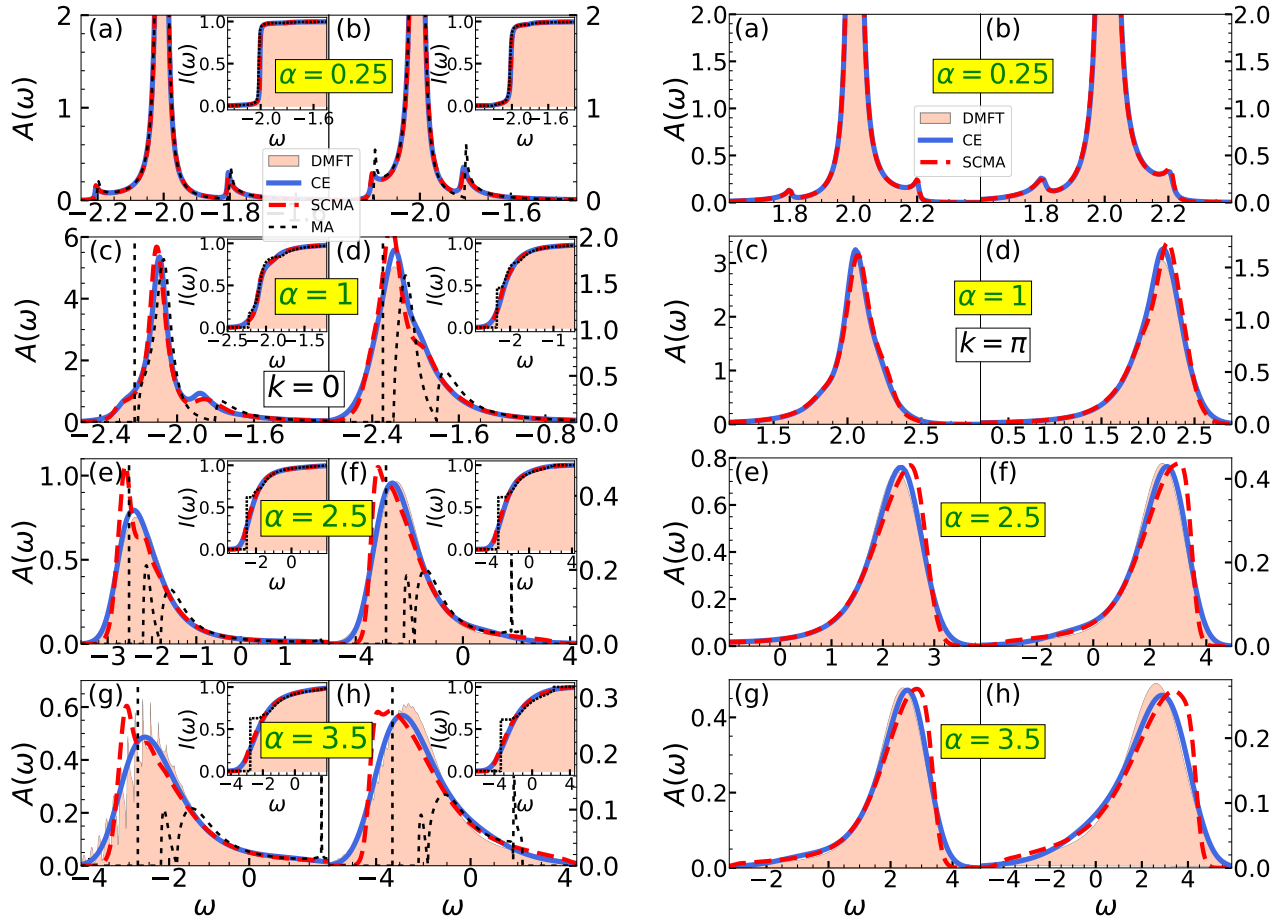
(i) Spectral functions for $\omega_0 = 0.5$ and $T = 0.3$. In the left panels $k = \pi/3$, while $k = 2\pi/3$ in the right panels.

(ii) Spectral functions for $\omega_0 = 0.5$ and $T = 0.7$. In the left panels $k = \pi/3$, while $k = 2\pi/3$ in the right panels.



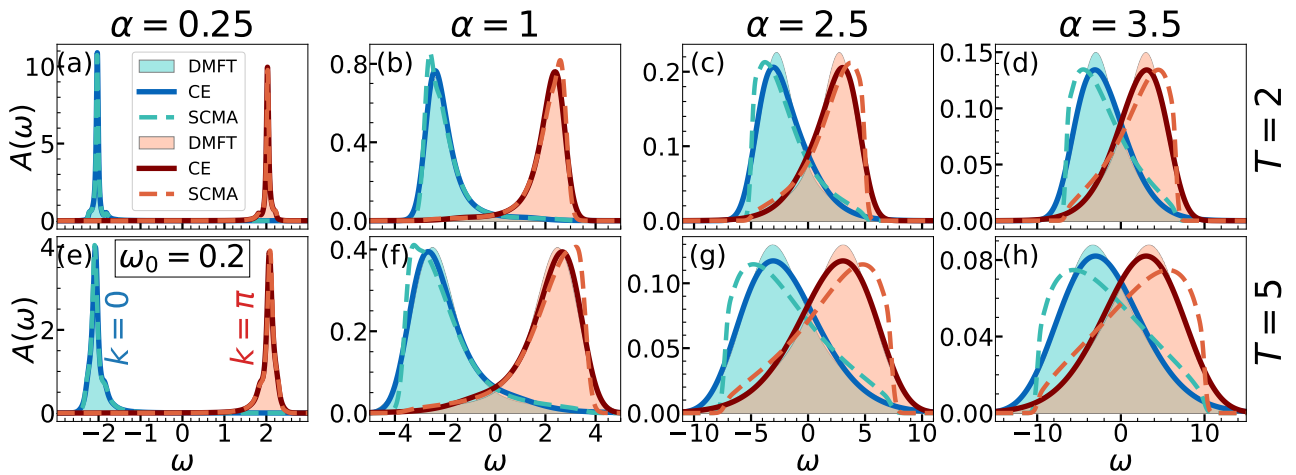
(iii) Spectral functions at higher temperatures for $\omega_0 = 0.5$ and $k = \pi/3, 2\pi/3$.

Figure 3.15: Comparison of the CE, DMFT, and SCMA spectral functions in 1D for $t_0 = 1$, $\omega_0 = 0.5$ and $k = \pi/3, 2\pi/3$.



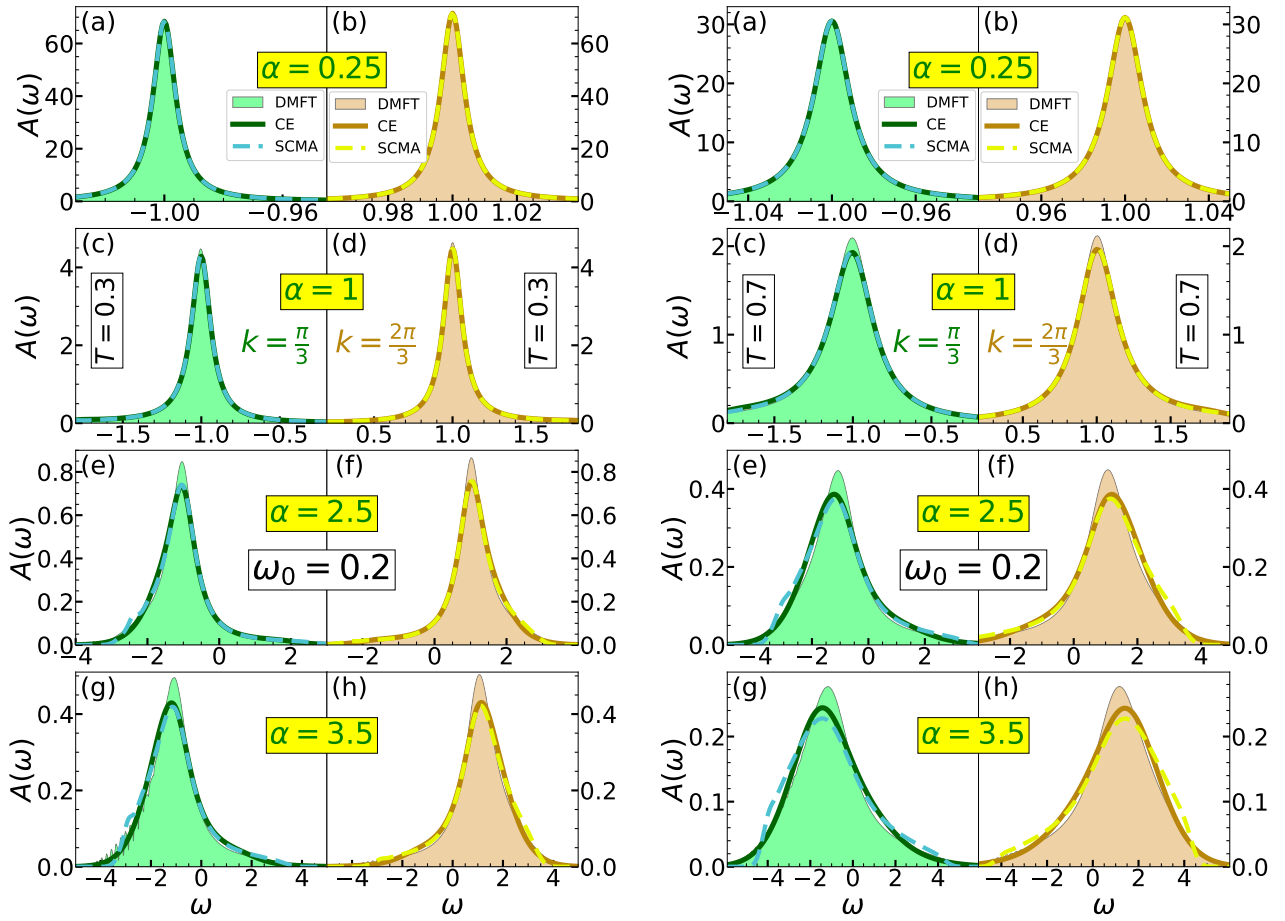
(i) Spectral functions for $\omega_0 = 0.2$ and $k = 0$. In the left panels $T = 0.3$, while $T = 0.7$ in the right panels. Insets show the integrated spectral weight $I(\omega) = \int_{-\infty}^{\infty} A(\omega) d\omega$.

(ii) Spectral functions for $\omega_0 = 0.2$ and $k = \pi$. In the left panels $T = 0.3$, while $T = 0.7$ in the right panels. Insets show the integrated spectral weight $I(\omega) = \int_{-\infty}^{\infty} A(\omega) d\omega$.



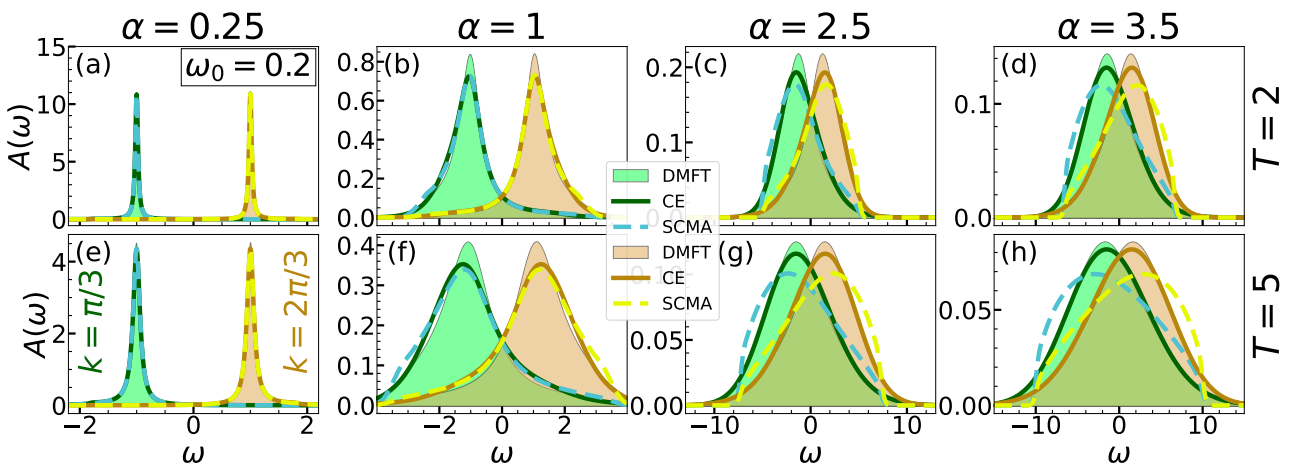
(iii) Spectral functions at higher temperatures for $\omega_0 = 0.2$ and $k = 0, \pi$.

Figure 3.16: Comparison of the CE, DMFT, SCMA, and MA spectral functions in 1D for $t_0 = 1$, $\omega_0 = 0.2$, and $k = 0, \pi$.



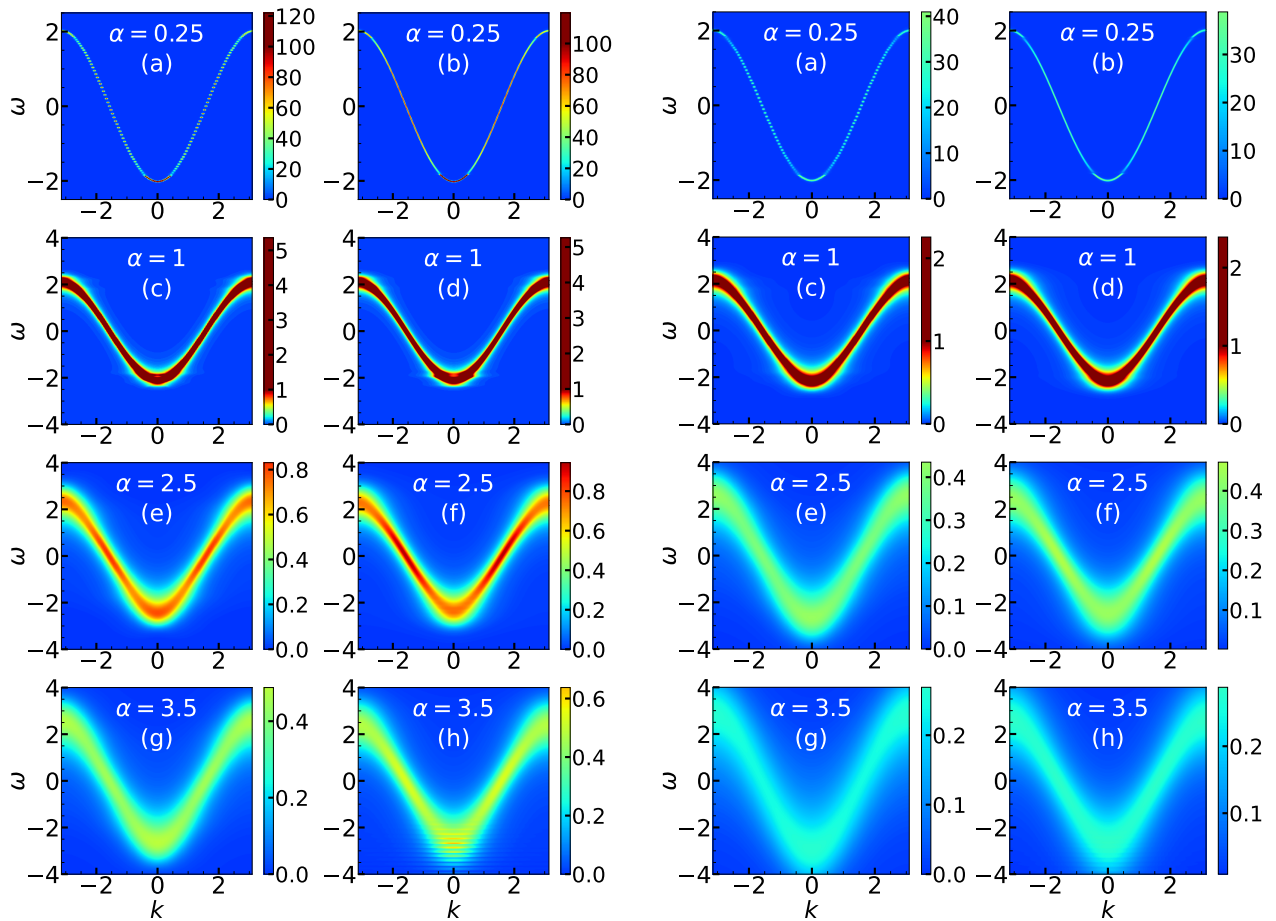
(i) Spectral functions for $\omega_0 = 0.2$ and $T = 0.3$. In the left panels $k = \pi/3$, while $k = 2\pi/3$ in the right panels.

(ii) Spectral functions for $\omega_0 = 0.2$ and $T = 0.7$. In the left panels $k = \pi/3$, while $k = 2\pi/3$ in the right panels.



(iii) Spectral functions at higher temperatures for $\omega_0 = 0.2$ and $k = \pi/3, 2\pi/3$.

Figure 3.17: Comparison of the CE, DMFT, and SCMA spectral functions in 1D for $t_0 = 1$, $\omega_0 = 0.2$ and $k = \pi/3, 2\pi/3$.



(i) Heat maps for $T = 0.3$. In the left panels, we present CE results, while the DMFT benchmark is presented in the right panels. Panels (c)–(h) use the same color coding, while panels (a) and (b) use different color coding.

(ii) Heat maps for $T = 0.7$. In the left panels, we present CE results, while the DMFT benchmark is presented in the right panels. Panels (c)–(h) use the same color coding, while panels (a) and (b) use different color coding.

Figure 3.18: Comparison of the CE and DMFT heat maps for $t_0 = 1$ and $\omega_0 = 0.2$.

Part III

Transport properties

Revisiting Linear Response Theory

This chapter does not contain original results. We only give a short overview of the linear response theory, which will be necessary for the calculation of optical conductivity and mobility in the subsequent chapters. We mostly follow Refs. [54] and [121].

1.1 Brief Overview and Introduction of the Most Important Quantities and Notation

The purpose of this section is to summarize the most general and most important results, without giving any formal proofs, and to establish a notation that will be used henceforth.

Let the total Hamiltonian of our system be

$$H_{\text{tot}} = H + H_1(t), \quad (1.1)$$

where H is the Holstein Hamiltonian, defined by Eq. (1.2) from Part I, while $H_1(t)$ is a perturbation of the form

$$H_1(t) = -\vec{A} \cdot \vec{F}(t). \quad (1.2)$$

Here, \vec{A} is an observable (operator), while \vec{F} is a classical field. Although this looks like a quite restrictive form of perturbation, it actually captures a wide variety of relevant cases, such as the introduction of electric or magnetic fields.

The change of expectation value (with respect to the case when there is no perturbation) of arbitrary observable B , is given by

$$\Delta\langle B \rangle(t) = \text{Tr} [\bar{\rho}(t)B] - \text{Tr} [\bar{\rho}_0 B], \quad (1.3)$$

where $\bar{\rho}(t)$ is the density matrix that corresponds to the total Hamiltonian, while $\bar{\rho}_0 = e^{-\beta H} / \text{Tr} [e^{-\beta H}]$ is the density matrix that corresponds to the Holstein Hamiltonian. To calculate this, we first need to find the time evolution of the density matrix $\bar{\rho}(t)$. As we will see, it is given by

$$\bar{\rho}(t) = \mathcal{L}(t, t_0) \bar{\rho}(t_0), \quad (1.4a)$$

$$\mathcal{L}(t, t_0) = e^{-itL_0} \hat{T}_t \exp \left\{ -i \int_{t_0}^t dt_1 e^{it_1 L_0} L_1(t_1) e^{-it_1 L_0} \right\} e^{it_0 L_0}, \quad (1.4b)$$

where L_0 and L_1 are the Liouville operators, defined by their action on arbitrary operator G

$$L_0 G = [H, G], \quad (1.5a)$$

$$L_1(t) G = [H_1(t), G]. \quad (1.5b)$$

Now, the linear response theory is obtained by approximating the time-ordered exponent in Eq. (1.4b) as a linear function with respect to L_1 . In this case, if we assume that there was no perturbation in the distant past $t \rightarrow -\infty$, then $\Delta\langle B\rangle(t)$ can be written as

$$\Delta\langle B\rangle(t) = \sum_j \int_{-\infty}^t dt_1 \phi_{BA_j}(t-t_1) F_j(t_1), \quad (1.6)$$

where

$$\phi_{BA}(t) = i\text{Tr} \{B[A(-t), \bar{\rho}_0]\} \quad (1.7)$$

is the so-called response function. In addition, we can also define other important quantities such as:

- the relaxation function

$$\Phi_{BA}(t) = \lim_{\varepsilon \rightarrow 0^+} \int_t^{\infty} \phi_{BA}(t_1) e^{-\varepsilon t_1} dt_1, \quad (1.8)$$

whose physical interpretation will be clearer in Sec. 1.3.

- the generalized susceptibility $\chi_{BA}(\omega)$. It is defined such that the following relation holds in the Fourier space

$$\Delta\langle B\rangle(\omega) = \sum_j F_j(\omega) \chi_{BA_j}(\omega). \quad (1.9)$$

For example, if we take B to be the current operator, A to be the dipole electric moment operator, and F to be the external electric field, then $\chi_{BA}(\omega)$ represents the optical conductivity. It can be related to the response function as follows

$$\chi_{BA}(\omega) = \int_0^{\infty} dt \phi_{BA}(t) e^{i\omega t - \varepsilon t}. \quad (1.10)$$

In the following sections, we will prove all of these relations and show many properties and different ways to express ϕ_{BA} , Φ_{BA} , and χ_{BA} .

1.2 Time Evolution of the Density Matrix

Here, we want to prove that the time evolution of the density matrix is given by Eq. (1.4). We start from Eq. (1.4a), defining $\mathcal{L}(t, t_0)$ as an evolution operator of the density matrix, and prove that it can be expressed as in Eq. (1.4b). Equivalently, we can also define $\mathcal{L}^{(1)}(t, t_0) = e^{itL_0} \mathcal{L}(t, t_0) e^{-it_0L_0}$, and prove that it is given by the time ordered exponential in (1.4b). To do so, let us first construct a differential equation that $\mathcal{L}^{(1)}(t, t_0)$ satisfies by evaluating its first derivative with respect to t

$$\dot{\mathcal{L}}^{(1)}(t, t_0) = e^{itL_0} iL_0 \mathcal{L}(t, t_0) + e^{itL_0} \dot{\mathcal{L}}(t, t_0) e^{-it_0L_0}. \quad (1.11)$$

The quantity $\dot{\mathcal{L}}(t, t_0)$ can be rewritten using the Liouville equation as follows

$$-i(L_0 + L_1(t)) \mathcal{L}(t, t_0) \rho(t_0) = -i(L_0 + L_1(t)) \rho(t) = \dot{\rho}(t) = \dot{\mathcal{L}}(t, t_0) \rho(t_0), \quad (1.12)$$

as it implies that

$$\dot{\mathcal{L}}(t, t_0) = -i(L_0 + L_1(t)) \mathcal{L}(t, t_0). \quad (1.13)$$

Plugging this back into Eq. (1.11), we get

$$\begin{aligned} \dot{\mathcal{L}}^{(1)}(t, t_0) &= -ie^{itL_0} L_1(t) \mathcal{L}(t, t_0) e^{-it_0L_0} = -i \underbrace{e^{itL_0} L_1(t) e^{-itL_0}}_{\equiv L_1(t,t)} \underbrace{e^{itL_0} \mathcal{L}(t, t_0) e^{-it_0L_0}}_{=\mathcal{L}^{(1)}(t,t_0)} \\ &= -iL_1(t,t) \mathcal{L}^{(1)}(t, t_0), \end{aligned} \quad (1.14)$$

where we introduced $L_1(t, t)$ to make the formulas somewhat simpler. There is also an initial condition $\mathcal{L}^{(1)}(t_0, t_0) = 1$. It is obvious that this differential equation can also be rewritten as an integral equation

$$\mathcal{L}^{(1)}(t, t_0) = 1 - i \int_{t_0}^t dt_1 L_1(t_1, t_1) \mathcal{L}^{(1)}(t_1, t_0). \quad (1.15)$$

This is now easy to solve using an iterative procedure

$$\begin{aligned} \mathcal{L}^{(1)}(t, t_0) &= 1 - i \int_{t_0}^t dt_1 L_1(t_1, t_1) \left[1 - i \int_{t_0}^{t_1} dt_2 L_1(t_2, t_2) \mathcal{L}^{(1)}(t_2, t_0) \right] \\ &= 1 - i \int_{t_0}^t dt_1 L_1(t_1, t_1) + (-i)^2 \int_{t_0}^t dt_1 \int_{t_0}^{t_1} dt_2 L_1(t_1, t_1) L_1(t_2, t_2) \\ &\quad + \dots + (-i)^n \int_{t_0}^t dt_1 \int_{t_0}^{t_1} dt_2 \dots \int_{t_0}^{t_{n-1}} dt_n L_1(t_1, t_1) \dots L_1(t_n, t_n) + \dots \end{aligned} \quad (1.16)$$

From the identity

$$\begin{aligned} \int_{t_0}^t dt_1 \int_{t_0}^{t_1} dt_2 \dots \int_{t_0}^{t_{n-1}} dt_n L_1(t_1, t_1) \dots L_1(t_n, t_n) \\ = \frac{1}{n!} \int_{t_0}^t dt_1 \int_{t_0}^{t_1} dt_2 \dots \int_{t_0}^{t_{n-1}} dt_n \hat{T}_t \{ L_1(t_1, t_1) \dots L_1(t_n, t_n) \}, \end{aligned} \quad (1.17)$$

we see that the solution can be written as

$$\mathcal{L}^{(1)}(t, t_0) = \hat{T}_t \exp \left\{ -i \int_{t_0}^t dt_1 L_1(t_1, t_1) \right\}. \quad (1.18)$$

Using the definition $\mathcal{L}^{(1)}(t, t_0) = e^{itL_0} \mathcal{L}(t, t_0) e^{-it_0L_0}$, we conclude that

$$\mathcal{L}(t, t_0) = e^{-itL_0} \hat{T}_t \exp \left\{ -i \int_{t_0}^t dt_1 e^{it_1L_0} L_1(t_1) e^{-it_1L_0} \right\} e^{it_0L_0}, \quad (1.19)$$

which completes the proof. □

1.3 Linear Response Approach

Equation (1.18) is exact. In the case when the external field is not too strong, this equation can be approximated as

$$\mathcal{L}^{(1)}(t, t_0) = 1 - i \int_{t_0}^t dt_1 L_1(t_1, t_1). \quad (1.20)$$

This constitutes the so-called linear response approach.

Let us now deduce the consequences of this approximation if we additionally suppose that the external field $F(t)$ is nonzero only for $t > t_0$. Hence,

$$\bar{\rho}(t < t_0) = \bar{\rho}(t_0) = \bar{\rho}_0 = \frac{e^{-\beta H}}{\text{Tr} [e^{-\beta H}]}. \quad (1.21)$$

From Eq. (1.19), and the fact that

$$L_0 \bar{\rho}_0 = 0, \quad (1.22)$$

we see that within the linear response theory, it follows that

$$\begin{aligned}
 \bar{\rho}(t) &= e^{-itL_0} \left(1 - i \int_{t_0}^t dt_1 e^{it_1L_0} L_1(t_1) e^{-it_1L_0} \right) \bar{\rho}_0 \\
 &= \bar{\rho}_0 - i \int_{t_0}^t dt_1 e^{i(t_1-t)L_0} L_1(t_1) \bar{\rho}_0 \\
 &\stackrel{(1.5b)}{=} \bar{\rho}_0 - i \int_{t_0}^t dt_1 e^{i(t_1-t)L_0} [H_1(t_1), \bar{\rho}_0] \\
 &\stackrel{(1.2)}{=} \bar{\rho}_0 + i \int_{t_0}^t dt_1 e^{i(t_1-t)L_0} [\vec{A}, \bar{\rho}_0] \vec{F}(t_1).
 \end{aligned} \tag{1.23}$$

In the second term, L_0 acts only on \vec{A} since \vec{F} is not an operator, while $\bar{\rho}_0$ commutes with L_0 . Hence, to proceed, it is sufficient to derive the following

$$\begin{aligned}
 e^{i(t_1-t)L_0} A &= \sum_{n=0}^{\infty} \frac{(i(t_1-t))^n}{n!} L_0^n A \\
 &\stackrel{(1.5a)}{=} \sum_{n=0}^{\infty} \frac{1}{n!} [i(t_1-t)H, [i(t_1-t)H, [\dots [i(t_1-t)H, A] \dots]]] \\
 &= e^{i(t_1-t)H} A e^{-i(t_1-t)H} \\
 &= A(t_1-t),
 \end{aligned} \tag{1.24}$$

where we used the Baker–Campbell–Hausdorff identity in the second-to-last line. Plugging this back into Eq. (1.23) and setting $t_0 \rightarrow -\infty$, we finally obtain

$$\bar{\rho}(t) = \bar{\rho}_0 + i \int_{-\infty}^t dt_1 [\vec{A}(t_1-t), \bar{\rho}_0] \vec{F}(t_1). \tag{1.25}$$

Hence, the response of arbitrary observable B reads as

$$\Delta\langle B \rangle(t) = \text{Tr} [\bar{\rho}(t)B] - \text{Tr} [\bar{\rho}_0 B] = i \int_{-\infty}^t dt_1 \text{Tr} \left\{ [\vec{A}(t_1-t), \bar{\rho}_0] B \right\} \vec{F}(t_1). \tag{1.26}$$

This can also be rewritten as

$$\boxed{\Delta\langle B \rangle(t) = i \int_{-\infty}^t dt_1 \sum_j \text{Tr} \left\{ [\vec{A}_j(t_1-t), \bar{\rho}_0] B \right\} \vec{F}_j(t_1) = \sum_j \int_{-\infty}^t dt_1 \phi_{BA_j}(t-t_1) F_j(t_1),} \tag{1.27}$$

where we derived the so-called response function $\phi_{BA}(t)$ as

$$\phi_{BA}(t) = i \text{Tr} \{ B [A(-t), \bar{\rho}_0] \}. \tag{1.28}$$

As we see, the response function illustrates how the system reacts to the external perturbation, but is independent of the external field $\vec{F}(t)$. Nevertheless, we can try out different choices of $\vec{F}(t)$ and see how the system reacts. One possibility is to use constant external field $F_j(t)$ (equal to unity) in the range $t \in (-\infty, 0)$ and then suddenly switch it off. In this case, Eq. (1.27), using the substitution $x = t - t_1$, implies that

$$\Delta\langle B \rangle(t) = \sum_j \int_0^{\infty} \phi_{BA_j}(x) \theta(x-t) dx \stackrel{\text{if } t \geq 0}{=} \sum_j \int_t^{\infty} \phi_{BA_j}(x) dx, \tag{1.29}$$

where θ is the Heaviside step function. This motivates the introduction of a new quantity¹

$$\Phi_{BA}(t) = \lim_{\varepsilon \rightarrow 0^+} \int_t^\infty \phi_{BA}(t_1) e^{-\varepsilon t_1} dt_1, \quad (1.30)$$

which is called the relaxation function.

1.4 Properties of Response and Relaxation Functions

1.4.1 Properties of $\phi_{BA}(t)$

Cyclic Properties

Using the cyclic property of the trace

$$\text{Tr} \{X[Y, Z]\} = \text{Tr} \{Z[X, Y]\} = \text{Tr} \{Y[Z, X]\}, \quad (1.31)$$

we immediately see that $\phi_{BA}(t)$ can be written in a few different ways

$$\phi_{BA}(t) = i \text{Tr} \{B[A(-t), \bar{\rho}_0]\} \quad (1.32a)$$

$$= i \text{Tr} \{\bar{\rho}_0[B, A(-t)]\} \quad (1.32b)$$

$$= i \text{Tr} \{A(-t)[\bar{\rho}_0, B]\}. \quad (1.32c)$$

Furthermore, using the fact that $\bar{\rho}_0$ commutes with H_0 , it follows that

$$\begin{aligned} \phi_{BA}(t) &= i \text{Tr} \{B[A(-t), \bar{\rho}_0]\} \\ &= i \text{Tr} \{B e^{-itH} [A, \bar{\rho}_0] e^{itH}\} \\ &= i \text{Tr} \{e^{itH} B e^{-itH} [A, \bar{\rho}_0]\} \\ &= i \text{Tr} \{B(t)[A, \bar{\rho}_0]\}. \end{aligned} \quad (1.33)$$

Thus, applying Eq. (1.31) once again we get

$$\phi_{BA}(t) = i \text{Tr} \{B(t)[A, \bar{\rho}_0]\} \quad (1.34a)$$

$$= i \text{Tr} \{\bar{\rho}_0[B(t), A]\} \quad (1.34b)$$

$$= i \text{Tr} \{A[\bar{\rho}_0, B(t)]\}. \quad (1.34c)$$

Symmetry Properties

The response function $\phi_{BA}(t)$ satisfies the following properties:

$$\phi_{BA}(t)^* = \phi_{BA}(t), \quad (1.35a)$$

$$\phi_{BA}(t) = -\phi_{AB}(-t). \quad (1.35b)$$

These can be proved by using the fact that

- $[X, Y]^\dagger = -[X^\dagger, Y^\dagger]$
- $A^\dagger = A$ and $B^\dagger = B$
- $A(-t)^\dagger = A(-t)$

¹Here, we also include the regularization parameter ε .

Hence, it follows that

$$\begin{aligned}\phi_{BA}(t)^* &= (i\text{Tr} \{B[A(-t), \bar{\rho}_0]\})^* = -i\text{Tr} \{[A(-t), \bar{\rho}_0]^\dagger B^\dagger\} \\ &= i\text{Tr} \{B[A(-t), \bar{\rho}_0]\} = \phi_{BA}(t),\end{aligned}\quad (1.36)$$

and

$$\phi_{BA}(t) \stackrel{(1.34c)}{=} i\text{Tr} \{A[\bar{\rho}_0, B(t)]\} = -i\text{Tr} \{A[B(t), \bar{\rho}_0]\} \stackrel{(1.32a)}{=} -\phi_{AB}(-t). \quad (1.37)$$

Furthermore, the so-called Onsager relation trivially follows from the time-reversal symmetry

$$\boxed{\phi_{BA}(t) = \varepsilon_A \varepsilon_B \phi_{AB}(t)}. \quad (1.38)$$

Here ε_A and ε_B are the parity signs of observables A and B with respect to time reversal.

Consequences of the Kubo Identity

As a consequence of Eqs. (E.2) and (E.4), that we derived in Appendix E, the response function can also be written as²

$$\boxed{\phi_{BA}(t) = \langle \tilde{A}\dot{B}(t) \rangle_0 = -\langle \tilde{B}(t)A \rangle_0 = -\langle \tilde{A}\dot{B}(t) \rangle_0}, \quad (1.39)$$

where the quantities with a tilde are defined as

$$\tilde{G} = G(i\nu_n = 0) = \int_0^\beta d\tau G(-i\tau). \quad (1.40)$$

The first equality in Eq. (1.39) is proven as follows

$$\phi_{BA}(t) \stackrel{(1.34a)}{=} i\text{Tr} \{B(t)[A, \bar{\rho}_0]\} \stackrel{(E.2)}{=} \text{Tr} \{B(t)\bar{\rho}_0\tilde{A}\} = \text{Tr} \{\tilde{A}B(t)\bar{\rho}_0\} = \langle \tilde{A}B(t) \rangle_0. \quad (1.41)$$

The second one is completely analogous

$$\phi_{BA}(t) \stackrel{(1.34c)}{=} -i\text{Tr} \{A[B(t), \bar{\rho}_0]\} \stackrel{(E.2)}{=} -\text{Tr} \{\tilde{B}(t)A\bar{\rho}_0\} = -\langle \tilde{B}(t)A \rangle_0, \quad (1.42)$$

while the third one is derived as a consequence of the second one

$$\phi_{BA}(t) = -\langle \tilde{B}(t)A \rangle_0 \stackrel{(E.4)}{=} -\langle \tilde{A}\dot{B}(t) \rangle_0. \quad (1.43)$$

1.4.2 Properties of $\Phi_{BA}(t)$

Basic Properties

From the definition of the relaxation function in Eq. (1.30) we can immediately see that it satisfies

$$\boxed{\lim_{t \rightarrow \infty} \Phi_{BA}(t) = 0}, \quad (1.44a)$$

$$\boxed{\dot{\Phi}_{BA}(t) = -\phi_{BA}(t)e^{-\varepsilon t}}. \quad (1.44b)$$

Furthermore, starting from Eq. (1.30), $\Phi_{BA}(t)$ can also be expressed as

$$\Phi_{BA}(t) = \int_t^\infty dt_1 \phi_{BA}(t_1) e^{-\varepsilon t_1} \stackrel{(1.39)}{=} - \int_t^\infty dt_1 \langle \tilde{A}\dot{B}(t) \rangle_0 e^{-\varepsilon t_1}. \quad (1.45)$$

Using the partial integration with $u = e^{-\varepsilon t_1}$ and $dv = \langle \tilde{A}\dot{B}(t) \rangle_0$, we obtain

$$\boxed{\Phi_{BA}(t) = \langle \tilde{A}\dot{B}(t) \rangle_0}. \quad (1.46)$$

²The expectation value is defined as $\langle G \rangle_0 = \text{Tr}[\bar{\rho}_0 G]$.

Symmetry Properties

The relaxation function $\phi_{BA}(t)$ satisfies the following properties:

$$\boxed{\Phi_{BA}(t)^* = \Phi_{BA}(t),} \quad (1.47a)$$

$$\boxed{\Phi_{BA}(-t) = \Phi_{AB}(t).} \quad (1.47b)$$

The first one of these is a direct consequence of Eq. (1.35a), and the definition of relaxation function (1.30). The second one can be proved as follows

$$\Phi_{BA}(-t) \stackrel{(1.46)}{=} \langle \tilde{A}B(-t) \rangle_0 = \langle \tilde{A}(t)B \rangle_0 \stackrel{(E.4)}{=} \langle \tilde{B}A(t) \rangle_0 \stackrel{(1.46)}{=} \Phi_{AB}(t). \quad (1.48)$$

In addition, $\Phi_{BA}(t)$ also satisfies the Onsager relation, as a consequence of time-inversion symmetry

$$\boxed{\Phi_{BA}(t) = \varepsilon_A \varepsilon_B \Phi_{AB}(t),} \quad (1.49)$$

where ε_A and ε_B are the parity signs of observables A and B with respect to time-reversal.

Fourier Properties

There is a direct consequence of these symmetry properties on $\Phi_{BA}(\omega)$ in the Fourier space

$$\boxed{\Phi_{BA}(\omega) = \Phi_{AB}(\omega)^*} \quad (1.50)$$

This is easily proved as follows:

$$\begin{aligned} \Phi_{BA}(\omega) &= \int_{-\infty}^{\infty} dt e^{i\omega t} \Phi_{BA}(t) \stackrel{t \rightarrow -t}{=} \int_{-\infty}^{\infty} dt e^{-i\omega t} \Phi_{BA}(-t) \stackrel{(1.47b)}{=} \int_{-\infty}^{\infty} dt e^{-i\omega t} \Phi_{AB}(t) \\ &\stackrel{(1.47a)}{=} \left[\int_{-\infty}^{\infty} dt e^{i\omega t} \Phi_{AB}(t) \right]^* = \Phi_{AB}(\omega)^*. \end{aligned} \quad (1.51)$$

1.5 Generalized Susceptibility

Definition and Relation to Response Function

Using the substitution $x = t - t_1$ in Eq. (1.27)

$$\Delta \langle B \rangle(t) = \sum_j \int_0^{\infty} dx \phi_{BA_j}(x) F_j(t-x) = \sum_j \int_{-\infty}^{\infty} dx \theta(x) \phi_{BA_j}(x) F_j(t-x), \quad (1.52)$$

and performing a Fourier transform on this convolution integral, leads us to

$$\boxed{\Delta \langle B \rangle(\omega) = \sum_j F_j(\omega) \chi_{BA_j}(\omega),} \quad (1.53)$$

where $\chi_{BA_j}(\omega)$ is the generalized susceptibility, which reads as

$$\boxed{\chi_{BA_j}(\omega) = \int_{-\infty}^{\infty} dt e^{i\omega t} \theta(t) \phi_{BA_j}(t) = \int_0^{\infty} dt e^{i\omega t} \phi_{BA_j}(t).} \quad (1.54)$$

Properties of $\chi_{BA}(\omega)$

The susceptibility $\chi_{BA}(\omega)$ satisfies the following properties:

$$\chi_{BA}(\omega)^* = \chi_{BA}(-\omega), \quad (1.55a)$$

$$\chi_{BA}(\omega) = \Phi_{BA}(t=0) + i\omega \int_0^\infty dt \Phi_{BA}(t) e^{i\omega t}, \quad (1.55b)$$

$$\chi_{BA}(\omega=0) = \Phi_{BA}(t=0) = \langle \tilde{A}B \rangle_0 = \langle \tilde{B}A \rangle_0. \quad (1.55c)$$

The first one of these is easily proved

$$\chi_{BA}(\omega)^* \stackrel{(1.54)}{=} \left[\int_0^\infty dt e^{i\omega t} \phi_{BA}(t) \right]^* \stackrel{(1.35a)}{=} \int_0^\infty dt e^{-i\omega t} \phi_{BA}(t) = \chi_{BA}(-\omega). \quad (1.56)$$

Equation (1.55b) is proved by introducing the regularization parameter in Eq. (1.54)

$$\chi_{BA}(\omega) = \int_0^\infty dt \phi_{BA}(t) e^{i\omega t - \varepsilon t}, \quad (1.57)$$

and using the partial integration with $u = e^{i\omega t}$ and $dv = \phi_{BA}(t) e^{-\varepsilon t}$. Since $v = -\Phi_{BA}(t)$, as a consequence of Eq. (1.44b), we obtain

$$\chi_{BA}(\omega) = -\Phi_{BA}(t) e^{i\omega t} \Big|_0^\infty + i\omega \int_0^\infty dt \Phi_{BA}(t) e^{i\omega t} \stackrel{(1.44a)}{=} \Phi_{BA}(0) + i\omega \int_0^\infty dt \Phi_{BA}(t) e^{i\omega t}, \quad (1.58)$$

which completes the proof of Eq. (1.55b). Before we proceed with our proof of Eq. (1.55c), let us note that the quantity

$$\tilde{\chi}_{BA}(\omega) = \int_0^\infty dt \Phi_{BA}(t) e^{i\omega t} \stackrel{(1.55b)}{=} \frac{\chi_{BA}(\omega) - \Phi_{BA}(t=0)}{i\omega} \stackrel{(1.55b)}{=} \frac{\chi_{BA}(\omega) - \chi_{BA}(\omega=0)}{i\omega}, \quad (1.59)$$

is often called the reduced susceptibility.

The only thing that remains is to show that Eq. (1.55c) is valid. This can be done as follows

$$\chi_{BA}(\omega=0) \stackrel{(1.55b)}{=} \Phi_{BA}(t=0) \stackrel{(1.46)}{=} \langle \tilde{A}B(t=0) \rangle_0 = \langle \tilde{A}B \rangle_0 \stackrel{(E.4)}{=} \langle \tilde{B}A \rangle_0. \quad (1.60)$$

Optical Conductivity from Linear Response Theory

Here, we will consider one of the applications of the formalism that we introduced in the last chapter. This chapter is also a review, and it does not contain original results. We again follow Refs. [54] and [121].

2.1 Basic Definitions

For us, the most important application of linear response theory is the ability to calculate the optical conductivity. To accomplish this, Ohm's law

$$\langle j_\alpha \rangle(\omega) = \sum_\gamma \sigma_{\alpha\gamma}(\omega) E_\gamma(\omega) \quad (2.1)$$

tells us that we should introduce the electric field $E_\gamma(\omega)$ and examine the response of the current density operator¹ $\langle j_\alpha \rangle(\omega)$. Theoretically, in order to incorporate the electric field, we need to add a perturbation to the Holstein Hamiltonian of the form

$$H_1(t) = -\vec{P} \cdot \vec{E}(t), \quad (2.2)$$

where \vec{P} is the electric dipole moment. This has the same form as Eq. (1.2), if we set $\vec{A} = \vec{P}$ and $\vec{F}(t) = \vec{E}(t)$. Hence, we can use all the results from the previous chapter. In particular, since the conductivity is a generalized susceptibility (see Eq. (1.53)), we can immediately deduce many different ways to express it

$$\begin{aligned} \sigma_{\alpha\gamma}(\omega) &= \chi_{j_\alpha P_\gamma}(\omega) \stackrel{(1.54)}{=} \int_0^\infty dt e^{i\omega t} \phi_{j_\alpha P_\gamma}(t) \stackrel{(1.39)}{=} \int_0^\infty dt e^{i\omega t} \langle \tilde{P}_\gamma j_\alpha(t) \rangle_0 \\ &\stackrel{(C.29)}{=} V \int_0^\infty dt e^{i\omega t} \langle \tilde{j}_\gamma j_\alpha(t) \rangle_0 \stackrel{(1.46)}{=} V \int_0^\infty dt e^{i\omega t} \Phi_{j_\alpha j_\gamma}(t). \end{aligned} \quad (2.3)$$

One immediate consequence of the previous line and the Onsager relation in Eq. (1.49) is the well-known fact that the conductivity tensor is symmetric $\sigma_{\alpha\gamma}(\omega) = \sigma_{\gamma\alpha}(\omega)$, but it can also be used in conjunction with Eq. (1.59) to derive the following relation

$$\sigma_{\alpha\gamma}(\omega) = V \frac{\chi_{j_\alpha j_\gamma}(\omega) - \chi_{j_\alpha j_\gamma}(\omega = 0)}{i\omega}, \quad (2.4)$$

The susceptibility $\chi_{j_\alpha j_\gamma}(\omega)$ from the last line can be connected to the current-current correlation function as follows

$$\chi_{j_\alpha j_\gamma}(\omega) \stackrel{(1.54)}{=} \int_0^\infty dt \phi_{j_\alpha j_\gamma}(\omega) e^{i\omega t} \stackrel{(1.34b)}{=} i \int_0^\infty dt e^{i\omega t} \langle [j_\alpha(t), j_\gamma] \rangle_0. \quad (2.5)$$

¹Indices α and γ denote the components of vectors and tensors.

2.2 Different Ways to Relate Optical Conductivity and Current-Current Correlation Functions

In the previous section, Eqs. (2.4) and (2.5) demonstrated how the optical conductivity can be related to the current-current correlation function. Here, we will show some various additional ways how this can be done. We note that we will here be focusing on the real part of the optical conductivity. This will be very helpful for our subsequent numerical implementations.

2.2.1 Expressions on a Real-Frequency Axis

Let us start from the result that we already obtained in Eq. (2.4). As a consequence of Eq. (1.55a), $\chi_{j_\alpha j_\gamma}(\omega = 0)/(i\omega)$ is purely imaginary. Hence

$$\boxed{\text{Re } \sigma_{\alpha\gamma}(\omega) = V \cdot \text{Re} \left(\frac{\chi_{j_\alpha j_\gamma}(\omega)}{i\omega} \right) \stackrel{(2.5)}{=} \frac{V}{\omega} \text{Re} \int_0^\infty dt e^{i\omega t} \langle [j_\alpha(t), j_\gamma] \rangle_0.} \quad (2.6)$$

Remark 22. As a consequence of Eq. (1.55a), we see that $\text{Re } \chi_{j_\alpha j_\gamma}(\omega)$ is symmetric while $\text{Im } \chi_{j_\alpha j_\gamma}(\omega)$ is antisymmetric function of ω . Hence, $\text{Re } \sigma_{\alpha\gamma}(\omega)$ is a symmetric function of ω , as seen from the expression above.

Another interesting expression for $\text{Re } \sigma_{\alpha\gamma}(\omega)$ can be derived by taking the real part of both sides of Eq. (2.3). The relaxation function $\Phi_{j_\alpha j_\gamma}(t)$ is an even, real function, as a consequence of Eqs. (1.47a), (1.47b), and (1.49). Hence, Re affects only the exponential term $e^{i\omega t}$, which as a result also becomes real and even function. Hence

$$\begin{aligned} \text{Re } \sigma_{\alpha\gamma}(\omega) &= \frac{V}{2} \text{Re} \int_{-\infty}^\infty dt e^{i\omega t} \Phi_{j_\alpha j_\gamma}(t) \stackrel{(1.46)}{=} \frac{V}{2} \text{Re} \int_{-\infty}^\infty dt e^{i\omega t} \langle \tilde{j}_\gamma j_\alpha(t) \rangle_0 \\ &= \frac{V}{2} \text{Re} \int_{-\infty}^\infty dt e^{i\omega t} \int_0^\beta d\tau \langle j_\gamma(-i\tau) j_\alpha(t) \rangle_0 \\ &= \frac{V}{2} \text{Re} \int_{-\infty}^\infty dt e^{i\omega t} \int_0^\beta d\tau \langle j_\gamma j_\alpha(t + i\tau) \rangle_0 \\ &\stackrel{(E.7)}{=} \frac{V}{2} \text{Re} \int_{-\infty}^\infty dt e^{i\omega t} \int_0^\beta d\tau \int_{-\infty}^\infty \frac{d\omega'}{2\pi} J_{j_\gamma j_\alpha}(\omega') e^{-i\omega'(t+i\tau)} \\ &= \frac{V}{2} \text{Re} J_{j_\gamma j_\alpha}(\omega) \frac{e^{\beta\omega} - 1}{\omega} = V \frac{1 - e^{-\beta\omega}}{2\omega} \text{Re} J_{j_\gamma j_\alpha}(\omega) e^{\beta\omega} \end{aligned} \quad (2.7)$$

Using the inverse Fourier transform of Eq. (E.9) leads us to

$$\text{Re } \sigma_{\alpha\gamma}(\omega) = V \frac{1 - e^{-\beta\omega}}{2\omega} \text{Re} \int_{-\infty}^\infty dt e^{i\omega t} \langle j_\alpha(t) j_\gamma \rangle_0. \quad (2.8)$$

Analogously, if we returned to Eq. (2.7), and used Eq. (E.8), we would obtain:

$$\text{Re } \sigma_{\alpha\gamma}(\omega) = V \frac{e^{\beta\omega} - 1}{2\omega} \text{Re} \int_{-\infty}^\infty dt e^{i\omega t} \langle j_\gamma j_\alpha(t) \rangle_0. \quad (2.9)$$

Remark 23. 1. Since we already proved that conductivity is a symmetric tensor $\sigma_{\alpha\gamma} = \sigma_{\gamma\alpha}$, this implies that we can interchange $\alpha \leftrightarrow \gamma$ in both Eqs. (2.8) and (2.9).

2. Due to invariance under time translations we can use $\langle j_\alpha(t) j_\gamma \rangle_0 = \langle j_\alpha j_\gamma(-t) \rangle_0$ and $\langle j_\gamma j_\alpha(t) \rangle_0 = \langle j_\gamma(-t) j_\alpha \rangle_0$ in both Eqs. (2.8) and (2.9).

3. Due to time-reversal symmetry, it holds that $\langle j_\alpha(t)j_\gamma \rangle_0 = \langle j_\alpha(-t)j_\gamma \rangle_0^*$. Hence, using the substitution $t \rightarrow -t$, we get

$$\int_{-\infty}^{\infty} dt e^{i\omega t} \langle j_\alpha(t)j_\gamma \rangle_0 = \int_{-\infty}^{\infty} dt e^{-i\omega t} \langle j_\alpha(-t)j_\gamma \rangle_0 = \left[\int_{-\infty}^{\infty} dt e^{i\omega t} \langle j_\alpha(t)j_\gamma \rangle_0 \right]^*, \quad (2.10)$$

we see that the expression in the previous line is real. This is the same integral, as in Eq. (2.9). Therefore, we do not need Re on the right-hand side of Eq. (2.9), and we can remove it. An analogous result holds also for Eq. (2.8). As a result, we obtain

$$\text{Re } \sigma_{\alpha\gamma}(\omega) = V \frac{1 - e^{-\beta\omega}}{2\omega} \int_{-\infty}^{\infty} dt e^{i\omega t} \langle j_\alpha(t)j_\gamma \rangle_0, \quad (2.11a)$$

$$\text{Re } \sigma_{\alpha\gamma}(\omega) = V \frac{e^{\beta\omega} - 1}{2\omega} \int_{-\infty}^{\infty} dt e^{i\omega t} \langle j_\gamma j_\alpha(t) \rangle_0. \quad (2.11b)$$

A more symmetric expression for $\text{Re } \sigma_{\alpha\gamma}(\omega)$ can be obtained as follows

$$\begin{aligned} \text{Re } \sigma_{\alpha\gamma}(\omega) &\stackrel{(2.11a)}{=} V \frac{1 - e^{-\beta\omega}}{2\omega} \int_{-\infty}^{\infty} dt e^{i\omega t} [\langle j_\alpha(t)j_\gamma \rangle_0 + \langle j_\gamma j_\alpha(t) \rangle_0] \\ &\quad - V \frac{1 - e^{-\beta\omega}}{2\omega} \int_{-\infty}^{\infty} dt e^{i\omega t} \langle j_\gamma j_\alpha(t) \rangle_0 \\ &\stackrel{(2.11b)}{=} V \frac{1 - e^{-\beta\omega}}{2\omega} \int_{-\infty}^{\infty} dt e^{i\omega t} [\langle j_\alpha(t)j_\gamma \rangle_0 + \langle j_\gamma j_\alpha(t) \rangle_0] - \frac{1 - e^{-\beta\omega}}{e^{\beta\omega} - 1} \text{Re } \sigma_{\alpha\gamma}(\omega), \end{aligned} \quad (2.12)$$

giving

$$\text{Re } \sigma_{\alpha\gamma}(\omega) = V \frac{\tanh\left(\frac{\beta\omega}{2}\right)}{2\omega} \int_{-\infty}^{\infty} dt e^{i\omega t} [\langle j_\alpha(t)j_\gamma \rangle_0 + \langle j_\gamma j_\alpha(t) \rangle_0]. \quad (2.13)$$

Furthermore, the terms in the square brackets are complex conjugates of each other. Therefore:

$$\text{Re } \sigma_{\alpha\gamma}(\omega) = V \frac{\tanh\left(\frac{\beta\omega}{2}\right)}{\omega} \int_{-\infty}^{\infty} dt e^{i\omega t} \text{Re} \langle j_\alpha(t)j_\gamma \rangle_0 \quad (2.14a)$$

$$= V \frac{\tanh\left(\frac{\beta\omega}{2}\right)}{\omega} \int_{-\infty}^{\infty} dt \cos(\omega t) \text{Re} \langle j_\alpha(t)j_\gamma \rangle_0. \quad (2.14b)$$

Some further insight can be gained by inspecting the spectral representation of the current-current correlation function (see Appendix E)

$$J_{j_\alpha j_\gamma}(\omega) \stackrel{(E.8)}{=} \int_{-\infty}^{\infty} dt e^{i\omega t} \langle j_\alpha j_\gamma(t) \rangle_0 \stackrel{(E.9)}{=} e^{-\beta\omega} \int_{-\infty}^{\infty} dt e^{i\omega t} \langle j_\gamma(t)j_\alpha \rangle_0 = e^{-\beta\omega} \int_{-\infty}^{\infty} dt e^{i\omega t} \langle j_\alpha j_\gamma(-t) \rangle_0, \quad (2.15)$$

where we, in the last equality, used the invariance under time reversal. If we now use a substitution $t \rightarrow -t$, we get

$$J_{j_\alpha j_\gamma}(\omega) = e^{-\beta\omega} J_{j_\alpha j_\gamma}(-\omega). \quad (2.16)$$

This is just one of the possible formulations of the fluctuation-dissipation theorem. It enables us to derive yet another form of the optical conductivity

$$\begin{aligned} \text{Re } \sigma_{\alpha\gamma}(\omega) &\stackrel{(2.11b)}{=} V \frac{e^{\beta\omega} - 1}{2\omega} \int_{-\infty}^{\infty} dt e^{i\omega t} \langle j_{\gamma} j_{\alpha}(t) \rangle_0 \stackrel{(E.7)}{=} V \frac{e^{\beta\omega} - 1}{2\omega} J_{j_{\gamma} j_{\alpha}}(\omega) \\ &\stackrel{(2.16)}{=} \frac{V}{2\omega} [J_{j_{\gamma} j_{\alpha}}(-\omega) - J_{j_{\gamma} j_{\alpha}}(\omega)] = \frac{V}{2\omega} \int_{-\infty}^{\infty} dt [e^{-i\omega t} \langle j_{\gamma} j_{\alpha}(t) \rangle_0 - e^{i\omega t} \langle j_{\gamma} j_{\alpha}(t) \rangle_0] \end{aligned} \quad (2.17)$$

Using now the invariance under time reversal and substitution $t \rightarrow -t$ in the first term, we obtain

$$\text{Re } \sigma_{\alpha\gamma}(\omega) = \frac{V}{2\omega} \int_{-\infty}^{\infty} dt e^{i\omega t} [\langle j_{\alpha}(t) j_{\gamma} \rangle_0 - \langle j_{\gamma} j_{\alpha}(t) \rangle_0]. \quad (2.18)$$

Let us note that although there is ω in the denominator, the DC conductivity can nevertheless be calculated directly, using Eq. (2.11a) and the fact that $\lim_{\omega \rightarrow 0} (1 - e^{-\beta\omega})/\omega = \beta$

$$\text{Re } \sigma_{\alpha\gamma}(\omega = 0) = \frac{V\beta}{2} \int_{-\infty}^{\infty} dt \langle j_{\alpha}(t) j_{\gamma} \rangle_0. \quad (2.19)$$

Up to now, we only showed how to calculate the conductivity from the current-current correlation function. However, we can also perform the calculation in the opposite direction. Using the inverse Fourier transform in Eq. (2.11a), we obtain

$$\langle j_{\alpha}(t) j_{\gamma} \rangle_0 = \int_{-\infty}^{\infty} \frac{d\omega}{2\pi V} e^{-i\omega t} \frac{2\omega}{1 - e^{-\beta\omega}} \text{Re } \sigma_{\alpha\gamma}(\omega). \quad (2.20)$$

2.2.2 Expressions on the Imaginary Axis

Using the substitution $t = -i\tau$ in Eq. (2.20), we get the current-current correlation function in imaginary time

$$\langle j_{\alpha}(-i\tau) j_{\gamma} \rangle_0 = \int_{-\infty}^{\infty} \frac{d\omega}{2\pi V} e^{-\omega\tau} \frac{2\omega}{1 - e^{-\beta\omega}} \text{Re } \sigma_{\alpha\gamma}(\omega). \quad (2.21)$$

The Fourier transform to Matsubara frequency space can also be easily carried out

$$\langle j_{\alpha}(i\nu_n) j_{\gamma} \rangle_0 = \int_{-\infty}^{\infty} \frac{d\omega}{2\pi V} \frac{2\omega}{1 - e^{-\beta\omega}} \text{Re } \sigma_{\alpha\gamma}(\omega) \int_0^{\beta} d\tau e^{i\nu_n\tau} e^{-\omega\tau} = \int_{-\infty}^{\infty} \frac{d\omega}{\pi V} \frac{\omega}{\omega - i\nu_n} \text{Re } \sigma_{\alpha\gamma}(\omega) \quad (2.22a)$$

$$= \int_{-\infty}^{\infty} \frac{d\omega}{\pi V} \frac{\omega^2}{\omega^2 + \nu_n^2} \text{Re } \sigma_{\alpha\gamma}(\omega) + i\nu_n \int_{-\infty}^{\infty} \frac{d\omega}{\pi V} \frac{\omega \text{Re } \sigma_{\alpha\gamma}(\omega)}{\omega^2 + \nu_n^2}, \quad (2.22b)$$

where we used that the second term in the last line is zero because the subintegral function is odd with respect to ω . Therefore

$$\langle j_{\alpha}(i\nu_n) j_{\gamma} \rangle_0 = \int_{-\infty}^{\infty} \frac{d\omega}{\pi V} \frac{\omega^2}{\omega^2 + \nu_n^2} \text{Re } \sigma_{\alpha\gamma}(\omega). \quad (2.23)$$

At the end of this section, we present another important identity

$$\chi_{j_{\alpha} j_{\gamma}}(i\nu_n) = \int_{-\infty}^{\infty} \frac{d\omega}{\pi} \frac{\text{Im } \chi_{j_{\alpha} j_{\gamma}}(\omega)}{\omega - i\nu_n} = \int_{-\infty}^{\infty} \frac{d\omega}{\pi V} \frac{\omega \text{Re } \sigma_{\alpha\gamma}(\omega)}{\omega - i\nu_n} = \langle j_{\alpha}(i\nu_n) j_{\gamma} \rangle_0. \quad (2.24)$$

The first equality is trivial, as the right-hand side is simply the Hilbert transform. The second equality is a direct consequence of

$$\text{Im } \chi_{j_{\alpha} j_{\gamma}}(\omega) \stackrel{(2.5)}{=} \text{Re} \int_0^{\infty} dt e^{i\omega t} \langle [j_{\alpha}(t), j_{\gamma}] \rangle_0 \stackrel{(2.6)}{=} \frac{\omega}{V} \text{Re } \sigma_{\alpha\gamma}(\omega). \quad (2.25)$$

The third equality is also trivial, as seen from Eq. (2.22a).

2.3 Optical Sum Rule

2.3.1 Optical Sum Rule in General

The previous sections demonstrated how the optical conductivity can be expressed using the current-current correlation functions. However, the calculation of both the current-current correlation functions and optical conductivity in practice can be very complex. This is why it is very important to have some results that can be used to crosscheck that our numerical implementation is in fact stable. One such result is the optical sum rule which states that the area under the curve $\text{Re}\sigma_{\alpha\gamma}(\omega)$ is exactly determined. In the following text, we derive the optical sum rule

$$\int_{-\infty}^{\infty} d\omega \text{Re}\sigma_{\alpha\alpha}(\omega) \stackrel{(2.18)}{=} V \int_{-\infty}^{\infty} \frac{d\omega}{2\omega} \int_{-\infty}^{\infty} dt e^{i\omega t} [\langle j_{\alpha}(t)j_{\alpha} \rangle_0 - \langle j_{\alpha}j_{\alpha}(t) \rangle_0]. \quad (2.26)$$

Let us now expand the right-hand side using the Lehmann spectral representation as follows

$$\int_{-\infty}^{\infty} d\omega \text{Re}\sigma_{\alpha\alpha}(\omega) = V \int_{-\infty}^{\infty} \frac{d\omega}{2\omega} \int_{-\infty}^{\infty} dt e^{i\omega t} \frac{1}{\mathcal{Z}} \sum_n \left\{ \langle n | e^{-\beta H} e^{iHt} j_{\alpha} \mathbb{1} e^{-iHt} j_{\alpha} | n \rangle - \langle n | e^{-\beta H} j_{\alpha} \mathbb{1} e^{iHt} j_{\alpha} e^{-iHt} | n \rangle \right\}, \quad (2.27)$$

where $|n\rangle$ is the energy basis, while $\mathbb{1}$ is an identity operator which we express as $\mathbb{1} = \sum_m |m\rangle\langle m|$. Hence

$$\int_{-\infty}^{\infty} d\omega \text{Re}\sigma_{\alpha\alpha}(\omega) = \frac{V}{\mathcal{Z}} \sum_{n,m} \int_{-\infty}^{\infty} \frac{d\omega}{2\omega} \int_{-\infty}^{\infty} dt e^{i\omega t} e^{-\beta E_n} e^{iE_n t} e^{-iE_m t} \langle n | j_{\alpha} | m \rangle \langle m | j_{\alpha} | n \rangle \quad (2.28)$$

$$- \frac{V}{\mathcal{Z}} \sum_{n,m} \int_{-\infty}^{\infty} \frac{d\omega}{2\omega} \int_{-\infty}^{\infty} dt e^{i\omega t} e^{-\beta E_n} e^{-iE_n t} e^{iE_m t} \langle n | j_{\alpha} | m \rangle \langle m | j_{\alpha} | n \rangle. \quad (2.29)$$

In the bottom line, we switch $n \leftrightarrow m$ and obtain

$$\begin{aligned} \int_{-\infty}^{\infty} d\omega \text{Re}\sigma_{\alpha\alpha}(\omega) &= \frac{V}{\mathcal{Z}} \sum_{n,m} \int_{-\infty}^{\infty} \frac{d\omega}{2\omega} |\langle n | j_{\alpha} | m \rangle|^2 (e^{-\beta E_n} - e^{-\beta E_m}) \int_{-\infty}^{\infty} dt e^{i(E_n - E_m + \omega)t} \\ &= \frac{V}{\mathcal{Z}} \sum_{n,m} \int_{-\infty}^{\infty} \frac{d\omega}{2\omega} |\langle n | j_{\alpha} | m \rangle|^2 (e^{-\beta E_n} - e^{-\beta E_m}) 2\pi \delta(E_n - E_m + \omega) \\ &= \frac{\pi V}{\mathcal{Z}} \sum_{n,m} |\langle n | j_{\alpha} | m \rangle|^2 (e^{-\beta E_n} - e^{-\beta E_m}) \frac{1}{E_m - E_n}. \end{aligned} \quad (2.30)$$

The matrix element can be rewritten using the definition of the current density operator in Eq. (C.29) as follows

$$V \langle n | j_{\alpha} | m \rangle = -i \langle n | [P_{\alpha}, H] | m \rangle = -i \langle n | P_{\alpha} H - H P_{\alpha} | m \rangle = -i(E_m - E_n) \langle n | P_{\alpha} | m \rangle, \quad (2.31)$$

where P is the polarization operator. Plugging this back into Eq. (2.30), we get

$$\begin{aligned} \int_{-\infty}^{\infty} d\omega \text{Re}\sigma_{\alpha\alpha}(\omega) &= \frac{-i\pi}{\mathcal{Z}} \sum_{n,m} \langle n | P_{\alpha} | m \rangle \langle m | j_{\alpha} | n \rangle (e^{-\beta E_n} - e^{-\beta E_m}) \\ &= \frac{-i\pi}{\mathcal{Z}} \sum_n e^{-\beta E_n} \langle n | P_{\alpha} \sum_m |m\rangle \langle m | j_{\alpha} | n \rangle + \frac{i\pi}{\mathcal{Z}} \sum_m e^{-\beta E_m} \langle m | j_{\alpha} \sum_n |n\rangle \langle n | P_{\alpha} | m \rangle \\ &= -\frac{i\pi}{\mathcal{Z}} \sum_n e^{-\beta E_n} \langle n | P_{\alpha} j_{\alpha} | n \rangle + \frac{i\pi}{\mathcal{Z}} \sum_n e^{-\beta E_n} \langle n | j_{\alpha} P_{\alpha} | n \rangle \end{aligned} \quad (2.32)$$

Therefore, we obtain

$$\int_{-\infty}^{\infty} d\omega \operatorname{Re} \sigma_{\alpha\alpha}(\omega) = -i\pi \langle [P_{\alpha}, j_{\alpha}] \rangle_0. \quad (2.33)$$

2.3.2 Optical Sum Rule for the Holstein Model

In the Holstein model, the polarization operator commutes with the interacting part of the Hamiltonian, so the current density operator is given by Eq. (C.37). Hence, the optical sum rule can be written as

$$\int_{-\infty}^{\infty} d\omega \operatorname{Re} \sigma_{\alpha\alpha}(\omega) = \frac{t_0\pi}{V} \sum_{\mathbf{r}_1, \mathbf{r}_2, \delta} \delta_{\alpha} r_{2\alpha} \left\langle \left[c_{\mathbf{r}_2}^{\dagger} c_{\mathbf{r}_2}, c_{\mathbf{r}_1+\delta}^{\dagger} c_{\mathbf{r}_1} \right] \right\rangle_0 = \frac{t_0\pi}{V} \sum_{\mathbf{r}, \delta} \delta_{\alpha}^2 c_{\mathbf{r}+\delta}^{\dagger} c_{\mathbf{r}}, \quad (2.34)$$

where δ goes over the nearest neighbor vectors. In the case of a 1D Holstein model, we can substitute $\delta_{\alpha}^2 \rightarrow 1$ and use the fact that the kinetic part of the Hamiltonian can be written as in Eq. (C.35), to obtain

$$\int_{-\infty}^{\infty} d\omega \operatorname{Re} \sigma_{\alpha\alpha}(\omega) = -\frac{\pi}{V} \langle H_{\text{kin}} \rangle_0 = 2 \int_0^{\infty} d\omega \operatorname{Re} \sigma_{\alpha\alpha}(\omega). \quad (2.35)$$

2.4 Diagrammatic Approach to Optical Conductivity

2.4.1 General Theory

Up to now, we have not taken into account the \mathbf{q} dependence of the optical conductivity. This generalization to arbitrary \mathbf{q} is actually quite straightforward [1, 68]

$$\sigma_{\alpha\gamma}(\mathbf{q}, \omega) = \frac{\chi_{j_{\alpha}j_{\gamma}}(\mathbf{q}, \omega) - \chi_{j_{\alpha}j_{\gamma}}(\mathbf{q}, \omega = 0)}{i\omega}, \quad (2.36)$$

where $\chi_{j_{\alpha}j_{\gamma}}(\mathbf{q}, \omega)$ is given by

$$\chi_{j_{\alpha}j_{\gamma}}(\mathbf{q}, \omega) = \chi_{j_{\alpha}j_{\gamma}}(\mathbf{q}, i\nu_n \rightarrow \omega + i0^+), \quad (2.37a)$$

$$\chi_{j_{\alpha}j_{\gamma}}(\mathbf{q}, i\nu_n) = \int_0^{\beta} d\tau e^{i\nu_n\tau} \frac{1}{N} \langle \hat{T}_{\tau} j^{\alpha}(\mathbf{q}, -i\tau) j^{\beta}(-\mathbf{q}, 0) \rangle. \quad (2.37b)$$

Remark 24. 1. A well-known result from many-body physics is that analytic continuation $i\nu_n \rightarrow \omega + i0^+$ of the time-ordered correlation function in the Matsubara space gives retarded correlation function in real frequency space. Hence, we see that Eqs. (2.37) and (2.5) are completely to each other.

2. We included the volume V from Eq. (2.4) into the definition of $\chi_{j_{\alpha}j_{\gamma}}(\mathbf{q}, \omega)$. This way, some equations will be a bit simpler, but most importantly the Feynman rules for the diagrammatic expansion of $\chi_{j_{\alpha}j_{\gamma}}(\mathbf{q}, \omega)$ will be the same as we formulated in Sec. 2.1.

3. Since we set the volume of the unit cell to be unity, we can interchange $V \leftrightarrow N$.

4. One might wonder how does N appear in the denominator of Eq. (2.37b), if we absorbed V from Eq. (2.4) into the definition of $\chi_{j_{\alpha}j_{\gamma}}(\mathbf{q}, \omega)$. The reason for this is that $j(\mathbf{q} = 0)$ and the current density operator that we used in Secs. 2.1 and 2.2 are related as $j(\mathbf{q} = 0) = Nj$.

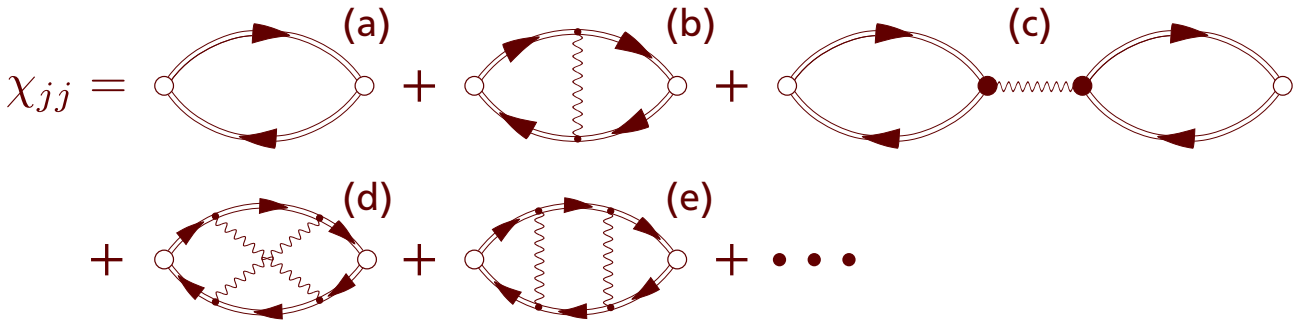


Figure 2.1: Feynman diagrams for $\chi_{j\alpha j\gamma}(\mathbf{q}, \omega)$.

Although we are mainly interested in the optical conductivity, the diagrammatic expansion is most easily formulated for $\chi_{j\alpha j\gamma}(\mathbf{q}, \omega)$. The first few diagrams are shown in Fig. 2.1. These are calculated using the Feynman rules we provided in Sec. 2.1 of Part I, with an additional rule that the empty circles at the beginning and the end of the diagrams represent free vertices $\gamma^\alpha(\mathbf{p} + \mathbf{q}, \mathbf{p})$ and $\gamma^\alpha(\mathbf{p}, \mathbf{p} + \mathbf{q})$; see Fig. 2.2.

The exact mathematical form of these quantities depends on the definition of the current density operator. It can be easily seen that $\gamma^\alpha(\mathbf{p}, \mathbf{p} + \mathbf{q})$ is different for the system in the continuum and on a lattice. Furthermore, even if we examine one particular lattice, there is freedom to choose between different, but physically equivalent expressions for the current density operator, and hence for free vertices as well. All of these are derived in Appendix C.



Figure 2.2: Feynman diagrams for free vertices $\gamma^\alpha(\mathbf{p} + \mathbf{q}, \mathbf{p})$ and $\gamma^\alpha(\mathbf{p}, \mathbf{p} + \mathbf{q})$

Let us now go back to Fig. 2.1, to introduce some useful terminology and provide a physical interpretation that will enable us to intuitively understand the significance of certain diagrams. The diagram in Fig. 2.1(a) is the so-called bubble term, while everything else represents the vertex corrections [1]. The bubble term represents the independent propagation of the electron-hole pair. Both the electron and hole are dressed, as seen from the fact that we use the interacting Green's function in Fig. 2.1(a), but the interaction between them is completely neglected. These are included in higher order terms, such as in Fig. 2.1(b). Actually, there is a whole class of terms analogous to Fig. 2.1(b) known as the *ladder diagrams*. The next term in this class is shown in Fig. 2.1(e), while all the other terms are obtained by adding vertical phonon lines that connect particle and hole propagators. In systems such as ours, with a low density of charge carriers, it is often expected that these diagrams will give dominant contributions. This is intuitively clear, as the scarcity of charge carriers causes the electron's repeated interactions with the same hole. There are also other classes of diagrams. One example is shown in Fig. 2.1(c), while its higher-order counterparts are obtained by adding additional phonon lines and fermion bubbles in a cascade. Actually, it turns out that, in the Holstein model, this entire class of diagrams is not contributing for the calculation of mobility. This will be proved in Chapter 5.

A reliable estimate of the vertex corrections is known to be a notoriously difficult task. In fact, their contribution in most systems is largely unknown. One of the goals of this thesis is to investigate the contribution of vertex corrections in one particular system - the Holstein model. This will be postponed until Chapters 5 and 6. Here, we only briefly overview some aspects of the diagrammatic approach.

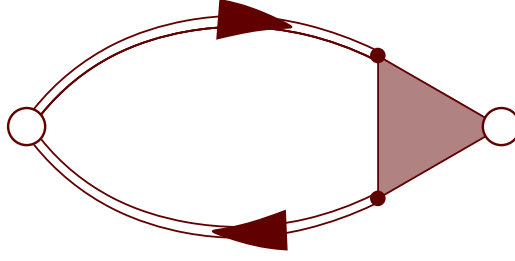


Figure 2.3: Alternative way to write Feynman diagrams for $\chi^{\mu\nu}$

The Feynman diagrams from Fig. 2.1 can also be written symbolically as in Fig. 2.3, where the shaded part represents the so-called renormalized vertex function $\Gamma^\gamma(\mathbf{p}, i\omega_n, \mathbf{p} + \mathbf{q}, i\omega_n + i\nu_m)$. Using this new quantity, $\chi_{j_\alpha j_\gamma}(\mathbf{q}, \omega)$ can now be written as

$$\chi_{j_\alpha j_\gamma}(\mathbf{q}, i\nu_m) \equiv -\frac{1}{N\beta} \sum_{\mathbf{p}, i\omega_n} \left[\gamma^\alpha(\mathbf{p} + \mathbf{q}, \mathbf{p}) G(\mathbf{p} + \mathbf{q}, i\omega_n + i\nu_m) \right. \\ \left. \times \Gamma^\gamma(\mathbf{p}, i\omega_n, \mathbf{p} + \mathbf{q}, i\omega_n + i\nu_m) G(\mathbf{p}, i\omega_n) \right]. \quad (2.38)$$

Equation (2.38) can also be taken as a definition of the renormalized vertex Γ^γ . We see that renormalized vertex Γ^γ now fully takes into account both the bubble part and the vertex corrections. Thus, finding Γ^γ and interacting Green's functions is sufficient the calculation of the current-current correlation function (i.e. optical conductivity), and hence represents the central quantity of our study.

Although it looks that the introduction of Γ^γ was unnecessary, the renormalized vertex function will enable us to easily formulate the so-called Ward identities. This identity is a consequence of the conservation of electric charge, and as such it establishes a relationship between the renormalized vertex function Γ^γ and the self-energy Σ . Therefore, for a given approximation in which Σ is calculated, the Ward identity dictates the vertex corrections that should be included in Γ^γ , in order not to violate the conservation of electric charge.

2.4.2 Bubble Approximation

The bubble term is completely determined by the one-particle properties of Green's functions. Here, we show how this term is calculated if the spectral function is known.

Restricting ourselves to the $\mathbf{q} = 0$ component, the direct application of Feynman rules imply that

$$\chi_{j_\alpha j_\alpha}(\mathbf{q} = 0, i\nu_m) = \text{bubble diagram} = -\frac{1}{N\beta} \sum_{\mathbf{k}, i\omega_n} v_{k_\alpha} G_{\mathbf{k}}(i\nu_m + i\omega_n) G_{\mathbf{k}}(i\omega_n) v_{k_\alpha}, \quad (2.39)$$

where v_{k_α} is the α -th component of the velocity $v_{\mathbf{k}} = \nabla_{\mathbf{k}} \varepsilon_{\mathbf{k}}$. Using the spectral representation of the Green's function

$$G_{\mathbf{k}}(i\omega_n) = \int_{-\infty}^{\infty} d\omega' \frac{A_{\mathbf{k}}(\omega')}{i\omega_n - \omega'}, \quad (2.40)$$

we see that $\chi_{j_\alpha j_\alpha}(\mathbf{q} = 0, i\nu_m)$ can be written as

$$\chi_{j_\alpha j_\alpha}(\mathbf{q} = 0, i\nu_m) = -\frac{1}{N\beta} \sum_{\mathbf{k}} v_{k_\alpha}^2 \int_{-\infty}^{\infty} d\omega' \int_{-\infty}^{\infty} d\omega'' A_{\mathbf{k}}(\omega') A_{\mathbf{k}}(\omega'') \\ \times \sum_{i\omega_n} \frac{1}{i\omega_n - \omega'} \frac{1}{i\omega_n + i\nu_m - \omega''}. \quad (2.41)$$

The sum over Matsubara frequencies is standardly calculated as

$$\frac{1}{\beta} \sum_{i\omega_n} F(i\omega_n) = \sum_{\text{poles of } F(z)} \text{Res} [f(z)F(z)], \quad (2.42)$$

where $f(z)$ is the Fermi-Dirac function

$$f(z) = \frac{1}{e^{\beta z} + 1}. \quad (2.43)$$

Plugging this back into Eq. (2.41), we obtain

$$\begin{aligned} \chi_{j_\alpha j_\alpha}(\mathbf{q} = 0, i\nu_m) = & -\frac{1}{N} \sum_{\mathbf{k}} v_{k_\alpha}^2 \int_{-\infty}^{\infty} d\omega' \int_{-\infty}^{\infty} d\omega'' A_{\mathbf{k}}(\omega') A_{\mathbf{k}}(\omega'') \\ & \times \left[\frac{f(\omega')}{\omega' + i\nu_m - \omega''} + \frac{f(\omega'' - i\nu_m)}{\omega'' - \omega' - i\nu_m} \right] \end{aligned} \quad (2.44)$$

The second term in the square brackets can be simplified

$$f(\omega'' - i\nu_m) = \frac{1}{e^{\beta(\omega'' - i\nu_m)} + 1} = \frac{1}{e^{\beta\omega''} + 1} = f(\omega''), \quad (2.45)$$

since $i\nu_m$ is the bosonic Matsubara frequency. Now, Eq. (2.44), after analytic continuation $i\nu_m \rightarrow \omega + i0^+$, becomes

$$\begin{aligned} \chi_{j_\alpha j_\alpha}(\mathbf{q} = 0, \omega) = & -\frac{1}{N} \sum_{\mathbf{k}} v_{k_\alpha}^2 \int_{-\infty}^{\infty} d\omega' \int_{-\infty}^{\infty} d\omega'' A_{\mathbf{k}}(\omega') A_{\mathbf{k}}(\omega'') \\ & \times \left[\frac{f(\omega')}{\omega' - \omega'' + \omega + i0^+} - \frac{f(\omega'')}{\omega' - \omega'' + \omega + i0^+} \right]. \end{aligned} \quad (2.46)$$

For the calculation of $\text{Re}\sigma_{\alpha\alpha}$, we only need the imaginary part of $\chi_{j_\alpha j_\alpha}(\mathbf{q} = 0, \omega)$, as implied by Eq. (2.6). The easiest way to calculate this is to use the Plemelj-Sokhotski theorem

$$\frac{1}{\omega' - \omega'' + \omega + i0^+} = \mathcal{P} \frac{1}{\omega' - \omega'' + \omega} - i\pi\delta(\omega' - \omega'' + \omega), \quad (2.47)$$

from which we obtain

$$\begin{aligned} \chi_{j_\alpha j_\alpha}(\mathbf{q} = 0, \omega) = & \frac{\pi}{N} \sum_{\mathbf{k}} v_{k_\alpha}^2 \int_{-\infty}^{\infty} d\omega' \int_{-\infty}^{\infty} d\omega'' A_{\mathbf{k}}(\omega') A_{\mathbf{k}}(\omega'') \\ & \times (f(\omega') - f(\omega'')) \delta(\omega' - \omega'' + \omega). \end{aligned} \quad (2.48)$$

Hence, using Eq. (2.6), we finally obtain

$$\boxed{\text{Re}\sigma_{\alpha\alpha}(\mathbf{q} = 0, \omega) = \frac{\pi}{N} \sum_{\mathbf{k}} v_{k_\alpha}^2 \int_{-\infty}^{\infty} d\omega' A_{\mathbf{k}}(\omega') A_{\mathbf{k}}(\omega' + \omega) \frac{f(\omega') - f(\omega' + \omega)}{\omega}}. \quad (2.49)$$

In our calculations, we normalize the optical conductivity to the concentration of charge carriers n_e

$$\mu(\omega) \equiv \frac{\text{Re}\sigma_{\alpha\alpha}(\mathbf{q} = 0, \omega)}{n_e} = \frac{\frac{\pi}{N} \sum_{\mathbf{k}} v_{k_\alpha}^2 \int_{-\infty}^{\infty} d\omega' A_{\mathbf{k}}(\omega') A_{\mathbf{k}}(\omega' + \omega) \frac{f(\omega') - f(\omega' + \omega)}{\omega}}{\frac{1}{N} \sum_{\mathbf{k}} \int_{-\infty}^{\infty} d\omega' A_{\mathbf{k}}(\omega') f(\omega')}. \quad (2.50)$$

As explained in Sec. 2.1 of Part I, at the end of this calculation we need to implement the prescription $A_{\mathbf{k}}(\omega') \rightarrow A_{\mathbf{k}}(\omega' + \tilde{\mu})$ and take the limit $\tilde{\mu} \rightarrow -\infty$, in order to make a connection between the

calculation that we performed in the grand canonical ensemble, and the formalism where there is only a single electron in the band. In conjunction, we shift the variable that we integrate over $\omega' \rightarrow \omega' - \tilde{\mu}$ and obtain

$$\mu_{\alpha\alpha}(\omega) = \lim_{\tilde{\mu} \rightarrow -\infty} \frac{\frac{\pi}{N} \sum_{\mathbf{k}} v_{k\alpha}^2 \int_{-\infty}^{\infty} d\omega' A_{\mathbf{k}}(\omega') A_{\mathbf{k}}(\omega' + \omega) \frac{f(\omega' - \tilde{\mu}) - f(\omega' + \omega - \tilde{\mu})}{\omega}}{\frac{1}{N} \sum_{\mathbf{k}} \int_{-\infty}^{\infty} d\omega' A_{\mathbf{k}}(\omega') f(\omega' - \tilde{\mu})}. \quad (2.51)$$

In this limit, it holds that $f(\nu - \tilde{\mu}) \approx e^{-\beta\nu} e^{\beta\tilde{\mu}}$. The factors $e^{\beta\tilde{\mu}}$ in the denominator and numerator cancel out, and we finally obtain

$$\mu_{\alpha\alpha}(\omega) = \frac{\pi \sum_{\mathbf{k}} v_{k\alpha}^2 \int_{-\infty}^{\infty} d\omega' A_{\mathbf{k}}(\omega') A_{\mathbf{k}}(\omega' + \omega) \frac{e^{-\beta\omega'} - e^{-\beta(\omega' + \omega)}}{\omega}}{\sum_{\mathbf{k}} \int_{-\infty}^{\infty} d\omega' A_{\mathbf{k}}(\omega') e^{-\beta\omega'}}. \quad (2.52)$$

In the limit $\omega \rightarrow 0$, this quantity is known as the (charge) mobility μ

$$\mu = \lim_{\omega \rightarrow 0} \mu_{\alpha\alpha}(\omega) = \frac{\pi\beta \sum_{\mathbf{k}} v_{k\alpha}^2 \int_{-\infty}^{\infty} d\omega' A_{\mathbf{k}}(\omega')^2 e^{-\beta\omega'}}{\sum_{\mathbf{k}} \int_{-\infty}^{\infty} d\omega' A_{\mathbf{k}}(\omega') e^{-\beta\omega'}}. \quad (2.53)$$

This is a very important physical quantity, and we will be calculating it in the Holstein model.

Remark 25. We will be calculating mobility and optical conductivity only for the 1D Holstein model. In that case $v_k = d\varepsilon_k/dk = 2t_0 \sin k$.

2.5 DMFT Optical Conductivity in the limit $d \rightarrow \infty$

In our numerical applications, we will be calculating optical conductivity and mobility within the cumulant expansion method, DMFT, SCMA, MA, and some methods that we will introduce later on in the thesis. For each of these methods, we can calculate the relevant quantities in the bubble approximation, using the formulas we derived in Sec. 2.4.2. However, those results would be incomplete without the full knowledge of the significance of the vertex corrections. Originally, in the case of the DMFT, this was answered by Khurana [122], and we review his work in this section.

In Chapter 1 of Part II, we explained that the DMFT equations are formally derived in the limit of an infinite number of dimensions $d \rightarrow \infty$ (in which case they provide an exact description of our system), but they can also be applied in the finite-dimensional case as well, in which case they provide an approximate description of our system. In the same manner, here we start by analyzing the DMFT optical conductivity in the limit $d \rightarrow \infty$. For this, it is useful to use the diagrammatic approach shown in Fig. 2.4.

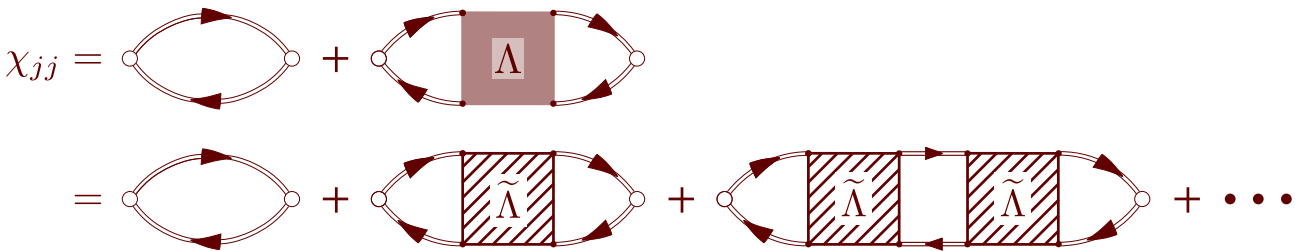


Figure 2.4: Another alternative way to write Feynman diagrams for $\chi^{\mu\nu}$

In the top line, we introduced the two-particle vertex function Λ , which completely takes into account the contribution of the vertex corrections. On the other hand, the bottom line introduced the irreducible

two-particle vertex function $\tilde{\Lambda}$, which plays the same role as the self-energy in the diagrammatic expansion of the Green's function. It has a property that it cannot be split into two pieces by cutting any two fermion lines. Otherwise, there would be overcounting of the diagrams. Hence, there are at least three distinct fermion paths between any two vertices. Thus, in a complete analogy to the analysis that we conducted in Sec. 1.4 of Part II, we see that the irreducible vertex function $\tilde{\Lambda}$ has to be diagonal in real-space representation, due to the scaling laws of the Green's functions in the limit $d \rightarrow \infty$. As a consequence, $\tilde{\Lambda}$ is momentum-independent in the Fourier space.

Remark 26. The conclusion that $\tilde{\Lambda}$ has at least three distinct paths between any two vertices is true only if we regard $\tilde{\Lambda}$ to be a part of the χ_{jj} correlation function, as shown in Fig. 2.4. Stated differently, this is only true if we regard all vertices of $\tilde{\Lambda}$ to be internal. This is sufficient for our analysis. However, it should be noted that this property is not necessarily satisfied if we consider $\tilde{\Lambda}$ to be an independent diagram. One such example is illustrated in Fig. 2.5. Therefore, even though $\tilde{\Lambda}$ by itself can have momentum dependence, only its local components give a nonvanishing contribution to the χ_{jj} . This is why we, in jargon, often say that $\tilde{\Lambda}$ is momentum independent quantity.

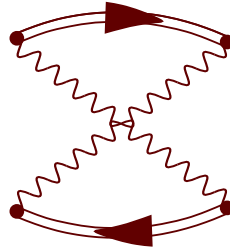


Figure 2.5: An example of an irreducible two-particle vertex function $\tilde{\Lambda}$.

The fact that $\tilde{\Lambda}$ is a momentum-independent quantity has a direct consequence on the vertex corrections for $\mathbf{q} = 0$ Fourier component of the optical conductivity, as we now demonstrate. The Feynman rules for any one of the vertex correction terms for $\chi_{j\alpha j\gamma}(\mathbf{q} = 0, i\nu_m)$ read as

$$\begin{aligned}
 & \text{Diagram: A vertex correction diagram showing a shaded box labeled } \tilde{\Lambda} \text{ connected to external lines. The diagram is part of a sum over } \mathbf{k} \text{ and } i\omega_n. \\
 & \propto \sum_{\mathbf{k}, i\omega_n} \underbrace{v_{k\alpha}}_{\text{odd function of } \mathbf{k}} \underbrace{G_{\mathbf{k}}(i\nu_m + i\omega_n)G_{\mathbf{k}}(i\omega_n)}_{\text{even function of } \mathbf{k}} \times \underbrace{\dots}_{\text{independent of } \mathbf{k}} = 0. \quad (2.54)
 \end{aligned}$$

Hence, we conclude that the vertex corrections vanish in the limit $d \rightarrow \infty$ for $\mathbf{q} = 0$. The reasoning that we used in Eq. (2.54) does not work for the bubble term which stays finite in the limit $d \rightarrow \infty$. This is because the bubble term has two vertices with the same momentum, giving $v_{k\alpha}^2$, which is an even function \mathbf{k} .

Numerical Results for the Mobility: Comparison Between Different Methods

In the previous chapter, we defined the charge mobility¹ as the DC conductivity, normalized to the concentration of charge carriers² n_e , i.e.

$$\mu = \frac{\sigma^{\text{DC}}}{n_e}. \quad (3.1)$$

We already emphasized that this quantity, although being routinely measured in experiments, is tremendously hard to calculate theoretically. Here, we examine the mobility in the 1D Holstein model, within the DMFT, CE, SCMA, and MA, using the bubble approximation we reviewed in the previous chapter. The results that we present are a product of our original work that was published in Ref. [87].

Remark 27. *The discussion on the importance of vertex corrections will be postponed until Chapters 5 and 6.*

3.1 Technical Details

In terms of the spectral functions, the charge mobility in the bubble approximation can be expressed as in Eq. (2.53). In our case, the dispersion is $\varepsilon_k = -2t_0 \cos k$, so Eq. (2.53) becomes

$$\mu = \frac{4\pi t_0^2 \beta \sum_k \int_{-\infty}^{\infty} d\nu A_k(\nu)^2 e^{-\nu/T} \sin^2 k}{\sum_k \int_{-\infty}^{\infty} d\nu A_k(\nu) e^{-\nu/T}}, \quad (3.2)$$

where the momenta k take the values $k_i = -\pi + \frac{2\pi i}{N}$ for $i = 0, 1, 2, \dots, N-1$. However, we are interested in the results in the thermodynamic limit, which correspond to $N \rightarrow \infty$. This is usually obtained by evaluating Eq. (3.2) for some finite N , which is then increased until the results fully converge.

Applying this within the DMFT, SCMA or MA is not numerically expensive, since the self-energy is local. For a given set of parameters (ω_0, g, T) we just need to calculate the self-energy once, and then the spectral functions for different values of momenta are obtained as

$$A_k(\omega) = -\frac{1}{\pi} \text{Im} \frac{1}{\omega - \varepsilon_k - \Sigma(\omega)}. \quad (3.3)$$

Therefore, once the self-energy is known, there are no numerically demanding calculations, and a very large number of k -points can be used to ensure the convergence of results. On the other hand, the

¹We often abbreviate the name, and simply call it the mobility.

²This quantity should also be normalized to the unit charge e , but we already set this to unity.

processing time required for the calculation of μ within the CE method rises linearly with the number of k -points we sum over. This is a consequence of the fact that the CE self-energy is not necessarily local. In practice, for every parameter regime the CE was applied to, we checked that $N = 64$ was large enough to be representative of the thermodynamic limit. This was also crosschecked using the DMFT.

However, the convergence with respect to the number of k points was not the only numerical challenge that was raised. In particular, the term $e^{-\nu/T}$ in Eq. (3.2) introduces numerical instabilities, as even a small numerical noise of $A_k(\nu)$ at $\nu \ll -1$ will be inflated and give an enormous overall error in the mobility. This is why the integrals in Eq. (3.2) require introducing some kind of negative frequency cutoff $\int_{-\infty}^{\infty} \rightarrow \int_{-\Lambda}^{\infty}$. We always check that the mobility results converge with respect to Λ . We note that this has to be done in all the methods (DMFT, SCMA, MA, and CE) we use. However, in the case of DMFT, SCMA, and MA, this is easily done due to the high numerical accuracy of our numerical implementations. On the other hand, the convergence with respect to Λ is much harder to achieve within the CE, as the Green's functions are initially calculated in the time-domain and require the use of numerical Fourier transform, which can introduce additional numerical errors. To overcome this, we have implemented a well-known interpolation scheme [123] in order to increase the precision of the Fourier transform. This is explained in detail in Appendix A. Nevertheless, there is still some numerical noise in the regimes of low temperatures and strong interactions which prevented us from precisely calculating the mobility in these cases. We note that we will only show the data where an accurate calculation was possible.

Remark 28. *Other than introducing numerical instabilities, there are also some important consequences of the exponential term $e^{-\nu/T}$ in Eq. (3.2). This term, despite the factor $\sin^2 k$ in the numerator of Eq. (3.2), implies that the largest contribution to the mobility most commonly comes from the spectral functions around the bottom of the band ($k \approx 0$), as they are typically situated at lower frequencies with respect to their higher momentum counterparts. This is favourable for the CE, as we have seen that the spectral function predictions of this method are more reliable for $k \approx 0$ than for $0 < k < \pi$.*

3.2 Results

In Fig. 3.1i, we present the DMFT, CE, and SCMA numerical results for the temperature dependence of the charge mobility in the bubble approximation. We also show the MA results in Fig. 3.1ii, but these will be only briefly discussed.

Very Weak Couplings

For very weak electron-phonon coupling, all methods are in agreement; see Fig. 3.1 for $\alpha \lesssim 0.25$. In this case, the electron-phonon scattering is weak, which is why the quasiparticle lifetime τ_k is long, and the linear time dependence dominates in the cumulant function. This last claim can be seen by inspecting Eq. (3.43) and Fig. 3.1(c), both from Part II. Although that figure demonstrates that the cumulant function is linear for large times, we need to keep in mind that, in the general case, the Green's function $G_k(t) = G_{k,0}(t) \exp(C_k(t))$ might already be attenuated before the cumulant actually starts being linear. However, since g is only a prefactor in Eq. (3.43) of Part II and the lifetime scales as $\tau_k \propto g^{-2}$ (see Eq. (3.45) of Part II), we see that if the electron-phonon coupling g is sufficiently weak, then the cumulant function will be linear for a long time before the Green's function attenuates. In fact, in this case, the cumulant function will be linear for most of the lifetime τ_k . Hence, we can approximate that Eq. (3.19) from Part II holds in the entire domain of time

$$C_k - i\varepsilon_k t \approx -i\tilde{E}_k t + \text{const}, \quad (3.4)$$

where the real and imaginary part of \tilde{E}_k correspond to the quasiparticle energy and lifetime

$$\text{Re}\tilde{E}_k = E_{p,k}; \quad \text{Im}\tilde{E}_k = -\frac{1}{2\tau_k}, \quad (3.5)$$

as we already proved in Sec. 3.2.3 of Part II. In this case, the Green's function is given by Eq. (3.1) of Part II, which reads as³

$$G_k(t) = -i\theta(t)e^{-i\tilde{E}_k t} \cdot \text{const}, \quad (3.6)$$

while the corresponding quantity in the Fourier space is given by

$$G_k(\omega) = \frac{\text{const}}{\omega - \tilde{E}_k} = \text{const} \cdot \frac{\omega - E_{p,k} - \frac{i}{2\tau_k}}{(\omega - E_{p,k})^2 + \left(\frac{1}{2\tau_k}\right)^2}. \quad (3.7)$$

The spectral function is then simply a Lorentzian

$$A_k(\omega) = \frac{1}{\pi} \frac{\frac{1}{2\tau_k}}{(\omega - E_{p,k})^2 + \left(\frac{1}{2\tau_k}\right)^2}, \quad (3.8)$$

where we set the constant from Eqs. (3.6) and (3.7) to 1, to ensure that the zeroth spectral sum rule is satisfied. Since we are considering the weak coupling limit, the lifetime τ_k is large, so the Lorentzian in Eq. (3.8) can be approximated as a Dirac delta function

$$A_k(\omega) \approx \delta(\omega - E_{p,k}). \quad (3.9)$$

However, we see that there is $A_k(\nu)^2$ in the numerator of Eq. (3.2). In this case, Eq. (3.9) is not suitable. Instead, we can use the fact that by squaring Eq. (3.8), we get a sharp function with a property that $\int_{-\infty}^{\infty} d\omega A_k(\omega)^2 = \tau_k \delta(\omega - E_{p,k})/\pi$. Hence, we can approximate

$$A_k(\omega)^2 = \frac{\tau_k}{\pi} \delta(\omega - E_{p,k}). \quad (3.10)$$

Plugging Eqs. (3.9) and (3.10) into Eq. (3.2), we obtain

$$\mu_{\text{weak}} \approx \frac{4t_0^2}{T} \frac{\sum_k \tau_k e^{-E_{p,k}/T} \sin^2 k}{\sum_k e^{-E_{p,k}/T}}, \quad (3.11)$$

where $E_{p,k}$ is given by Eq. (3.65) of Part II and Eq. (2.23) of Part I. We checked that Eq. (3.11) is in agreement with numerical results from Fig. 3.1i in the case of very weak couplings. In addition, we see that at high temperatures Eq. (3.11) further simplifies as $e^{-E_{p,k}/T} \approx 1$. In this case, the lifetime is inversely proportional to the temperature $\tau_k \propto 1/T$, as seen from Eq. (3.45) of Part II, which implies the power law behavior of the mobility

$$\mu_{\text{weak}} \propto 1/T^2. \quad (3.12)$$

Once again, we emphasize that this conclusion holds only for very weak electron-phonon couplings, where the assumption of weak scattering is still satisfied despite the high temperatures⁴; see Figs. 3.1i(a) and 3.1i(b) for $\alpha = 0.25$ and Fig. 3.1i(c) for $\alpha = \sqrt{2}/10$.

³The constant in Eq. (3.6) is, of course, not the same constant as in Eq. (3.4).

⁴In the case of extremely high temperatures $T \rightarrow \infty$, due to intense scattering of electrons and phonons, the lifetime tends to zero, and our assumptions no longer continue to hold true, meaning that it cannot be expected that $\mu_{\text{weak}} \propto 1/T^2$ continues to hold. In fact, the limit $T \rightarrow \infty$ will be discussed in the following text.

Somewhat Stronger Couplings

If α (for fixed ω_0) is a little bit larger than the case we already analyzed (but still small), the DMFT, CE, and SCMA all remain in agreement; see Fig. 3.1i(a) for $\alpha \leq 1$ and Figs. 3.1i(b) and 3.1i(c) for $\alpha \leq 0.5$. However, the range of validity of the MA is smaller, and it proves to be reliable only for much weaker interactions, such as $\alpha \lesssim 0.25$ in Fig. 3.1ii(a), $\alpha \lesssim 0.25$ in Fig. 3.1ii(b), and $\alpha \lesssim \sqrt{2}/10$ in Fig. 3.1ii(c). In the case of somewhat stronger couplings, MA starts to deviate from other methods, which is more pronounced at lower temperatures. This is expected as the MA takes into account only the lowest-order Feynman diagram, which is why we focus on the predictions of other methods.

In the regimes of somewhat stronger couplings, we see that there is a universal power law behavior at higher temperatures $\mu \propto T^{-3/2}$; see Fig. 3.1i(a) for $1/\sqrt{2} \leq \alpha \leq 2.5$, Fig. 3.1i(b) for $0.5 \leq \alpha \leq 2$ and Fig. 3.1i(c) for $0.5 \leq \alpha \leq 1$. Within the CE method, this can be explained as follows. If the temperature is sufficiently high, the Green's function in the time domain is quickly damped, which is why $C_k(t)$ can be approximated with just the lowest order (quadratic) Taylor expansion around $t = 0$, which reads as

$$C_k(t) \approx \frac{t^2}{2} \cdot \left. \frac{d^2 C_k(t)}{dt^2} \right|_{t=0} = -g^2(2n_{\text{ph}} + 1) \frac{t^2}{2}, \quad (3.13)$$

as a consequence of Eqs. (3.8) and (3.44), both from Part II.

Therefore, the corresponding Green's function (see Eq. (3.1) of Part II) is thus a Gaussian

$$G_k(t) = -i\theta(t)e^{-i\varepsilon_k t} e^{-\frac{g^2}{2}(2n_{\text{ph}}+1)t^2}, \quad (3.14)$$

which also implies the Gaussian spectral function

$$A_k(\omega) = \frac{e^{-\frac{(\omega-\varepsilon_k)^2}{2g^2(2n_{\text{ph}}+1)}}}{\sqrt{2\pi g^2(2n_{\text{ph}}+1)}}. \quad (3.15)$$

This form of the spectral function, as we now demonstrate, allows us to completely analytically evaluate the expression in Eq. (3.2). In particular, we directly see that

$$\int_{-\infty}^{\infty} d\nu A_k(\nu) e^{-\beta\nu} = e^{\frac{1}{2}g^2(2n_{\text{ph}}+1)\beta^2} e^{-\beta\varepsilon_k}, \quad (3.16a)$$

$$\int_{-\infty}^{\infty} d\nu A_k(\nu)^2 e^{-\beta\nu} = \frac{1}{2\sqrt{g^2(2n_{\text{ph}}+1)\pi}} e^{\frac{1}{4}g^2(2n_{\text{ph}}+1)\beta^2} e^{-\beta\varepsilon_k}. \quad (3.16b)$$

Now, Eq. (3.2) is evaluated by changing the sum over momenta to integral, as follows

$$\begin{aligned} \mu_{\text{high}-T} &= \frac{4\pi t_0^2 \beta \sum_k \sin^2 k \frac{1}{2\sqrt{g^2(2n_{\text{ph}}+1)\pi}} e^{\frac{1}{4}g^2(2n_{\text{ph}}+1)\beta^2} e^{-\beta\varepsilon_k}}{\sum_k e^{\frac{1}{2}g^2(2n_{\text{ph}}+1)\beta^2} e^{-\beta\varepsilon_k}} \\ &= \frac{2\pi t_0^2 \beta}{e^{\frac{1}{4}g^2(2n_{\text{ph}}+1)\beta^2} \sqrt{g^2(2n_{\text{ph}}+1)\pi}} \frac{\sum_k e^{2\beta t_0 \cos k} \sin^2 k}{\sum_k e^{2\beta t_0 \cos k}} \\ &= t_0^2 \beta e^{-\frac{1}{4}g^2(2n_{\text{ph}}+1)\beta^2} \sqrt{\frac{\pi}{g^2(2n_{\text{ph}}+1)}} \frac{\int_{-\pi}^{\pi} dk e^{2\beta t_0 \cos k} (1 - \cos(2k))}{\int_{-\pi}^{\pi} dk e^{2\beta t_0 \cos k}}. \end{aligned} \quad (3.17)$$

This is now easily evaluated using the integral representation of the modified Bessel functions of the first kind I_n , which reads as

$$I_n(z) = \frac{1}{\pi} \int_0^{\pi} e^{z \cos \theta} \cos(n\theta) d\theta. \quad (3.18)$$

Therefore

$$\int_{-\pi}^{\pi} e^{2\beta t_0 \cos k} = 2\pi I_0(2\beta t_0), \quad (3.19)$$

$$\int_{-\pi}^{\pi} e^{2\beta t_0 \cos k} \cos(2k) = 2\pi I_2(2\beta t_0). \quad (3.20)$$

If we additionally use the recurrence relation $I_0(z) - I_2(z) = \frac{2}{z} I_1(z)$, we also see that

$$\int_{-\pi}^{\pi} e^{2\beta t_0 \cos k} (1 - \cos(2k)) = 2\pi (I_0(2\beta t_0) - I_2(2\beta t_0)) = \frac{2\pi}{\beta t_0} I_1(2\beta t_0). \quad (3.21)$$

Plugging this back into Eq. (3.17), we finally obtain

$$\mu_{\text{high-}T} = \frac{t_0}{g} \sqrt{\frac{\pi}{2n_{\text{ph}} + 1}} \exp\left(-\frac{g^2(2n_{\text{ph}} + 1)}{4T^2}\right) \frac{I_1\left(\frac{2t_0}{T}\right)}{I_0\left(\frac{2t_0}{T}\right)}, \quad (3.22)$$

Since we are working in the high-temperature limit, the previous expression can be further simplified using

$$2n_{\text{ph}} + 1 \approx 2T/\omega_0, \quad \text{for large } T, \quad (3.23a)$$

$$I_1(2t_0/T)/I_0(2t_0/T) \approx t_0/T, \quad \text{for large } T. \quad (3.23b)$$

Combining this with Eq. (3.22), we finally obtain the result we were looking for

$$\mu_{\text{high-}T} \propto T^{-3/2}, \quad \text{for } T \gg t_0, \omega_0. \quad (3.24)$$

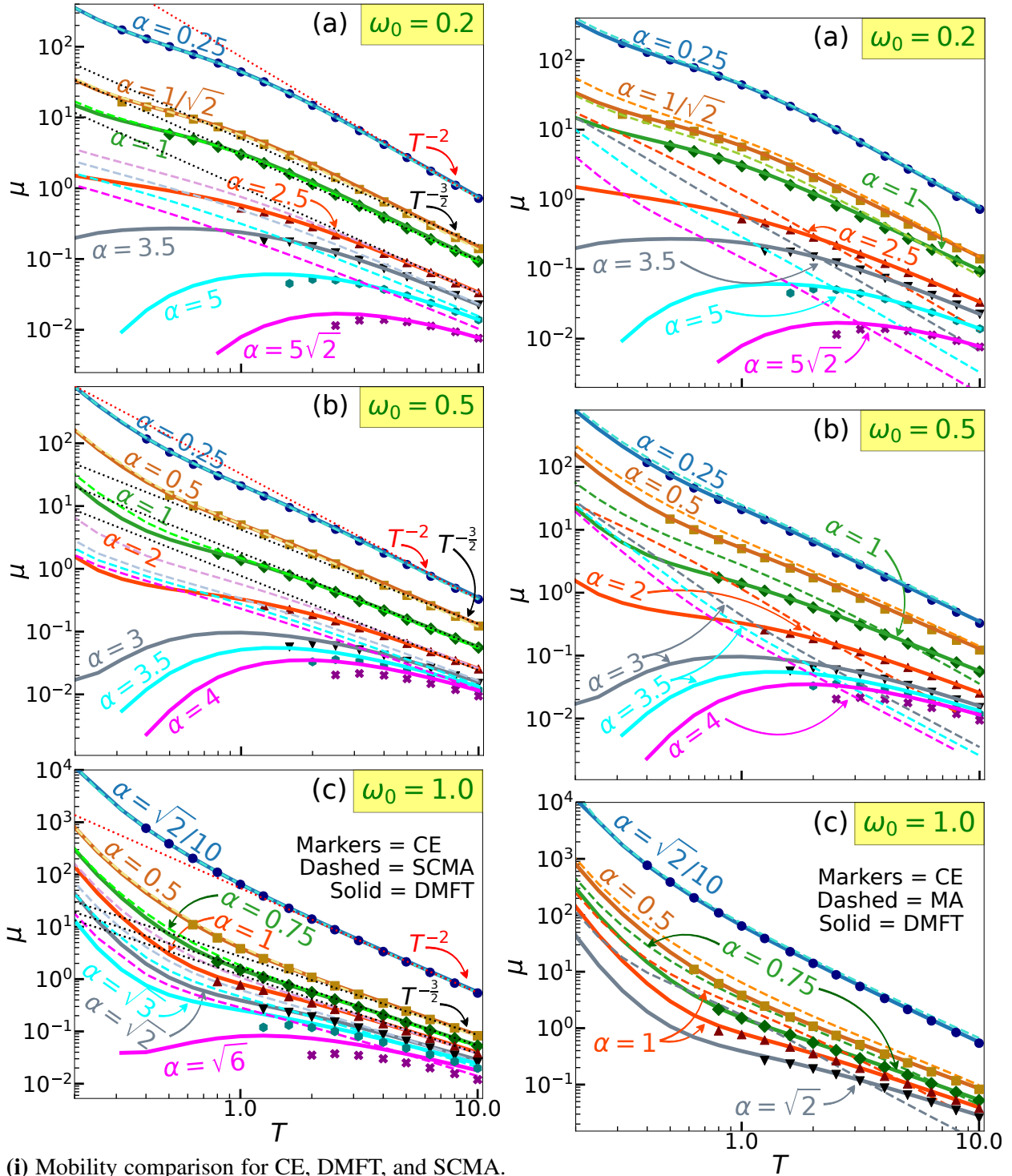
Remark 29. *The result, obtained by substituting Eq. (3.23) into Eq. (3.22), coincides with the mobility obtained by combining the Einstein relation, between the mobility and diffusion coefficient, with the Marcus formula [4, 124].*

The conclusion that we have reached in Eq. (3.24) should be quite general. For the derivation of this result, we only used the fact that the temperature is very high, without any assumptions on the strength of the electron-phonon coupling. This seems to contradict the result in Eq. (3.12). However, this is not the case. As we already noted, Eq. (3.12) is valid in the regime of high temperatures and weak electron-phonon coupling, but not in the case of extremely high temperatures where the assumption of weak scattering breaks down. Therefore, even for weak couplings, we can expect that the temperature dependence of the mobility would eventually transition to the power law behavior of the form $\mu \propto T^{-3/2}$, for extremely high temperatures⁵.

Intermediate and Strong Couplings

In the case of intermediate and strong electron-phonon coupling, MA is practically useless; for example, see Fig. 3.1ii (a) for $\alpha \gtrsim 2.5$. On the other hand, the SCMA gives satisfactory results for high temperatures and intermediate electron-phonon couplings, but it deviates from the DMFT at lower temperatures (see, e.g., Fig. 3.1i(a) for $\alpha = 2.5$ and Fig. 3.1i(b) for $\alpha = 2$) and also for stronger coupling strength (see, e.g., Fig. 3.1i(a) for $\alpha > 2.5$ and Fig. 3.1i(b) for $\alpha > 2$). At these stronger couplings, the DMFT predicts the non-monotonic mobility, where a region of decreasing mobility with decreasing temperature is ascribed to the hopping transport in phenomenological theories [60, 124]. The strong coupling mobility is better described by the CE than SCMA, although low-temperature results are missing due to our inability to converge the results with respect to the cutoff Λ .

⁵We note that in the regimes of stronger electron-phonon couplings, higher temperatures are required for the asymptotic behavior $\mu \propto T^{-3/2}$ to be reached, as can be seen from the results in Fig. 3.1.



(i) Mobility comparison for CE, DMFT, and SCMA. The dotted red (black) lines are auxiliary lines with the power law behavior $\mu \propto T^{-2}$ ($\mu \propto T^{-3/2}$). Here $t_0 = 1$.

(ii) Mobility comparison for CE, DMFT, and MA.

Figure 3.1: Temperature dependence of the mobility for the CE, DMFT, MA, and SCMA.

Ward Identity and its Consequences

As we briefly discussed in Sec. 2.4, the conservation of electric charge imposes a relation between the renormalized vertex function and the self-energy. This relation is known as the *Ward identity* [1, 125–127]. The proof of this identity for the zero temperature case can be found in Ref. [127]. This identity was also known to be satisfied in the finite-temperature case as well, since the sketch of the derivation appeared in Ref. [125]. Nevertheless, we are not aware of any references where that proof has been presented in detail. This is what we will be doing in this chapter. We note that our proof is more general than the one that was sketched in Ref. [125], as we allow for a larger flexibility in the choice of the current density operator.

4.1 Introduction and Mathematical Formulation of the Ward identity

Since the charge conservation represents a relation between the current \mathbf{j} and the density n , it is useful to use a 4-vector¹ notation $j^\mu = (n, \mathbf{j})^T$ where these quantities are unified into a single object² j^μ . In addition, we also use $r \equiv (-i\tau, \mathbf{r})^T$, $p \equiv (i\omega, \mathbf{p})$, $\sum_p \equiv \sum_{i\omega} \sum_{\mathbf{p}}$, as well as³ $\sum_r \equiv \int_0^\beta d\tau \sum_{\mathbf{r}}$. It is now completely natural to generalize $\chi_{j_\alpha j_\gamma}(\mathbf{q}, \omega)$ from Eq. (2.37) by introducing a correlation function between 4-currents⁴

$$\chi_{jj}^{\mu\nu}(\mathbf{q}, \tau) = \frac{1}{N} \langle \hat{T}_\tau j^\mu(\mathbf{q}, \tau) j^\nu(-\mathbf{q}, 0) \rangle, \quad (4.1)$$

and also to introduce the 4-vector generalization of the renormalized current vertex Γ^ν (compare with Eq. (2.38)) as follows

$$\chi^{\mu\nu}(q) \equiv -\frac{1}{N\beta} \sum_p \left[\gamma^\mu(\mathbf{p} + \mathbf{q}, \mathbf{p}) G(p + q) \Gamma^\nu(p, p + q) G(p) \right]. \quad (4.2)$$

Since the renormalized vertex Γ^ν fully takes into account both the bubble part and the vertex corrections, it represents the central quantity of our study [1, 128]. The Ward identity is formulated using this quantity:

¹We use the following convention for the metric $\eta = [-1, 1, 1, 1]$

²A detailed discussion and derivation of the current operator j^μ , both in the continuum and on a lattice, was presented in Appendix C (a brief overview is given in Sec. C.7). For now, it suffices to know that the current can be expressed as in Eq. (C.121), with a symmetry property given in Eq. (C.122).

³In the case of the continuum we should replace the discrete lattice coordinate \mathbf{r} with a continuous variable \mathbf{x} , and hence $\sum_{\mathbf{r}} \leftrightarrow \int_{-\infty}^{\infty} d\mathbf{x}$.

⁴In order to make the notation somewhat simpler, in this chapter we often write an argument of a function in imaginary time as τ instead of $-i\tau$.

Theorem 3 (Ward identity). *Let us consider the hypercubic lattice where p and q are arbitrary 4-momenta, G is the interacting Green's function and Γ^μ is the renormalized vertex function. Then, the conservation of charge implies that the following identity holds*

$$\boxed{G(p)^{-1} - G(p+q)^{-1} = \Delta^\mu(q)\Gamma_\mu(p+q, p)}. \quad (4.3)$$

where the Einstein summation convention has been used, while $\Delta^\mu(q)$ is given by⁵ Eqs. (C.110) and (C.124).

Remark 30. *In the limit of long wavelength $\mathbf{q} \rightarrow 0$, the Ward identity holds even for lattices that are not hypercubic, and also for the system in the continuum. In both of these cases $\Delta(\mathbf{q}) = \mathbf{q}$.*

4.2 Proof of the Ward Identity

We now present the proof in the finite-temperature case, but we note that the same proof also works at $T = 0$, in real time, if we replace $\int_0^\beta d\tau \leftrightarrow \int_{-\infty}^\infty dt$ and $\frac{1}{\beta} \sum_{i\omega} \leftrightarrow \int_{-\infty}^\infty \frac{d\omega}{2\pi}$.

4.2.1 Definition of Correlation Function $\Lambda^\mu(r_1, r_2, r_3)$

Since the proof of the Ward identity is not completely straightforward, let us try to motivate the main ideas: In Sec. 4.1, we noted that the Ward identity (4.3) is a consequence of the charge conservation

$$\frac{\partial n_{\mathbf{q}}}{\partial \tau} + \Delta(\mathbf{q}) \cdot \mathbf{j}_{\mathbf{q}}(\tau) = 0. \quad (4.4)$$

Hence, it is natural to try to apply this for $j^\mu(\mathbf{q}, \tau)$ in the correlation function $\chi^{\mu\nu}(\mathbf{q}, \tau)$, which is connected to the renormalized vertex function. However, it turns out that it would be much more useful if the creation and annihilation operators in the expression for current $j^\nu(-\mathbf{q}, \tau = 0) = \sum_{\mathbf{p}} c_{\mathbf{p}}^\dagger \gamma^\nu(\mathbf{p} - \mathbf{q}, \mathbf{p}) c_{\mathbf{p}-\mathbf{q}}$ appeared in different imaginary times $c_{\mathbf{p}}^\dagger(\tau_1)$ and $c_{\mathbf{p}-\mathbf{q}}(\tau_2)$. This could be emulated by defining a new auxiliary quantity instead of the current-current correlation function, such as $\langle \hat{T}_\tau j_{\mathbf{q}}^\mu(\tau) c_{\mathbf{k}}(\tau_x) c_{\mathbf{k}+\mathbf{q}}^\dagger(\tau_y) \rangle$. However, somewhat less cumbersome expressions are obtained in the coordinate space, where we can fully utilize the compact 4-vector notation. This is why we introduce

$$\Lambda^\mu(r_1, r_2, r_3) = \langle \hat{T}_\tau j^\mu(r_3) c(r_1) c^\dagger(r_2) \rangle. \quad (4.5)$$

This function satisfies

$$\Lambda^\mu(r_1, r_2, r_3) = \Lambda^\mu(r_1 - r_2, 0, r_3 - r_2) = \Lambda^\mu(r_1 - r_3, r_2 - r_3, 0) = \Lambda^\mu(0, r_2 - r_1, r_3 - r_1), \quad (4.6)$$

as a consequence of the temporal and space translation symmetry of the system. In the real-time formalism (at $T = 0$), this defines Λ^μ on the whole domain of its variables. On the other hand, we need to be more careful in imaginary time formalism. It turns out that Eq. (4.5) formally converges only for $\tau_{\min} < \tau_{\text{intermediate}} < \tau_{\max} < \beta + \tau_{\min}$. For example, if $\tau_3 > \tau_1 > \tau_2$, then:

$$\begin{aligned} \Lambda^\mu(r_1, r_2, r_3) &= \frac{1}{\mathcal{Z}} \text{Tr} \left[e^{-\beta H} e^{\tau_3 H} j_{\mathbf{r}_3}^\mu e^{-H\tau_3} e^{H\tau_1} c_{\mathbf{r}_1} e^{-H\tau_1} e^{H\tau_2} c_{\mathbf{r}_2}^\dagger e^{-H\tau_2} \right] \\ &= \frac{1}{\mathcal{Z}} \text{Tr} \left[e^{-H(\beta - \tau_3 + \tau_2)} j_{\mathbf{r}_3}^\mu e^{-H(\tau_3 - \tau_1)} c_{\mathbf{r}_1} e^{-H(\tau_1 - \tau_2)} c_{\mathbf{r}_2}^\dagger \right], \end{aligned} \quad (4.7)$$

⁵The corresponding current operator is given by Eq. (C.108)

which converges for $\tau_2 < \tau_1 < \tau_3 < \beta + \tau_2$. In other regions (in τ space) we will define Λ^μ , such that certain properties are satisfied⁶. Let us motivate what those properties are: in this example ($\tau_2 < \tau_1 < \tau_3 < \beta + \tau_2$), notice that $\tau_3 - \beta < \tau_2 < \tau_1 < \tau_3$. Hence

$$\begin{aligned}
 \Lambda^\mu(\mathbf{r}_1, \tau_1, \mathbf{r}_2, \tau_2, \mathbf{r}_3, \tau_3 - \beta) &= \text{Tr} \left[e^{-\beta H} e^{H\tau_1} c_{\mathbf{r}_1} e^{-H\tau_1} e^{H\tau_2} c_{\mathbf{r}_2}^\dagger e^{-H\tau_2} e^{H(\tau_3 - \beta)} j_{\mathbf{r}_3}^\mu e^{-H(\tau_3 - \beta)} \right] \\
 &= \text{Tr} \left[e^{-\beta H} e^{\tau_3 H} j_{\mathbf{r}_3}^\mu e^{-H\tau_3} e^{H\tau_1} c_{\mathbf{r}_1} e^{-H\tau_1} e^{H\tau_2} c_{\mathbf{r}_2}^\dagger e^{-H\tau_2} \right] \\
 &= \Lambda^\mu(r_1, r_2, r_3),
 \end{aligned} \tag{4.8}$$

where the cyclic property of trace was used in the second line. We also used the fact that the current operator commutes with all operators under time ordering. As a result, we see that we can extend the definition of Λ^μ to regions where Eq. (4.5) does not formally converge, such that Λ^μ is periodic (with period β) with respect to τ_3 : $\Lambda^\mu(\mathbf{r}_1, \tau_1, \mathbf{r}_2, \tau_2, \mathbf{r}_3, \tau_3 \pm \beta) = \Lambda^\mu(r_1, r_2, r_3)$. Analogous reasoning can be used to impose that Λ^μ is antiperiodic (with period β), with respect to τ_2 and τ_3

$$\Lambda^\mu(\mathbf{r}_1, \tau_1, \mathbf{r}_2, \tau_2 \pm \beta, \mathbf{r}_3, \tau_3) = -\Lambda^\mu(r_1, r_2, r_3), \tag{4.9}$$

$$\Lambda^\mu(\mathbf{r}_1, \tau_1 \pm \beta, \mathbf{r}_2, \tau_2, \mathbf{r}_3, \tau_3) = -\Lambda^\mu(r_1, r_2, r_3). \tag{4.10}$$

Therefore, we successfully extended the definition of Λ^μ to the whole τ domain. We note that these periodic/antiperiodic conditions are consistent with translational invariance.

4.2.2 Definition of $\tilde{\Gamma}^\mu$

As a reminder, we introduced the correlation function Λ^μ since the consequences of the charge conservation (4.4) are much more directly reflected on this quantity than on current-current correlation function $\chi^{\mu\nu}$. However, to proceed with the proof of the Ward identity, we first need to find a relation that connects Λ^μ with the renormalized vertex function Γ^μ . To do so, we first introduce a new quantity $\tilde{\Gamma}^\mu(r_1, r_2, r_3)$ such that

$$\Lambda^\mu(r_1, r_2, r_3) = \sum_{r'_1} \sum_{r'_2} G(r_1 - r'_1) \tilde{\Gamma}^\mu(r'_1, r'_2, r_3) G(r'_2 - r_2). \tag{4.11}$$

Although this looks quite abstract, it turns out that this new quantity, in the Fourier space, is actually the same as the renormalized vertex function $\Gamma^\mu(p, p + q)$ from Eq. (4.2). We will prove this in the following sections, but before that, let us first inspect some properties of $\tilde{\Gamma}^\mu$: First of all $\tilde{\Gamma}^\mu$ is invariant under spatial translations $\mathbf{r}_1 \rightarrow \mathbf{r}_1 + \mathbf{a}$, $\mathbf{r}_2 \rightarrow \mathbf{r}_2 + \mathbf{a}$, $\mathbf{r}_3 \rightarrow \mathbf{r}_3 + \mathbf{a}$. This is easily checked from Eq. (4.11) as a consequence of the fact that both Λ^μ and the Green's function G are invariant under such transformations. Furthermore, $\tilde{\Gamma}^\mu(r'_1, r'_2, r_3)$ inherited from $\Lambda^\mu(r_1, r_2, r_3)$ the periodicity with respect to τ_3 , with period β . However, we cannot say anything about the (anti)periodicity with respect to τ'_1 or τ'_2 , as the integration over these variables is performed only in the domain⁷ $(0, \beta)$ in Eq. (4.11). Outside of this interval $\tilde{\Gamma}^\mu$ does not even have to be defined. However, we want to define $\tilde{\Gamma}^\mu$ on the whole interval of τ'_1 and τ'_2 , such that the subintegral function in Eq. (4.11) becomes periodic with respect to both τ'_1 and τ'_2 with period β . To do so, we must impose that $\tilde{\Gamma}^\mu(r'_1, r'_2, r_3)$ is antiperiodic with respect to τ'_1 and τ'_2 . This is a consequence of the fact that $G(r_1 - r'_1)$ and $G(r'_2 - r_2)$ have such properties. Now, it turns out that $\tilde{\Gamma}_\mu$ also posses a symmetry with respect to temporal translations. This can be proved as follows: first we use arbitrary τ to translate $\tau_1 \rightarrow \tau_1 + \tau$, $\tau_2 \rightarrow \tau_2 + \tau$, $\tau_3 \rightarrow \tau_3 + \tau$ in Eq. (4.11), and use the fact that Λ^μ is invariant under such transformation. Then, in the integrals

⁶We note that this is exactly the same approach that is used for defining the finite temperature Green's function in imaginary time.

⁷As we noted, $\sum_r \equiv \int_0^\beta d\tau \sum_r$

over the imaginary times (in the right-hand side of Eq. (4.11)), we use substitutions $\tau_1' \rightarrow \tau_1' + \tau$, $\tau_2' \rightarrow \tau_2' + \tau$, after which the domain of integration becomes $(\tau, \beta + \tau)$. After these transformations, the Green's functions remain unchanged. At last, we use the property that the whole subintegral function in Eq. (4.11) is periodic with a period β . Hence, we can restore the domain over which we integrate from $(\tau, \beta + \tau)$ back to $(0, \beta)$. As a result, all quantities in Eq. (4.11) remain unchanged, except for the fact that all temporal variables in $\tilde{\Gamma}_\mu$ are shifted by τ . This is only possible if $\tilde{\Gamma}_\mu$ possesses a symmetry with respect to temporal translations. This completes our proof⁸.

All of these properties finally enable us to define the Fourier series of $\tilde{\Gamma}^\mu$ as

$$\tilde{\Gamma}^\mu(p, p + q) = \sum_{r_2} \sum_{r_3} \tilde{\Gamma}^\mu(0, r_2, r_3) e^{i(pr_2 + qr_3)}. \quad (4.12)$$

We note that due to (anti)periodic properties that we examined, q^0 is bosonic, while p^0 is fermionic Matsubara frequency. Before we prove that $\tilde{\Gamma}^\mu$ from Eq. (4.12) is indeed the same as Γ^μ from (4.2), let us first show different forms of Fourier transforms. This will be quite useful for us since $\tilde{\Gamma}^\mu$ is defined in the coordinate space (see Eq. (4.11)), while Γ^μ is defined in k-space (see Eq. (4.2)).

4.2.3 Fourier Transform

The purpose of this section is twofold:

- We define the convention that will be used for the Fourier transform.
- Due to the translational invariance of the system, we will see that it is possible to introduce some arbitrary (free) parameters in the Fourier transform. This gives us the freedom to choose them conveniently in our analysis later.

$$\tilde{\Gamma}^\mu(r_1, r_2, r_3)$$

Translational invariance of $\tilde{\Gamma}^\mu$ enabled us to write its Fourier transform as in Eq. (4.12). However, the translational invariance can also be used to introduce an arbitrary (free) parameter as follows⁹:

$$\begin{aligned} \tilde{\Gamma}_\mu(p, p + q) &= \sum_{r_2} \sum_{r_3} \tilde{\Gamma}_\mu(0, r_2, r_3) e^{ipr_2 + iqr_3} \\ &= \left[\begin{array}{l} r_2 \rightarrow r_2 - r_1 \\ r_3 \rightarrow r_3 - r_1 \end{array} \right] \\ &= \sum_{r_2} \sum_{r_3} \tilde{\Gamma}_\mu(0, r_2 - r_1, r_3 - r_1) e^{i[p(r_2 - r_1) + q(r_3 - r_1)]} \\ &= \sum_{r_2} \sum_{r_3} \tilde{\Gamma}_\mu(r_1, r_2, r_3) e^{i[p(r_2 - r_1) + q(r_3 - r_1)]}. \end{aligned} \quad (4.13)$$

Here, r_1 is an arbitrary parameter.

⁸We note that the properties of (anti)periodicity with period β , and temporal translational invariance are not mutually contradictory since we have an even number "antiperiodic" (τ_1 and τ_2) variables.

⁹The combination of periodic (antiperiodic) variable τ_3 (τ_2) of $\tilde{\Gamma}^\mu$ with bosonic (fermionic) Matsubara frequency q^0 (p^0) has a consequence that the whole subintegral function is periodic with respect to both τ_2 and τ_3 . Hence, the domain of integration, of both τ_2 and τ_3 , can always be shifted $(0, \beta) \leftrightarrow (\tau_1, \beta + \tau_1)$ for arbitrary τ_1 .

$$\boxed{G(r_1 - r'_1)}$$

In a completely analogous manner, we can introduce an arbitrary (free) parameter r' into the Fourier transform of the Green's function

$$G(p) = \sum_r e^{-ip(r-r')} G(r - r') = \sum_r e^{ip(r-r')} G(r' - r), \quad (4.14)$$

$$\boxed{\Lambda^\mu(r_1, r_2, r_3)}$$

The quantity $\Lambda^\mu(r_1, r_2, r_3)$ was (originally¹⁰) defined in Eq. (4.5), as a correlation function between current, annihilation and creation operators. It is thus natural that the convention for the Fourier transform of Λ^μ follows the convention for \mathbf{j}_q , c_p and c_k^\dagger , which (in the case of spatial coordinates) read as:

$$j_q^\mu = \sum_{\mathbf{r}} e^{-i\mathbf{q}\mathbf{r}} j^\mu(\mathbf{r}), \quad (4.15a)$$

$$c_p = \frac{1}{\sqrt{N}} \sum_{\mathbf{r}} e^{-i\mathbf{p}\mathbf{r}} c_{\mathbf{r}}, \quad (4.15b)$$

$$c_k^\dagger = \frac{1}{\sqrt{N}} \sum_{\mathbf{r}} e^{i\mathbf{k}\mathbf{r}} c_{\mathbf{r}}^\dagger. \quad (4.15c)$$

We note that the factor $1/\sqrt{N}$ in Eqs. (4.15b) and (4.15c) is standard convention, as we want to keep the property that c and c^\dagger transform as $c_\lambda^\dagger = \sum_i \langle i|\lambda\rangle c_i^\dagger$ and $c_\lambda = \sum_i \langle \lambda|i\rangle c_i$, when the basis is changed $\{|i\rangle\} \rightarrow \{|\lambda\rangle\}$.

Dirac Identity in the Matsubara space

In the real-time formalism, we can get a nice identity¹¹ if we successively apply Fourier and inverse Fourier transform to an arbitrary function F . The same can be done in the Matsubara space as well

$$F(\tau) = \frac{1}{\beta} \sum_{i\omega_n} e^{-i\omega_n\tau} \int_0^\beta d\tau' e^{i\omega_n\tau'} F(\tau') \quad (4.16)$$

$$= \frac{1}{\beta} \int_0^\beta d\tau' \sum_{i\omega_n} e^{-i\omega_n(\tau-\tau')} F(\tau') \quad (4.17)$$

$$= \frac{1}{\beta} \int_0^\beta d\tau' \sum_{i\omega_n} e^{-i\omega_n(\tau'-\tau)} F(\tau') \quad (4.18)$$

In the last line we used the fact that Matsubara frequencies are symmetric, so we can use a substitution $i\omega_n \rightarrow -i\omega_n$.

4.2.4 Proof that $\tilde{\Gamma}^\mu(p, p+q) \equiv \Gamma^\mu(p, p+q)$

Let us first remind ourselves that the main purpose of the renormalized vertex function in our study is to use it in Eq. (4.2) to calculate the current-current correlation function. In that sense, we will say that

¹⁰Afterwards we imposed that it has certain symmetry properties with respect to temporal variables; see Sec. 4.2.1

¹¹Which is basically just one of the ways to represent the Dirac delta function

$\tilde{\Gamma}^\mu(p, p+q)$ is identical with $\Gamma^\mu(p, p+q)$ if it produces the same result when inserted into Eq. (4.2). Hence, our task is to prove that $\chi^{\mu\nu}(q)$ coincides with the following quantity

$$\tilde{\chi}^{\mu\nu}(q) \equiv -\frac{1}{N\beta} \sum_p \left[\gamma^\mu(\mathbf{p} + \mathbf{q}, \mathbf{p}) G(p+q) \tilde{\Gamma}^\nu(p, p+q) G(p) \right]. \quad (4.19)$$

Since renormalized vertex function was defined in Eq. (4.11) in coordinate space, let us first use the inverse Fourier transform on both $\tilde{\Gamma}^\nu$ and G .

$$\tilde{\chi}^{\mu\nu}(q) = -\frac{1}{N\beta} \sum_p \left[\gamma^\mu(\mathbf{p} + \mathbf{q}, \mathbf{p}) \sum_{r'_1} e^{i(p+q)(r'_1-r_1)} G(r_1 - r'_1) \sum_{r''_2, r_3} \tilde{\Gamma}^\nu(r''_1, r''_2, r_3) e^{i[p(r''_2-r''_1)+q(r_3-r''_1)]} \sum_{r_2} G(r'_2 - r_2) e^{ip(r_2-r'_2)} \right]. \quad (4.20)$$

Here, r_1, r''_1 and r'_2 are arbitrary parameters. We can now conveniently choose $r''_1 = r'_1$ and $r'_2 = r''_2$.¹² Hence

$$\tilde{\chi}^{\mu\nu}(q) = -\frac{1}{N\beta} \sum_{p, r_2, r_3} \left[\gamma^\mu(\mathbf{p} + \mathbf{q}, \mathbf{p}) e^{-i(p+q)r_1} e^{iqr_3} e^{ipr_2} \times \sum_{r'_1, r''_2} G(r_1 - r'_1) \tilde{\Gamma}^\nu(r'_1, r''_2, r_3) G(r''_2 - r_2) \right]. \quad (4.21)$$

The bottom line in Eq. (4.21) can be recognized and $\Lambda^\nu(r_1, r_2, r_3)$ from Eq. (4.11), giving

$$\tilde{\chi}^{\mu\nu}(q) = -\frac{1}{N\beta} \sum_{p, r_2, r_3} e^{-i(p+q)r_1} e^{ipr_2} e^{iqr_3} \gamma^\mu(\mathbf{p} + \mathbf{q}, \mathbf{p}) \Lambda^\nu(r_1, r_2, r_3). \quad (4.22)$$

It is now convenient to separate the spatial and temporal coordinates. Thus, we can now set the arbitrary parameter $r_1^0 \equiv \tau_1 = 0$. Since \mathbf{r}_1 is still arbitrary, we can sum over this parameter, and divide everything with the number of \mathbf{k} -points (which is equal to N).

$$\tilde{\chi}^{\mu\nu}(q) = -\frac{1}{N\beta} \sum_{\mathbf{p}} \gamma^\mu(\mathbf{p} + \mathbf{q}, \mathbf{p}) \sum_{i\omega_p} \int_0^\beta d\tau_2 \int_0^\beta d\tau_3 e^{-i\omega_p \tau_2} e^{-i\omega_q \tau_3} \times \frac{1}{N} \sum_{\mathbf{r}_1, \mathbf{r}_2, \mathbf{r}_3} e^{-i(\mathbf{p}+\mathbf{q})\mathbf{r}_1} e^{i\mathbf{p}\mathbf{r}_2} e^{i\mathbf{q}\mathbf{r}_3} \Lambda^\nu(\mathbf{r}_1, 0, \mathbf{r}_2, \tau_2, \mathbf{r}_3, \tau_3). \quad (4.23)$$

Using the convention from Eq. (4.15), we can see that the bottom line of Eq. (4.23) is equal to

$$\Lambda^\nu(\mathbf{p} + \mathbf{q}, 0, \mathbf{p}, \tau_2, -\mathbf{q}, \tau_3) = \Lambda^\nu(\mathbf{p} + \mathbf{q}, -\tau_3, \mathbf{p}, \tau_2 - \tau_3, -\mathbf{q}, 0), \quad (4.24)$$

where we used the temporal translational invariance to obtain the last equality. Plugging this back into Eq. (4.23), using the substitution $\tau_2 \rightarrow \tau_2 + \tau_3$, and using the fact that the whole subintegral function is periodic with respect to τ_2 with period β , such that we can shift the domain of integration from $(\tau_3, \beta + \tau_3)$ back to $(0, \beta)$, we get

¹²However, we cannot choose for example $r_1 = r_2$, as r_1 "sees" r_2 as a variable. The choice $r''_1 = r'_1$ was allowed (same for $r'_2 = r''_2$) as the free parameter r''_1 is situated inside the integrals over r''_2 and r_3 , where r'_1 is taken to be constant (i.e. r''_1 sees r'_1 as a constant). Of course, we can later interchange the integrals, resulting in the fact that r''_1 no longer sees r'_1 as a constant, but this is allowed due to the Fubini's theorem.

$$\tilde{\chi}^{\mu\nu}(q) = -\frac{1}{N\beta} \sum_{\mathbf{p}} \gamma^\mu(\mathbf{p} + \mathbf{q}, \mathbf{p}) \sum_{i\omega_p} \int_0^\beta d\tau_2 \int_0^\beta d\tau_3 e^{-i\omega_p(\tau_2+\tau_3)} e^{-i\omega_q\tau_3} \times \Lambda^\nu(\mathbf{p} + \mathbf{q}, -\tau_3, \mathbf{p}, \tau_2, -\mathbf{q}, 0). \quad (4.25)$$

Let us now use the substitution $\tau_3 \rightarrow -\tau_3$ and, similarly as before, use the periodicity to shift the domain of integration back to $(0, \beta)$. We get

$$\tilde{\chi}^{\mu\nu}(q) = -\frac{1}{N} \sum_{\mathbf{p}} \gamma^\mu(\mathbf{p} + \mathbf{q}, \mathbf{p}) \int_0^\beta d\tau_3 e^{i\omega_q\tau_3} \times \frac{1}{\beta} \sum_{i\omega_p} \int_0^\beta d\tau_2 e^{-i\omega_p(\tau_2-\tau_3)} \Lambda^\nu(\mathbf{p} + \mathbf{q}, \tau_3, \mathbf{p}, \tau_2, -\mathbf{q}, 0). \quad (4.26)$$

The bottom line of the previous expression can be simplified using the identity in Eq. (4.18)

$$\tilde{\chi}^{\mu\nu}(q) = -\frac{1}{N} \sum_{\mathbf{p}} \gamma^\mu(\mathbf{p} + \mathbf{q}, \mathbf{p}) \int_0^\beta d\tau_3 e^{i\omega_q\tau_3} \Lambda^\nu(\mathbf{p} + \mathbf{q}, \tau_3, \mathbf{p}, \tau_3, -\mathbf{q}, 0). \quad (4.27)$$

Since we have only one temporal variable left, we will change the label of the dummy variable $\tau_3 \rightarrow \tau$. Furthermore, since τ is restricted to the values between 0 and β , we can represent Λ^μ using Eq. (4.5)

$$\tilde{\chi}^{\mu\nu}(q) = -\frac{1}{N} \sum_{\mathbf{p}} \int_0^\beta d\tau e^{i\omega_q\tau} \gamma^\mu(\mathbf{p} + \mathbf{q}, \mathbf{p}) \langle \hat{T}_\tau j_{-\mathbf{q}}^\nu(0) c_{\mathbf{p}+\mathbf{q}}(\tau) c_{\mathbf{p}}^\dagger(\tau) \rangle. \quad (4.28)$$

Under \hat{T}_τ we can arbitrarily interchange the operators as long as we keep track of the minus signs. Hence

$$\tilde{\chi}^{\mu\nu}(q) = \frac{1}{N} \int_0^\beta d\tau e^{i\omega_q\tau} \langle \hat{T}_\tau \sum_{\mathbf{p}} c_{\mathbf{p}}^\dagger(\tau) \gamma^\mu(\mathbf{p} + \mathbf{q}, \mathbf{p}) c_{\mathbf{p}+\mathbf{q}}(\tau) j_{-\mathbf{q}}^\nu(0) \rangle \quad (4.29)$$

Now, we recognize the current operator from Eq. (C.121) and obtain

$$\tilde{\chi}^{\mu\nu}(q) = \frac{1}{N} \int_0^\beta d\tau e^{i\omega_q\tau} \langle \hat{T}_\tau j_{\mathbf{q}}^\mu(\tau) j_{-\mathbf{q}}^\nu(0) \rangle. \quad (4.30)$$

This coincides with $\chi^{\mu\nu}(q)$, as seen from Eqs. (2.37b) and (4.1). This completes the proof that $\tilde{\Gamma}^\mu = \Gamma^\mu$.

This property enables us to apply the charge conservation from Eq. (4.4) directly in Eq. (4.5), and connect the obtained result to the renormalized vertex function via Eq. (4.11). In order to do that, we first need to figure out how to differentiate expressions which have time ordering operator. This will be discussed in the next section.

4.2.5 Differentiation under the Time-Ordering Operator

Theorem 4. *Let:*

$$A(\tau_1, \tau_2, \tau_3) = \hat{T}_\tau Z(\tau_3) X(\tau_1) Y(\tau_2), \quad (4.31)$$

where \hat{T}_τ is the time-ordering operator, X and Y are arbitrary fermionic operators¹³, while Z is some bosonic operator¹⁴. Then:

$$\frac{\partial A}{\partial \tau_3} = \hat{T}_\tau \frac{\partial Z}{\partial \tau_3} X Y + \delta(\tau_3 - \tau_1) \hat{T}_\tau [Z, X] Y + \delta(\tau_3 - \tau_2) \hat{T}_\tau X [Z, Y], \quad (4.32)$$

where $[,]$ is the commutator.

¹³In our case these are annihilation and creation operators

¹⁴In our case this is the current operator.

Proof. Let us write out the time dependence in the time-ordering operator explicitly:

$$\begin{aligned}
 A(\tau_1, \tau_2, \tau_3) = & ZXY\theta(\tau_3 - \tau_1)\theta(\tau_1 - \tau_2) \\
 & - ZYX\theta(\tau_3 - \tau_2)\theta(\tau_2 - \tau_1) \\
 & + XYZ\theta(\tau_1 - \tau_2)\theta(\tau_2 - \tau_3) \\
 & + XZY\theta(\tau_1 - \tau_3)\theta(\tau_3 - \tau_2) \\
 & - YZX\theta(\tau_2 - \tau_3)\theta(\tau_3 - \tau_1) \\
 & - YXZ\theta(\tau_2 - \tau_1)\theta(\tau_1 - \tau_3).
 \end{aligned} \tag{4.33}$$

Hence:

$$\begin{aligned}
 \frac{\partial A}{\partial \tau_3} = & \hat{T}_\tau \frac{\partial Z}{\partial \tau_3} XY \\
 & + ZXY\delta(\tau_3 - \tau_1)\theta(\tau_1 - \tau_2) \\
 & - ZYX\delta(\tau_3 - \tau_2)\theta(\tau_2 - \tau_1) \\
 & - XYZ\delta(\tau_2 - \tau_3)\theta(\tau_1 - \tau_2) \\
 & - XZY(\delta(\tau_1 - \tau_3)\theta(\tau_3 - \tau_2) - \delta(\tau_3 - \tau_2)\theta(\tau_1 - \tau_3)) \\
 & + YZX(\delta(\tau_2 - \tau_3)\theta(\tau_3 - \tau_1) - \delta(\tau_3 - \tau_1)\theta(\tau_2 - \tau_3)) \\
 & + YXZ\delta(\tau_1 - \tau_3)\theta(\tau_2 - \tau_1).
 \end{aligned} \tag{4.34}$$

Let us now group the terms with a common delta function:

$$\begin{aligned}
 \frac{\partial A}{\partial \tau_3} - \hat{T}_\tau \frac{\partial Z}{\partial \tau_3} XY = & \delta(\tau_3 - \tau_1) \left[\theta(\tau_1 - \tau_2)(ZXY - XZY) \right. \\
 & \left. - \theta(\tau_2 - \tau_1)(YZX - YXZ) \right] \\
 & + \delta(\tau_3 - \tau_2) \left[\theta(\tau_1 - \tau_2)(XZY - XYZ) \right. \\
 & \left. - \theta(\tau_2 - \tau_1)(ZYX - YZX) \right]
 \end{aligned} \tag{4.35}$$

Hence:

$$\frac{\partial A}{\partial \tau_3} = \hat{T}_\tau \frac{\partial Z}{\partial \tau_3} XY + \delta(\tau_3 - \tau_1) \hat{T}_\tau [Z, X]Y + \delta(\tau_3 - \tau_2) \hat{T}_\tau X[Z, Y]. \tag{4.36}$$

□

Our next task is to find the consequences of charge conservation (4.4) on Λ^μ and then deduce how is that connected to the renormalized vertex function using Eq. (4.11).

4.2.6 The Consequences of Charge Conservation on Λ^μ

Since the charge conservation in Eq. (4.4) contains $\frac{\partial n_{\mathbf{a}}}{\partial \tau}$, let us first use Eq. (4.36) to differentiate $\Lambda^0(r_1, r_2, r_3)$ with respect to τ_3 . We will restrict ourselves to the case then $\tau_1, \tau_2, \tau_3 \geq 0$. In this case Λ^μ can be expressed as in Eq. (4.5). We obtain:

$$\begin{aligned}
 \frac{\partial \Lambda^0(r_1, r_2, r_3)}{\partial \tau_3} = & \langle \hat{T}_\tau \frac{\partial n(r_3)}{\tau_3} c(r_1) c^\dagger(r_2) \rangle \\
 & + \delta(\tau_3 - \tau_1) \langle \hat{T}_\tau [n(r_3), c(r_1)] c^\dagger(r_2) \rangle \\
 & + \delta(\tau_3 - \tau_2) \langle \hat{T}_\tau c(r_1) [n(r_3), c^\dagger(r_2)] \rangle
 \end{aligned} \tag{4.37}$$

The delta functions ensure that we are always dealing with equal time commutators. To calculate these, we express the density as $n(r_3) = c^\dagger(r_3)c(r_3)$, and use $[AB, C] = A\{B, C\} - \{A, C\}B$, which is needed as the fields $c^\dagger(r)$ are fermionic

$$\begin{aligned}\delta(\tau_3 - \tau_1)[n(r_3), c(r_1)] &= -\delta(\tau_3 - \tau_1)\{c^\dagger(r_3), c(r_1)\}c(r_3) \\ &= -c(r_3)\delta(r_3 - r_1),\end{aligned}\quad (4.38)$$

$$\begin{aligned}\delta(\tau_3 - \tau_2)[n(r_3), c^\dagger(r_2)] &= \delta(\tau_3 - \tau_2)c^\dagger(r_3)\{c(r_3), c^\dagger(r_2)\} \\ &= c^\dagger(r_3)\delta(r_3 - r_2).\end{aligned}\quad (4.39)$$

Plugging this back into Eq. (4.37), and using the definition of the finite-temperature Green's function $G(r - r') = -\langle \hat{T}c(r)c^\dagger(r') \rangle$, we get

$$\begin{aligned}\frac{\partial \Lambda^0(r_1, r_2, r_3)}{\partial \tau_3} &= \langle \hat{T}_\tau \frac{\partial n(r_3)}{\tau_3} c(r_1) c^\dagger(r_2) \rangle \\ &\quad \delta(r_1 - r_3)G(r_3 - r_2) - \delta(r_2 - r_3)G(r_1 - r_3).\end{aligned}\quad (4.40)$$

It would be useful if we rewrote the previous expression in the \mathbf{k} -space, to make it easier to directly use the charge conservation from Eq. (4.4). To do so, we first note that if we apply the following $\int d\mathbf{r}_1 e^{-i\mathbf{p}(\mathbf{r}_1 - \mathbf{r}_2)} \int d\mathbf{r}_3 e^{-i\mathbf{q}(\mathbf{r}_3 - \mathbf{r}_2)}$ to Eq. (4.5), we obtain $\langle \hat{T}_\tau j_{\mathbf{q}}(\tau_3) c_{\mathbf{p}}(\tau_1) c_{\mathbf{p}+\mathbf{q}}^\dagger(\tau_2) \rangle$. This is easily seen, but we demonstrate it explicitly using the translational symmetry of the system

$$\begin{aligned}& \frac{1}{N^2} \sum_{\mathbf{p}, \mathbf{q}} e^{i\mathbf{q}(\mathbf{r}_3 - \mathbf{r}_2)} e^{i\mathbf{p}(\mathbf{r}_1 - \mathbf{r}_2)} \langle \hat{T}_\tau j_{\mathbf{q}}^\mu(\tau_3) c_{\mathbf{p}}(\tau_1) c_{\mathbf{p}+\mathbf{q}}^\dagger(\tau_2) \rangle \\ &= \frac{1}{N^2} \sum_{\mathbf{p}, \mathbf{q}} e^{i\mathbf{q}(\mathbf{r}_3 - \mathbf{r}_2)} e^{i\mathbf{p}(\mathbf{r}_1 - \mathbf{r}_2)} \\ & \times \langle \sum_{\mathbf{r}'_3} e^{-i\mathbf{q}\mathbf{r}'_3} j_{\mathbf{r}'_3}^\mu(\tau_3) \frac{1}{\sqrt{N}} \sum_{\mathbf{r}'_1} e^{-i\mathbf{r}'_1 \mathbf{p}} c_{\mathbf{r}'_1}(\tau_1) \frac{1}{\sqrt{N}} \sum_{\mathbf{r}'_2} e^{i\mathbf{r}'_2 (\mathbf{p} + \mathbf{q})} c_{\mathbf{r}'_2}^\dagger(\tau_2) \rangle \\ &= \frac{1}{N^3} \sum_{\mathbf{r}'_1, \mathbf{r}'_2, \mathbf{r}'_3} \langle j_{\mathbf{r}'_3}^\mu(\tau_3) c_{\mathbf{r}'_1}(\tau_1) c_{\mathbf{r}'_2}^\dagger(\tau_2) \rangle \underbrace{\sum_{\mathbf{p}} e^{i\mathbf{p}(\mathbf{r}_1 - \mathbf{r}_2 - \mathbf{r}'_1 + \mathbf{r}'_2)}}_{N\delta_{\mathbf{r}_1 + \mathbf{r}'_2, \mathbf{r}'_1 + \mathbf{r}_2}} \underbrace{\sum_{\mathbf{q}} e^{i\mathbf{q}(\mathbf{r}_3 - \mathbf{r}_2 - \mathbf{r}'_3 + \mathbf{r}'_2)}}_{N\delta_{\mathbf{r}'_2 + \mathbf{r}_3, \mathbf{r}_2 + \mathbf{r}'_3}} \\ &= \frac{1}{N} \sum_{\mathbf{r}'_3} \langle j_{\mathbf{r}'_3}^\mu(\tau_3) c_{\mathbf{r}_1 + \mathbf{r}'_3 - \mathbf{r}_3}(\tau_1) c_{\mathbf{r}'_3 + \mathbf{r}_2 - \mathbf{r}_3}^\dagger(\tau_2) \rangle \\ &= \frac{1}{N} \sum_{\mathbf{r}'_3} \langle j_{\mathbf{r}'_3}^\mu c_{\mathbf{r}_1} c_{\mathbf{r}_2}^\dagger \rangle \\ &= \Lambda^\mu(r_1, r_2, r_3)\end{aligned}\quad (4.41)$$

Therefore, let us apply $\int d\mathbf{r}_1 e^{-i\mathbf{p}(\mathbf{r}_1 - \mathbf{r}_2)} \int d\mathbf{r}_3 e^{-i\mathbf{q}(\mathbf{r}_3 - \mathbf{r}_2)}$ to both sides of Eq. (4.40). Before that, we can use the translational invariance of the system, and set $r_2 = 0$ everywhere. We get

$$\begin{aligned}\frac{\partial}{\partial \tau_3} \Lambda^0(\mathbf{p}, \tau_1, \mathbf{p} + \mathbf{q}, 0, \mathbf{q}, \tau_3) &= \langle \hat{T}_\tau \frac{\partial n_{\mathbf{q}}(\tau_3)}{\partial \tau_3} c_{\mathbf{p}}(\tau_1) c_{\mathbf{p}+\mathbf{q}}^\dagger(0) \rangle \\ &\quad + \delta(\tau_1 - \tau_3)G(\mathbf{p} + \mathbf{q}, \tau_1) - \delta(\tau_3)G(\mathbf{p}, \tau_1).\end{aligned}\quad (4.42)$$

Due to the Eq. (4.4), the first line on the right-hand side is

$$-\mathbf{\Delta}(\mathbf{q}) \cdot \vec{\Lambda}(\mathbf{p}, \tau_1, \mathbf{p} + \mathbf{q}, 0, \mathbf{q}, \tau_3).$$

Hence,

$$\begin{aligned} \frac{\partial}{\partial \tau_3} \Lambda^0(\mathbf{p}, \tau_1, \mathbf{p} + \mathbf{q}, 0, \mathbf{q}, \tau_3) + \mathbf{\Delta}(\mathbf{q}) \cdot \vec{\Lambda}(\mathbf{p}, \tau_1, \mathbf{p} + \mathbf{q}, 0, \mathbf{q}, \tau_3) = \\ + \delta(\tau_1 - \tau_3) G(\mathbf{p} + \mathbf{q}, \tau_1) - \delta(\tau_3) G(\mathbf{p}, \tau_1). \end{aligned} \quad (4.43)$$

On the left-hand side of the previous equation, we can use Eq. (4.11), to see the consequences of this identity on the renormalized vertex function¹⁵. This will be the last piece needed for the proof of the Ward identity.

4.2.7 Putting all the Pieces Together

Let us first express $\Lambda^\mu(r_1, r_2, r_3)$ from Eq. (4.11) using the Green's functions and renormalized vertex function in the Fourier space, in order to make a connection with in Eq. (4.43) more easily.

$$\begin{aligned} \Lambda^\mu(r_1, r_2, r_3) &= \sum_{r'_1, r'_2} G(r_1 - r'_1) \Gamma^\mu(r'_1, r'_2, r_3) G(r'_2 - r_2) \\ &= \frac{1}{(N\beta)^4} \sum_{r'_1, r'_2} \sum_{p_1} e^{ip_1(r_1 - r'_1)} G(p_1) \\ &\quad \times \sum_{p_2, q_2} e^{-ip_2(r'_2 - r'_1)} e^{-iq_2(r_3 - r'_1)} \Gamma^\mu(p_2, p_2 + q_2) \\ &\quad \times \sum_{p_3} e^{ip_3(r'_2 - r_2)} G(p_3) \\ &= \frac{1}{(N\beta)^2} \sum_{p_1, q_2} G(p_1) \Gamma^\mu(p_1 - q_2, p_1) G(p_1 - q_2) e^{ip_1 r_1} e^{-iq_2 r_3} e^{-ir_2(p_1 - q_2)} \end{aligned} \quad (4.44)$$

As before, we are free to set $r_2 = 0$ due to the translational invariance, and we Fourier transform the spacial part by applying $\int d\mathbf{r}_1 e^{-i\mathbf{p}\mathbf{r}_1} \int d\mathbf{r}_3 e^{-i\mathbf{q}\mathbf{r}_3}$. We get

$$\begin{aligned} \Lambda^\mu(\mathbf{p}, \tau_1, \mathbf{p} + \mathbf{q}, 0, \mathbf{q}, \tau_3) &= \frac{1}{\beta^2} \sum_{i\omega_{p_1}, i\omega_{q_2}} G(\mathbf{p}, i\omega_{p_1}) \\ &\quad \times \Gamma^\mu(\mathbf{p} + \mathbf{q}, i\omega_{p_1} - i\omega_{q_2}, \mathbf{p}, i\omega_{p_1}) G(\mathbf{p} + \mathbf{q}, i\omega_{p_1} - i\omega_{q_2}) e^{-i\omega_{p_1} \tau_1} e^{i\omega_{q_2} \tau_3}. \end{aligned} \quad (4.45)$$

Using this, we can calculate the expression given by the left-hand side of Eq. (4.43), obtaining

$$\begin{aligned} \frac{\partial}{\partial \tau_3} \Lambda^0(\mathbf{p}, \tau_1, \mathbf{p} + \mathbf{q}, 0, \mathbf{q}, \tau_3) + \mathbf{\Delta}(\mathbf{q}) \cdot \vec{\Lambda}(\mathbf{p}, \tau_1, \mathbf{p} + \mathbf{q}, 0, \mathbf{q}, \tau_3) \\ = \frac{1}{\beta^2} \sum_{i\omega_{p_1}, i\omega_{q_2}} e^{-i\omega_{p_1} \tau_1} e^{i\omega_{q_2} \tau_3} G(\mathbf{p}, i\omega_{p_1}) \left[i\omega_{q_2} \Gamma^0(\mathbf{p} + \mathbf{q}, i\omega_{p_1} - i\omega_{q_2}, \mathbf{p}, i\omega_{p_1}) \right. \\ \left. + \mathbf{\Delta}(\mathbf{q}) \cdot \vec{\Gamma}(\mathbf{p} + \mathbf{q}, i\omega_{p_1} - i\omega_{q_2}, \mathbf{p}, i\omega_{p_1}) \right] G(\mathbf{p} + \mathbf{q}, i\omega_{p_1} - i\omega_{q_2}). \end{aligned} \quad (4.46)$$

Let us now equate right-hand sides of Eqs. (4.46) and (4.43), and apply

$\int_0^\beta d\tau_1 e^{i\omega_p \tau_1} \int_0^\beta d\tau_3 e^{i\omega_q \tau_3}$ to both sides. We get:

$$G(p + q) - G(p) = G(p) \Delta^\mu(q) \Gamma_\mu(p + q, p) G(p + q) \quad (4.47)$$

If we divide both sides by $G(p + q) \cdot G(p)$

$$G^{-1}(p) - G^{-1}(p + q) = \Delta^\mu(q) \Gamma_\mu(p + q, p) \quad (4.48)$$

This completes the proof of the Ward identity. \square

¹⁵We note that we already proved that $\vec{\Gamma} = \Gamma$ in Sec. 4.2.4.

Remark 31. In the long wavelength limit $\mathbf{q} \rightarrow 0$, the Ward identity can be written as

$$\boxed{G^{-1}(p) - G^{-1}(p + q) = q^\mu \Gamma_\mu(p + q, p)} \quad (4.49)$$

Remark 32. If make the substitutions $q \rightarrow -q, p \rightarrow p + q$, and multiply both sides by -1 , we obtain a Ward identity for $\Gamma^\mu(p + q, p)$ instead of $\Gamma^\mu(p, p + q)$

$$\boxed{G^{-1}(p) - G^{-1}(p + q) = -\Delta^\mu(-q) \Gamma_\mu(p, p + q)} \quad (4.50)$$

4.3 Consequence of the Ward Identity

Let us now inspect some direct consequences of the Ward identity (4.3). For example, if we set $\mathbf{q} = 0$ in Eq. (4.3), analytically continue the results to the real frequency axis, and use the Dyson equation, we get the following expression for Γ^0 that is diagonal with respect to momentum variables

$$\boxed{\Gamma^0(\mathbf{p}, \omega_p + \omega_q; \mathbf{p}, \omega_p) = 1 - \frac{\Sigma_{\mathbf{p}}(\omega_p + \omega_q) - \Sigma_{\mathbf{p}}(\omega_p)}{\omega_q}} \quad (4.51)$$

One might raise the question of whether a similar expression could be derived for $\vec{\Gamma}$ as well. It turns out that this is possible only if we impose some quite restrictive conditions.

Theorem 5. Let $\Gamma^0(\mathbf{p} + \mathbf{q}, \omega_p + \omega_q; \mathbf{p}, \omega_p)$ and $\vec{\Gamma}(\mathbf{p} + \mathbf{q}, \omega_p + \omega_q; \mathbf{p}, \omega_p)$ be the density-density and the current-current correlation functions¹⁶. If, in the long wavelength limit $\mathbf{q} \approx 0$, these functions are analytic and $\Gamma^0(\mathbf{p} + \mathbf{q}, \omega_p + \omega_q; \mathbf{p}, \omega_p)$ is an even function of \mathbf{q} , then the following relations hold

$$\boxed{\vec{\Gamma}(\mathbf{p}, \omega_p + \omega_q; \mathbf{p}, \omega_p) = \nabla_{\mathbf{p}} \varepsilon_{\mathbf{p}} + \nabla_{\mathbf{p}} \Sigma_{\mathbf{p}}(\omega_p + \omega_q)} \quad (4.52)$$

Here, $\Sigma_{\mathbf{p}}(\omega_p)$ is the self-energy of the system, while $\varepsilon_{\mathbf{p}}$ is the noninteracting dispersion relation.

Remark 33. The first term on the right-hand side of Eq. (4.52) is equal to the free current vertex in the long wavelength limit, while the second term gives the contribution of vertex corrections.

Proof. Starting from the Ward identity (4.3), analytically continuing results to the real-frequency axis, and using the Dyson equation we see that

$$\Delta^\mu(q) \Gamma_\mu(p + q, p) = G^{-1}(p) - G^{-1}(p + q) = \varepsilon_{\mathbf{p}+\mathbf{q}} - \varepsilon_{\mathbf{p}} + \Sigma(p + q) - \Sigma(p) - \omega_q. \quad (4.53)$$

In the long wavelength limit $\mathbf{q} \rightarrow 0$ we can approximate the right-hand side using

$$\begin{aligned} \varepsilon_{\mathbf{p}+\mathbf{q}} - \varepsilon_{\mathbf{p}} &\approx \mathbf{q} \cdot \nabla_{\mathbf{p}} \varepsilon_{\mathbf{p}}, \\ \Sigma(p + q) &\approx \Sigma(\mathbf{p}, \omega_p + \omega_q) + \mathbf{q} \cdot \nabla_{\mathbf{p}} \Sigma(\mathbf{p}, \omega_p + \omega_q). \end{aligned} \quad (4.54)$$

On the other hand, the left hand side can be approximated as follows in the long wavelength limit $\mathbf{q} \rightarrow 0$

$$\Delta^\mu(q) \Gamma_\mu(p + q, p) \approx \mathbf{q} \cdot \vec{\Gamma}(\mathbf{p} + \mathbf{q}, \omega_p + \omega_q, \mathbf{p}, \omega_p) - \omega_q \Gamma^0(\mathbf{p} + \mathbf{q}, \omega_p + \omega_q, \mathbf{p}, \omega_p). \quad (4.55)$$

Up to a linear order in \mathbf{q} , using the fact that Γ^0 is an even function of \mathbf{q} , the previous expression can be written as

$$\Delta^\mu(q) \Gamma_\mu(p + q, p) \approx \mathbf{q} \cdot \vec{\Gamma}(\mathbf{p}, \omega_p + \omega_q, \mathbf{p}, \omega_p) - \omega_q \Gamma^0(\mathbf{p}, \omega_p + \omega_q, \mathbf{p}, \omega_p). \quad (4.56)$$

¹⁶Here, we abandon the 4-vector notation and switch back to the usual representation where momenta and frequencies are separated.

Plugging this back into Eq. (4.53) and grouping the terms that are of zeroth and first order with respect to \mathbf{q} , we get

$$0 = [\omega_q - \omega_q \Gamma^0(\mathbf{p}, \omega_p + \omega_q, \mathbf{p}, \omega_p) + \Sigma(\mathbf{p}, \omega_p) - \Sigma(\mathbf{p}, \omega_p + \omega_q)] + \mathbf{q} \cdot [\vec{\Gamma}(\mathbf{p}, \omega_p + \omega_q, \mathbf{p}, \omega_p) - \nabla_{\mathbf{p}} \varepsilon_{\mathbf{p}} - \nabla_{\mathbf{p}} \Sigma(\mathbf{p}, \omega_p + \omega_q)] \quad (4.57)$$

Since \mathbf{q} is arbitrary, we see that Eq. (4.52) directly follows from the previous line, which completes the proof. \square

Another consequence of the Ward identity is that we can always find the diagonal components of the renormalized vertex function

Theorem 6. *The diagonal components of the renormalized vertex function are completely determined by the self-energy of the system and read as*

$$\boxed{\begin{aligned} \vec{\Gamma}(\mathbf{p}, \omega_p; \mathbf{p}, \omega_p) &= \nabla_{\mathbf{p}} \varepsilon_{\mathbf{p}} + \nabla_{\mathbf{p}} \Sigma_{\mathbf{p}}(\omega_p), \\ \Gamma^0(\mathbf{p}, \omega_p; \mathbf{p}, \omega_p) &= 1 - \partial_{\omega_p} \Sigma_{\mathbf{p}}(\omega_p) \equiv \frac{1}{Z}. \end{aligned}} \quad (4.58)$$

Proof. Starting from Eq. (4.3), and expanding both sides to linear order in q^μ , we straightforwardly obtain Eq. (4.58). \square

Vertex Corrections in the Holstein Model: Analytical Considerations

5.1 Introduction

As discussed in Chapter 2, the mobility and the optical conductivity are completely determined by the current-current correlation function, and the latter can be calculated directly using the Feynman diagrams. In the case of the Holstein model, the first few of these diagrams are presented in Fig. 2.1, while their physical meaning was discussed in Sec. 2.4. Using the procedure we reviewed in Sec. 2.4.2, we calculated the charge mobility in Chapter 3, within the DMFT, CE, SCMA, and MA, by taking into account only the diagram in Fig. 2.1(a), known as the bubble term. However, the question of vertex corrections was not addressed at all. This is what we will do here and in the subsequent chapter. We note that although the technical aspect of our work relies on the methodology that was worked out in Refs. [1, 127], the results that we obtain about the vertex corrections in the Holstein model are an original contribution that has yet to be published.

5.2 The Limit of Weak Electron-Phonon Coupling

In Parts I and II of this thesis, we saw that for sufficiently weak electron-phonon coupling strength g , the single particle properties can be accurately described using only the (self-consistent) Migdal approximation. Therefore, one might argue that we can select the most relevant diagrams in the perturbative expansion of Fig. 2.1, where for the full fermion propagator we use the Green's function in the (SC)MA approximation, and as a result, obtain an accurate description of the transport properties in the weak coupling limit. However, such analysis requires caution, as there are two questions that one needs to address: i) which diagrams in Fig. 2.1 are the most relevant, that should be included in our calculations? ii) can we guarantee that the approximations that we use are in accordance with the Ward identity (see Chapter 4), i.e., with the conservation of electric charge? We will initially focus on the second question, in the cases when the single-particle properties are described by the MA and SCMA. These will be investigated in Secs. 5.2.1 and 5.2.2, respectively, where we will conclude that for the Ward identity to be satisfied it is sufficient to take the bubble approximation, both in the MA and SCMA case. Then, we will come back to the first question in Sec. 5.2.3, in the context of mobility. We will find all Feynman diagrams that contribute in the leading order (with respect to g) to mobility and prove that all of them are vanishing. This shows that there are no vertex corrections of mobility in the weak coupling limit, and its accurate description can be obtained using the bubble approximation within the SCMA.

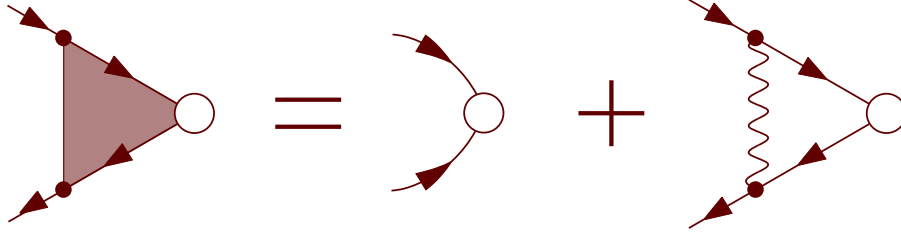


Figure 5.1: Renormalized vertex function Γ^μ needed for the Ward identity to be satisfied within the Migdal approximation.

5.2.1 The Migdal Approximation and the Ward Identity

Let us now investigate which diagrams should be included in the vertex corrections, for the Ward identity to be satisfied, if the single-particle properties are described using the Migdal approximation. Starting from Eq. (4.3), we see that¹

$$\begin{aligned}\Delta(q)^\mu \Gamma_\mu(p+q, p) &= G_{\text{MA}}^{-1}(p) - G_{\text{MA}}^{-1}(p+q) \\ &= \Sigma_{\text{MA}}(p+q) - \Sigma_{\text{MA}}(p) + \varepsilon_{\mathbf{p}+\mathbf{q}} - \varepsilon_{\mathbf{p}} - q^0 \\ &\approx \Sigma_{\text{MA}}(p+q) - \Sigma_{\text{MA}}(p) + \Delta(q)^\mu \gamma_\mu(\mathbf{p} + \mathbf{q}, \mathbf{p}).\end{aligned}\quad (5.1)$$

In the last line we used the Ward identity for the free theory; see Eq. (C.125). Furthermore, using Eq. (2.16) from Part I, we can express the self-energy in the Migdal approximation as² $\Sigma_{\text{MA}}(p) = -\frac{g^2}{N\beta} \sum_k D(p-k)G_0(k)$, where G_0 is the free propagator. Hence

$$\begin{aligned}\Delta(q)^\mu \Gamma_\mu(p+q, p) &= -\frac{g^2}{N\beta} \sum_k [D(p+q-k)G_0(k) - D(p-k)G_0(k)] \\ &\quad + \Delta(q)^\mu \gamma_\mu(\mathbf{p} + \mathbf{q}, \mathbf{p}).\end{aligned}\quad (5.2)$$

Using the substitution $k \rightarrow k+q$ in the first term, we get

$$\begin{aligned}\Delta(q)^\mu \Gamma_\mu(p+q, p) &= -\frac{g^2}{N\beta} \sum_k D(p-k) [G_0(k+q) - G_0(k)] + \Delta(q)^\mu \gamma_\mu(\mathbf{p} + \mathbf{q}, \mathbf{p}) \\ &= -\frac{g^2}{N\beta} \sum_k D(p-k)G_0(k+q)G_0(k) [G_0^{-1}(k) - G_0^{-1}(k+q)] \\ &\quad + \Delta(q)^\mu \gamma_\mu(\mathbf{p} + \mathbf{q}, \mathbf{p}).\end{aligned}\quad (5.3)$$

If we once again use the Ward identity for the free theory (see Eq. (C.125)), on the terms in the square bracket, the previous expression becomes

$$\begin{aligned}\Delta(q)^\mu \Gamma_\mu(p+q, p) &= \Delta(q)^\mu \left[\gamma_\mu(\mathbf{p} + \mathbf{q}, \mathbf{p}) - \frac{g^2}{N\beta} \sum_k D(p-k) \right. \\ &\quad \left. \times G_0(k+q)G_0(k)\gamma_\mu(\mathbf{k} + \mathbf{q}, \mathbf{k}) \right].\end{aligned}\quad (5.4)$$

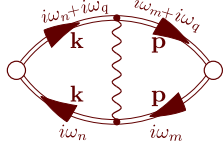
While this expression does not uniquely determine Γ^μ , we can nevertheless conclude that the solution

$$\Gamma_\mu(p+q, p) = \gamma_\mu(\mathbf{p} + \mathbf{q}, \mathbf{p}) - \frac{g^2}{N\beta} \sum_k D(p-k)G_0(k+q)G_0(k)\gamma_\mu(\mathbf{k} + \mathbf{q}, \mathbf{k}),\quad (5.5)$$

¹We use the standard four-notation; see Secs. C.7 and 4.1.

²The Feynman rules are given in Fig. 2.1 of Part I.

is in accordance with the Ward identity. Diagrammatically, this Γ^μ can be represented as in Fig 5.1, which corresponds to the diagrams for χ_{jj} shown in Figs. 2.1(a) and 2.1(b). The first term in Eq. (5.5) is the free current vertex (it corresponds to the first term on the right-hand side of Fig 5.1 and to the χ_{jj} diagram in Fig. 2.1(a)), while the second term is the vertex correction (it corresponds to the second term on the right-hand side of Fig 5.1 and to the χ_{jj} diagram in Fig. 2.1(b)). In the long-wavelength limit $\mathbf{q} \rightarrow 0$, the vertex correction term (i.e., the diagram in Fig. 2.1(b)) is not contributing, as seen from



$$\propto \sum_{\mathbf{k}} G(\mathbf{k}, i\omega_n) G(\mathbf{k}, i\omega_n + i\omega_q) \gamma_i(\mathbf{k}, \mathbf{k}) = 0. \quad (5.6)$$

The previous expression is zero since $G(\mathbf{k})$ is an even function of momenta, $\gamma_i(\mathbf{k}, \mathbf{k})$ is odd, while the phonon propagator does not depend on momenta at all. We note that this is only true in the long wavelength limit $\mathbf{q} \rightarrow 0$. Otherwise, Eq. (5.6) would contain terms of the form $G(\mathbf{k} + \mathbf{q})$, that would not be even under the transformation $\mathbf{k} \rightarrow -\mathbf{k}$. Therefore, the presented analysis proves that in the long wavelength limit $\mathbf{q} \rightarrow 0$, the Ward identity is satisfied if the current-current correlation function is calculated in the bubble approximation, while the single-particle properties are calculated in the Migdal approximation.

5.2.2 The Self-Consistent Migdal Approximation and the Ward Identity

Let us now repeat our analysis, investigating which diagrams should be included in the vertex corrections, for the Ward identity to be satisfied, if the single-particle properties are now described using the self-consistent Migdal approximation. This is very similar to the Migdal approximation, which we already thoroughly examined in Sec. 5.2.1. We again start from Eq. (4.3), this time in the case $\Sigma = \Sigma_{\text{SCMA}}$

$$\begin{aligned} \Delta(q)^\mu \Gamma_\mu(p + q, p) &= G_{\text{SCMA}}^{-1}(p) - G_{\text{SCMA}}^{-1}(p + q) \\ &= \Sigma_{\text{SCMA}}(p + q) - \Sigma_{\text{SCMA}}(p) + \Delta(q)^\mu \gamma_\mu(\mathbf{p} + \mathbf{q}, \mathbf{p}). \end{aligned} \quad (5.7)$$

In the SCMA, the self-energy is given by the Feynman diagram in Fig. 2.4(a) from Part II. Using the Feynman rules, given in Fig. 2.1 from Part I, we see that it can be written as follows

$$\Sigma_{\text{SCMA}}(p) = -\frac{g^2}{N\beta} \sum_k D(p - k) G_{\text{SCMA}}(k). \quad (5.8)$$

Since this is completely analogous to the expressions we had in Sec. 5.2.1, we deduce that Eq. (5.3), upon substituting $G_0 \rightarrow G_{\text{SCMA}}$, remains valid

$$\begin{aligned} \Delta(q)^\mu \Gamma_\mu(p + q, p) &= \Delta(q)^\mu \gamma_\mu(\mathbf{p} + \mathbf{q}, \mathbf{p}) - \frac{g^2}{N\beta} \sum_k D(p - k) \\ &\quad \times G_{\text{SCMA}}(k + q) G_{\text{SCMA}}(k) [G_{\text{SCMA}}^{-1}(k) - G_{\text{SCMA}}^{-1}(k + q)]. \end{aligned} \quad (5.9)$$

The terms in the square brackets can be written in terms of the renormalized vertex function, using the Ward identity (see Eq. (4.3))

$$\begin{aligned} \Delta(q)^\mu \Gamma_\mu(p + q, p) &= \Delta(q)^\mu [\gamma_\mu(\mathbf{p} + \mathbf{q}, \mathbf{p}) - \frac{g^2}{N\beta} \sum_k D(p - k) \\ &\quad \times G_{\text{SCMA}}(k + q) G_{\text{SCMA}}(k) \Gamma_\mu(k + q, k)]. \end{aligned} \quad (5.10)$$

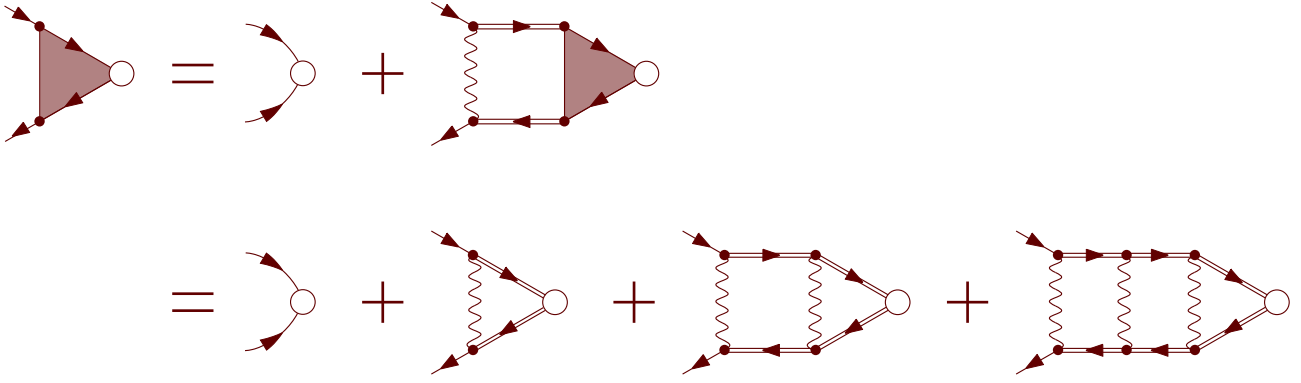


Figure 5.2: Renormalized vertex function Γ^μ needed for the Ward identity to be satisfied within the self-consistent Migdal approximation.

Thus, we can read off that the following solution for the renormalized vertex function is in accordance with the Ward identity

$$\Gamma_\mu(p+q, p) = \gamma_\mu(\mathbf{p} + \mathbf{q}, \mathbf{p}) - \frac{g^2}{N\beta} \sum_k D(p-k) G_{\text{SCMA}}(k+q) G_{\text{SCMA}}(k) \Gamma_\mu(k+q, k). \quad (5.11)$$

This is an equation for Γ_μ , which needs to be solved self-consistently. Diagrammatically, this Equation can be represented as the first line in Fig. 5.2, while the second line represents the corresponding solution, known as the *ladder approximation*, that is obtained by the iterative application of Eq. (5.11) on itself. In terms of the diagrams for the current-current correlation function, it is represented as the sum of diagrams in Figs. 2.1(a) and 2.1(b), as well as the higher order diagrams which are obtained by adding vertical phonon lines that connect particle and hole propagators. Hence, within this approach, the vertex corrections are determined by the ladder diagrams. However, each of these diagrams is vanishing in the long-wavelength limit $\mathbf{q} \rightarrow 0$, as seen from

$$\begin{array}{c} \text{Diagram: A vertex with two fermion lines (momentum } \mathbf{k} \text{) and a phonon line (momentum } \mathbf{q} \text{). The fermion lines are labeled } i\omega_n \text{ and } i\omega_n + i\omega_q \text{, and the phonon line is labeled } i\omega_n \text{. The vertex is shaded.} \end{array} \propto \sum_{\mathbf{k}} G(\mathbf{k}, i\omega_n) G(\mathbf{k}, i\omega_n + i\omega_q) \gamma_i(\mathbf{k}, \mathbf{k}) = 0. \quad (5.12)$$

This can be understood by noting that the phonon line in the Feynman diagram carries the momentum, but the phonon propagator is actually momentum independent. Hence, we see that only the left current vertex and the two fermion Green's functions, which we see in the Figure above, depend on \mathbf{k} . Since the fermion Green's functions are an even function of \mathbf{k} , and the current vertex is odd, we conclude that Eq. (5.12) must be vanishing due to the sum over \mathbf{k} . This completes our analysis, which proves that in the long wavelength limit $\mathbf{q} \rightarrow 0$, the Ward identity is satisfied if the current-current correlation function is calculated in the bubble approximation, while the single-particle properties are calculated in the self-consistent Migdal approximation.

Remark 34. In our analysis, we always restricted ourselves to the long wavelength case $\mathbf{q} \approx 0$.

5.2.3 Vertex Corrections of Mobility in the Weak Coupling Limit

Estimating the contribution of vertex corrections in the exact solution requires summing up all the diagrams in the perturbative expansion (see Fig. 2.1), and comparing the obtained results to the one we would obtain using only the bubble approximation. For some of these vertex correction diagrams, we can immediately see that they are not contributing in the limit of long wavelengths $\mathbf{q} \rightarrow 0$. As we

have already seen, this was the case for the ladder diagrams, which turned out to be vanishing due to the fact that the phonon propagator is momentum independent, while the Green's function and the free current vertex turned out to be even and odd, respectively, under the transformation $\mathbf{k} \rightarrow -\mathbf{k}$. In a completely analogous way, we can see that the diagram in Fig. 2.1(c), as well as its higher-order counterparts (i.e., the ring diagrams), are also zero in the limit $\mathbf{q} \rightarrow 0$. Yet, evaluating other diagrams, can be more complex. Luckily, since we are interested only in the mobility in the weak coupling regime, it is not necessary to evaluate each of these diagrams exactly. Instead, for a given vertex correction diagram, it is sufficient to take into account only the leading order term³, with respect to the electron-phonon coupling strength, which scales as g^{-2} [1]. This significantly simplifies our analysis, as the vast majority of diagrams are not contributing in the leading order $\sim g^{-2}$, and we thus need to find only those that do. Let us now analyze the scaling, with respect to g , of different diagrams.

To accomplish this, let us first note that for sufficiently weak coupling, the spectral function and its square can be approximated as in Eqs. (3.9) and (3.10), while the lifetime τ_k scales as g^{-2} , as seen from Eq. (3.45) of Part II. This implies that $A_k \sim g^0$ and $A_k^2 \sim g^{-2}$, which in conjunction with Eq. (2.53) directly leads to the conclusion that the bubble term of mobility does in fact scale as g^{-2} , in the leading order. The vertex correction diagrams can be analyzed in a similar way, with additional notes that: i) $\text{Re}G \sim g^0$ ii) the leading order term in $(\text{Re}G)^2$ scales as g^{-2} iii) each phonon propagator introduces a factor of $D \sim g^2$. Therefore, out of all vertex correction diagrams with n phonon propagators, the leading order contribution (with respect to g) will be given by the ones in which each of $2(n+1)$ fermion propagators has a pair with the same 4-momentum. A contribution of such diagram would have the same scaling as the bubble term, since $g^{2n} \cdot g^{-2(n+1)} \sim g^{-2}$. However, all such diagrams (ladder diagrams, ring diagrams) are vanishing. Hence, we conclude that there are no vertex corrections to the mobility in the weak coupling limit of the Holstein model. Since the SCMA gives an accurate single-particle description of the Holstein model in the weak coupling limit, and since the bubble approximation within SCMA is in accordance with the Ward identity, we conclude that the mobility in the weak coupling limit is accurately described using the bubble approximation within SCMA.

5.3 Vertex Corrections in the Atomic Limit

Let us now investigate the importance of vertex corrections in the vicinity of the atomic limit (small $t_0 \approx 0$). First we note that every Feynman diagram for the current-current correlation function has two current vertices, and each of them is already proportional to t_0 . Thus, in the lowest order perturbation theory with respect to the hopping parameter t_0 , all the other elements of the Feynman diagrams (fermion and phonon propagators) can be taken to be strictly at the atomic limit. Both of these propagators are analytically known and are of course \mathbf{k} independent at the atomic limit. As a consequence, all the \mathbf{k} dependence is in the current vertex, which is an odd function of \mathbf{k} . Since the \mathbf{k} is summed over, we conclude that all vertex corrections are vanishing. The bubble part is nevertheless still nonzero, as there are two current vertices with same \mathbf{k} , giving an overall even function, which as a consequence does not vanish after the summation over \mathbf{k} is performed.

³This is justified, since the mobility in the bubble approximation, in the weak coupling limit, as we will see in the text below, also scales as g^{-2} .

Vertex Corrections in the Holstein Model: Numerical Considerations

6.1 Introduction and Benchmarks

In the last chapter, we concluded that the vertex corrections of the mobility in the Holstein model are vanishing in the weak coupling and atomic limits. However, so far, we do not know anything outside of these two limiting cases. This is why we now continue our analysis by numerically examining the significance of vertex corrections in a wide range of regimes. We note that in this chapter the central quantity of our interest is the optical conductivity, which provides more information than the mobility alone. The quality of our analysis is restricted by the quality of the results that we are able to acquire for both exact optical conductivity, as well as the optical conductivity in the bubble approximation. As detailed in Chapter 2, the calculation of exact optical conductivity can be reduced to the calculation of the current-current correlation function. Nevertheless, this is highly nontrivial to evaluate. Calculations on the imaginary axis are possible [50, 129], but analytic continuation to the real axis presents a formidable obstacle. This is why real-time (or frequency) methods are often preferred. One such method is the momentum-space hierarchical equations of motion (HEOM), which was developed very recently by Janković [49]. Using HEOM, it is possible to obtain numerically exact results for the current-current correlation function in the 1D Holstein model. This is currently a state-of-the-art method that represents a natural generalization of the HEOM method that was used for the calculation of single-particle properties; see Sec. 2.5.1 of Part II and Ref. [83].

On the other hand, using the fact that the DMFT neglects the vertex corrections (see Sec. 2.5 and Ref. [122]), but gives very accurate spectral functions, we see that those can be used in Eq. (2.52) to obtain practically exact results for the optical conductivity in the bubble approximation. Therefore, the discrepancy between DMFT and HEOM results serves as a measure of the importance of the vertex corrections.

Remark 35. *One of the reasons why our analysis of vertex corrections is important is because in contrast to model Hamiltonians, the numerically exact approaches are not possible in real materials, and the calculation of the optical conductivity thus requires the use of approximate methods. The bubble approximation is commonly employed, but the contribution of vertex corrections largely remains unknown. In fact, even for model Hamiltonians, the contribution of vertex corrections in a wide range of parameter regimes is often unknown, although some progress has been made [130]. We now have a unique opportunity to gain some intuition about these questions in one particular system - the Holstein model.*

To obtain the DMFT results, we first use the algorithm from Fig. 1.2 of Part II to obtain the self-energy and spectral functions, and then we calculate the optical conductivity normalized to the concentration of charge carriers using Eq. (2.52). As for the numerical calculation of mobility (see

Chapter 3), the exponential factor $e^{-\beta\omega'}$ in Eq. (2.52) causes numerical instabilities, forcing us to introduce negative frequency cutoff $\int_{-\infty}^{\infty} \rightarrow \int_{-\Lambda}^{\infty}$ for the calculation of integrals. The calculation is repeated for different values of parameter Λ , which is decreased until the results fully converge. In addition, we also check that the results converge with respect to the number of k points used in Eq. (2.52), which need to be large enough in order to faithfully represent the thermodynamic limit. If the results have not fully converged, this can often be reflected in the optical sum rule (see Eq. (2.35))

$$\int_{-\infty}^{\infty} d\omega \mu(\omega) = \frac{\pi}{N} \sum_k 2t_0 \cos k \int_{-\infty}^{\infty} d\omega A_k(\omega) e^{-\beta\omega}, \quad (6.1)$$

which we also always check to be satisfied. The current-current correlation function on the real and imaginary time axis is then obtained simply using Eqs. (2.20) and (2.21).

We note that, as for the single-particle properties (see Sec. 2.5.1 of Part II), the HEOM method for the calculation of the current-current correlation function requires convergence with respect to two parameters: the number of lattice sites N , and the maximum hierarchy depth D . However, numerical problems arise if the electron-phonon coupling constant is too strong, if the temperature is too low, or if the phonon frequency is too small.

In addition to HEOM, we also use the QMC method [129] to crosscheck our results. Within this method, the current-current correlation function is calculated directly, on both the real and imaginary time axis. However, in practice, it is not always possible to obtain these results for large enough times t , required for the use of Eq. (2.11) and extraction of the optical conductivity. This is why the QMC will only be used as a benchmark for the current-current correlation functions.

Remark 36. *We note that Veljko Janković has not only developed the methodology for the HEOM method, but has also generated all the data we will be using in this thesis as a benchmark. On the other hand, the QMC data that we use were provided to us by Nenad Vukmirović and Suzana Miladić, as a result of their joint work.*

6.2 Optical Conductivity in the Weak Coupling Regime

In Chapter 5, we analytically proved that the vertex corrections of mobility are vanishing in the weak coupling limit. Here, we use numerical calculations of the optical conductivity and the current-current correlation function to support those findings. The results are shown in Fig. 6.1.

Remark 37. *The optical conductivity will always be normalized to the concentration of charge carriers n_e , and such quantity will be denoted by $\mu(\omega)$ (earlier this was sometimes denoted by $\mu_{\alpha\alpha}(\omega)$). This will not always be emphasized, but it is nevertheless something one could guess, since we are working in the limit $n_e \rightarrow 0$.*

We see that the DMFT is in excellent agreement with HEOM and QMC benchmarks. In Fig. 6.1(b₁), there seems to be a tiny discrepancy between the HEOM and DMFT results. However, even this difference is not due to the vertex corrections, but actually due to the finite-size effects. To prove this, we implemented the DMFT on a lattice with a finite number of lattice sites N . The results are shown in Fig. 6.2. As we see, the DMFT results for $N = 160$ (which is the same as used in HEOM; see Table 6.1) are not fully converged, but they are on the verge of doing so. In addition, the difference between the DMFT results for $N = 160$ and $N = 300$ looks very similar to the difference between HEOM and DMFT in Fig. 6.1(b₁). On the other hand, Fig. 6.2 demonstrates that $N = 160$ is sufficient for the imaginary part of the current-current correlation function to converge. This is in accordance with Fig. 6.1(c₁). Thus, taking everything into account, we conclude that the discrepancy in Fig. 6.1(b₁) must be due to the finite-size effects.

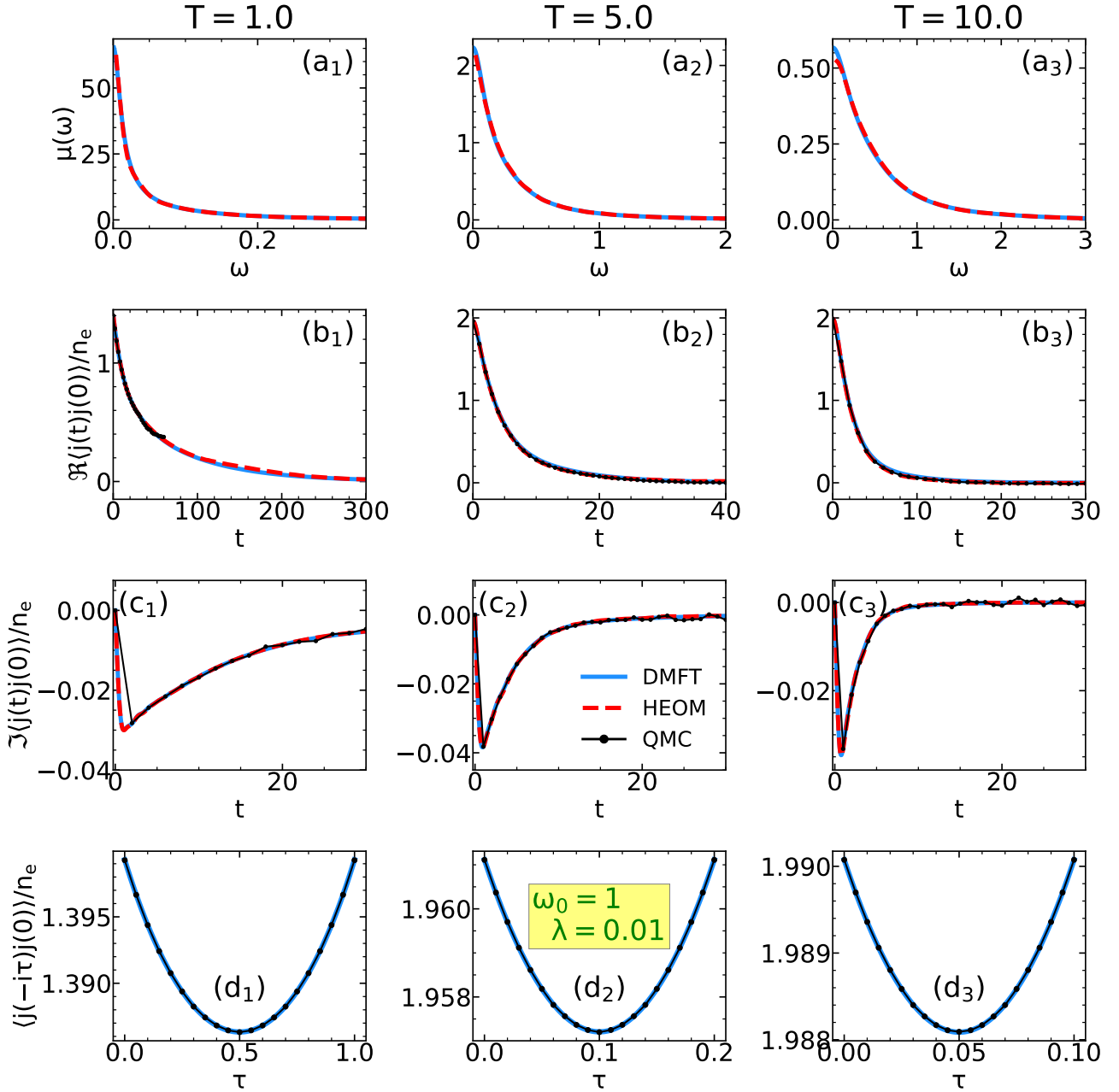


Figure 6.1: Optical conductivities and current-current correlation functions in real and imaginary times in the weak coupling limit $\omega_0 = 1$, $\lambda = 0.01$. All quantities are normalized to the concentration of charge carriers.

Table 6.1: Number of lattice sites N and the maximum hierarchy depth D that correspond to HEOM/QMC results in Fig. 6.1.

Parameters	N_{HEOM}	D_{HEOM}	N_{QMC}
$\omega_0 = 1$ $\lambda = 0.01$ $T = 1.0$	160	2	60
$\omega_0 = 1$ $\lambda = 0.01$ $T = 5.0$	40	3	60
$\omega_0 = 1$ $\lambda = 0.01$ $T = 10.0$	40	3	60

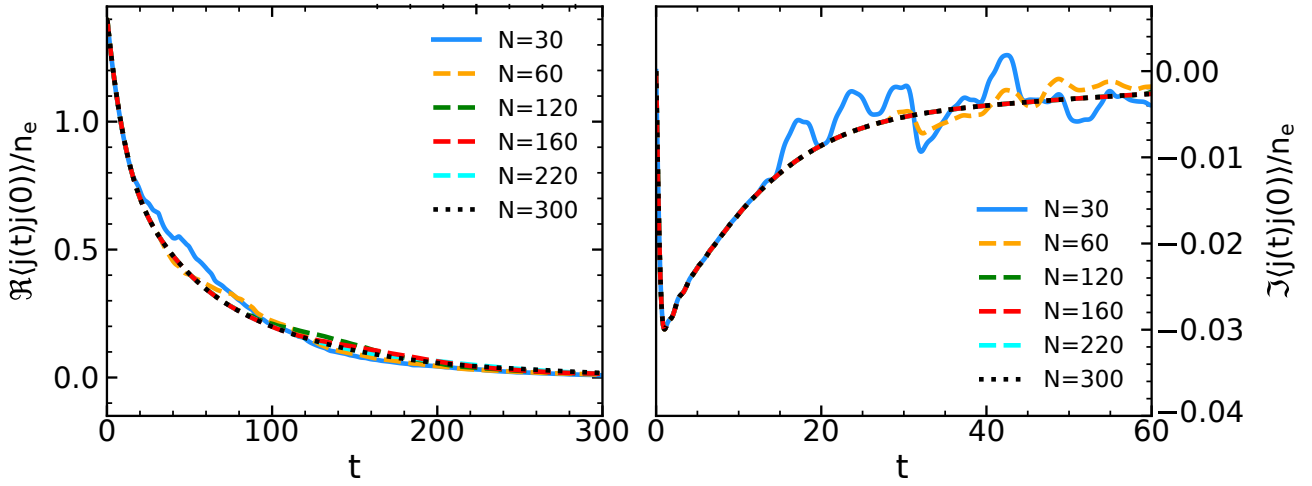


Figure 6.2: Finite-size effects in the current-current correlation function for $\omega_0 = 1$, $\lambda = 0.01$, and $T = 1$.

6.3 Optical Conductivity for Intermediate and Strong Electron-Phonon Coupling

The results for intermediate coupling are presented in Figs. 6.3 and 6.4, while the corresponding values of HEOM/QMC chain lengths and maximum hierarchy depth are displayed in Table 6.2. We observe that the vertex corrections are substantial for $\lambda = 0.5$ (see Figs. 6.3(a₁)–6.3(a₂)). A discrepancy between the DMFT and HEOM/QMC results is also evident in Figs. 6.3(b₁)–6.3(b₂) and Figs. 6.3(c₁)–6.3(c₂). However, the DMFT and QMC data for the imaginary-time current-current correlation function are in very good agreement; see Figs. 6.3(d₁)–6.3(d₂). Looking at it the other way around, we conclude that a tiny change in the imaginary axis data can lead to an enormous difference in the real axis data. This demonstrates why it is extremely difficult to extract reliable information about the optical conductivity from the data on the imaginary-time (or frequency) axis, and why real-time (or frequency) methods are often preferred. From now on, we will not be showing any results of the imaginary-time correlation functions.

For $\lambda = 1$ we observe that vertex corrections in $\mu(\omega)$ are also considerable, but it seems that the difference between DMFT and HEOM predictions is not as drastic for $\mu(\omega = 0)$; see Figs. 6.4(a₁)–6.4(a₂). However, we should keep in mind that the temperature in both of these regimes is relatively high, and that the comparison for lower temperatures cannot be performed due to the unavailability of the HEOM results. In fact, in Fig. 6.3 we could observe that although HEOM predicted a huge correction for $\mu_{\text{DMFT}}(\omega = 0)$ at $T = 1$, the relative difference between $\mu_{\text{DMFT}}(\omega = 0)$ and $\mu_{\text{HEOM}}(\omega = 0)$ was drastically reduced at $T = 10$. Another interesting feature that we point out is that vertex corrections can both increase and decrease the bubble mobility: $\mu_{\text{HEOM}}(\omega = 0) > \mu_{\text{DMFT}}(\omega = 0)$ at Fig. 6.4(a₁), while $\mu_{\text{DMFT}}(\omega = 0) > \mu_{\text{HEOM}}(\omega = 0)$ at Fig. 6.4(a₂).

An analysis that we have now presented unfortunately cannot be easily repeated in the case of strong electron-phonon coupling $\lambda = 2$, as the HEOM data are not available. Therefore, we only present the DMFT and QMC results in Fig. 6.5. We see that while the DMFT is in agreement with QMC for small t , the difference between these methods can be observed for larger times. However, it is hard to quantitatively estimate the significance of vertex corrections in this case for $\mu(\omega)$, as accurate QMC results are not available for long enough times.

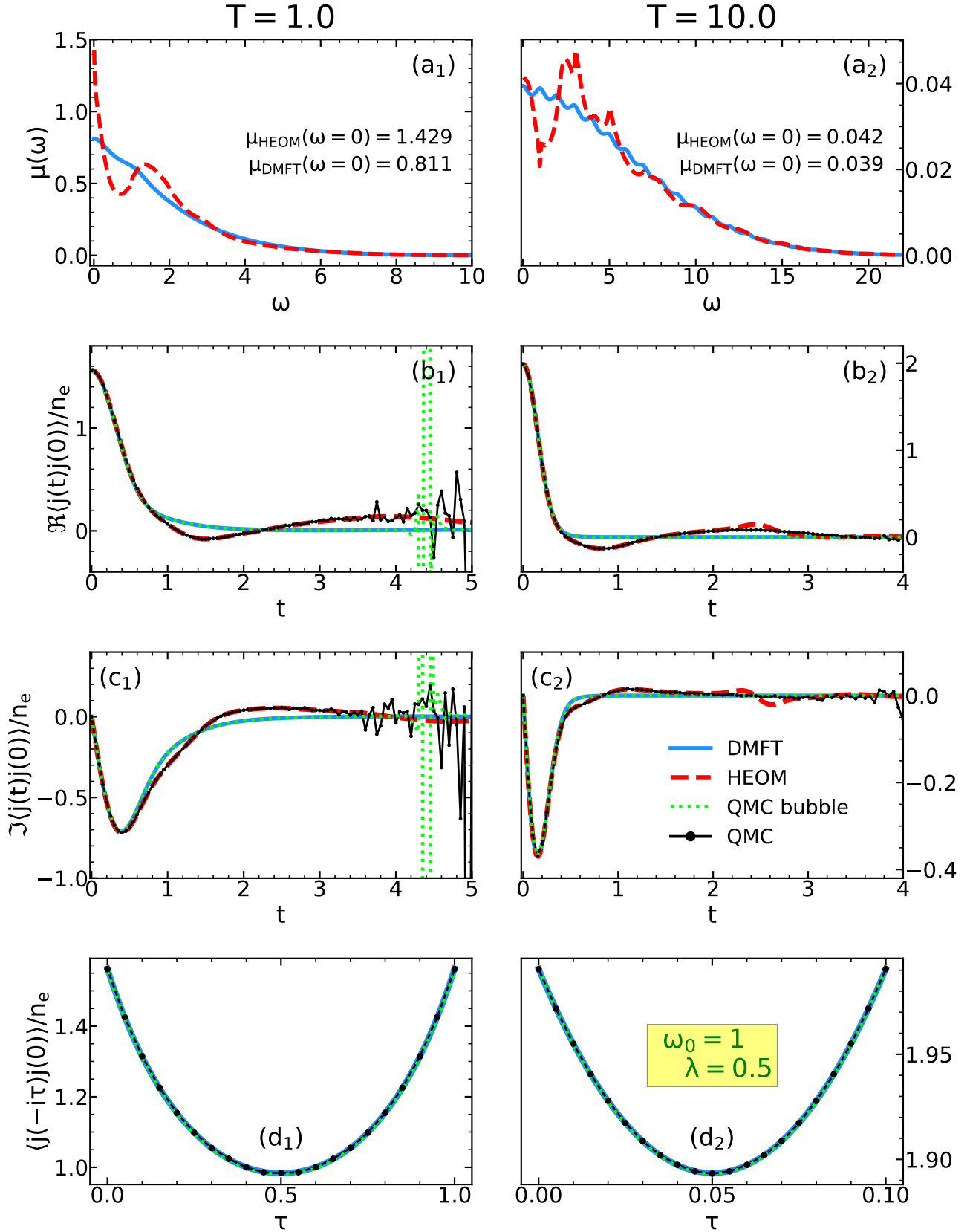


Figure 6.3: Optical conductivities and current-current correlation functions in real and imaginary times in the intermediate coupling regime $\omega_0 = 1.0$, $\lambda = 0.5$. All quantities are normalized to the concentration of charge carriers.

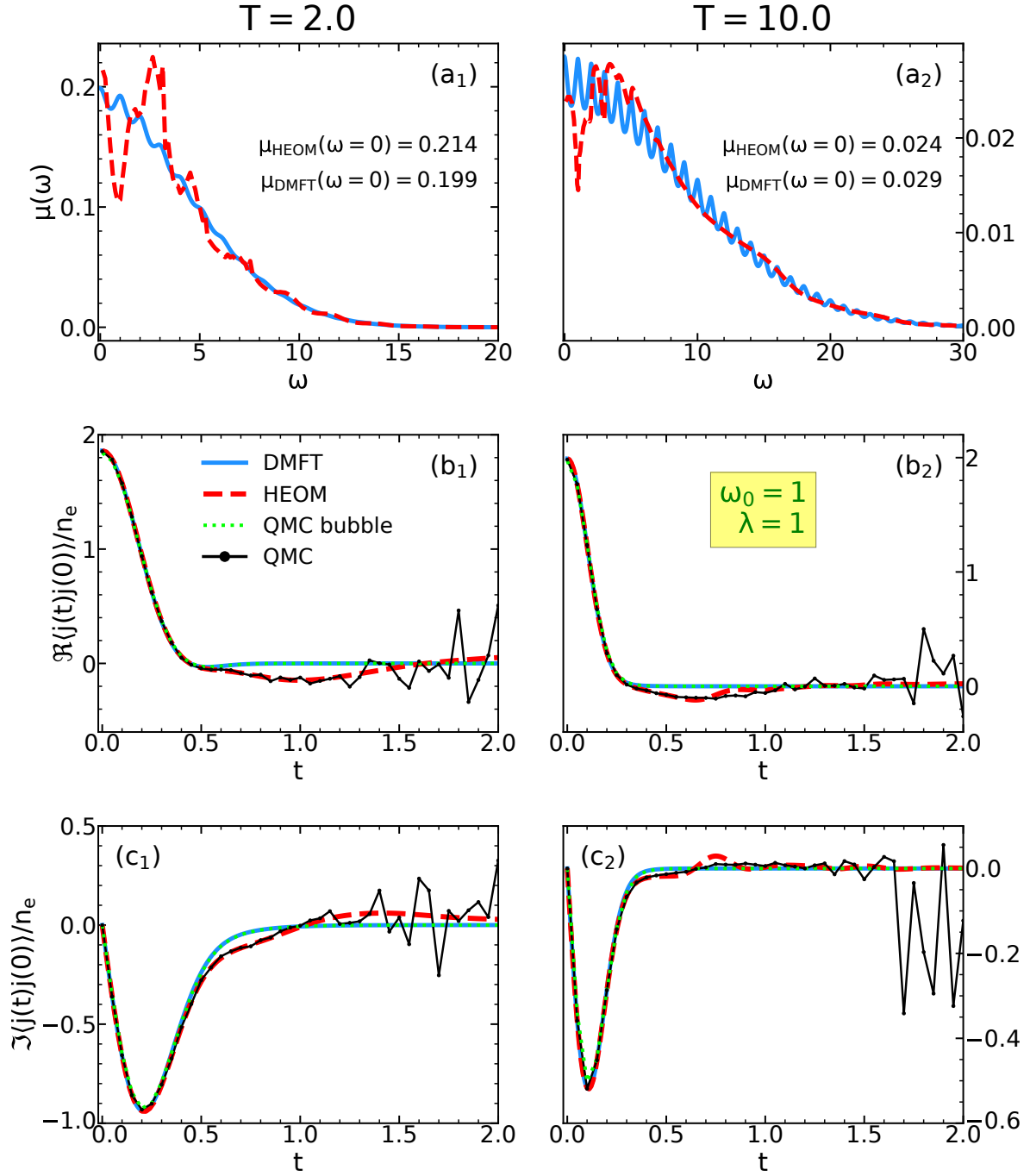


Figure 6.4: Optical conductivities and real-time current-current correlation functions in the intermediate coupling regime $\omega_0 = 1.0$, $\lambda = 1.0$. All quantities are normalized to the concentration of charge carriers.

Table 6.2: Number of lattice sites N and the maximum hierarchy depth D that correspond to HEOM/QMC results in Figs. 6.3 and 6.4.

Parameters	N_{HEOM}	D_{HEOM}	N_{QMC}
$\omega_0 = 1$ $\lambda = 0.5$ $T = 1.0$	13	6	10
$\omega_0 = 1$ $\lambda = 0.5$ $T = 10.0$	5	21	10
$\omega_0 = 1$ $\lambda = 1.0$ $T = 2.0$	7	12	7
$\omega_0 = 1$ $\lambda = 1.0$ $T = 10.0$	7	12	7

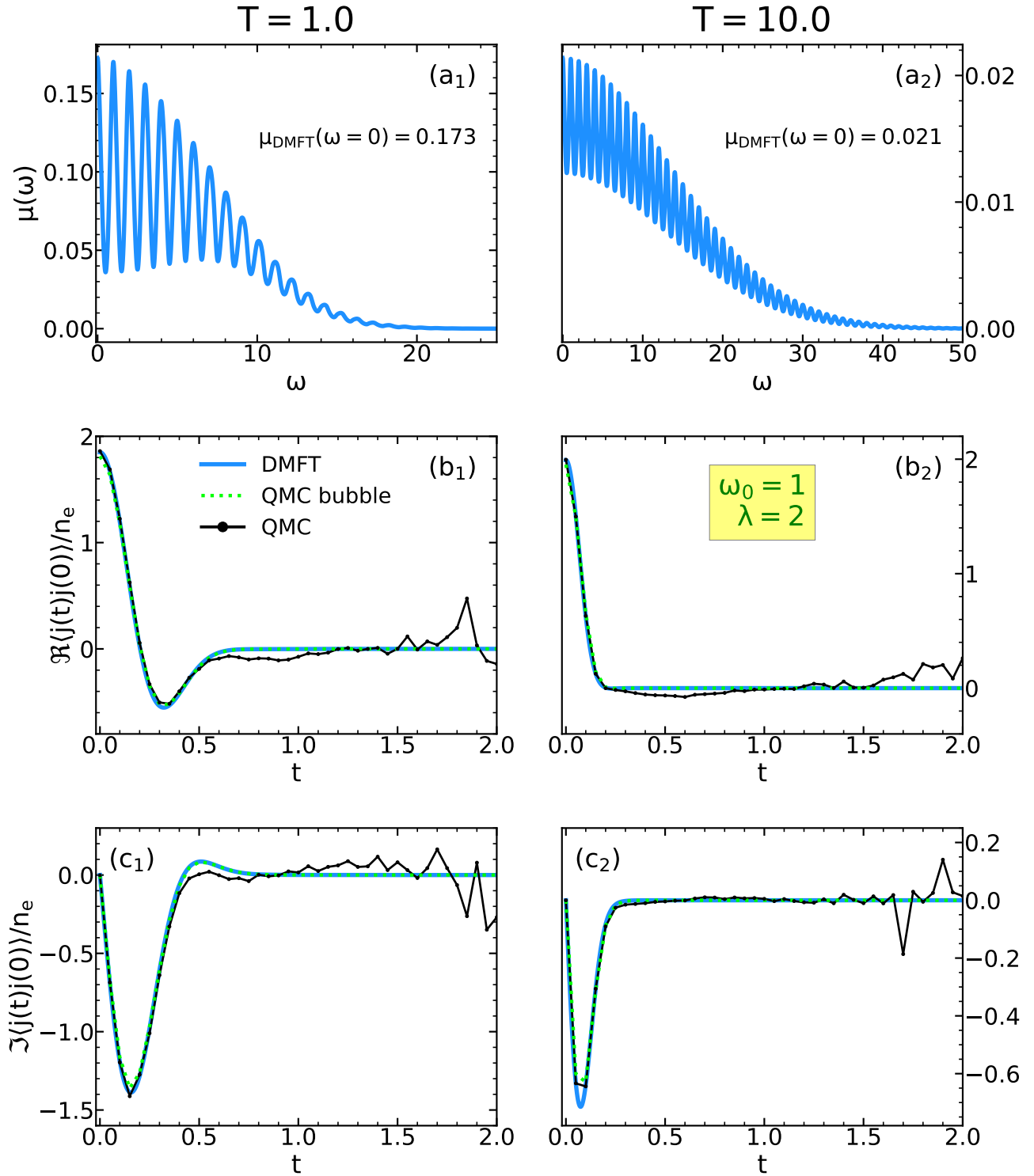


Figure 6.5: Optical conductivities and real-time current-current correlation functions in the strong coupling regime $\omega_0 = 1.0$, $\lambda = 2.0$. All quantities are normalized to the concentration of charge carriers. Here, $N_{\text{QMC}} = 10$.

6.4 Optical Conductivity Close to the Adiabatic Limit

Let us now investigate the optical conductivity close to the adiabatic limit (i.e., the case when ω_0 is small). In this regime, the constituents of crystal lattice¹ oscillate slowly around their equilibrium position, causing the electron to observe a disordered system on a short timescale $t \lesssim \omega_0^{-1}$. However, this is a *dynamical* disorder. As a consequence, there is no Anderson localization, and the electrons' motion starts being diffusive for large times $t \gg \omega_0^{-1}$. This is relevant for the study of organic semiconductors, as the oscillations of their composing molecules are slow due to their large masses and weak restoring Van der Waals forces. The mobility in these systems is described using the so-called transient localization scenario [124] that takes into account both the short- and long-time behavior of electrons. Although an interesting idea for future work, we will not apply the transient localization scenario in our analysis, but will instead focus on the behavior of the system at timescales² $t \lesssim \omega_0^{-1}$, which can be described using only the static disorder. Therefore, our description of optical conductivity will be inadequate for $\omega \lesssim \omega_0$ (we will get Anderson insulator for $\omega = 0$), but the predictions for $\omega \gtrsim \omega_0$ will be quite reliable. This will hopefully enable us to reproduce one of the characteristic features, which is the finite frequency peak in optical conductivity (also called the displaced Drude peak) [49, 124]. This will be an important crosscheck for HEOM results.

6.4.1 Replacing Phonons with Static Disorder

From the electron's point of view, the molecules constituting the crystal lattice look like a static disorder on short timescales $t \lesssim \omega_0^{-1}$, because they are displaced from their equilibrium positions, but do not have enough time to move. Stated more formally, in this case, it is possible to remove the phonons from the Hamiltonian, and replace them with a single particle random potential that is diagonal in the coordinate space. This can be seen by rewriting the interaction term of the Hamiltonian as follows

$$H_{\text{el-ph}} = -g \sum_i (a_i + a_i^\dagger) n_i = -g \sqrt{2\omega_0} \sum_i X_i n_i, \quad (6.2)$$

where $n_i = c_i^\dagger c_i$, while X_i is the coordinate operator of i -th molecule. In the case we are considering $t \lesssim \omega_0^{-1}$, the operator X_i in Eq. (6.2) can be treated classically by replacing it with a random variable with an appropriate probability distribution $p(x)$. Then, the calculation of arbitrary quantity requires repeating the calculation for many different classical realizations X_i (taken from probability distribution $p(x)$), and averaging the end result.

Since we are working in the limit of vanishing electron concentration, $p(x)$ is actually solely determined by the phononic part of the Hamiltonian

$$H_{\text{ph}} = \omega_0 a^\dagger a, \quad (6.3)$$

and is thus given by

$$p(x) = \frac{1}{\mathcal{Z}_p} \sum_{n=0}^{\infty} e^{-\beta n \omega_0} |\langle x | \psi_n \rangle|^2 = \frac{1}{\mathcal{Z}_p} \langle x | \underbrace{\sum_{n=0}^{\infty} e^{-\beta n \omega_0} |\psi_n \rangle \langle \psi_n|}_{\equiv e^{-\beta H}} | x \rangle = \frac{1}{\mathcal{Z}_p} \langle x | e^{-\beta H_{\text{ph}}} | x \rangle, \quad (6.4)$$

where \mathcal{Z}_p is the partition function and ψ_n are the eigenstates of Eq. (6.3) (i.e., they are Hermite functions). From Eq. (6.4) we see that $p(x)$ is just a density matrix of the harmonic oscillator in coordinate representation, which can be found in many books [131–133]. We follow along Ref [131], and formulate:

¹In the remaining part of this chapter, the constituents of crystal lattice will be simply referred to as molecules (as it is the case for organic semiconductors).

²In the Fourier space, this corresponds to frequencies $\omega \gtrsim \omega_0$.

Theorem 7. *The probability distribution $p(x)$ is a Gaussian*

$$p(x) = \frac{1}{\sigma\sqrt{2\pi}} e^{-\frac{x^2}{2\sigma^2}}, \quad \sigma^2 = \frac{1}{2\omega_0} \operatorname{cth} \left(\frac{\beta\omega_0}{2} \right). \quad (6.5)$$

Proof. We start from Eq. (6.3), and drop the term $\frac{1}{\mathcal{Z}_p}$, which is justified as long as we normalize $p(x)$ at the end of the calculation. Since $p(x)$ is no longer normalized, it does not provide any useful information for a single value of x . This is why we want to examine its value when we vary the argument, i.e. $p(x + dx)$. It can be expressed using the momentum operator P as follows

$$p(x + dx) = \langle x + dx | e^{-\beta H_{\text{ph}}} | x + dx \rangle = p(x) + idx \langle x | [P, e^{\beta H_{\text{ph}}}] | x \rangle. \quad (6.6)$$

This was obtained using the fact that the momentum operator is the generator of the translations

$$|x + dx\rangle = e^{-idxP} |x\rangle \approx (1 - idxP) |x\rangle. \quad (6.7)$$

Our task is thus reduced to the calculation of the second term in Eq. (6.6). This could be easily accomplished if there was the coordinate operator instead of the momentum operator in Eq. (6.6) (since X acts trivially on $|x\rangle$). In that sense, the following lemma practically solves our problem:

Lemma 3. *The following relation always holds*

$$[P, e^{-\beta H_{\text{ph}}}] = i\omega_0 \{X, e^{-\beta H_{\text{ph}}}\} \operatorname{th} \left(\frac{\beta\omega_0}{2} \right), \quad (6.8)$$

where $\{, \}$ is the anticommutator.

Proof. Since $P \propto a - a^\dagger$, it is useful to examine what happens if we try to commute a (and a^\dagger) with $e^{-\beta H_{\text{ph}}} = e^{-\beta\omega_0 a^\dagger a}$. This is facilitated using the famous Baker–Campbell–Hausdorff formula

$$e^B A e^{-B} = A + [B, A] + \frac{1}{2!} [B, [B, A]] + \dots \quad (6.9)$$

giving:

$$e^{-\beta\omega_0 a^\dagger a} a e^{\beta\omega_0 a^\dagger a} = a - \beta\omega_0 [a^\dagger a, a] + \frac{\beta^2 \omega_0^2}{2!} [a^\dagger a, [a^\dagger a, a]] + \dots = a e^{\beta\omega_0}. \quad (6.10)$$

Hence:

$$e^{-\beta\omega_0 a^\dagger a} a = e^{\beta\omega_0} a e^{-\beta\omega_0 a^\dagger a}, \quad (6.11a)$$

and analogously

$$e^{-\beta\omega_0 a^\dagger a} a^\dagger = e^{-\beta\omega_0} a^\dagger e^{-\beta\omega_0 a^\dagger a}. \quad (6.11b)$$

We would now like to add/subtract these two equations and somehow get the terms proportional to $a - a^\dagger$, giving momentum operator, and terms proportional to $a + a^\dagger$, giving coordinate operator. This can be accomplished by writing the exponential $e^{\beta\omega_0}$ as

$$e^{\beta\omega_0} = \frac{1+x}{1-x} \implies x = \operatorname{th} \left(\frac{\beta\omega_0}{2} \right) \quad (6.12)$$

Eqs. (6.11a) and (6.11b) become:

$$\left[1 - \operatorname{th} \left(\frac{\beta\omega_0}{2} \right) \right] e^{-\beta\omega_0 a^\dagger a} a = \left[1 + \operatorname{th} \left(\frac{\beta\omega_0}{2} \right) \right] a e^{-\beta\omega_0 a^\dagger a} \quad (6.13a)$$

$$\left[1 + \operatorname{th} \left(\frac{\beta\omega_0}{2} \right) \right] e^{-\beta\omega_0 a^\dagger a} a^\dagger = \left[1 - \operatorname{th} \left(\frac{\beta\omega_0}{2} \right) \right] a^\dagger e^{-\beta\omega_0 a^\dagger a} \quad (6.13b)$$

Subtracting Eq. (6.13b) from Eq. (6.13a) and simplifying the obtained expression, we get

$$[a - a^\dagger, e^{-\beta H}] = -\{a + a^\dagger, e^{-\beta H}\} \text{th} \left(\frac{\beta \omega_0}{2} \right). \quad (6.14)$$

Multiplying both sides with $-i\sqrt{\frac{\omega_0}{2}}$ we finally obtain

$$[P, e^{-\beta H}] = i\omega_0 \{X, e^{-\beta H}\} \text{th} \left(\frac{\beta \omega_0}{2} \right), \quad (6.15)$$

which proves the lemma. \square

Let us now continue the proof of Theorem 7, and go back to Eq. (6.6)

$$\frac{dp(x)}{dx} = -\omega_0 \text{th} \left(\frac{\beta \omega_0}{2} \right) \langle x | \{X, e^{-\beta H}\} | x \rangle = -2\omega_0 \text{th} \left(\frac{\beta \omega_0}{2} \right) x p(x). \quad (6.16)$$

This is a simple differential equation whose solution is exactly the Gaussian in Eq. (6.5). This completes our proof. \square

Therefore, we conclude that in the case we are considering, the electron-phonon interaction can be replaced with an interaction of the form

$$H_{int} \rightarrow \sum_i \varepsilon_i n_i; \quad \varepsilon_i = -g\sqrt{2\omega_0} X_i. \quad (6.17)$$

where X_i can now be understood as a classical random variable with a probability distribution that is given in Eq. (6.5). To make this even more simple, ε_i can also be regarded as a random variable with the appropriate distribution. Since the distribution of X is given by the Gaussian (see Eq. (6.5)), we conclude that ε will also have a Gaussian distribution, centered around zero, with the following variance

$$\sigma_\varepsilon^2 \equiv \text{Var} [\varepsilon] = 2\omega_0 g^2 \text{Var} [X] = g^2 \text{cth} \left(\frac{\beta \omega_0}{2} \right) = 2g^2 \left(\frac{1}{2} + \frac{1}{e^{\beta \omega_0} - 1} \right). \quad (6.18)$$

Hence, the probability distribution for ε is given by:

$$p_\varepsilon(\varepsilon) = \frac{1}{\sigma_\varepsilon \sqrt{2\pi}} e^{-\frac{\varepsilon^2}{2\sigma_\varepsilon^2}}. \quad (6.19)$$

6.4.2 Anderson Approach

So far, we have seen that for the short-time dynamics, the electron-phonon interaction term in the Hamiltonian can be replaced by Eq. (6.17), where ε_i is the random variable with a probability distribution given by Eq. (6.19). Hence, the phonons are completely removed from the picture, and the total Hamiltonian is given by

$$H = -t_0 \sum_i \left(c_i^\dagger c_{i+1} + H.c. \right) + \sum_i \varepsilon_i n_i. \quad (6.20)$$

In the case when there is only N lattice sites in the system, the Hamiltonian can be written in the following matrix form

$$H = \begin{bmatrix} \varepsilon_0 & -t_0 & 0 & 0 & \dots & 0 & 0 & 0 & -t_0 \\ -t_0 & \varepsilon_1 & -t_0 & 0 & \dots & 0 & 0 & 0 & 0 \\ 0 & -t_0 & \varepsilon_1 & -t_0 & \dots & 0 & 0 & 0 & 0 \\ 0 & 0 & -t_0 & \varepsilon_2 & \dots & 0 & 0 & 0 & 0 \\ \vdots & \vdots & \vdots & \vdots & \vdots & \vdots & \vdots & \vdots & \vdots \\ 0 & 0 & 0 & 0 & \dots & \varepsilon_{N-4} & -t_0 & 0 & 0 \\ 0 & 0 & 0 & 0 & \dots & -t_0 & \varepsilon_{N-3} & -t_0 & 0 \\ 0 & 0 & 0 & 0 & \dots & 0 & -t_0 & \varepsilon_{N-2} & t_0 \\ -t_0 & 0 & 0 & 0 & \dots & 0 & 0 & -t_0 & \varepsilon_{N-1} \end{bmatrix}, \quad (6.21)$$

where the periodic boundary conditions were assumed. The most straightforward way to solve this is to simply use the exact diagonalization. As a result, we would get eigenvectors $|n\rangle$ and eigenvalues E_n that can be used to obtain the optical conductivity from Eq. (2.18) as follows³

$$\begin{aligned} \text{Re}\sigma(\omega) &= \frac{N}{2\omega} \int_{-\infty}^{\infty} dt e^{i\omega t} [\langle j(t)j \rangle - \langle jj(t) \rangle] \\ &= \frac{N}{2\omega} \int_{-\infty}^{\infty} dt e^{i\omega t} \frac{1}{\mathcal{Z}} \sum_n e^{-\beta E_n} [\langle n|j(t)\mathbb{1}j|n\rangle - \langle n|j\mathbb{1}j(t)|n\rangle], \end{aligned} \quad (6.22)$$

where $\mathbb{1}$ is the identity operator and $\mathcal{Z} = \sum_n e^{-\beta E_n}$ is the partition function. If we now expand the identity operator as $\mathbb{1} = \sum_m |m\rangle\langle m|$, we get

$$\begin{aligned} \text{Re}\sigma(\omega) &= \frac{N}{2\omega} \int_{-\infty}^{\infty} dt \frac{e^{i\omega t}}{\mathcal{Z}} \sum_{n,m} |\langle n|j|m\rangle|^2 (e^{it(E_n - E_m)} - e^{-it(E_n - E_m)}) e^{-\beta E_n} \\ &= \frac{N}{2\omega \mathcal{Z}} \sum_{n,m} [e^{-\beta E_n} - e^{-\beta E_m}] |\langle n|j|m\rangle|^2 \int_{-\infty}^{\infty} dt e^{it(\omega + E_n - E_m)} \\ &= \frac{N\pi}{\omega \mathcal{Z}} \sum_{n,m} |\langle n|j|m\rangle|^2 [e^{-\beta E_n} - e^{-\beta E_m}] \delta(\omega - E_m + E_n). \end{aligned} \quad (6.23)$$

In this case, the concentration of electrons is $1/N$, implying that

$$\mu(\omega) = \frac{\pi}{\omega \mathcal{Z}} \sum_{n,m} |\langle n|Nj|m\rangle|^2 [e^{-\beta E_n} - e^{-\beta E_m}] \delta(\omega - E_m + E_n), \quad (6.24)$$

where the matrix element is easily calculated using Eq. (C.34). As we already emphasized, within this approach we should be able to reproduce the displaced Drude peak. However, this method is not able to correctly reproduce $\mu(\omega)$ for $\omega \lesssim \omega_0$, and it incorrectly gives an Anderson insulator for $\mu(\omega = 0)$.

Remark 38. From Eq. (6.24), we see that $\mu(\omega)$ is given as a series of Dirac delta peaks. Therefore, to plot this quantity we will always use a Lorentzian representation of delta functions with some small half-width η . However, we note that broadening η is only used for plotting, whereas all calculations are performed exactly (within this method).

6.4.3 Coherent Potential Approximation

Before we move on to the results, let us first note that the same DMFT procedure we reviewed in Chapter 1 of Part II, can be also applied to the Hamiltonian with disorder in Eq. (6.20), instead of the full Holstein Hamiltonian. This constitutes the so-called coherent potential approximation (CPA). The advantage of CPA is that its application is not restricted to the Holstein model, but can also be applied to much more general systems. However, it does not take into account the vertex corrections. Nevertheless, this technique was widely used for the study of disordered systems [134]. Now, we have a unique opportunity to quantitatively examine the reliability of this method in one particular model, the Holstein model, by comparing its predictions for the optical conductivity with the DMFT, which calculates the bubble term almost exactly.

In practice, the CPA is, in our case, applied as follows: We start with an initial guess⁴ for the self-energy $\Sigma(\omega)$, calculate the local Green's function $G(\omega)$ using⁵ Eq. (1.108) from Part II, and obtain $G_0(\omega)$ from the Dyson equation

$$G_0(\omega)^{-1} = G(\omega)^{-1} + \Sigma(\omega). \quad (6.25)$$

³We already set the lattice constant to unity, so we can freely interchange $V \leftrightarrow N$.

⁴The algorithm is so stable that we can practically use any function as an initial guess.

⁵This is the local Green's function for the 1D case.

Then, we find the impurity Green's function G_{imp} , which is actually just a resolvent $1/(G_0(\omega)^{-1} - \varepsilon)$ that needs to be averaged over the many different realizations of the random variable ε , with a probability distribution that we derived in Eq. (6.19)

$$\begin{aligned} G_{\text{imp}}(\omega) &= \left\langle (G_0(\omega)^{-1} - \varepsilon)^{-1} \right\rangle = \int_{-\infty}^{\infty} d\varepsilon \frac{p_\varepsilon(\varepsilon)}{G_0(\omega)^{-1} - \varepsilon} \\ &= \frac{1}{\sigma_\varepsilon} \sqrt{\frac{\pi}{2}} e^{-\frac{1}{2\sigma_\varepsilon^2 G_0(\omega)^2}} \left[-i + \operatorname{erfi} \left(\frac{1}{\sqrt{2}\sigma_\varepsilon G_0(\omega)} \right) \right], \end{aligned} \quad (6.26)$$

where erfi is the imaginary error function. The self-energy in the next iteration is obtained by again using the Dyson equation

$$\Sigma(\omega) = G_0^{-1}(\omega) - G_{\text{imp}}^{-1}(\omega), \quad (6.27)$$

which closes the loop. This is now repeated until the condition for convergence $G_{\text{imp}}(\omega) = G(\omega)$ is reached (up to some predefined accuracy). As a result, we obtain the self-energy that can now be used to calculate the spectral function as

$$A_k(\omega) = -\frac{1}{\pi} \operatorname{Im} \frac{1}{\omega - \Sigma(\omega) - \varepsilon_k}, \quad (6.28)$$

and also the optical conductivity and current-current correlation functions using Eqs. (2.52) and (2.11), respectively.

Remark 39. *The self-energy in the CPA method is, analogous to the DMFT, k -independent.*

6.4.4 Numerical Results

The numerical results for optical conductivity and current-current correlation function in the regime $\omega_0 = 1/3$ are presented in Fig. 6.6, while the numerical parameters for HEOM are displayed in Table 6.3. In panels 6.6(a₁)–6.6(a₂) we see that the contribution of vertex corrections is substantial (compare HEOM and DMFT). We also observe that in contrast to Fig. 6.3(a₁), where $\mu_{\text{HEOM}}(\omega = 0)$ was significantly larger than $\mu_{\text{DMFT}}(\omega = 0)$ for low temperature regime, here the roles are reversed.

While the vertex corrections are responsible for the difference between the predictions of the DMFT/CPA and HEOM/Anderson, let us now compare the methods within each of these categories separately. We see a remarkable agreement between DMFT and CPA. Of course, the CPA method by construction cannot capture the vertex corrections, but apart from that, despite being simple, displays the far-reaching capabilities for the calculation of the optical conductivity in the bubble approximation. Although we show the results for only two different temperatures in Fig. 6.6, we actually conducted comparisons in a wide range of electron-phonon couplings and temperatures, and we always found an excellent agreement between DMFT and CPA. We note that one of the known shortcomings of CPA is the fact that it cannot predict an insulating behavior $\mu_{\text{Anderson}}(\omega = 0) = 0$. However, this is actually better in our case, since we are dealing with dynamic, instead of static, disorder.

A good agreement can also be observed between HEOM and Anderson approach, as the latter is capable of capturing the most prominent feature of the spectrum - the displaced Drude peak. The only significant discrepancy between Anderson and HEOM can be observed $\omega \lesssim \omega_0$, where we know that Anderson approach gives incorrect predictions due to the fact that it does not take into account the dynamical motion of molecules. We note that due to Anderson localization we should get $\mu_{\text{Anderson}}(\omega = 0) = 0$, but the results in Figs. 6.6(a₁)–6.6(a₂) suggest otherwise. The reason for this apparent contradiction lies in the fact that we used artificial broadening for plotting the Anderson

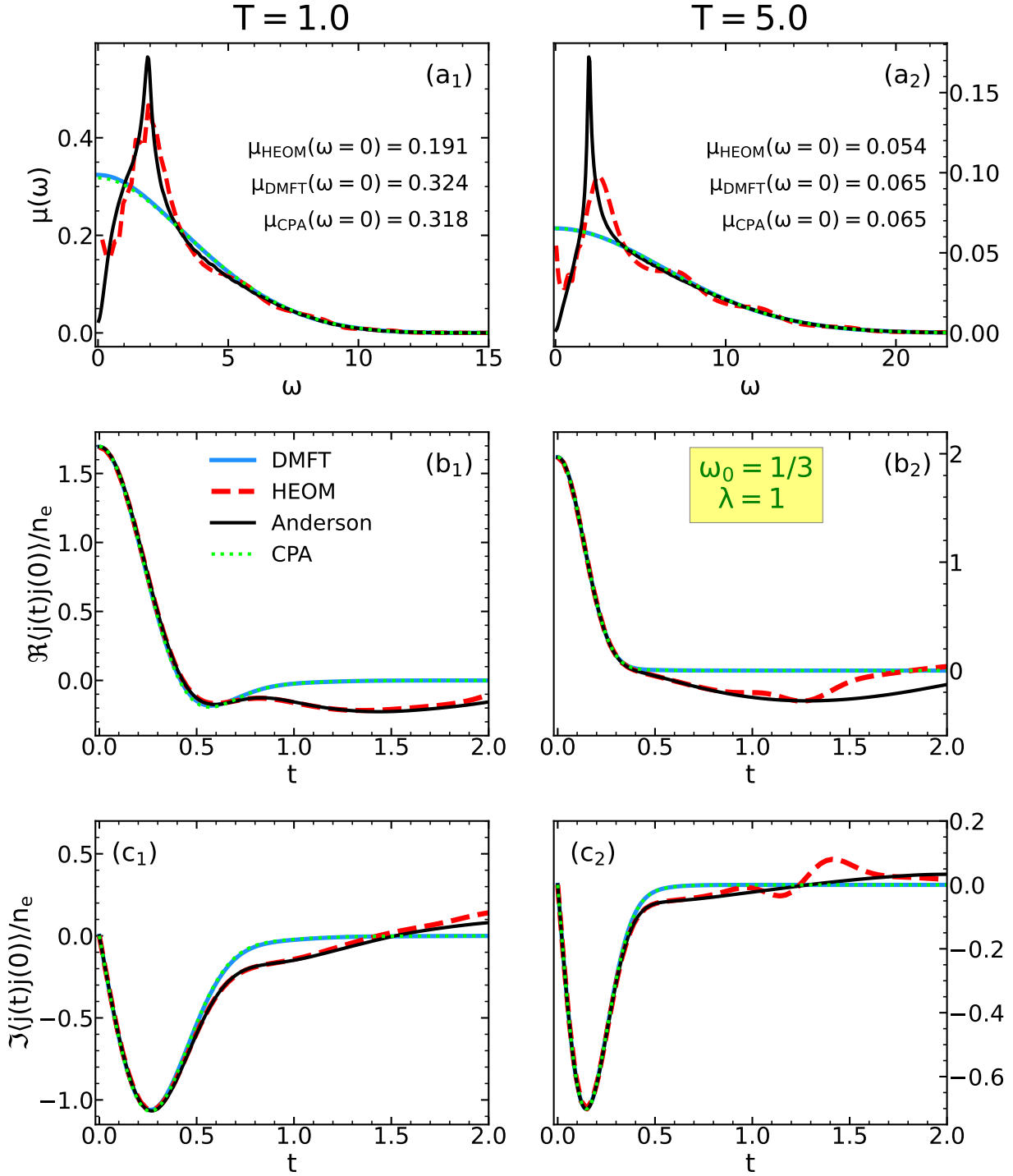


Figure 6.6: Optical conductivities and real-time current-current correlation functions in the regime close to the adiabatic limit $\omega_0 = 1/3$, $\lambda = 1$. All quantities are normalized to the concentration of charge carriers. In panels (a) and (b), we use the Lorentzian broadening with half-width $\eta = 0.05$ for Anderson results.

Table 6.3: Number of lattice sites N and the maximum hierarchy depth D that correspond to HEOM results in Figs 6.6.

Parameters	N_{HEOM}	D_{HEOM}
$\omega_0 = 1/3$ $\lambda = 1$ $T = 1$	7	12
$\omega_0 = 1/3$ $\lambda = 1$ $T = 5$	6	15

results in Figs. 6.6(a₁)–6.6, by replacing the Dirac delta functions in Eq. (6.24) with their Lorentzian representations. This was avoided in the case of the current-current correlation functions, which were calculated using a formula that is obtained by plugging Eq. (6.24) into Eq. (2.20)

$$\frac{1}{n_e} \langle j(t)j \rangle = \frac{1}{Z} \sum_{m,n} e^{-it(E_m - E_n)} e^{-\beta E_n} |\langle n | N j | m \rangle|^2. \quad (6.29)$$

In this expression there are no delta functions, so no broadening was needed. In accordance to the results for $\mu(\omega)$, we see that HEOM and Anderson are in agreement for small times; see Figs. 6.6(b₁)–6.6(b₂) and Figs. 6.6(c₁)–6.6(c₂).

6.5 Optical Conductivity in the Regimes where the Phonon Frequency is Large

Since the HEOM data are here largely unavailable, and also since we already gave a thorough analysis of the vertex corrections in other regimes, we just present the results in Fig. 6.7 without further discussion.

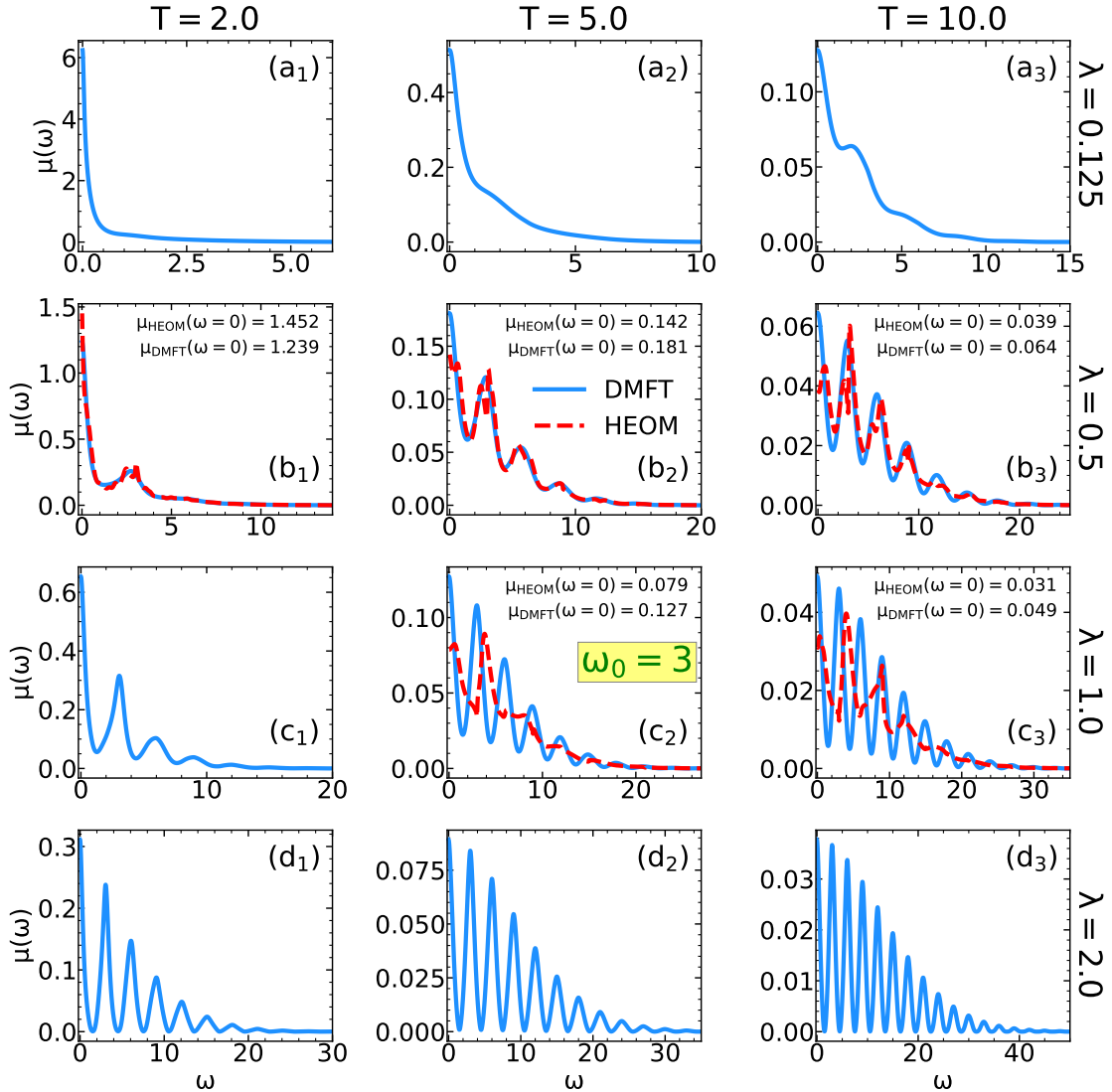


Figure 6.7: Optical conductivities, normalized to the concentration of charge carriers, close to the antiadiabatic limit $\omega_0 = 3$.

Table 6.4: Number of lattice sites N and the maximum hierarchy depth D that correspond to the HEOM results in Fig. 6.7.

Parameters	N_{HEOM}	D_{HEOM}
$\omega_0 = 3 \quad \lambda = 0.5 \quad T = 2.0$	10	8
$\omega_0 = 3 \quad \lambda = 0.5 \quad T = 5.0$	7	12
$\omega_0 = 3 \quad \lambda = 0.5 \quad T = 10.0$	5	19
$\omega_0 = 3 \quad \lambda = 1.0 \quad T = 5.0$	7	12
$\omega_0 = 3 \quad \lambda = 1.0 \quad T = 10.0$	5	21

Conclusions

In this thesis, we gave a comprehensive study of single particle and transport properties of the Holstein model, which was introduced in Part I. Part II was devoted solely to the single particle properties, or more specifically to the calculation of quantities such as effective mass, ground state energy, spectral functions, and correlation functions in imaginary time, using different methods. For this purpose, in Chapter 1 we reviewed the dynamical mean field theory and showed how this method can be applied to the Holstein model in a stable and numerically inexpensive way. Since the impurity problem was already solved analytically in Ref. [56], in terms of the continued fraction expansion, the stability of the DMFT algorithm (see Fig. 1.2) rested upon our ability to accurately evaluate the local Green's function on a real frequency axis. As this cannot be done using a straightforward trapezoid integration due to the strong numerical instabilities, we developed a numerical scheme that solves this problem in Sec. 1.8. In addition, we showed that the local Green's function can actually be evaluated analytically in 1D and 2D cases with nearest neighbor hopping. As a result, in these cases, we obtained that a single iteration of the DMFT algorithm in Fig. 1.2 has an analytic solution. Having in mind that a convergence of a DMFT loop in a typical (not too extreme) regime requires only on the order of 10 iterations, it is clear how incredibly numerically cheap this method really is.

The numerical efficiency and stability of the DMFT became important only after we have concluded that this method gives accurate and reliable predictions in the Holstein model, irrespective of the parameter regime. This was established in Chapter 2. To be more precise, we observed a remarkable agreement between the DMFT predictions and the best available results in the literature for the effective mass, the ground state energy, and the spectral functions, which were calculated for weak, intermediate, and strong electron-phonon coupling strength coupling, as well as close to the atomic limit. In addition, we calculated the first nine spectral sum rules exactly, and numerically checked that DMFT satisfies all of them. We also showcased the superiority of the DMFT compared to the (self-consistent) Migdal approximation, which is a commonly used method. Comparisons of the imaginary time correlation functions between various methods were also conducted. However, we saw that it is very hard to draw conclusions from the imaginary axis data, as even a tiny difference in the imaginary axis correlation functions can correspond to substantial differences in spectral functions. All our findings from Chapter 2 can be summarized by saying that DMFT provides approximate, but exceptionally accurate and numerically cheap results for the single-particle properties of the Holstein model.

Our results now establish the DMFT as one of the best benchmarks for the Holstein model, against which other methods can be tested. One such method is the (second-order) CE method, which was examined in Chapter 3. CE is increasingly popular because it can be easily applied to different models and to real materials as well. This is why it was important to examine its range of validity, which we did using the Holstein model as a testing ground. In our comprehensive analysis, we applied the CE method in a broad temperature range for three phonon frequencies $\omega_0/t_0 = 0.2, 0.5$ and 1, covering regimes from weak to strong electron-phonon couplings. We mostly focused on the 1D system in the thermodynamic limit, but some of the results were shown also in 2D and 3D. To avoid numerical instabilities and to reach high numerical precision, we derived a number of analytical expressions and we used the Levin's collocation method in calculations of the cumulant, as well as an interpolation scheme for the Fourier transform in corresponding calculations of the spectral functions. The quasiparticle properties and spectral functions were shown in comparison to the DMFT and SCMA results.

We observed that at weak coupling (roughly corresponding to $m_0/m^* \gtrsim 0.9$) CE, DMFT, and SCMA give very similar spectral functions. Most of the spectral weight for $k = 0$ is in the quasiparticle peak, while a small satellite is rather well reproduced in all three methods. As the interaction increases, a clear difference in the spectral functions emerges. Nevertheless, the positions of the CE and DMFT quasiparticle and the first satellite peak at low temperatures are in rather good agreement. Furthermore, the overall spectral weight distribution is in a decent agreement even though the satellite peaks are

more pronounced in DMFT for stronger electron-phonon coupling. Roughly speaking, there is a decent agreement in 1D up to the interactions corresponding to $m_0/m^* \sim 0.5$. Interestingly, the agreement between the CE and DMFT spectral functions persists also for $k = \pi$, although CE does not capture a tiny quasiparticle peak. In this case, the DMFT spectral weight almost merges to a single broad peak. We note that the disagreement between the predictions of the CE and the reliable benchmark that was observed in Ref. [116] for $k = \pi$, is solely due to considering a lattice of finite $N = 6$ size [87], while our results demonstrate that those discrepancies are significantly reduced in the thermodynamic limit $N \rightarrow \infty$. However, the deviation of CE from the exact solution is most obvious for intermediate momenta where the CE solution merges to a single peak, while the satellite structure is seen in DMFT. At high temperatures, the CE gives decent results, much better than the SCMA, and one might suspect that the CE would be exact in the limit $T \rightarrow \infty$. However, this is not the case as we proved using the spectral sum rules. It turns out that the CE gives the exact spectral moments only up to the order $n = 4$, while it incorrectly predicts the prefactor in the leading order term (with respect to T , when $T \rightarrow \infty$) for $n = 5$.

For a correct interpretation of the results that we obtained in Chapter 3, we always need to keep in mind the potential of our methods for the application in other models and real materials. CE and MA are both relatively simple and inexpensive to apply, which is why the comparison between these two methods seems the most fair. Although the DMFT appears computationally superior to CE, we note that the numerical efficiency that we achieved with DMFT is restricted to the Holstein model. For predicting the properties of real materials, CE remains numerically cheap, while the required numerical resources for the application of the DMFT are vastly increased. In addition, the issue of nonlocal correlations may also emerge. Nevertheless, DMFT is very useful as a reliable benchmark in the Holstein model, as it can be used as a judge, to decide which of the other methods performs the best. Having this in mind, our results readily demonstrated that CE is vastly superior to MA. Furthermore, we also obtained that the CE gives slightly better results than the self-consistent MA (i.e., the SCMA), despite the fact that the CE does not require any self-consistent calculations. Of course, for a definitive answer on the range of validity of CE in connection with ab initio calculations, one needs to perform a similar analysis for both the Fröhlich model and for other models as well, which can be used for a realistic description of the electronic spectra and charge transport in real materials. A useful hint in this direction is provided by Ref. [112] which shows that the CE, around the bottom of the band, gives promising results for the spectral function even in the case when the phonons have a dispersion [135].

In Part III of this thesis, we provided an in-depth study of transport properties in the Holstein model. In particular, we concentrated on the study of optical conductivity, normalized to the concentration of charge carriers $\mu(\omega)$, and a DC version of this quantity, i.e., the mobility $\mu \equiv \mu(\omega = 0)$. Both of these were calculated using the linear response theory. Within this formalism, $\mu(\omega)$ is naturally written as a sum of the so-called bubble term, which is completely determined by the single-particle properties, while the remaining contribution is known as the vertex corrections. In practice, the vertex corrections are notoriously hard to calculate, which is why the bubble approximation is usually employed in real materials. This is why it is of paramount importance to understand both the capabilities of different methods to produce accurate results in the bubble approximation, as well as the importance of vertex corrections, which are usually neglected without justification. Our goal was to answer these questions on one particular example - the Holstein model.

Since the single-particle properties were already well studied in Part II, we used them in Chapter 3 of Part III to calculate the mobility using the DMFT, CE, SCMA, and MA. As before, the DMFT was used as a benchmark, which is justified due to its excellent capabilities for accurately predicting the spectral functions, as we already discussed. The agreement between DMFT and CE was quite good. This is the case even for stronger electron-phonon couplings, where the CE indicated that it is capable of capturing non-monotonic behavior of $\mu(T)$, with a region of increasing mobility with temperature, which is usually assigned to hopping conduction in phenomenological theories. For strong electron-phonon coupling, the CE mobility results were obtained only for $T \gtrsim t_0$, since a very small numerical

noise at frequencies $\omega \ll E_p$ affects a precise calculation of mobility at lower temperatures. While it would be ambitious to expect that the CE would continue to produce reliable results even for low-temperature mobility in the strong coupling case, this method nevertheless produced quality results well beyond the regimes where we would expect a perturbative method to be trustworthy. This was not the case for the SCMA and MA, which were clearly worse. However, we note that SCMA provided a significant improvement to the mobility predictions of MA. For high temperatures, we observed that the temperature dependence of mobility within CE, DMFT, and SCMA assumed a universal form: for weak electron-phonon coupling $\mu \propto T^{-2}$, while for somewhat stronger coupling $\mu \propto T^{-3/2}$. These high-temperature limits were also obtained analytically within the CE. While one might find it surprising that the CE was able to produce any meaningful results for μ , due to its inability to correctly capture the spectral functions for $k \not\approx 0$ and $k \not\approx \pi$, we note that $k \approx 0$ are actually giving the largest contribution for μ in the case of small concentration of charge carriers, which we are considering. To summarize, we argue that the CE will be most useful in calculations of charge mobility, as has already been done in ab initio calculations for SrTiO₃ [98] and naphthalene [99].

This analysis would not be complete without examining the contribution of the vertex corrections. In Chapter 5, we analytically proved that the vertex corrections of mobility are actually vanishing in the weak coupling and atomic limits of the Holstein model. In all other regimes, we numerically studied the vertex corrections of optical conductivity, by comparing the bubble approximation results, obtained using the DMFT, and the numerically exact predictions of the hierarchical equations of motion (HEOM) method, which we took from the literature. The discrepancy between these results determined the significance of the vertex corrections. Our numerical results explicitly showed that while the vertex corrections for small electron-phonon coupling strengths are vanishing, there are substantial vertex corrections in both the intermediate coupling and near-adiabatic regimes. In addition, we saw that these vertex corrections can lead to an increase in mobility (compared to the bubble result) in some regimes, while leading to a decrease in other regimes. While a natural continuation of this line of research would be to repeat this analysis in the Fröhlich model, we note that the Holstein model currently stands as a unique electron-phonon model where such an in-depth study, that we presented, was possible. Another way, which is actually within our reach, to build upon these results is to study the near-adiabatic regime more deeply, where the so-called displaced Drude peak is observed both in HEOM solution and in the Anderson approach. This suggests that the transient localization theory [124] would produce interesting results. We leave this for our future work.

Part V
Appendices



Numerical Fourier Transform of Green's functions

In this section, we will show how to do numerical Fourier transform and inverse Fourier transform of the Green's functions using the FFT algorithm.

A.1 Transform $G(t) \rightarrow G(\omega)$

At first glance, this seems to be pretty straightforward. However, the problem arises because the Riemann approximation

$$G(\omega) = \int_{-\infty}^{\infty} dt G(t) e^{i\omega t} \approx \Delta t \sum_n G(t_n) e^{i\omega t_n}, \quad (\text{A.1})$$

fails for large ω . Namely, no matter how small¹ Δt is, for large enough ω , the "integrand" will make several oscillations in the interval $(t_n, t_n + \Delta t)$. In order to overcome these difficulties, we use some kind of interpolation scheme for the Green's function and integrate analytically. This idea originated from Ref. [123], and we here review the main ideas from that reference.

It is not advisable to use ordinary Lagrange interpolating polynomial

$$G(t) = \sum_{i=0}^{N-1} G(t_i) \prod_{j \neq i} \frac{t - t_j}{t_i - t_j}, \quad (\text{A.2})$$

not only because it is highly impractical (since the order of polynomial N is so large²), but also because high-degree polynomials have a notorious ability to "wobble", thus potentially producing serious errors. Instead, we will use a piecewise polynomial which will be obtained by using the interpolation on only a few nearest points. In the cubic case, which we will examine, we need four nearest points. Two of those points are located on the left (from the point t we are examining), whereas the other two points are on the right, if the point t is not located in the first (t_0, t_1) or in the last sub-interval (t_{N-2}, t_{N-1}) . Otherwise, we are forced to take one point on one side and three on the other. This will cause some complication as we will see.

Notice that Lagrange interpolation polynomial in Eq. (A.2) is linear in $G(t_i)$. In fact $G(t_i)$ is multiplied by

$$\prod_{j \neq i} \frac{t - t_j}{t_i - t_j} = \prod_{j \neq i} \frac{t - t_i + t_i - t_j}{t_i - t_j} = \prod_{j \neq i} \left[1 + \frac{t - t_i}{\Delta t} \frac{1}{i - j} \right] = K_i \left(\frac{t - t_i}{\Delta t} \right). \quad (\text{A.3})$$

¹We always assume that both t -grid and ω -grid are equidistant.

²Although the symbol N , in the whole thesis, was reserved for the number of lattice points, here we use it to denote the number of points on a t grid.

Since, our $G(t)$ will be approximated as a piecewise Lagrange polynomial, that means that it can also be cast into form

$$G(t) = \sum_{j=0}^{N-1} G(t_j) K_j \left(\frac{t-t_j}{\Delta t} \right). \quad (\text{A.4})$$

In this case, the product in Eq. (A.3) does not go over all j , but only over four nearest j . That means that K_j would be the same for all j if there were no boundary points. To account for the boundary points, we will rewrite K_j as a term that is independent of j and another, correction term C_j which will account for these boundary points

$$G(t) = \sum_{j=0}^{N-1} G(t_j) K \left(\frac{t-t_j}{\Delta t} \right) + \sum_j G(t_j) C_j \left(\frac{t-t_j}{\Delta t} \right). \quad (\text{A.5})$$

The kernel function K can be obtained using (A.3), but technically it is probably easier to obtain it by interpolating a few key values: $K(0) = 1$ and $K(n) = 0$ for $n \in \mathbb{Z} \setminus \{0\}$ - this condition ensures the consistency condition $G(t = t_j) = G(t_j)$. Of course, $K(x)$ is always obtained by interpolating to the nearest four points - two to the left and two to the right. Implementing this, we obtain

$$\begin{aligned} K(x) &= \frac{1}{2}(x-1)(x+1)(x-2)\theta(x)\theta(1-x) \\ &\quad - \frac{1}{2}(x-1)(x+1)(x+2)\theta(-x)\theta(x+1) \\ &\quad - \frac{1}{6}(x-1)(x-2)(x-3)\theta(2-x)\theta(x-1) \\ &\quad + \frac{1}{6}(x+1)(x+2)(x+3)\theta(-1-x)\theta(x+2). \end{aligned} \quad (\text{A.6})$$

The correction terms are also easily obtained and read as

$$C_0(x) = -\frac{1}{6}(x-1)(x-2)(x-3)\theta(x)\theta(2-x) - K(x), \quad (\text{A.7a})$$

$$\begin{aligned} C_1(x) &= \frac{1}{2}(x-1)(x+1)(x-2)\theta(x+1)\theta(1-x) \\ &\quad - \frac{1}{6}(x-1)(x-2)(x-3)\theta(x-1)\theta(2-x) - K(x), \end{aligned} \quad (\text{A.7b})$$

$$\begin{aligned} C_2(x) &= -\frac{1}{2}(x-1)(x+1)(x+2)\theta(-x)\theta(x+2) \\ &\quad + \frac{1}{2}(x-1)(x+1)(x-2)\theta(x)\theta(1-x) \\ &\quad - \frac{1}{6}(x-1)(x-2)(x-3)\theta(x-1)\theta(2-x) - K(x), \end{aligned} \quad (\text{A.7c})$$

$$C_3(x) = \frac{1}{6}(x+1)(x+2)(x+3)\theta(x+3)\theta(-2-x). \quad (\text{A.7d})$$

These correction terms (C_0, C_1, C_2, C_3) are a consequence of the fact that t_0 is a boundary point. Additional correction terms ($C_{N-1}, C_{N-2}, C_{N-3}, C_{N-4}$) should arise due to the fact that t_{N-1} is also a boundary point, but these are now easily obtained using the symmetry condition $C_{N-1-j}(x) = C_j(x)$. Having this in mind, we can go back to Eq. (A.5) and perform the analytic integration

$$\begin{aligned} G(\omega) &= \int_{-\infty}^{\infty} dt G(t) e^{i\omega t} \\ &= \sum_{j=0}^{N-1} G(t_j) \int_{-\infty}^{\infty} dt K \left(\frac{t-t_j}{\Delta t} \right) e^{i\omega t} + \sum_{j=0}^{N-1} G(t_j) \int_{-\infty}^{\infty} dt C_j \left(\frac{t-t_j}{\Delta t} \right) e^{i\omega t}. \end{aligned} \quad (\text{A.8})$$

In the first integral we will use the substitution $x = \frac{t-t_j}{\Delta t}$, whereas in the second one, we will use $x = \frac{t-t_{min}}{\Delta t}$. We obtain

$$G(\omega) = \sum_{j=0}^{N-1} \Delta t e^{i\omega t_j} G(t_j) \tilde{K}(\theta) + \sum_j \Delta t e^{i\omega t_{min}} G(t_j) \tilde{C}_j(\theta), \quad (\text{A.9})$$

where

$$\theta = \omega \Delta t, \quad (\text{A.10a})$$

$$\tilde{K}(\theta) = \int_{-\infty}^{\infty} dx e^{i\theta x} K(x), \quad (\text{A.10b})$$

$$\tilde{C}_j(\theta) = \int_{-\infty}^{\infty} e^{i\theta x} C_j(x-j). \quad (\text{A.10c})$$

The second term in Eq. (A.9) has only a few terms. It is thus easy to compute. On the other hand, the first term can be computationally expensive, so we will try to use FFT to compute it. Setting

$$\omega_{min} = 0; \quad \Delta\omega\Delta t = \frac{2\pi}{N}; \quad \omega_n = n\Delta\omega; \quad n = 0, 1, \dots, \frac{N}{2} - 1, \quad (\text{A.11})$$

and using the same conventions for the FFT as python

$$\hat{f}_k = \sum_{j=0}^{N-1} f_j e^{-ijk\frac{2\pi}{N}} \equiv \text{FFT}[f_j]_k, \quad (\text{A.12a})$$

$$f_k = \frac{1}{N} \sum_{j=0}^{N-1} \hat{f}_j e^{ijk\frac{2\pi}{N}} \equiv \text{IFFT}[\hat{f}_j]_k, \quad (\text{A.12b})$$

where i is the imaginary unit and the number of data points is of the form $N = 2^l$, $l \in \mathbb{N}$, we see that the first term in Eq. (A.9) can be easily evaluated using

$$\sum_{j=0}^{N-1} G(t_j) e^{i\omega_n j \Delta t} = N \cdot \text{IFFT}[G(t_j)]_n. \quad (\text{A.13})$$

The second term in Eq. (A.9) is calculated directly. We note that due to the symmetry condition $C_{N-1-j}(x) = C_j(-x)$

$$\begin{aligned} \tilde{C}_{N-1-j}(\theta) &= \int_{-\infty}^{\infty} dx e^{i\theta x} C_{N-1-j}(x - N + 1 + j) = \int_{-\infty}^{\infty} dx e^{i\theta x} C_j(N - 1 - j - x) \\ &= \int_{-\infty}^{\infty} dy e^{i\theta(N-1-y)} C_j(y - j) = e^{i\theta(N-1)} \tilde{C}_j(\theta)^* \\ &= e^{i\omega(t_{max}-t_{min})} \tilde{C}_j(\theta)^*. \end{aligned} \quad (\text{A.14})$$

Hence, combining everything obtained so far we get

$$\begin{aligned} G(\omega_n) &= \Delta t e^{i\omega_n t_{min}} \left[N \tilde{K}(\theta) \cdot \text{IFFT}[G(t_j)]_n \right] \\ &\quad + \Delta t e^{i\omega_n t_{min}} \left[\tilde{C}_0(\theta) G(t_{min}) + \tilde{C}_1(\theta) G(t_{min} + \Delta t) + \dots \right] \\ &\quad + \Delta t e^{i\omega_n t_{max}} \left[\tilde{C}_0(\theta)^* G(t_{max}) + \tilde{C}_1(\theta)^* G(t_{max} - \Delta t) + \dots \right]. \end{aligned} \quad (\text{A.15})$$

The second and third lines have only a few terms. In our cubic case, each of them has only four terms. We note that the negative frequencies $\omega < 0$ are obtained using a similar procedure as the one we presented after we use the substitution $t \rightarrow -t$ in Eq. (A.1).

The only thing that remains is to calculate $\tilde{K}(\theta)$ and $\tilde{C}_j(\theta)$. This can be obtained straightforwardly using (A.10), (A.6) and (A.7). We get

$$\tilde{K}(\theta) = \frac{6 + \theta^2}{3\theta^4} [3 - 4 \cos \theta + \cos 2\theta], \quad (\text{A.16a})$$

$$\tilde{C}_0(\theta) = \frac{-42 + 5\theta^2 + (6 + \theta^2)(8 \cos \theta - \cos 2\theta)}{6\theta^4} + i \frac{-12\theta + 6\theta^3 + (6 + \theta^2) \sin 2\theta}{6\theta^4}, \quad (\text{A.16b})$$

$$\tilde{C}_1(\theta) = \frac{14(3 - \theta^2) - 7(6 + \theta^2) \cos \theta}{6\theta^4} + i \frac{30\theta - 5(6 + \theta^2) \sin \theta}{6\theta^4} \quad (\text{A.16c})$$

$$\tilde{C}_2(\theta) = \frac{-4(3 - \theta^2) + 2(6 + \theta^2) \cos \theta}{3\theta^4} + i \frac{-12\theta + 2(6 + \theta^2) \sin \theta}{3\theta^4}, \quad (\text{A.16d})$$

$$\tilde{C}_3(\theta) = \frac{2(3 - \theta^2) - (6 + \theta^2) \cos \theta}{6\theta^4} + i \frac{6\theta - (6 + \theta^2) \sin \theta}{6\theta^4}. \quad (\text{A.16e})$$

We note that this numerical scheme has a removable numerical singularity at $\theta = 0$. To avoid that, we can use the Taylor expansion of $\tilde{K}(\theta)$, $\tilde{C}_0(\theta)$, $\tilde{C}_1(\theta)$, $\tilde{C}_2(\theta)$ and $\tilde{C}_3(\theta)$ around $\theta = 0$.

A.2 Transform $G(\omega) \rightarrow G(t)$

To perform the inverse Fourier transform by definition, we need to evaluate

$$G(t) = \int_{-\infty}^{\infty} \frac{d\omega}{2\pi} G(\omega) e^{-i\omega t}. \quad (\text{A.17})$$

It seems logical that we can evaluate this integral using a procedure analogous to the one we presented in the previous section. However, now there is an additional problem, since $G(\omega)$ has a high-frequency tail of the form $\sim \frac{1}{\omega}$, as can be seen using the partial integration, the fact that the Green's function is retarded $G(t < 0) = 0$

$$\begin{aligned} G(\omega) &= \int_0^{\infty} dt G(t) e^{i\omega t} \\ &= G(t) \frac{e^{i\omega t}}{i\omega} \Big|_0^{\infty} - \int_0^{\infty} dt G'(t) \frac{e^{i\omega t}}{i\omega} \\ &= -\frac{G(0)}{i\omega} - \left[-G'(t) \frac{e^{i\omega t}}{\omega^2} \Big|_0^{\infty} + \int_0^{\infty} dt G''(t) \frac{e^{i\omega t}}{\omega^2} \right] \\ &= \frac{iG(0)}{\omega} - \frac{G'(0)}{\omega^2} - \frac{1}{\omega^2} \int_0^{\infty} dt G''(t) e^{i\omega t}, \end{aligned} \quad (\text{A.18})$$

and employing the Riemann-Lebesgue lemma to show that the last term goes to zero faster than $\frac{1}{\omega^2}$, meaning

$$G(\omega) \sim \frac{iG(0)}{\omega} - \frac{G'(0)}{\omega^2} \quad \text{as } \omega \rightarrow \pm\infty. \quad (\text{A.19})$$

As a consequence of this high-frequency tail, $G(\omega)$ falls off very slowly to zero for $\omega \rightarrow \infty$, forcing us to use an extremely large domain in ω in order to get somewhat decent results. We would like to avoid this since $G(\omega)$ is most often calculated using some numerical algorithm, which means that obtaining $G(\omega)$ in a large ω domain would require a significant amount of computational time.

One of the ways to deal with this issue is to rewrite the Green's function as

$$G(\omega) = \underbrace{[G(\omega) - T(\omega)]}_{\equiv G^{\text{n.t.}}(\omega)} + T(\omega), \quad (\text{A.20})$$

where $T(\omega)$ denotes the high-frequency tail of $G(\omega)$. Now, we can perform the inverse Fourier transform on $G^{\text{n.t.}}(\omega)$ using a procedure, completely analogous to the one we presented in the previous section, since this quantity now has no high-frequency tail. Since this was already explained in detail in Sec. A.1, we focus on performing an inverse Fourier transform on $T(\omega)$. This can be done analytically. Here, we show how this is done using the idea from the TRIQS software library [136].

From Eq. (A.19), we see that $T(\omega)$ is of the form

$$T(\omega) = \frac{t_1}{\omega} + \frac{t_2}{\omega^2}, \quad (\text{A.21})$$

where t_1 and t_2 need to be determined, as $G(0)$ and $G'(0)$ are not initially known. This can be easily done using fitting, or using the spectral sum rules.

Before we proceed, let us note that we unwillingly introduced the singularity at $\omega = 0$. This can pose some serious problems for numerical considerations of $G^{\text{n.t.}}(\omega)$, so we will have to modify our tail function before going further. We want to modify $T(\omega)$ in such a way that we get the same asymptotic behavior (up to a square order in $\frac{1}{\omega}$) and we also do not want to create any additional singularities. This can be done by adding a conveniently chosen infinite series of the form $\frac{1}{\omega^{3+n}}$ to the Eq. (A.21). There are many ways to do this, and we present only one of them

$$\begin{aligned} T(\omega) &= t_1 \left[\frac{1}{\omega} - \frac{1}{\omega^3} + \frac{1}{\omega^5} + \dots \right] + t_2 \left[\frac{1}{\omega^2} - \frac{1}{\omega^4} + \frac{1}{\omega^6} + \dots \right] \\ &= \frac{t_1 \omega}{1 + \omega^2} + \frac{t_2}{1 + \omega^2} \\ &= \frac{\frac{1}{2}(t_1 + it_2)}{\omega + i} + \frac{\frac{1}{2}(t_1 - it_2)}{\omega - i}. \end{aligned} \quad (\text{A.22})$$

This way we removed all singularities from the real axis $T(0) = t_2$. One additional problem (that is not completely obvious) can arise if this tail function has a large peak near $\omega \approx 0$, and if our ω grid is not dense enough. We can fix this without introducing a finer grid by modifying our tail function again. We will introduce the parameter a , that will be conveniently chosen, which will smear off our peak

$$\begin{aligned} T(\omega) &= \frac{t_1}{a} \left[\frac{a}{\omega} - \frac{a^3}{\omega^3} + \frac{a^5}{\omega^5} + \dots \right] + \frac{t_2}{a^2} \left[\frac{a^2}{\omega^2} - \frac{a^4}{\omega^4} + \frac{a^6}{\omega^6} + \dots \right] \\ &= \frac{t_1 \omega}{a^2 + \omega^2} + \frac{t_2}{a^2 + \omega^2} \\ &= \frac{\frac{1}{2}(t_1 + i \frac{t_2}{a})}{\omega + ia} + \frac{\frac{1}{2}(t_1 - i \frac{t_2}{a})}{\omega - ia}. \end{aligned} \quad (\text{A.23})$$

Now, our peak will be smaller $T(0) = \frac{t_2}{a^2}$. It turns out that good results are usually obtained by setting

$$a = c \cdot \sqrt{N} \Delta\omega, \quad (\text{A.24})$$

where N is the number of data points used, and $c > 1$ is arbitrary number such that $c \ll \sqrt{N}$. It is recommended to make c as large as possible, but $c = 1$ will be just fine in most situations.

Since we finally found our tail function in Eq.(A.23), we can now transform it to the time domain analytically. This is easily done using the:

$$\int_{-\infty}^{\infty} \frac{d\omega}{2\pi} \frac{e^{-i\omega t}}{\omega + ia} = -ie^{-at}\theta(t), \quad (\text{A.25a})$$

$$\int_{-\infty}^{\infty} \frac{d\omega}{2\pi} \frac{e^{-i\omega t}}{\omega - ia} = ie^{at}\theta(-t). \quad (\text{A.25b})$$

Both of these relations can be trivially proven using Cauchy's residue formula. Now, the time-domain tail function takes the form:

$$T(t) = \frac{1}{2}(t_1 + i\frac{t_2}{a})(-i)e^{-at}\theta(t) + \frac{1}{2}(t_1 - i\frac{t_2}{a})ie^{at}\theta(-t). \quad (\text{A.26})$$

Now, we have everything we need to perform both the Fourier and inverse Fourier transforms in a numerically efficient and accurate way.

Numerical Integration Scheme for the Calculation of Highly-Oscillating Functions in the CE Method

The purpose of this appendix is to show a numerical procedure for the calculation of the cumulant function $C_{\mathbf{k}}(t)$ in the Holstein model. To achieve this, we start from Eq. (3.43) of Part II. This expression can be separated into two terms

$$C_{\mathbf{k}}(t) = -g^2 t \int_0^t dx iD(x) e^{ix\varepsilon_{\mathbf{k}}} J_0(2t_0 x)^d + g^2 \int_0^t dx x iD(x) e^{ix\varepsilon_{\mathbf{k}}} J_0(2t_0 x)^d. \quad (\text{B.1})$$

In practice, the cumulant function is stored on a computer as an array $[C_{\mathbf{k}}(t_0), C_{\mathbf{k}}(t_1) \dots C_{\mathbf{k}}(t_G)]$, which represent the values of $C_{\mathbf{k}}(t)$ for times $[t_0 = 0, t_1 \dots t_G]$ (this array of times will be referred to as the t -grid). Therefore, to avoid integrating over the same interval multiple times, it is much better to divide both of the integrals \int_0^t in Eq. (B.1) into a sum of integrals of the form $\int_{t_{i-1}}^{t_i}$, where t_i are times from the previously defined t -grid

$$C_{\mathbf{k}}(t) = -g^2 t \sum_{j=0}^{G-1} \int_{t_j}^{t_{j+1}} dx iD(x) e^{ix\varepsilon_{\mathbf{k}}} J_0(2t_0 x)^d + g^2 \sum_{j=0}^{G-1} \int_{t_j}^{t_{j+1}} dx x iD(x) e^{ix\varepsilon_{\mathbf{k}}} J_0(2t_0 x)^d. \quad (\text{B.2})$$

The numerical procedure for the integration of each of these intervals is the same¹, so we focus on just one of them, say, $t \in (t_{i-1}, t_i)$. From now on, to shorten the notation, we denote $a \equiv t_i$ and $b \equiv t_{i+1}$. Therefore, all the integrals in Eq. (B.2) can be written in the following form

$$I = \int_a^b dx g(x) e^{ir_1 x} J_0(r_2 x)^d, \quad (\text{B.3})$$

where $g(x)$ is either a linear or a constant function, while² $r_1 = \varepsilon_{\mathbf{k}} \pm \omega_0$, and $r_2 = 2t_0$. Now, our task is reduced, and we just need to find a numerical scheme for the calculation of the integral in Eq. (B.3). Luckily, this has already been studied by Levin for arbitrary r_1 and r_2 and slowly varying $g(x)$ [119]. In the rest of this appendix, we review this method in the 1D ($d = 1$), 2D ($d = 2$), and 3D ($d = 3$) cases.

B.1 Overview of the Main Ideas

The main idea is to rewrite the subintegral function in Eq. (B.3) as a scalar product of two columns $|\tilde{g}(x)\rangle$ and $|\tilde{J}(x)\rangle$, whose elements are functions

$$I = \int_a^b dx \langle \tilde{g}(x) | \tilde{J}(x) \rangle. \quad (\text{B.4})$$

¹Actually, there is one exception; see Remark 40.

²The phonon propagator is defined below Eq. (3.43) of Part II, and is given by $iD(t) = (n_{\text{ph}} + 1)e^{-i\omega_0 t} + n_{\text{ph}}e^{i\omega_0 t}$.

Column $|\tilde{g}(x)\rangle$ should consist exclusively of slowly-varying functions, while all the highly-oscillating functions should be contained in $|\tilde{J}(x)\rangle$, with the property that

$$\frac{d|\tilde{J}(x)\rangle}{dx} = \hat{A}(x)|\tilde{J}(x)\rangle, \quad (\text{B.5})$$

where $\hat{A}(x)$ is some matrix of slowly-varying functions. If we can accomplish that, then the integral from Eq. (B.4) can be written as

$$I = \int_a^b dx \frac{d}{dx} \langle \tilde{f}(x) | \tilde{J}(x) \rangle = \langle \tilde{f}(b) | \tilde{J}(b) \rangle - \langle \tilde{f}(a) | \tilde{J}(a) \rangle, \quad (\text{B.6})$$

where we introduced a new quantity $|\tilde{f}(x)\rangle$, which satisfies

$$\left(\frac{d}{dx} + \hat{A}^\dagger(x) \right) |\tilde{f}(x)\rangle = |\tilde{g}(x)\rangle. \quad (\text{B.7})$$

Since both $\hat{A}^\dagger(x)$ and $|\tilde{g}(x)\rangle$ are slowly-varying, there also exists a slowly-varying particular solution of Eq. (B.7). Therefore, this differential equation can then, following Levin [119], be approximately solved by formally expanding

$$|\tilde{f}(x)\rangle = \sum_{k=1}^M u_k(x) [c_k \ d_k \ \dots]^T, \quad (\text{B.8})$$

into a basis set of polynomials $u_k(x) = (x - \frac{a+b}{2})^{k-1}$ and determining the unknown polynomial coefficients c_k, d_k, \dots by imposing that Eq. (B.7) is exactly satisfied at M uniformly distributed collocation points³ $x_j = a + \frac{(j-1)(b-a)}{M-1}$, $j = 1 \dots M$. The initial problem is thus reduced to a simple linear algebra problem, which is always easy to solve.

B.2 1D Case

In the 1D case ($d = 1$), columns $|\tilde{g}(x)\rangle$ and $|\tilde{J}(x)\rangle$ assume the following form

$$|\tilde{g}(x)\rangle = [g(x) \ 0]^T, \quad (\text{B.9a})$$

$$|\tilde{J}(x)\rangle = e^{ir_1 x} [J_0(r_2 x) \ J_1(r_2 x)]^T, \quad (\text{B.9b})$$

where $J_0(x)$ and $J_1(x)$ are the Bessel functions of the first kind, of zeroth and first order. The matrix $\hat{A}(x)$, such that Eq. (B.5) holds, is given by

$$\hat{A}(x) = \begin{bmatrix} ir_1 & -r_2 \\ r_2 & ir_1 - \frac{1}{x} \end{bmatrix}. \quad (\text{B.10})$$

The unknown coefficients c_k and d_k , which determine the column function

$$|\tilde{f}(x)\rangle = \sum_{k=1}^M u_k(x) [c_k \ d_k]^T, \quad (\text{B.11})$$

are obtained from the following set of $2M$ linear equations

$$\begin{bmatrix} \mathcal{C} & \mathcal{C}^d \\ \mathcal{D}^c & \mathcal{D} \end{bmatrix} \begin{bmatrix} c_1 \\ \vdots \\ c_M \\ d_1 \\ \vdots \\ d_M \end{bmatrix} = \begin{bmatrix} g(x_1) \\ \vdots \\ g(x_M) \\ 0 \\ \vdots \\ 0 \end{bmatrix}. \quad (\text{B.12})$$

³This is known as the M -point collocation approximation.

Here, $\mathcal{C}, \mathcal{C}^d, \mathcal{D}^c, \mathcal{D}$ are $M \times M$ matrices that read as

$$\mathcal{C}_{ij} = u'_j(x_i) - ir_1 u_j(x_i) \quad (\text{B.13a})$$

$$\mathcal{C}_{ij}^d = r_2 u_j(x_i) \quad (\text{B.13b})$$

$$\mathcal{D}_{ij} = u'_j(x_i) - \left(ir_1 + \frac{1}{x_i} \right) u_j(x_i) \quad (\text{B.13c})$$

$$\mathcal{D}_{ij}^c = -r_2 u_j(x_i). \quad (\text{B.13d})$$

The solution of Eq. (B.3) for $d = 1$ is now obtained using Eq. (B.6), where $|\tilde{J}(x)\rangle$ is given by Eq. (B.9b), and $|\tilde{f}(x)\rangle$ is given by Eq. (B.11), with the coefficients $c_1, \dots, c_M, d_1, \dots, d_M$ that are obtained by solving Eq. (B.12).

B.3 2D Case

In the 2D case, the relevant quantities are given by

$$|\tilde{g}(x)\rangle = [g(x) \ 0 \ 0]^T, \quad (\text{B.14a})$$

$$|\tilde{J}(x)\rangle = e^{ir_1 x} [J_0(r_2 x)^2 \ J_0(r_2 x) J_1(r_2 x) \ J_1(r_2 x)^2]^T, \quad (\text{B.14b})$$

$$\hat{A}(x) = \begin{bmatrix} ir_1 & -2r_2 & 0 \\ r_2 & ir_1 - \frac{1}{x} & -r_2 \\ 0 & 2r_2 & ir_1 - \frac{2}{x} \end{bmatrix}. \quad (\text{B.14c})$$

The column

$$|\tilde{f}(x)\rangle = \sum_{k=1}^M u_k(x) [c_k \ d_k \ e_k]^T \quad (\text{B.15})$$

is determined by c_k, d_k and e_k , which are obtained as a solution of the following system of $3M$ linear equations

$$\begin{bmatrix} \mathcal{C} & \mathcal{C}^d & \mathcal{C}^e \\ \mathcal{D}^c & \mathcal{D} & \mathcal{D}^e \\ \mathcal{E}^c & \mathcal{E}^d & \mathcal{E} \end{bmatrix} \begin{bmatrix} c_1 \\ \vdots \\ c_M \\ d_1 \\ \vdots \\ e_1 \\ \vdots \end{bmatrix} = \begin{bmatrix} g(x_1) \\ \vdots \\ g(x_M) \\ 0 \\ \vdots \\ 0 \\ \vdots \end{bmatrix}. \quad (\text{B.16})$$

Here, $\mathcal{C}, \mathcal{C}^d \dots \mathcal{E}$ are $M \times M$ matrices. Elements of \mathcal{C}_{ij} and \mathcal{C}_{ij}^d are the same as in Eq. (B.13), while $\mathcal{C}_{ij}^e = \mathcal{E}_{ij}^c = 0$. All the other elements are given by:

$$\mathcal{D}_{ij}^c = -2r_2 u_j(x_i) \quad (\text{B.17a})$$

$$\mathcal{D}_{ij}^e = 2r_2 u_j(x_i) \quad (\text{B.17b})$$

$$\mathcal{D}_{ij} = u'_j(x_i) - \left(ir_1 + \frac{1}{x_i} \right) u_j(x_i) \quad (\text{B.17c})$$

$$\mathcal{E}_{ij} = u'_j(x_i) - \left(ir_1 + \frac{2}{x_i} \right) u_j(x_i) \quad (\text{B.17d})$$

$$\mathcal{E}_{ij}^d = -r_2 u_j(x_i) \quad (\text{B.17e})$$

Therefore, the solution of Eq. (B.3) for $d = 2$ is found by first solving Eq. (B.16) for $c_1, \dots, c_M, d_1, \dots, d_M, e_1, \dots, e_M$, using this to calculate $|\tilde{f}(x)\rangle$ in Eq. (B.15), and along with Eq. (B.14b), plugging this into Eq. (B.6).

B.4 3D Case

The procedure that was presented so far is actually quite easily generalized to the 3D case as well. Here, the quantities of interest are easily derived and read as

$$|\tilde{g}(x)\rangle = [g(x) \ 0 \ 0 \ 0]^T, \quad (\text{B.18a})$$

$$|\tilde{J}(x)\rangle = e^{ir_1x} [J_0(r_2x)^3 \ J_0(r_2x)^2 J_1(r_2x) \ J_0(r_2x) J_1(r_2x)^2 \ J_1(r_2x)^3]^T, \quad (\text{B.18b})$$

$$\hat{A}(x) = \begin{bmatrix} ir_1 & -3r_2 & 0 & 0 \\ r_2 & ir_1 - \frac{1}{x} & -2r_2 & 0 \\ 0 & 2r_2 & ir_1 - \frac{2}{x} & -r_2 \\ 0 & 0 & 3r_2 & ir_1 - \frac{3}{x} \end{bmatrix}, \quad (\text{B.18c})$$

$$|\tilde{f}(x)\rangle = \sum_{k=1}^M u_k(x) [c_k \ d_k \ e_k \ f_k]^T, \quad (\text{B.18d})$$

where the coefficients c_k , d_k , e_k and f_k satisfy

$$\begin{bmatrix} \mathcal{C} & \mathcal{C}^d & \mathcal{C}^e & \mathcal{C}^f \\ \mathcal{D}^c & \mathcal{D} & \mathcal{D}^e & \mathcal{D}^f \\ \mathcal{E}^c & \mathcal{E}^d & \mathcal{E} & \mathcal{E}^f \\ \mathcal{F}^c & \mathcal{F}^d & \mathcal{F}^e & \mathcal{F} \end{bmatrix} \begin{bmatrix} c_1 \\ \vdots \\ c_M \\ d_1 \\ \vdots \\ e_1 \\ \vdots \\ f_1 \\ \vdots \end{bmatrix} = \begin{bmatrix} g(x_1) \\ \vdots \\ g(x_M) \\ 0 \\ \vdots \\ 0 \\ \vdots \\ 0 \\ \vdots \end{bmatrix}. \quad (\text{B.19})$$

Here \mathcal{C}_{ij} , \mathcal{C}_{ij}^d , \mathcal{C}_{ij}^e , \mathcal{D}_{ij} , \mathcal{D}_{ij}^e , \mathcal{E}_{ij}^c and \mathcal{E}_{ij} are the same as in Eqs. (B.13) and (B.17), while $\mathcal{C}_{ij}^f = \mathcal{F}_{ij}^c = \mathcal{D}_{ij}^f = \mathcal{F}_{ij}^d = 0$. All other elements are given by:

$$\mathcal{E}_{ij}^d = -2r_2 u_j(x_i), \quad (\text{B.20a})$$

$$\mathcal{E}_{ij}^f = 3r_2 u_j(x_i), \quad (\text{B.20b})$$

$$\mathcal{D}_{ij}^c = -3r_2 u_j(x_i), \quad (\text{B.20c})$$

$$\mathcal{F}_{ij}^e = -r_2 u_j(x_i), \quad (\text{B.20d})$$

$$\mathcal{F}_{ij} = u_j'(x_i) - \left(ir_1 + \frac{3}{x_i} \right) u_j(x_i). \quad (\text{B.20e})$$

Therefore, in a complete analogy to 1D and 2D, the solution of Eq. (B.3) for $d = 3$ is calculated using Eq. (B.6), where $|\tilde{J}(x)\rangle$ and $|\tilde{f}(x)\rangle$ are given by Eqs. (B.18b) and (B.18d), respectively. Thus, our numerical scheme has been completely specified.

Remark 40. We note that Eqs. (B.13), (B.17) and (B.20) explicitly demonstrate that our numerical scheme is singular at $x = 0$. This does not pose any problems, as the subintegral function in our initial expression (B.3) is not highly-oscillatory around $x = 0$. Therefore, the trapezoid scheme can be applied there.



Current Operator in Quantum Mechanics

C.1 Introduction

This text is devoted to the derivation of the current density operator in two different, but relevant cases:

- *In the continuum case* - this is a standard derivation that can be found in many texts; for example see Ref. [128]. The standard idea is to modify the kinetic term of the Hamiltonian, using the minimal substitution $\mathbf{p} \rightarrow \mathbf{p} - e_0\mathbf{A}$. Then, the current density is derived straightforwardly from its most general definition $\mathbf{j}(\mathbf{r}) = -\frac{\delta H}{\delta \mathbf{A}(\mathbf{r})}$, which is motivated in Sec. C.2.
- *In the case of a lattice, with a tight-binding Hamiltonian that includes only the nearest-neighbor hopping* - while the total current can easily be derived [1], the derivation of the Fourier components of the current is more involved. Analogous to the minimal substitution in the continuum case, here we use the Pierels substitution $t_{ij} \rightarrow t_{ij} e^{-i \int_{\mathbf{R}_i}^{\mathbf{R}_j} d\mathbf{r} \mathbf{A}(\mathbf{r}, t)}$ to include the vector potential $\mathbf{A}(\mathbf{r})$ in the Hamiltonian. Before the application of the definition $\mathbf{j}(\mathbf{r}) = -\frac{\delta H}{\delta \mathbf{A}(\mathbf{r})}$, it is standard to restrict the derivation to the case when the field $\mathbf{A}(\mathbf{r})$ slowly varies on the atomic scale, such that $\int_{\mathbf{R}_i}^{\mathbf{R}_j} d\mathbf{r} \mathbf{A}(\mathbf{r}, t)$ can be approximated as a linear combination $\mathbf{A}(\mathbf{R}_i, t)$ and $\mathbf{A}(\mathbf{R}_j, t)$. For example, in the 1D case we can approximate:

1.
$$\int_{R_i}^{R_j} dx A(x, t) \approx \frac{R_j - R_i}{2} (A(R_i, t) + A(R_j, t)). \quad (\text{C.1})$$

In this approach, which has for example been used Ref. [126], the left-hand side of Eq. C.1 has been approximated as a single trapezoid.

2.
$$\int_{R_i}^{R_j} dx A(x, t) \approx (R_j - R_i) A(R_j, t). \quad (\text{C.2})$$

Here, $\int_{R_i}^{R_j} dx A(x, t)$ has been approximated as a single rectangle, where the height of that rectangle is taken to be $A(R_j, t)$. Similarly, we can also take the height of the rectangle to be $A(R_i, t)$

$$\int_{R_i}^{R_j} dx A(x, t) \approx (R_j - R_i) A(R_i, t). \quad (\text{C.3})$$

As we will see, neither Eq. (C.2), nor Eq. (C.3) leads to the Hermitian Hamiltonian. This problem can be solved by combining approximations in Eqs. (C.2) and (C.3) in the following way: approximation (C.2) is used for the hopping from site j to site i , whereas approximation (C.3) is used for its Hermitian conjugate term. This approach has been used by Refs. [125, 137].

These two approaches lead to two different expressions for the current operator. It turns out that Eq. (C.1) will lead to a real current vertex, while the combination of Eqs. (C.2) and (C.3) will lead to a complex current vertex. Both of these have certain advantages and disadvantages, as we will discuss later in detail.

C.2 Some General Remarks on the Definition of the Current Density Operator

Here, we discuss some model-independent ways in which the current operator is defined. Typically, the current operator \mathbf{j} is calculated either by finding such \mathbf{j} that the continuity equation is satisfied

$$\partial_\mu j^\mu(\mathbf{r}, t) = 0 \iff \frac{\partial \rho}{\partial t} = -\text{div } \mathbf{j}(\mathbf{r}, t), \quad (\text{C.4})$$

or directly by using

$$\boxed{\mathbf{j}(\mathbf{r}) = -\frac{\delta H}{\delta \mathbf{A}(\mathbf{r}, t)}} \quad (\text{C.5})$$

where H is the Hamiltonian of the theory, in which the vector potential has been introduced. Since the continuity Equation (C.4) has been thoroughly studied in any textbook on electromagnetism, we will here give the motivation only for Eq. (C.5).

For this, we first recall from classical mechanics that the Lagrangian of the system of particles in an electromagnetic field is given by

$$L = \sum_i \left[\frac{1}{2} m_i v_i^2 + q_i \mathbf{v}_i \cdot \mathbf{A}(\mathbf{r}_i) - q_i \varphi(\mathbf{r}_i) \right] - V(\mathbf{r}_1, \mathbf{r}_2 \dots). \quad (\text{C.6})$$

Then, we switch to the Hamiltonian description of the system

$$\mathbf{p}_i \equiv \frac{\partial L}{\partial \mathbf{v}_i} = m_i \mathbf{v}_i + q_i \mathbf{A}(\mathbf{r}_i) \quad (\text{C.7a})$$

$$H = \sum_i \mathbf{p}_i \cdot \mathbf{v}_i - L \quad (\text{C.7b})$$

$$= \sum_i \left[\mathbf{v}_i \cdot (\mathbf{p}_i - q_i \mathbf{A}(\mathbf{r}_i)) - \frac{1}{2} m_i v_i^2 - q_i \varphi(\mathbf{r}_i) \right] - V(\mathbf{r}_1, \mathbf{r}_2 \dots) \quad (\text{C.7c})$$

$$= \sum_i \left[\frac{1}{2m_i} (\mathbf{p}_i - q_i \mathbf{A}(\mathbf{r}_i))^2 - q_i \varphi(\mathbf{r}_i) \right] - V(\mathbf{r}_1, \mathbf{r}_2 \dots). \quad (\text{C.7d})$$

We note that the last line could be obtained directly by using the minimal coupling description $\mathbf{p}_i \rightarrow \mathbf{p}_i - q_i \mathbf{A}(\mathbf{r}_i)$ in the Hamiltonian formalism.

Now the current will pop out by inspecting the variation of the Hamiltonian δH , as a response to the variation of the vector potential $\delta \mathbf{A}$

$$\delta H = H(\mathbf{A} + \delta \mathbf{A}) - H(\mathbf{A}) = - \sum_i \frac{q_i \delta \mathbf{A}(\mathbf{r}_i)}{m_i} (\mathbf{p}_i - q_i \mathbf{A}(\mathbf{r}_i)) \quad (\text{C.8})$$

$$= - \sum_i q_i \mathbf{v}_i \delta \mathbf{A}(\mathbf{r}_i) = - \int d\mathbf{r} \underbrace{\sum_i q_i \mathbf{v}_i \delta(\mathbf{r} - \mathbf{r}_i)}_{\equiv \mathbf{j}(\mathbf{r})} \delta \mathbf{A}(\mathbf{r}) \quad (\text{C.9})$$

$$= - \int d\mathbf{r} \mathbf{j}(\mathbf{r}) \delta \mathbf{A}(\mathbf{r}) \quad (\text{C.10})$$

The last line directly implies Eq. (C.5), which completes our motivation. \square

C.3 Current Density Operator in the Case of a Continuum

We restrict ourselves to the case of the spinless systems, which are relevant for our study, while the generalization to the case with spin is straightforward. In our case, the corresponding Hamiltonian reads as

$$H = \int d\mathbf{r} \psi^\dagger(\mathbf{r}) \frac{[\mathbf{p} - e_0 \mathbf{A}(\mathbf{r})]^2}{2m_0} \psi(\mathbf{r}) + \dots \quad (\text{C.11})$$

$$= \frac{1}{2m_0} \int d\mathbf{r} \psi^\dagger(\mathbf{r}) [ie_0 \nabla \mathbf{A} + ie_0 \mathbf{A} \nabla + e_0^2 \mathbf{A}^2] \psi(\mathbf{r}) + \dots, \quad (\text{C.12})$$

where the dots \dots denote the terms with no \mathbf{A} dependence. As we want to use Eq. (C.5), we need to transform the term with $\nabla \mathbf{A}$, by using the integration by parts

$$\frac{1}{2m_0} \int d\mathbf{r} \psi^\dagger(\mathbf{r}) ie_0 \nabla \mathbf{A}(\mathbf{r}) \psi(\mathbf{r}) = -\frac{ie_0}{2m_0} \int d\mathbf{r} \mathbf{A}(\mathbf{r}) (\nabla \psi^\dagger(\mathbf{r})) \psi(\mathbf{r}), \quad (\text{C.13})$$

where the surface term has been neglected. Hence

$$H = \frac{e_0}{2m_0} \int d\mathbf{r} \left[-(\nabla \psi^\dagger(\mathbf{r})) i \mathbf{A}(\mathbf{r}) \psi(\mathbf{r}) + \psi^\dagger(\mathbf{r}) i \mathbf{A}(\mathbf{r}) \nabla \psi(\mathbf{r}) + e_0 \mathbf{A}(\mathbf{r})^2 \psi^\dagger(\mathbf{r}) \psi(\mathbf{r}) \right] + \dots \quad (\text{C.14})$$

Using Eq. (C.5), we directly obtain the current density operator:

$$\begin{aligned} j(\mathbf{r}) &= j^p(\mathbf{r}) + j^d(\mathbf{r}) \\ j^p(\mathbf{r}) &= \frac{ie_0}{2m_0} [(\nabla \psi^\dagger(\mathbf{r})) \psi(\mathbf{r}) - \psi^\dagger(\mathbf{r}) \nabla \psi(\mathbf{r})] \\ j^d(\mathbf{r}) &= -\frac{e_0^2}{m_0} \mathbf{A}(\mathbf{r}) \psi^\dagger(\mathbf{r}) \psi(\mathbf{r}) \end{aligned} \quad (\text{C.15})$$

To transform these relations to the Fourier space we use:

$$j(\mathbf{q}) = \int d\mathbf{r} j(\mathbf{r}) e^{-i\mathbf{q}\mathbf{r}}, \quad (\text{C.16})$$

$$\psi^\dagger(\mathbf{r}) = \frac{1}{\sqrt{V}} \sum_{\mathbf{k}} e^{-i\mathbf{k}\mathbf{r}} c_{\mathbf{k}}^\dagger, \quad (\text{C.17})$$

$$\psi(\mathbf{r}) = \frac{1}{\sqrt{V}} \sum_{\mathbf{k}} e^{i\mathbf{k}\mathbf{r}} c_{\mathbf{k}}, \quad (\text{C.18})$$

$$c_{\mathbf{k}}^\dagger = \frac{1}{\sqrt{V}} \int d\mathbf{r} e^{i\mathbf{k}\mathbf{r}} \psi^\dagger(\mathbf{r}), \quad (\text{C.19})$$

$$c_{\mathbf{k}} = \frac{1}{\sqrt{V}} \int d\mathbf{r} e^{-i\mathbf{k}\mathbf{r}} \psi(\mathbf{r}), \quad (\text{C.20})$$

obtaining

$$j^p(\mathbf{q}) = \frac{ie_0}{2m_0 V} \int d\mathbf{r} e^{-i\mathbf{q}\mathbf{r}} \left[\sum_{\mathbf{k}_1, \mathbf{k}_2} -i\mathbf{k}_1 - i\mathbf{k}_2 \right] e^{-i\mathbf{k}_1 \mathbf{r} + i\mathbf{k}_2 \mathbf{r}} c_{\mathbf{k}_1}^\dagger c_{\mathbf{k}_2} \quad (\text{C.21})$$

$$= \frac{e_0}{2m_0} \sum_{\mathbf{k}} (2\mathbf{k} + \mathbf{q}) c_{\mathbf{k}}^\dagger c_{\mathbf{k}+\mathbf{q}}, \quad (\text{C.22})$$

and

$$j^d(\mathbf{q}) = -\frac{e_0^2}{m_0 V} \int d\mathbf{r} e^{-i\mathbf{q}\mathbf{r}} A(\mathbf{r}) \sum_{\mathbf{k}_1, \mathbf{k}_2} e^{-i\mathbf{k}_1\mathbf{r} + i\mathbf{k}_2\mathbf{r}} c_{\mathbf{k}_1}^\dagger c_{\mathbf{k}_2} \quad (\text{C.23})$$

$$= -\frac{e_0^2}{m_0 V} \sum_{\mathbf{k}_1, \mathbf{k}_2} c_{\mathbf{k}_1}^\dagger c_{\mathbf{k}_2} A(\mathbf{q} + \mathbf{k}_1 - \mathbf{k}_2) \quad (\text{C.24})$$

$$= -\frac{e_0^2}{m_0 V} \sum_{\mathbf{k}_1, \mathbf{k}_2} A(\mathbf{k}_1 - \mathbf{k}_2) c_{\mathbf{k}_1}^\dagger c_{\mathbf{k}_2 + \mathbf{q}}. \quad (\text{C.25})$$

Hence:

$$\begin{aligned} j(\mathbf{q}) &= j^p(\mathbf{q}) + j^d(\mathbf{q}) \\ j^p(\mathbf{q}) &= \frac{e_0}{2m_0} \sum_{\mathbf{k}} (2\mathbf{k} + \mathbf{q}) c_{\mathbf{k}}^\dagger c_{\mathbf{k} + \mathbf{q}}, \\ j^d(\mathbf{q}) &= -\frac{e_0^2}{m_0 V} \sum_{\mathbf{k}_1, \mathbf{k}_2} A(\mathbf{k}_1 - \mathbf{k}_2) c_{\mathbf{k}_1}^\dagger c_{\mathbf{k}_2 + \mathbf{q}}. \end{aligned} \quad (\text{C.26})$$

C.4 Current Density Operator in the Case of a Lattice

C.4.1 Full Current Operator

If we are interested only in the full current operator (corresponding to $\mathbf{q} = 0$ Fourier components), and not its other Fourier components, we can easily calculate it as a time derivative of the polarization operator

$$\mathbf{j}_{\text{tot}} \equiv \frac{\partial \mathbf{P}}{\partial t} = -i[\mathbf{P}, H]. \quad (\text{C.27})$$

This definition can be motivated by the continuity equation

$$\frac{\partial \mathbf{P}}{\partial t} = \int d\mathbf{r} \frac{\partial \rho}{\partial t} \mathbf{r} = - \int d\mathbf{r} (\text{div } \mathbf{j}) \mathbf{r} = \int d\mathbf{r} \mathbf{j} (\text{div } \mathbf{r}) = \int d\mathbf{r} \mathbf{j} \equiv \mathbf{j}_{\text{tot}}. \quad (\text{C.28})$$

If we are not interested in the \mathbf{r} dependence, then we can simply define the current density operator to be

$$\mathbf{j} = \frac{\mathbf{j}_{\text{tot}}}{V} = \frac{1}{V} \frac{\partial \mathbf{P}}{\partial t} = -\frac{i}{V} [\mathbf{P}, H]. \quad (\text{C.29})$$

Remark 41. We always set the volume of a unit cell to unity. Hence, we can always use the number of lattice sites N instead of the volume V (and vice versa) in all our formulas.

Remark 42. In the case of the Holstein model, only the kinetic part of the Hamiltonian contributes in Eq. (C.29), as the interaction term commutes with the polarization operator.

1D Case with Tight-binding Hamiltonian and Nearest-neighbor Interaction

Let us now calculate j from Eq. (C.29) in the case of 1D tight-binding Hamiltonian with nearest-neighbor hopping. In this case:

$$H_{\text{kin}} = - \sum_{\langle j_1, j_2 \rangle} t_{j_1 j_2} c_{j_1}^\dagger c_{j_2} = -t_0 \sum_i (c_r^\dagger c_{r+1} + h.c.), \quad (\text{C.30})$$

$$P = e_0 \sum_j j c_j^\dagger c_j. \quad (\text{C.31})$$

It is now straightforward to substitute Eqs. (C.30) and (C.31) to Eq. (C.29) and to obtain:

$$j = \frac{ie_0t_0}{N} \sum_{j,r} j \left[c_j^\dagger c_j, c_r^\dagger c_{r+1} \right] + h.c. \quad (C.32)$$

$$= \frac{ie_0t_0}{N} \sum_r (r c_r^\dagger c_{r+1} - (r+1) c_r^\dagger c_{r+1}) + h.c., \quad (C.33)$$

where we used the following relation between the commutator $[,]$ and the anticommutator $\{, \}$: $[AB, C] = A \{B, C\} - \{A, C\} B$ and $[A, BC] = \{A, B\} C - B \{A, C\}$. Hence,

$$j = \frac{ie_0t_0}{N} \sum_r (c_{r+1}^\dagger c_r - c_r^\dagger c_{r+1}) = \frac{e_0}{N} \sum_k v_k c_k^\dagger c_k, \quad (C.34)$$

where $v_k = \nabla_k \varepsilon_k = 2t_0 \sin k$.

Tight-binding Hamiltonian with Nearest-neighbor Interaction in an Arbitrary Number of Dimensions

The 1D results can easily be generalized to an arbitrary number of dimensions, in the case of hypercubic lattice. We just need to introduce the vector δ that goes over the nearest neighbor vectors. Using this, the Hamiltonian and polarization operator read as¹

$$H_{kin} = -t_0 \sum_{\mathbf{r}, \delta} c_{\mathbf{r}}^\dagger c_{\mathbf{r}+\delta} \quad (C.35)$$

$$\mathbf{P} = e_0 \sum_{\mathbf{r}} \mathbf{r} c_{\mathbf{r}}^\dagger c_{\mathbf{r}}, \quad (C.36)$$

while the calculation of the current is analogous to the 1D case, giving

$$\mathbf{j} = \frac{ie_0t_0}{V} \sum_{\mathbf{r}, \delta} \delta \cdot c_{\mathbf{r}+\delta}^\dagger c_{\mathbf{r}} = \frac{e_0}{V} \sum_{\mathbf{k}} v_{\mathbf{k}} c_{\mathbf{k}}^\dagger c_{\mathbf{k}}, \quad (C.37)$$

where $v_{\mathbf{k}} = \nabla_{\mathbf{k}} \varepsilon_{\mathbf{k}}$.

Remark 43. *In the rest of this chapter and generally, in this thesis, we set $e_0 = 1$, unless stated otherwise.*

C.4.2 Fourier Components of the Current Density Operator

If we are interested in the current density operator in the Fourier space, or equivalently as a function of lattice coordinate, then the result in Eq. (C.34) is not satisfactory. In order to use the current definition from Eq. (C.5), we first need to introduce the vector potential in the tight-binding Hamiltonian. This can be done by modifying the hopping parameter t_{ij} via the Peierls substitution²

$$t_{j_1 j_2} \rightarrow t_{j_1 j_2} e^{-i \int_{\mathbf{R}_{j_1}}^{\mathbf{R}_{j_2}} d\mathbf{r} \mathbf{A}(\mathbf{r}, t)}. \quad (C.38)$$

Let us now restrict ourselves to the 1D case, and assume that the vector potential does not vary too much on the atomic scale. We will derive the current operators starting from Eq. (C.1) and Eqs. (C.2) and (C.3), as we explained in Sec. C.1.

¹Here, we assume that for every nearest neighbor at δ , there is another nearest neighbour at $-\delta$.

²There should also be e_0 in the exponent, but we already set $e_0 = 1$.

We will see that a more symmetric approximation from Eq. (C.1) leads to the real current vertex, but the drawback is that $\text{div } \mathbf{j}$ cannot be properly defined in the coordinate space. On the other hand, the divergence of current is easily defined if we start from Eqs. (C.2) and (C.3), but the current vertex turns out to be complex. Thus, we see that both of these approaches has certain advantages and limitations. These will be discussed in detail below.

C.4.2.1 Current Density Operator using Approximation from Eq. (C.1)

1D Case

In this case, the 1D nearest-neighbour Hamiltonian becomes

$$H = -t_0 \sum_j \left[e^{-\frac{i}{2}(A(j)+A(j+1))} c_j^\dagger c_{j+1} + e^{\frac{i}{2}(A(j)+A(j+1))} c_{j+1}^\dagger c_j \right] + \dots, \quad (\text{C.39})$$

where \dots denote the terms that do not depend on $A(j)$. The current density operator is now obtained using³ Eq. (C.5)

$$j_r \equiv -\frac{\delta H}{\delta A(r)} \quad (\text{C.40})$$

$$= t_0 \sum_j \left[-\frac{i}{2} e^{-\frac{i}{2}(A(j)+A(j+1))} (\delta_{j,r} + \delta_{j+1,r}) c_j^\dagger c_{j+1} + h.c. \right] \quad (\text{C.41})$$

$$= -\frac{it_0}{2} \left[c_r^\dagger c_{r+1} e^{-\frac{i}{2}(A(r)+A(r+1))} + c_{r-1}^\dagger c_r e^{-\frac{i}{2}(A(r)+A(r-1))} \right] + h.c. \quad (\text{C.42})$$

Let us now approximate the exponential using the Taylor series, up to a linear order, and collect the terms with and without A dependence. These correspond to diamagnetic and paramagnetic terms of current density, respectively

$$j_r = j_r^p + j_r^d \quad (\text{C.43})$$

$$j_r^p = \frac{it_0}{2} \left[c_r^\dagger c_{r-1} + c_{r+1}^\dagger c_r - c_r^\dagger c_{r+1} - c_{r-1}^\dagger c_r \right] \quad (\text{C.44})$$

$$j_r^d = -\frac{t_0}{4} \left[(A(r) + A(r+1)) c_r^\dagger c_{r+1} + (A(r) + A(r-1)) c_{r-1}^\dagger c_r \right] + h.c. \quad (\text{C.45})$$

Due to our assumption that the vector potential slowly varies on the atomic scale, we can further approximate $A(r+1) \approx A(r-1) \approx A(r)$ in the diamagnetic term. Hence

$$j_r^d = -\frac{t_0}{2} A(r) \left[c_r^\dagger c_{r+1} + c_{r-1}^\dagger c_r + c_{r+1}^\dagger c_r + c_r^\dagger c_{r-1} \right]. \quad (\text{C.46})$$

Since the goal of our work is to calculate the response functions in the linear response theory, and these are connected to the correlation functions in the absence of the external potential, from now on we will concentrate on the paramagnetic term $j_r \equiv j_r^p$. To obtain its the Fourier components, we use

$$j_q = \sum_r e^{-iqr} j_r, \quad (\text{C.47a})$$

$$c_r^\dagger = \frac{1}{\sqrt{N}} \sum_{k_1} e^{-ik_1 r} c_{k_1}^\dagger, \quad (\text{C.47b})$$

$$c_r = \frac{1}{\sqrt{N}} \sum_{k_2} e^{ik_2 r} c_{k_2}. \quad (\text{C.47c})$$

³In the case of a lattice, the right-hand side of Eq. (C.5) should be divided by the volume of the unit lattice, but this was set to unity.

We get

$$j_q = \frac{it_0}{2N} \sum_{r,k_1,k_2} e^{-iqr} [e^{-ik_2} + e^{-ik_1} - e^{ik_2} - e^{ik_1}] e^{i(k_2-k_1)r} c_{k_1}^\dagger c_{k_2} \quad (\text{C.48})$$

$$= t_0 \sum_k [\sin(k) + \sin(k+q)] c_k^\dagger c_{k+q} \quad (\text{C.49})$$

This can also be written as:

$$j_q = 2t_0 \sum_k \sin\left(k + \frac{q}{2}\right) \cos\left(\frac{q}{2}\right) c_k^\dagger c_{k+q} \quad (\text{C.50})$$

The Case of a Tight-Binding Hamiltonian with Nearest-neighbor Interaction in an Arbitrary Number of Dimensions

All of these results are easily generalized to the higher-dimensional case⁴. We just give the result for the paramagnetic current, which is all we actually need

$$\mathbf{j}^p(\mathbf{r}) = \frac{it_0}{2} \sum_{\delta} \left(c_{\mathbf{r}}^\dagger c_{\mathbf{r}-\delta} + c_{\mathbf{r}+\delta}^\dagger c_{\mathbf{r}} \right) \delta \quad (\text{C.51})$$

where δ goes over the nearest neighbour vectors. The Fourier transform of the paramagnetic current is also easily obtained and reads as

$$\mathbf{j}(\mathbf{q}) = \frac{it_0}{2} \sum_{\mathbf{k}, \delta} \delta [e^{-i\delta\mathbf{k}} + e^{-i\delta(\mathbf{k}+\mathbf{q})}] c_{\mathbf{k}}^\dagger c_{\mathbf{k}+\mathbf{q}} \quad (\text{C.52})$$

Due to inversion symmetry, for every nearest neighbor at δ , there is another nearest neighbor situated at $-\delta$. Hence, we can introduce the notation $\sum_{\tilde{\delta}}$ which denotes a sum that goes over half of the nearest neighbors, such that the other half is obtained as $-\tilde{\delta}$. In this case, the last expression can be written as

$$\mathbf{j}(\mathbf{q}) = 2t_0 \sum_{\mathbf{k}, \tilde{\delta}} \tilde{\delta} \sin\left(\mathbf{k} \tilde{\delta} + \frac{\mathbf{q} \tilde{\delta}}{2}\right) \cos\left(\frac{\mathbf{q} \tilde{\delta}}{2}\right) c_{\mathbf{k}}^\dagger c_{\mathbf{k}+\mathbf{q}}. \quad (\text{C.53})$$

C.4.2.2 Current Density Operator using Approximation from Eqs. (C.2) and (C.3)

1D Case

If we straightforwardly applied approximation (C.2), then the corresponding Hamiltonian would be given by

$$H = -t_0 \sum_j \left[e^{-iA(j+1)} c_j^\dagger c_{j+1} + e^{iA(j)} c_{j+1}^\dagger c_j \right] + \dots \quad (\text{C.54})$$

This Hamiltonian is not Hermitian. As we already assumed that the vector potential is slowly varying on the atomic scale, we could fix this problem by hand, by approximating $A(j) \approx A(j+1)$. On the other hand, this can also be done by using approximation (C.2) on the hopping terms $c_j^\dagger c_{j+1}$, while using approximation (C.3) on the hopping terms $c_{j+1}^\dagger c_j$. In this case, the Hamiltonian becomes

$$H = -t_0 \sum_j \left[e^{-iA(j+1)} c_j^\dagger c_{j+1} + e^{iA(j+1)} c_{j+1}^\dagger c_j \right] + \dots, \quad (\text{C.55})$$

⁴We assume that a lattice has inversion symmetry.

where dots ... denote the terms that do not depend on $A(j)$. The current density operator is now obtained using Eq. (C.5)

$$j_r \equiv -\frac{\delta H}{\delta A(r)} \quad (\text{C.56})$$

$$= -it_0 e^{-iA(r)} c_{r-1}^\dagger c_r + it_0 e^{iA(r)} c_r^\dagger c_{r-1} \quad (\text{C.57})$$

$$= it_0 \left[c_r^\dagger c_{r-1} - c_{r-1}^\dagger c_r \right] - t_0 \left[c_r^\dagger c_{r-1} + c_{r-1}^\dagger c_r \right] A(r) + \dots, \quad (\text{C.58})$$

where dots ... denote the higher order terms with respect to A . From here, we can read off the paramagnetic and diamagnetic terms:

$$\begin{aligned} j_r &\equiv j_r^p + j_r^d \\ j_r^p &= it_0 \left[c_r^\dagger c_{r-1} - c_{r-1}^\dagger c_r \right] \\ j_r^d &= -t_0 \left[c_r^\dagger c_{r-1} + c_{r-1}^\dagger c_r \right] A(r) \end{aligned} \quad (\text{C.59})$$

Again, we concentrate on the paramagnetic term $j_r \equiv j_r^p$, which is the only one that gives a contribution in the calculation of response functions in the linear response theory. Its Fourier components can straightforwardly be calculated using Eq. (C.47)

$$j_q = \frac{it_0}{N} \sum_{r,k_1,k_2} e^{-iqr} \left[e^{-ik_2 r} - e^{ik_1 r} \right] e^{i(k_2 - k_1)r} c_{k_1}^\dagger c_{k_2} \quad (\text{C.60})$$

Hence,

$$j_q = it_0 \sum_k \left[e^{-i(k+q)} - e^{ik} \right] c_k^\dagger c_{k+q}. \quad (\text{C.61})$$

The Case of a Tight-binding Hamiltonian with Nearest-neighbor Interaction in an Arbitrary Number of Dimensions

The derivations that we presented can easily be repeated for the higher-dimensional case. As in the 1D case, in order to keep the Hamiltonian Hermitian after the Pierels substitution, we need to use different approximations for the hopping terms going from site j to i , and for hopping terms going from i to j . This is why Eq. (C.35) is not convenient for our purpose. Instead, we will restrict ourselves to the case of a lattice with inversion symmetry. In this case, it is better to write the Hamiltonian (before introducing the vector potential) as

$$H_{kin} = -t_0 \sum_{\mathbf{r}, \tilde{\delta}} \left(c_{\mathbf{r}}^\dagger c_{\mathbf{r}+\tilde{\delta}} + c_{\mathbf{r}+\tilde{\delta}}^\dagger c_{\mathbf{r}} \right), \quad (\text{C.62})$$

where the sum over $\tilde{\delta}$ goes over only a half of the nearest-neighbours, such that all nearest neighbours are obtained using $\tilde{\delta}$ and $-\tilde{\delta}$. For example, in the cubic lattice $\tilde{\delta}$ would go over $[1, 0, 0]$, $[0, 1, 0]$ and $[0, 0, 1]$. Now, analogous to the 1D case, the vector potential is introduced as follows

$$H_{kin} = -t_0 \sum_{\mathbf{r}, \tilde{\delta}} \left(c_{\mathbf{r}}^\dagger c_{\mathbf{r}+\tilde{\delta}} e^{-i\tilde{\delta}\mathbf{A}(\mathbf{r}+\tilde{\delta})} + c_{\mathbf{r}+\tilde{\delta}}^\dagger c_{\mathbf{r}} e^{i\tilde{\delta}\mathbf{A}(\mathbf{r}+\tilde{\delta})} \right). \quad (\text{C.63})$$

The paramagnetic current is also easily calculated, and reads as

$$\mathbf{j}^p(\mathbf{r}) = it_0 \sum_{\tilde{\delta}} \left(c_{\mathbf{r}}^\dagger c_{\mathbf{r}-\tilde{\delta}} - c_{\mathbf{r}-\tilde{\delta}}^\dagger c_{\mathbf{r}} \right) \tilde{\delta}, \quad (\text{C.64})$$

while its Fourier transform is given by

$$\mathbf{j}(\mathbf{q}) = it_0 \sum_{\mathbf{k}, \tilde{\delta}} \tilde{\delta} \left(e^{-i\tilde{\delta}(\mathbf{k}+\mathbf{q})} - e^{i\tilde{\delta}\mathbf{k}} \right) c_{\mathbf{k}}^\dagger c_{\mathbf{k}+\mathbf{q}} \quad (\text{C.65})$$

C.5 Continuity Equation and its Consequences

The Case of Continuum

Eqs. (C.26), (C.50) and (C.61) were all derived from Eq. (C.5). It is not immediately clear whether each of these expressions satisfies the continuity equation. In the case of Eq. (C.26), this can be easily explicitly checked. To do so, we first transform the continuity equation

$$\text{div } \mathbf{j}(\mathbf{r}, t) = -\frac{\partial \rho}{\partial t} = i[\rho(\mathbf{r}), H] \quad (\text{C.66})$$

into the Fourier space

$$\mathbf{q} j(\mathbf{q}) = [\rho(\mathbf{q}), H] = [\rho(\mathbf{q}), H_{kin}]. \quad (\text{C.67})$$

In the last equality, we restricted ourselves to the case when only the kinetic part of the Hamiltonian does not commute with the particle density. This is true for the models we are considering.

Eq. (C.67) can now explicitly be checked, both in the most general case when \mathbf{A} is finite, and in the special case when we take only the paramagnetic part of the current operator (in which case we must also set $\mathbf{A} = 0$ in H_{kin}). We will now prove that continuity equation holds in the most general case. In order to calculate commutator in Eq. (C.67), we first use Eqs. (C.17) and (C.18) to express H_{kin} from Eq. (C.12) using creation/annihilation operators in the Fourier space⁵

$$H_{kin} = \frac{1}{2m_0V} \sum_{\mathbf{k}_1, \mathbf{k}_2} \int d\mathbf{r} e^{-i\mathbf{k}_1\mathbf{r}} \left(\mathbf{k}_2^2 - e_0(-i\nabla)\mathbf{A}(\mathbf{r}) - e_0\mathbf{A}(\mathbf{r})(-i\nabla) + e_0^2\mathbf{A}(\mathbf{r})^2 \right) e^{i\mathbf{k}_2\mathbf{r}} c_{\mathbf{k}_1}^\dagger c_{\mathbf{k}_2}. \quad (\text{C.68})$$

Using the integration by parts in the second term in the brackets, we get

$$H_{kin} = \frac{1}{2m_0V} \sum_{\mathbf{k}_1, \mathbf{k}_2} \int d\mathbf{r} e^{-i\mathbf{k}_1\mathbf{r}} \left(\mathbf{k}_2^2 + e_0(-i\tilde{\nabla})\mathbf{A}(\mathbf{r}) - e_0\mathbf{A}(\mathbf{r})(-i\nabla) + e_0^2\mathbf{A}(\mathbf{r})^2 \right) e^{i\mathbf{k}_2\mathbf{r}} c_{\mathbf{k}_1}^\dagger c_{\mathbf{k}_2}. \quad (\text{C.69})$$

Hence,

$$H_{kin} = \frac{1}{2m_0V} \sum_{\mathbf{k}_1, \mathbf{k}_2} \int d\mathbf{r} e^{-i\mathbf{k}_1\mathbf{r}} \left[\mathbf{k}_2^2 - e_0(\mathbf{k}_1 + \mathbf{k}_2)\mathbf{A}(\mathbf{r}) + e_0^2\mathbf{A}(\mathbf{r})^2 \right] e^{i\mathbf{k}_2\mathbf{r}} c_{\mathbf{k}_1}^\dagger c_{\mathbf{k}_2} \quad (\text{C.70})$$

$$= \frac{1}{2m_0V} \sum_{\mathbf{k}_1, \mathbf{k}_2} \left[V \mathbf{k}_2^2 \delta_{\mathbf{k}_1, \mathbf{k}_2} - e_0(\mathbf{k}_1 + \mathbf{k}_2)\mathbf{A}(\mathbf{k}_1 - \mathbf{k}_2) + e_0^2\mathbf{A}^2(\mathbf{k}_1 - \mathbf{k}_2) \right] c_{\mathbf{k}_1}^\dagger c_{\mathbf{k}_2}, \quad (\text{C.71})$$

where $\mathbf{A}^2(\mathbf{k}_1 - \mathbf{k}_2)$ is the Fourier transform of $\mathbf{A}^2(\mathbf{r})$, and not the square of the Fourier transform. The right-hand side of Eq. (C.67) now reads as

$$[\rho(\mathbf{q}), H_{kin}] = \frac{e_0}{2m_0V} \sum_{\mathbf{k}_1, \mathbf{k}_2, \mathbf{k}_3} \left[c_{\mathbf{k}_3}^\dagger c_{\mathbf{k}_3+\mathbf{q}}, c_{\mathbf{k}_1}^\dagger c_{\mathbf{k}_2} \right] \times \left(V \mathbf{k}_2^2 \delta_{\mathbf{k}_1, \mathbf{k}_2} - e_0(\mathbf{k}_1 + \mathbf{k}_2)\mathbf{A}(\mathbf{k}_1 - \mathbf{k}_2) + e_0^2\mathbf{A}^2(\mathbf{k}_1 - \mathbf{k}_2) \right). \quad (\text{C.72})$$

⁵Exclusively for the purpose of this derivation, we reintroduce e_0 , as was done in Sec. C.3.

The commutator is calculated as follows

$$\left[c_{\mathbf{k}_3}^\dagger c_{\mathbf{k}_3+\mathbf{q}}, c_{\mathbf{k}_1}^\dagger c_{\mathbf{k}_2} \right] = c_{\mathbf{k}_3}^\dagger c_{\mathbf{k}_2} \delta_{\mathbf{k}_3+\mathbf{q}, \mathbf{k}_1} - c_{\mathbf{k}_1}^\dagger c_{\mathbf{k}_3+\mathbf{q}} \delta_{\mathbf{k}_3, \mathbf{k}_2}. \quad (\text{C.73})$$

Hence,

$$\begin{aligned} [\rho(\mathbf{q}), H_{kin}] &= \frac{e_0}{2m_0V} \sum_{\mathbf{k}_1, \mathbf{k}_2} \left(c_{\mathbf{k}_1-\mathbf{q}}^\dagger c_{\mathbf{k}_2} - c_{\mathbf{k}_1}^\dagger c_{\mathbf{k}_2+\mathbf{q}} \right) \\ &\quad \times \left(V \mathbf{k}_2^2 \delta_{\mathbf{k}_1, \mathbf{k}_2} - e_0(\mathbf{k}_1 + \mathbf{k}_2) \mathbf{A}(\mathbf{k}_1 - \mathbf{k}_2) + e_0^2 \mathbf{A}^2(\mathbf{k}_1 - \mathbf{k}_2) \right). \end{aligned} \quad (\text{C.74})$$

This can be further simplified if we make the substitution $\mathbf{k}_1 \rightarrow \mathbf{k}_1 + \mathbf{q}$, $\mathbf{k}_2 \rightarrow \mathbf{k}_2 + \mathbf{q}$ in the terms proportional to $c_{\mathbf{k}_1-\mathbf{q}}^\dagger c_{\mathbf{k}_2}$

$$\begin{aligned} [\rho(\mathbf{q}), H_{kin}] &= \frac{e_0}{2m_0} \sum_{\mathbf{k}} [(\mathbf{k} + \mathbf{q})^2 - \mathbf{k}^2] c_{\mathbf{k}}^\dagger c_{\mathbf{k}+\mathbf{q}} \\ &\quad - \frac{e_0^2}{2m_0V} \sum_{\mathbf{k}_1, \mathbf{k}_2} 2\mathbf{q} \mathbf{A}(\mathbf{k}_1 - \mathbf{k}_2) c_{\mathbf{k}_1}^\dagger c_{\mathbf{k}_2+\mathbf{q}} \\ &= \frac{e_0}{2m_0} \underbrace{\sum_{\mathbf{k}} (2\mathbf{k}\mathbf{q} + \mathbf{q}^2) c_{\mathbf{k}}^\dagger c_{\mathbf{k}+\mathbf{q}}}_{\mathbf{q} j^p(\mathbf{q})} - \frac{e_0^2}{m_0V} \underbrace{\sum_{\mathbf{k}_1, \mathbf{k}_2} \mathbf{q} \mathbf{A}(\mathbf{k}_1 - \mathbf{k}_2) c_{\mathbf{k}_1}^\dagger c_{\mathbf{k}_2+\mathbf{q}}}_{\mathbf{q} j^d(\mathbf{q})} \\ &= \mathbf{q} j(\mathbf{q}). \end{aligned} \quad (\text{C.75})$$

This proves that the definition of current operator from Eq. (C.26) satisfies the continuity Equation (C.67).

The Case of a Lattice

In the case of a lattice, things are a little more subtle. In this case, the system is discrete, so the spacial derivative $\frac{\partial}{\partial x}$ as an operation does not exist in the usual sence. This is also true for the divergence operator. Hence, one cannot check whether the continuity equation, in the form of Eq. (C.66), is satisfied or not. Instead, we can assume that it is satisfied, and use this assumption to derive the form of the divergence operator on the lattice. To do so, we need to start from Eq. (C.66), with a slightly different notation since the system is now discrete

$$\text{div } \mathbf{j}_{\mathbf{r}} = -\frac{\partial n_{\mathbf{r}}(t)}{\partial t}, \quad (\text{C.76})$$

use the Heisenberg equation

$$\text{div } \mathbf{j}_{\mathbf{r}} = i[n_{\mathbf{r}}, H_{kin}], \quad (\text{C.77})$$

and calculate the commutator on the right-hand side.

1D Case

In the case, H_{kin} is given by Eq. (C.30), so the commutator is calculated as follows

$$\text{div } j_r \equiv i[n_r, H_{kin}] = -it_0 \sum_{r_1} [c_{r_1}^\dagger c_r, c_{r_1}^\dagger c_{r_1+1}] + h.c. \quad (\text{C.78})$$

$$= it_0 \left(c_{r+1}^\dagger c_r - c_r^\dagger c_{r+1} - c_r^\dagger c_{r-1} + c_{r-1}^\dagger c_r \right) \quad (\text{C.79})$$

In the case when the current⁶ is defined as in Sec. C.4.2.1, we see that the continuity equation can be written as

$$\text{div } j_r = j_{r+1} - j_r. \quad (\text{C.80})$$

This is a somewhat natural definition of the divergence on a discrete lattice, for a 1D system. However, it is important to note that the particular form of the divergence in Eq. (C.80) depends on the definition of the current density operator. In the case of the current operator from Sec. C.4.2.2, it is actually impossible to rewrite the right-hand side of Eq. (C.79) as a linear combination of current operators at different lattice sites. Luckily, this is not a problem for us, as we are actually interested in the Fourier version of the continuity equation. This is because in our study, we are interested in the restrictions that the continuity equation places upon the vertex functions in the \mathbf{k} space. In the following, we show that $\text{div } j_r$ in the Fourier space can always be written using j_q .

$$\mathcal{F}[\text{div } j_r](q) = i[n_q, H_{kin}] \quad (\text{C.81})$$

$$= i \sum_{k_1, k_2} \varepsilon_{k_2} [c_{k_1}^\dagger c_{k_1+q}, c_{k_2}^\dagger c_{k_2}] \quad (\text{C.82})$$

$$= i \sum_k (\varepsilon_{k+q} - \varepsilon_k) c_k^\dagger c_{k+q} \quad (\text{C.83})$$

$$= -2it_0 \sum_k (\cos(k+q) - \cos(k)) c_k^\dagger c_{k+q} \quad (\text{C.84})$$

In the case when the current is given by Eq. (C.59), this becomes

$$\mathcal{F}[\text{div } j_r](q) = -it_0 \sum_k [e^{-i(k+q)} - e^{ik}] c_k^\dagger c_{k+q} \quad (\text{C.85})$$

$$- it_0 \sum_k [e^{i(k+q)} - e^{-ik}] c_k^\dagger c_{k+q} \quad (\text{C.86})$$

This can be further simplified as

$$\mathcal{F}[\text{div } j_r](q) = (e^{iq} - 1) j_q. \quad (\text{C.87})$$

On the other hand, if the current density is given by Eq. (C.50), then it is better to transform Eq. (C.84) as

$$\mathcal{F}[\text{div } j_r](q) = 4it_0 \sum_k \sin\left(k + \frac{q}{2}\right) \sin\left(\frac{q}{2}\right) c_k^\dagger c_{k+q} \quad (\text{C.88})$$

$$= 2i \tan\left(\frac{q}{2}\right) j_q \quad (\text{C.89})$$

Hence, in both of these cases, we can write

$$\mathcal{F}[\text{div } j_r](q) = i\Delta(q)j_q. \quad (\text{C.90})$$

We note that $\Delta(q)$ satisfies the property that

$$\Delta(q) \approx q, \quad \text{for } q \rightarrow 0. \quad (\text{C.91})$$

Hence, the result in the long wavelength limit coincides with the continuum result, which is expected.

⁶We emphasize once again that we consider only the paramagnetic part of the current density operator

Higer Dimensional Case

Analogous to Eq. (C.83), we can write

$$\mathcal{F}[\text{div } \mathbf{j}_r](\mathbf{q}) = i \sum_{\mathbf{k}} (\varepsilon_{\mathbf{k}+\mathbf{q}} - \varepsilon_{\mathbf{k}}) c_{\mathbf{k}}^\dagger c_{\mathbf{k}+\mathbf{q}}, \quad (\text{C.92})$$

where $\varepsilon_{\mathbf{k}}$ is now given by

$$\varepsilon_{\mathbf{k}} = -t_0 \sum_{\delta} e^{i\delta\mathbf{k}}. \quad (\text{C.93})$$

Hence,

$$\mathcal{F}[\text{div } \mathbf{j}_r](\mathbf{q}) = -it_0 \sum_{\mathbf{k}, \delta} [e^{i\delta(\mathbf{k}+\mathbf{q})} - e^{i\delta\mathbf{k}}] c_{\mathbf{k}}^\dagger c_{\mathbf{k}+\mathbf{q}}. \quad (\text{C.94})$$

If we now introduce the symbol $\tilde{\delta}$, whose meaning was explained in Sec. C.4.2.1 and C.4.2.2, then the previous expression can be cast into the following form⁷

$$\mathcal{F}[\text{div } \mathbf{j}_r](\mathbf{q}) = -it_0 \sum_{\mathbf{k}, \tilde{\delta}} [e^{i\tilde{\delta}(\mathbf{k}+\mathbf{q})} + e^{-i\tilde{\delta}(\mathbf{k}+\mathbf{q})} - e^{i\tilde{\delta}\mathbf{k}} - e^{-i\tilde{\delta}\mathbf{k}}] c_{\mathbf{k}}^\dagger c_{\mathbf{k}+\mathbf{q}} \quad (\text{C.95})$$

$$= 4it_0 \sum_{\mathbf{k}, \tilde{\delta}} \sin\left(\mathbf{k}\tilde{\delta} + \frac{\mathbf{q}\tilde{\delta}}{2}\right) \sin\left(\frac{\mathbf{q}\tilde{\delta}}{2}\right) c_{\mathbf{k}}^\dagger c_{\mathbf{k}+\mathbf{q}}. \quad (\text{C.96})$$

If we restrict ourselves to the case of hypercubic lattice, in arbitrary number of dimensions, then this can also be written as

$$\boxed{\mathcal{F}[\text{div } \mathbf{j}_r](\mathbf{q}) = i\Delta(\mathbf{q}) \cdot \mathbf{j}(\mathbf{q})}, \quad (\text{C.97})$$

where $\Delta(\mathbf{q})$ is given by

$$\boxed{\Delta(\mathbf{q}) = 2 \sum_{\tilde{\delta}} \tan\left(\frac{\mathbf{q}\tilde{\delta}}{2}\right) \tilde{\delta}}, \quad (\text{C.98})$$

in the case when we use the current operator from Sec. C.4.2.1, while

$$\boxed{\Delta(\mathbf{q}) = -i \sum_{\tilde{\delta}} [e^{i\tilde{\delta}\mathbf{q}} - 1] \tilde{\delta}}, \quad (\text{C.99})$$

corresponds to the current operator from Sec. C.4.2.2. As we already noted, the continuum case is obtained by taking

$$\boxed{\Delta(\mathbf{q}) = \mathbf{q}} \quad (\text{C.100})$$

We conclude this section by stating a version of the continuity equation, both in real and imaginary time ($\tau = it$), which is valid both in the continuum and on a lattice

$$\boxed{\begin{aligned} \frac{\partial n_{\mathbf{q}}}{\partial t} + i\Delta(\mathbf{q}) \cdot \mathbf{j}_{\mathbf{q}}(t) &= 0 \\ \frac{\partial n_{\mathbf{q}}}{\partial \tau} + \Delta(\mathbf{q}) \cdot \mathbf{j}_{\mathbf{q}}(\tau) &= 0 \end{aligned}} \quad (\text{C.101})$$

⁷Here, we implicitly assume that for every nearest neighbour situated at δ , there is another nearest neighbour at $-\delta$.

C.6 General Form of the Current Operator

In previous sections we saw that there are different ways in which the exponent in the Pierels substitution (see Eq. (C.38)) can be approximated in the case when the field varies slowly on the atomic scale. We showed two different approaches, given in Eqs. (C.39) and (C.55), lead to two different current operators. Furthermore, the continuity equation is a bit different for each of these cases, but can always be written in the form of Eq. (C.101), with a suitable choice of $\Delta(\mathbf{q})$. Here, we give a more general derivation of the current operator and continuity equation, such that the current operators from previous sections turn out to be special cases.

Current Operator in Coordinate Representation

After the Pierels substitution, the Hamiltonian reads as

$$H = -t_0 \sum_{\mathbf{r}} \sum_{\delta} c_{\mathbf{r}}^{\dagger} c_{\mathbf{r}+\delta} \cdot \exp \left(-i \int_{\mathbf{r}}^{\mathbf{r}+\delta} d\mathbf{r} \mathbf{A}(\mathbf{r}) \right), \quad (\text{C.102})$$

where δ goes over the nearest-neighbours. If the field $\mathbf{A}(\mathbf{r})$ varies slowly on the atomic scale, the integral inside the exponential can be approximated as a scalar product of the displacement vector between the nearest neighbours and the linear combination of $\mathbf{A}(\mathbf{r})$ at the endpoints. Before we do this, we introduce the parameter $\tilde{\delta}$, as explained in Sec. C.4.2 in order to make the Hamiltonian more explicitly Hermitian

$$H = -t_0 \sum_{\mathbf{r}} \sum_{\tilde{\delta}} \left[c_{\mathbf{r}}^{\dagger} c_{\mathbf{r}+\tilde{\delta}} e^{-i \frac{m\mathbf{A}(\mathbf{r})+n\mathbf{A}(\mathbf{r}+\tilde{\delta})}{m+n} \tilde{\delta}} + c_{\mathbf{r}+\tilde{\delta}}^{\dagger} c_{\mathbf{r}} e^{i \frac{m\mathbf{A}(\mathbf{r})+n\mathbf{A}(\mathbf{r}+\tilde{\delta})}{m+n} \tilde{\delta}} \right] \quad (\text{C.103})$$

The current operator then reads as

$$\mathbf{j}(\mathbf{r}) = -\frac{\delta H}{\delta \mathbf{A}(\mathbf{r})} = -\frac{it_0}{m+n} \sum_{\tilde{\delta}} \left(mc_{\mathbf{r}}^{\dagger} c_{\mathbf{r}+\tilde{\delta}} + nc_{\mathbf{r}-\tilde{\delta}}^{\dagger} c_{\mathbf{r}} \right) \tilde{\delta} + \frac{it_0}{m+n} \sum_{\tilde{\delta}} \left(mc_{\mathbf{r}+\tilde{\delta}}^{\dagger} c_{\mathbf{r}} + nc_{\mathbf{r}}^{\dagger} c_{\mathbf{r}-\tilde{\delta}} \right) \tilde{\delta}. \quad (\text{C.104})$$

We now see that the current operator from Eq. (C.51) is obtained by setting $m = n$ in the previous equation, while the current from Eq. (C.64) is obtained by setting $m = 0$.

Current Operator in Momentum Representation

The momentum representation is obtained by using

$$\mathbf{j}(\mathbf{q}) = \sum_{\mathbf{r}} e^{-i\mathbf{q}\mathbf{r}} \mathbf{j}(\mathbf{r}), \quad (\text{C.105})$$

$$c_{\mathbf{r}}^{\dagger} = \frac{1}{\sqrt{N}} \sum_{\mathbf{k}} e^{-i\mathbf{k}\mathbf{r}} c_{\mathbf{k}}^{\dagger}, \quad (\text{C.106})$$

$$c_{\mathbf{r}} = \frac{1}{\sqrt{N}} \sum_{\mathbf{k}} e^{i\mathbf{k}\mathbf{r}} c_{\mathbf{k}}. \quad (\text{C.107})$$

We get:

$$\mathbf{j}(\mathbf{q}) = \frac{it_0}{m+n} \sum_{\mathbf{k}} \sum_{\tilde{\delta}} \left[-m e^{i(\mathbf{k}+\mathbf{q})\tilde{\delta}} - n e^{i\mathbf{k}\tilde{\delta}} + m e^{-i\mathbf{k}\tilde{\delta}} + n e^{-i(\mathbf{k}+\mathbf{q})\tilde{\delta}} \right] \tilde{\delta} c_{\mathbf{k}}^{\dagger} c_{\mathbf{k}+\mathbf{q}}. \quad (\text{C.108})$$

Continuity Equation in the Case of Hypercubic Lattice

Theorem 8. *In the case of hypercubic lattice with nearest-neighbour hopping, the continuity equation can be written as*

$$\frac{\partial n_{\mathbf{q}}}{\partial t} + i\Delta(\mathbf{q}) \cdot \mathbf{j}_{\mathbf{q}}(t) = 0, \quad (\text{C.109})$$

where $\Delta(\mathbf{q})$ is given by

$$\Delta(\mathbf{q}) = \sum_{\tilde{\delta}} \frac{2\tilde{\delta}}{\cot \frac{\mathbf{q}\tilde{\delta}}{2} + i\frac{m-n}{m+n}} \quad (\text{C.110})$$

while $\tilde{\delta}$ goes over the orthonormal vectors $[1, 0, 0 \dots], [0, 1, 0 \dots], [1, 0, 0 \dots] \dots$

Proof. As explained in Sec. C.5, the continuity equation reads as

$$\text{div } \mathbf{j}_{\mathbf{r}} = -\frac{\partial n_{\mathbf{r}}(t)}{\partial t} = i[n_{\mathbf{r}}, H_{kin}]. \quad (\text{C.111})$$

which can be rewritten in the Fourier space as follows

$$\mathcal{F}[\text{div } \mathbf{j}_{\mathbf{r}}](\mathbf{q}) = i \sum_{\mathbf{k}} (\varepsilon_{\mathbf{k}+\mathbf{q}} - \varepsilon_{\mathbf{k}}) c_{\mathbf{k}}^{\dagger} c_{\mathbf{k}+\mathbf{q}}. \quad (\text{C.112})$$

Hence, our task reduces to show that the scalar product $i\Delta(\mathbf{q}) \cdot \mathbf{j}_{\mathbf{q}}$, using $\Delta(\mathbf{q})$ from Eq. (C.110) and $\mathbf{j}_{\mathbf{q}}$ from Eq. (C.108), is equal to the right-hand side of Eq. (C.112). To do so, it turns out that it is much more convenient to rewrite $\mathbf{j}(\mathbf{q})$ as

$$\begin{aligned} \mathbf{j}(\mathbf{q}) &= t_0 \sum_{\mathbf{k}, \tilde{\delta}} \tilde{\delta} \left(\sin(\mathbf{k}\tilde{\delta}) + \sin((\mathbf{k} + \mathbf{q})\tilde{\delta}) \right) c_{\mathbf{k}}^{\dagger} c_{\mathbf{k}+\mathbf{q}} \\ &+ \frac{it_0(m-n)}{m+n} \sum_{\mathbf{k}, \tilde{\delta}} \tilde{\delta} \left(\cos(\mathbf{k}\tilde{\delta}) - \cos((\mathbf{k} + \mathbf{q})\tilde{\delta}) \right) c_{\mathbf{k}}^{\dagger} c_{\mathbf{k}+\mathbf{q}}. \end{aligned} \quad (\text{C.113})$$

Now, it is straightforward to derive the following

$$\begin{aligned} i\Delta(\mathbf{q}) \cdot \mathbf{j}_{\mathbf{q}} &= it_0 \sum_{\tilde{\delta}_1, \tilde{\delta}_2} \frac{2\tilde{\delta}_1 \cdot \tilde{\delta}_2}{\cot \frac{\mathbf{q}\tilde{\delta}_1}{2} + i\frac{m-n}{m+n}} \sum_{\mathbf{k}} \left(\sin(\mathbf{k}\tilde{\delta}_2) + \sin((\mathbf{k} + \mathbf{q})\tilde{\delta}_2) \right) c_{\mathbf{k}}^{\dagger} c_{\mathbf{k}+\mathbf{q}} \\ &- \frac{t_0(m-n)}{m+n} \sum_{\tilde{\delta}_1, \tilde{\delta}_2} \frac{2\tilde{\delta}_1 \cdot \tilde{\delta}_2}{\cot \frac{\mathbf{q}\tilde{\delta}_1}{2} + i\frac{m-n}{m+n}} \sum_{\mathbf{k}} \left(\cos(\mathbf{k}\tilde{\delta}_2) - \cos((\mathbf{k} + \mathbf{q})\tilde{\delta}_2) \right) c_{\mathbf{k}}^{\dagger} c_{\mathbf{k}+\mathbf{q}}. \end{aligned} \quad (\text{C.114})$$

We can eliminate the sum over $\tilde{\delta}_2$ because $\{\tilde{\delta}\}$ forms an orthonormal set of vectors. Furthermore, using $\sin x + \sin y = 2 \sin \left(\frac{x+y}{2} \right) \cos \left(\frac{x-y}{2} \right)$ and $\cos x - \cos y = -2 \sin \left(\frac{x+y}{2} \right) \sin \left(\frac{x-y}{2} \right)$ we get

$$\begin{aligned} i\Delta(\mathbf{q}) \cdot \mathbf{j}_{\mathbf{q}} &= it_0 \sum_{\tilde{\delta}, \mathbf{k}} \frac{4}{\cot \frac{\mathbf{q}\tilde{\delta}}{2} + i\frac{m-n}{m+n}} \sin \left(\frac{2\mathbf{k} + \mathbf{q}}{2} \tilde{\delta} \right) \cos \left(\frac{\mathbf{q}\tilde{\delta}}{2} \right) c_{\mathbf{k}}^{\dagger} c_{\mathbf{k}+\mathbf{q}} \\ &- \frac{t_0(m-n)}{m+n} \sum_{\tilde{\delta}, \mathbf{k}} \frac{4}{\cot \frac{\mathbf{q}\tilde{\delta}}{2} + i\frac{m-n}{m+n}} \sin \left(\frac{2\mathbf{k} + \mathbf{q}}{2} \tilde{\delta} \right) \sin \left(\frac{\mathbf{q}\tilde{\delta}}{2} \right) c_{\mathbf{k}}^{\dagger} c_{\mathbf{k}+\mathbf{q}}. \end{aligned} \quad (\text{C.115})$$

This can be further simplified as

$$i\Delta(\mathbf{q}) \cdot \mathbf{j}_{\mathbf{q}} = 4it_0 \sum_{\mathbf{k}, \tilde{\delta}} \sin \left(\frac{2\mathbf{k} + \mathbf{q}}{2} \tilde{\delta} \right) \sin \left(\frac{\mathbf{q}\tilde{\delta}}{2} \right) c_{\mathbf{k}}^{\dagger} c_{\mathbf{k}+\mathbf{q}}. \quad (\text{C.116})$$

This is equal to $\mathcal{F}[\text{div } \mathbf{j}_{\mathbf{r}}](\mathbf{q})$, as seen from Eqs. (C.112) and (C.96). This completes our proof. \square

C.7 Some Properties of the (Paramagnetic) Current Operator

Compact Notation for all (Paramagnetic) Current Operators

One universal property for the paramagnetic currents in Eqs. (C.26), (C.50), (C.61) and (C.108) is the fact that all of them can be written in the form:

$$j_i(\mathbf{q}) = \sum_{\mathbf{k}} c_{\mathbf{k}}^\dagger \gamma_i(\mathbf{k} + \mathbf{q}, \mathbf{k}) c_{\mathbf{k}+\mathbf{q}}, \quad (\text{C.117})$$

where

$$\gamma_i(\mathbf{k} + \mathbf{q}, \mathbf{k}) = \frac{it_0}{m+n} \sum_{\tilde{\delta}} \left[-m e^{i(\mathbf{k}+\mathbf{q})\tilde{\delta}} - n e^{i\mathbf{k}\tilde{\delta}} + m e^{-i\mathbf{k}\tilde{\delta}} + n e^{-i(\mathbf{k}+\mathbf{q})\tilde{\delta}} \right] \tilde{\delta}, \quad (\text{C.118})$$

in the case of a lattice, while in the continuum

$$\gamma_i(\mathbf{k} + \mathbf{q}, \mathbf{k}) = \frac{1}{m_0} \left(\mathbf{k} + \frac{\mathbf{q}}{2}, \right) \quad (\text{C.119})$$

where m_0 is the mass of the electron. Furthermore, even the density operator is of that form

$$n(\mathbf{q}) = \sum_{\mathbf{r}} e^{-i\mathbf{q}\mathbf{r}} c_{\mathbf{r}}^\dagger c_{\mathbf{r}} = \frac{1}{N} \sum_{\mathbf{r}, \mathbf{k}_1, \mathbf{k}_2} e^{-i\mathbf{r}(\mathbf{q}+\mathbf{k}_1-\mathbf{k}_2)} c_{\mathbf{k}_1}^\dagger c_{\mathbf{k}_2} = \sum_{\mathbf{k}} c_{\mathbf{k}}^\dagger c_{\mathbf{k}+\mathbf{q}}. \quad (\text{C.120})$$

This motivates the introduction of 4-vector notation, with $j^0(\mathbf{q}) = n(\mathbf{q})$ $\gamma^0(\mathbf{k} + \mathbf{q}, \mathbf{k}) = 1$, and metric $\eta = [-1, 1, 1, 1]$

$$j^\mu(\mathbf{q}) = \sum_{\mathbf{k}} c_{\mathbf{k}}^\dagger \gamma^\mu(\mathbf{k} + \mathbf{q}, \mathbf{k}) c_{\mathbf{k}+\mathbf{q}}. \quad (\text{C.121})$$

In general, we see that γ^μ satisfies

$$\gamma^\mu(\mathbf{k} + \mathbf{q}, \mathbf{k}) = \gamma^\mu(\mathbf{k}, \mathbf{k} + \mathbf{q})^*. \quad (\text{C.122})$$

Furthermore, we can also state the continuity equation in the 4-vector notation, which is valid both for a continuum and on a lattice

$$\Delta^\mu(q) j_\mu(q) = 0, \quad (\text{C.123})$$

where we used the 4-momentum q . The zeroth component of $\Delta^\mu(q)$ is given by

$$\Delta^0(q) = q^0 \quad (\text{C.124})$$

while other three components correspond to $\Delta^i(\mathbf{q})$ from Eq. (C.110).

Remark 44. In the real space formulation, $q^0 = \omega_q$, while $q^0 = i\omega_q$ in the Matsubara space.

Ward Identity for the Special case of a Free Theory

From Eqs. (C.98) and (C.99) we can easily derive one of the special cases of the Ward identity:

$$\Delta^\mu(q) \gamma_\mu(k + q, k) = \varepsilon_{\mathbf{k}+\mathbf{q}} - \varepsilon_{\mathbf{k}} - q^0 = G(k)^{-1} - G(k + q)^{-1}. \quad (\text{C.125})$$



Using Continued Fraction Expansion for Representing Diagonal Elements of the Inverse of Tridiagonal Matrix

D.1 Statement of the Problem and Introduction of Notation

Definition 1. A matrix is tridiagonal if the only non-zero elements are the ones that are located on its main diagonal and the first diagonals above and below the main diagonal

$$M = \begin{bmatrix} a_0 & b_1 & 0 & 0 & 0 & \dots \\ b_1 & a_1 & b_2 & 0 & 0 & \dots \\ 0 & b_2 & a_2 & b_3 & 0 & \dots \\ 0 & 0 & b_3 & a_3 & b_4 & \dots \\ \vdots & \vdots & \vdots & \vdots & \vdots & \ddots \end{bmatrix}. \quad (\text{D.1})$$

Remark 45. We use the convention in which the indices of $N \times N$ matrix are going from $i = 0 \dots N-1$.

Our task is to show how can the elements $(M^{-1})_{nn}$ be expressed analytically in terms of the continued fraction expansion. From the standard linear algebra course, we know that

$$(M^{-1})_{nn} = \frac{\bar{M}_n^n}{\det(M)}, \quad (\text{D.2})$$

where \bar{M}_n^n is the determinant of the matrix obtained by deleting the n -th row and n -th column of matrix M . Before calculating these quantities, we introduce a notation that will make our formulas more compact. Hence, we define

Definition 2. Minor of the second kind $\bar{M}_{j_1 j_2 \dots}^{i_1 i_2 \dots}$ is a determinant of matrix that is obtained by deleting rows $i_1, i_2 \dots$ and columns $j_1, j_2 \dots$ from a square matrix M .

Definition 3. Let:

$$D_0 \equiv \det(M) \quad (\text{D.3a})$$

$$D_1 \equiv \bar{M}_0^0 \quad (\text{D.3b})$$

$$D_2 \equiv \bar{M}_{01}^{01}, \quad (\text{D.3c})$$

\vdots

$$D_n \equiv \bar{M}_{01 \dots n-1}^{01 \dots n-1} \quad (\text{D.3d})$$

\vdots

Definition 4. Let M be a square matrix, while $i_1, i_2 \dots i_n$ and $j_1, j_2 \dots j_n$ are the indices that denote rows and columns, respectively. Then, a minor of the first kind $\widetilde{M}_{j_1 j_2 \dots j_n}^{i_1 i_2 \dots i_n}$ represents a determinant of a $n \times n$ matrix, which is obtained by extracting the elements of M which are situated at the intersection of rows $i_1, i_2 \dots$ and columns $j_1, j_2 \dots$.

For example, \widetilde{M}_{j}^i is equal to the element of matrix M that is situated at i -th row and j -th column. On the other hand, $\widetilde{M}_{j_1 j_2}^{i_1 i_2}$ is a determinant of 2×2 matrix. Let us now create a definition, analogous to Def. 3, only this time for the minors of the first kind.

Definition 5. Let:

$$\widetilde{D}_0 \equiv 1 \quad (\text{D.4a})$$

$$\widetilde{D}_1 \equiv \widetilde{M}_0^0 \quad (\text{D.4b})$$

$$\widetilde{D}_2 \equiv \widetilde{M}_{01}^{01} \quad (\text{D.4c})$$

⋮

$$\widetilde{D}_n \equiv \widetilde{M}_{01 \dots n-1}^{01 \dots n-1} \quad (\text{D.4d})$$

⋮

for arbitrary positive n . If $n < 0$, then $\widetilde{D}_n \equiv 0$.

D.2 Some Useful Identities

As we already noted, $(M^{-1})_{nn}$ can be evaluated using the Eq. (D.2), which, using our new notation, can be expressed as follows

$$(M^{-1})_{nn} = \frac{\overline{M}_n^n}{D_0}, \quad (\text{D.5})$$

To calculate this, we follow a four-step process:

1. Express \overline{M}_n^n in terms of D_n and \widetilde{D}_n .
2. Derive the recurrence relation for D_n .
3. Derive the recurrence relation for \widetilde{D}_n .
4. Express D_0 in terms of D_n and \widetilde{D}_n .

Let us do this step by step.

Expressing \overline{M}_n^n in terms of D_n and \widetilde{D}_n .

Using the fact that the determinant of the block diagonal matrix is simply given by the product of the determinants of each block, we see that

$$\overline{M}_n^n = \begin{vmatrix} a_0 & b_1 & 0 & \cdots & 0 & 0 & 0 & \cdots & 0 & 0 \\ b_1 & a_1 & b_2 & \cdots & 0 & 0 & 0 & \cdots & 0 & 0 \\ 0 & b_2 & a_2 & \cdots & 0 & 0 & 0 & \cdots & 0 & 0 \\ \vdots & \vdots & \vdots & \vdots & \vdots & \vdots & \vdots & \vdots & \vdots & \vdots \\ 0 & 0 & 0 & \cdots & b_{n-1} & a_{n-1} & b_n & 0 & 0 & \cdots \\ 0 & 0 & 0 & \cdots & 0 & b_n & a_n & b_{n+1} & 0 & \cdots \\ 0 & 0 & 0 & \cdots & 0 & 0 & b_{n+1} & a_{n+1} & b_{n+2} & \cdots \\ 0 & 0 & 0 & \cdots & 0 & 0 & 0 & b_{n+2} & a_{n+2} & \cdots \\ 0 & 0 & 0 & \cdots & 0 & 0 & 0 & 0 & b_{n+3} & \cdots \\ 0 & 0 & 0 & \cdots & 0 & 0 & 0 & 0 & 0 & \cdots \\ \vdots & \vdots & \vdots & \vdots & \vdots & \vdots & \vdots & \vdots & \vdots & \ddots \end{vmatrix} = \tilde{D}_n D_{n+1}. \quad (\text{D.6})$$

Recurrence Relation for D_n

Let us first start from D_0 , and expand this matrix along the $i = 0$ column

$$D_0 = \begin{vmatrix} a_0 & b_1 & 0 & 0 & \cdots \\ b_1 & a_1 & b_2 & 0 & \cdots \\ 0 & b_2 & a_2 & b_3 & \cdots \\ \vdots & \vdots & \vdots & \vdots & \ddots \end{vmatrix} = a_0 D_1 - b_1 \begin{vmatrix} b_1 & 0 & 0 & 0 & \cdots \\ b_2 & a_2 & b_3 & 0 & \cdots \\ 0 & b_3 & a_3 & b_4 & \cdots \\ \vdots & \vdots & \vdots & \vdots & \ddots \end{vmatrix} = a_0 D_1 - b_1^2 D_2. \quad (\text{D.7})$$

However, since D_n has the same form as D_0 , we can immediately conclude that

$$D_n = a_n D_{n+1} - b_{n+1}^2 D_{n+2}. \quad (\text{D.8})$$

Recurrence Relation for \tilde{D}_n

Let us expand \tilde{D}_n along the last row

$$\tilde{D}_n = \begin{vmatrix} a_0 & b_1 & 0 & \cdots & 0 & 0 & 0 \\ b_1 & a_1 & b_2 & \cdots & 0 & 0 & 0 \\ 0 & b_2 & a_2 & \cdots & 0 & 0 & 0 \\ \vdots & \vdots & \vdots & \vdots & \vdots & \vdots & \vdots \\ 0 & 0 & 0 & \cdots & b_{n-2} & a_{n-2} & b_{n-1} \\ 0 & 0 & 0 & \cdots & 0 & b_{n-1} & a_{n-1} \end{vmatrix} = a_{n-1} \tilde{D}_{n-1} - b_{n-1} \begin{vmatrix} a_0 & b_1 & 0 & \cdots & 0 & 0 & 0 \\ b_1 & a_1 & b_2 & \cdots & 0 & 0 & 0 \\ 0 & b_2 & a_2 & \cdots & 0 & 0 & 0 \\ \vdots & \vdots & \vdots & \vdots & \vdots & \vdots & \vdots \\ 0 & 0 & 0 & \cdots & b_{n-3} & a_{n-3} & b_{n-2} \\ 0 & 0 & 0 & \cdots & 0 & 0 & b_{n-1} \end{vmatrix} = a_{n-1} \tilde{D}_{n-1} - b_{n-1}^2 \tilde{D}_{n-2}. \quad (\text{D.9})$$

Expressing D_0 in terms of D_n and \tilde{D}_n

Theorem 9. For $n \geq 0$, it holds that

$$D_0 = D_n \tilde{D}_n - b_n^2 \tilde{D}_{n-1} D_{n+1}. \quad (\text{D.10})$$

Proof. For $n = 0$, this is trivial since $\tilde{D}_0 = 1$ and $\tilde{D}_{-1} = 0$. For $n = 1$, this is also easy to see as a consequence of Eq. (D.7), since $\tilde{D}_1 = a_0$. For other n , we can proceed using the method of induction: we assume that Eq. (D.10) holds for n , and try to prove that it holds for $n + 1$. We will do this using the recurrence relations in Eqs. (D.8) and (D.9)

$$\begin{aligned}
D_0 &= \tilde{D}_n D_n - b_n^2 \tilde{D}_{n-1} D_{n+1} \\
&= \tilde{D}_n D_n - b_n^2 \tilde{D}_{n-1} \frac{D_n + b_{n+1}^2 D_{n+2}}{a_n} \\
&= \tilde{D}_n (D_n + b_{n+1}^2 D_{n+2}) - b_{n+1}^2 \tilde{D}_n D_{n+2} - \frac{b_n^2}{a_n} \tilde{D}_{n-1} (D_n + b_{n+1}^2 D_{n+2}) \\
&= \left(a_n \tilde{D}_n - b_n^2 \tilde{D}_{n-1} \right) \frac{D_n + b_{n+1}^2 D_{n+2}}{a_n} - b_{n+1}^2 \tilde{D}_n D_{n+2} \\
&= D_{n+1} \tilde{D}_{n+1} - b_{n+1}^2 \tilde{D}_n D_{n+2}. \tag{D.11}
\end{aligned}$$

We obtained that Eq. (D.10) holds for $n + 1$. Thus, this completes the proof. \square

D.3 Evaluation of $(M^{-1})_{nn}$ for Arbitrary n

Now, we finally have everything we need (see Eqs. (D.5), (D.6), (D.8), (D.9), and (D.10)) to derive analytical expression for $(M^{-1})_{nn}$, in terms of the continued fraction expansion

$$\begin{aligned}
(M^{-1})_{nn} &= \frac{\bar{M}_n^n}{D_0} = \frac{\tilde{D}_n D_{n+1}}{\tilde{D}_n D_n - b_n^2 \tilde{D}_{n-1} D_{n+1}} = \frac{1}{\frac{D_n}{D_{n+1}} - b_n^2 \frac{\tilde{D}_{n-1}}{\tilde{D}_n}} \\
&= \frac{1}{\frac{a_n D_{n+1} - b_{n+1}^2 D_{n+2}}{D_{n+1}} - b_n^2 \frac{\tilde{D}_{n-1}}{a_{n-1} \tilde{D}_{n-1} - b_{n-1}^2 \tilde{D}_{n-2}}} \\
&= \frac{1}{a_n - b_{n+1}^2 \frac{D_{n+2}}{a_{n+1} D_{n+2} - b_{n+2}^2 D_{n+3}} - \frac{b_n^2}{a_{n-1} - b_{n-1}^2 \frac{\tilde{D}_{n-2}}{a_{n-2} \tilde{D}_{n-2} - b_{n-2}^2 \tilde{D}_{n-3}}}} \\
&= \frac{1}{a_n - \frac{b_{n+1}^2}{a_{n+1} - \frac{b_{n+2}^2}{a_{n+2} - \frac{b_{n+3}^2}{\ddots}}} - \frac{b_n^2}{a_{n-1} - \frac{b_{n-1}^2}{a_{n-2} - \frac{b_{n-2}^2}{\ddots}}}. \tag{D.12}
\end{aligned}$$

As we see, there are two continued fractions in the denominator. In the first, the index keeps increasing, so it is infinite in the case when the matrix M is also infinite. The second continued fraction is always finite.

Some General Operator Identities

In order to make the subsequent equations shorter, it is useful to introduce the following notation

$$\tilde{G} = G(i\nu_n = 0) = \int_0^\beta d\tau G(-i\tau), \quad (\text{E.1})$$

where $G(-i\tau)$ is an arbitrary operator in imaginary time $\tau = it$. Now we can formulate

Theorem 10 (Kubo identity). *Let G be an arbitrary operator and $\bar{\rho}_0$ the density matrix. Then*

$$[G, \bar{\rho}_0] = -i\bar{\rho}_0\tilde{G}. \quad (\text{E.2})$$

Proof.

$$\begin{aligned} [G, \bar{\rho}_0] &= \frac{1}{\mathcal{Z}} [G, e^{-\beta H}] = \frac{1}{\mathcal{Z}} (Ge^{-\beta H} - e^{-\beta H}G) = \frac{e^{-\beta H}}{\mathcal{Z}} (e^{\beta H}Ge^{-\beta H} - G) \\ &= \bar{\rho}_0 (G(-i\beta) - G(0)) = \bar{\rho}_0 \int_0^\beta d\tau \frac{\partial}{\partial \tau} G(-i\tau) = -i\bar{\rho}_0 \int_0^\beta d\tau \dot{G}(-i\tau) \\ &= -i\bar{\rho}_0\tilde{G}. \end{aligned} \quad (\text{E.3})$$

□

Another useful identity can be formulated as follows

Theorem 11. *Let G_1 and G_2 be arbitrary operators. Then*

$$\langle \tilde{G}_1 G_2 \rangle_0 = \langle \tilde{G}_2 G_1 \rangle_0, \quad (\text{E.4})$$

where the expectation value is defined as $\langle G \rangle_0 = \text{Tr}\{\bar{\rho}_0 G\}$.

Proof. Starting from

$$\langle \tilde{G}_1 G_2 \rangle_0 \stackrel{(\text{E.1})}{=} \int_0^\beta d\tau \langle G_1(-i\tau) G_2 \rangle_0 \stackrel{\lambda=\beta-\tau}{=} \int_0^\beta d\lambda \text{Tr} \left[\frac{e^{-\beta H}}{\mathcal{Z}} e^{iH(i\lambda-i\beta)} G_1 e^{-iH(i\lambda-i\beta)} G_2 \right], \quad (\text{E.5})$$

and using the cyclic property of the trace, we obtain

$$\begin{aligned} \langle \tilde{G}_1 G_2 \rangle_0 &= \int_0^\beta d\lambda \text{Tr} \left[\frac{e^{-\beta H}}{\mathcal{Z}} G_2 e^{-H\lambda} G_1 e^{H\lambda} \right] = \int_0^\beta d\lambda \text{Tr} [\bar{\rho}_0 e^{H\lambda} G_2 e^{-H\lambda} G_1] \\ &= \int_0^\beta d\lambda \langle G_2(-i\lambda) G_1 \rangle_0 = \langle \tilde{G}_2 G_1 \rangle_0. \end{aligned} \quad (\text{E.6})$$

□

Spectral Representation

Definition 6. Spectral density $J_{AB}(\omega)$ of the correlation function $\langle AB(t) \rangle_0$ is defined such that it satisfies

$$\langle AB(t) \rangle_0 = \int_{-\infty}^{\infty} \frac{d\omega}{2\pi} J_{AB}(\omega) e^{-i\omega t}. \quad (\text{E.7})$$

Equivalently, $J_{AB}(\omega)$ could also be defined as

$$J_{AB}(\omega) = \int_{-\infty}^{\infty} dt e^{i\omega t} \langle AB(t) \rangle_0, \quad (\text{E.8})$$

which is just an inverse Fourier transform of Eq. (E.7). Now, the fluctuation-dissipation theorem can be formulated as follows

Theorem 12.

$$\langle B(t)A \rangle_0 = \int_{-\infty}^{\infty} \frac{d\omega}{2\pi} J_{AB}(\omega) e^{\beta\omega} e^{-i\omega t}. \quad (\text{E.9})$$

Proof.

$$\begin{aligned} \langle B(t)A \rangle_0 &= \frac{1}{\mathcal{Z}} \text{Tr} [e^{-\beta H} e^{itH} B e^{-itH} A] = \frac{1}{\mathcal{Z}} \text{Tr} [e^{i(t+i\beta)H} B e^{-i(t+i\beta)H} e^{-\beta H} A] \\ &= \langle AB(t+i\beta) \rangle_0 \stackrel{(\text{E.7})}{=} \int_{-\infty}^{\infty} \frac{d\omega}{2\pi} J_{AB}(\omega) e^{-i\omega(t+i\beta)}. \end{aligned} \quad (\text{E.10})$$

□

Spectral Sum Rules: Numerical DMFT vs Analytical Results

Here, we numerically calculate the spectral sum rules from the DMFT, in a wide range of parameter regimes, and compare them to the results obtained using the exact expressions from Eq. (2.15) of Part II. The results are shown in Tables F.1–F.17. We see that there is a remarkable agreement in all the regimes we examined, which span from weak to strong coupling and from low to high temperatures. This is just another demonstration of the quality of the DMFT results.

Table F.1: Spectral sum rules for $\omega_0 = 1.0, g = 1.0$ at different temperatures.

n	$T = 0.3$		$T = 0.5$		$T = 0.7$	
	Exact	DMFT	Exact	DMFT	Exact	DMFT
0	1.00×10^0	1.00×10^0	1.00×10^0	1.00×10^0	1.00×10^0	1.00×10^0
1	-2.00×10^0	-2.00×10^0	-2.00×10^0	-2.00×10^0	-2.00×10^0	-2.00×10^0
2	5.07×10^0	5.06×10^0	5.31×10^0	5.31×10^0	5.63×10^0	5.63×10^0
3	-1.13×10^1	-1.13×10^1	-1.22×10^1	-1.22×10^1	-1.35×10^1	-1.35×10^1
4	3.16×10^1	3.15×10^1	3.69×10^1	3.69×10^1	4.44×10^1	4.44×10^1
5	-6.57×10^1	-6.55×10^1	-8.18×10^1	-8.18×10^1	-1.06×10^2	-1.06×10^2
6	2.24×10^2	2.23×10^2	3.07×10^2	3.07×10^2	4.43×10^2	4.43×10^2
7	-3.18×10^2	-3.14×10^2	-5.10×10^2	-5.07×10^2	-8.50×10^2	-8.45×10^2
8	2.07×10^3	2.07×10^3	3.40×10^3	3.40×10^3	5.95×10^3	5.96×10^3

n	$T = 1.0$		$T = 2.0$		$T = 3.0$	
	Exact	DMFT	Exact	DMFT	Exact	DMFT
0	1.00×10^0	1.00×10^0	1.00×10^0	1.00×10^0	1.00×10^0	1.00×10^0
1	-2.00×10^0	-2.00×10^0	-2.00×10^0	-2.00×10^0	-2.00×10^0	-2.00×10^0
2	6.16×10^0	6.16×10^0	8.08×10^0	8.08×10^0	1.01×10^1	1.01×10^1
3	-1.57×10^1	-1.57×10^1	-2.33×10^1	-2.33×10^1	-3.12×10^1	-3.12×10^1
4	5.85×10^1	5.85×10^1	1.23×10^2	1.23×10^2	2.13×10^2	2.13×10^2
5	-1.52×10^2	-1.52×10^2	-3.85×10^2	-3.85×10^2	-7.32×10^2	-7.32×10^2
6	7.42×10^2	7.42×10^2	2.76×10^3	2.76×10^3	6.87×10^3	6.87×10^3
7	-1.67×10^3	-1.66×10^3	-8.17×10^3	-8.14×10^3	-2.31×10^4	-2.30×10^4
8	1.29×10^4	1.29×10^4	8.63×10^4	8.62×10^4	3.11×10^5	3.11×10^5

n	$T = 5.0$		$T = 7.0$		$T = 10.0$	
	Exact	DMFT	Exact	DMFT	Exact	DMFT
0	1.00×10^0	1.00×10^0	1.00×10^0	1.00×10^0	1.00×10^0	1.00×10^0
1	-2.00×10^0	-2.00×10^0	-2.00×10^0	-2.00×10^0	-2.00×10^0	-2.00×10^0
2	1.40×10^1	1.40×10^1	1.80×10^1	1.80×10^1	2.40×10^1	2.40×10^1
3	-4.71×10^1	-4.71×10^1	-6.31×10^1	-6.31×10^1	-8.71×10^1	-8.71×10^1
4	4.64×10^2	4.64×10^2	8.12×10^2	8.12×10^2	1.51×10^3	1.51×10^3
5	-1.76×10^3	-1.76×10^3	-3.24×10^3	-3.24×10^3	-6.30×10^3	-6.30×10^3
6	2.42×10^4	2.42×10^4	5.86×10^4	5.86×10^4	1.55×10^5	1.55×10^5
7	-9.19×10^4	-9.17×10^4	-2.36×10^5	-2.35×10^5	-6.53×10^5	-6.52×10^5
8	1.78×10^6	1.78×10^6	5.95×10^6	5.95×10^6	2.22×10^7	2.22×10^7

Table F.2: Sum rules for $\omega_0 = 1, g = \sqrt{2}$ at different temperatures.

n	$T = 0.3$		$T = 0.5$		$T = 1.0$	
	Exact	DMFT	Exact	DMFT	Exact	DMFT
0	1.00×10^0	1.00×10^0	1.00×10^0	1.00×10^0	1.00×10^0	1.00×10^0
1	-2.00×10^0	-2.00×10^0	-2.00×10^0	-2.00×10^0	-2.00×10^0	-2.00×10^0
2	6.15×10^0	6.15×10^0	6.63×10^0	6.63×10^0	8.33×10^0	8.33×10^0
3	-1.46×10^1	-1.46×10^1	-1.65×10^1	-1.65×10^1	-2.33×10^1	-2.33×10^1
4	5.41×10^1	5.41×10^1	6.81×10^1	6.81×10^1	1.29×10^2	1.29×10^2
5	-1.10×10^2	-1.10×10^2	-1.54×10^2	-1.54×10^2	-3.60×10^2	-3.60×10^2
6	6.07×10^2	6.08×10^2	9.38×10^2	9.38×10^2	2.92×10^3	2.92×10^3
7	-4.07×10^2	-3.99×10^2	-1.06×10^3	-1.05×10^3	-6.11×10^3	-6.07×10^3
8	1.03×10^4	1.03×10^4	1.89×10^4	1.89×10^4	9.41×10^4	9.41×10^4
	$T = 3.0$		$T = 5.0$		$T = 10.0$	
0	1.00×10^0	1.00×10^0	1.00×10^0	1.00×10^0	1.00×10^0	1.00×10^0
1	-2.00×10^0	-2.00×10^0	-2.00×10^0	-2.00×10^0	-2.00×10^0	-2.00×10^0
2	1.61×10^1	1.61×10^1	2.41×10^1	2.41×10^1	4.40×10^1	4.40×10^1
3	-5.44×10^1	-5.44×10^1	-8.63×10^1	-8.63×10^1	-1.66×10^2	-1.66×10^2
4	6.30×10^2	6.30×10^2	1.52×10^3	1.52×10^3	5.42×10^3	5.42×10^3
5	-2.34×10^3	-2.34×10^3	-6.11×10^3	-6.11×10^3	-2.34×10^4	-2.34×10^4
6	3.91×10^4	3.91×10^4	1.55×10^5	1.55×10^5	1.09×10^6	1.09×10^6
7	-1.36×10^5	-1.36×10^5	-6.09×10^5	-6.08×10^5	-4.74×10^6	-4.74×10^6
8	3.42×10^6	3.42×10^6	2.22×10^7	2.22×10^7	3.10×10^8	3.10×10^8

Table F.3: Sum rules for $\omega_0 = 1, g = 0.5$ at different temperatures.

n	$T = 0.3$		$T = 0.5$		$T = 0.7$	
	Exact	DMFT	Exact	DMFT	Exact	DMFT
0	1.00×10^0	1.00×10^0	1.00×10^0	1.00×10^0	1.00×10^0	1.00×10^0
1	-2.00×10^0	-2.00×10^0	-2.00×10^0	-2.00×10^0	-2.00×10^0	-2.00×10^0
2	4.27×10^0	4.27×10^0	4.33×10^0	4.33×10^0	4.41×10^0	4.41×10^0
3	-8.82×10^0	-8.82×10^0	-9.06×10^0	-9.06×10^0	-9.38×10^0	-9.38×10^0
4	1.92×10^1	1.92×10^1	2.02×10^1	2.02×10^1	2.16×10^1	2.16×10^1
5	-3.94×10^1	-3.94×10^1	-4.24×10^1	-4.24×10^1	-4.65×10^1	-4.65×10^1
6	8.90×10^1	8.90×10^1	9.96×10^1	9.96×10^1	1.15×10^2	1.15×10^2
7	-1.74×10^2	-1.74×10^2	-2.02×10^2	-2.02×10^2	-2.43×10^2	-2.42×10^2
8	4.33×10^2	4.33×10^2	5.33×10^2	5.33×10^2	6.86×10^2	6.86×10^2
	$T = 1.0$		$T = 3.0$		$T = 5.0$	
0	1.00×10^0	1.00×10^0	1.00×10^0	1.00×10^0	1.00×10^0	1.00×10^0
1	-2.00×10^0	-2.00×10^0	-2.00×10^0	-2.00×10^0	-2.00×10^0	-2.00×10^0
2	4.54×10^0	4.54×10^0	5.51×10^0	5.51×10^0	6.51×10^0	6.51×10^0
3	-9.91×10^0	-9.91×10^0	-1.38×10^1	-1.38×10^1	-1.78×10^1	-1.78×10^1
4	2.40×10^1	2.40×10^1	4.46×10^1	4.46×10^1	7.15×10^1	7.15×10^1
5	-5.38×10^1	-5.38×10^1	-1.22×10^2	-1.22×10^2	-2.19×10^2	-2.19×10^2
6	1.43×10^2	1.43×10^2	4.75×10^2	4.75×10^2	1.11×10^3	1.11×10^3
7	-3.21×10^2	-3.20×10^2	-1.37×10^3	-1.36×10^3	-3.59×10^3	-3.58×10^3
8	1.00×10^3	1.00×10^3	6.73×10^3	6.72×10^3	2.35×10^4	2.35×10^4

Table F.4: Sum rules for $\omega_0 = 1, g = 0.75$ at different temperatures.

n	$T = 0.3$		$T = 0.7$		$T = 1.0$	
	Exact	DMFT	Exact	DMFT	Exact	DMFT
0	1.00×10^0	1.00×10^0	1.00×10^0	1.00×10^0	1.00×10^0	1.00×10^0
1	-2.00×10^0	-2.01×10^0	-2.00×10^0	-2.00×10^0	-2.00×10^0	-2.00×10^0
2	4.60×10^0	4.62×10^0	4.92×10^0	4.92×10^0	5.22×10^0	5.22×10^0
3	-9.85×10^0	-9.88×10^0	-1.11×10^1	-1.11×10^1	-1.23×10^1	-1.23×10^1
4	2.39×10^1	2.40×10^1	3.00×10^1	3.00×10^1	3.65×10^1	3.65×10^1
5	-4.96×10^1	-4.97×10^1	-6.83×10^1	-6.83×10^1	-8.88×10^1	-8.88×10^1
6	1.33×10^2	1.33×10^2	2.14×10^2	2.14×10^2	3.15×10^2	3.15×10^2
7	-2.36×10^2	-2.36×10^2	-4.45×10^2	-4.43×10^2	-7.25×10^2	-7.22×10^2
8	8.52×10^2	8.56×10^2	1.91×10^3	1.91×10^3	3.52×10^3	3.52×10^3
	$T = 3.0$		$T = 5.0$		$T = 10.0$	
0	1.00×10^0	1.00×10^0	1.00×10^0	1.00×10^0	1.00×10^0	1.00×10^0
1	-2.00×10^0	-2.00×10^0	-2.00×10^0	-2.00×10^0	-2.00×10^0	-2.00×10^0
2	7.41×10^0	7.41×10^0	9.64×10^0	9.64×10^0	1.53×10^1	1.53×10^1
3	-2.11×10^1	-2.11×10^1	-3.00×10^1	-3.00×10^1	-5.25×10^1	-5.25×10^1
4	9.97×10^1	9.97×10^1	1.94×10^2	1.94×10^2	5.63×10^2	5.63×10^2
5	-3.14×10^2	-3.14×10^2	-6.84×10^2	-6.84×10^2	-2.23×10^3	-2.23×10^3
6	1.94×10^3	1.94×10^3	5.93×10^3	5.93×10^3	3.30×10^4	3.30×10^4
7	-6.19×10^3	-6.17×10^3	-2.14×10^4	-2.13×10^4	-1.34×10^5	-1.34×10^5
8	5.25×10^4	5.25×10^4	2.55×10^5	2.54×10^5	2.72×10^6	2.72×10^6

Table F.5: Sum rules for $\omega_0 = 1, g = \sqrt{3}$ at different temperatures.

n	$T = 0.4$		$T = 1.0$		$T = 2.0$	
	Exact	DMFT	Exact	DMFT	Exact	DMFT
0	1.00×10^0	1.00×10^0	1.00×10^0	1.00×10^0	1.00×10^0	1.00×10^0
1	-2.00×10^0	-2.00×10^0	-2.00×10^0	-2.00×10^0	-2.00×10^0	-2.00×10^0
2	7.54×10^0	7.54×10^0	1.05×10^1	1.05×10^1	1.62×10^1	1.62×10^1
3	-1.91×10^1	-1.91×10^1	-3.10×10^1	-3.10×10^1	-5.40×10^1	-5.40×10^1
4	9.46×10^1	9.46×10^1	2.28×10^2	2.28×10^2	6.38×10^2	6.38×10^2
5	-2.00×10^2	-2.00×10^2	-6.56×10^2	-6.56×10^2	-2.25×10^3	-2.25×10^3
6	1.66×10^3	1.66×10^3	7.51×10^3	7.51×10^3	3.97×10^4	3.97×10^4
7	-7.53×10^2	-7.33×10^2	-1.49×10^4	-1.48×10^4	-1.22×10^5	-1.21×10^5
8	4.47×10^4	4.48×10^4	3.55×10^5	3.55×10^5	3.50×10^6	3.50×10^6
	$T = 3.0$		$T = 5.0$		$T = 10.0$	
0	1.00×10^0	1.00×10^0	1.00×10^0	1.00×10^0	1.00×10^0	1.00×10^0
1	-2.00×10^0	-2.00×10^0	-2.00×10^0	-2.00×10^0	-2.00×10^0	-2.00×10^0
2	2.22×10^1	2.22×10^1	3.41×10^1	3.41×10^1	6.40×10^1	6.40×10^1
3	-7.77×10^1	-7.77×10^1	-1.25×10^2	-1.25×10^2	-2.45×10^2	-2.45×10^2
4	1.27×10^3	1.27×10^3	3.17×10^3	3.17×10^3	1.17×10^4	1.17×10^4
5	-4.85×10^3	-4.85×10^3	-1.31×10^4	-1.31×10^4	-5.13×10^4	-5.13×10^4
6	1.17×10^5	1.17×10^5	4.83×10^5	4.82×10^5	3.54×10^6	3.54×10^6
7	-4.13×10^5	-4.12×10^5	-1.92×10^6	-1.92×10^6	-1.55×10^7	-1.54×10^7
8	1.52×10^7	1.52×10^7	1.03×10^8	1.03×10^8	1.50×10^9	1.50×10^9

Table F.6: Sum rules for $\omega_0 = 0.2, g = 0.05$ at different temperatures.

n	$T = 0.3$		$T = 0.5$		$T = 0.7$	
	Exact	DMFT	Exact	DMFT	Exact	DMFT
0	1.00×10^0	1.00×10^0	1.00×10^0	1.00×10^0	1.00×10^0	1.00×10^0
1	-2.00×10^0	-2.00×10^0	-2.00×10^0	-2.00×10^0	-2.00×10^0	-2.00×10^0
2	4.01×10^0	4.01×10^0	4.01×10^0	4.01×10^0	4.02×10^0	4.02×10^0
3	-8.03×10^0	-8.03×10^0	-8.05×10^0	-8.05×10^0	-8.07×10^0	-8.07×10^0
4	1.61×10^1	1.61×10^1	1.62×10^1	1.62×10^1	1.62×10^1	1.62×10^1
5	-3.23×10^1	-3.23×10^1	-3.25×10^1	-3.25×10^1	-3.27×10^1	-3.27×10^1
6	6.48×10^1	6.48×10^1	6.54×10^1	6.54×10^1	6.60×10^1	6.60×10^1
7	-1.30×10^2	-1.30×10^2	-1.32×10^2	-1.32×10^2	-1.33×10^2	-1.33×10^2
8	2.61×10^2	2.61×10^2	2.65×10^2	2.65×10^2	2.69×10^2	2.69×10^2
	$T = 1.0$		$T = 3.0$		$T = 5.0$	
0	1.00×10^0	1.00×10^0	1.00×10^0	1.00×10^0	1.00×10^0	1.00×10^0
1	-2.00×10^0	-2.00×10^0	-2.00×10^0	-2.00×10^0	-2.00×10^0	-2.00×10^0
2	4.03×10^0	4.03×10^0	4.08×10^0	4.08×10^0	4.13×10^0	4.13×10^0
3	-8.10×10^0	-8.10×10^0	-8.30×10^0	-8.30×10^0	-8.50×10^0	-8.50×10^0
4	1.64×10^1	1.64×10^1	1.71×10^1	1.71×10^1	1.78×10^1	1.78×10^1
5	-3.30×10^1	-3.30×10^1	-3.51×10^1	-3.51×10^1	-3.72×10^1	-3.72×10^1
6	6.68×10^1	6.68×10^1	7.27×10^1	7.27×10^1	7.89×10^1	7.89×10^1
7	-1.35×10^2	-1.35×10^2	-1.50×10^2	-1.50×10^2	-1.67×10^2	-1.67×10^2
8	2.74×10^2	2.74×10^2	3.14×10^2	3.14×10^2	3.58×10^2	3.58×10^2

Table F.7: Sum rules for $\omega_0 = 0.2, g = 0.2$ at different temperatures.

n	$T = 0.3$		$T = 0.5$		$T = 0.7$	
	Exact	DMFT	Exact	DMFT	Exact	DMFT
0	1.00×10^0	1.00×10^0	1.00×10^0	1.00×10^0	1.00×10^0	1.00×10^0
1	-2.00×10^0	-2.00×10^0	-2.00×10^0	-2.00×10^0	-2.00×10^0	-2.00×10^0
2	4.12×10^0	4.12×10^0	4.20×10^0	4.20×10^0	4.28×10^0	4.28×10^0
3	-8.49×10^0	-8.49×10^0	-8.80×10^0	-8.80×10^0	-9.12×10^0	-9.12×10^0
4	1.78×10^1	1.78×10^1	1.89×10^1	1.89×10^1	2.02×10^1	2.02×10^1
5	-3.71×10^1	-3.71×10^1	-4.05×10^1	-4.05×10^1	-4.43×10^1	-4.43×10^1
6	7.84×10^1	7.84×10^1	8.88×10^1	8.88×10^1	1.00×10^2	1.00×10^2
7	-1.65×10^2	-1.65×10^2	-1.93×10^2	-1.93×10^2	-2.26×10^2	-2.25×10^2
8	3.53×10^2	3.53×10^2	4.31×10^2	4.30×10^2	5.23×10^2	5.22×10^2
	$T = 1.0$		$T = 3.0$		$T = 5.0$	
0	1.00×10^0	1.00×10^0	1.00×10^0	1.00×10^0	1.00×10^0	1.00×10^0
1	-2.00×10^0	-2.00×10^0	-2.00×10^0	-2.00×10^0	-2.00×10^0	-2.00×10^0
2	4.40×10^0	4.40×10^0	5.20×10^0	5.20×10^0	6.00×10^0	6.00×10^0
3	-9.60×10^0	-9.60×10^0	-1.28×10^1	-1.28×10^1	-1.60×10^1	-1.60×10^1
4	2.21×10^1	2.21×10^1	3.71×10^1	3.71×10^1	5.60×10^1	5.60×10^1
5	-5.02×10^1	-5.02×10^1	-1.00×10^2	-1.00×10^2	-1.68×10^2	-1.68×10^2
6	1.20×10^2	1.20×10^2	3.18×10^2	3.18×10^2	6.71×10^2	6.71×10^2
7	-2.81×10^2	-2.80×10^2	-9.17×10^2	-9.14×10^2	-2.18×10^3	-2.17×10^3
8	6.91×10^2	6.90×10^2	3.18×10^3	3.16×10^3	9.86×10^3	9.83×10^3

Table F.8: Sum rules for $\omega_0 = 0.2, g = 0.5$ at different temperatures.

n	$T = 0.3$		$T = 0.5$		$T = 0.7$	
	Exact	DMFT	Exact	DMFT	Exact	DMFT
0	1.00×10^0	1.00×10^0	1.00×10^0	1.00×10^0	1.00×10^0	1.00×10^0
1	-2.00×10^0	-2.00×10^0	-2.00×10^0	-2.00×10^0	-2.00×10^0	-2.00×10^0
2	4.78×10^0	4.78×10^0	5.27×10^0	5.27×10^0	5.76×10^0	5.76×10^0
3	-1.11×10^1	-1.11×10^1	-1.30×10^1	-1.30×10^1	-1.50×10^1	-1.50×10^1
4	2.85×10^1	2.85×10^1	3.84×10^1	3.84×10^1	4.99×10^1	4.99×10^1
5	-7.04×10^1	-7.04×10^1	-1.04×10^2	-1.04×10^2	-1.44×10^2	-1.44×10^2
6	1.93×10^2	1.93×10^2	3.36×10^2	3.36×10^2	5.42×10^2	5.42×10^2
7	-4.98×10^2	-4.97×10^2	-9.66×10^2	-9.63×10^2	-1.68×10^3	-1.68×10^3
8	1.45×10^3	1.44×10^3	3.43×10^3	3.42×10^3	7.10×10^3	7.08×10^3
	$T = 1.0$		$T = 3.0$		$T = 5.0$	
0	1.00×10^0	1.00×10^0	1.00×10^0	1.00×10^0	1.00×10^0	1.00×10^0
1	-2.00×10^0	-2.00×10^0	-2.00×10^0	-2.00×10^0	-2.00×10^0	-2.00×10^0
2	6.51×10^0	6.51×10^0	1.15×10^1	1.15×10^1	1.65×10^1	1.65×10^1
3	-1.80×10^1	-1.80×10^1	-3.80×10^1	-3.80×10^1	-5.80×10^1	-5.80×10^1
4	6.99×10^1	6.99×10^1	2.90×10^2	2.90×10^2	6.60×10^2	6.60×10^2
5	-2.19×10^2	-2.19×10^2	-1.12×10^3	-1.12×10^3	-2.72×10^3	-2.72×10^3
6	9.90×10^2	9.90×10^2	1.10×10^4	1.10×10^4	4.11×10^4	4.11×10^4
7	-3.34×10^3	-3.33×10^3	-4.51×10^4	-4.50×10^4	-1.79×10^5	-1.79×10^5
8	1.75×10^4	1.75×10^4	5.60×10^5	5.60×10^5	3.52×10^6	3.52×10^6

Table F.9: Sum rules for $\omega_0 = 0.2, g = 0.75$ at different temperatures.

n	$T = 0.3$		$T = 0.5$		$T = 0.7$	
	Exact	DMFT	Exact	DMFT	Exact	DMFT
0	1.00×10^0	1.00×10^0	1.00×10^0	1.00×10^0	1.00×10^0	1.00×10^0
1	-2.00×10^0	-2.00×10^0	-2.00×10^0	-2.00×10^0	-2.00×10^0	-2.00×10^0
2	5.75×10^0	5.75×10^0	6.85×10^0	6.85×10^0	7.96×10^0	7.96×10^0
3	-1.49×10^1	-1.49×10^1	-1.93×10^1	-1.93×10^1	-2.37×10^1	-2.37×10^1
4	4.93×10^1	4.93×10^1	7.99×10^1	7.99×10^1	1.18×10^2	1.18×10^2
5	-1.41×10^2	-1.41×10^2	-2.55×10^2	-2.55×10^2	-4.05×10^2	-4.05×10^2
6	5.27×10^2	5.27×10^2	1.25×10^3	1.25×10^3	2.46×10^3	2.46×10^3
7	-1.60×10^3	-1.60×10^3	-4.26×10^3	-4.24×10^3	-9.01×10^3	-8.98×10^3
8	6.77×10^3	6.75×10^3	2.46×10^4	2.46×10^4	6.65×10^4	6.64×10^4
	$T = 1.0$		$T = 3.0$		$T = 5.0$	
0	1.00×10^0	1.00×10^0	1.00×10^0	1.00×10^0	1.00×10^0	1.00×10^0
1	-2.00×10^0	-2.00×10^0	-2.00×10^0	-2.00×10^0	-2.00×10^0	-2.00×10^0
2	9.64×10^0	9.64×10^0	2.09×10^1	2.09×10^1	3.21×10^1	3.21×10^1
3	-3.05×10^1	-3.05×10^1	-7.54×10^1	-7.54×10^1	-1.20×10^2	-1.20×10^2
4	1.90×10^2	1.90×10^2	1.11×10^3	1.11×10^3	2.78×10^3	2.78×10^3
5	-6.96×10^2	-6.96×10^2	-4.68×10^3	-4.68×10^3	-1.22×10^4	-1.22×10^4
6	5.47×10^3	5.47×10^3	9.30×10^4	9.30×10^4	3.90×10^5	3.90×10^5
7	-2.14×10^4	-2.13×10^4	-4.13×10^5	-4.12×10^5	-1.78×10^6	-1.78×10^6
8	2.10×10^5	2.10×10^5	1.08×10^7	1.08×10^7	7.58×10^7	7.58×10^7

Table F.10: Sum rules for $\omega_0 = 0.2, g = 1.0$ at different temperatures.

n	$T = 0.3$		$T = 0.5$		$T = 0.7$	
	Exact	DMFT	Exact	DMFT	Exact	DMFT
0	1.00×10^0	1.00×10^0	1.00×10^0	1.00×10^0	1.00×10^0	1.00×10^0
1	-2.00×10^0	-2.00×10^0	-2.00×10^0	-2.00×10^0	-2.00×10^0	-2.00×10^0
2	7.11×10^0	7.11×10^0	9.07×10^0	9.07×10^0	1.11×10^1	1.11×10^1
3	-2.02×10^1	-2.02×10^1	-2.81×10^1	-2.81×10^1	-3.60×10^1	-3.60×10^1
4	8.79×10^1	8.79×10^1	1.63×10^2	1.63×10^2	2.63×10^2	2.63×10^2
5	-2.83×10^2	-2.83×10^2	-5.81×10^2	-5.81×10^2	-9.93×10^2	-9.93×10^2
6	1.47×10^3	1.47×10^3	4.23×10^3	4.23×10^3	9.33×10^3	9.34×10^3
7	-4.99×10^3	-4.97×10^3	-1.60×10^4	-1.59×10^4	-3.72×10^4	-3.72×10^4
8	3.11×10^4	3.10×10^4	1.45×10^5	1.45×10^5	4.46×10^5	4.46×10^5
	$T = 1.0$		$T = 3.0$		$T = 5.0$	
0	1.00×10^0	1.00×10^0	1.00×10^0	1.00×10^0	1.00×10^0	1.00×10^0
1	-2.00×10^0	-2.00×10^0	-2.00×10^0	-2.00×10^0	-2.00×10^0	-2.00×10^0
2	1.40×10^1	1.40×10^1	3.40×10^1	3.40×10^1	5.40×10^1	5.40×10^1
3	-4.79×10^1	-4.79×10^1	-1.28×10^2	-1.28×10^2	-2.08×10^2	-2.08×10^2
4	4.58×10^2	4.58×10^2	3.14×10^3	3.14×10^3	8.22×10^3	8.22×10^3
5	-1.82×10^3	-1.82×10^3	-1.38×10^4	-1.38×10^4	-3.69×10^4	-3.69×10^4
6	2.29×10^4	2.29×10^4	4.69×10^5	4.69×10^5	2.05×10^6	2.05×10^6
7	-9.60×10^4	-9.58×10^4	-2.14×10^6	-2.14×10^6	-9.53×10^6	-9.53×10^6
8	1.57×10^6	1.57×10^6	9.73×10^7	9.73×10^7	7.11×10^8	7.11×10^8

Table F.11: Sum rules for $\omega_0 = 0.2, g = \sqrt{2}$ at different temperatures.

n	$T = 0.3$		$T = 0.5$		$T = 0.7$	
	Exact	DMFT	Exact	DMFT	Exact	DMFT
0	1.00×10^0	1.00×10^0	1.00×10^0	1.00×10^0	1.00×10^0	1.00×10^0
1	-2.00×10^0	-2.00×10^0	-2.00×10^0	-2.00×10^0	-2.00×10^0	-2.00×10^0
2	1.02×10^1	1.02×10^1	1.41×10^1	1.41×10^1	1.81×10^1	1.81×10^1
3	-3.25×10^1	-3.25×10^1	-4.81×10^1	-4.81×10^1	-6.40×10^1	-6.40×10^1
4	2.18×10^2	2.18×10^2	4.65×10^2	4.65×10^2	8.08×10^2	8.08×10^2
5	-7.91×10^2	-7.90×10^2	-1.83×10^3	-1.83×10^3	-3.32×10^3	-3.31×10^3
6	6.81×10^3	6.80×10^3	2.34×10^4	2.34×10^4	5.66×10^4	5.65×10^4
7	-2.57×10^4	-2.55×10^4	-9.60×10^4	-9.56×10^4	-2.41×10^5	-2.40×10^5
8	2.85×10^5	2.83×10^5	1.61×10^6	1.61×10^6	5.46×10^6	5.44×10^6
	$T = 1.0$		$T = 3.0$		$T = 5.0$	
0	1.00×10^0	1.00×10^0	1.00×10^0	1.00×10^0	1.00×10^0	1.00×10^0
1	-2.00×10^0	-2.00×10^0	-2.00×10^0	-2.00×10^0	-2.00×10^0	-2.00×10^0
2	2.41×10^1	2.41×10^1	6.40×10^1	6.40×10^1	1.04×10^2	1.04×10^2
3	-8.79×10^1	-8.79×10^1	-2.48×10^2	-2.48×10^2	-4.08×10^2	-4.08×10^2
4	1.50×10^3	1.50×10^3	1.17×10^4	1.17×10^4	3.14×10^4	3.14×10^4
5	-6.39×10^3	-6.39×10^3	-5.26×10^4	-5.26×10^4	-1.44×10^5	-1.44×10^5
6	1.50×10^5	1.50×10^5	3.49×10^6	3.49×10^6	1.57×10^7	1.57×10^7
7	-6.61×10^5	-6.60×10^5	-1.63×10^7	-1.62×10^7	-7.39×10^7	-7.39×10^7
8	2.07×10^7	2.07×10^7	1.46×10^9	1.46×10^9	1.09×10^{10}	1.09×10^{10}

Table F.12: Sum rules for $\omega_0 = 0.5, g = 0.05$ at different temperatures.

n	$T = 0.3$		$T = 0.5$		$T = 0.7$	
	Exact	DMFT	Exact	DMFT	Exact	DMFT
0	1.00×10^0	1.09×10^0	1.00×10^0	1.00×10^0	1.00×10^0	1.00×10^0
1	-2.00×10^0	-2.18×10^0	-2.00×10^0	-2.00×10^0	-2.00×10^0	-2.00×10^0
2	4.00×10^0	4.37×10^0	4.01×10^0	4.00×10^0	4.01×10^0	4.01×10^0
3	-8.01×10^0	-8.74×10^0	-8.02×10^0	-8.02×10^0	-8.03×10^0	-8.03×10^0
4	1.61×10^1	1.75×10^1	1.61×10^1	1.61×10^1	1.61×10^1	1.61×10^1
5	-3.21×10^1	-3.50×10^1	-3.22×10^1	-3.22×10^1	-3.23×10^1	-3.23×10^1
6	6.43×10^1	7.02×10^1	6.46×10^1	6.45×10^1	6.48×10^1	6.48×10^1
7	-1.29×10^2	-1.40×10^2	-1.29×10^2	-1.29×10^2	-1.30×10^2	-1.30×10^2
8	2.58×10^2	2.82×10^2	2.60×10^2	2.59×10^2	2.61×10^2	2.61×10^2
	$T = 1.0$		$T = 3.0$		$T = 5.0$	
0	1.00×10^0	1.00×10^0	1.00×10^0	1.00×10^0	1.00×10^0	1.00×10^0
1	-2.00×10^0	-2.00×10^0	-2.00×10^0	-2.00×10^0	-2.00×10^0	-2.00×10^0
2	4.01×10^0	4.01×10^0	4.03×10^0	4.03×10^0	4.05×10^0	4.05×10^0
3	-8.04×10^0	-8.04×10^0	-8.12×10^0	-8.12×10^0	-8.20×10^0	-8.20×10^0
4	1.61×10^1	1.61×10^1	1.64×10^1	1.64×10^1	1.67×10^1	1.67×10^1
5	-3.24×10^1	-3.24×10^1	-3.32×10^1	-3.32×10^1	-3.41×10^1	-3.41×10^1
6	6.51×10^1	6.51×10^1	6.75×10^1	6.75×10^1	6.99×10^1	6.99×10^1
7	-1.31×10^2	-1.31×10^2	-1.37×10^2	-1.37×10^2	-1.43×10^2	-1.43×10^2
8	2.63×10^2	2.63×10^2	2.80×10^2	2.80×10^2	2.97×10^2	2.97×10^2

Table F.13: Sum rules for $\omega_0 = 0.5, g = 0.2$ at different temperatures.

n	$T = 0.3$		$T = 0.5$		$T = 0.7$	
	Exact	DMFT	Exact	DMFT	Exact	DMFT
0	1.00×10^0	1.00×10^0	1.00×10^0	1.00×10^0	1.00×10^0	1.00×10^0
1	-2.00×10^0	-2.00×10^0	-2.00×10^0	-2.00×10^0	-2.00×10^0	-2.00×10^0
2	4.06×10^0	4.06×10^0	4.09×10^0	4.09×10^0	4.12×10^0	4.12×10^0
3	-8.21×10^0	-8.21×10^0	-8.33×10^0	-8.33×10^0	-8.45×10^0	-8.45×10^0
4	1.68×10^1	1.68×10^1	1.72×10^1	1.72×10^1	1.76×10^1	1.76×10^1
5	-3.41×10^1	-3.41×10^1	-3.53×10^1	-3.53×10^1	-3.66×10^1	-3.66×10^1
6	6.99×10^1	6.99×10^1	7.34×10^1	7.34×10^1	7.73×10^1	7.73×10^1
7	-1.42×10^2	-1.42×10^2	-1.52×10^2	-1.52×10^2	-1.62×10^2	-1.62×10^2
8	2.93×10^2	2.93×10^2	3.18×10^2	3.18×10^2	3.47×10^2	3.47×10^2
	$T = 1.0$		$T = 3.0$		$T = 5.0$	
0	1.00×10^0	1.00×10^0	1.00×10^0	1.00×10^0	1.00×10^0	1.00×10^0
1	-2.00×10^0	-2.00×10^0	-2.00×10^0	-2.00×10^0	-2.00×10^0	-2.00×10^0
2	4.16×10^0	4.16×10^0	4.48×10^0	4.48×10^0	4.80×10^0	4.80×10^0
3	-8.63×10^0	-8.63×10^0	-9.90×10^0	-9.90×10^0	-1.12×10^1	-1.12×10^1
4	1.83×10^1	1.83×10^1	2.35×10^1	2.35×10^1	2.92×10^1	2.92×10^1
5	-3.87×10^1	-3.87×10^1	-5.45×10^1	-5.45×10^1	-7.33×10^1	-7.33×10^1
6	8.36×10^1	8.36×10^1	1.36×10^2	1.36×10^2	2.08×10^2	2.08×10^2
7	-1.79×10^2	-1.79×10^2	-3.30×10^2	-3.29×10^2	-5.51×10^2	-5.50×10^2
8	3.95×10^2	3.95×10^2	8.73×10^2	8.71×10^2	1.70×10^3	1.70×10^3

Table F.14: Sum rules for $\omega_0 = 0.5, g = 0.5$ at different temperatures.

n	$T = 0.3$		$T = 0.5$		$T = 0.7$	
	Exact	DMFT	Exact	DMFT	Exact	DMFT
0	1.00×10^0	1.00×10^0	1.00×10^0	1.00×10^0	1.00×10^0	1.00×10^0
1	-2.00×10^0	-2.00×10^0	-2.00×10^0	-2.00×10^0	-2.00×10^0	-2.00×10^0
2	4.37×10^0	4.37×10^0	4.54×10^0	4.54×10^0	4.73×10^0	4.73×10^0
3	-9.34×10^0	-9.34×10^0	-1.00×10^1	-1.00×10^1	-1.08×10^1	-1.08×10^1
4	2.11×10^1	2.11×10^1	2.41×10^1	2.41×10^1	2.75×10^1	2.75×10^1
5	-4.62×10^1	-4.62×10^1	-5.53×10^1	-5.53×10^1	-6.62×10^1	-6.62×10^1
6	1.08×10^2	1.08×10^2	1.40×10^2	1.40×10^2	1.81×10^2	1.81×10^2
7	-2.37×10^2	-2.37×10^2	-3.28×10^2	-3.27×10^2	-4.49×10^2	-4.48×10^2
8	5.74×10^2	5.74×10^2	8.80×10^2	8.78×10^2	1.33×10^3	1.33×10^3
	$T = 1.0$		$T = 3.0$		$T = 5.0$	
0	1.00×10^0	1.00×10^0	1.00×10^0	1.00×10^0	1.00×10^0	1.00×10^0
1	-2.00×10^0	-2.00×10^0	-2.00×10^0	-2.00×10^0	-2.00×10^0	-2.00×10^0
2	5.02×10^0	5.02×10^0	7.01×10^0	7.01×10^0	9.00×10^0	9.00×10^0
3	-1.20×10^1	-1.20×10^1	-1.99×10^1	-1.99×10^1	-2.79×10^1	-2.79×10^1
4	3.32×10^1	3.32×10^1	8.55×10^1	8.55×10^1	1.62×10^2	1.62×10^2
5	-8.49×10^1	-8.49×10^1	-2.76×10^2	-2.76×10^2	-5.79×10^2	-5.79×10^2
6	2.59×10^2	2.59×10^2	1.43×10^3	1.43×10^3	4.24×10^3	4.24×10^3
7	-6.92×10^2	-6.90×10^2	-4.93×10^3	-4.92×10^3	-1.62×10^4	-1.61×10^4
8	2.35×10^3	2.34×10^3	3.10×10^4	3.09×10^4	1.49×10^5	1.49×10^5

Table F.15: Sum rules for $\omega_0 = 0.2, g = 0.75$ at different temperatures.

n	$T = 0.3$		$T = 0.5$		$T = 0.7$	
	Exact	DMFT	Exact	DMFT	Exact	DMFT
0	1.00×10^0	1.00×10^0	1.00×10^0	1.00×10^0	1.00×10^0	1.00×10^0
1	-2.00×10^0	-2.00×10^0	-2.00×10^0	-2.00×10^0	-2.00×10^0	-2.00×10^0
2	4.82×10^0	4.82×10^0	5.22×10^0	5.22×10^0	5.64×10^0	5.64×10^0
3	-1.10×10^1	-1.10×10^1	-1.26×10^1	-1.26×10^1	-1.43×10^1	-1.43×10^1
4	2.87×10^1	2.87×10^1	3.67×10^1	3.67×10^1	4.64×10^1	4.64×10^1
5	-6.79×10^1	-6.79×10^1	-9.41×10^1	-9.41×10^1	-1.27×10^2	-1.27×10^2
6	1.90×10^2	1.90×10^2	3.05×10^2	3.05×10^2	4.73×10^2	4.73×10^2
7	-4.49×10^2	-4.47×10^2	-7.97×10^2	-7.94×10^2	-1.34×10^3	-1.33×10^3
8	1.39×10^3	1.39×10^3	2.97×10^3	2.97×10^3	5.87×10^3	5.86×10^3
	$T = 1.0$		$T = 3.0$		$T = 5.0$	
0	1.00×10^0	1.00×10^0	1.00×10^0	1.00×10^0	1.00×10^0	1.00×10^0
1	-2.00×10^0	-2.00×10^0	-2.00×10^0	-2.00×10^0	-2.00×10^0	-2.00×10^0
2	6.30×10^0	6.30×10^0	1.08×10^1	1.08×10^1	1.53×10^1	1.53×10^1
3	-1.69×10^1	-1.69×10^1	-3.48×10^1	-3.48×10^1	-5.28×10^1	-5.28×10^1
4	6.34×10^1	6.34×10^1	2.49×10^2	2.49×10^2	5.56×10^2	5.56×10^2
5	-1.88×10^2	-1.88×10^2	-9.26×10^2	-9.26×10^2	-2.23×10^3	-2.23×10^3
6	8.37×10^2	8.37×10^2	8.59×10^3	8.59×10^3	3.15×10^4	3.15×10^4
7	-2.59×10^3	-2.58×10^3	-3.36×10^4	-3.35×10^4	-1.32×10^5	-1.32×10^5
8	1.39×10^4	1.39×10^4	4.03×10^5	4.03×10^5	2.46×10^6	2.46×10^6

Table F.16: Sum rules for $\omega_0 = 0.5, g = 1.0$ at different temperatures.

n	$T = 0.3$		$T = 0.5$		$T = 0.7$	
	Exact	DMFT	Exact	DMFT	Exact	DMFT
0	1.00×10^0	1.00×10^0	1.00×10^0	1.00×10^0	1.00×10^0	1.00×10^0
1	-2.00×10^0	-2.00×10^0	-2.00×10^0	-2.00×10^0	-2.00×10^0	-2.00×10^0
2	5.47×10^0	5.47×10^0	6.16×10^0	6.16×10^0	6.92×10^0	6.92×10^0
3	-1.34×10^1	-1.34×10^1	-1.62×10^1	-1.62×10^1	-1.92×10^1	-1.92×10^1
4	4.13×10^1	4.13×10^1	5.89×10^1	5.89×10^1	8.11×10^1	8.11×10^1
5	-1.06×10^2	-1.06×10^2	-1.66×10^2	-1.66×10^2	-2.47×10^2	-2.47×10^2
6	3.73×10^2	3.73×10^2	7.20×10^2	7.20×10^2	1.28×10^3	1.28×10^3
7	-9.22×10^2	-9.18×10^2	-2.02×10^3	-2.01×10^3	-3.93×10^3	-3.92×10^3
8	3.97×10^3	3.96×10^3	1.10×10^4	1.09×10^4	2.59×10^4	2.59×10^4
	$T = 1.0$		$T = 3.0$		$T = 5.0$	
0	1.00×10^0	1.00×10^0	1.00×10^0	1.00×10^0	1.00×10^0	1.00×10^0
1	-2.00×10^0	-2.00×10^0	-2.00×10^0	-2.00×10^0	-2.00×10^0	-2.00×10^0
2	8.08×10^0	8.08×10^0	1.60×10^1	1.60×10^1	2.40×10^1	2.40×10^1
3	-2.38×10^1	-2.38×10^1	-5.56×10^1	-5.56×10^1	-8.76×10^1	-8.76×10^1
4	1.22×10^2	1.22×10^2	6.19×10^2	6.19×10^2	1.50×10^3	1.50×10^3
5	-4.03×10^2	-4.03×10^2	-2.48×10^3	-2.48×10^3	-6.35×10^3	-6.35×10^3
6	2.61×10^3	2.61×10^3	3.74×10^4	3.74×10^4	1.50×10^5	1.50×10^5
7	-8.79×10^3	-8.75×10^3	-1.55×10^5	-1.54×10^5	-6.57×10^5	-6.56×10^5
8	7.35×10^4	7.34×10^4	3.11×10^6	3.11×10^6	2.09×10^7	2.09×10^7

Table F.17: Sum rules for $\omega_0 = 0.5, g = \sqrt{2}$ at different temperatures.

n	$T = 0.3$		$T = 0.5$		$T = 0.7$	
	Exact	DMFT	Exact	DMFT	Exact	DMFT
0	1.00×10^0	1.00×10^0	1.00×10^0	1.00×10^0	1.00×10^0	1.00×10^0
1	-2.00×10^0	-2.00×10^0	-2.00×10^0	-2.00×10^0	-2.00×10^0	-2.00×10^0
2	6.93×10^0	6.93×10^0	8.33×10^0	8.33×10^0	9.84×10^0	9.84×10^0
3	-1.87×10^1	-1.87×10^1	-2.43×10^1	-2.43×10^1	-3.03×10^1	-3.03×10^1
4	7.95×10^1	7.95×10^1	1.30×10^2	1.30×10^2	1.97×10^2	1.97×10^2
5	-2.25×10^2	-2.25×10^2	-4.10×10^2	-4.10×10^2	-6.72×10^2	-6.72×10^2
6	1.21×10^3	1.21×10^3	2.85×10^3	2.85×10^3	5.79×10^3	5.79×10^3
7	-3.07×10^3	-3.05×10^3	-8.53×10^3	-8.49×10^3	-1.92×10^4	-1.91×10^4
8	2.34×10^4	2.34×10^4	8.31×10^4	8.30×10^4	2.30×10^5	2.29×10^5
	$T = 1.0$		$T = 3.0$		$T = 5.0$	
0	1.00×10^0	1.00×10^0	1.00×10^0	1.00×10^0	1.00×10^0	1.00×10^0
1	-2.00×10^0	-2.00×10^0	-2.00×10^0	-2.00×10^0	-2.00×10^0	-2.00×10^0
2	1.22×10^1	1.22×10^1	2.81×10^1	2.81×10^1	4.40×10^1	4.40×10^1
3	-3.97×10^1	-3.97×10^1	-1.03×10^2	-1.03×10^2	-1.67×10^2	-1.67×10^2
4	3.28×10^2	3.28×10^2	2.09×10^3	2.09×10^3	5.39×10^3	5.39×10^3
5	-1.20×10^3	-1.20×10^3	-8.86×10^3	-8.86×10^3	-2.37×10^4	-2.37×10^4
6	1.34×10^4	1.34×10^4	2.51×10^5	2.51×10^5	1.08×10^6	1.08×10^6
7	-4.86×10^4	-4.85×10^4	-1.08×10^6	-1.08×10^6	-4.84×10^6	-4.84×10^6
8	7.50×10^5	7.50×10^5	4.19×10^7	4.19×10^7	3.00×10^8	3.00×10^8

Bibliography

- [1] G. Mahan, *Many-Particle Physics* (Kluwer Academic, New York, 2000).
- [2] F. Giustino, *Rev. Mod. Phys.* **89**, 015003 (2017).
- [3] Z. Bai, D. He, S. Fu, Q. Miao, S. Liu, M. Huang, K. Zhao, Y. Wang, and X. Zhang, *Nano Select* **3**, 1112 (2022).
- [4] N. Prodanović and N. Vukmirović, *Phys. Rev. B* **99**, 104304 (2019).
- [5] A. Y. Sosorev, *Materials & Design* **192**, 108730 (2020).
- [6] M. Tinkham, *Introduction to Superconductivity* (Courier Corporation, 2004).
- [7] J. Noffsinger, E. Kioupakis, C. G. Van de Walle, S. G. Louie, and M. L. Cohen, *Phys. Rev. Lett.* **108**, 167402 (2012).
- [8] M. Fox, *Optical Properties of Solids* (American Association of Physics Teachers, 2002).
- [9] H. Fröhlich, *Advances in Physics* **3**, 325 (1954).
- [10] U. Rössler, *Solid State Theory: An Introduction* (Springer Science & Business Media, 2009).
- [11] L. D. Landau, *Phys. Z. Sowjet.* **3**, 664 (1933).
- [12] S. Pekar, *Zh. Eksp. Teor. Fiz* **16**, 341 (1946).
- [13] S. Pekar, *Zh. Eksp. Teor. Fiz* **16**, 335 (1946).
- [14] S. Pekar, *Zh. Eksp. Teor. Fiz* **17**, 868 (1947).
- [15] S. Pekar, *Zh. Eksp. Teor. Fiz* **18**, 933 (1948).
- [16] L. Landau and S. Pekar, *Zh. Eksp. Teor. Fiz* **18**, 419 (1948).
- [17] H. Fröhlich, H. Pelzer, and S. Zienau, *The London, Edinburgh, and Dublin Philosophical Magazine and Journal of Science* **41**, 221 (1950).
- [18] T. Holstein, *Ann. Phys.* **8**, 325 (1959).
- [19] S. Pekar, *Research in Electron Theory of Crystals*, Tech. Rep. (1951) [English edition: US AEC Transl. AEC-tr-555 (1963)].

- [20] N. Bogoliubov, *Uspekhi Mat. Nauk* **2**, 3 (1950).
- [21] S. Tyablikov, *Zhur. Eksptl'. i Teoret. Fiz.* **21** (1951).
- [22] A. Alexandrov, *Polarons in Advanced Materials*, Vol. 103 (2007).
- [23] C. Franchini, M. Reticcioli, M. Setvin, and U. Diebold, *Nature Reviews Materials* **6**, 560 (2021).
- [24] L. Vidmar, J. Bonča, M. Mierzejewski, P. Prelovšek, and S. A. Trugman, *Phys. Rev. B* **83**, 134301 (2011).
- [25] B. Kloss, D. R. Reichman, and R. Tempelaar, *Phys. Rev. Lett.* **123**, 126601 (2019).
- [26] C. Brockt and E. Jeckelmann, *Phys. Rev. B* **95**, 064309 (2017).
- [27] J. Stolpp, J. Herbrych, F. Dorfner, E. Dagotto, and F. Heidrich-Meisner, *Phys. Rev. B* **101**, 035134 (2020).
- [28] Y. Murakami, P. Werner, N. Tsuji, and H. Aoki, *Phys. Rev. B* **91**, 045128 (2015).
- [29] D. Jansen, J. Stolpp, L. Vidmar, and F. Heidrich-Meisner, *Phys. Rev. B* **99**, 155130 (2019).
- [30] J. H. Fetherolf, D. Golež, and T. C. Berkelbach, *Phys. Rev. X* **10**, 021062 (2020).
- [31] A. S. Mishchenko, N. Nagaosa, and N. Prokof'ev, *Phys. Rev. Lett.* **113**, 166402 (2014).
- [32] M. Kang, S. W. Jung, W. J. Shin, Y. Sohn, S. H. Ryu, T. K. Kim, M. Hoesch, and K. S. Kim, *Nature materials* **17**, 676 (2018).
- [33] R. M. Martin, L. Reining, and D. M. Ceperley, *Interacting Electrons: Theory and Computational Approaches* (Cambridge University Press, 2016).
- [34] A. A. Abrikosov, I. Dzyaloshinskii, L. P. Gorkov, and R. A. Silverman, *Methods of Quantum Field Theory in Statistical Physics* (Dover, New York, NY, 1975).
- [35] A. Damascelli, Z. Hussain, and Z.-X. Shen, *Rev. Mod. Phys.* **75**, 473 (2003).
- [36] S. Moser, L. Moreschini, J. Jaćimović, O. S. Barišić, H. Berger, A. Magrez, Y. J. Chang, K. S. Kim, A. Bostwick, E. Rotenberg, L. Forró, and M. Grioni, *Phys. Rev. Lett.* **110**, 196403 (2013).
- [37] Z. Wang, S. Mckeown Walker, A. Tamai, Y. Wang, Z. Ristic, F. Y. Bruno, A. De La Torre, S. Riccò, N. Plumb, M. Shi, *et al.*, *Nature materials* **15**, 835 (2016).
- [38] I. Lang and Y. A. Firsov, *Zh. Eksp. Teor. Fiz.* **43**, 1843 (1962), [*Sov. Phys. JETP* **16**, 1301 (1963)].
- [39] A. S. Alexandrov and J. T. Devreese, *Advances in Polaron Physics* (Springer, 2010).
- [40] E. Jeckelmann and S. R. White, *Phys. Rev. B* **57**, 6376 (1998).
- [41] C. Zhang, E. Jeckelmann, and S. R. White, *Phys. Rev. B* **60**, 14092 (1999).
- [42] P. E. Kornilovitch, *Phys. Rev. Lett.* **81**, 5382 (1998).
- [43] A. H. Romero, D. W. Brown, and K. Lindenberg, *The Journal of chemical physics* **109**, 6540 (1998).
- [44] A. H. Romero, D. W. Brown, and K. Lindenberg, *Phys. Rev. B* **59**, 13728 (1999).

- [45] J. Bonča, S. A. Trugman, and I. Batistić, *Phys. Rev. B* **60**, 1633 (1999).
- [46] J. Bonča, S. A. Trugman, and M. Berciu, *Phys. Rev. B* **100**, 094307 (2019).
- [47] D. Jansen, J. Bonča, and F. Heidrich-Meisner, *Phys. Rev. B* **102**, 165155 (2020).
- [48] J. L. M. van Mechelen, D. van der Marel, C. Grimaldi, A. B. Kuzmenko, N. P. Armitage, N. Reyren, H. Hagemann, and I. I. Mazin, *Phys. Rev. Lett.* **100**, 226403 (2008).
- [49] V. Janković, *The Journal of Chemical Physics* **159**, 094113 (2023).
- [50] A. S. Mishchenko, N. Nagaosa, G. De Filippis, A. de Candia, and V. Cataudella, *Phys. Rev. Lett.* **114**, 146401 (2015).
- [51] G. Schubert, G. Wellein, A. Weisse, A. Alvermann, and H. Fehske, *Phys. Rev. B* **72**, 104304 (2005).
- [52] D. Jansen and F. Heidrich-Meisner, *Phys. Rev. B* **108**, L081114 (2023).
- [53] G. L. Goodvin, M. Berciu, and G. A. Sawatzky, *Phys. Rev. B* **74**, 245104 (2006).
- [54] R. Kubo, *Journal of the physical society of Japan* **12**, 570 (1957).
- [55] A. Migdal, *Zh. Eksp. Teor. Fiz.* **34**, 1438 (1958), [*Sov. Phys. JETP* **7**, 996 (1958)].
- [56] S. Ciuchi, F. de Pasquale, S. Fratini, and D. Feinberg, *Phys. Rev. B* **56**, 4494 (1997).
- [57] P. E. Kornilovitch, *Europhysics Letters* **59**, 735 (2002).
- [58] A. Georges, G. Kotliar, W. Krauth, and M. J. Rozenberg, *Rev. Mod. Phys.* **68**, 13 (1996).
- [59] S. Fratini, F. de Pasquale, and S. Ciuchi, *Phys. Rev. B* **63**, 153101 (2001).
- [60] S. Fratini and S. Ciuchi, *Phys. Rev. Lett.* **91**, 256403 (2003).
- [61] L.-C. Ku, S. A. Trugman, and J. Bonča, *Phys. Rev. B* **65**, 174306 (2002).
- [62] P. Mitrić, V. Janković, N. Vukmirović, and D. Tanasković, *Phys. Rev. Lett.* **129**, 096401 (2022).
- [63] K. Held, *Advances in physics* **56**, 829 (2007).
- [64] W. Metzner and D. Vollhardt, *Phys. Rev. Lett.* **62**, 324 (1989).
- [65] F. Schwabl, *Statistical Mechanics* (Springer Science & Business Media, 2006).
- [66] A. Altland and B. D. Simons, *Condensed Matter Field Theory* (Cambridge University Press, 2010).
- [67] J. W. Negele, *Quantum Many-Particle Systems* (CRC Press, 2018).
- [68] P. Coleman, *Introduction to Many-Body Physics* (Cambridge University Press, 2015).
- [69] J. Hubbard, *Proceedings of the Royal Society of London. Series A. Mathematical and Physical Sciences* **281**, 401 (1964).
- [70] W. Metzner, *Phys. Rev. B* **43**, 8549 (1991).
- [71] O. S. Barišić, *Phys. Rev. B* **76**, 193106 (2007).

- [72] M. Berciu, *Phys. Rev. Lett.* **97**, 036402 (2006).
- [73] Y. Tanimura, *J. Comp. Phys.* **153**, 020901 (2020).
- [74] R.-X. Xu and Y. J. Yan, *Phys. Rev. E* **75**, 031107 (2007).
- [75] J. Jin, X. Zheng, and Y. Yan, *J. Comp. Phys.* **128**, 234703 (2008).
- [76] D. Hou, R. Wang, X. Zheng, N. Tong, J. Wei, and Y. Yan, *Phys. Rev. B* **90**, 045141 (2014).
- [77] Z. Li, N. Tong, X. Zheng, D. Hou, J. Wei, J. Hu, and Y. Yan, *Phys. Rev. Lett.* **109**, 266403 (2012).
- [78] L. Chen, Y. Zhao, and Y. Tanimura, *The Journal of Physical Chemistry Letters* **6**, 3110 (2015), pMID: 26267210.
- [79] L. Song and Q. Shi, *J. Comp. Phys.* **142**, 174103 (2015).
- [80] L. Song and Q. Shi, *J. Comp. Phys.* **143**, 194106 (2015).
- [81] I. S. Dunn, R. Tempelaar, and D. R. Reichman, *J. Comp. Phys.* **150**, 184109 (2019).
- [82] Y. Yan, T. Xing, and Q. Shi, *J. Comp. Phys.* **153**, 204109 (2020).
- [83] V. Janković and N. Vukmirović, *Phys. Rev. B* **105**, 054311 (2022).
- [84] H. D. Raedt and A. Lagendijk, *Phys. Rev. Lett.* **49**, 1522 (1982).
- [85] H. De Raedt and A. Lagendijk, *Phys. Rev. B* **27**, 6097 (1983).
- [86] H. De Raedt and A. Lagendijk, *Phys. Rev. B* **30**, 1671 (1984).
- [87] P. Mitrić, V. Janković, N. Vukmirović, and D. Tanasković, *Phys. Rev. B* **107**, 125165 (2023).
- [88] B. I. Lundqvist, *Physik der kondensierten Materie* **9**, 236 (1969).
- [89] D. C. Langreth, *Phys. Rev. B* **1**, 471 (1970).
- [90] L. Hedin, *Physica Scripta* **21**, 477 (1980).
- [91] O. Gunnarsson, V. Meden, and K. Schönhammer, *Phys. Rev. B* **50**, 10462 (1994).
- [92] G. D. Mahan, *Phys. Rev.* **145**, 602 (1966).
- [93] D. Dunn, *Canadian Journal of Physics* **53**, 321 (1975).
- [94] B. Holm and F. Aryasetiawan, *Phys. Rev. B* **56**, 12825 (1997).
- [95] G. Antonius, Y.-H. Chan, and S. G. Louie, *Phys. Rev. Research* **2**, 043296 (2020).
- [96] C. Verdi, F. Caruso, and F. Giustino, *Nature Communications* **8** (2017), 10.1038/ncomms15769.
- [97] J. P. Nery, P. B. Allen, G. Antonius, L. Reining, A. Miglio, and X. Gonze, *Phys. Rev. B* **97**, 115145 (2018).
- [98] J.-J. Zhou and M. Bernardi, *Phys. Rev. Research* **1**, 033138 (2019).
- [99] B. K. Chang, J.-J. Zhou, N.-E. Lee, and M. Bernardi, *npj Computational Materials* **8**, 1 (2022).

- [100] S. M. Story, J. J. Kas, F. D. Vila, M. J. Verstraete, and J. J. Rehr, *Phys. Rev. B* **90**, 195135 (2014).
- [101] J. Lischner, D. Vigil-Fowler, and S. G. Louie, *Phys. Rev. B* **89**, 125430 (2014).
- [102] F. Caruso and F. Giustino, *Phys. Rev. B* **92**, 045123 (2015).
- [103] J. S. Zhou, J. Kas, L. Sponza, I. Reshetnyak, M. Guzzo, C. Giorgetti, M. Gatti, F. Sottile, J. Rehr, and L. Reining, *The Journal of chemical physics* **143**, 184109 (2015).
- [104] B. Gumhalter, V. Kovač, F. Caruso, H. Lambert, and F. Giustino, *Phys. Rev. B* **94**, 035103 (2016).
- [105] D. Vigil-Fowler, S. G. Louie, and J. Lischner, *Phys. Rev. B* **93**, 235446 (2016).
- [106] V. c. v. Vlček, E. Rabani, and D. Neuhauser, *Phys. Rev. Materials* **2**, 030801 (2018).
- [107] J. S. Zhou, M. Gatti, J. J. Kas, J. J. Rehr, and L. Reining, *Phys. Rev. B* **97**, 035137 (2018).
- [108] J. Ma and J. Cao, *J. Chem. Phys.* **142**, 094106 (2015).
- [109] L. Cupellini, F. Lipparini, and J. Cao, *J. Phys. Chem. B* **124**, 8610 (2020).
- [110] J. A. Nöthling, T. Mančal, and T. Krüger, *J. Chem. Phys.* **157**, 095103 (2022).
- [111] J. J. Kas, J. J. Rehr, and L. Reining, *Phys. Rev. B* **90**, 085112 (2014).
- [112] P. J. Robinson, I. S. Dunn, and D. R. Reichman, *Phys. Rev. B* **105**, 224305 (2022).
- [113] B. Pandey and P. B. Littlewood, arXiv preprint arXiv:2201.06715 (2022).
- [114] N. Kandolf, C. Verdi, and F. Giustino, *Phys. Rev. B* **105**, 085148 (2022).
- [115] A. S. Mishchenko, N. V. Prokof'ev, A. Sakamoto, and B. V. Svistunov, *Phys. Rev. B* **62**, 6317 (2000).
- [116] P. J. Robinson, I. S. Dunn, and D. R. Reichman, *Phys. Rev. B* **105**, 224304 (2022).
- [117] R. Kubo, *Journal of the Physical Society of Japan* **17**, 1100 (1962).
- [118] E. Meeron, *The Journal of Chemical Physics* **27**, 1238 (1957).
- [119] D. Levin, *Journal of Computational and Applied Mathematics* **67**, 95 (1996).
- [120] G. B. Arfken, H. J. Weber, and F. E. Harris, *Mathematical Methods for Physicists: A Comprehensive Guide* (Academic Press, 2011).
- [121] K. B. Tsiberkin and D. Kadyrov, *Physics of Nonequilibrium Processes: Linear Response Theory (in Russian)* (2015).
- [122] A. Khurana, *Phys. Rev. Lett.* **64**, 1990 (1990).
- [123] W. H. Press, S. A. Teukolsky, W. T. Vetterling, and B. P. Flannery, *Numerical Recipes: The Art of Scientific Computing* (Cambridge University Press, 2007).
- [124] S. Fratini, D. Mayou, and S. Ciuchi, *Adv. Funct. Mater.* **26**, 2292 (2016).
- [125] H. Hafermann, E. G. C. P. van Loon, M. I. Katsnelson, A. I. Lichtenstein, and O. Parcollet, *Phys. Rev. B* **90**, 235105 (2014).

- [126] D. Bergeron, V. Hankevych, B. Kyung, and A.-M. S. Tremblay, *Phys. Rev. B* **84**, 085128 (2011).
- [127] J. R. Schrieffer, *Theory of Superconductivity*, Advanced book classics (Perseus, 1999).
- [128] H. Bruus and K. Flensberg, *Many-Body Quantum Theory in Condensed Matter Physics: An Introduction* (OUP Oxford, 2004).
- [129] S. Miladić and N. Vukmirović, *Phys. Rev. B* **107**, 184315 (2023).
- [130] J. Vučičević, J. Kokalj, R. Žitko, N. Wentzell, D. Tanasković, and J. Mravlje, *Phys. Rev. Lett.* **123**, 036601 (2019).
- [131] C. Cohen-Tannoudji, B. Diu, and F. Laloe, *Quantum Mechanics* **1**, 898 (1986).
- [132] L. D. Landau and E. M. Lifshitz, *Quantum Mechanics: Non-Relativistic Theory*, Vol. 3 (Elsevier, 2013).
- [133] W. Greiner, L. Neise, and H. Stöcker, *Thermodynamics and Statistical Mechanics* (Springer Science & Business Media, 2012).
- [134] R. J. Elliott, J. A. Krumhansl, and P. L. Leath, *Rev. Mod. Phys.* **46**, 465 (1974).
- [135] J. Bonča and S. A. Trugman, *Phys. Rev. B* **103**, 054304 (2021).
- [136] O. Parcollet, M. Ferrero, T. Ayrat, H. Hafermann, I. Krivenko, L. Messio, and P. Seth, *Computer Physics Communications* **196**, 398 (2015).
- [137] J. Vučičević and R. Žitko, *Phys. Rev. B* **104**, 205101 (2021).

Biography of the Author

Petar Mitrić was born on August 23rd, 1995 in Belgrade, Republic of Serbia, where he completed his elementary and high school education. He started his Bachelor of Science studies at the Faculty of Physics, University of Belgrade in 2014, and graduated in July 2018 with a GPA of 9.97/10.00. During his studies, he was awarded the Đordje Živanović award (2016/2017) for the best third-year student at the Faculty of Physics, as well as the Dositeja fellowship (2017/2018 and 2018/2019) from the Serbian Ministry of Youth and Sports. However, his most significant achievement during this period was receiving the Student of Generation award (2017/2018) at the end of his bachelor studies, marking him as the best-performing student in his entire graduating class at the Faculty of Physics. After that, he started his MSc studies in 2018 at the same faculty, and completed them in 2019 with a GPA of 10.00/10.00. His master's thesis, titled *Canonical Structure of the Teleparallel Equivalent of General Relativity*, was done under the supervision of Dr. Branislav Cvetković, complemented by a close collaboration with Dr. Milutin Blagojević.

Petar Mitrić started his doctoral studies in November 2019, also at the Faculty of Physics, University of Belgrade, specializing in the field of condensed matter physics. His research was entirely conducted at the Scientific Computing Laboratory of the Institute of Physics Belgrade, under the supervision of Dr. Darko Tanasković. His research is mainly focused on studying the electron-phonon interaction and its consequences on single-particle and transport properties. During his doctoral studies, Petar Mitrić has published three peer-reviewed research papers, of which papers 1 and 2 are directly connected to the topic of his thesis

1. **P. Mitrić**, V. Janković, N. Vukmirović, and D. Tanasković, "*Spectral Functions of the Holstein Polaron: Exact and Approximate Solutions*", *Phys. Rev. Lett.* **129**, 096401 (2022).
2. **P. Mitrić**, V. Janković, N. Vukmirović, and D. Tanasković, "*Cumulant Expansion in the Holstein Model: Spectral Functions and Mobility*", *Phys. Rev. B* **107**, 125165 (2023).
3. C. Martin, V. Martinez, M. Opačić, S. Djurdjić-Mijin, **P. Mitrić**, A. Umićević, . A. Poudel, I. Sydoryk, W. Ren, R. M. Martin, D. B. Tanner, N. Lazarević, C. Petrovic, and D. Tanasković, "*Optical Conductivity and Vibrational Spectra of the Narrow-gap Semiconductor FeGa₃*", *Phys. Rev. B* **165151**, 165151 (2023).

Изјава о ауторству

Име и презиме аутора – **Петар Митрић**

Број индекса – **8009/2019**

Изјављујем

да је докторска дисертација под насловом

Spectral Functions and Mobility of the Holstein Polaron

(Спектралне функције и покретљивост Холштајновог поларона)

- резултат сопственог истраживачког рада;
- да дисертација у целини ни у деловима није била предложена за стицање друге дипломе према студијским програмима других високошколских установа;
- да су резултати коректно наведени и
- да нисам кршио ауторска права и користио интелектуалну својину других лица.

У Београду, 19.12.2023.

Потпис аутора



Изјава о истоветности штампане и електронске верзије докторског рада

Име и презиме аутора – **Петар Митрић**

Број индекса – **8009/2019**

Студијски програм – Физика кондензоване материје и статистичка физика

Наслов рада – **Spectral Functions and Mobility of the Holstein Polaron**

(Спектралне функције и покретљивост Холштајновог поларона)

Ментор – др **Дарко Танасковић**


Изјављујем да је штампана верзија мог докторског рада истоветна електронској верзији коју сам предао ради похрањивања у **Дигиталном репозиторијуму Универзитета у Београду**.

Дозвољавам да се објаве моји лични подаци везани за добијање академског назива доктора наука, као што су име и презиме, година и место рођења и датум одбране рада.

Ови лични подаци могу се објавити на мрежним страницама дигиталне библиотеке, у електронском каталогу и у публикацијама Универзитета у Београду.

У Београду, 19.12.2023.

Потпис аутора



Изјава о коришћењу

Овлашћујем Универзитетску библиотеку „Светозар Марковић“ да у Дигитални репозиторијум Универзитета у Београду унесе моју докторску дисертацију под насловом:

Spectral Functions and Mobility of the Holstein Polaron

(Спектралне функције и покретљивост Холштајновог поларона)

која је моје ауторско дело.

Дисертацију са свим прилозима предао сам у електронском формату погодном за трајно архивирање.


Моју докторску дисертацију похрањену у Дигиталном репозиторијуму Универзитета у Београду и доступну у отвореном приступу могу да користе сви који поштују одредбе садржане у одабраном типу лиценце Креативне заједнице (Creative Commons) за коју сам се одлучио.

1. Ауторство (CC BY)
2. Ауторство – некомерцијално (CC BY-NC)
3. Ауторство – некомерцијално – без прерада (CC BY-NC-ND)
4. Ауторство – некомерцијално – делити под истим условима (CC BY-NC-SA)
5. Ауторство – без прерада (CC BY-ND)
6. Ауторство – делити под истим условима (CC BY-SA)

(Молимо да заокружите само једну од шест понуђених лиценци. Кратак опис лиценци је саставни део ове изјаве).

У Београду, 19.12.2023.

Потпис аутора



1. **Ауторство.** Дозвољаваате умножавање, дистрибуцију и јавно саопштавање дела, и прераде, ако се наведе име аутора на начин одређен од стране аутора или даваоца лиценце, чак и у комерцијалне сврхе. Ово је најслободнија од свих лиценци.
2. **Ауторство – некомерцијално.** Дозвољаваате умножавање, дистрибуцију и јавно саопштавање дела, и прераде, ако се наведе име аутора на начин одређен од стране аутора или даваоца лиценце. Ова лиценца не дозвољава комерцијалну употребу дела.
3. **Ауторство – некомерцијално – без прерада.** Дозвољаваате умножавање, дистрибуцију и јавно саопштавање дела, без промена, преобликовања или употребе дела у свом делу, ако се наведе име аутора на начин одређен од стране аутора или даваоца лиценце. Ова лиценца не дозвољава комерцијалну употребу дела. У односу на све остале лиценце, овом лиценцом се ограничава највећи обим права коришћења дела.
4. **Ауторство – некомерцијално – делити под истим условима.** Дозвољаваате умножавање, дистрибуцију и јавно саопштавање дела, и прераде, ако се наведе име аутора на начин одређен од стране аутора или даваоца лиценце и ако се прерада дистрибуира под истом или сличном лиценцом. Ова лиценца не дозвољава комерцијалну употребу дела и прерада.
5. **Ауторство – без прерада.** Дозвољаваате умножавање, дистрибуцију и јавно саопштавање дела, без промена, преобликовања или употребе дела у свом делу, ако се наведе име аутора на начин одређен од стране аутора или даваоца лиценце. Ова лиценца дозвољава комерцијалну употребу дела.
6. **Ауторство – делити под истим условима.** Дозвољаваате умножавање, дистрибуцију и јавно саопштавање дела, и прераде, ако се наведе име аутора на начин одређен од стране аутора или даваоца лиценце и ако се прерада дистрибуира под истом или сличном лиценцом. Ова лиценца дозвољава комерцијалну употребу дела и прерада. Слична је софтверским лиценцама, односно лиценцама отвореног кода.